DISCLAIMER
The publication of papers in International Journal of Engineering does not imply that the editorial board, reviewers or publisher accept, approve or endorse the data and conclusions of authors.

CONTENTS

Transactions A: Basics

International Journal of Engineering

Functionalized Halloysite Nanotubes and Graphene Oxide Nanosheets Fillers Incorporated in UF Membranes for Oil/Water Separation

M. Amid, N. Nabian*, M. Delavar

Department of Chemical Engineering, University of Science and Technology of Mazandaran, Behshahr, Iran

P A P E R   I N F O

A B S T R A C T

Novel ultrafiltration mixed matrix membranes combined by dual nanofillers Graphene Oxide + Functionalized Halloysite Nanotubes (GO/FHNTs) were prepared. In this work, we improved the performance and properties of polycarbonate-based membranes for oil/water separation applications. The morphology and other properties of the fabricated membranes were characterized by different analytical method including Field Emission Scanning Electron Microscope (FESEM), Fourier-transform infrared spectroscopy (FTIR), contact angle goniometer, and mechanical strength apparatus. The obtained results confirmed that addition of GO/FHNTS had a positive effect on hydrophilicity and tensile strength. Also, the water permeation of the optimum GO0.25-FHNT0.75 membrane was about 2.5 times more than pure polycarbonate. Overall results showed that all membranes reached 100% oil separation efficiency at various ultrafiltration times. Furthermore, the optimum membrane showed a flux recovery ratio of more than 90% where the permeate fluxes of feed solutions with 100 ppm and 200 ppm olive oil concentrations were reduced to only about 5.5% and 6% after three regeneration cycles, respectively.

1. INTRODUCTION

Today, the separation of oil from water has received a lot of attention. One of the main reasons in this regard is the increasing demand for purified and clean water. Oily wastewater is the product of various industries such as steel, food industry and pharmacy. These wastewaters can also enter to open water during oil exploration and transportation [1]. Nowadays, the scarcity of clean water has become a serious problem, due to the rapid increase in population and industrial activities [2, 3]. The most common methods of purifying oily wastewater can be named as centrifugal systems, cyclones, electrostatic precipitation, and membrane filtration [4-6]. Among the various techniques, membrane filtration is a more effective and efficient one for separating oil from wastewaters, especially oil emulsions. The advantages of membrane separation are high selectivity, low maintenance cost, low required space, high efficiency, and no need for chemical additives [7-9]. Hence,

different studies have been done by researchers in which membrane separation processes were used for the decontamination of oily pollutants [10-13]. Among these applied pressure gradient membrane processes, ultrafiltration systems are of great importance owing to their lower required pressures compared to others [14, 15]. Nowadays, mixed matrix membranes (MMMs) containing organic/inorganic fillers are recommended in this regard. MMMs with more efficient separation, high mechanical strength, good processing ability and long-term stability represent the basic standards for the commercialization of industrial applications [16]. Ismail et al. [17] synthesized polyvinylidene fluoride mixed matrix membranes, including HMO nanoparticles in order to eliminate oils. The obtained results represented that the flux of membranes containing HMO nanoparticles was 10 times greater than that of pure PVDF with an oil separation efficiency of 93%. In another study, Vatanpour et al. [18] synthesized polyethersulfone (PES) based mixed matrix membranes

Corresponding Author Institutional Email: nimanabian@mazust.ac.ir (N. Nabian)

using multi-walled carbon nanotubes and titanium oxide coating and then compared them with each other. The results revealed that the hydrophilicity was increased in membranes containing multi-walled carbon nanotubes. Water permeation was also increased significantly in membranes containing carbon nanotubes with titanium oxide coating. Furthermore, Zirepour et al. [19] fabricated a mixed matrix of ultrafiltration membrane containing multi-walled carbon nanotubes. The results showed that these nanotubes had a positive effect on the permeate flux and mechanical strength of the membrane and improved membrane efficiency for the treatment of organic wastewater.

Halloysite nanotubes (HNTs) are more easily modified than other nanomaterials and possess a relatively low price. A group of researchers synthesized a series of novel PES based mixed matrix membranes by blending functionalized HNTs to improve the hydrophilicity and reusability of membranes [20-23]. A utilization of halloysite nanotubes in combination with other nanoparticles as new membrane fillers has been reported in the literature [24]. As an example, Ikhsan et al. [25] investigated the effect of halloysite nanotubes / hydrous iron oxide nanocomposites on a polymer-based composite matrix membrane at different ratios. Their obtained results confirmed that with increasing the nanocomposite up to 23.88 wt%, the contact angle of the membrane decreased from 81.9° to 50.3°. Mixed matrix membranes containing nanoparticles exhibited a water permeation of 650 $L.m^{-2}.h^{-1}$ and oil removal efficiency equal to 99.7%. As another candidate to be combined with HNTs, graphene oxide (GO) nanomaterials can improve membrane performance because of their extremely high aspect ratio, excellent hydrophilicity, their easy surface functionalization, and excellent enhancement of membrane properties [26]. Therefore, GO-based membranes incorporated with halloysite nanotubes were prepared for the improvement of membrane separation processes [27]. The results obtained by Zhu et al. [28] demonstrated that by the addition of halloysite nanotubes to polyethersulfone membrane containing GO nanoparticles, the permeate flux was increased from 288.6 $L.m^{-2}.h^{-1}$ to 716 $L.m^{-2}.h^{-1}$. In addition, some groups of researchers developed a new strategy to improve the performance of HNT/GO membranes through functionalization of halloysite nanotubes via modifiers in order to avoid the accumulation of nanotubes in polymeric solutions [29]. Poly(4-vinylpyridine) (P4VP) was used as a modifier by Zhang et al. [30] to produce a functionalized halloysite nanotubes incorporated in polyethersulfone (PES) based membranes. Zhan et al. [31] fabricated polyarylene ether nitrile (PEN) MMMs for oil removal applications by adding different loadings of polydopamine (PDA) modified halloysite nanotubes to the membranes containing GO nanomaterials. The resulting composite

membranes showed a separation efficiency of more than 99%. In similar studies, the authors changed the ratios of PDA modified halloysite nanotubes to graphene oxide nanoparticles in the cellulose acetate membrane matrix being used in oil/water separation [32-34]. Moreover, it was described elsewhere that sodium dodecyl sulfate (SDS) could be a useful modifier enhancing the dispersion of halloysite nanotubes [1, 2]. Based on the findings reported in the literature, it is not presented anywhere that how the oil/water separation performance of the mixed matrix membranes containing both GO-HNT nanomaterials changes if SDS is used for the functionalization of halloysite nanotubes. Among diverse types of polymers being utilized for the preparation of polymeric membranes, polycarbonate (PC) is an appealing material due to its remarkable features like reasonable chemical stability, good physical toughness, and relatively low price [1, 2]. Therefore, the aim of this study is to prepare polycarbonate based mixed matrix membranes comprising both graphene oxide nanosheets (GO) and sodium dodecyl sulfate functionalized HNTs (FHNT) with three various GO/FHNT ratios. The effects of the simultaneous presence of these hydrophilic nanomaterials on the membrane properties like porosity, mean pore size, and hydrophilicity as well as its performance such as permeability, oil rejection and flux recovery ratio were investigated.

2. MATERIALS AND METHODS

Commercial graphene oxide nanosheets, acetone, polyvinyl pyrrolidone (PVP), N-methyl-2-pyrrolidone (NMP), halloysite nanotubes (HNTs), polycarbonate (grade: 0710), sodium dodecyl sulfate (SDS) and Olive oil was used in this study that introduced mentioned materials in our previous work [35].

2. 1. Preparation of Membranes   In this study, four membranes including a pure polycarbonate membrane and three mixed matrix membranes intercalated by both nanomaterials of commercial graphene oxide nanosheets and the functionalized halloysite nanotubes were synthesized in different weight ratios of fillers. The synthesis of functionalized halloysite nanotubes is clearly stated in our previous work [35]. First of all, the predetermined ratios of graphene oxide nanoparticles to functionalized halloysite nanotubes are added to the solution containing NMP and PVP and the resulting mixture was placed on a stirrer at 65°C for 24 hours to completely disperse the nanoparticles into the solution. Then, predetermined amounts of polycarbonate added to the dope solution. The glycerol is then added to the solution and placed on the heater. Thus, the dope solution is prepared for the preparation of MMMs. After spreading the polymeric solution on a flat glass plane, it

was sunk in a cubic container full of water to complete the phase inversion process leading to the formation of the membrane. Later, the synthesis procedure was followed by the detaching the synthesized membrane from the glass plate, the membrane is placed in distilled water. Dope solution ingredients of all fabricated membranes is summarized in Table 1.

2. 2. Characterization Analyses

The transmission electron microscopy (TEM) is a special apparatus for determining the structure and morphology of the synthesized materials, which makes it possible to study the morphological characteristics of samples with high resolution and high magnification. In this study, TEM (Philips, Netherlands) analysis was used to identify the dispersion level as well as the morphology of the functionalized nanotubes. Furthermore, the FESEM apparatus (MIRA3TESCAN-XMU, Czech Republic) was used in this work for the characterization of the commercial HNTs, the modified ones as well as the synthesized membranes. The common feature for most polymers is that they are non-conductive and therefore they definitely need to be coated before implementing this test. In this case, FESEM can be used in low voltage and current conditions. Fourier transform infrared spectroscopy (FTIR) is commonly used to study chemical bonds. The FTIR apparatuses, namely Shimadzu (Japan) and Bomem MB-100 (Canada) were used to determine the presence of the functional groups of the prepared halloysite nanotubes and the fabricated membranes, respectively.

2. 3. Water Contact Angle

By a contact angle measurement system, the hydrophilicity properties of the samples can be investigated. The contact angle refers to the angle that a water droplet makes with a solid surface. With an increase in the wettability feature, the water contact angle decreases. In this study, in order to assess the synthesized membranes' hydrophilicity, the contact angles between water and the membranes' surfaces were obtained using the contact angle measuring instrument (Data physics OCA 15 Plus, Germany). It should be noted that the volume of one drop of water on the membrane surface is equal to 4 microliters. For each

sample, photography was done three times and their average contact angle value was reported.

2. 4. Mechanical Strength

In this study, the mechanical strength tests were done by a universal machine (H10KS, England). Three samples were tested for each membrane and the average tensile strength was reported.

2. 5. Porosity and Mean Pore Size

Porosity is considered as another remarkable index for the evaluation of membrane characteristics. To calculate this parameter, at first, the dry weights of 5 pieces of each membrane (3 cm^2) were measured. Then, these pieces of the dry membrane were soaked in distilled water for 48 h. After that, for the removal of extra water from the membrane surface, a filter paper was applied and subsequently weighing the wet membranes was repeated. Finally, the membrane porosity was calculated by Equation (1) and average of them was reported [36]:

$$\varepsilon = \frac{\frac{m_{wet}-m_{dry}}{\rho_{water}}}{\frac{m_{wet}-m_{dry}}{\rho_{water}}+\frac{m_{dry}}{\rho_{PC}}} \tag{1}$$

where m_{dry} is the weight of dry membrane and m_{wet} is the wet one (g). ρ_{PC} and ρ_{water} represent the density of polycarbonate (1.22 g/cm^3) and that of water (0.998 g/cm^3), respectively.

Also, the following equation was used for the calculation of membrane mean pore size [37]:

$$r_{average} = \sqrt{\frac{8\mu l q(2.9-1.75\varepsilon)}{\varepsilon\, A\, \Delta P}} \tag{2}$$

where μ refers to the viscosity of water at 25 ˚C in Pascal-seconds, l represents thickness of fabricated membranes in meter, q refers to water flow in cubic meters per seconds, ΔP represents the atmospheric operation pressure in Pascal, and A refers to surface area of membrane in square meters.

2. 6. Water Permeation

Water permeation (J in L.m^{-2}.h^{-1}) was calculated by Equation (3) [38]:

$$J = \frac{Q}{A\Delta t} \tag{3}$$

where Q shows the volume of collected permeate in liter, Δt refers to the duration of permeate collection in hour. Meanwhile, the pressures used to achieve the membrane water permeation were 1, 1.5, and 2 bar. It is notable that to measure the permeate flux and oil removal efficiency of synthesized membranes an ultrafiltration setup was applied. The process diagram of this setup is shown in previous work schematically [35].

2. 7. Oil Removal Efficiency

To measure the efficiency of membranes in olive oil/aqueous solution separation, at first, the membrane was used for thirty

TABLE 1. Dope solution ingredients of prepared membranes

Membrane code	PC (wt%)	NMP (wt%)	PVP (wt%)	Glycerol (wt%)	GO (wt%)	FHNT (wt%)
Pristine PC	12	82.13	5	0.87	0	0
GO0.25-FHNT0.75	12	81.13	5	0.87	0.25	0.75
GO0.5-FHNT0.5	12	81.13	5	0.87	0.5	0.5
GO0.75-FHNT0.25	12	81.13	5	0.87	0.75	0.25

minutes where the tank in the ultrafiltration set-up was filled with deionized water to minimize the effects of membrane compactness. Then, the tests continued in which an emulsion of olive oil in water flowed through the UF setup instead of water. In this test, although the concentration of feed solution varied, the other feed parameters were remained unchanged like the pressure of 1 bar and the flow rate of 1 L/min. Using Equation (4), the efficiency of membranes in the removal of olive oil (R in percent form) was estimated [39]:

$$R = \frac{C_F - C_P}{C_F} \qquad (4)$$

where C_P and C_F represent the olive oil concentration in the collected permeate and feed tank, respectively.

2. 8. Antifouling Tests   The optimum was reused to antifouling test. For this purpose, the pure water flux of membrane was measured again (J_2). After that, the flux recovery ratio (FRR) of the optimal membrane was calculated by Equation (5) [40]:

$$FRR = \frac{J_2}{J_1} \times 100 \qquad (5)$$

where J_2 and J_1 (L.m^{-2}.h^{-1}) refer to the water permeation of the membrane after and before the oil removal test, respectively.

3. RESULTS AND DISCUSSION

3. 1. Characterization of Graphene Oxide Nanomaterials and Functionalized Halloysite Nanotubes

3. 1. 1. FESEM   The FESEM images of HNTs and functionalized ones are displayed in Figures 1A and 1B, respectively. It can be confirmed that the HNTs are aggregated, while the FHNTs are in a uniform distribution of nanotubes as well as a decrease in their particle size.

3. 1. 2. TEM Analysis   Results of TEM analysis for FHNTs and GO are shown in Figures 2A, and 2B, respectively. Figure 2A represents the tubular structure of functionalized halloysite nanotubes at different magnifications. Similar findings were reported by Lun et al. [2]. In a study conducted by Cheng et al. [41] the functionalized halloysite nanotubes with sodium dodecyl sulfate showed much lower agglomeration and more uniform distribution. Moreover, based on Figure 2B, the surface roughness and amorphous structure of the graphene oxide nanomaterials can be observed [42].

3. 1. 3. FTIR Analysis of FHNTs   The FTIR spectra of functionalized halloysite nanotubes are discussed in
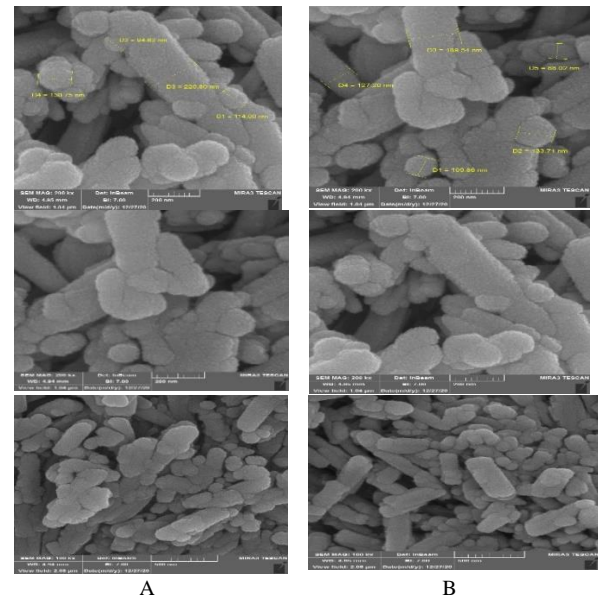
Figure 1. FESEM images of A) Commericial HNTs, B) Functionalized HNTs
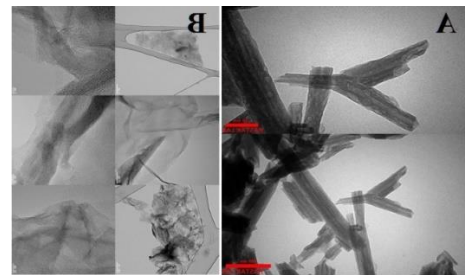
Figure 2. TEM analysis of A) Functionalized halloysite nanotubes and B) GO nanomaterials

our previous study [35]. Briefly, the five peaks confirming the presence of sodium dodecyl sulfate appeared in the FTIR image of sodium dodecyl sulfate functionalized halloysite nanotubes.

3. 2. Characterization of Synthesized Pristine PC and MMMs
3. 2. 1. Morphology of Membranes   The upside surface and cross-sectional FESEM results of the blank PC and GO0.25-FHNT0.75 mixed matrix membranes are shown in Figures 3a and 3b, respectively.

By comparing Figures 3a and 3b, it can be seen that the membrane containing nanoparticles has a more spongy structure than the pure polycarbonate membrane. This result can be attributed to the bonds between nanoparticles and the membrane matrix. Various studies have shown that created bonds can affect the mixing process [43]. The reduction in the rate of replacement between coagulant and solvent in the synthesis process of mixed matrix membranes, created membranes with a
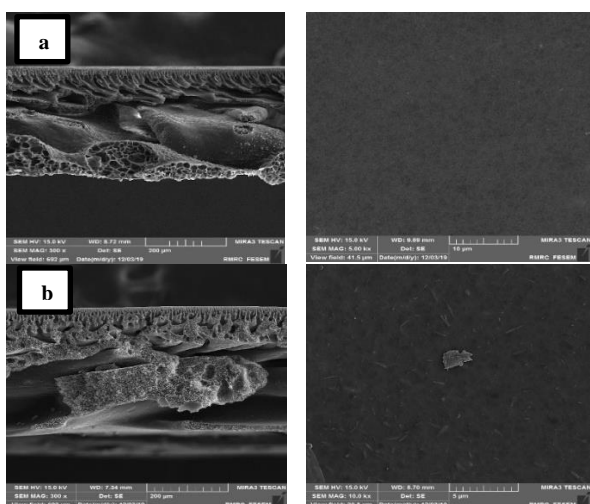
Figure 3. Cross section and top surface of a) blank PC b) GO-FHNT0.75 mixed matrix membrane

Figure 4. FTIR spectra of blank PC and mixed matrix membranes

more spongy structure than blank membrane [44]. Also, by addition of functionalized HNTs and GO nanomaterials results in the formation of the larger macro-pores in the sub-layer of the membrane, which can be due to the fact that the functionalized HNTs and GO nanomaterials are naturally hydrophilic [45-47]. Furthermore, the top layer of the blank PC has a uniform and smooth surface. But, referring to the upside surface image of GO0.25-FHNT0.75 mixed matrix membrane, GO nanosheets in the center of the picture as well as uniformly distributed nanotubes (FHNTs) can be seen, which verifies the presence of both nanomaterials.

3. 2. 2. Functional Groups   The results of FTIR analysis is presented in Figure 4. The functional groups of blank PC and mixed matrix membranes containing GO and FHNTs were in detail discussed in our previous work [35, 47]. In brief, the peaks at 1081 cm^{-1}, 1260 cm^{-1}, 1365 cm^{-1}, 1466 cm^{-1}, 1505 cm^{-1}, 1772 cm^{-1}, and 2854 cm^{-1} correspond to the vibrations of chemical bonds in the blank polycarbonate membrane. The peak appeared at 3465 cm^{-1} is related to adsorbed water. Furthermore, the peaks at 1241 cm^{-1}, 1466 cm^{-1}, and 2922 cm^{-1} are attributed to the presence of functionalized HNTs in the membrane matrix. The bond between SDS-HNTs and PC polymeric material can be assigned to the hydrogen bond between the surface hydroxyl group of the HNTs and the carbonyl group of polycarbonate as well as the hydrophobic-hydrophobic interaction between the alkyl chain of SDS molecules and the benzene ring present in the polycarbonate matrix. The peaks appeared at 1037 cm^{-1}, 1056 cm^{-1}, 1380 cm^{-1}, 1631 cm^{-1}, and 1729 cm^{-1}, and 3433 cm^{-1} are assigned to different functional groups of GO nanosheets.

3. 2. 3. Mechanical Strength   The results of mechanical strength of prepared membranes are shown
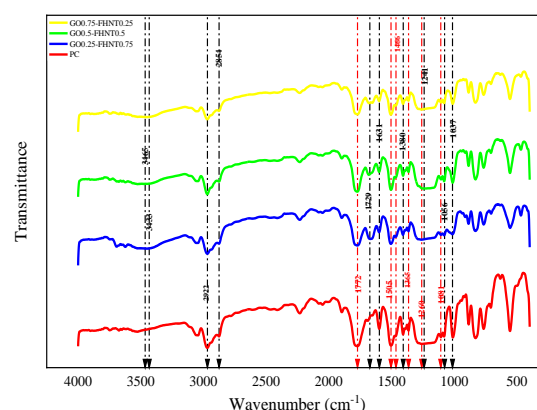
in Figure 5. It can be confirmed that addition of nanomaterials, increased the tensile strength and Young's modulus and elongation increased. It can be related to the presence of epoxide functional groups in GO nanomaterials [48]. On the other hand, when the GO loading increased to 0.75 wt%, these mechanical parameters exhibited a decreasing trend. It can be related to the agglomeration of nanosheets in the polymeric solution. In similar studies, the same results were reported [49-50]. Moreover, although GO0.75-FHNT0.25 possessed a GO loading of more than 0.5 wt% after which the mechanical parameters decreased, it still exhibited tensile strength and elongation values greater than those of GO0.25-FHNT0.75 MMM. It can be attributed to the better dispersion of functionalized halloysite nanotubes and a stronger bond between functionalized halloysite nanotubes and polymeric matrix [51].

3. 2. 4. Hydrophilicity   Figure 6 shows the contact angle of synthesized membranes. The obtained results confirm that adding GO nanomaterials and FHNTs
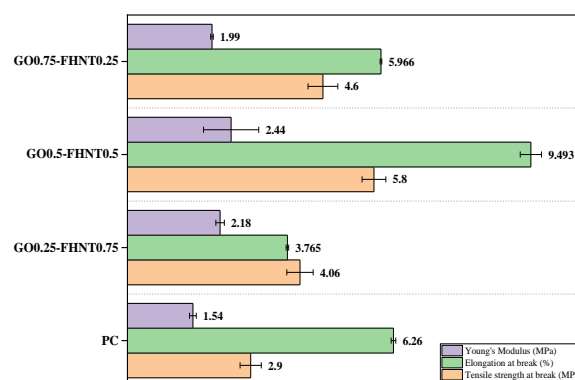
Figure 5. Mechanical strength of mixed matrix membranes
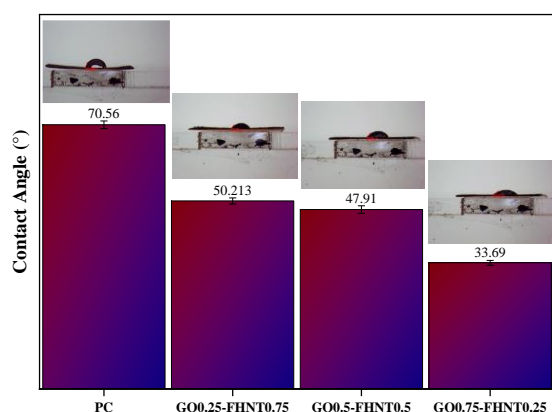
Figure 6. Water contact angle of synthesized membrane

enhanced the hydrophilicity of mixed matrix membranes in comparison with that of blank PC membrane. It can be attributed to the hydrophilic groups attached on GO and FHNTs. Also, SDS as amphiphilic material, could produce a large amount of hydrophilic cavity and functional groups of functionalized halloysite nanotubes [52].

3. 2. 5. Porosity and Mean Pore Size   The porosity and mean pore size of synthesized membranes are presented in Figure 7. As shown in Figure 7, the porosity quantities of mixed matrix membranes were bigger than that value achieved for the pure polycarbonate membrane. Also, by increasing the loadings of GO nanomaterials, porosity values reduced. In can be due to a rise in the viscosity of the polymeric solution, as a result of a reduction in the substitution rate of coagulant and solvent in the phase inversion procedure [53, 54]. In addition, because of the tubular structure of halloysite nanotubes, they make the membranes porous after being dispersed in the dope solution [35, 55].
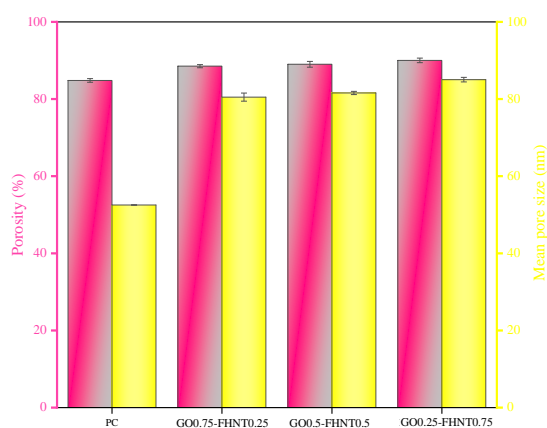
The overall results of membranes mean pore size confirmed that mean pore sizes of mixed matrix membranes were more than that of the pure membrane. But, an enhancement in the loading of GO nanomaterials shows a negative effect on the mean pore size because of strong hydrogen bonds between GO nanosheets and the polymeric solution [42].

3. 2. 6. Ultrafiltration Experiments   For the investigation of the performance of synthesized membranes, some tests were carried out using the ultrafiltration setup such as water permeation, oil separation, and membrane regeneration that will be described in the following sections.

3. 2. 6. 1. Water Permeation   Regarding the obtained results of water permeation displayed in Figure 8, the water permeation of mixed matrix membranes improved around 3 times in comparison to blank PC. It can be due to the hydrophilic nature of these added nanomaterials. In addition, the enhancement in the water permeation of GO0.25-FHNT0.75 compared with GO0.75-FHNT0.25 from 1237.5 $L.m^{-2}.h^{-1}$ to 1025 $L.m^{-2}.h^{-1}$ can be attributed to the greater hydrophilicity of halloysite nanotubes and its hollow tubular structure that offers a wide range of channels for water permeation [55-57] as well as the agglomeration of GO nanomaterials [58-60]. Based on these obtained data of water permeation as well as porosity and water contact angle values, GO0.25-FHNT0.75 mixed matrix membrane selected as the optimal membrane.

3. 2. 6. 2. Oil Separation of Selected Membranes The effect of feed concentration on the separation efficiency of olive oil by the optimal membrane in ultrafiltration tests at 1 bar and ambient temperature was investigated and the results are shown in Figures 9. For this purpose, the feed solution was prepared in 100-200

Figure 7. Porosity and mean pore size of membranes
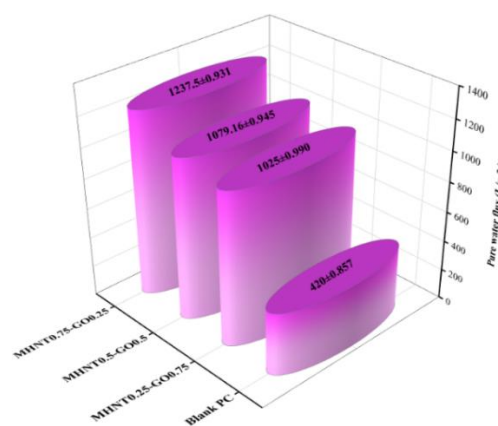
Figure 8. Water permeation of blank PC and mixed matrix membranes

ppm oil concentrations, and subsequently the selected membrane was examined for the efficiency of olive oil separation using the as-prepared feed solution.

To interpret the results displayed in Figure 9, this point is noteworthy that as the UF process begins, the presence of quite open membrane pores allows some oil particles to come out from the other side of the membrane. Over time, some pores become blocked with oil particles, and as a result, oil separation efficiency

increases up to 100%. But, the times to reach this separation efficiency decreased from 225 min for the blank PC to 165 minutes for the GO0.25-FHNT0.75 membrane at 100 ppm feed concentration. Also, with increasing the concentration of the feed solution, the time to achieve 100% separation increased. In addition, for the investigation of membrane fouling, the curves of permeate flux versus time are plotted in Figures 9A, 9B and 9C for each feed concentration. In detail, the blank PC membrane possessed the lower permeate flux compared with the optimal GO0.25-FHNT0.75 MMM.

3. 2. 6. 3. Reusability of Optimal Membrane
After ultrafiltration experiments, the optimal membrane was used in reusability test and the results were plotted in Figure 10. In other words, GO0.25-FHNT0.75 mixed matrix membrane was evaluated in terms of regeneration. In this case, the used membrane was washed after oil separation ultrafiltration tests by acetone solution (20% v/v). After that, the water permeation of washed membrane was measured again. This method was repeated for three times. Finally, the flux recovery ratio was calculated by Equation (5). The obtained results showed that with increasing feed concentration, the FRR decreased [35, 47]. It can be due to the blockage of some pores and not complete cleaning of membrane pores by acetone solution. Furthermore, the permeate fluxes of feed solutions with 100 ppm and 200 ppm olive oil concentrations were reduced only about 5.5% and 6% after three cycles, respectively [61].

Figure 9. Permeate flux and separation efficiency of blank PC and the optimal mixed matrix membrane at A) 100 ppm, B) 150 ppm, C) 200 ppm, 1 bar and 25°C
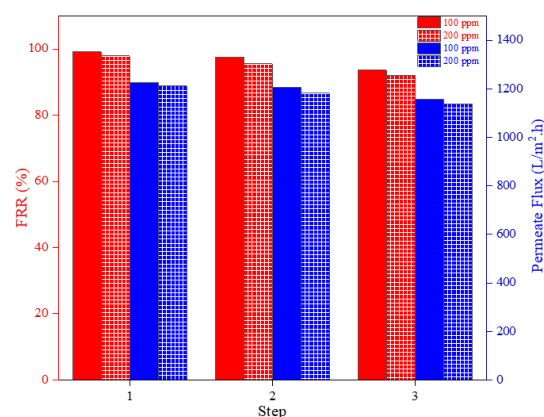
Figure 10. FRR results of GO0.25-FHNT0.75 mixed matrix membrane

4. CONCLUSION

In this work, polycarbonate membranes were synthesized in which the functionalized HNTs and GO nanomaterials were added in the dope solution of the membrane simultaneously. According to the FESEM images, the mixed matrix membrane showed a more spongy structure

compared to the blank PC membrane. In addition, the water permeation results showed that the best wettability was related to GO0.25-FHNT0.75 mixed matrix membrane.

Also, water contact angle of FHNT/GO membrane compared to blank PC membrane decreased from 70.56° to 33.69°. As a result, water permeation of FHNT/GO mixed matrix membrane increased by 2.9 times compared to blank PC membrane.

The overall results of mean pore size of membranes confirmed that the mean pore size of FHNT/GO mixed matrix membranes increased about 1.5 times compared to blank PC membrane.

The pure polycarbonate membrane and the optimum GO0.25-FHNT0.75 mixed matrix membrane were used for ultrafiltration experiments of olive oil removal from water. The UF results confirmed that synthesized membranes had a desirable ability for olive oil removal up to 100% separation efficiency. Finally, the reusability of GO0.25-FHNT0.75 membrane was checked and the obtained data confirmed that the mentioned membrane was well regenerated with a flux recovery ratio of more than 93% after three cycles.

5. REFERENCES

1. Cheng, Z.-L., Chang, X.-Y., Liu, Z. and Qin, D.-Z., "Surface-modified halloysite nanotubes as fillers applied in reinforcing the performance of polytetrafluoroethylenezhi-lin cheng et al. Surface-modified hnts applied in ptfe", *Clay Minerals*, Vol. 53, No. 4, (2018), 643-656. https://doi.org/10.1180/clm.2018.48

2. Lun, H., Ouyang, J. and Yang, H., "Enhancing dispersion of halloysite nanotubes via chemical modification", *Physics and Chemistry of Minerals*, Vol. 41, No. 4, (2014), 281-288. https://doi.org/10.1007/s00269-013-0646-9

3. Moghadassi, A., Hamidi, A., Hosseini, S. and Bagheripour, E., "Fabrication and characterization of novel mixed matrix polyethersulfone based nanofiltration membrane modified by ilmenite", *International Journal of Engineering, Transactions A: Basics*, Vol. 30, No. 1, (2017), 7-14. doi: 10.5829/idosi.ije.2017.30.01a.02

4. Gude, V.G., "Desalination and sustainability–an appraisal and current perspective", *Water Research*, Vol. 89, (2016), 87-106. https://doi.org/10.1016/j.watres.2015.11.012

5. Obotey Ezugbe, E. and Rathilal, S., "Membrane technologies in wastewater treatment: A review", *Membranes*, Vol. 10, No. 5, (2020), 89. **https://doi.org/10.3390/membranes10050089**

6. Abadi, S.R.H., Sebzari, M.R., Hemati, M., Rekabdar, F. and Mohammadi, T., "Ceramic membrane performance in microfiltration of oily wastewater", *Desalination*, Vol. 265, No. 1-3, (2011), 222-228. https://doi.org/10.1016/j.desal.2010.07.055

7. Akhair, S., Harun, Z., Basri, H., Ahmad, R., Rashid, A. and Azhar, F.H., "Hydrophobicity properties of graphite and reduced graphene oxide of the polysulfone (PSF) mixed matrix membrane", *International Journal of Engineering, Transactions B: Applications*, Vol. 31, No. 8, (2018), 1381-1388. doi: 10.5829/ije.2018.31.08b.29

8. Gholami, F., Zinadini, S., Zinatizadeh, A., Noori, E. and Rafiee, E., "Preparation and characterization of an antifouling polyethersulfone nanofiltration membrane blended with graphene oxide/ag nanoparticles", *International Journal of Engineering, Transactions A: Basics*, Vol. 30, No. 10, (2017), 1425-1433. doi: 10.5829/ije.2017.30.10a.02

9. Delavar, M., Bakeri, G. and Hosseini, M., "Fabrication of polycarbonate mixed matrix membranes containing hydrous manganese oxide and alumina nanoparticles for heavy metal decontamination: Characterization and comparative study", *Chemical Engineering Research and Design*, Vol. 120, (2017), 240-253. https://doi.org/10.1016/j.cherd.2017.02.029

10. Lively, R.P. and Sholl, D.S., "From water to organics in membrane separations", *Nature Materials*, Vol. 16, No. 3, (2017), 276-279. https://doi.org/10.1038/nmat4860

11. Bagheri, M., Sangpour, P., Badiei, E. and Pazouki, M., "Graphene oxide antibacterial sheets: Synthesis and characterization (research note)", *International Journal of Engineering, Transactions C: Aspects*, Vol. 27, No. 12, (2014), 1803-1808. doi: 10.5829/idosi.ije.2014.27.12c.01

12. Cai, Y., Chen, D., Li, N., Xu, Q., Li, H., He, J. and Lu, J., "Nanofibrous metal–organic framework composite membrane for selective efficient oil/water emulsion separation", *Journal of Membrane Science*, Vol. 543, (2017), 10-17. https://doi.org/10.1016/j.memsci.2017.08.047

13. Chen, W., Su, Y., Zheng, L., Wang, L. and Jiang, Z., "The improved oil/water separation performance of cellulose acetate-graft-polyacrylonitrile membranes", *Journal of Membrane Science*, Vol. 337, No. 1-2, (2009), 98-105. https://doi.org/10.1016/j.memsci.2009.03.029

14. Zinadini, S., Moradi, M., and Zinatizadeh, A. A. L. "Influence of operating variables on performance of nanofiltration membrane for dye removal from synthetic wastewater using response surface methodology" *International Journal of Engineering, Transactions C: Aspects*, Vol. 29, No. 12, (2016), 1650-1658. doi: 10.5829/idosi.ije.2016.29.12c.03

15. Mohammadipour, E., Nabian, N. and Delavar, M., "Novel pvc-melamine mixed matrix membranes for the sirius red removal from aqueous solutions: Experimental study and rsm modeling", *Journal of Water Process Engineering*, Vol. 47, (2022), 102752. https://doi.org/10.1016/j.jwpe.2022.102752

16. Li, Y.S., Yan, L., Xiang, C.B. and Hong, L.J., "Treatment of oily wastewater by organic–inorganic composite tubular ultrafiltration (UF) membranes", *Desalination*, Vol. 196, No. 1-3, (2006), https://doi.org/10.1016/j.desal.2005.11.021

17. Ismail, N., Salleh, W., Awang, N., Ahmad, S., Rosman, N., Sazali, N. and Ismail, A., "Pvdf/hmo ultrafiltration membrane for efficient oil/water separation", *Chemical Engineering Communications*, Vol. 208, No. 4, (2021), 463-473. https://doi.org/10.1080/00986445.2019.1650035

18. Vatanpour, V., Madaeni, S.S., Moradian, R., Zinadini, S. and Astinchap, B., "Novel antibifouling nanofiltration polyethersulfone membrane fabricated from embedding tio2 coated multiwalled carbon nanotubes", *Separation and Purification Technology*, Vol. 90, (2012), 69-82. https://doi.org/10.1016/j.seppur.2012.02.014

19. Zirehpour, A., Rahimpour, A., Jahanshahi, M. and Peyravi, M., "Mixed matrix membrane application for olive oil wastewater treatment: Process optimization based on taguchi design method", *Journal of Environmental Management*, Vol. 132, (2014), 113-120. https://doi.org/10.1016/j.jenvman.2013.10.028

20. Lannelongue, G., Gonzalez-Benito, J. and Quiroz, I., "Environmental management and labour productivity: The moderating role of capital intensity", *Journal of Environmental Management*, Vol. 190, (2017), 158-169. https://doi.org/10.1016/j.jenvman.2016.11.051

21. Yu, L., Zhang, Y., Zhang, H. and Liu, J., "Development of a molecular separation membrane for efficient separation of low-molecular-weight organics and salts", *Desalination*, Vol. 359, (2015), 176-185. https://doi.org/10.1016/j.desal.2014.12.044

22. Wei, A., Liu, B., Zhao, H., Chen, Y., Wang, W., Ma, Y., Yang, H. and Liu, S., "Synthesis and formation mechanism of flowerlike architectures assembled from ultrathin nio nanoflakes and their adsorption to malachite green and acid red in water", *Chemical Engineering Journal*, Vol. 239, (2014), 141-148. https://doi.org/10.1016/j.cej.2013.10.079

23. Costa, E.P., Roccamante, M., Amorim, C.C., Oller, I., Pérez, J.A.S. and Malato, S., "New trend on open solar photoreactors to treat micropollutants by photo-fenton at circumneutral ph: Increasing optical pathway", *Chemical Engineering Journal*, Vol. 385, (2020), 123982. https://doi.org/10.1016/j.cej.2019.123982

24. Zhu, L., Wang, H., Bai, J., Liu, J. and Zhang, Y., "A porous graphene composite membrane intercalated by halloysite nanotubes for efficient dye desalination", *Desalination*, Vol. 420, (2017), 145-157. https://doi.org/10.1016/j.desal.2017.07.008

25. Ikhsan, S.N.W., Yusof, N., Aziz, F., Misdan, N., Ismail, A.F., Lau, W.-J., Jaafar, J., Salleh, W.N.W. and Hairom, N.H.H., "Efficient separation of oily wastewater using polyethersulfone mixed matrix membrane incorporated with halloysite nanotube-hydrous ferric oxide nanoparticle", *Separation and Purification Technology*, Vol. 199, (2018), 161-169. https://doi.org/10.1016/j.seppur.2018.01.028

26. Yang, L., Tang, B. and Wu, P., "Uf membrane with highly improved flux by hydrophilic network between graphene oxide and brominated poly (2, 6-dimethyl-1, 4-phenylene oxide)", *Journal of Materials Chemistry A*, Vol. 2, No. 43, (2014), 18562-18573. https://doi.org/10.1039/C4TA03790A

27. Lim, S., Park, M.J., Phuntsho, S., Mai-Prochnow, A., Murphy, A.B., Seo, D. and Shon, H., "Dual-layered nanocomposite membrane incorporating graphene oxide and halloysite nanotube for high osmotic power density and fouling resistance", *Journal of Membrane Science*, Vol. 564, (2018), 382-393. https://doi.org/10.1016/j.memsci.2018.06.055

28. Zhu, Y., Chen, P., Nie, W. and Zhou, Y., "Greatly improved oil-in-water emulsion separation properties of graphene oxide membrane upon compositing with halloysite nanotubes", *Water, Air, & Soil Pollution*, Vol. 229, No. 3, (2018), 1-9. https://doi.org/10.1007/s11270-018-3757-6

29. Zeng, G., He, Y., Ye, Z., Yang, X., Chen, X., Ma, J. and Li, F., "Novel halloysite nanotubes intercalated graphene oxide based composite membranes for multifunctional applications: Oil/water separation and dyes removal", *Industrial & Engineering Chemistry Research*, Vol. 56, No. 37, (2017), 10472-10481. https://doi.org/10.1021/acs.iecr.7b02723

30. Zhang, J., Zhang, Y., Chen, Y., Du, L., Zhang, B., Zhang, H., Liu, J. and Wang, K., "Preparation and characterization of novel polyethersulfone hybrid ultrafiltration membranes bending with modified halloysite nanotubes loaded with silver nanoparticles", *Industrial & Engineering Chemistry Research*, Vol. 51, No. 7, (2012), 3081-3090. https://doi.org/10.1021/ie202473u

31. Zhan, Y., He, S., Wan, X., Zhao, S. and Bai, Y., "Thermally and chemically stable poly (arylene ether nitrile)/halloysite nanotubes intercalated graphene oxide nanofibrous composite membranes for highly efficient oil/water emulsion separation in harsh environment", *Journal of Membrane Science*, Vol. 567, (2018), 76-88. https://doi.org/10.1016/j.memsci.2018.09.037

32. Li, F., Yu, Z., Shi, H., Yang, Q., Chen, Q., Pan, Y., Zeng, G. and Yan, L., "A mussel-inspired method to fabricate reduced graphene oxide/g-c3n4 composites membranes for catalytic decomposition and oil-in-water emulsion separation", *Chemical Engineering Journal*, Vol. 322, (2017), 33-45. https://doi.org/10.1016/j.cej.2017.03.145

33. Di Luccio, M., Nobrega, R. and Borges, C.P., "Microporous anisotropic phase inversion membranes from bisphenol a polycarbonate: Effect of additives to the polymer solution", *Journal of Applied Polymer Science*, Vol. 86, No. 12, (2002), 3085-3096. https://doi.org/10.1002/app.11338

34. Feng, J., Hao, J., Du, J. and Yang, R., "Using tga/ftir tga/ms and cone calorimetry to understand thermal degradation and flame retardancy mechanism of polycarbonate filled with solid bisphenol a bis (diphenyl phosphate) and montmorillonite", *Polymer Degradation and Stability*, Vol. 97, No. 4, (2012), 605-614. https://doi.org/10.1016/j.polymdegradstab.2012.01.011

35. Amid, M., Nabian, N. and Delavar, M., "Fabrication of polycarbonate ultrafiltration mixed matrix membranes including modified halloysite nanotubes and graphene oxide nanosheets for olive oil/water emulsion separation", *Separation and Purification Technology*, Vol. 251, (2020), 117332. https://doi.org/10.1016/j.seppur.2020.117332

36. Delavar, M., Bakeri, G., Hosseini, M. and Nabian, N., "Fabrication and characterization of polyvinyl chloride mixed matrix membranes containing high aspect ratio anatase titania and hydrous manganese oxide nanoparticle for efficient removal of heavy metal ions: Competitive removal study", *The Canadian Journal of Chemical Engineering*, Vol. 98, No. 7, (2020), 1558-1579. https://doi.org/10.1002/cjce.23725

37. Yuliwati, E., Ismail, A., Matsuura, T., Kassim, M. and Abdullah, M., "Effect of modified pvdf hollow fiber submerged ultrafiltration membrane for refinery wastewater treatment", *Desalination*, Vol. 283, (2011), 214-220. https://doi.org/10.1016/j.desal.2011.03.049

38. Yuan, X., Li, W., Zhu, Z., Han, N. and Zhang, X., "Thermo-responsive pvdf/psma composite membranes with micro/nanoscale hierarchical structures for oil/water emulsion separation", *Colloids and Surfaces A: Physicochemical and Engineering Aspects*, Vol. 516, (2017), 305-316. https://doi.org/10.1016/j.colsurfa.2016.12.047

39. Saadati, J. and Pakizeh, M., "Separation of oil/water emulsion using a new psf/pebax/f-mwcnt nanocomposite membrane", *Journal of the Taiwan Institute of Chemical Engineers*, Vol. 71, (2017), 265-276. https://doi.org/10.1016/j.jtice.2016.12.024

40. Safarpour, M., Khataee, A. and Vatanpour, V., "Preparation of a novel polyvinylidene fluoride (PVDF) ultrafiltration membrane modified with reduced graphene oxide/titanium dioxide (tio2) nanocomposite with enhanced hydrophilicity and antifouling properties", *Industrial & Engineering Chemistry Research*, Vol. 53, No. 34, (2014), 13370-13382. https://doi.org/10.1021/ie502407g

41. Cheng, Z.-L., Chang, X.-Y. and Liu, Z., "Surface modification of halloysite nanotubes grafted by dodecylamine and their application in reinforcing polytetrafluoroethylene", *Clay Minerals*, Vol. 54, No. 2, (2019), 219-225. https://doi.org/10.1180/clm.2019.29

42. Nasirizadeh, N., Ghaani, M., Shekari, Z. and Shateri-Khalilabad, M., "Novel non enzymatic tbhq modified electrochemical sensor for hydrogen peroxide determination in different beverage samples", *Journal of the Brazilian Chemical Society*, Vol. 27, (2016), 1577-1586. https://doi.org/10.5935/0103-5053.20160037

43. Chang, X., Wang, Z., Quan, S., Xu, Y., Jiang, Z. and Shao, L., "Exploring the synergetic effects of graphene oxide (go) and polyvinylpyrrodione (PVP) on poly (vinylylidenefluoride)(pvdf) ultrafiltration membrane performance", *Applied Surface Science*, Vol. 316, (2014), 537-548. https://doi.org/10.1016/j.apsusc.2014.07.202

44. Zinadini, S., Zinatizadeh, A.A., Rahimi, M., Vatanpour, V. and Zangeneh, H., "Preparation of a novel antifouling mixed matrix pes membrane by embedding graphene oxide nanoplates", *Journal of Membrane Science*, Vol. 453, (2014), 292-301. https://doi.org/10.1016/j.memsci.2013.10.070

45. Narasimha Rao, C., Subbarayudu, K., Vijaya, Y. and Venkata Subbaiah, M., "Adsorption of ni (ii) from aqueous solution by

activated carbons derived from tobacco stem", *Desalination and Water Treatment*, Vol. 54, No. 12, (2015), 3392-3399. https://doi.org/10.1080/19443994.2014.910837

46. Wang, Z., Yu, H., Xia, J., Zhang, F., Li, F., Xia, Y. and Li, Y., "Novel go-blended pvdf ultrafiltration membranes", *Desalination*, Vol. 299, (2012), 50-54. https://doi.org/10.1016/j.desal.2012.05.015

47. Amid, M., Nabian, N. and Delavar, M., "Performance evaluation and modeling study of pc blended membranes incorporated with sds-modified and unmodified halloysite nanotubes in the separation of oil from water", *Journal of Environmental Chemical Engineering*, Vol. 9, No. 4, (2021), 105237. https://doi.org/10.1016/j.jece.2021.105237

48. Nasir, M.. "Graphene Based Membrane Modified Silica Nanoparticles (GO/SiO$_2$-Psf) for Seawater Desalination and Wastewater Treatment: Salt Rejection and Dyes" *International Journal of Engineering, Transactions A: Basics*, Vol. 36, No. 4, (2023), 698-708, doi: 10.5829/ije.2023.36.04a.09

49. Qi, B., Lu, S., Xiao, X., Pan, L., Tan, F. and Yu, J., "Enhanced thermal and mechanical properties of epoxy composites by mixing thermotropic liquid crystalline epoxy grafted graphene oxide", *Express Polymer Letters*, Vol. 8, No. 7, (2014). DOI: 10.3144/expresspolymlett.2014.51

50. Shen, X.-J., Liu, Y., Xiao, H.-M., Feng, Q.-P., Yu, Z.-Z. and Fu, S.-Y., "The reinforcing effect of graphene nanosheets on the cryogenic mechanical properties of epoxy resins", *Composites Science and Technology*, Vol. 72, No. 13, (2012), 1581-1587. https://doi.org/10.1016/j.compscitech.2012.06.021

51. Foorginejad, A., Taheri, M., & Mollayi, N.. "A non-destructive ultrasonic testing approach for measurement and modelling of tensile strength in rubbers", *International Journal of Engineering, Transactions C: Aspects*, Vol. 33, No. 12, (2020), 2549-2555. doi: 10.5829/ije.2020.33.12c.16

52. Saif, M.J., Asif, H.M. and Naveed, M., "Properties and modification methods of halloysite nanotubes: A state-of-the-art review", *Journal of the Chilean Chemical Society*, Vol. 63, No. 3, (2018), 4109-4125. http://dx.doi.org/10.4067/s0717-97072018000304109

53. Gianni, E., Avgoustakis, K., Pšenička, M., Pospíšil, M. and Papoulis, D., "Halloysite nanotubes as carriers for irinotecan: Synthesis and characterization by experimental and molecular simulation methods", *Journal of Drug Delivery Science and Technology*, Vol. 52, (2019), 568-576. https://doi.org/10.1016/j.jddst.2019.05.001

54. Han, M.-J. and Nam, S.-T., "Thermodynamic and rheological variation in polysulfone solution by pvp and its effect in the preparation of phase inversion membrane", *Journal of Membrane Science*, Vol. 202, No. 1-2, (2002), 55-61. https://doi.org/10.1016/S0376-7388(01)00718-9

55. Liang, W., Ge, X., Ge, J., Li, T., Zhao, T., Chen, X., Song, Y., Cui, Y., Khan, M. and Ji, J., "Reduced graphene oxide embedded with mq silicone resin nano-aggregates for silicone rubber composites with enhanced thermal conductivity and mechanical performance", *Polymers*, Vol. 10, No. 11, (2018), 1254. https://doi.org/10.3390/polym10111254

56. Ng, E.-P., Subari, S.N.M., Marie, O., Mukti, R.R. and Juan, J.-C., "Sulfonic acid functionalized mcm-41 as solid acid catalyst for tert-butylation of hydroquinone enhanced by microwave heating", *Applied Catalysis A: General*, Vol. 450, (2013), 34-41. https://doi.org/10.1016/j.apcata.2012.09.055

57. Farokhi, B., Rezaei, M., Kiamehr, Z. and Hosseini, S., "A new approach to provide high water permeable polyethersulfone based nanofiltration membrane by air plasma treatment", *International Journal of Engineering, Transactions C: Aspects*, Vol. 32, No. 3, (2019), 354-359. doi: 10.5829/ije.2019.32.03c.01

58. Yuan, P., Southon, P.D., Liu, Z., Green, M.E., Hook, J.M., Antill, S.J. and Kepert, C.J., "Functionalization of halloysite clay nanotubes by grafting with γ-aminopropyltriethoxysilane", *The Journal of Physical Chemistry C*, Vol. 112, No. 40, (2008), 15742-15751. https://doi.org/10.1021/jp805657t

59. Taleghani, H.G., Ghoreyshi, A.A. and Najafpour, G., "Lactic acid production with in situ extraction in membrane bioreactor", *Applied Food Biotechnology*, Vol. 4, No. 1, (2017), 27-34. https://doi.org/10.22037/afb.v4i1.13686

60. Taleghani, H.G., Ghoreyshi, A.A. and Najafpour, G.D., "Thin film composite nanofiltration membrane for lactic acid production in membrane bioreactor", *Biochemical Engineering Journal*, Vol. 132, (2018), 152-160. https://doi.org/10.1016/j.bej.2018.01.020

61. Abdollahzadeh Sharghi, E., Shorgashti, A. and Bonakdarpour, B., "The study of organic removal efficiency and membrane fouling in a submerged membrane bioreactor treating vegetable oil wastewater", *International Journal of Engineering, Transactions C: Aspects*, Vol. 29, No. 12, (2016), 1642-1649. doi: 10.5829/idosi.ije.2016.29.12c.02

Persian Abstract

چکیده

در این مطالعه، به منظور بهبود عملکرد غشاهای پلی یکربناتی برای تصفیه پساب‌های روغنی، غشاهای ماتریس مخلوط اولترافیلتراسیون جدید توسط نانوپرکننده اکسید گرافن و نانولوله های هالویسیت عامل دار شده، سنتز شدند. مورفولوژی و سایر خواص غشاهای ساخته شده توسط میکروسکوپ الکترونی روبشی انتشار میدانی، طیف‌سنج FTIR، زاویه تماس و دستگاه مقاومت مکانیکی مشخصه یابی شدند. نتایج بدست‌آمده تأیید کرده است که افزودن GO/FHNTs تأثیر مثبتی بر آب‌دوستی و استحکام کششی دارد. همچنین فلاکس اب خالص غشای بهینه GO0.25-FHNT0.75 حدود ۲.۵ برابر بیشتر از پلی کربنات خالص بود. نتایج کلی نشان داده است که همه غشاها در زمان‌های مختلف فرآیند اولترافیلتراسیون، به بازده ۱۰۰ درصد جداسازی روغن از آب رسیدند. علاوه بر این، غشای بهینه نسبت بازیابی شار بیش از ۹۰ درصد را نشان داد است. در عملیات بازیابی غشا، شار نفوذی محلول‌های خوراک با غلظت‌های ppm ۱۰۰و ppm۲۰۰ روغن زیتون به ترتیب تنها حدود ۵/۵ درصد و ۶ درصد پس از سه چرخه بازسازی کاهش یافته است.

International Journal of Engineering

Enhancing Seismic Design of Non-structural Components Implementing Artificial Intelligence Approach: Predicting Component Dynamic Amplification Factors

B. D. Bhavani[a], S. P. Challagulla[a], E. Noroozinejad Farsangi*[b], I. Hossain[c], M. Manne[d]

[a] Department of Civil Engineering, Koneru Lakshmaiah Education Foundation, Vaddeswaram, Guntur, India
[b] Faculty of Civil and Surveying Engineering, Graduate University of Advanced Technology, Kerman, Iran
[c] School of Natural Sciences and Mathematics, Ural Federal University, Yekaterinburg, Russia
[d] Department of Civil Engineering, Birla Institute of Technology and Science -Pilani, Hyderabad Campus, Telangana, India

A B S T R A C T

The seismic performance of non-structural components (NSCs) has been the focus of intensive study during the last few decades. Modern building codes define design forces on components using too simple relationships. The component accelerates faster than the floor acceleration to which it is connected. Therefore, component dynamic amplification factors (CDAFs) are calculated in this work to quantify the amplification in the acceleration of NSCs for the various damping ratios and tuning ratios of the NSC, and the primary structural periods. From the analysis results, it was observed that CDAF peaks are either underestimated or overestimated by the code-based formulae. A prediction model to ascertain the CDAFs was also developed using artificial neural networks (ANNs). Following that, the suggested model is contrasted with the established relationships from the past research. The ANN model's coefficient of correlation (R) was 0.97. Hence, using an ANN algorithm reduces the necessity of laborious and complex analysis.

doi: 10.5829/ije.2023.36.07a.02

1. INTRODUCTION

Non-structural components (NSCs) cannot withstand loads [1]. Non-structural components damage may cause both immediate and long-term financial losses. The damage of components, especially expensive and important equipment in important structures may impair the functionality of buildings [2-5]. These results show that NSC seismic performances are just as significant as structural component seismic performances. The current Standards and Guidelines were mostly produced using empirical methodologies built from earlier experiences and engineering skills [6]. To keep NSCs secure and guarantee that the building can remain operating after an earthquake, non-structural components must be constructed for earthquakes. To do this, it is necessary to calculate the floor response spectrum (FRS) at the location where the NSC is connected to the main system.

Using a decoupled analysis method, the floor response spectrum (FRS) approach, is used [7-15]. Without considering the impact of the secondary system, the fundamental structure is dynamically analyzed first. The time history of the acceleration response is supplied to a component at floor level where it is mounted to create the FRS. The resulting FRS may thus be used to determine the maximum force for the NSCs. According to research on dynamic behaviour of components subjected to ground motion, the likelihood of NSC damage would be enhanced if the primary structure's response was amplified [16]. Researchers began studying FRS generating methods in the 1970s. A method for producing the FRS using the ground response spectra was created by Yasui et al. [17]. For the purpose of accurately identifying floor acceleration spectra, a unique method is created and verified [18]. To study the seismic requirements on nuclear plants, Jiang et al. [19] created

Corresponding Author Email: noroozinejad@kgut.ac.ir
(E. Noroozinejad Farsangi)

floor response spectra. They found that the FRS from analysis showed significant fluctuations, especially in tuning circumstances. Investigations have been done on the floor response spectrum of complex structures [20-24]. The most recent research [25] investigated how a stiffness irregularity affected the FRS and found that the floor response's amplitude is larger at the soft story position. None of the FRS generating approaches that have been extensively discussed in the relevant literature [19, 23, 26, 27] can reliably measure the amplification in the acceleration of the non-structural components.

Component dynamic amplification factors, which represent the amplification of NSCs, are significant in the production of FRS. Hence, using a component dynamic amplification factor, the current work investigates how to quantify such amplification. Hence, for primary structures subject to seismic loads, the aforementioned factors were examined. The amplification factors and those discovered from the code-based formulations were contrasted. An attempt has been made in this study to develop the prediction model for the CDAF. The existing models [28, 29] for the determination of CDAF have not been considered the effect of a damping ratio of the NSC. As a result, this study proposed a prediction model for the CDAF spectrum based on data-driven methods. Data-driven methods like Machine learning (ML) techniques are superior in the establishment of relations between various input and output variables than conventional regression analysis [10, 30-32]. To be more specific, an ML model including Artificial Neural Network (ANN) was utilized to develop the CDAF spectra. By contrasting the amplification factors computed from the ML model with the factors acquired from the existing relations, the constructed prediction model based on the ML technique was verified.

The following is how the paper is organized: In section 2, the mathematical model is described. The selection and scale of ground motions are shown in section 3. The CDAF is described in section 4. The ANN model's details are presented in section 5. The suggested ANN prediction model's validation is shown in section 6. The final part draws brief conclusions (i.e., section 7).

2. DESCRIPTION OF MODEL

The basic structure in the current investigation is an acceleration sensitive NSC linked to a SDOF, as shown in Figure 1. The primary structure's (ξ_p) viscous damping ratio is taken as 5%. It is possible to calculate the primary structure's reaction for a given set of ground movements using Equation (1).

$$m_p\ddot{x} + c_p\dot{x} + k_px = -m_p\ddot{x}_g \qquad (1)$$

where m_p, c_p, and k_p are the mass, damping and stiffness for the primary structure: $c_p = 2m_p\xi_p\omega_p$; ω_p is the
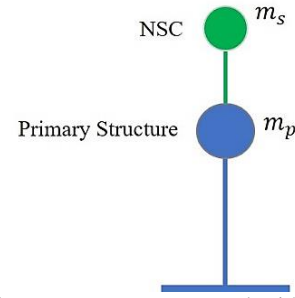
Figure 1. Primary structure connected with non-structural component

primary structure's frequency; $\dot{x}$ and $\ddot{x}$ are the relative velocity and acceleration; $\ddot{x}_g$ is the ground acceleration; $(\ddot{x} + \ddot{x}_g)$: primary structure's absolute acceleration. The resulting absolute acceleration response may be transformed into pseudo-acceleration response spectra in accordance with Equation (2) produce the FRS.

$$m_s\ddot{x}_s + c_s\dot{x}_s + k_sx_s = -m_p(\ddot{x} + \ddot{x}_g) \qquad (2)$$

where m_s, c_s, and k_s are the mass, damping, and stiffness for the NSC: $c_s = 2m_s\xi_s\omega_s$; ω_s and ξ_s are the NSC's frequency and damping ratio; x_s, $\dot{x}_s$, and $\ddot{x}_s$, are the relative displacement, velocity, and acceleration, respectively. Equations (1) and (2) are differential equations, which are then solved numerically using the Runge-Kutta technique.

3. GROUND MOTIONS

Realistic responses are produced by the seismic response evaluation process using actual ground motion recordings [33-38]. Such records are easily accessible through the NGA-West 2 Database of the Pacific Earthquake Engineering Research Centre (PEER) [39]. Hence, 11 horizontal ground motion excitations have been taken into account in the current research for the hard soil type in accordance with ASCE 7-16 [28]. Based on shear wave velocity (V_{S30}), ground motions are chosen to depict hard soil in accordance with National Earthquake Hazard Reduction Program (NEHRP) [40] criteria. Table 1 displays the specifics of the excitation. Since they can greatly reduce the computational time compared to many ground motions, spectrum compatible ground motions are used in this investigation [41]. To create spectrum-compatible seismic excitations, the time-domain spectral matching method [42] is applied. The IS 1893:2016 target spectra and average spectra of ground motions are shown in Figure 2. The average spectrum must remain above 90% of the target spectrum in accordance with ASCE 7-16. This figure shows that mean spectra are much more than 90% of the target spectra.

TABLE 1. Ground motions information

Earthquake	Year	Station	M_w	R_{jb} (km)
Helena_ Montana-01	1935	Carroll College	6	2.07
Helena_ Montana-02	1935	Helena Fed Bldg	6	2.09
Kern County	1952	Pasadena - CIT Athenaeum	7.36	122.65
Kern County	1952	Santa Barbara Courthouse	7.36	81.3
Kern County	1952	Taft Lincoln School	7.36	38.42
Southern Calif	1952	San Luis Obispo	6	73.35
Parkfield	1966	Cholame - Shandon Array #12	6.19	17.64
Parkfield	1966	San Luis Obispo	6.19	63.34
Parkfield	1966	Temblor pre-1969	6.19	15.96
Borrego Mtn	1968	Pasadena - CIT Athenaeum	6.63	207.14
Borrego Mtn	1968	San Onofre - So Cal Edison	6.63	129.11
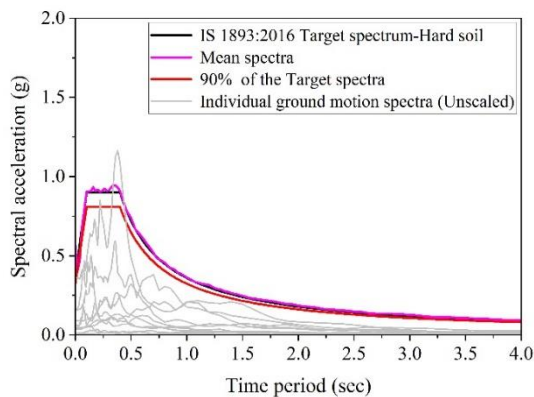
Figure 2. Mean and target spectra

4. COMPONENT DYNAMIC AMPLIFICATION FACTOR

The component's acceleration in relation to the floor acceleration is examined in this section. Elastic SDOF systems make up the NSCs examined in this study. In comparison to the main structure, the NSC's mass is thought to be quite low. Floor response spectra (FRS) is a decoupled approach that evaluates the primary system and non-structural component separately in a predetermined sequence. The linear time history analysis's input is scaled ground motions. From the model at the floor, absolute acceleration responses are collected and fed into the NSC to produce the relevant FRS. With a 5% damping ratio, the FRS was attained.

The FRS is performed, and its results are normalized by the appropriate peak floor acceleration (PFA). The component dynamic amplification factor is represented by the ratio FRS/PFA (CDAF). Understanding the seismic behaviour of non-structural components requires knowledge of the CDAF [12, 13]. Figure 3 shows the CDAF spectra for different primary structural periods for a 5% damping ratio of the NSC. The vibration period (T_p) of the primary structures shown in the Figure 3 represent the very stiff to flexible structures. The peak in the CDAF spectra was observed in the range of $0.7 \leq T_s/T_p \leq 1$ for the considered primary structures. The definitions of ASCE 7-16 [28] are contrasted with the CDAF in the present study. According to ASCE 7-16, for flexible NSCs with vibration periods greater than 0.06 seconds, the components amplification factor (a_p) is 2.5. The value of the amplification factor for stiff NSCs ($T_s < 0.06$ sec) is 1. It is clear from Figure 3 that the CDAF peaks are either underestimated or overestimated by the ASCE 7 standards.

Since NSCs come in a variety of periods and damping ratios (ξ_s), it is necessary to evaluate the impact of these characteristics on the seismic behaviour of non-structural components [43]. Determining component dynamic amplification factors for various ξ_s (0.1%, 0.2%, 0.5%, 1%, 2%, 5%, and 10%) is the purpose of this work. The CDAF spectrum for various damping ratios (0.1%, 2%, and 10%) is shown in Figure 4. As predicted, lower ξ_s values led to greater amplification factor values. The damping ratio of NSC is discovered to have a greater impact on the main structure's vibration periods. It is important to note that the impact of ξ_s is negligible for both extremely short and very long NSC periods. To do so, this work tried to create a prediction model for the CDAF utilizing machine learning methods such as artificial neural networks (ANNs). Amplification factors were determined for various ξ_s (0.1%, 0.2%, 0.5%, 1%, 2%, 5%, and 10%), tuning ratios, T_s/T_p (0 to 40 with 0.5 increment), and primary structural periods, T_p (0.1 to 1 s, with 0.1 increment, and 1.25, 1.5, 2, 2.5, 3, 3.5, and 4 s).
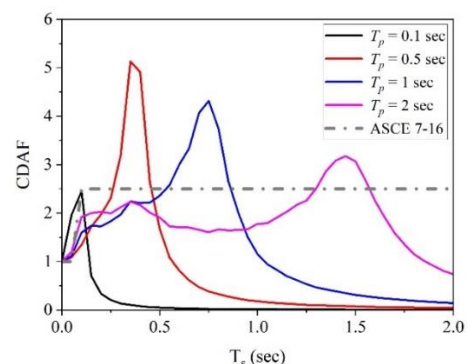
Figure 3. Component dynamic amplification factors for different primary structural periods
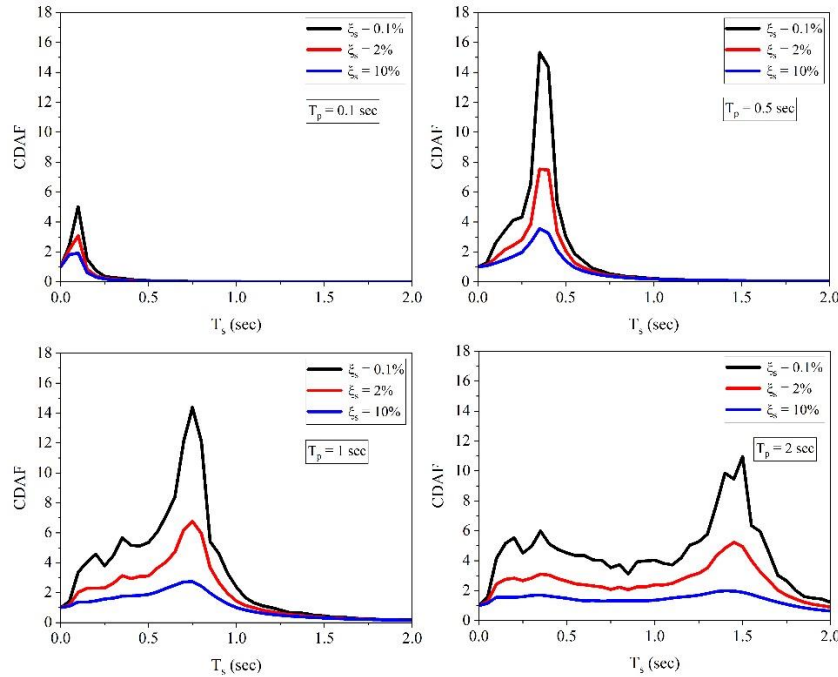
Figure 4. Component dynamic amplification factors at different NSC damping ratios

5. ARTIFICIAL NEURAL NETWORK (ANN) MODEL

Biological neural networks are simplified models that are used to express ANNs analytically. Massive data sets, difficult problems, and muddled circumstances may all be handled by neural networks. Because of this, neural networks are frequently a more accurate instrument for forecasting than traditional computational methods [44]. The current study employs a two layered feed-forward neural network to precisely forecast the CDAF. One of two levels, the other being the output layer, is the hidden layer. With only one hidden layer, neural networks can accurately estimate any function [45]. The tuning ratio (T_s/T_p), damping ratio (ξ_s) of the NSC, and primary structural period (T_p) are all considered as model inputs. The predicted output of the model is represented by the CDAF values. The performance of the model is more strongly influenced by the architecture of the networks. Insufficient hidden neurons will make learning harder for the network. Yet, the likelihood of the network overfitting the training set increases with the number of hidden neurons. By experimenting with the number of hidden neurons, we were able to fix the set with the lowest mean squared error (MSE). The optimal number was determined to be 35 hidden nodes, which corresponds to that number. Consequently, the 35 neurons in the hidden layer were considered while creating the ANN 3-35-1 model (Figure 5). The hidden neurons must be trained using an appropriate learning
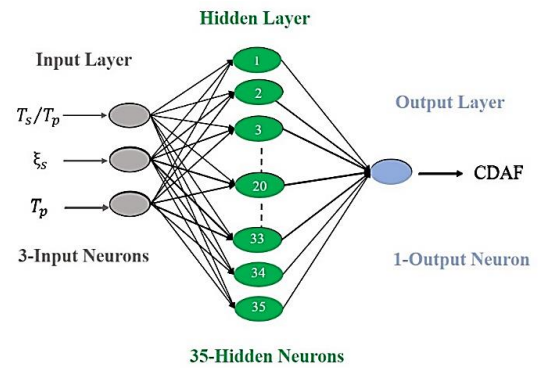
Figure 5. ANN 3-35-1 model

method. The network is trained using the Bayesian Regularization (BR) back propagation (BP) method. Moreover, the output and hidden layers both employ the Tan-sigmoid transfer function. Using the MATLAB R2019b environment, the neural network model for this investigation was developed. In all, 9639 CDAF values representing 17 primary structural periods, 81 NSC tuning ratios, and 7 NSC damping ratios were generated by simulation in this work. A training set, which makes up 70% of the whole dataset, and a testing set, which makes up 30% of the total dataset, are further separated into each dataset. The complete dataset must be pre-processed before training. The dataset must be normalized between -1.0 and 1.0 to give the variables an

equal weight. Using Equation (3), this normalization may be carried out.

$$x_n = \frac{2(x - x_{min})}{(x_{max} - x_{min})} - 1 \qquad (3)$$

where x_n is the normalized value. x_{min}, x_{max}, are the minimum and maximum values of the variable x, respectively. By specifying the performance assessment functions, the ANN model's predictive power is assessed. In this study, performance was measured using the mean square error (MSE), and coefficient of correlation (R). The performance functions (Equations (4) and (5)) are defined as follows:

$$MSE = \frac{\Sigma(y_s - y_p)^2}{N} \qquad (4)$$

$$R = \sqrt{\frac{\Sigma y_s^2 - \Sigma(y_s - y_p)^2}{\Sigma y_s^2}} \qquad (5)$$

where, N is the number of data points, and y_s and y_p are the simulated and predicted outputs. Table 2 displays the model's performance results. The error (MSE) should be as low as feasible, and the R value ought to be high. The connection between the predicted CDAF and the simulated CDAF is shown in Figure 6. The component dynamic amplification factor values are accurately predicted by the model, as seen by the correlation coefficient's proximity to unity.

6. VALIDATION OF THE ANN PREDICTION MODEL

This section looked at how well the ANN model predicted the dynamic amplification factors of non-structural parts that were connected to the main structure. For this validation, the damping ratios of NSC (0.6% and 3%) were used to construct the CDAF spectra of the primary structure under consideration. The ANN prediction model is not developed using the damping ratio values that were taken into consideration for validation. The predicted and simulated CDAF spectra are displayed in Figure 7. The predicted and simulated spectra for each of the instances under consideration have a comparably high level of agreement. Table 3 displays the maximum and lowest parameters used in creating the

TABLE 2. Results of the ANN model's performance

Dataset	R	MSE
Training	0.974	0.0019
Testing	0.966	0.0022
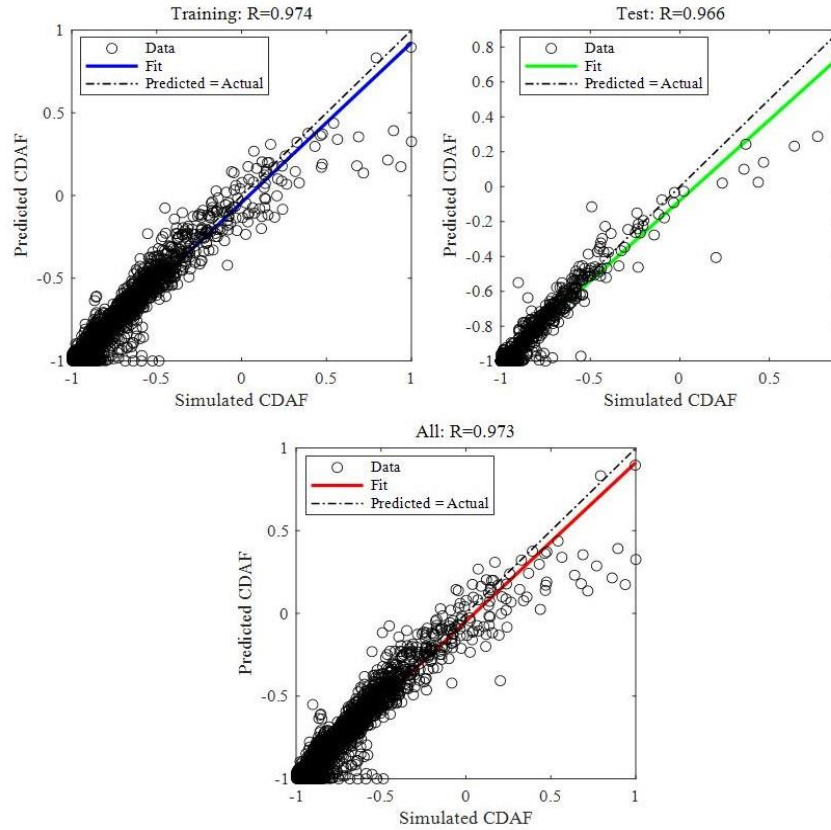
Figure 6. CDAF predicted by ANN and simulations
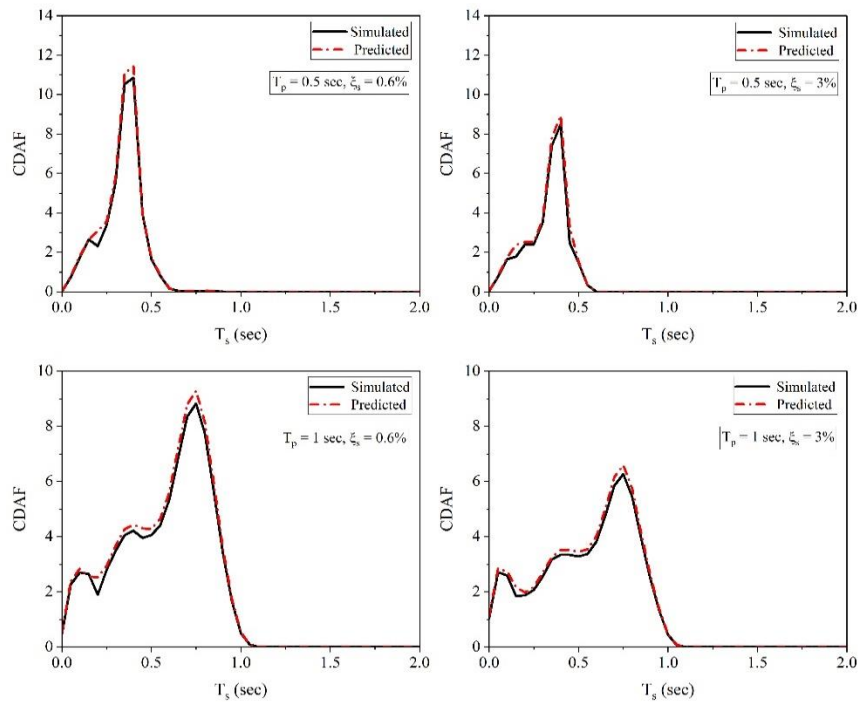
Figure 7. Comparison of simulated and ANN's predicted CDAF spectra

TABLE 3. Limits of various variables

	Input variables			Output
	T_p (sec)	T_s/T_p	ξ_s (%)	CDAF
Max	4.0	40.0	10.0	19.598
Min	0.1	0.00	0.1	0.000

ANN model. Thus, neural networks may be used to analyze the seismic behaviour of non-structural components. The ANN analysis approach reduces computational time by skipping the typical complicated analysis.

7. CONCLUSIONS

Component dynamic amplification factors are crucial because they represent the amplification of NSCs in the floor response spectrum. Hence, the present study explores the quantification of such amplification by means of a component dynamic amplification factor. The primary structure is therefore examined for the aforementioned factors. The amplification factors are compared to those found in the code-based formulae. The study allows for the following conclusions to be drawn:

- The component dynamic amplification factors show significant peak values in the range of $0.7 \leq T_s/T_p \leq 1$ for the considered primary structures.

- The damping ratio (ξ_s) of NSC has a greater impact on the dynamic amplification factors at vibration periods of the primary structure.
- The influence of ξ_s is negligible for both extremely short and very long NSC periods.
- The ASCE 7's definition under- or overestimates the amplification factors for periods closer to the vibration periods of the primary structure. So, the impacts of the dynamic properties of the NSC and primary structure should be included in the present code-based formulation.
- Machine learning (ML) technique like ANN is utilized to develop the prediction model for CDAF spectra. ANN is proved to be more effective and powerful tool in this study for establishing the relation between the input and output variables.

8. REFERENCES

1.   Filiatrault, A., and Sullivan, T. "Performance-based seismic

design of nonstructural building components: The next frontier of earthquake engineering." *Earthquake Engineering and Engineering Vibration*, Vol. 13, No. 1, (2014), 17-46. DOI:10.1007/s11803-014-0238-9

2. Shang, Q., Wang, T., and Li, J. "Seismic fragility of flexible pipeline connections in a base isolated medical building." *Earthquake Engineering and Engineering Vibration*, Vol. 18, No. 4, (2019), 903-916. https://doi.org/10.1007/s11803-019-0542-5

3. Di Sarno, L., Magliulo, G., D'Angela, D., and Cosenza, E. "Experimental assessment of the seismic performance of hospital cabinets using shake table testing." *Earthquake Engineering & Structural Dynamics*, Vol. 48, No. 1, (2019), 103-123. https://doi.org/10.1002/eqe.3127

4. Challagulla, S. P., Parimi, C., Mohan, S. C., and Farsangi, E. N. "Seismic Response of Building Structures with Sliding Non-structural Elements." *International Journal of Engineering, Transactions B: Applications*, Vol. 33, No. 2, (2020), 205-212. DOI: 10.5829/IJE.2020.33.02B.04

5. Nateghi, F. "Earthquake Evaluation of the Non Structural Elements in a Thermal Power Plant." *International Journal of Engineering, Transactions A: Basics*, Vol. 29, No. 1, (2016), 8-13. DOI: 10.5829/idosi.ije.2016.29.01a.02

6. Anajafi, H., and Medina, R. A. "Evaluation of ASCE 7 equations for designing acceleration-sensitive nonstructural components using data from instrumented buildings." *Earthquake Engineering & Structural Dynamics*, Vol. 47, No. 4, (2018), 1075-1094. https://doi.org/10.1002/eqe.3006

7. Suarez, L. E., and Singh, M. P. "Floor response spectra with structure–equipment interaction effects by a mode synthesis approach." *Earthquake Engineering & Structural Dynamics*, Vol. 15, No. 2, (1987), 141-158. https://doi.org/10.1002/eqe.4290150202

8. Adam, C. "Dynamics of elastic–plastic shear frames with secondary structures: Shake table and numerical studies." *Earthquake Engineering & Structural Dynamics*, Vol. 30, No. 2, (2001), 257-277. https://doi.org/10.1002/1096-9845(200102)30:2<257::AID-EQE7>3.0.CO;2-J

9. Menon, A., and Magenes, G. "Definition of seismic input for out-of-plane response of masonry walls: II. Formulation." *Journal of Earthquake Engineering*, Vol. 15, No. 2, (2011), 195-213. https://doi.org/10.1080/13632460903494446

10. Challagulla, S. P., Bhargav, N. C., and Parimi, C. "Evaluation of damping modification factors for floor response spectra via machine learning model." In *Structures*, Vol. 39, 679-690. Elsevier. https://doi.org/10.1016/j.istruc.2022.03.071

11. Rahman, M. M., Nahar, T. T., Kim, D., and Park, D.-W. "Location Sensitivity of Non-structural Component for Channel-type Auxiliary Building Considering Primary-secondary Structure Interaction." *International Journal of Engineering, Transactions A: Basics*, Vol. 35, No. 7, (2022). doi: 10.5829/ije.2022.35.07a.06

12. Pesaralanka, V., Challagulla, S. P., Vicencio, F., Chandra Babu, P. S., Hossain, I., Jameel, M., and Ramakrishna, U. "Influence of a Soft Story on the Seismic Response of Non-Structural Components." *Sustainability*, Vol. 15, No. 4, (2023), 2860. https://doi.org/10.3390/su15042860

13. Challagulla, S. P., Kontoni, D.-P. N., Suluguru, A. K., Hossain, I., Ramakrishna, U., and Jameel, M. "Assessing the Seismic Demands on Non-Structural Components Attached to Reinforced Concrete Frames." *Applied Sciences*, Vol. 13, No. 3, (2023), 1817. https://doi.org/10.3390/app13031817

14. Hossain, I., Velkin, V. I., and Shcheklein, S. E. "Experimental study in reduction of two phase flow induced vibration." In MATEC web of conferences, Vol. 211, EDP Sciences 2018. https://doi.org/10.1051/matecconf/201821116001

15. Hossain, I., Velkin, V. I., and Shcheklein, S. E. "The study of passive vibration dampers in pipelines using PIV-methodology for single phase flow." *WIT Transactions on Ecology and the Environment*, Vol. 224, (2017), 565-570. DOI: 10.2495/ESUS170521

16. D'Angela, D., Magliulo, G., and Cosenza, E. "Seismic damage assessment of unanchored nonstructural components taking into account the building response." *Structural Safety*, Vol. 93, , (2021), 102126. https://doi.org/10.1016/j.strusafe.2021.102126

17. Yasui, Y., Yoshihara, J., Takeda, T., and Miyamoto, A. "Direct generation method for floor response spectra," (1993).

18. Vukobratović, V., and Fajfar, P. "A method for the direct determination of approximate floor response spectra for SDOF inelastic structures." *Bulletin of Earthquake Engineering*, Vol. 13, No. 5, (2015), 1405-1424. https://doi.org/10.1007/s10518-014-9667-0

19. Jiang, W., Li, B., Xie, W. C., and Pandey, M. D. "Generate floor response spectra: Part 1. Direct spectra-to-spectra method." *Nuclear Engineering and Design*, Vol. 293, (2015), 525-546. https://doi.org/10.1016/j.nucengdes.2015.05.034

20. Calvi, P. M., and Sullivan, T. J. "Estimating floor spectra in multiple degree of freedom systems." *Earthquakes and Structures*, Vol. 7, No. 1, (2014), 17-38. http://dx.doi.org/10.12989/eas.2014.7.1.017

21. Zhai, C. H., Zheng, Z., Li, S., Pan, X., and Xie, L. L. "Seismic response of nonstructural components considering the near-fault pulse-like ground motions." *Earthquake and Structures*, Vol. 10, No. 5, (2016), 1213-1232. https://doi.org/10.12989/eas.2016.10.5.1213

22. Petrone, C., Magliulo, G., and Manfredi, G. "Floor response spectra in RC frame structures designed according to Eurocode 8." *Bulletin of Earthquake Engineering*, Vol. 14, No. 3, (2016), 747-767. https://doi.org/10.1007/s10518-015-9846-7

23. Berto, L., Bovo, M., Rocca, I., Saetta, A., and Savoia, M. "Seismic safety of valuable non-structural elements in RC buildings: Floor Response Spectrum approaches." *Engineering Structures*, Vol. 205, No. October 2019, (2020), 110081. https://doi.org/10.1016/j.engstruct.2019.110081

24. Shang, Q., Li, J., and Wang, T. "Floor acceleration response spectra of elastic reinforced concrete frames." *Journal of Building Engineering*, Vol. 45, (2022), 103558. https://doi.org/10.1016/j.jobe.2021.103558

25. Landge, M. V., and Ingle, R. K. "Comparative study of floor response spectra for regular and irregular buildings subjected to earthquake." *Asian Journal of Civil Engineering*, Vol. 22, No. 1, (2021), 49-58. https://doi.org/10.1007/s42107-020-00297-1

26. Singh, M. P., and Suarez, L. E. "Seismic response analysis of structure-equipment systems with non-classical damping effects." *Earthquake Engineering & Structural Dynamics*, Vol. 15, No. 7, (1987), 871-888. https://doi.org/10.1002/eqe.4290150708

27. Perez, Y. M., Guerra, E. M., Bazan-zurita, E., Engineer, P., Associates, R., Engineer, S. P., Associates, R., and Associates, R. "Seismic response of equipment supported on structures," (2015). 23rd Conference on Structural Mechanics in Reactor Technology Manchester, United Kingdom - August 10-14, 2015

28. ASCE. "Minimum design loads and associated criteria for buildings and other structures (ASCE/SEI 7-16)." American Society of Civil Engineers (ASCE) Reston, VA.

29. (BSSC), B. S. S. C. "NEHRP recommended seismic provisions for new buildings and other structures (fema p-750)." Report Prepared for the Federal Emergency Management Agency (FEMA). National Institute of Building Sciences Washington, DC.

30. van Kooten, R. T., Bahadoer, R. R., ter Buurkes de Vries, B., Wouters, M. W. J. M., Tollenaar, R. A. E. M., Hartgrink, H. H.,

Putter, H., and Dikken, J. L. "Conventional regression analysis and machine learning in prediction of anastomotic leakage and pulmonary complications after esophagogastric cancer surgery." *Journal of Surgical Oncology*, (2022). https://doi.org/10.1002/jso.26910

31. Challagulla, S. P., Parimi, C., and Anmala, J. "Prediction of spectral acceleration of a light structure with a flexible secondary system using artificial neural networks." *International Journal of Structural Engineering*, Vol. 10, No. 4, (2020), 353-379. https://doi.org/10.1504/IJSTRUCTE.2020.109857

32. Bhargav, N. C., Challagulla, S. P., and Farsangi, E. N. "Prediction Model for Significant Duration of Strong Motion in India." *Journal of Applied Science and Engineering*, Vol. 26, No. 2, (2022), 279-292. https://doi.org/10.6180/jase.202302_26(2).0014

33. Bagheri, B., Nivedita, K. A., and Firoozabad, E. S. "Comparative damage assessment of irregular building based on static and dynamic analysis." *International Journal of Civil and Structural Engineering*, Vol. 3, No. 3, (2013), 505.

34. Senaldi, I., Magenes, G., Penna, A., Galasco, A., and Rota, M. "The effect of stiffened floor and roof diaphragms on the experimental seismic response of a full-scale unreinforced stone masonry building." *Journal of Earthquake Engineering*, Vol. 18, No. 3, (2014), 407-443. https://doi.org/10.1080/13632469.2013.87694635.

35. Aydin, E., Öztürk, B., Kebeli, Y. E., and Gültepe, G. "An Experimental Study on the Effects of Different Pendulum Damper Designs on Structural Behavior." In Seismic Isolation, Energy Dissipation and Active Vibration Control of Structures: 17th World Conference on Seismic Isolation (17WCSI), 240-253. Springer.

36. Ozturk, B., Cetin, H., and Aydin, E. "Optimum vertical location and design of multiple tuned mass dampers under seismic excitations." In *Structures*, Vol. 41, 1141-1163. Elsevier. https://doi.org/10.1016/j.istruc.2022.05.014

37. Ozturk, B., Cetin, H., Dutkiewicz, M., Aydin, E., and Noroozinejad Farsangi, E. "On the Efficacy of a Novel Optimized Tuned Mass Damper for Minimizing Dynamic Responses of Cantilever Beams." *Applied Sciences*, Vol. 12, No. 15, (2022), 7878. https://doi.org/10.3390/app12157878

38. Praveen, O., Pithadiya, M., and Gopikrishna, K. "Influence of Real Ground Motion Records in Performance Assessment of RC Buildings." *International Journal of Engineering*, *Transactions C: Aspects,* Vol. 32, No. 12, (2019), 1745-1752. https://doi.org/10.5829/ije.2019.32.12c.07

39. Center, P. "PEER ground motion database." Pacific Earthquake Engineering Research Center, University of California, Berkeley, CA, http://ngawest2. berkeley. edu, (2013).

40. [NEHRP], N. E. H. R. P. "NEHRP Recommended Seismic Provisions for New Buildings and Other Structures." Part 1, Provisions, (2009).

41. Khy, K., Chintanapakdee, C., and Wijeyewickrema, A. C. "Application of conditional mean spectrum in nonlinear response history analysis of tall buildings on soft soil." *Engineering Journal*, Vol. 23, No. 1, (2019), 135-150. https://doi.org/10.4186/ej.2019.23.1.135

42. Alatik, L., and Abrahamson, N. "An improved method for nonstationary spectral matching." *Earthquake Spectra*, Vol. 26, No. 3, (2010), 601-617. https://doi.org/10.1193/1.3459159

43. Aragaw, L. F., and Calvi, P. M. "Earthquake-induced floor accelerations in base-rocking wall buildings." *Journal of Earthquake Engineering*, Vol. 25, No. 5, (2021), 941-969. https://doi.org/10.1080/13632469.2018.1548393

44. Jeng, D. S., Cha, D. H., and Blumenstein, M. "Application of neural network in civil engineering problems." In *P*roceedings of the International Conference on Advances in the Internet, Processing, Systems and Interdisciplinary Research. Citeseer.

45. Hornik, K., Stinchcombe, M., and White, H. "Multilayer feedforward networks are universal approximators." *Neural Networks*, Vol. 2, No. 5, (1989), 359-366. https://doi.org/10.1016/0893-6080(89)90020-8

Persian Abstract

چکیده

عملکرد لرزه ای اجزای غیر سازه ای در طول چند دهه اخیر مورد توجه محققین بوده است. قوانین ساختمانی نوین، نیروهای طراحی را بر روی اجزا با استفاده از روابط بسیار ساده تعریف می کنند. معمولا اجزای غیرسازه ای متصل به یک کف سازه ای شتابی بیشتر از طبقه ای که به آن متصل هستند می گیرند. بنابراین، ضرایب تشدید دینامیکی اجزا در این کار برای کمی سازی میزان تشدید در شتاب اجزای غیر سازه ای برای نسبت‌های مختلف میرایی و نسبت‌های تنظیم شده اجزای غیر سازه ای، و پریودهای ارتعاشی اصلی سازه محاسبه می‌شوند. از نتایج تجزیه و تحلیل به دست آمده، مشاهده شد که نقاط پیک CDAF توسط فرمول‌های مبتنی بر آیین نامه های فعلی مقادیر را دست پایین در نظر گرفته یا بیش از حد برآورد می‌نمایند. برای رفع این مشکل، یک مدل پیش‌بینی برای تعیین CDAFs با استفاده از شبکه‌های عصبی مصنوعی (ANN) توسعه داده شده است. ضریب همبستگی مدل 0.97 بود. از این رو، استفاده از یک الگوریتم ANN ضرورت تجزیه و تحلیل پیچیده را تا حد قابل توجهی کاهش می دهد.

International Journal of Engineering

A Fuzzy Fusion Framework for Generating Purpose-oriented Texts

M. Tayefeh Mahmoudi*[a], K. Badie[b]

[a] Data Analysis & Processing Research Group, IT Research Faculty, ICT Research Institute, Iran
[b] E-Content & E-Services Research Group, IT Research Faculty, ICT Research Institute, Iran

A B S T R A C T

Fusing textual information, as type of information fusion, has been of great significance to those interested in making informative texts out of the existing ones. The main idea behind text fusion, like any other type of information fusion, is to merge the partial texts from different sources in such a way that the outcome can hold a reasonably high relevance with regard to certain objectives. In this paper, a fuzzy framework is proposed for text generation, according to which a range of relevant texts are merged to yield producing a new text that can help the users fulfill a certain functionality in plausible manner. The focal point in our approach with regard to fusion is the distance between the class prototype of a text on the one side and the feature vectors belonging to different subsets of the existing texts on the other side. Results of experiments, show that the suggested framework can be a suitable alternatives for performing fusion in the cases that the identity of the existing texts from the viewpoint of the texts considered is unclear. This would turn into an effective utilization of the existing texts for the purpose of generating new texts.

1. INTRODUCTION

In recent years, text fusion has been of great significance to those interested in making informative texts out of the existing ones [1]. Texts fusion, in this way, has got numerous applications with regard to issues such as text summarization and text mining as well [2, 3]. The main idea behind text fusion, like any type of information fusion, is to merge partial texts from different sources in such a way that the outcome can hold a reasonably high relevance with regard to certain objectives.

Provided that organizational texts can help their users perform their functionalities in a reasonable way, one interesting application of text fusion is to merge the existing texts in such a manner that the outcome can hold such characteristic. For instance, if the functionality under consideration is "planning", the purpose of text fusion would be to provide a new text through merging the existing one, that can help planners do their functionality of planning in a plausible manner. Since the functionalities of a text may occasionally share similar aspects that could reflect in the way their essential

segments show up in the corresponding texts, we therefore need to make use of those approaches to fusion which can handle the ambiguity or uncertainty which may arise due to such sort of similarity in functionalities. In this sense, fuzzy logic can be considered as a helpful means for handling this uncertainty or ambiguity. Taking this point into account, a fuzzy framework is proposed in this paper for text fusion according to which a variety of texts are to be selected whose merging can yield a high expectation for helping the user fulfill a certain functionality.

The main concern in our approach is the distance between the prototypical classes of text considered for a variety of pre-defined functionalities on the one side, and the feature vectors belonging to different subsets of the existing texts, on the other side. Feature vectors in our approach are represented in terms of a number of membership degrees, each standing for the status of affiliation toward a certain feature in the desired class of text. In this paper, to evaluate the performance of our proposed framework we decided to compare it with the performance of OWA operators which are well- known

---

for information fusion purposes. Therefore, beside the proposed framework as a novel approach to text fusion, a part of the novelty in our work lies in examining the capability of OWA operators in fusing the textual information from the viewpoint of synthesizing a new text that can meet certain goals. Results of experimentation show that the suggested framework can be regarded a suitable alternative for fusion in the case that the identity of the existing texts from the viewpoint of the considered functionalities is not clear.

2. RELATED WORKS

By text integration or fusion, we mean to blend or fuse some pre-experienced texts to finally form a new text which can meet certain goals and /or certain criteria. A classical approach to integrating text can lie in multi-document text summarization according to which a final summery is to be made based on the information encapsulated in each document [4]. The main assumption in case of such an approach is that, each document may include its own peculiar information that can contribute to the final summery. Many methods have been proposed for multi-document text summarization out of which the recent works based on using deep neural networks are of particular significance [5]. The significance of deep neural net based text summarization mostly goes back to the fact that past experiences of summarization through joining different parts (from different documents) would have the ability to realize a new summary in a promising way. Another perspective in text integration can be met in integrating and blending concepts for creative generation of stories [6, 7] and automatic story telling [8] specially for generating game scenarios. Within this context, those who design games may generate and also explore some scenarios of game with high complexity through three main stages of domain implementation, solution generation and story board generation based on a kind of composition between the related items [9]. It seems that the main advantage of the proposed framework, compared to deep neural network-based document summarization, is no need for training patterns due to its dependence on the presence of linguistically-significant notions (such as What, Where, When, …) while considering some membership functions. In fact the effect of the very training which is essential to operationalizing deep neural network is somewhat encapsulated in the corresponding membership functions.

Fusion of dynamic web contents/ services through an extreme personalization as well as heterogeneous devices together with a interaction channels using content caching and adaptive aggregation algorithms as well as fuzzy utility based patterns mining are typical examples for fusion [10, 11].

Semantic data/information integration using fuzzy rules may also be widely used for text fusion [12], datasets integration [13] and information fusion [14] as well. Here, the relevant information is fused on the basis of a kind of logical reasoning to enhance the power of current semantic web systems [15] and search engines [16]. In this respect, the process of fuzzy conceptual matching can help an efficient retrieval of intelligent information and knowledge, and would be able to be integrated into the other commercial search engines [16]. Information fusion under fuzzy environment can also be applied for retrieving fuzzy information, whose fuzzy numbers are to represent the strength degrees according to which criteria of priority are met for the documents [17]. On the basis of the concept of fusing enterprise information, a kind of neural network has been presented which functions on the ground of choquet fuzzy integral [18].

Beside the above approaches, compositional adaptation techniques used in case-based reasoning have also the ability to combine the experienced sources (of information), like book chapters or texts to be used in learning in the form of a new configuration that can serve the current problems of teaching or research/ development support in a plausible manner [19, 20]. Although the propositions used for presenting the resources have crisp nature, it can however be possible to make use of fuzzy logic in these approaches both at representation and inference levels to provide the final solution in a favorable way.

Concept composition can also be considered as an approach to creating textual contents [21, 22].

In the meantime, due to the achievements of issues like semantic web, many researchers have tended to developing digital libraries based on ontological structures to share exchange and retrieval information efficiency [23]. Moreover, fuzzy queries have also been taken into account to build their queries in a more precise way in order to give assistance to readers for searching information [24]. In this regard, fuzzy ontology is utilized to present uncertain information in the case of digital libraries whereas fuzzy queries are used to retrieve information from this ontology. It is obvious that, using such a system can give more precise integrational results [24, 25]. It should also be mentioned that, collecting large amount of documents, in the way delivered by the search engines in Internet, is difficult and time-consuming for users to read and analyze. Here, the burden of managing information can be greatly eased through detecting common and distinctive topics within a set of documents as well as generating multi-document summaries. To achieve this goal, we first apply the well-known ordered weighted averaging (OWA) fusion operator to text fusion while examining the results, and then propose a new fuzzy framework according to which the input text is transformed into a set of membership degrees with

regard to a set of nominal values, and an appropriate distance function is then considered to measure the distance between the feature vector comprising these membership degrees and the ideal prototype vectors already defined for the prototype classes of a text. In both cases (applying OWA operators and proposed framework) possible types of texts (research, development, analysis, …) are represented in terms of a variety of key segments whose nominal values (L, M, H) take part in characterizing the types of the texts. Here, linguistically significant notions like What, Where, When , Who, … are used to determine the status of each nominal value. We found out through experimentation that the results obtained through the new framework is quite close to those obtained through applying AVG OWA. Moreover it was perceived that the proposed framework functions better than i) MIN OWA in the sense of avoiding the items in the resulted text which are not necessarily compatible with the requirements of the desired key segment, and ii) MAX OWA in the sense of observing some crucial items in the resulted text which are usually neglected by this operator mostly due to the point that text fusion through MAX OWA calls for severe

constraints. The benefit of such an approach goes back to the fact that the input texts are treated in a generic way thus providing a chance for the system to merge them in a way as generic as possible.

3. THE PROPOSED APPROACH

3. 1. Basic Concepts   The basic idea behind our approach is based on the point that there exists a number of key segments in a text whose status of emphasis gives sense to the type of functionality which is expected to be performed by it when a text is exposed to its user. A partial ontology of these key segments that ought to be observed by texts authors in some way is shown in Figure 1 [26]. This ontology has in reality been designed to describe each key segment in depths; in such a way that the entire key segments can be differentiated properly in the input text.

Taking this ontology into account, each class of text functionality can be represented in terms of the related key segments as features and their values as the feature's values. The feature's values in our approach are Low (L),
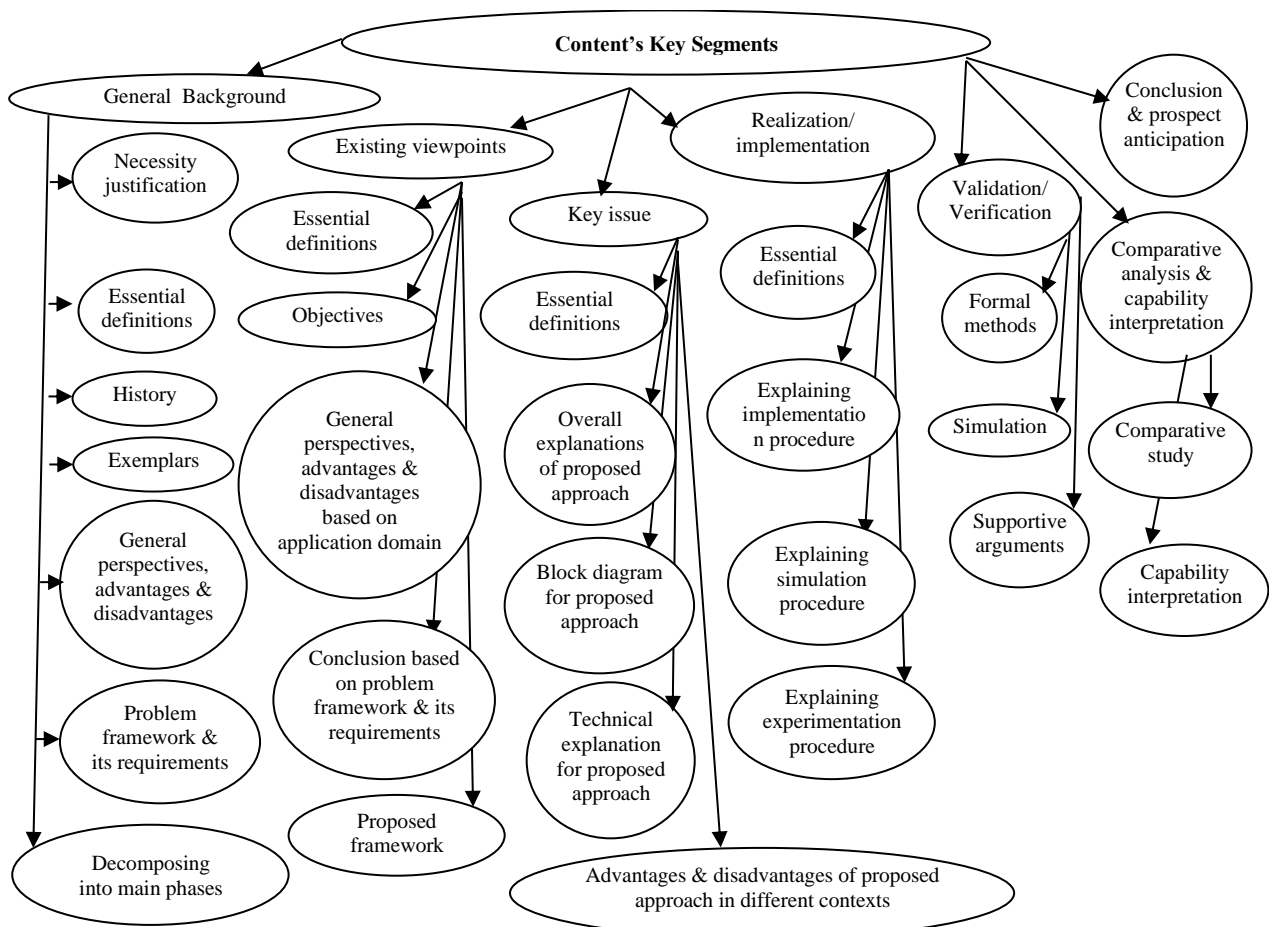
Figure 1. The Ontology of Text's Key Segments

Medium (M) and High (H), which are decided based on the status of the explanations regarding linguistically-significant notions such as What, Which, Who, Whom, Where, When, How and Why that are the items to be tackled in generating texts. Having represented classes of text functionality in the above manner, our main objective would be to find a certain combination, out of the existing texts, whose similarity degree regarding the corresponding features' values in the desired class of functionality as the purpose of fusion can be sufficiently high. To show the similarity degree, in our approach, membership degrees of the existing features' values with regard to the prototypical values for the same features in the desired class of text functionality are taken into account. These prototypical values are in reality the quantitative versions of the linguistic variable values "L", "M" and "H" which have been considered to indicate the status of the existing key segments (General Background, Existing Viewpoints, …) for different text functionalities. In our approach we decided to consider "1" for "L", "2" for "M" and "3" for "H" as the simplest version. The ground for calculating such a measure is decided to be the total number of the predicates as well as the arguments, which tackle the afore-mentioned linguistically- significant notions for each key segment as an feature. This is because, provided that these notions are significant from the view-point of a text's status of richness, the status of the related predicates/arguments can naturally be a good indicator to show how far it can be regarded close to the corresponding feature value in the desired class of text functionality. To show that a certain combination of texts (with certain functionalities), belongs adequately to a certain class of text functionality, in our approach we make use of a number of criteria that tackle respectively (i) the fact that the similarity of this combination to the desired class ought to be more than the corresponding similarities for the other combinations, and (ii) the fact that this similarity ought to be more than a certain threshold.

3. 2. The Proposed Approach Based on Text Fusion

The main point in our framework is merging a range of relevant texts to yield producing a new text that can help the users fulfill a certain functionality. It would thus be important to first select those texts as the input texts whose topics are somewhat similar in some aspects. Having done so, the next step would be to identify the significant key segments in each input text through detecting the entities which have been realized to be essential for each key segment as illustrated in the ontology of Figure 1. To perform this task, linguistically significant notions such as What, Where, Who, … are searched for, to determine the status of membership degrees with regard to the considered linguistic variable values "L", "M" and "H" for the corresponding key

segments. As the next step, the possible combinations of the feature vectors comprising these membership degrees are constituted, and out of these combinations those which hold the minimum distance toward the prototypical feature vectors predefined for each text functionality, are selected as the most appropriate alternatives for fusion. Below, the above mentioned steps are discussed in detail. Figure 2 illustrates the essential steps to the proposed framework for fusion.

3. 2. 1. Text Functionalities and Status of Linguistic Variable Values for the Selected Features

With respect to fusion issues, identifying the features of those texts that are to be fused, is of great importance.

To facilitate the fusion process, the major key segments (Figure 1) are used as the features: General Background, Existing viewpoints, Key issue, Proposed approach realization/ implementation, Validation/ Verification, Comparative analysis & capability interpretation, Conclusion & prospect anticipation. We have realized that such features are consistent for a variety of texts whose functionality is to help users with their tasks in the corresponding organizations. Interestingly the key segments discussed above are also popular among many knowledge workers like those involved in research, innovation, development, planning and analysis issues with the final goal of disseminating their works' results in terms of suitable texts. Examples for the important functionalities in an organization, are Planning/ Scheduling, Research, Innovation, Development/ Optimization/ Improvement. Education/ Promotion, Analysis/ Assessment/ Assurance, Guidance, and Justification.

As far as linguistically significant notions are concerned, "L" (Low), "M" (Medium) and "H" (High)
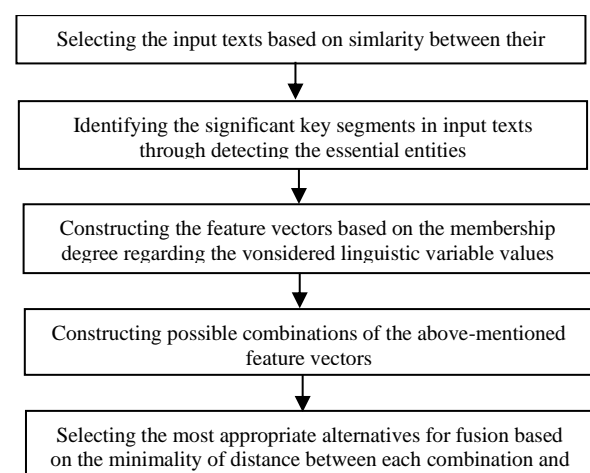
Figure 2. The steps essential to the proposed framework for fusion

stand for the extent that notions like "What", "Who", "Whom", "Where", "When", "How", and "Why", are to be addressed to create a partial text for each of the afore-mentioned key segments. For example with regard to the key segment "General Background", the items with regard to "Necessity", "Essential Definitions", "History", "Exemplars", "General Perspectives", "Advantages & Disadvantages", "Requirements of Problem Framework", and "Main Phases" are considered as "Whats", the agents who have taken part in the "History" of an issue are considered as "Whose", the space and time where a "framework" can function well are considered as "Wheres" and "Whens", the way a problem framework works as well as the way a problem is "decomposed into main phases" are considered as "Hows", and finally the reason that the "necessity" of an issue is justified as well as the reasons a "framework" may or may not function properly with regard to certain situations are considered as "Whys". Referring to Figure 1, the interpretation of "Whats", "Whose", "Whoms", "Wheres", "Whens", "Hows" and "Whys" can be equally performed for the other types of key segment taking into account their hyponyms. It is to be noted that the nominal values already agreed for each functionality are responsible for doing this task to indicate how far the above-mentioned notions ought to be addressed. Table 1 illustrates the status of the corresponding nominal values with regard to these notions.

We may see from the table that the depth of a notion depends on the amount of a nominal value. Let us say, the notion "How" is also called for when we have a transition from the nominal value "L" to the nominal value "M", and in the same manner, by transition from "M" to "H", the notion "Why", which organically stands for an explanation with more depth, would be worth being added.

Taking this point into account, for each feature, the fuzzy membership functions can be considered based on the nominal values already discussed. Table 2 shows the corresponding nominal values for the selected text features. The membership functions for these values are also shown in Figure 3.

TABLE 1. Status of the nominal values

Nominal Value	Status of Linguistically Significant notions
L (Low)	Addresses What, Where, When, Who , and Whom
M (Medium)	Addresses What, Where, When, Who, Whom, and How
H (High)	Addresses What, Where, When, Who, Whom, How, and Why

TABLE 2. Status of linguistic variables values for the selected features taking into account the existing functionalities

Input Text Features	Research	Development / Planning	General Learning	Justification	Innovation	Analysis/ Assessment
General Background	H	M	L	L	M	L
Existing Viewpoints	H	M	H	L	M	L
Key Issue	H	M	M	M	M	M
Proposed Approach Realization/ Implementation	H	M	L	M	L	M
Validation/ Verification	H	M	L	M	L	H
Comparative Analysis & Capability Interpretation	H	M	L	L	L	L
Conclusion & Prospect Anticipation	H	H	L	L	L	L
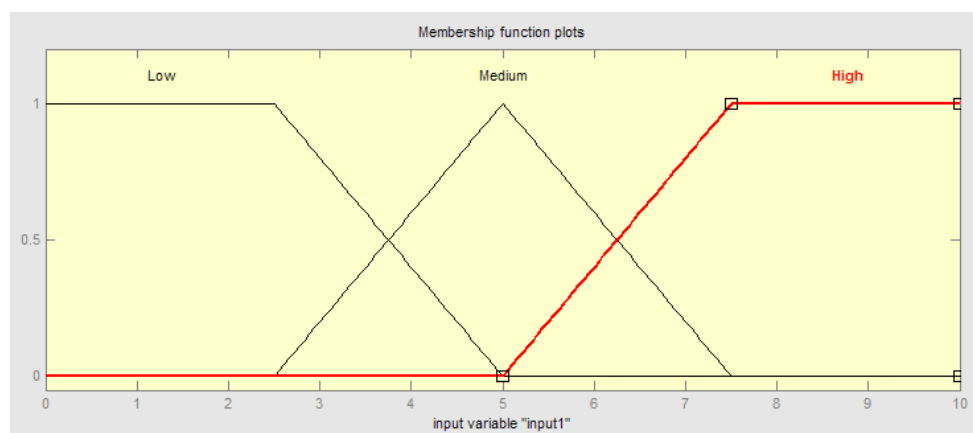
Figure 3. Membership functions for each of the linguistic variable values for the features in the text

3. 2. 2. Process of Fusion Using Weights   In order to perform fusion, we first need to make a membership degree matrix for each input text document within which each row represents the status of membership degrees for the related key segment. Figure 4(a) illustrates such a matrix for the i-th and jth text documents.

To fuse these texts documents, all their combination forms have to be considered. For instance, if there are three texts documents to be fused, the possible combinations would be as follows:

(doc i) , (doc j), (doc k), (doc i , doc j), (doc I, doc k), (doc j, doc k), (doc I, doc j, doc k)

Let us consider the combination of the ith and jth text documents. Taking into account the matrix representation for each text (as shown in Figure 4(a)), the result of fusion can be represented as the matrix of Figure 4(b).

To obtain a text suitable for a certain functionality, matrix of each texts' functionalities, which is represented in Table 2, has to be compared with the equivalent membership degrees from the matrix of document.

Suppose that our purpose is to select a combination of texts which can best fit the functionality of "research".

To figure out the best combination for fusion, the following conditions should be satisfied as the necessary criteria.

Condition 1: distance (Research, Xi) < distance (Development, Xi), distance (Learning, Xi),…..

Condition 2: (distance (Development, Xi)- distance (Research, Xi)) + (distance (learning, Xi) – distance (Research, Xi))... $\rightarrow$ Max

Based on the type of the functionality expected from fusion, the coefficients called "importance coefficient" is to be considered for different functionalities, in order to

improve the process of selecting the best combination. To achieve this, the conditions are changed to the following forms:

$$d(R, X_i) = (d_1^{i_R}, d_2^{i_R}, ..., d_7^{i_R})$$

$$\sum_{j=1}^{7} w\, d_j^{i^2_R X}$$

$$\sum_{j=1}^{7} w\, d_j^{i^2_R} < \sum_{j=1}^{7} w\, d_j^{i^2_D}, \sum_{j=1}^{7} w\, d_j^{i^2_P}, ...$$

$$(\sum_{j=1}^{7} w\, d_j^{i^2_D} - \sum_{j=1}^{7} w\, d_j^{i^2_R}) + (\sum_{j=1}^{7} w\, d_j^{i^2_P} - \sum_{j=1}^{7} w\, d_j^{i^2_R}) + ... -\,-> \max$$

To determine the importance coefficient (w), suppose that WL=1, WM=2, WH=3, for each function, W should be calculated per each feature in a way that $\sum w = 1$ can be satisfied.

For instance, weights for each feature can be calculated as follows:

W_H: 3 3 3 3   3 3 3
Research : [H H H H H H H]
$W_{Research}$: [3/21 3/21 3/21 3/21 3/21 3/21 3/21]

While for Learning the same weights would better be calculated as follows:

$W_{L,M,H}$:   1 3 2 1 1 1 1
Learning:[L H M L L L L]
$W_{Learning}$: [1/10 3/10 2/10 1/10 1/10 1/10 1/10]

It is to be noted that Ws can also be determined by OWA. For this purpose, three forms of OWA for the discussed importance coefficients are considered as follows [27, 28]:
- Max: or oring aggregation operator is given by: W' = [l, 0,..., 0]
- Min: or anding aggregation operator is given by: W' = [0, 0,..., 1]
- Average: W' = [1/n, 1/n,..., 1/n]

In this approach, the best combinations for the existing functions are calculated and upon the requested objective, the combination results are represented and compared with the results achieved for applying OWA.

4. EXPERIMENTAL RESULTS

To validate the performance of the proposed framework, a number of texts with unclear nature from the view-point of the desired class of functionality were selected as the input texts. These texts are the research papers addressed in the literature [29, 30] as $text_1$, $text_2$ and $text_3$. Let us say, $text_1$ is on "Particle Swarm Optimization" (as mentioned in the literature [29]), $text_2$ is on "Evolving the Structure of the Particle Swarm Optimization Algorithms" (as mentioned in the literature [30]), and $text_3$ is on "Optimization of Nonlinear Constrained Particle Swarm" (as mentioned in the literature). We

Figure 4. (a) Matrix for the i-th and jth text documents (b) Fusion of matrix i-th and jth text documents

selected these research papers as input texts since they address the same topic of "particle swarm", so as to conduct fusion in a way that can make sense with regard to the considered text's key labels (General Background, Existing Viewpoint, Key Issue, …). Experimentation was done in such a manner that, each input text was investigated from the perspective of the key segments as the features discussed in the paper, taking into account the status of the nominal values belonging to them. As discussed in section 3.2.1, these nominal values stand for the extent that notions like "What", "Who", "Whom", "Where", "When", "How" and "Why" are addressed in the way already discussed with regard to the ontology of the key segments in Figure 1.

Result of experimentation for each feature has been shown in Table 3 by a separate color for the three input texts. The number of predicates/ arguments detected for each feature in the input texts is also mentioned in Table 3.

Having normalized the given numbers in Table 4 into the range of [1 10] using

X= Lower band+ (Upper band – Lower band) α /Max

process is performed based on the weights that have been explained in the previous section.

In this example, as the presupposed range is [1 10] and the Max value is 200, the normalizing formula would be:

$$x=1+(10-1)\alpha/200$$

Simulation results are presented in Table 4. As it is seen, each number defines the status of the texts that are appropriate to be combined for a certain functionality.

The feature values for the selected texts for fusion are as follows:

General Background, Existing viewpoints, Key issue, Proposed approach realization/ Implementation, Validation/ Verification, Comparative analysis & capability interpretation, Conclusion & prospect anticipation.

$Text_1$: [50, 10, 35, 26, 200, 15, 4] → Normalized $Text_1$: [3.25, 1.45, 2.57, 2.17, 10, 1.67, 1.18]
$Text_2$: [4, 21, 37, 70, 0, 14, 5] → Normalized $Text_2$: [1.18, 1.94, 2.66, 4.15, 1, 1.63, 1.22]
$Text_3$: [7, 11, 18, 45, 0, 29, 8] → Normalized $Text_3$: [1.31, 1.49, 1.81, 3.02, 1, 2.30, 1.36]

The orders of certain functionalities which have been considered as the purpose of fusion are respectively: research, development, learning, justification, guidance, innovation and analysis.

The results of fusion with the mentioned feature values are as follows. As it is illustrated, to generate text for "research", combination of $Text_2$ and $Text_3$ are appropriate according to the proposed approach, while to generate a text for "development/planning", the

combination of $Text_1$ & $Text_3$ would be suitable. In the same way, we may have different combinations of texts based on the type of the desired functionality.

Results of applying Max OWA reveal that, if the objective is to have a text for "research", $Text_2$ is more suitable, while for having a text for "development/planning", $Text_1$ is appropriate.

Applying Min OWA shows that the combination of $Text_1$ and $Text_2$ leads to a proper result once "research" has been considered as the desired text functionality. Finally, applying AVG OWA, illustrates the same results as those obtained by applying the proposed framework. Figure 5 shows the results obtained.

For the moment, to combine the texts, the parts corresponding to the related features are just added together, paying no attention to the fact that they may have some common parts. This may lead to a possible presence of somewhat similar parts in the text obtained as the result of fusion. To circumvent this problem, a variety of techniques such as semantic information

TABLE 3. Number of predicates for each feature in selected Texts

Text's Key Labels	Text Functionalities		
	$Text_1$ [29]	$Text_2$ [30]	$Text_3$ [31]
General Background	50	4	7
Existing Viewpoints	10	21	11
Key Issue	35	37	18
Proposed Approach Realization/ Implementation	26	70	45
Validation/ Verification	200	0	0
Comparative Analysis & Capability Interpretation	15	14	29
Conclusion & Prospect Anticipation	4	5	8

TABLE 4. Definition of simulation results

Numerical Result	Suitable Text
0	None of the combinations are suitable for the desired functionality
1	$Text_1$ is suitable for the desired functionality
2	$Text_2$ is suitable for the desired functionality
3	$Text_3$ is suitable for the desired functionality
4	The combination of $Text_1$ and $Text_2$ are suitable for the desired functionality
5	The combination of $Text_1$ and $Text_3$ are suitable for the desired functionality
6	The combination of $Text_2$ and $Text_3$ are suitable for the desired functionality
7	The combination of $Text_1$ and $Text_2$ and $Text_3$ are suitable for the desired functionality

Each Number Shows Which Combination of Texts Are Appropriate for Purpose-Oriented Fusion

0: None of the Texts is good for fusion
1: Text1 is good for fusion
2: Text2 is good for fusion
4: Text1 & Text2
5: Text1 & Text3
6: Text2 & Text3
7: Text1 & Text2 & Text3
The results of Proposed Approach for Fusion :
6   5   0   0   0   0   0

The results of Max OWA:
2   1   0   0   0   0   0

The results of Min OWA:
4   0   0   0   0   0   0

The results of AVG OWA:
6   5   0   0   0   0   0

Figure 5. Implementation Results for Fusion

processing as well as natural language processing may come effective to resolve this kind of overlap or redundancy. Approaching this problem can be considered as a continuation of the present work in future.

Figure 6 shows a part of the result of text fusion that has been obtained through the above mentioned fusion methods. It should be noticed that our proposed framework for fusion in some sense can be regarded as an approach to summarization since its main concern is to pick out those parts in the input text whose significance is in the way they comply with some desired functionalities. Let us say, it can be regarded as a kind of multi-document summarization with respect to certain functionalities for a text (research, planning, assessment, …) taking into account text's key labels (such as "General Background", "Existing Viewpoints", "Proposed Approach Realization Implementation", …) as the important aspects in a summery.

Research Text

Proposed Approach: Fusion of $Text_2$ [30] and $Text_3$

General Background:

The partial texts obtained through applying our framework to $Text_2$ [30]

Particle Swarm Optimization (PSO) is a population based stochastic optimization technique well developed in literature [8]. Standard PSO algorithm randomly initializes a group of particles (solutions) and then searches for optima by updating all particles along a number of generations. In any iteration, each particle is updated by following some rules [16]. Standard model implies that particles are updated synchronously [16]. This means that the current position and speed for a particle is computed taking into account only information from the previous generation of particles.

The partial texts obtained through applying our framework to $Text_3$

The particle swarm optimization algorithm (PSOA) was firstly proposed in literature [4, 5] and has deserved some attention during the last years in the global optimization field. PSOA is based on the population of agents or particles and tries to simulate its social behavior in optimal exploration of problem space. During time (iterations in the optimization context) each agent possesses a velocity vector that is a stochastic combination of its previous velocity and the distances of its current position to its own best ever position and to the best ever swarm position. The weights of the last two directions are controlled by two parameters called cognitive and social parameters [6].
PSOA belongs to a class of stochastic algorithms for global optimization and its main advantages are the easily parallelization and simplicity. PSOA seems to outperform the genetic algorithm for some difficult programming classes, namely the unconstrained global optimization problems [6]. In spite of the referred advantages, PSOA possesses some drawbacks, namely its parameters dependency and the slow convergence rate in the vicinity of the global minimum.

MAX OWA: $Text_2$ [30]

General Background:

The partial texts obtained through applying MAX OWA to $Text_2$ [30]

Particle Swarm Optimization (PSO) is a population based stochastic optimization technique well developed [8]. Standard PSO algorithm randomly initializes a group of particles (solutions) and then searches for optima by updating all particles along a number of generations. In any iteration, each particle is updated by following some rules [16]. Standard model implies that particles are updated synchronously [16]. This means that the current position and speed for a particle is computed taking into account only information from the previous generation of particles.

MIN OWA: Fusion of Text$_1$ [29] & Text$_2$ [30]

General Background:

The partial texts obtained through applying MIN OWA to fuse Text$_1$ [29] & Text$_2$ [30]

Although the principle of Particle Swarm Optimization is a quite new approach, its ancestors reach back into history as it emerged from biological research and simulation on swarming animals. The first computer-related work in this area was provided by Craig Reynolds which published a paper about simulating bird swarms in literature [6]. The idea was to simulate realistic swarms mainly for computer graphics and movies. The result was some simulated swarm of whose the individuals called \Boids\ [7]. These were directed by three simple rules, which were implemented and caused a near-realistic swarming behaviour:
- Separation: Do not run into flockmates
- Alignment: Align the own heading to the average of the neighbours
- Cohesion: Move toward the average position of neighbours.

For making this possible a new software was written named MASSIVE which controls this mass of agent technology-equipped computer actors (CGIs) and their states.

A quite funny anecdote about this battle sequence is that in the early testing-runs it was working way too good. The directors noticed some group of orcs which fled the battle because they were too scared. This was adjusted later on, as orcs are said to fear nothing at all...

The concepts embedded into the Boids were refined and later led into some new area of computer graphics which is called behavioral animation. The most impressive usage are probably the immense battle sequences in the trilogy Lord of the Rings where about 250,000 individual fighters.

AVG OWA: Fusion of Text$_2$ [30] and Text$_3$
General Background:

The partial texts obtained through applying AVG OWA to fuse Text$_2$ [30] & Text$_3$
From Text$_2$ [30]

Particle Swarm Optimization (PSO) is a population based stochastic optimization technique developed in literature [8]. Standard PSO algorithm randomly initializes a group of particles (solutions) and then searches for optima by updating all particles along a number of generations. In any iteration, each particle is updated by following some rules [16]. Standard model implies that particles are updated synchronously [16]. This means that the current position and speed for a particle is computed taking into account only information from the previous generation of particles.

From Text$_3$

The particle swarm optimization algorithm (PSOA) was firstly proposed in literature [4, 5] and has deserved some attention during the last years in the global optimization field. PSOA is based on the population of agents or particles and tries to simulate its social behavior in optimal exploration of problem space. During time (iterations in the optimization context) each agent possesses a velocity vector that is a stochastic combination of its previous velocity and the distances of its current position to its own best ever position and to the best ever swarm position. The weights of the last two directions are controlled by two parameters called cognitive and social parameters [6].

PSOA belongs to a class of stochastic algorithms for global optimization and its main advantages are the easily parallelization and simplicity. PSOA seems to outperform the genetic algorithm for some difficult programming classes, namely the unconstrained global optimization problems [6]. In spite of the referred advantages, PSOA possesses some drawbacks, namely its parameters dependency and the slow convergence rate in the vicinity of the global minimum.

Figure 6. The results of Texts Fusion

5. CONCLUDING REMARKS

A fuzzy framework was presented in this paper, which is capable of fusing the input texts in such a manner that the outcome can have the claim of belonging to certain text functionalities by considering a number of text's key labels. As discussed in the paper, each class of text functionality is represented in terms of some key segments as features and the related values, which are decided based on the status of the explanations regarding some linguistically- significant notions. It was discussed that the membership degrees of the features' values in a combination of texts is calculated based on the total number of the predicates/ arguments that tackle them for each key segment as a feature. To show that a certain combination of texts belongs sufficiently to a certain class of functionality, we made use of a variety of criteria that can assure this belongingness in a reasonable manner. Results of an experimentation on some texts (picked out from some research papers) show the fact that

the proposed framework can be a suitable alternative for performing fusion in the cases that the class identity of the input text documents is unclear. Moreover, It should be noticed that the proposed framework for fusion can be regarded as an approach to multi-document summarization as well since its main concern is to pick out those parts in the input texts whose significance is in the way they comply with some desired functionalities.

As the final point, it is observed that, from the viewpoint of fusion methodology, the proposed approach to text fusion can be regarded similar to the fusion operator AVG OWA. This seems to be mainly due to the smooth distribution of weights in both AVG OWA –based fusion and our proposed framework as well.

6. REFERENCES

1. Ying, L., Zhe, W., Jie, F., Tingge, Z., Linna, L. and Jiming, L., "Multi-modal public opinion analysis based on image and text fusion", *Journal of Frontiers of Computer Science & Technology*, Vol. 16, No. 6, (2022), 1260. doi: 10.3778/j.issn.1673-9418.2110056.

2. Ernst, O., Caciularu, A., Shapira, O., Pasunuru, R., Bansal, M., Goldberger, J. and Dagan, I., "Proposition-level clustering for multi-document summarization", in Proceedings of the 2022 Conference of the North American Chapter of the Association for Computational Linguistics: Human Language Technologies. (2022), 1765-1779.

3. Srividya, K., Mirayababu, K. and Mary Sowjanya, A., "Mining interesting aspects of a product using aspect-based opinion mining from product reviews (research note)", *International Journal of Engineering*, Vol. 30, No. 11, (2017), 1707-1713. doi: 10.5829/ije.2017.30.11b.11.

4. Nazari, N. and Mahdavi, M., "A survey on automatic text summarization", *Journal of AI and Data Mining*, Vol. 7, No. 1, (2019), 121-135. doi: 10.22044/JADM.2018.6139.1726.

5. Ma, C., Zhang, W.E., Guo, M., Wang, H. and Sheng, Q.Z., "Multi-document summarization via deep learning techniques: A survey", *ACM Computing Surveys*, Vol. 55, No. 5, (2022), 1-37. doi: https://doi.org/10.1145/3529754.

6. Fauconnier, G. and Turner, M., "Conceptual integration networks", *Cognitive science*, Vol. 22, No. 2, (1998), 133-187.

7. Pereira, F.C. and Cardoso, A., "Conceptual blending and the quest for the holy creative process", in Second Workshop on Creative Systems, Approaches to Creativity in Artificial Intelligence and Cognitive Science, European Conference on Artificial Intelligence (ECAI 2002), Lyon, France, July. (2002).

8. Yu, M.-H., Li, J., Chan, Z., Yan, R. and Zhao, D., "Content learning with structure-aware writing: A graph-infused dual conditional variational autoencoder for automatic storytelling", in Proceedings of the AAAI Conference on Artificial Intelligence. Vol. 35, (2021), 6021-6029.

9. Zubek, R., "Elements of game design, MIT Press, (2020).

10. Ravi, J., Yu, Z. and Shi, W., "A survey on dynamic web content generation and delivery techniques", *Journal of Network and Computer Applications*, Vol. 32, No. 5, (2009), 943-960. https://doi.org/10.1016/j.jnca.2009.03.005

11. Mohbey, K., "High fuzzy utility based frequent patterns mining approach for mobile web services sequences", *International Journal of Engineering*, *Transactions B: Applications,* Vol. 30, No. 2, (2017), 182-191. doi: 10.5829/idosi.ije.2017.30.02b.04.

12. Nikolov, N. and Stoehr, P., "Integrating biomedical publications with existing metadata", in 2008 21st IEEE International Symposium on Computer-Based Medical Systems, IEEE. (2008), 653-655.

13. Kieler, B., "Semantic data integration across different scales: Automatic learning generalization rules", *International Archives of Photogrammetry, Remote Sensing and Spatial Information Sciences*, Vol. 37, No., (2008), 685-690.

14. Hong-Sheng, S., "Multi-source fuzzy information fusion method based on bayesian optimal classifier", *Acta Automatica Sinica*, Vol. 34, No. 3, (2008), 282-287.

15. Nikravesh, M., "Beyond the semantic web: Fuzzy logic-based web intelligence", *Soft Computing in Ontologies and Semantic Web*, (2006), 149-209. doi: 10.1007/978-3-540-33473-6_7.

16. Nikravesh, M., Takagi, T., Tajima, M., Shinmura, A., Ohgaya, R., Taniguchi, K., Kawahara, K., Fukano, K. and Aizawa, A., "Enhancing the power of search engines and navigations based on conceptual model: Web intelligence", *Soft Computing for Information Processing and Analysis*, (2005), 35-92. https://doi.org/10.1007/3-540-32365-1_3

17. Lee, H.-S., Chou, M.-T., Tseng, W.-K., Fang, H.-H. and Yeh, C.-H., "A new information fusion method for fuzzy information retrieval", in Knowledge-Based Intelligent Information and Engineering Systems: 11th International Conference, KES 2007, XVII Italian Workshop on Neural Networks, Vietri sul Mare, Italy, September 12-14, 2007. Proceedings, Part II 11, Springer., (2007), 1293-1298.

18. Wang, Z., "A new approach to enterprise information fusion: Choquet-fuzzy-integral-based neural network", in Third International Conference on Natural Computation (ICNC 2007), IEEE. Vol. 5, (2007), 212-216.

19. Arshadi, N. and Badie, K., "A compositional approach to solution adaptation in case-based reasoning and its application to tutoring library", in Proceedings of 8th German Workshop on Case-Based Reasoning. Lammerbuckel. Vol. 11, (2000).

20. Tayefeh Mahmoudi, M., Badie, K., Moosaee, M. and Souri, A., "A compositional adaptation-based approach for recommending learning resources in software development", *International Journal of Engineering*, *Transactions A: Basics,* Vol. 35, No. 7, (2022), 1317-1329. doi: 10.5829/IJE.2022.35.07A.11.

21. Wang, P., Zamora, J., Liu, J., Ilievski, F., Chen, M. and Ren, X., "Contextualized scene imagination for generative commonsense reasoning", arXiv preprint arXiv:2112.06318, (2021).

22. Mahmoudi, M.T., Badie, K., Kharrat, M., Khamaneh, S.B. and Khales, M.Y., "Content personalization in organizations via composing a source content model with user model", in IC-AI, (2008), 943-949.

23. Petty, M.D. and Weisel, E.W., Model composition and reuse, in Model engineering for simulation. 2019, Elsevier.57-85.

24. Lin, B.Y., Zhou, W., Shen, M., Zhou, P., Bhagavatula, C., Choi, Y. and Ren, X., "Commongen: A constrained text generation challenge for generative commonsense reasoning", arXiv preprint arXiv:1911.03705, (2019).

25. Sharma, A. and Kumar, S., "Machine learning and ontology-based novel semantic document indexing for information retrieval", *Computers & Industrial Engineering*, Vol. 176, (2023), 108940. https://doi.org/10.1016/j.cie.2022.108940

26. Wang, H., Du, J., Li, M. and Li, W., An ontology-based query system for university domain, in Advances in natural computation, fuzzy systems and knowledge discovery. 2021, Springer.632-643.

27. Quan, T.T., Hui, S.C. and Cao, T.H., "Ontology-based fuzzy retrieval for digital library", in Asian Digital Libraries. Looking

Back 10 Years and Forging New Frontiers: 10th International Conference on Asian Digital Libraries, ICADL 2007, Hanoi, Vietnam, December 10-13, 2007. Proceedings 10, Springer. (2007), 95-98.

28. Badie, K., Kharrat, M., Mahmoudi, M.T., Mirian, M.S., Ghazi, T.M. and Babazadeh, S., Ontology-driven creation of contents: Making efficient interaction between organizational users and their surrounding tasks, in User interface design for virtual environments: Challenges and advances. 2012, IGI Global.156-170.

29. Yager, R.R., "On ordered weighted averaging aggregation operators in multicriteria decisionmaking", *IEEE Transactions on Systems, Man, and Cybernetics*, Vol. 18, No. 1, (1988), 183-190.

30. Alcantud, J.C.R., Santos-García, G. and Akram, M., "Owa aggregation operators and multi-agent decisions with n-soft sets", *Expert Systems with Applications*, Vol. 203, (2022), 117430. https://doi.org/10.1016/j.eswa.2022.117430

Persian Abstract

چکیده

همجوشی اطلاعات متنی، به عنوان نوعی از همجوشی اطلاعات، برای آنان که علاقمند به استخراج و تولید محتواهای حاوی اطلاعات از میان متون موجود هستند، از اهمیت بسزایی برخوردار گردیده است. ایده اصلی که در پس همجوشی متن همانند هرنوع دیگری ازهمجوشی اطلاعات وجود دارد،ادغام بخشهایی از متون برگرفته از منابع مختلف است به قسمی که نتیجه حاصل از انسجام منطقی ای در راستای اهداف خاص مورد انتظار از متن برخوردار باشد.در این مقاله یک چارچوب فازی جهت تولید متن پیشنهاد می شود که برمبنای آن بخشهایی از متون مرتبط طوری با هم ادغام گردند که نیاز کاربر رابصورت قابل قبولی برآورده سازند. نکته اصلی در چارچوب پیشنهادی ما در خصوص همجوشی، فاصله میان طبقه نمونه متن از یکسو و بردار ویژگی های زیرمجموعه های مختلف از متون موجوداز سوی دیگر است. نتایج حاصل از آزمایش نشان می دهد که چارچوب پیشنهادی می تواند جایگزین مناسبی برای انجام همجوشی در مواردی باشد که هویت متون موجوداز وضوح کافی برخوردار نباشد. این امر منجر به تولید کارآمد متون جدید بر مبنای متون موجود می گردد.

International Journal of Engineering

Optimal Load Shedding for Voltage Collapse Prevention Following Overloads in Distribution System

S. Sundarajoo*, D. M. Soomro

Faculty of Electrical and Electronic Engineering, Universiti Tun Hussein Onn Malaysia (UTHM), Parit Raja, Batu Pahat, Johor, Malaysia

P A P E R   I N F O

A B S T R A C T

Load shedding is generally regarded as the final option to evade voltage collapse and blackout following major overloads. The traditional method of load shedding curtails random loads regardless of their importance until the system's voltage is improved. Shedding random loads without considering their priority will lead to power interruption in vital infrastructures. Hence, to improve the existing power system protection scheme, development of a more effective and efficient load shedding method is necessary. In this paper, an optimal under voltage load shedding (UVLS) method is proposed for optimum prediction of amount of load shed and the best location for load curtailment. Moreover, the proposed method is designed to maintain the vital loads in the system during the load shedding process. In this work, the stability index (SI) and feed-forward backpropagation neural network (FFBPNN) were adopted to avoid voltage collapse and blackout by mitigating voltage instability following overloads in distribution system. The performance of the proposed method to several overload scenarios is investigated. Case studies performed on the IEEE 33-bus system exposed significant robustness and performance of the recommended technique. Compared to other approaches, the proposed approach is efficient in counteracting under-shedding occurrence, enhancing the voltage profile, and improving the stability of the system, whilst maintaining vital loads in the system during load shedding.

doi: 10.5829/ije.2023.36.07a.04

1. INTRODUCTION

In the past several decades, many large-scale blackout incidents have occurred [1]. These incidents are not acceptable because they result in massive catastrophes to society's economic and social advancement. Protection measure via under voltage load shedding (UVLS) is the final and effective option to counteract a voltage instability situation [2]. Moreover, UVLS is used to prevent voltage collapse and power blackouts [3].

Various UVLS methodologies have been used to maintain system stability [4]. The trend of recent studies reflects the development of load shedding methodologies using computational intelligence (CI) methods. Using CI methods, nonlinear problems can be solved effortlessly. Consequently, many researchers have utilized CI methods in order to optimize the load shedding algorithm by minimizing the voltage drop and fulfilling all the constraints [5].

Singh et al. [6] optimized a load shedding problem based on voltage dependent load model, considering the stability constraints using black hole (BH) optimization. A metaheuristic algorithm known as moth swarm algorithm (MSA) was used by sayed et al. [7] to optimally solve a load shedding problem by minimizing the amount of load shed, reducing real power loss, and improving voltage profile. Another metaheuristic algorithm known as, improved moth flame optimization (IMFO), was applied by Sayed et al. [8] to lower the load shedding amount, enhanced the loadability of the network and prevent voltage collapse. Another UVLS method was proposed by Modarresi et al. [9] which has estimateds the load shedding amount based on the local measurements employing an adaptive neuro-fuzzy inference system (ANFIS).

A hybrid technique incorporating genetic algorithm (GA) and particle swarm optimization (PSO) to obtain the optimum amount of load to be shed for overloaded

Corresponding Author Institutional Email: he190076@siswa.uthm.edu.my (S. Sundarajoo)

systems was presented by Larik et al. [10]. To sum up, the major shared disadvantages of the aforementioned CI based load shedding frameworks were high computational time and pre-mature convergence. These drawbacks can result in non-optimal load shedding.

Cruz et al. [11], applied a reliability index, the system average interruption duration index, known as SAIDI, during load shedding optimization along with PSO to improve the reliability of distribution systems. Javadi and Amraee [12] presented a mixed integer programming (MIP), and loading margin based UVLS model to minimize the amount of load shedding. Tian and Mou [13] proposed a system analysis-based dispersed load curtailment framework in order to prevent voltage collapse by adopting a segmentation technique utilizing voltage control sensitivity. However, these papers did not consider the priority of load (i.e., vital, semi-vital, and non-vital) while applying the load shedding strategy. Thus, the performance of the aforementioned UVLS algorithms may not be adequate.

In order to address this issue, Sarwar et al. [14] used a mixed integer linear programming (MILP) method while considering the load priority and load ranking using voltage stability index. Similarly, by considering the load priority, a method to predict the minimum load shedding amount was reported by Mansouri et al. [15]. However, in the abovementioned papers, overload problems in the distribution system are ignored. Therefore, the effectiveness of these UVLS methods to prevent voltage collapse following overloads in distribution system may not be satisfactory.

From the discussion above, it can be noted that considerable efforts are accomplished to propose new UVLS frameworks. However, a substantial number of past works on load shedding schemes are developed for transmission systems, and only a scant number of past works are reported for distribution systems. Similarly, the voltage stability issues are ignored in most of the previous studies. It is worth noting that the distribution system is close to the electricity users [16]. Thus, distribution system needs utmost attention and robustness. Moreover, distribution system interacts with oversensitive consumers such as health care, industrial and digital loads. The most important aim of the present distribution system is to offer valuable and continuous electricity to the users [16]. Likewise, the electricity users expect the least number of blackouts [17]. Also, the present distribution systems are more severely overloaded to meet the growing load demand. Therefore, the distribution system's stability and protection should be improved.

To satisfy the aforesaid crucial but unaddressed inadequacies, this paper develops an UVLS scheme by adopting stability index (SI) and artificial neural network (ANN) to tackle overloaded situations and prevent voltage collapse in distribution systems. The proposed UVLS technique is applied on a well-known benchmark system, the IEEE 33-bus system with different overload scenarios. The main contributions of this work are three-fold:

- A comparatively minor fraction of the past studies adopted SI as an indicator to determine the stability of buses in the system. Similarly, meager interest has been given to ANN based approaches for UVLS. Therefore, SI and ANN are incorporated for the first time to be applied for a load shedding strategy. By doing so, the computational time is fast, and the result obtained is optimal. Also, this study may assist future works to implement SI and ANN for various optimal load shedding strategies.

- The proposed load shedding framework consists of three main modules, namely SI module (SIM), system load priority module (SLPM), and ANN module (ANNM), to perform optimal load shedding following overloads in the distribution system. By employing these modules, the proposed method can optimally determine the adequate load curtailment amount and the best location for load curtailment whilst preventing under-shedding.

- The proposed algorithm considers the priority of the loads in the system (vital, semi-vital, and non-vital) to avoid power interruption in critical infrastructures such as healthcare facilities during load shedding. This is achieved by using the load priority limit data of the network.

The rest of this article consists of the following sections: Section 2 concisely demonstrates the proposed strategy. Section 3 discusses the efficacy of the proposed technique by simulations on the IEEE 33-bus system. Lastly, section 4 concludes the research paper.

2. PROPOSED METHOD

In this work, the fundamental objectives in designing an optimal UVLS methodology are: (1) to enhance the voltage profile of the system by shedding an optimum amount of load, (2) to find the optimum location to shed the load, and (3) to prevent the vital loads in the system from being shed during the UVLS process. The outline of the suggested UVLS procedure is presented in a block diagram, as exhibited in Figure 1. The details of the modules used in this work are described in the following subsections.

2. 1. Stability Index Module   Generally, SI is used to assess the stability condition of the buses in a system [18]. SI will receive real-time voltage of sending and receiving bus, active and reactive power of receiving bus, and the resistance and reactance values of each line from the distribution system data and load flow analysis.

Accordingly, SI can be applied as an indicator in this work to determine the weak buses in the system that could lead to voltage collapse following overloads. By doing so, the optimum locations to shed the loads in the system can be determined. Hence, this paper incorporates the SI as a module known as SIM.

SI is derived from a standard two-bus distribution network, as presented in Figure 2. The equation of SI is stated in Equation (1):

$$SI_r = |V_s|^4 - \left[4(P_r x_{ij} - Q_s r_{ij})^2 - 4(P_r r_{ij} - Q_s x_{ij})^2\right]|V_s|^2 \tag{1}$$

where, SI_r is the receiving bus's SI value, the sending end bus voltage is V_s, the real power at the receiving bus and the reactive power at the sending bus are P_r and Q_s, respectively. The resistance and reactance of line $i - j$ are r_{ij} and x_{ij}.

Note that larger SI value is required for buses in the system to be stable against voltage instability and prevent voltage collapse when the load demand increases. As a rule of thumb, voltage collapse is expected to occur as the SI value approaches to zero. In order to improve the SI value to a satisfactory value, the system's loading must be reduced. This can be achieved by shedding some loads from certain buses in the system. The total amount of load to be curtailed from the optimum locations identified by the SIM should be determined by applying an appropriate technique. As mentioned earlier, ANN is used as the tool to find the optimum load shedding amount in this work.

2. 2. System Load Priority Module The SLPM is implemented to identify the type of loads in each bus of the system. As mentioned before, the proposed method curtails loads from the non-vital loads at first. Therefore, the type of loads (vital, semi-vital, and non-vital) are required to be known. This is done to prevent the proposed method from shedding vital loads in the network. The type of loads in each bus of the system is categorized according to the importance of the loads. The loads include residential loads, industrial loads, commercial loads, and uninterruptible loads. Uninterruptible loads include health care, navigation, military, and public service loads. The uninterruptible loads are vital loads and should be served without any disconnection. For those purposes, the proposed load shedding method will shed loads in each bus of the system according to the load priority category rather than shedding random loads in each bus. This will ensure the vital loads in each bus of the system to operate without any interruption.

2. 3. Artificial Neural Network Module ANN commences computations to imitate the learning procedures of the human brain [19]. ANN is one of the CI techniques that can be employed as a tool to achieve the optimal solution. As reported by Qiao et al. [20], ANN is the most capable algorithm to curtail loads, which are optimum. For that capability, ANN is implemented to find the optimum load shedding amount in this paper.

The ANNM implemented in this paper retrieves the load priority data from the SLPM. The ANNM plays a significant part in predicting the optimal amount of load to be curtailed from the optimum locations determined by the SIM. Input, hidden, and output layers are the three composition layers required to model a feed forward neural network with error backpropagation learning (FFBPNN).

The input layer is the first layer, the output layer is the last layer, and the layer in the middle of the input and output layer is the hidden layer. Every neuron in a particular layer is linked to each neuron in the following layer. In this paper, the type of training used to train the neural network is known as backpropagation.

Backpropagation is a type of supervised training. The FFBPNN model is designed with two inputs in the input layer and one output in the output layer. The inputs of the
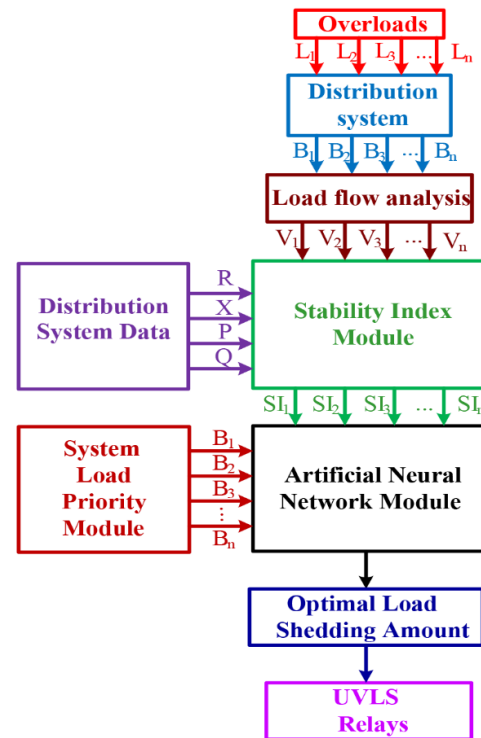
Figure 1. Proposed load shedding scheme outline
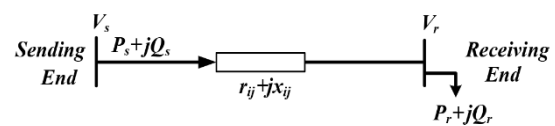
Figure 2. Two-bus system

FFBPNN model are comprised of post-overload active load demand at bus i, signified as P_i, and percentage of vital load requirement at bus i, represented as X_i. The hidden layers are comprised of one layer of nodes between input and output layers. The output layer of the network consists of one output which is the amount of load to be shed, denoted as P_{shed}. The neural network model used in this module is presented in Figure 3.

The Levenberg-Marquardt (LM) algorithm is utilized to solve the optimization problem in FFBPNN. LM algorithm is one of the most efficient algorithms for fast convergence rate and least error [13, 20]. The training data set is divided into three portions; 70% utilization for training, 15% for validation to decrease overfitting, and 15% for testing to achieve a decisive result. At times, the output of the network may distinguish from the targets after training, especially when the data set varies. Hence, stochastic gradient descent is employed in backpropagation to reduce the error in order to obtain a suitable network output.

The cross-validation methodology is adopted to achieve the finest training. By doing so, the most efficient FFBPNN is stimulated. One hidden layer is kept permanent, while the number of neurons is varied in each trial to obtain the minimum value of the mean square error (MSE). Throughout the procedure of determining the suitable total neurons in the hidden layer, approximately 50 tests were conducted starting from 1 to 50 neurons. Finally, the network with the minimum value of MSE is chosen to be used to obtain the optimal load shedding amount. Figure 4 represents the overall framework of the ANNM for the proposed method. The comprehensive methodology of the recommended approach is shown in the flowchart as presented in Figure 5.

3. SIMULATION RESULTS

To prove the efficacy of the suggested technique, the IEEE 33-bus system, a well-known distribution system,
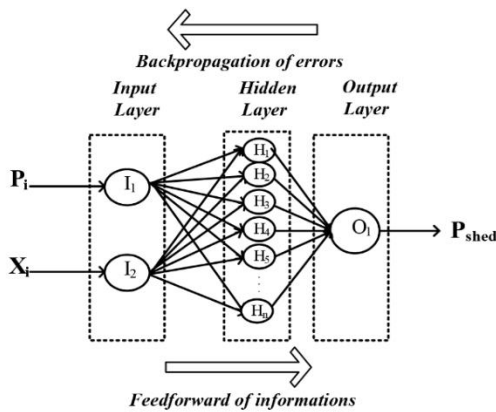
Figure 3. Neural-network model used in ANNM
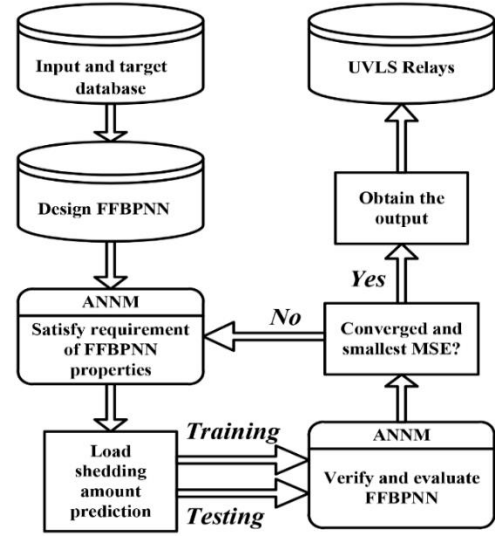
Figure 4. Overall framework of the ANNM
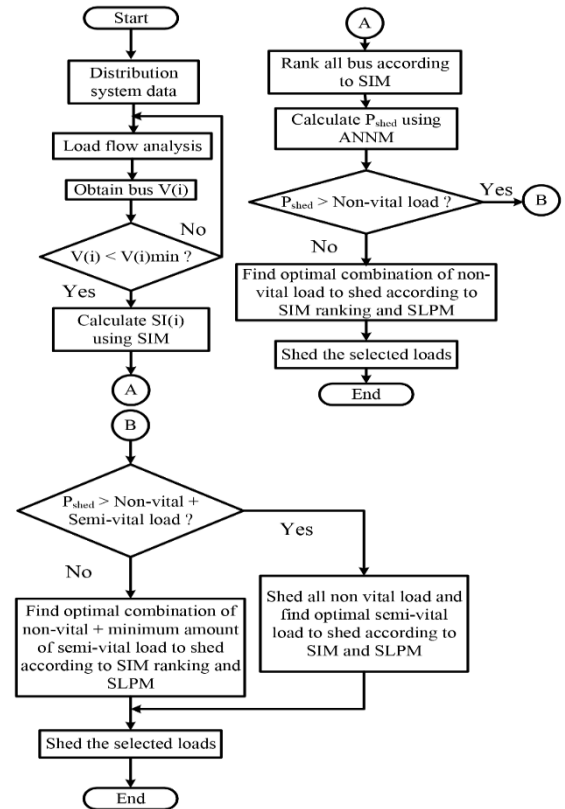
Figure 5. Flowchart of proposed method

is used, as shown in Figure 6. Baran and Wu [21] established the IEEE 33-bus system. The test network comprised 33 buses, 32 branches, and 33 constant loads. The 33-bus system operates at a rated voltage of 12.66kV. The bus data and line data of the 33-bus system were obtained from Montoya et al. [22]. In the original case, the total power demand of the system is 3.715MW

and 2.3Mvar. The load priority limits comprising the percentage of vital loads in each bus are listed in Table 1.

To assess the robustness of the proposed method following overloads, three scenarios, namely without overload, 25% overload, and 50% overload, are stimulated. Additionally, four case studies were conducted comprising the aforementioned scenarios to examine the system's response to the proposed load shedding method. The details of the case studies are listed in Table 2. Additionally, the proposed method will be compared with the conventional and PSO based load shedding method to verify the efficacy of the proposed technique at the end of this section.

The simulations are performed in MATLAB environment in a 64-bit computer with i7-4720 2.60GHz CPU and 8.0GB RAM.
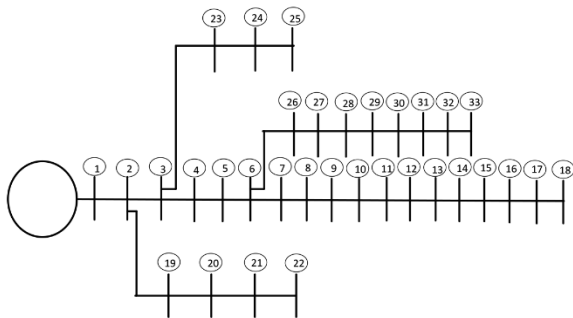
Figure 6. One line diagram of IEEE 33-bus system

TABLE 1. Vital load percentage for IEEE 33-bus

Bus	Percentage (%)	Bus	Percentage (%)
1	0	18	34
2	34	19	60
3	23	20	53
4	64	21	20
5	15	22	50
6	43	23	4
7	35	24	15
8	21	25	10
9	5	26	59
10	21	27	2
11	0	28	28
12	52	29	15
13	11	30	55
14	47	31	25
15	57	32	30
16	61	33	3
17	37		

TABLE 2. Case studies

Case	Description
1	Without load shedding
2	With proposed load shedding technique
3	With conventional load shedding technique
4	With PSO based load shedding technique

3. 1. Case 1: Without Load Shedding   The first case for the overload scenarios is without any load shedding method. As the system is exposed to massive overloads, the voltage profile and the SI values of every bus reduce, as shown in Figure 7. In this situation, the voltage profile of the system falls below the allowable limit (0.9 pu) for scenarios with an overload of 25% and 50%. Hence, it is clear that the network requires a load curtailment strategy to prevent voltage collapse and instability.

3. 2. Case 2: With Proposed Method   In this case, the proposed method is simulated. The ANN structure used in the proposed method is as presented in Table 3. The proposed method allows shedding of loads at weak buses according to the SIM, while the vital loads in every bus of the system are maintained according to the SLPM. The summary of the proposed UVLS results are presented in Table 4.

Furthermore, Figure 8 shows the voltage profile, the SI values, the percentage of load shed, and the amount of load shed. According to Figure 8, the system's voltage profile is guaranteed for every overload scenario, where the computed voltage of every bus in the system is above 0.92 pu, which is higher than the permissible voltage of 0.9 pu.

3. 3. Case 3: With Conventional Method   In this case, the conventional UVLS method was simulated using the voltage levels and the amount of load to be shed for every voltage level as listed in Table 5.
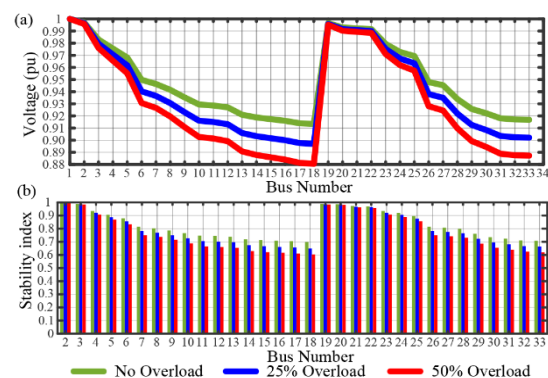
Figure 7. Without load shedding: (a) System voltage profile (b) System SI values

TABLE 3. Neural network training parameters

Parameter	Descriptions
Input layer	1
Input layer neurons	2
Hidden layers	1
Hidden layer neurons	10
Output layer	1
Output layer neurons	1
Layer 1 activation function	Tansig
Layer 2 activation function	Purelin
Performance function	Mean squared error (MSE)
Maximum epoch	1000
Maximum validation checks	6

TABLE 4. Proposed method results summary

Overload scenarios (%)	0%	25%	50%
Total load shed amount (MW)	0	1.18	2.10
Total load shed percentage (%)	0	0.25	0.38
Minimum voltage (pu)	0.91	0.92	0.921
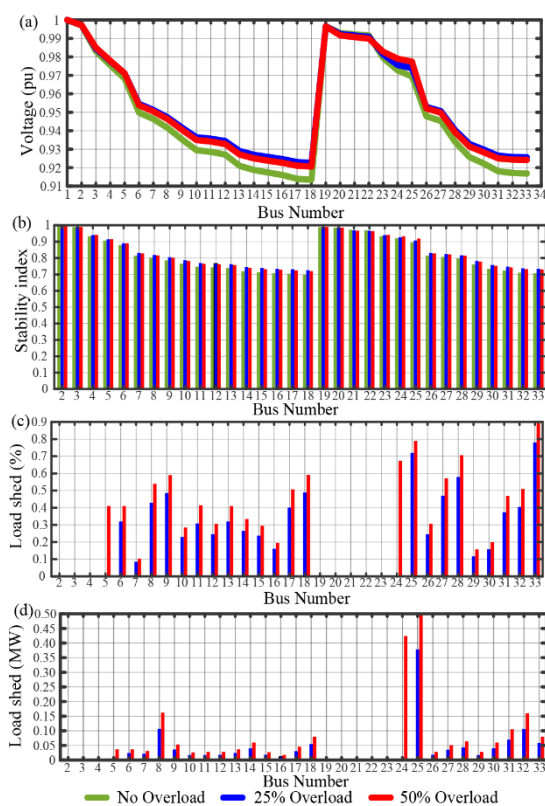
Figure 8. With proposed load shedding method: (a) System voltage profile (b) System SI values (c) Load shed percentage (d) Load shed amount

TABLE 5. Conventional load shedding stages

Stage	Voltage Threshold (pu)	Load Shedding Value (%)
1	0.9	20
2	0.88	20
3	0.86	10

The voltage profile, percentage of load shed, and the amount of load shed with the conventional method are shown in Figure 9, whereas Table 6 summarizes the results obtained using the conventional UVLS method. It is evident from Table 6 that the conventional method shed insufficient amount of load for each overload scenario. This condition is known as under-shedding, which leads to instability of the system and may result in voltage collapse and cascaded blackouts.

3. 4. Case 4: With PSO Method   In this case, one of the most employed and well-known CI methods, the PSO algorithm has been utilized for load shedding procedure. The PSO is used to obtain the optimal load shed amount. Minimization of load shedding amount is taken as the objective of the optimization model. By doing so, the
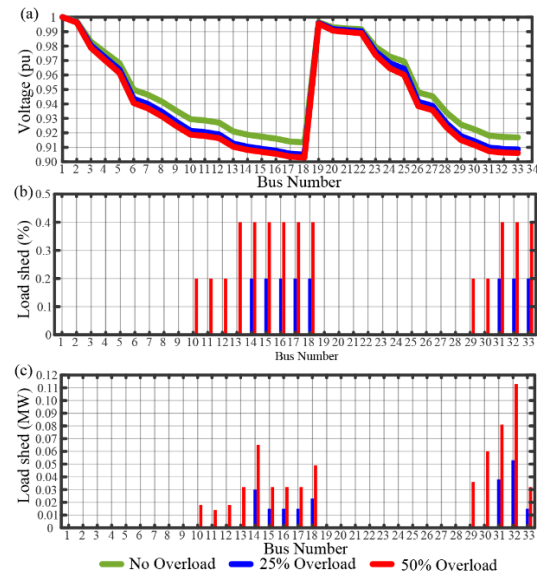
Figure 9. With conventional UVLS method: (a) System voltage profile (b) Load shed percentage (c) Load shed amount

TABLE 6. Conventional UVLS results summary

Overload scenarios (%)	0%	25%	50%
Total load shed amount (MW)	0	0.20	0.62
Total load shed percentage (%)	0	0.04	0.11
Minimum voltage (pu)	0.91	0.905	0.903

PSO based optimal load shedding method is simulated to be compared with the results achieved by the proposed approach for further validation. The voltage profile, load curtailment percentage, and the amount of load shedding obtained utilizing PSO based load shedding method are given in Figure 10. Table 7 summarizes the results obtained using that method. It can be noticed from Table 7 that the PSO based method also resulted in under-shedding and it failed to improve the voltage profile above the acceptable limit.

3. 5. Comparative Study Results   A feasible UVLS method should be capable of curtailing the mismatch amount of load and preserving the system voltage to prevent voltage collapse and blackout. The three different methods examined in this paper for scenarios of 25% overload and 50% overload are compared in this section as shown in Table 8.

It can be noticed from Table 8 that the amount of load shed by the conventional technique and the PSO technique are lower than the amount of power imbalance. This creates an under-shedding event due to the inadequate load shedding performed for the overload events. On the contrary, the proposed method does not suffer from under-shedding in every overload scenario. This is due to the ability of the proposed technique to find the load curtailment amount, optimally.
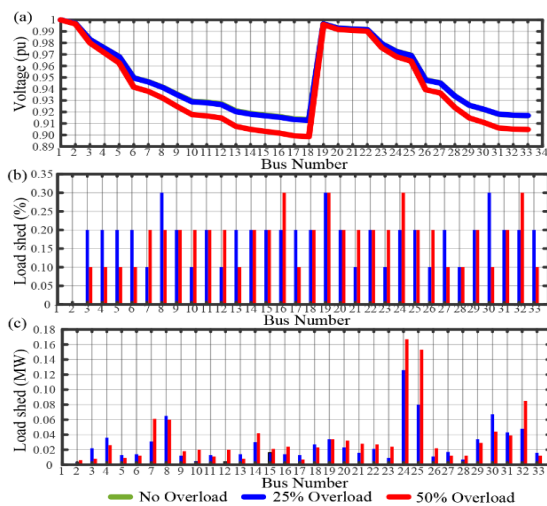
Figure 10. With PSO based load shedding method: (a) System voltage profile (b) Load shed percentage (c) Load shed amount

TABLE 7. PSO-UVLS results summary

Overload scenarios (%)	0%	25%	50%
Total load shed amount (MW)	0	0.89	1.10
Total load shed percentage (%)	0	0.19	0.20
Minimum voltage (pu)	0.91	0.913	0.89

TABLE 8. Comparative study results

Overload	Parameter	Proposed	PSO	Conventional
25%	Power imbalance (MW)	0.92	0.92	0.92
	Amount of load shed (MW)	1.18	0.89	0.20
	Under-shedding (MW)	-	0.03	0.72
	Minimum voltage (pu)	0.92	0.913	0.905
50%	Power imbalance (MW)	1.85	1.85	1.85
	Amount of load shed (MW)	2.10	1.10	0.62
	Under-shedding (MW)	-	0.75	1.23
	Minimum voltage (pu)	0.921	0.89	0.903

4. CONCLUSION

This paper proposed an optimal UVLS method to mitigate voltage collapse following overloads in distribution network. Some of the prominent features of the proposed method include, managing power imbalances, preventing under-shedding, and improving load shedding efficiency by maintaining vital loads during load shedding. The proposed method can determine the best location for load shedding using SIM. Furthermore, an intelligent FFBPNN-based method is designed to predict load curtailment amount efficiently using ANNM. On the other hand, the vital loads in the system were maintained according to the SLPM. The proposed approach was tested on the IEEE 33-bus test network and the results were compared with other approaches. The results from simulation unveiled that the proposed method can significantly prevent voltage collapse following overloads in distribution system.

5. ACKNOWLEDGEMENTS

6. REFERENCES

1. Sundarajoo, S., and Soomro, D. M. "Under voltage load shedding and penetration of renewable energy sources in distribution systems: a review." *International Journal of Modelling and Simulation*, (2022), 1-19. https://doi.org/10.1080/02286203.2022.2143191

2. Nemouchi, H., Tiguercha, A., and Ladjici, A. A. "An adaptive

decentralized under voltage load shedding in distribution networks." *International Transactions on Electrical Energy Systems*, Vol. 30, No. 11, (2020), e12592. https://doi.org/10.1002/2050-7038.12592

3. Maresch, K., Marchesan, G., Junior, G. C., and Borges, A. "An underfrequency load shedding scheme for high dependability and security tolerant to induction motors dynamics." *Electric Power Systems Research*, Vol. 196, (2021), 107217. https://doi.org/10.1016/j.epsr.2021.107217

4. Khamis, A., Khatib, T., Aishah, N. M., and Ridzuan, R. "A novel research clustering scheme using bibliometric analysis : A case study of global trend in electrical power system load shedding." *Iranian Journal of Science and Technology, Transactions of Electrical Engineering*, (2021). https://doi.org/10.1007/s40998-021-00430-z

5. Dreidy, M., Mokhlis, H., and Mekhilef, S. "Application of meta-heuristic techniques for optimal load shedding in islanded distribution network with high penetration of solar PV Generation." *Energies*, Vol. 10, No. 2, (2017), 150. https://doi.org/10.3390/en10020150

6. Singh, P., Arya, R., Titare, L. S., and Arya, L. D. "Optimal load shedding to avoid risks of voltage collapse using black hole algorithm." *Journal of The Institution of Engineers (India): Series B*, Vol. 102, (2021), 261-276. https://doi.org/10.1007/s40031-021-00543-3

7. Sayed, F., Kamel, S., Yu, J., and Jurado, F. "Optimal load shedding of power system including optimal TCSC allocation using moth swarm algorithm." *Iranian Journal of Science and Technology, Transactions of Electrical Engineering*, Vol. 44, (2020), 741-765. https://doi.org/10.1007/s40998-019-00255-x

8. Sayed, F., Kamel, S., Taher, M. A., and Jurado, F. "Enhancing power system loadability and optimal load shedding based on TCSC allocation using improved moth flame optimization algorithm." *Electrical Engineering*, Vol. 103, (2021), 205-225. https://doi.org/10.1007/s00202-020-01072-w

9. Modarresi, J., Gholipour, E., and Khodabakhshian, A. "New adaptive and centralised under-voltage load shedding to prevent short-term voltage instability." *IET Generation, Transmission & Distribution*, Vol. 12, No. 11, (2018), 2530-2538. https://doi.org/10.1049/iet-gtd.2017.0783

10. Larik, R. M., Mustafa, M. W., Aman, M. N., Jumani, T. A., Sajid, S., and Panjwani, M. K. "An improved algorithm for optimal load shedding in power systems." *Energies*, Vol. 11, No. 7, (2018), 1808. https://doi.org/10.3390/en11071808

11. Cruz, L. M., Alvarez, D. L., Al-Sumaiti, A. S., and Rivera, S. "Load curtailment optimization using the PSO algorithm for enhancing the reliability of distribution networks." *Energies*, Vol. 13, No. 12, (2020), 3236. https://doi.org/10.3390/en13123236

12. Javadi, M., and Amraee, T. "Mixed integer linear formulation for undervoltage load shedding to provide voltage stability." *IET Generation, Transmission & Distribution*, Vol. 12, No. 9, (2018), 2095–2104. https://doi.org/10.1049/iet-gtd.2017.1118

13. Tian, A., and Mou, X. "A network analysis-based distributed load shedding strategy for voltage collapse prevention." *IEEE Access*, Vol. 7, (2019), 161375-161384.

14. Sarwar, S., Mokhlis, H., Othman, M., Muhammad, M. A., Laghari, J. A., Mansor, N. N., Mohamad, H., and Pourdaryaei, A. "A mixed integer linear programming based load shedding technique for improving the sustainability of islanded distribution systems." *Sustainability (Switzerland)*, Vol. 12, No. 15, (2020). https://doi.org/10.3390/SU12156234

15. Mansouri, H. R., Mozafari, B., Soleymani, S., and Mohammadnezhad, H. "A new optimal distributed strategy to mitigate the phase imbalance in smart grids." *International Journal of Engineering, Transactions C: Aspects*, Vol. 33, No. 12, (2020), 2489-2495. https://doi.org/10.5829/ije.2020.33.12c.08

16. Murty, V. V. S. N., and Kumar, A. "Voltage regulation and loss minimization in reconfigured distribution systems with capacitors and OLTC in the presence of PV penetration." *Iranian Journal of Science and Technology, Transactions of Electrical Engineering*, Vol. 3, , (2020). https://doi.org/10.1007/s40998-020-00389-3

17. Zare, H., Khanalizadeh Eini, M., and Esmaeili, A. "Stabilization of voltage and current in the distribution networks using APF and TSC." *International Journal of Engineering, Transactions B: Applications*, Vol. 35, No. 5, (2022), 1064-1073. https://doi.org/10.5829/IJE.2022.35.05B.21

18. Danish, M. S. S., Senjyu, T., Danish, S. M. S., Sabory, N. R., Narayanan, K., and Mandal, P. "A recap of voltage stability indices in the past three decades." *Energies*, Vol. 12, No. 8, (2019), 1544. https://doi.org/10.3390/en12081544

19. Al-Ani, B. R. K., and Erkan, E. T. "A study of load demand forecasting models in electricity using artificial neural networks and fuzzy logic model." *International Journal of Engineering, Transactions C: Aspects*, Vol. 35, No. 6, (2022), 1111-1118. https://doi.org/10.5829/ije.2022.35.06c.02

20. Qiao, J., Wang, L., Yang, C., and Gu, K. "Adaptive levenberg-marquardt algorithm based echo state network for chaotic time series prediction." *IEEE Access*, Vol. 6, (2018), 10720-10732. https://doi.org/10.1109/ACCESS.2018.2810190

21. Baran, M. E., and Wu, F. F. "Network reconfiguration in distribution systems for loss reduction and load balancing." *IEEE Power Engineering Review*, Vol. 9, No. 4, (1989), 101-102. https://doi.org/10.1109/MPER.1989.4310642

22. Montoya, O. D., Gil-González, W., and Grisales-Noreña, L. F. "An exact MINLP model for optimal location and sizing of DGs in distribution networks: A general algebraic modeling system approach." *Ain Shams Engineering Journal*, Vol. 11, No. 2, (2020), 409-418. https://doi.org/10.1016/j.asej.2019.08.011

Persian Abstract

چکیده

کاهش بار به طور کلی به عنوان گزینه نهایی برای جلوگیری از فروپاشی ولتاژ و خاموشی پس از اضافه بارهای عمده در نظر گرفته می شود. روش سنتی کاهش بار، بارهای تصادفی را بدون توجه به اهمیت آنها تا زمانی که ولتاژ سیستم بهبود یابد، محدود می کند. ریزش بارهای تصادفی بدون در نظر گرفتن اولویت آنها منجر به قطع برق در زیرساخت های حیاتی می شود. از این رو، برای بهبود طرح حفاظتی سیستم قدرت موجود، توسعه یک روش کاهش بار موثرتر و کارآمدتر ضروری است. در این مقاله، یک روش بهینه کاهش بار تحت ولتاژ (UVLS) برای پیش‌بینی بهینه مقدار بار ریخته‌شده و بهترین مکان برای کاهش بار پیشنهاد شده است. علاوه بر این، روش پیشنهادی برای حفظ بارهای حیاتی در سیستم در طول فرآیند کاهش بار طراحی شده است. در این کار، شاخص پایداری (SI) و شبکه عصبی پس انتشار پیش‌خور (FFBPNN) برای جلوگیری از فروپاشی و خاموشی ولتاژ با کاهش ناپایداری ولتاژ به دنبال اضافه‌بار در سیستم توزیع، اتخاذ شد. عملکرد روش پیشنهادی برای چندین سناریو اضافه بار بررسی شده است. مطالعات موردی انجام شده بر روی سیستم ۳۳ گذرگاهی IEEE استحکام و عملکرد قابل توجه تکنیک توصیه شده را نشان داد. در مقایسه با سایر روش‌ها، رویکرد پیشنهادی در مقابله با وقوع کم‌ریزش، افزایش پروفیل ولتاژ، و بهبود پایداری سیستم و در عین حال حفظ بارهای حیاتی در سیستم در طول ریزش بار، کارآمد است.

International Journal of Engineering

J o u r n a l   H o m e p a g e :   w w w . i j e . i r

Energy Collector Based on Piezoelectric Nano Materials in the Power Supply System to Improve the Efficiency of Industrial Internet of Things (IIoT) for Industry 4.0

X. Kang*

College of Logistics Information, Henan Logistics Vocational College, Xinxiang, China

P A P E R   I N F O

A B S T R A C T

Due to the strong electromechanical coupling, small size and high sensitivity, piezoelectric nanomaterials have been widely used in generators, sensors and other fields. In this paper, the characteristics of energy collector in IIoT power supply system based on piezoelectric nano-materials are analyzed. PVDF piezoelectric nanofibers are prepared by electrospinning technology. The material and control chips are integrated into a bimodal piezoelectric energy collector. The effectiveness is analyzed experimentally. The experimental results show that the resonant frequency of energy collection varies with the length of the cantilever arm. When the length of the cantilever arm is 12mm, the installation error of 1.0mm length leads to 3.5% of the resonant frequency error. The optimal load of piezoelectric vibration collectors with different cantilever arms is 400K. The output power of CUB, BRG and BTG are 50.7 μ W 55.6 μ W and 51.8 μ W, respectively. At the same time, the working frequency band of energy collectors with various cantilever structures is 12Hz to 18Hz. The optimal excitation frequency is 16Hz. In summary, the energy collector of power system constructed by piezoelectric nano-materials proposed by many researchers has high efficiency, which can provide a quick solution for IIOT in Industry 4.0 and enhance the power generation mechanism. It is of great significance to the development of IIOT in practice.

doi: 10.5829/ije.2023.36.07a.05

1. INTRODUCTION

The mini energy collectors based on environmental energy acquisition and conversion technology have received extensive attention at industry 4.0 [1]. The micro-vibration energy collector converts the vibration energy in the environment into electric energy, which has the advantages of green environmental protection. The technology has the advantages of simple structure, low maintenance cost and small size. It has important practical value in wireless sensor network systems such as environmental safety and structural health monitoring and has become the potential research direction in the field of micro energy for industry 4.0. The vibration energy collector has a high-quality factor and high output performance during resonance, but the resonant frequency cannot be changed with the vibration frequency of the environment. The bandwidth is narrow.

It cannot work with the vibration environment with a large frequency variation. However, for a specific application environment, the vibration generally has some dominant frequencies. At these dominant frequencies, the vibration energy density is large, and the peak point is corresponding to the spectrogram. To maximize the output power of the micro-vibration energy collector, the resonant frequency must be consistent with the dominant frequency in the environment.

The Industrial Internet of Things (IIoT) is powered by traditional batteries. The battery life is limited and needs frequent replacement. This conventional technology increases environmental pollution as well. The energy collector supplies power to ultra-low-power microprocessor devices by extracting energy from the surrounding environment (such as wind, heat and vibration). Since the vibration energy collector has the characteristics of low cost and high power, it has attracted

the interest of researchers. At present, the vibration electromechanical conversion mechanism is mainly realized by three mechanisms of electrostatic field, electromagnetic field and piezoelectric energy. Among them, piezoelectric vibration energy collectors do not require additional power when converting mechanical energy to electrical energy. It has positives of easy fabrication, simple electromechanical structure and high power density. Therefore, the piezoelectric vibration energy collector became a hot area of research in the field of micro energy research for industry 4.0. The energy collector in the IoT power supply system can convert the surplus mechanical energy into electrical energy in the environment. It has the advantages of wide application range and high output voltage. It can supply power to low-power sensors [2]. However, most of the research on piezoelectric energy collectors focuses on the energy harvesting performance in the atmospheric environment, and the characteristic analysis has still to be further explored. In addition, traditional piezoelectric power generation materials such as ZnO still have problems such as high toxicity, poor flexibility or low mechanical durability, which restricts their practical application in the field of micro-nano-scale piezoelectric power generation in industry 4.0. Polyvinylidene fluoride (PVDF) is an organic piezoelectric material with excellent piezoelectric properties, good flexibility and biological phase fusion. PVDF piezoelectric nano fibers are prepared by electrospinning technology. The material can be applied to the energy collector in an IIoT power supply system based on piezoelectric nano materials, which is of great significance for improving collection performance and promoting the development of the IIoT [3]. The energy collector based on piezoelectric nanomaterials has attracted wide attention from researchers. This piezoelectric "Nano-generator" converts dynamic mechanical energy into a higher piezoelectric energy, producing a pulsed AC high-voltage output to the external circuit that can be used to drive low-power microelectronic devices and nano-sensor devices in industry 4.0 to promote IIoT. It has shown great potential for building self-powered systems.

Most of the research studies on piezoelectric nano materials, piezoelectric power generation devices and self-powered systems focus on the collection of energy generated during solid state contact. It is necessary to artificially input mechanical energy and control it to produce stable dynamic changes to achieve stable continuous electric pulse output [4]. The spontaneous acquisition should also be achieved along with the continuous electric pulse. Compared with the air flow in an open environment [5], the microfluidic chip technology can control the gas phase or liquid phase fluid in a smaller enclosed space. Therefore, it is an ideal platform for constructing micro-nano-scale power supply systems. The challenge is the assembly of piezoelectric materials in the chip and the oscillation under the action of micro fluids to construct the microfluidic energy collectors. In addition, it has also been widely used in the manufacture of masks. In the modern medical market, this material can effectively reduce the harm of airborne virus transmission [6]. In the nano biosensor, it also effectively reduces the impact of plant pathogens on crop productivity [7]. During COVID-19, nanomaterials played an important role in the medical Internet of Things industry, effectively improving the performance of biosensors [8].

The energy collector is usually composed of a cantilever beam and a mass, which is a typical second-order vibration system. The resonant frequency is determined by the stiffness of the cantilever beam, the equivalent mass of the system and the pre-stress. The commonly used adjustment methods include cantilever beam length adjustment, pre-stress adjustment and mass adjustment. The cantilever beam length adjustment method is simpler [9]. However, for the mini energy collector of a micro-electromechanical system, once the length of the cantilever beam cannot be changed after the process is completed, other adjustment methods can be used. In addition, smart masks driven by the nano Internet of Things can effectively resist hazardous substances in the air, so as to protect human health. At the same time, the nano Internet of Things has inspired the emergence of intelligent plant pathogen diagnosis biosensors, making them develop towards the fifth generation of intelligent biosensors based on 2D MXenes, and gradually being applied to hospitals. It is worth noting that by 2021, the global market scale of the nano Internet of Things has reached 38.8 billion yuan, with a huge market scale and broad prospects. However, there is still a gap in the scale of the current nano Internet of Things market in China, which is mainly reflected in the investment of private capital. There are also gaps in the corresponding research. The research on nanotechnology in China is still in infancy, and there is still a big gap between China and foreign countries.

1. 1. Related Work   To produce dynamic changes to achieve stable electric pulse output, Hao et al. [6] have assembled an airflow conditioning structure and combined it with a piezoelectric power generation device. The spontaneous pulse without interference in the mechanical energy of the fluid form can produce a stable electrical output. This result is of great significance for promoting piezoelectric power generation devices and their applications in industry 4.0 for self-powered systems. Almonacid et al. [10] have changed the pre-stress of the cantilever beam by magnetic attraction and repulsive force. The resonance frequency is adjusted between 67.6-98Hz, but the structure is somewhat complicated. Zhuang et al. [11] have processed the cantilever beam using MEMS technology, and printed the colloidal mixture of zinc particles. By changing the mud concentration and viscosity at the resonant

frequency of 0.1, Hz can be changed at a minimum, but the operation is difficult. Wang et al. [12] have changed the centroid of the mass by rotating the screw on the mass to realize the adjustment of the resonant frequency of the device. The screwing and unscrewing of the screw can increase or decrease the resonant frequency. The result can be directly adjusted in the range of 130-180 Hz for generating quick power.

Many scholars have done a lot of research work to improve the performance of piezoelectric energy collectors for industry 4.0. Lu et al. [13] have used the method of optimizing parameters to establish mathematical theoretical models to broaden the frequency. But they ignore the relationship between internal impedance and optimal load impedance of energy collectors. It does not accurately indicate the nature of maximizing output power. Abasian and Tabesh [14] have studied broadband by using the method of adjusting the frequency. However, this kind of situation can only work when the frequency changes slowly. The accuracy of the frequency regulator is higher, and the intelligent micro-regulator is difficult to implement. Arunkumar et al. [15] have introduced the dynamic amplifier to build the mathematical model to study the broadband piezoelectric energy collector, but it ignores the electromechanical coupling effect of the energy collector.

Xie at al. [16] have used dynamic amplifiers to determine the electromechanical model and studied the effects of dynamic amplifiers on output power, but they ignored the effects of system damping and load resistance on system performance. In response to the above drawbacks, the characteristics of the energy collector in the IoT power supply system based on piezoelectric Nano materials are analyzed. The prepared PVDF Nano fibers are used to construct the piezoelectric energy collector in the IoT power supply system. The characteristics are analyzed effectively by the characteristic analysis method, which provides a basis for improving the performance of the piezoelectric energy collector.

There is a scope for further innovations to generate quick power for Industrial IoT and for industry 4.0, Hence, the energy collector based on piezoelectric Nano materials in the power supply system is proposed in this paper.

1. 2. Research Contributions   In this paper, the author has described PVDF piezoelectric Nano fibers.

By using electrospinning technology, these PVDF piezoelectric Nanofibers are prepared, which are then applied to the energy collector of the IoT power supply system to analyze the features of the energy collector. This concept assists in improving the performance of the piezoelectric energy collector.

Piezoelectric Energy Collector Modeling and theoretical concepts are discussed in the paper. The

distributed parameter model and Single-degree-of-freedom model are also analyzed.

To analyze the characteristics of the vibration energy collector, a single-degree-of-freedom model is used.

The characteristics of energy collectors in power supply systems based on piezoelectric nanomaterials are discussed with three topologies, including CUB (uniform cantilever beam structure), BRG (the non-uniform cantilever beam structure with rectangular grooves) and BTG (the non-uniform cantilever beam structure with triangular grooves).

The results show that the output voltage and performance of the non-uniform cantilever beam structure (BRG) with rectangular grooves is significantly higher than that of CUB and BTG under different load conditions. The output power is much larger than that of the uniform cantilever beam structure.

The specific latest technology is shown in Figure 1.

The research is structured into 5 sections. The proposed research is described in section 2. Results are discussed in section 3. Development of the Industrial IoT's and devices are discussed in section 4. The outcome is discussed in section 5 as conclusions.

2. PROPOSED METHOD

2. 1. Preparation of PVDF Nanofibers   The PVDF piezoelectric nano fibers are prepared through electrospinning technology. The material is applied to the energy collector of the IoT power supply system based on piezoelectric nano materials to analyze the features of the energy collector. The PVDF powder (molecular weight 534000, Sigma-Aldrich) is used as a precursor. Acetone and N-dimethylformamide (DMF, both purchased from Sinopharm Group) are used to configure an electrospinning precursor. Microelectrodes and microfluidic chip abrasives are prepared using AZ5214-ESU9-GM1070 photoresist. Microfluidic chips are assembled using polydimethylsiloxane two-component silicone rubber (PDMS, Sylgard 184).

DMF and acetone are mixed in a ratio of 3:7 by volume and stirred uniformly. The concentration of the PVDF precursor fluid is configured as needed. A certain amount of PVDF powder is weighed, mixed with the
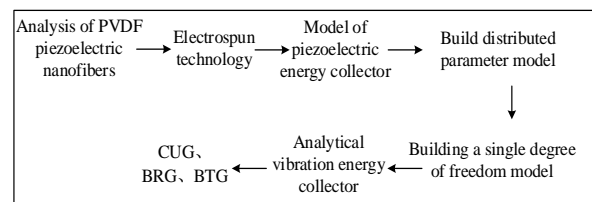
Figure 1. Schematic diagram of the overall concept and corresponding technologies of the research organization of the paper

mixture of DMF and acetone. It is heated and stirred for 2 hours at 60°C to obtain the clear transparent liquid as the electrospinning precursor solution. The precursor fluid is drawn into the syringe and the syringe is mounted on a microinjection pump (Longerpump TJP-3A/W0109-1B). The syringe needle is joined to the positive pole of the DC voltage source, and the two aluminum foils attached to the receiving plate are joined to the negative pole of the DC voltage source [17]. The direction of the needle is perpendicular to the surface of the receiving plate and the distance is 15 cm. Thereafter, spinning is carried out under the conditions of a voltage of 13 kV, a propulsion speed of 50 L/min, an ambient temperature and humidity of 35°C and 30% RH, respectively. The PV wafer is attached to the parallel aluminum foil of the receiving plate to receive PVDF nanofibers. The spinning time is 30 min. After the end of the spinning, the substrate covered with the PVDF nanofibers is taken out and placed in a drying oven at 80°C for 1h to remove excess solvent. The obtained white fiber membrane is the prepared PVDF Nanofiber.

2. 2. The Construction of Piezoelectric Energy Collector and Theoretical Model

The prepared PVDF nanofibers are applied to an energy collector of an IoT power supply system. The structural diagram of the piezoelectric vibration energy collector in the IoT power supply system is shown in Figure 1. The entire energy collector consists of the single-degree-of-freedom piezoelectric bimorph cantilever system with a concentrated mass M_t at the end and the elastic-amplifier system consisting of a spring-mass-damping. The piezoelectric cantilever system consists of the metal substrate, the bimorph (integrated by piezoelectric nanofibers and a control chip), the terminal concentrated mass M_t, and the load circuit. The bimorphs PZT1 and PZT2 are bonded to the upper and lower surfaces of the metal substrate by epoxy resin. They are polarized in the thickness direction [18]. The polarization directions are opposite (as shown in Figure 2 "↓" and "↑"). They are connected in series to the applied load resistor R_L. The resistance is the equivalent impedance of the AC-DC circuit, filter circuit, and resistor R connected to the electrical output of the energy collector. The change in load resistance R_L reflects the change in the equivalent impedance at the output.

The Elastic Amplifier system consists of a spring mass damping system, with mass, stiffness and damping coefficients of M_b, K_b and C_b, respectively. The left end of the piezoelectric bimorph cantilever is fixed to the mass M_b of the elastic amplifier. The elastic amplifier is mounted on the foundation. y is the fundamental vibration displacement. i is the current flowing through the load resistor R_L. Through the elastic amplifier
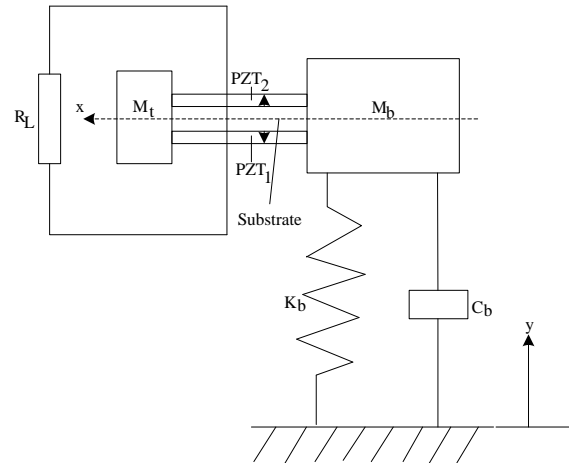
Figure 2. Piezoelectric cantilever vibration energy harvester structure

system, the vibration generated by the foundation is amplified and transmitted to the piezoelectric bimorph cantilever system. It amplifies the bending vibration displacement of the piezoelectric bimorph cantilever system to improve the output capacity of the energy collector.

2. 3. Theoretical Models

The theoretical model of cantilever beam-mass block structure has distribution parameter model and single degrees of freedom model. The distributed parameter model requires an equation to calculate the frequency. This process is complicated and has high precision. In the actual operation process, because of installation error in the dimensions of the piezoelectric cantilever beam, the distributed parameter model also causes an error in the resonant frequency of the structure.

The single-degree-of-freedom model simplifies the structure into a spring-mass system. The single-degree-of-freedom model is used to analyze the characteristics of the vibration energy collector. The single degree of freedom model of the vibration energy collector is shown in Figure 3.
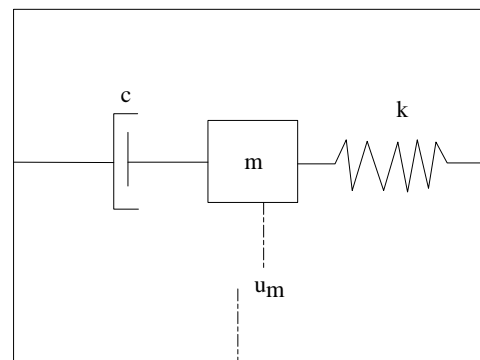
Figure 3. Single degree of freedom equivalent model

The cantilever beam is equivalent to the spring with a spring constant k. The system mass m is the sum of the mass m_0 and the equivalent mass m^* of the piezoelectric cantilever. Where, $m^* = \dfrac{33}{140} m_b$. m_b is the mass of the cantilever beam. The damping coefficient c of the system includes mechanical damping and electrical damping, which is approximately equivalent to linear viscous damping [8]. The vibration Equation (1) is as follows:

$$m\ddot{u}_m + c\dot{u}_m + k u_m = ma \tag{1}$$

where u_m is the displacement of the centroid in the z direction. a is the environmental acceleration.

The resonant frequency of the vibrating energy collector is given in Equation (2).

$$f = \frac{1}{2\pi}\sqrt{\frac{k}{m}} \tag{2}$$

By changing the mass m, the adjustment of the structural resonance frequency can be achieved [19]. In the equilibrium state, the concentrated force F_m is exerted by the centroid of the mass. The elastic restoring force $F = -k u_m$ of the cantilever is balanced.

The displacement $u(x)$ of the cantilever beam is shown in Equation (3):

$$u(x) = \frac{F_m}{6EI} x^2 \left[3(l + l_m/2) - x \right] \quad x \in [0,l] \tag{3}$$

where EI is the section bending stiffness of the cantilever beam; l and l_m are the length of the cantilever beam and the mass. The centroid displacement of the mass is shown in Equation (4):

$$u_m = u(l) + \frac{l_m}{2}\frac{\partial u(x)}{\partial x}\Big|_{x=l} \tag{4}$$

The elastic coefficient of the cantilever beam can be obtained from the mechanical equilibrium relationship as given in Equation (5).

$$k = -\frac{F}{u_m} = \frac{12EI}{4l^3 + 6l^2 l_m + 3l l_m^2} \tag{5}$$

2. 4. Characteristics of Energy Collector (EC)
The piezoelectric EC theoretical model is used to analyze the characteristics of the energy collector. The characteristics are based on energy collected, voltage amplitude, motion displacement and output voltage. This sub-section derives the EC characteristics through mathematical modeling.

The energy collector output voltage amplitude and phase angle expression are given in Equations (6) and (7).

$$V = \frac{U\omega^2}{\kappa\sqrt{\left(\lambda_e^2(A) - \omega^2\right)^2 + 4\delta_e^2(A)\omega^2}} \tag{6}$$

$$\vartheta_V = \tan^{-1}\left[-\frac{2\delta_e(A)\omega}{\lambda_e^2(A) - \omega^2}\right] + \tan^{-1}\frac{a_3}{\lambda} \tag{7}$$

where, $\delta_e(A)$ represents the attenuation coefficient of the amplitude function of piecewise linear piezoelectric system with single degree of freedom. $\lambda_e(A)$ represents the equivalent linear natural frequency of a single-degree-of-freedom piecewise linear piezoelectric system. $\kappa = \sqrt{a_3^2 + \lambda^2}/(a_2\lambda)$ represents the proportional parameter between the system's motion displacement and the output voltage.

Considering the proportional relationship between the output voltage of the energy collector and the motion displacement [20], the displacement solution characteristics of the energy collector are first determined. Assuming that the motion displacement kinetic singularity of the energy collector dynamic differential equation is (A_0, ϑ_0), the expressions of the energy collector's displacement and the initial phase angle versus time are given in Equation (8).

$$\begin{cases} \dfrac{dA}{dt} = -\dfrac{U\omega^2}{2\lambda}\sin\vartheta - \delta_e(A)A \\[2ex] \dfrac{d\vartheta}{dt} = -\dfrac{U\omega^2}{2\lambda A}\cos\vartheta + \lambda_e(A) - \omega \end{cases} \tag{8}$$

The singularity (A_0, ϑ_0) corresponding to the steady-state motion needs to satisfy the following relationship as given in Equations (9) and (10).

$$-\frac{U\omega^2}{2\lambda}\sin\vartheta_0 - \delta_e(A_0)A_0 = 0 \tag{9}$$

$$-\frac{U\omega^2}{2\lambda A_0}\cos\vartheta_0 + \lambda_e(A_0) - \omega = 0 \tag{10}$$

To analyze the characteristic of the output voltage cycle of the EC [21], a small amount of disturbance $(\Delta A_0, \Delta \vartheta_0)$ is applied to the stable point of the energy collector. The expression is given in Equation (11).

$$\begin{cases} A = A_0 + \Delta A \\ \vartheta = \vartheta_0 + \Delta\vartheta \end{cases} \tag{11}$$

Equation (9) is substituted into Equation (11) to obtain Equation (12).

$$\begin{cases} \dfrac{dA_0}{dt} + \dfrac{d(\Delta A)}{dt} = -\dfrac{U\omega^2}{2\lambda}\sin(\vartheta_0 + \Delta\vartheta) - \delta_e(A_0)(A_0 + \Delta A) \\[2ex] \dfrac{d\vartheta_0}{dt} + \dfrac{d(\Delta\vartheta)}{dt} = -\dfrac{U\omega^2}{2\lambda(A_0 + \Delta A)}\cos(\vartheta_0 + \Delta\vartheta) + \lambda_e(A_0) - \omega \end{cases} \tag{12}$$

where, $\dfrac{dA_0}{dt}$ and $\dfrac{d\vartheta_0}{dt}$ are substituted into Equation (12), and the results are subjected to Taylor series expansion processing. Considering that ΔA and $\Delta\vartheta$ are small

disturbances, the higher order values of ΔA and $\Delta \vartheta$ are negligible relative to the one-time term. Therefore, only the ones of ΔA and $\Delta \vartheta$ are retained, and the expressions of $\dfrac{d(\Delta A)}{dt}$ and $\dfrac{d(\Delta \vartheta)}{dt}$ are show in Equation (13).

$$\begin{cases} \dfrac{d(\Delta A)}{dt} = \left(-\delta_e(A_0)\right)\Delta A + \left(-\dfrac{U\omega^2}{2\lambda}\cos\vartheta_0\right)\Delta\vartheta \\ \dfrac{d(\Delta\vartheta)}{dt} = \left(-\dfrac{U\omega^2}{2\lambda A_0^2}\cos\vartheta_0\right)\Delta A + \left(-\dfrac{U\omega^2}{2\lambda A_0}\sin\vartheta_0\right)\Delta\vartheta \end{cases} \qquad (13)$$

To obtain the characteristic criteria of increments ΔA and $\Delta \vartheta$, the expression including excitation frequency ω and steady-state motion singularity A_0 is used to replace $\dfrac{U\omega^2}{2\lambda}\cos\vartheta_0$ and $\dfrac{U\omega^2}{2\lambda}\sin\vartheta_0$, as shown in Equation (14).

$$\begin{cases} \dfrac{d(\Delta A)}{dt} = -\delta_e(A_0)\Delta A + \left(\omega - \lambda_e(A_0)\right)A_0\Delta\vartheta \\ \dfrac{d(\Delta\vartheta)}{dt} = \left(\omega - \lambda_e(A_0)\right)\dfrac{1}{A_0}\Delta A - \delta_e(A_0)\Delta\vartheta \end{cases} \qquad (14)$$

The characteristic Equation (14) is derived by Equations (15) to (17).

$$\begin{vmatrix} C_1 - i & C_2 \\ C_3 & C_4 - i \end{vmatrix} = \begin{vmatrix} -\delta_e(A_0) - i & \left(\omega - \lambda_e(A_0)\right)A_0 \\ \left(\omega - \lambda_e(A_0)\right)\dfrac{1}{A_0} & -\delta_e(A_0) - i \end{vmatrix} = 0 \qquad (15)$$

Then

$$p = -(C_1 + C_4) = 2\delta_e(A_0) \qquad (16)$$

$$q = (C_1 C_4 - C_2 C_3) = \delta_e^2(A_0) - \left(\omega - \lambda_e(A_0)\right)^2 \qquad (17)$$

The characteristic equation of Equation (15) can be derived by Equation (18).

$$i^2 + pi + q = 0 \qquad (18)$$

At the same time, the value of the discriminant Δ can be obtained as in Equation (19).

$$\Delta = p^2 - 4q = \left(2\delta_e(A_0)\right)^2 - 4\left(\delta_e^2(A_0) - \left(\omega - \lambda_e(A_0)\right)^2\right) \\ = 4\left(\omega - \lambda_e(A_0)\right)^2 \geq 0 \qquad (19)$$

Based on the theory of motion stability, since the value of the discriminant Δ is always greater than or equal to zero, the characteristics of the energy collectors is determined by the value of p and q.

When $q < 0$, the two roots of Equation (18) are real roots and different signs. The singularity at this time is unstable, and the steady state motion of the energy collector cannot be achieved [22]. When $q > 0$ and $p > 0$, the singularity is stable, and the steady state motion of the energy collector can be achieved. At the same time, since $p = 2\delta_e(A_0)$ is the equivalent attenuation coefficient of the energy collector amplitude, indicating that the positive damping $p > 0$ is always true. Therefore, the piecewise linear system stability condition is given in Equation (20).

$$q = \delta_e^2(A_0) - \left(\omega - \lambda_e(A_0)\right)^2 > 0 \qquad (20)$$

Combined with Equation (19), the relationship between the output voltage and the motion displacement of the energy collectors is $V = \dfrac{a_2\lambda}{\sqrt{a_3^2 + \lambda^2}}$. The branch characteristics of the energy collector's output voltage amplitude-frequency curve are analyzed.

3. RESULTS

3. 1. Experimental Environment

PVDF piezoelectric Nano fibers prepared by electrospinning technology are used to construct energy collectors in piezoelectric nano material-based IoT power supply systems. The characteristic test instrument of the energy collectors in the constructed piezoelectric nano material-based IoT power supply system is shown in Figure 4.

The energy collector is mounted on the exciter. The sinusoidal signal generated by the signal generator drives the exciter through the power amplifier. The data acquisition module acquires the signal of the acceleration sensor. At the excitation acceleration of 6m/s², the frequency is swept from small to large. The output voltage of the collector is measured by an oscilloscope, and the output voltage at resonance maximized. The resonance frequency of the collected vibration energy collector varies with the length of the cantilever beam as shown in Figure 5.

3. 2. Experimental Observations

From the experimental results in Figure 5, the theoretical

Figure 4. Piezoelectric micro-vibration energy harvester physical map
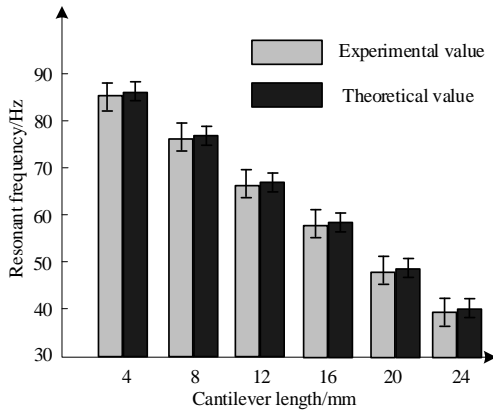
Figure 5. Vibration energy collector resonant frequency with cantilever beam length results

calculation results of the single degree of freedom model established in this paper are slightly higher than the experimental measurements. The error is extremely small. The main reason for the error is that the bending moment of the cantilever beam and the rotation effect of the mass are not considered in the single degree of freedom model. It is not suitable for the characteristic analysis of the mass collector and the short cantilever beam structure energy collector. In addition, the looseness of the base to the cantilever beam causes the increase in the effective length of the cantilever beam. When the length of the cantilever beam is 12 mm, an installation error of 1.0 mm length will cause an error of 3.5% of the resonance frequency.

To effectively analyze the characteristics of energy collectors in IoT power supply systems based on piezoelectric nano materials, the energy collector characteristics of three topologies with CUB, BRG and BTG are studied. When the excitation frequency is 11 Hz and the acceleration is $6m/s^2$, the voltage effective values of the three piezoelectric vibration energy collectors vary with load, as shown in Figure 6.
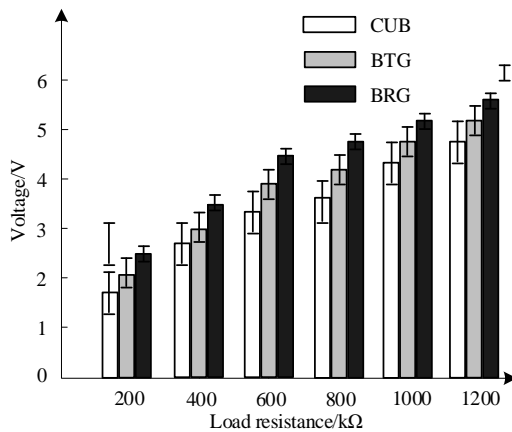
From Figure 6, the output voltage of the non-uniform cantilever beam structure (BRG) with rectangular grooves is significantly higher than that of CUB and BTG under different load conditions. This shows that BRG with rectangular grooves outperforms the other two topological energy collectors.

When the excitation frequency is 11 Hz and the acceleration is $6m/s^2$, the output power of the three piezoelectric vibration energy collectors varies with load in Figure 7.

From the experimental results in Figure 7, the optimal load of the piezoelectric vibration collectors of different cantilever structures is 400 K, but their output powers are different. The uniform cantilever beam structure (CUB), the non-uniform cantilever beam structure (BRG) with rectangular grooves, and the non-uniform cantilever beam structure (BTG) with triangular grooves have output powers of 50.7 μW, 55.6 μW and 51.8 μW, respectively. The experimental results show that the output of the piezoelectric vibration energy collector of the non-uniform cantilever beam structure with grooves is high. Among the cantilever beams with different topologies, the non-uniform cantilever beam structure with rectangular grooves has the best performance. The output power is much larger than that of the uniform cantilever beam structure.

The characteristics of piezoelectric vibration energy collectors are studied and the relationship between the output power and the excitation frequency is explored experimentally. When the excitation amplitude is 1mm, the load impedance is 250 kΩ. The excitation acceleration is $6m/s^2$. The relationship between the output voltage and the excitation frequency of the three kinds of topological piezoelectric vibration energy collectors is shown in Figure 8.

When the excitation amplitude is 1mm, the load impedance is 250 kΩ, and the excitation acceleration is $6m/s^2$. The relationship between the output power and the excitation frequency of the three topological piezoelectric vibration energy collectors is shown in Figure 9.

Figure 6. Output voltage varies with load
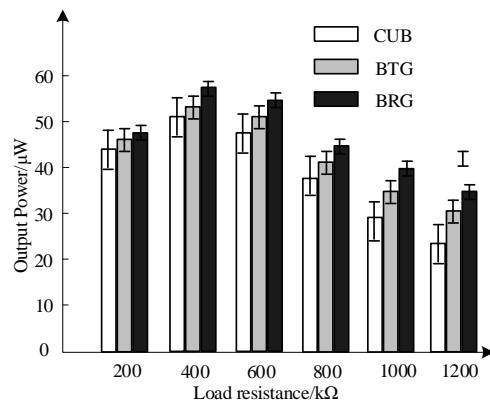
Figure 7. Output power varies with load
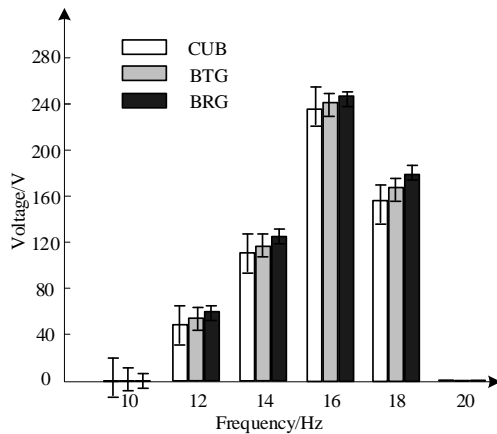
Figure 8. Output voltage varies with load
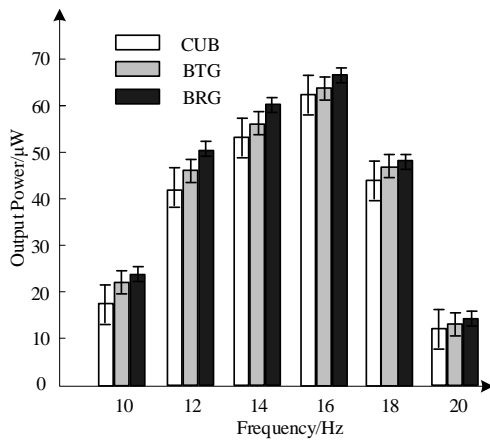
Figure 9. Output power varies with load

It can be seen from the experimental results of Figures 8 and 9 that the operating frequency of the piezoelectric vibration energy collector is between 12 Hz and 18Hz. The working bandwidth is 6 Hz. In the entire operating frequency band, the output voltage and output power of the piezoelectric energy collector with the rectangular and triangular grooved beam topology is always greater than the power of the piezoelectric energy collector of the uniform beam topology. Among the different structural grooves, the performance of the rectangular groove is the best. The optimum excitation frequency of all piezoelectric vibration generators is 16 Hz. The maximum output power at the optimum excitation frequency is 60.5 μW, 62.4 μW and 66.1 μW, respectively. The experimental results show that the energy collector output voltage and output power based on the rectangular slot are significantly larger than the uniform cantilever beam structure. The output power of the energy collector based on different topologies is related to the excitation frequency.

The above experimental results show that the performance of the piezoelectric energy collector based

on the non-uniform thickness of the cantilever beam is better than that of the piezoelectric energy collector based on the uniform cantilever beam structure. The non-uniform cantilever beam with rectangular groove has the best performance. The energy collectors of various cantilever structures have an operating frequency band of 12Hz to 18Hz and an optimum excitation frequency of 16Hz. The characteristics of the single-degree-of-freeness energy collector under the best matching resistance are shown in Table 1.

The experimental results in Table 1 are compared with those of the single-free elastic system piezoelectric cantilever energy collector made by Wang et al. [12]. The piezoelectric crystal materials have different characteristics, and the resonant frequencies are different between the short-circuit state and the open-circuit state. However, the electrical output characteristics and vibration characteristics of the two have the same trend with the frequency and the output power with the load resistance. The validity of the energy collector characteristic analysis in the IoT power supply system based on piezoelectric nanomaterials is verified.

4. DISCUSSION

The development of the Industrial IoT is the most promising technology for the promotion of industry 4.0 and global market opportunity. In 2020, there are more than 30 billion IoT devices in the industry supporting IIoT worldwide. Ideally, billions of smart devices will connect to the wireless networks through IIoT. The battery life of devices is a significant topic to study, because installing a battery in a small device is not feasible in all circumstances. In addition, battery maintenance and replacement costs are very high.

In recent years, the development of the IIoT has attracted a large amount of investment, especially for improving the battery life of the devices. However, generating power quickly for billions of devices is a challenging game. Researchers have proposed innovative

TABLE 1. Comparison of energy harvester characteristics under the best matching resistance

Resistance	Node	Single degree of freedom
		Peak
43.4 kΩ	Working frequency/Hz	44.7
	Output Power/mW	444.9
91.8 kΩ	Working frequency/Hz	45.4
	Output Power/mW	436.3
140.2kΩ	Working frequency/Hz	46.1
	Output Power/mW	427.7
	Bandwidth/Hz	6

solutions for this problem. Although traditional battery power supplies can solve the power supply problem, they must be purchased, maintained, and post-processed. When the equipment is installed in a remote location, it is more difficult to maintain the power supply [23]. As an alternative, energy harvesting technology can directly power remote IoT devices and sensors with great performance. The energy collector of the IoT power supply system based on piezoelectric Nano materials studied in this paper is an effective power supply facility designed by energy harvesting technology. PVDF piezoelectric Nano fibers are prepared by electrospinning technology with excellent piezoelectric properties and good flexibility and bio-phase PVDF organic piezoelectric materials. The energy collector applied to the IoT power supply system is prepared using this material to increase collection performance.

With the energy harvesting solution, the power system can operate independently. Energy harvesting is a procedure to collect energy that is available in the environment and transform it into electrical energy. The converted power can be utilized directly or can be preserved for future use. For remote deployment devices that do not have access to the local grid, energy harvesting solutions excel in providing alternative power to a wide range of electronic devices. The energy collected can be derived from radio energy, vibrational kinetic energy of the piezoelectric element, pressure energy, or light energy of the photovoltaic cell. The collected energy is transformed into electrical energy and stored in the durable storage battery. Energy harvesting systems typically include circuitry for generating or harvesting energy. In this paper, the nano materials are used to collect energy and to transform it into electric energy to promote renewable solutions in industry 4.0.

5. CONCLUSIONS

Industrial development for generating renewable energy solutions is the most promising research area nowadays. The renewable solutions are utilizing science and technologies to achieve the goal. The battery life of devices/equipment is a serious issue to address. Battery maintenance and replacement costs are very high. The innovative technique is proposed based on nano materials to generate renewable energy solutions by using energy collector. The energy is then converted into the desired form to generate renewable energy solutions. In this paper, the renewable energy solution is presented by utilizing the characteristics of the energy collector in the power supply systems of industry 4.0 based on piezoelectric nano materials to enhance the quick power generation. The PVDF piezoelectric nano fibers with high aspect ratio are prepared by electrospinning technology. The prepared PVDF piezoelectric nano fibers are applied to the energy collector of the power

supply system in industry 4.0, and their characteristics are further analyzed. Two models are discussed in the paper, namely, single-degree-of-freedom model and distributed parameter model. Piezoelectric vibration energy collectors and the relationship between the output power and excitation frequency has been studied in this paper. The results demonstrate that the performance of the rectangular groove is the best. The optimum excitation frequency of all piezoelectric vibration generators is 16Hz. The maximum output power at the optimum excitation frequency is 60.5 μW, 62.4 μW and 66.1 μW, respectively. The energy collector in the IIoT power supply system based on piezoelectric Nano materials adopts dynamic technique to improve collection performance and generate quick power for improving the performance of energy-based equipment in industry 4.0. In future, energy harvesting solution can be applied where the power system can operate independently. It collects energy that is available in environment and transforms it into electrical energy. This converted power can be utilized directly or can be preserved for future use. The research work has important reference significance for the future industry 4.0 energy collection and conversion. The research still has some defects. Due to limited time and resources, sample data collection is relatively simple. Further analysis is needed in the future.

6. DATA AVAILABILITY

The data can be shared on valid request.

7. REFERENCES

1. Zhan, H., Tian, H., Niu, B. and Li, C., "Time-frequency analysis method based on multi-resolution gaussian filter bank", *Journal of China Electronic Science Research Institute*, Vol. 12, No. 6, (2017), 655-661. https://doi.org/10.3969/j.issn.1673-5692.2017.06.017

2. Nan, Y., Tan, D., Shao, J., Willatzen, M. and Wang, Z.L., "2d materials as effective cantilever piezoelectric nano energy harvesters", *ACS Energy Letters*, Vol. 6, No. 6, (2021), 2313-2319. https://doi.org/10.1021/acsenergylett.1c00901

3. Kaur, M., "Elitist multi-objective bacterial foraging evolutionary algorithm for multi-criteria based grid scheduling problem", in 2016 International Conference on Internet of Things and Applications (IOTA), IEEE. (2016), 431-436.

4. Hao, J., Yi, M. and Fan, J., "Modeling and simulation of magnetic field strength distribution characteristics of ingot electromagnetic casting", *Comp Simulat*, Vol. 36, (2019), 40-243. https://doi.org/10.3969/j.issn.1006-9348.2019.05.048

5. Choi, N., Kim, D., Lee, S.-J. and Yi, Y., "A fog operating system for user-oriented iot services: Challenges and research directions", *IEEE Communications Magazine*, Vol. 55, No. 8, (2017), 44-51. https://doi.org/10.1109/MCOM.2017.1600908

6. Aktas, O., Kangama, M., Linyu, G., Ding, X., Carpenter, M. and Salje, E., "Probing the dynamic response of ferroelectric and ferroelastic materials by simultaneous detection of elastic and

piezoelectric properties", *Journal of Alloys and Compounds*, Vol. 903, (2022), 163857. https://doi.org/10.1016/j.jallcom.2022.163857

7. Cheng, G., Lu, Y. and Venkatesh, T., "Indentation of piezoelectric micro-and nanostructures", *International Journal of Modern Physics B*, Vol. 36, No. 09n11, (2022), 2240035. https://doi.org/10.1142/S0217979222400355

8. Chaudhary, V., Khanna, V., Awan, H.T.A., Singh, K., Khalid, M., Mishra, Y.K., Bhansali, S., Li, C.-Z. and Kaushik, A., "Towards hospital-on-chip supported by 2d mxenes-based 5th generation intelligent biosensors", *Biosensors and Bioelectronics*, Vol. 220, (2023), 114847. https://doi.org/10.1016/j.bios.2022.114847

9. Lee, C.Y., Kim, W.C., Kim, H.J., Huh, H.D., Park, S., Choi, S.H., Kim, K.B., Min, C.K., Kim, S.H. and Shin, D.O., "Comparative dosimetric characterization for different types of detectors in high-energy electron beams", *Journal of the Korean Physical Society*, Vol. 70, (2017), 317-324. https://doi.org/10.3938/jkps.70.317

10. Almonacid, F., Fernandez, E.F., Mellit, A. and Kalogirou, S., "Review of techniques based on artificial neural networks for the electrical characterization of concentrator photovoltaic technology", *Renewable and Sustainable Energy Reviews*, Vol. 75, (2017), 938-953. https://doi.org/10.1016/j.rser.2016.11.075

11. Zhuang, T., Ren, M., Gao, X., Dong, M., Huang, W. and Zhang, C., "Insulation condition monitoring in distribution power grid via iot-based sensing network", *IEEE Transactions on Power Delivery*, Vol. 34, No. 4, (2019), 1706-1714. https://doi.org/10.1109/TPWRD.2019.2918289

12. Wang, Y., Li, H. and Li, X., "A case of on-chip memory subsystem design for low-power cnn accelerators", *IEEE Transactions on Computer-Aided Design of Integrated Circuits and Systems*, Vol. 37, No. 10, (2017), 1971-1984. https://doi.org/10.1109/tcad.2017.2778060

13. Lu, F., Wang, Y., Wang, X., Liao, X., He, Z. and Yan, Z., "Study on the collaborative discharge of a double superconducting pulsed power supply based on htsppt modules", *IEEE Transactions on Applied Superconductivity*, Vol. 28, No. 2, (2017), 1-7. https://doi.org/10.1109/TASC.2017.2776269

14. Abasian, A. and Tabesh, A., "Characterization of piezoelectric energy harvesters using frequency-weighted impedance method", *IEEE Transactions on Industrial Electronics*, Vol. 65, No. 10, (2018), 7954-7962. https://doi.org/10.1109/TIE.2018.2803722

15. Chandrasekhar, A., Alluri, N.R., Sudhakaran, M., Mok, Y.S. and Kim, S.-J., "A smart mobile pouch as a biomechanical energy harvester towards self-powered smart wireless power transfer applications", *Nanoscale*, Vol. 9, No. 28, (2017), 9818-9824. https://doi.org/10.1039/c7nr00110j

16. Xie, X., Carpinteri, A. and Wang, Q., "A theoretical model for a piezoelectric energy harvester with a tapered shape", *Engineering Structures*, Vol. 144, (2017), 19-25. https://doi.org/10.1016/j.engstruct.2017.04.050

17. Wu, W.-H., Kuo, K.-C., Lin, Y.-H. and Tsai, Y.-C., "Non-contact magnetic cantilever-type piezoelectric energy harvester for rotational mechanism", *Microelectronic Engineering*, Vol. 191, (2018), 16-19. https://doi.org/10.1016/j.mee.2018.01.026

18. Acciari, G., Caruso, M., Miceli, R., Riggi, L., Romano, P., Schettino, G. and Viola, F., "Piezoelectric rainfall energy harvester performance by an advanced arduino-based measuring system", *IEEE Transactions on Industry Applications*, Vol. 54, No. 1, (2017), 458-468. https://doi.org/10.1109/TIA.2017.2752132

19. Arroyo, E., Jia, Y., Du, S., Chen, S.-T. and Seshia, A.A., "Experimental and theoretical study of a piezoelectric vibration energy harvester under high temperature", *Journal of Microelectromechanical Systems*, Vol. 26, No. 6, (2017), 1216-1225. https://doi.org/10.1109/JMEMS.2017.2723626

20. Mareschal, B., Kaur, M., Kharat, V. and Sakhare, S.S., "Convergence of smart technologies for digital transformation", *Tehnički glasnik*, Vol. 15, No. 1, (2021), II-IV. https://doi.org/10.31803/tg-20210225102651

21. Jiang, L., Sakhare, S.R. and Kaur, M., "Impact of industrial 4.0 on environment along with correlation between economic growth and carbon emissions", *International Journal of System Assurance Engineering and Management*, (2021), 1-9. https://doi.org/10.1007/s13198-021-01456-6

22. Fechet, R., Petrariu, A.I. and Graur, A., "Partial discharge and internet of things: A switchgear cell maintenance application using microclimate sensors", *Sensors*, Vol. 21, No. 24, (2021), 8372. https://doi.org/10.3390/s21248372

23. Zhang, L., Guo, J. and Xing, Y., "Bending analysis of functionally graded one-dimensional hexagonal piezoelectric quasicrystal multilayered simply supported nanoplates based on nonlocal strain gradient theory", *Acta Mechanica Solida Sinica*, Vol. 34, (2021), 237-251. https://doi.org/10.1007/s10338-020-00204-w

Persian Abstract

چکیده

با توجه به اتصال الکترومکانیکی قوی، اندازه کوچک و حساسیت بالا، نانومواد پیزوالکتریک به طور گسترده ای در ژنراتورها، حسگرها و سایر زمینه ها استفاده شده است. در این مقاله، ویژگی‌های کلکتور انرژی در سیستم منبع تغذیه IIoT مبتنی بر نانومواد پیزوالکتریک تحلیل می‌شود. نانوالیاف پیزوالکتریک PVDF با فناوری الکتروریسی تهیه می‌شوند. مواد و تراشه های کنترل در یک جمع کننده انرژی پیزوالکتریک دووجهی یکپارچه شده اند. اثربخشی به صورت تجربی تجزیه و تحلیل می شود. نتایج تجربی نشان می دهد که فرکانس رزونانس جمع آوری انرژی با طول بازوی کنسول تغییر می کند. هنگامی که طول بازوی کنسول ۱۲ میلی متر است، خطای نصب ۱.۰ میلی متر طول منجر به ۳.۵٪ از خطای فرکانس رزونانس می شود. بار بهینه کلکتورهای ارتعاش پیزوالکتریک با بازوهای مختلف کنسول ۴۰۰ K است. توان خروجی BTG و BRG، CUB به ترتیب ۵۰.۷ μ W، ۵۵.۶ μ W و ۵۱.۸ μ W است. در عین حال، باند کاری فرکانس کلکتورهای انرژی با ساختارهای مختلف کنسولی ۱۲ هرتز تا ۱۸ هرتز است. فرکانس بهینه تحریک ۱۶ هرتز است. به طور خلاصه، جمع کننده انرژی سیستم قدرت ساخته شده توسط نانومواد پیزوالکتریک که توسط بسیاری از محققان پیشنهاد شده است، راندمان بالایی دارد که می تواند راه حلی سریع برای IIOT در Industry 4.0 ارائه کند و مکانیسم تولید برق را افزایش دهد. برای توسعه IIOT در عمل اهمیت زیادی دارد.

International Journal of Engineering

Performance Analysis of Bi-directional Improved Hybrid Three Quasi Z source Converter

R. Alla*, A. Chowdhury

Department of Electrical Engineering, Sardar Vallabhbhai National Institute of Technology, Surat, India

A B S T R A C T

Bi-directional power converters are utilized for effective management of available electrical energy associated with renewable energy systems with the use of an energy storage system. Improved hybrid three quasi z source converter (IHTQZSC) is proposed in this paper which has been providing a higher voltage gain without any switched capacitor or charge pump cells. IHTQZSC has been intended for bi-directional power transfer and control applications in this paper. The converter ensures a widespread voltage gain in a single stage DC↔AC power conversion system with lesser shoot-through time instants. The competence of the converter is acclaimed with voltage stress, current stress, peak switching device power and power losses compared with the other high voltage gain converters. Impact of voltage gain and power drawn by the converter on the efficiency has been explained. The four-quadrant power control is achieved with the constant switching frequency predictive controller. The DC-link voltage of the converter is controlled with a PI controller, and a predictive controller is used for the grid current tracking. The bi-directional working of the converter is illustrated with MATLAB/Simulink software

doi: 10.5829/ije.2023.36.07a.06

1. INTRODUCTION

Recent developments in the fields of renewable energy extraction, electric vehicles (EVs) and energy storage systems (ESS) are associated with an efficient power electronic interface (PEI). PEI plays a critical role in DC-DC, DC-AC, AC-AC and AC-DC power conversion systems either by step-up or step-down the voltage and allowing uni-directional or bi-directional power transfer. High gain DC-DC converter along with 9 level multilevel inverter is used for interfacing hybrid energy system to the utility [1]. An interleaved DC-DC converter has been designed to reduce voltage stress and providing higher voltage gain compared with a conventional boost converter [2]. The diode bridge rectifier (DBR) is used along with a further stage of DC-DC converter in uni-directional AC-DC power conversion [3, 4]. A voltage source converter (VSC) is used on behalf of DBR for AC-DC power conversion, popularly known as a PWM rectifier, which can improve the power quality on the source side and allows bi-directional power transferring

[5-8]. So far, the different PEI discussed are of two-stage power conversion systems. A DBR or a VSC facilitates in rectification stage and a DC-DC converter is accustomed to either step-up or step-down the dc voltage [9]. Bi-directional PEI is preferred over uni-directional PEI, particularly in EVs and ESS, as it reduces the cost and volume of the system. Furthermore, AC-DC bi-directional PEI is capable of maintaining an active and reactive power balance in the system.

Impedance source converters (ISC) are providing higher voltage gain in a single-stage power conversion system. Shoot-through phenomena in VSC are avoided with the introduction of dead time in between switching devices on the same leg. Dead-time is no need to provide among the switches of the same leg in ISC. Shoot-through states (STS) are intended for voltage boost functionality in ISC, whereas STS are avoided in VSC. These shortcomings in VSC are overcome with the ISC, which can use the STS to boost the input voltage while the power is transferring to the loads in normal switching states. The family of ISC is developed based on the

* Corresponding Author Email: *ramanjaneyulualla@gmail.com* (R. Alla)

operating principle of the basic z source converter (ZSC) [10]. Quasi Z source converter (QZSC) inherits the features of ZSC without any change in voltage gain, developed to provide a common DC-rail with reduced capacitor stress [11].

Further, different ISC are developed to meet high voltage gain, reduced voltage and current stresses [12-16]. QZSC is facilitated as a bi-directional DC-DC converter [17]. Battery assisted ZSC with an ultra-capacitor as an input source is worked as a bi-directional converter for electric drive applications [18]. All regions of locomotive operation are discussed with bi-directional ZSC [19]. The working of ISC depends on the insertion of STS along with the conventional switching states. The pulse width modulation (PWM) methods are developed to include STS along with non shoot-through switching states (nSTS) for the voltage buck-boost action of ISC, among which simple boost control (SBC) method is eminently implemented in most of the applications [20]. The DC-link voltage of the ISC are regulated along with the inductor current ripples with a dual-loop control method, requires two PI controllers [21]. ISC has been developed with switched capacitor or charge pump based configuration. It has been identified that atleast a capacitor is carrying a load current in these converters, which can increase the rating of the capacitor such that size and cost of the converters has been increased [22-25]. MPC is a very attractive control method that can be implemented for most power electronic applications. PI controllers are not needed with the MPC. Direct MPC has been changed to working at a constant switching frequency in a grid-connected IHTQZC [26]. The comparison of traditional VSC and ZSC is carried out in fuel cell applications [27].

Significant research has to be enforced to analyze the performance of high voltage gain bi-directional ISC in various applications. Low voltage gain ZSC and QZSC are assigned in most of the applications so far developed. This paper elaborates on the ability of high voltage gain IHTQZSC among other ISC by considering the details about the voltage and current stresses, pea switching device power and power losses that occurred in the converters. This paper addresses bi-directional power conversion working of IHTQZSC. Instead of two PI controllers [20] for DC-link voltage regulation, a single PI controller is addressed in this paper. The grid current of the converter is controlled with a predictive controller (PC), which accomplishes a constant switching frequency. Section 2 of the article explains the bi-directional IHTQZSC configuration and working. Voltage gain, voltage stress, current stresses and power losses in the impedance network of high voltage gain ISC are presented in section 3. DC-link voltage control and grid current control are discussed in section 4. The performance of the converter providing reactive power support to the grid and the bi-directional power flow

capability is illustrated with the SimPower System tool in MATLAB software, in section 5 of this paper.

2. MATHEMATICAL MODEL OF IHTQZSC

Impedance network consists inductors (L_1, L_2, L_3 and L_4), capacitors (C_1, C_2, C_3, C_4, C_5 and C_6) and bi-directional switches (S_1, S_2 and S_3) inserted in between dc source and the VSC. The configuration of the bi-directional IHTQZSC is shown in Figure 1. Switches are introduced in place of diodes of [27], for allowing bi-directional power. For a VSC, the relation between peak AC voltage (v_{peak}) and the DC-link voltage (V_{DC}) is expressed in Equation (1):

$$v_{peak} = M \frac{V_{DC}}{2} \tag{1}$$

where M is modulation index.

The converter steps-up the input voltage of the battery (V_{Bat}) for maintaining the required DC-link voltage V_{DC} at PWM inverter and feeding power into the grid. Similarly, the converter steps-down the voltage V_{DC} at the PWM rectifier to meet V_{Bat} and feeding the power into the DC source. Therefore, the converter operation is explained firstly as a PWM inverter with input voltage boost mode, and secondly, PWM rectifier with voltage buck mode.

2. 1. STS Operation of IHTQZSC as PWM Inverter with Voltage Boost   The voltage boost operation is achieved with the insertion of STS in addition to nSTS. The converter undergoes shoot-through, at a time duration of $d_{ST}T$ for a switching cycle of time period T, so that the switches in the three legs are turned on simultaneously and it causes $V_{DC}=0$. Hence the zero power, i.e., $P_{Grid}=0$ transfers to the grid represented with dashed lines shown in Figure 2.

Here d_{ST} is the shoot-through duty ratio. The switches S_1, S_2 and S_3 in the converter are turned off in this mode. It allows capacitors to discharge energy into the inductors. The voltage across the inductors, switches,
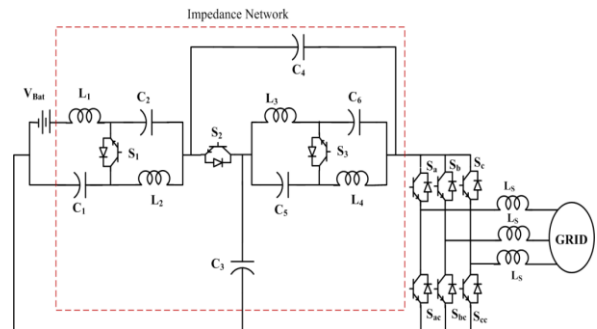
Figure 1. Circuit Diagram of IHTQZSC
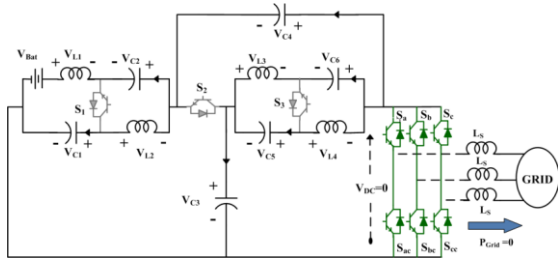
Figure 2. IHTQZSC as PWM inverter in STS

current through the diodes and capacitors are expressed in Equations (2) to (8):

$$v_{L1} = v_{C2} + v_{C4} + V_{Bat} \; ; \; v_{L2} = v_{C1} + v_{C4} \tag{2}$$

$$v_{L3} = v_{C3} + v_{C6} \; ; \; v_{L4} = v_{C3} + v_{C5} \tag{3}$$

$$v_{S1} = v_{C1} + v_{C2} + v_{C4} \; ; \; v_{S2} = v_{C3} + v_{C4} \tag{4}$$

$$v_{S3} = v_{C3} + v_{C5} + v_{C6} \tag{5}$$

$$i_{C1} = -i_{L2} \; ; \; i_{C2} = -i_{L1} \; ; \; i_{S1} = i_{S2} = i_{S3} = 0 \tag{6}$$

$$i_{C3} = -(i_{L3} + i_{L4}) \; ; \; i_{C4} = -(i_{L1} + i_{L2}) \tag{7}$$

$$i_{C5} = -i_{L3} \; ; \; i_{C6} = -i_{L4} \tag{8}$$

2. 2. nSTS operation of IHTQZSC as PWM Inverter with Voltage Boost   General sinusoidal pulse width modulated (SPWM) signals are sent to the switches in the three legs of the converter at a time duration of (1-d_{ST})T. The switches S_1, S_2 and S_3 in the converter are turned on to allow charging of the capacitors as shown in Figure 3.

In nSTS mode, the energy from the dc source is fed into the grid. Every switch in the converter has a duty ratio of (1-d_{ST}) in nSTS mode. The voltage across the inductors, diodes, current through the switches and capacitors are expressed in Equations (9) to (16):

$$v_{L1} = -v_{C1} + v_{Bat} \; ; \quad v_{L2} = -v_{C2} \; ; \tag{9}$$
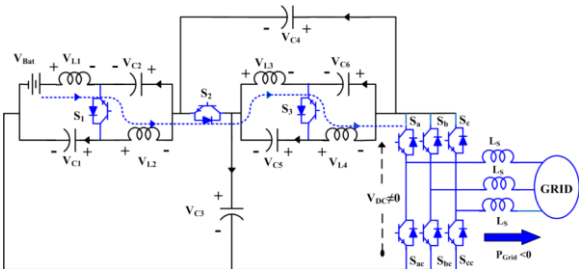
Figure 3. IHTQZSC as PWM inverter in nSTS

$$v_{L3} = -v_{C5} \; ; \; v_{L4} = -v_{C6} \; ; \; v_{DC} = v_{C3} + v_{C4} \tag{10}$$

$$v_{S1} = v_{S2} = v_{S3} = 0 \tag{11}$$

$$i_{L1} + i_{C2} = i_{L2} + i_{C1} = i_{S1} \tag{12}$$

$$i_{L3} + i_{C6} = i_{L4} + i_{C5} = i_{S3} \tag{13}$$

$$i_{L2} + i_{C4} - i_{C2} = i_{L3} + i_{C3} - i_{C5} = i_{S2} \tag{14}$$

$$i_{C4} + i_{C6} = i_{L4} - i_{Con} \; ; \tag{15}$$

$$i_{Con} = S_a i_a + S_b i_b + S_c i_c \tag{16}$$

According to the volt-s and ampere-s balance principle the steady state voltage across capacitors and current through the inductors are expressed in Equations (17) to (23). Equation (1) has been expressed in terms of G in Equation (22). For a SBC [20], M=1- d_{ST}. Here I_{Con} is the average current through the converter terminals and R_L is the equivalent resistance about the power injected into the grid.

$$V_{C1} = \frac{1 - 3d_{ST}}{(1 - 4d_{ST})} V_{Bat} \tag{17}$$

$$V_{C2} = V_{C5} = V_{C6} = \frac{d_{ST}}{(1 - 4d_{ST})} V_{Bat} \tag{18}$$

$$V_{C4} = \frac{2d_{ST}}{(1 - 4d_{ST})} V_{Bat} \tag{19}$$

$$V_{C3} = \frac{1 - d_{ST}}{(1 - 4d_{ST})} V_{Bat} \tag{20}$$

$$V_{DC} = \frac{1}{(1 - 4d_{ST})} V_{Bat} \; ; B_{ST} = \frac{1}{(1 - 4d_{ST})} \tag{21}$$

$$v_{peak} = G \frac{V_{DC}}{2} \; ; \; G = M B_{ST} \tag{22}$$

$$I_{L1} = \frac{1 - d_{ST}}{(1 - 4d_{ST})} I_{Con} \; ; I_{Con} = \frac{(1 - d_{ST}) V_{DC}}{R_L}$$
$$I_{L1} = I_{L2} = I_{L3} = I_{L4} \tag{23}$$

2. 3. STS Operation of IHTQZSC as PWM Rectifier with Voltage Buck Action   The VSC acts as a PWM rectifier. The DC-link voltage V_{DC} is stepped down to meet the battery voltage V_{Bat} with power flowing from the grid to the battery. Reverse phenomena occur here, in comparison with section 2.1. Thereby the voltage across

the inductors and current through the capacitors are expressed with a negative sign compared with the equations represented in section 2.1. The insertion of STS provides voltage buck action. Figure 4 illustrates the STS operation of the converter, at a time duration of $d_{CK}T$, makes the switches in the three legs are turned on simultaneously, causes $V_{DC}=0$ and hence the zero power, i.e., $P_{Grid}=0$ transfers to the battery from the grid represented with dashed lines. The switches S_1, S_2 and S_3 in the converter are turned off in this mode, allows the inductors to charge the capacitors.

2. 4. nSTS Operation of IHTQZSC as PWM Rectifier with Voltage Buck Action
Similar to section 2.2, switches S_1, S_2 and S_3 in the converter are turned on, the energy from the grid is fed into the battery as well as the capacitors are discharging shown in Figure 5. Every switch in the converter has a duty ratio of ($1-d_{CK}$). The voltage across the inductors and current through the capacitors are expressed with negative sign. The steady state voltage across capacitors, dc-link voltage and inductor currents are expressed in Equations (24) to (30). Here I_{Bat} is the current drawn by the DC source. Both PWM inverter working and PWM rectifier working are accomplished with the insertion of STS for a time interval of $d_{ST}T$ or $d_{CK}T$. Based on Equations (21) and (29), $d_{ST}=d_{CK}$.

3. PARAMETER DESIGN OF IHTQZSC

Voltage stress and current stress of every component in the configuration of the IHTQZSC are deduced for the
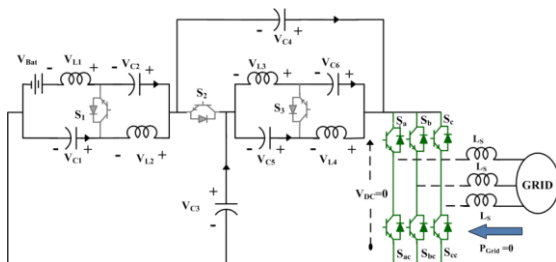
Figure 4. IHTQZSC as PWM Rectifier in STS operation
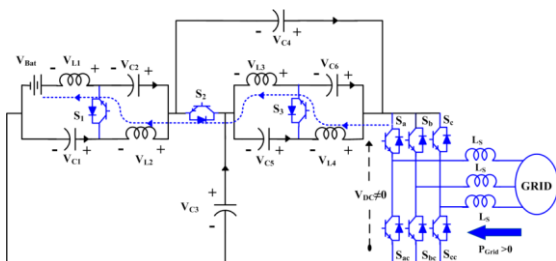
Figure 5. IHTQZSC as PWM Rectifier in nSTS operation

design of active and passive components. The voltage and current stresses are equal in the converter while working as a PWM inverter or PWM rectifier since the shoot-through duty ratio values are equal. The values of capacitances expressed in Equations (31) and (32) are selected based on their voltage stress, which is maximum in STS. Hence the Equations (6) to (8) are considered for capacitance calculation by allowing a ripple percentage of r_v in capacitor voltage.

$$V_{C1} = (1 - 3d_{CK})V_{DC} \tag{24}$$

$$V_{C2} = V_{C5} = V_{C6} = d_{CK}V_{DC} \tag{25}$$

$$V_{C3} = (1 - 2d_{CK})V_{DC} \tag{26}$$

$$V_{C4} = 2d_{CK}V_{DC} \tag{27}$$

$$V_{Bat} = (1 - 4d_{CK})V_{DC} \tag{28}$$

$$V_{Bat} = B_{CK}V_{DC} ; B_{CK} = (1 - 4d_{CK}) \tag{29}$$

$$I_{L1} = I_{L2} = I_{L3} = I_{L4} = I_{Bat} = \frac{1 - d_{CK}}{(1 - 4d_{CK})}I_{Con} \tag{30}$$

The current stress through the inductors is maximum in STS, hence Equations (2) and (3) are chosen for evaluating the inductance value by allowing a percentage current ripple of r_i. Inductance value is expressed in Equation (33). Voltage stress across the switches and current stress in the switches are expressed in Equation (34).

$$C_1 = \frac{d_{ST}(1 - 4d_{ST})I_{Bat}}{r_v(1 - 3d_{ST})V_{Bat}f_S}$$
$$C_2 = C_5 = C_6 = \frac{(1 - 4d_{ST})I_{Bat}}{r_v V_{Bat}f_S} \tag{31}$$

$$C_3 = \frac{d_{ST}(1 - 4d_{ST})I_{Bat}}{r_v(1 - 2d_{ST})V_{Bat}f_S}$$
$$C_4 = \frac{0.5(1 - 4d_{ST})I_{Bat}}{r_v V_{Bat}f_S} \tag{32}$$

$$L_1 = L_2 = L_3 = L_4 = \frac{d_{ST}(1 - d_{ST})V_{Bat}}{r_i(1 - 4d_{ST})I_{Bat}f_S} \tag{33}$$

$$V_{S1} = V_{S2} = V_{S3} = V_{DC}$$
$$V_{Sa} = V_{Sb} = V_{Sc} = V_{Saa} = V_{Sbb} = V_{Scc} = V_{DC}$$
$$I_{S1} = I_{S2} = I_{S3} = B_{ST}I_{Con} \tag{34}$$
$$I_{Sa} = I_{Sb} = V_{Sc} = I_{Saa} = I_{Sbb} = I_{Scc} = \frac{4I_{Bat}}{3}$$

$$i_{ST} = I_{L1} + I_{L2} + I_{L3} + I_{L4} \tag{35}$$

$$i_{Sa} = \frac{1}{2}i_a + \frac{i_{ST}}{3} \tag{36}$$

$$i_{peak} = \frac{4P_{Grid}}{3V_{Bat}M\cos\varphi} \tag{37}$$

The product of voltage and current stress provides peak switching device power (SDP) of the converter. Shoot-through current and switch S_a current through the switches in the converter legs [28] is expressed in Equations (35) and (36). i_{Sa} has a maximum value when i_a is at its peak value, expressed in Equation (37). The current through switch S_a has a peak current of either i_{Sa} or i_{peak}. Total SDP of IHTQZSC is sum of the SDP of the switches in the converter and expressed in Equation (38):

$$SDP = V_{S1}I_{S1} + V_{S2}I_{S2} + V_{S3}I_{S3} + 6V_{DC}\max\left\{i_{Sa} \text{ or } i_{peak}\right\} \tag{38}$$

3. 1. Power Losses　　The total power losses in the impedance network are due to the losses in inductors, capacitors and switches. Power loss in the inductors and capacitors are given in Equations (39) and (40). r_{ind}, r_{cap} and r_d are the internal resistances of the inductors, capacitors and the switches. t_{on} and t_{off} are the turn on and turn off transition times of the switches at a switching frequency of f_s. The Ohmic losses and switching losses in the impedance network and converter legs are expressed in Equations (41) and (44).

$$P_{ind} = 4(1 - d_{ST})^2 B_{ST}^2 I_{Con}^2 r_{ind} \tag{39}$$

$$P_{Cap} = 12I_{Bat}^2 \frac{d_{ST}}{(1 - d_{ST})} r_{cap} \tag{40}$$

$$P_{Nw-ohm} = (I_{S1rms}^2 + I_{S2rms}^2 + I_{S3rms}^2)r_D \tag{41}$$

$$P_{Nw-turn} = (V_{S1}I_{S1} + V_{S2}I_{S2} + V_{S3}I_{S3})\frac{t_{on} + t_{off}}{2}f_s \tag{42}$$

$$I_{inv-sw,rms} = \sqrt{\frac{16}{9}d_{ST}I_{LI}^2 + \frac{16}{9}\frac{P_{Grid}^2(1 - d_{ST})}{G^2 V_{Bat}^2 \cos^2\varphi}} \tag{43}$$

3. 2. Comparative Analysis with other High Voltage Gain ISC　　The voltage boost factor (B_{ST}), maximum voltage and current stress in the converter elements and peak SDP are preferred for the identification of the competence of IHTQZSC with another high voltage gain ISC. It has been noticed that IHTQZSC provides a wider voltage gain compared with other higher voltage gain ISC with a lower shoot-through duty ratio has shown in Figure 6(a). The maximum value of the capacitor voltage stress of IHTQZSC is lower than the voltage stress reported in literature [14, 15] at higher voltage gain requirements. Except Zhu et al. [12] reported that the remaining converters have an equal amount of maximum inductor current stress listed in Table 1. IHTQZSC has a lower switch current stress compared with current stress in the switches reported by Jagan et al. [14] and Zhu et al. [15]. The proposed converter has a lower value of maximum voltage stress in the switches of the impedance network. IHTQZSC has a nearer SDP value considered by Jagan et al. [14] and Zhu et al. [15] are shown in Figure 6(b).

$$P_{inv-sw} = 6\left\{\frac{16}{9}d_{ST}I_{Bat}^2 + \frac{16}{9}\frac{P_{Grid}^2(1 - d_{ST})}{G^2 V_{Bat}^2 \cos^2\varphi}\right\}r_d \tag{44}$$

$$P_{inv-turn} = 6V_{DC}\frac{I_{ST}}{3}\frac{t_{on} + t_{off}}{2}f_S \tag{45}$$

TABLE 1. Voltage and Current Stress of IHTQZSC

	[12]	[13]	[14]	[15]	Pst - IHTQZSC
$\frac{V_{CMax}}{V_{Bat}}$	$B_{ST}(1 - d_{ST})/(1 + d_{ST})$	B_{ST}	$d_{ST}(2 - d_{ST})B_{ST}$	$d_{ST}(3 - 2d_{ST})B_{ST}$	$(1 - 2d_{ST})B_{ST}$
$\frac{I_{LMax}}{I_{Con}}$	$B_{ST}(1 - d_{ST})/(1 + d_{ST})$	$(1 - d_{ST})B_{ST}$	$(1 - d_{ST})B_{ST}$	$(1 - d_{ST})B_{ST}$	$(1 - d_{ST})B_{ST}$
$\frac{I_{SMax}}{I_{Con}}$	B_{ST}	$(1 - d_{ST})B_{ST}$	B_{ST}	B_{ST}	B_{ST}
$\frac{V_{SMax}}{V_{Bat}}$	B_{ST} $B_{ST}(1 - d_{ST})/(1 + d_{ST})$ $B_{ST}d_{ST}/(1 + d_{ST})$	B_{ST} $d_{ST}B_{ST}$ $(1 - d_{ST})B_{ST}$	B_{ST} $d_{ST}B_{ST}$ $(1 - d_{ST})B_{ST}$	B_{ST} $d_{ST}B_{ST}$ $(1 - d_{ST})B_{ST}$	B_{ST}

V_{SMAX}, V_{CMAX}　Maximum voltage in switch and capacitors; I_{LMAX}, I_{LMAX}　Maximum current through switches and inductors

(a)

(b)
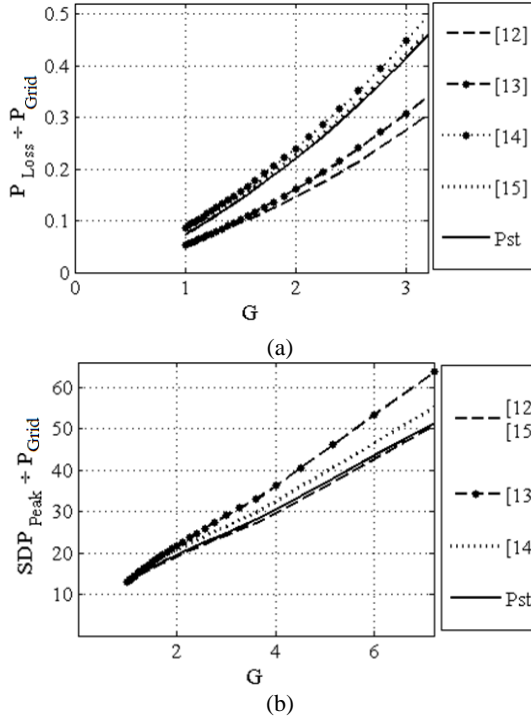
Figure 6. (a) Power loss variation with G (b) SDP variation with G

The converters reported by Jagan et al. [14], Zhu et al. [15] and IHTQZSC are having very nearer voltage gain and an equal amount of inductor maximum current stress. The maximum current stress and voltage stress in the switches of IHTQZSC are lower than other converters. IHTQZSC has lower SDP compared with reported data by Nozadian eta l. [13] Jagan et al [14] and has a very nearer SDP value compared with data reported by Zhu et al. [12] and Zhu et al. [15]. Hence the power losses are considered for highlighting the significance of IHTQZSC, plotted in Figure 6(a). It has been verified that IHTQZSC has a lower power loss compared to data reported by Jagan et al. [14] and Zhu et al. [15] among high voltage gain non-coupled ISC.

4. CONTROL METHOD

CSF-PC controller is utilizing for the controlling of IHTQZSC [27] as shown in Figure 7. The converter has been controlled on DC-side of the converter to attain a constant DC-link voltage V_{DC}. But V_{DC} has been varying from zero to a peak value. Hence it can be challenging to control direct V_{DC}. That's why V_{DC} has been expressed as a sum of V_{C3} and V_{C4}. The DC-link voltage V_{DC} is regulated with a PI controller. The bode diagram in dotted line shown in Figure 11 represents a negative gain margin and phase margin due to RHP zero makes the
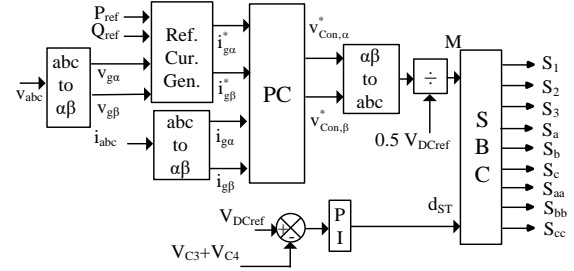
Figure 7. Grid-Tied IHTQZSC with CSF-PC

uncompensated system becomes unstable. With the proper selection of parameters kp=0.0003 and ki=0.02 in PI controller, bode diagram for the compensated system represented in solid line in Figure 7 exhibits system stability.

PC is implemented for grid current tracking by predicting the two orthogonal voltage vectors. Here R_S is considered for the filter resistance and V_{Con} is the voltage across the converter. v_{abc} and i_{abc} are grid voltage and currents. The grid current equation is expressed in Equation (46). The predicted grid current during a sampling time of T_S with Euler's approximation is represented in $\alpha\beta$ reference frame in Equation (47).

$$L_S \frac{di_{abc}}{dt} = -R_S i_{abc} + v_{Con} - v_{abc} \tag{46}$$

$$i_{g\alpha\beta}(k+1) = \left(1 - \frac{R_S T_s}{L_S}\right) i_{g\alpha\beta}(k) + \frac{T_s}{L_S}\left(v_{Con,\alpha\beta}(k) - v_{g\alpha\beta}(k)\right) \tag{47}$$

$$C = C_\alpha + C_\beta$$
$$C_\alpha = \left(\left|i_{g\alpha}^*(k+1) - i_{g\alpha}(k+1)\right|\right)^2 ; \tag{48}$$
$$C_\beta = \left(\left|i_{g\beta}^*(k+1) - i_{g\beta}(k+1)\right|\right)^2$$

$$i_{g\alpha}^* = \frac{2}{3}(P_{ref} v_{g\alpha} + Q_{ref} v_{g\beta}) \tag{49}$$

$$i_{g\beta}^* = \frac{2}{3}(P_{ref} v_{g\beta} - Q_{ref} v_{g\alpha}) \tag{50}$$

The quadratic cost function is defined for identifying the optimal switching vectors mentioned in Equation (48). $i_{g\alpha}^*$ and $i_{g\beta}^*$ are the reference values of grid current, evaluated by considering the required amount of active and reactive powers P_{ref} and Q_{ref} injected or consumed from the grid, respectively. The predicted orthogonal voltage vectors $V_{Con,\alpha}^*$ and $V_{Con,\beta}^*$ are obtained with the maxima-minima concept represented in Equation (51).

$$v^{*}_{Con,\alpha} = -\frac{L_S}{T_S}A; A = \left(1 - \frac{R_S T_S}{L_S}\right)i_{g\alpha}(k) + \frac{T_S}{L_S}v_{g\alpha}(k) - i^{*}_{g\alpha}(k+1)$$

$$v^{*}_{Con,\beta} = -\frac{L_S}{T_S}B; B = \left(1 - \frac{R_S T_S}{L_S}\right)i_{g\beta}(k) + \frac{T_S}{L_S}v_{g\beta}(k) - i^{*}_{g\beta}(k+1)$$

(51)

V_{DC} has been controlled with PI controller by generating d_{ST} and the four-quadrant operation of power is controlled with the implementation of PC for grid current tracking by generating $v^{*}_{Con,\alpha}$ and $v^{*}_{Con,\beta}$. These optimal voltage vectors send the modulating signals to the SBC along with d_{ST} from the PI controller. Constant switching frequency is obtained with the use of a modulator in the SBC controller, operates the converter in STS and nSTS mode.

5. RESULTS AND DISCUSSION

Performance of IHTQZSC has been analysed during the four-quadrant power control with MATLAB Simulink results. The direction of i_{abc} is considered positive when the converter acts as PWM rectifier feeding power into the DC source. The system parameters are - Inductance 1mH, Capacitance 470μf, switching frequency 10kHz, grid voltage 220Vrms, grid inductance 15mH, input voltage 200V and sampling time of 25μs.

Active power (P) and reactive power (Q) along with i_{abc} and v_{abc} are chosen grid side parameters for the identification of the converter response. V_{Bat}, V_{C3}, V_{DC} and inductor current or DC source current I_{L1} are considered as DC side parameters.
QI , QII, QIII and QIV are quadrants

Figure 8 shows the response of the converter while operating in Q_I, consumes P of 1000W at unity power factor (upf) up to 0.4s and afterward absorbs Q of 1000VAr. It means the converter acts as a PWM rectifier and provides VAr support to the grid. Hence the peak of i_{abc} has been changed to 5.23A from 3.7A. The controller affords a quick response from the converter with a change in Q. The converter draws a DC source current of 5A at V_{Bat} of 200V and maintaining V_{C3} at and 306.6V, V_{DC} at 413V. The converter shifts its operation from Q_I to Q_{IV} at 0.6s with a change in Q from 1000VAr to -750VAr. Such that, i_{abc} has been changed its peak value from 5.23A to 4.63A. The DC source side parameter values are continued without any variation as there is no change in V_{Bat} observed in Figure 9.

After 0.8 s, the converter acts as a PWM Inverter change its operation from Q_{IV} to Q_{III} with a change in P from 1000W to -2000W as well as change in Q from -750VAr to -500VAr. The response of the converter is shown in Figure 10. The peak of i_{abc} has been changed from 4.63A to 7.63A. The DC source current I_{L1} has been shifted to 10A with a change in P. A sudden shift in P caused a small voltage dip in V_{C3} and V_{DC} of the converter and restored within a single cycle. The
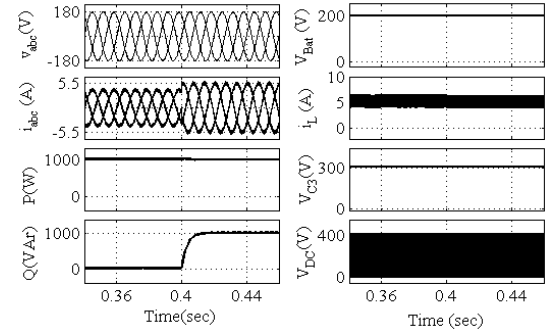
Figure 8. Response of IHTQZSC working in Q_I
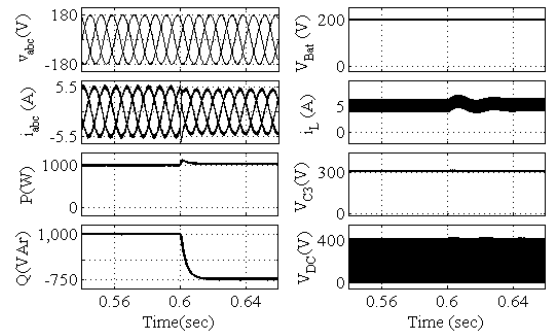
Figure 9. Response of IHTQZSC during Q_I to Q_{IV}
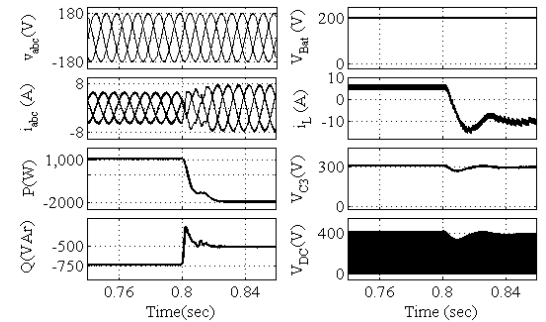
Figure 10. Response of IHTQZSC during QIV to QIII

converter shifts its operation from Q_{III} to Q_{II} after 1 s due to a change in Q from -500VAr to 1200VAr. i_{abc} has been changed its peak value to 8.63A from 7.63A as shown in Figure 11. The DC source side parameters are continued, with constant V_{Bat}.

The transition of converter operation from Q_{II} to Q_I occurred at 1.2s observed in Figure 12, with the change in Q from 1200VAr to zero VAr. Simultaneously V_{Bat} has been reduced to 125V from 200V. With the change in V_{Bat} along with Q change, i_{abc}, i_{L1}, V_{C3}, and V_{DC} of the converter are disturbed for a period of three cycles and restored back to steady-state with the values at 7.4A, 10A, 281V and 438.2V, respectively. The impact of converter voltage gain and the power drawn from the converter on efficiency is shown in Figure 13.
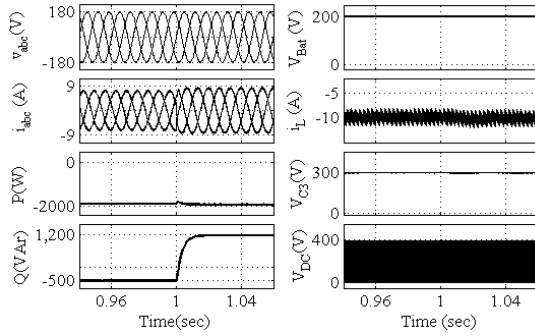
Figure 11. Response of IHTQZSC during QIII to QII
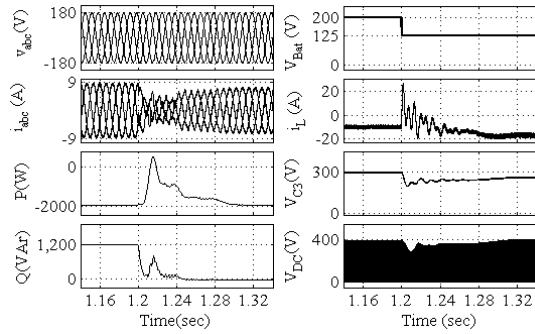
Figure 12. Response of IHTQZSC during QII to QI
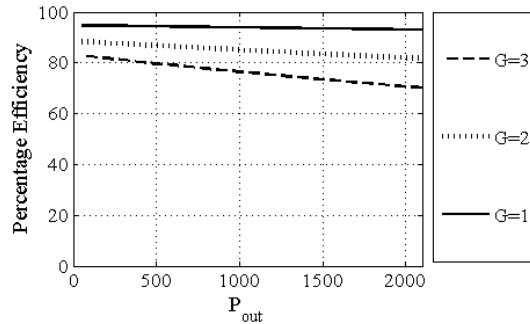
Figure 13. The efficiency variation of IHTQZSC

6. CONCLUSION

IHTQZSC ensures a wider range of voltage gain, among other high voltage gains ISC does not need any switching capacitors or charge pump cells. The voltage stress in the switching devices, capacitors, the current stress in the inductors and switching devices are deduced in this paper. The worthiness of the converter has been commended by comparing the voltage stress and current stress, peak SDP and power losses in the present converter with another high gain ISC. The converter has been working in all four quadrants, by injecting or consuming both active and reactive powers with the use of a predictive controller implemented for grid current tracking with a good dynamic response with the change

in dc source voltage as well as grid power. With the ability of bi-directional power control, high voltage gain, lower voltage stress and current stress in the converter elements with lesser peak SDP, the converter can be utilized in electric vehicles, energy storage systems, and in hybrid energy source systems.

7. REFERENCES

1. Gobimohan, S., "Active power quality improvement for unified renewable energy system with multilevel inverter and pekf controllers", *Energy Sources, Part A: Recovery, Utilization, and Environmental Effects*, Vol. 42, No. 21, (2020), 2603-2622. doi: 10.1080/15567036.2019.1612486.

2. Ye, H., Jin, G., Fei, W. and Ghadimi, N., "High step-up interleaved dc/dc converter with high efficiency", *Energy Sources, Part A: Recovery, Utilization, and Environmental Effects*, (2020), 1-20. doi: 10.1080/15567036.2020.1716111.

3. Ananthapadmanabha, B., Maurya, R. and Arya, S.R., "Improved power quality switched inductor cuk converter for battery charging applications", *IEEE Transactions on Power Electronics*, Vol. 33, No. 11, (2018), 9412-9423. doi: 10.1109/TPEL.2018.2797005.

4. Gupta, J., Maurya, R. and Arya, S.R., "On-board electric vehicle battery charger with improved power quality and reduced switching stress", *IET Power Electronics*, Vol. 13, No. 13, (2020), 2885-2894. doi: 10.1049/iet-pel.2019.0962.

5. Bhavya, K., Rama Rao, P. and Ravi Srinivas, L., "Performance evaluation of weighted feedback based upqc under various power quality issues", *International Journal of Engineering, Transactions C: Aspects,* Vol. 36, No. 3, (2023), 441-449. doi: 10.5829/ije.2023.36.03c.02.

6. Tan, K.M., Padmanaban, S., Yong, J.Y. and Ramachandaramurthy, V.K., "A multi-control vehicle-to-grid charger with bi-directional active and reactive power capabilities for power grid support", *Energy*, Vol. 171, (2019), 1150-1163. doi: 10.1016/j.energy.2019.01.053.

7. Chung, I.-Y., Liu, W., Schoder, K. and Cartes, D.A., "Integration of a bi-directional dc–dc converter model into a real-time system simulation of a shipboard medium voltage dc system", *Electric Power Systems Research*, Vol. 81, No. 4, (2011), 1051-1059. doi: 10.1109/ESTS.2009.4906531.

8. Yong, J.Y., Ramachandaramurthy, V.K., Tan, K.M. and Selvaraj, J., "Experimental validation of a three-phase off-board electric vehicle charger with new power grid voltage control", *IEEE Transactions on Smart Grid*, Vol. 9, No. 4, (2016), 2703-2713. doi: 10.1109/TSG.2016.2617400.

9. Tavassoli, F., Ghoreishy, H., Adabi, J. and Rezanejad, M., "An advanced modulation technique featuring common mode voltage suppression for three-phase neutral point clamped back to back converters", *International Journal of Engineering, Transactions B: Applications,,* Vol. 35, No. 11, (2022), 2220-2228. doi: 10.5829/ije.2022.35.11b.17.

10. Gadalla, B., Schaltz, E., Zhou, D. and Blaabjerg, F., "Lifetime prediction of boost, z-source and y-source converters in a fuel cell hybrid electric vehicle application", *Electric Power Components and Systems*, Vol. 46, No. 18, (2018), 1979-1991. doi: 10.1080/15325008.2018.1528316.

11. Karimi, M., Mahdavi, M. and Torki Harchegani, A., "A new soft switching qzsc converter by using coupled inductor", *Electric Power Components and Systems*, Vol. 46, No. 3, (2018), 270-277. doi: 10.1080/15325008.2018.1444687.

12. Zhu, M., Yu, K. and Luo, F.L., "Switched inductor z-source inverter", *IEEE Transactions on Power Electronics*, Vol. 25, No. 8, (2010), 2150-2158. doi: 10.1109/TPEL.2010.2046676.

13. Nozadian, M.H.B., Babaei, E., Hosseini, S.H. and Asl, E.S., "Steady-state analysis and design considerations of high voltage gain switched z-source inverter with continuous input current", *IEEE Transactions on Industrial Electronics*, Vol. 64, No. 7, (2017), 5342-5350. doi: 10.1109/TIE.2017.2677315.

14. Jagan, V., Kotturu, J. and Das, S., "Enhanced-boost quasi-z-source inverters with two-switched impedance networks", *IEEE Transactions on Industrial Electronics*, Vol. 64, No. 9, (2017), 6885-6897. doi: 10.1109/TIE.2017.2688964.

15. Zhu, X., Zhang, B. and Qiu, D., "A new nonisolated quasi-z-source inverter with high voltage gain", *IEEE Journal of Emerging and Selected Topics in Power Electronics*, Vol. 7, No. 3, (2018), 2012-2028. doi: 10.1109/JESTPE.2018.2873805.

16. Shen, H., Zhang, B. and Qiu, D., "Hybrid z-source boost dc–dc converters", *IEEE Transactions on Industrial Electronics*, Vol. 64, No. 1, (2016), 310-319. doi: 10.1109/TIE.2016.2607688.

17. Kafle, Y.R., Hasan, S.U. and Town, G.E., "Quasi-z-source based bidirectional dc-dc converter and its control strategy", *Chinese Journal of Electrical Engineering*, Vol. 5, No. 1, (2019), 1-9. doi: 10.23919/CJEE.2019.000001.

18. Hu, S., Liang, Z. and He, X., "Ultracapacitor-battery hybrid energy storage system based on the asymmetric bidirectional z-source topology for ev", *IEEE Transactions on Power Electronics*, Vol. 31, No. 11, (2015), 7489-7498. doi: 10.1109/TPEL.2015.2493528.

19. Vijayan, V. and Ashok, S., "High-performance bi-directional z-source inverter for locomotive drive application", *IET Electrical Systems in Transportation*, Vol. 5, No. 4, (2015), 166-174. doi: 10.1049/iet-est.2014.0053.

20. Siwakoti, Y.P., Peng, F.Z., Blaabjerg, F., Loh, P.C. and Town, G.E., "Impedance-source networks for electric power conversion part i: A topological review", *IEEE Transactions on Power Electronics*,   Vol. 30, No. 2, (2014), 699-716. doi: 10.1109/TPEL.2014.2329859.

21. Ellabban, O., Van Mierlo, J. and Lataire, P., "A dsp-based dual-loop peak dc-link voltage control strategy of the z-source inverter", *IEEE Transactions on Power Electronics*, Vol. 27, No. 9, (2012), 4088-4097. doi: 10.1109/TPEL.2012.2189588.

22. Zhang, Y., Liu, Q., Gao, Y., Li, J. and Sumner, M., "Hybrid switched-capacitor/switched-quasi-z-source bidirectional dc–dc converter with a wide voltage gain range for hybrid energy sources evs", *IEEE Transactions on Industrial Electronics*, Vol.   66,   No.   4,   (2018),   2680-2690.   doi: 10.1109/TIE.2018.2850020.

23. Kumar, A., Xiong, X., Pan, X., Reza, M., Beig, A.R. and Al Jaafari, K., "A wide voltage gain bidirectional dc–dc converter based on quasi z-source and switched capacitor network", *IEEE Transactions on Circuits and Systems II: Express Briefs*, Vol. 68, No. 4, (2020), 1353-1357. doi: 10.1109/TCSII.2020.3033048.

24. Veerachary, M. and Kumar, P., "Analysis and design of quasi-z-source equivalent dc–dc boost converters", *IEEE Transactions on Industry Applications*, Vol. 56, No. 6, (2020), 6642-6656. doi: 10.1109/TIA.2020.3021372.

25. Zhang, Y., Fu, C., Sumner, M. and Wang, P., "A wide input-voltage range quasi-z-source boost dc–dc converter with high-voltage gain for fuel cell vehicles", *IEEE Transactions on Industrial Electronics*, Vol. 65, No. 6, (2017), 5201-5212. doi: 10.1109/TIE.2017.2745449.

26. Alla, R. and Chowdhury, A., "Csf-pc based grid tied improved hybrid three quasi z source converter", *COMPEL-The International Journal for Computation and Mathematics in Electrical and Electronic Engineering*, Vol. 39, No. 4, (2020), 927-942. doi: 10.1108/COMPEL-01-2020-0062.

27. Shen, M., Joseph, A., Wang, J., Peng, F.Z. and Adams, D.J., "Comparison of traditional inverters and $ z $-source inverter for fuel cell vehicles", *IEEE Transactions on Power Electronics*, Vol.   22,   No.   4,   (2007),   1453-1463.   doi: 10.1109/PET.2004.1393815.

Persian Abstract

چکیده

مبدل‌های قدرت دو جهته برای مدیریت مؤثر انرژی الکتریکی موجود مرتبط با سیستم‌های انرژی تجدیدپذیر با استفاده از سیستم ذخیره‌سازی انرژی مورد استفاده قرار می‌گیرند. مبدل هیبریدی سه شبه منبع z (IHTQZSC) در این مقاله پیشنهاد شده است که افزایش ولتاژ بالاتری را بدون هیچ خازن سوئیچ یا سلول پمپ شارژ ارائه می دهد. در این مقاله IHTQZSC برای کاربردهای انتقال قدرت و کنترل دو جهته ای را در یک سیستم تبدیل توان DC↔AC تک مرحله ای با لحظه های تیراندازی کمتر تضمین می کند. صلاحیت مبدل با تنش ولتاژ، تنش جریان، توان دستگاه سوئیچینگ پیک و تلفات توان در مقایسه با دیگر مبدل های افزایش ولتاژ بالا تحسین شده است. تأثیر افزایش ولتاژ و توان گرفته شده توسط مبدل بر بازده توضیح داده شده است. کنترل توان چهار ربعی با کنترل کننده پیش بینی فرکانس سوئیچینگ ثابت به دست می آید. ولتاژ DC-link مبدل با یک کنترل کننده PI کنترل می شود و یک کنترل کننده پیش بینی برای ردیابی جریان شبکه استفاده می شود. کار دو طرفه مبدل با نرم افزار MATLAB/Simulink نشان داده شده است.

International Journal of Engineering

A Numerical Modelling Approach to Assess Deformations of Horseshoe Cavern on Account of Rock Mass Characteristics and Discontinuities

S. Kuili*[a], V. R. Sastry[b]

[a] Department of Civil Engineering, NIT Karnataka, Surathkal, Mangalore, India
[b] Department of Mining Engineering, NIT Karnataka, Surathkal, Mangalore, India

A B S T R A C T

Caverns are massive underground openings excavated for purposes like defense installations and nuclear waste disposal which becomes challenging for weak strata consisting of fractured rock masses and may result in future calamities. This study is dedicated to ascertain stability of a horseshoe cavern in different types of granitic rock masses as well as fractured rocks. Two different types of granitic formations are accounted and displacements obtained along cavern periphery have been illustrated in the preliminary part of this study. An increment in vertical displacement at the crown of 260% and lateral displacement of almost 170% for both walls were observed for moderately weathered rock. Further, implications due to orientation and frequency of joint sets on the displacements incurred has also been explored. This study acquires its novelty by considering combinations of joint sets with varying spacings for investigating their implications on cavern walls. Presence of discontinuities depicted that horizontal joint spaced closely increased the deformation magnitude which reduced with decrement in joint frequency. Subsequently, along with horizontal joints at 4m interval, vertical and oblique joints sets were also incorporated at different frequencies. Consideration of vertical joints at 2m spacing with horizontal joints resulted in 313.2% increase in vertical displacement at cavern crown as well as 340% and 363% increase in lateral deformation at the left and right wall, respectively in comparison to intact rock. In case of oblique joints spaced at 2m with horizontal joints, increment in vertical deformation at the crown proliferated to 329% in comparison to intact rock.

1. INTRODUCTION

The scope of better mechanisms related to ground control and advancements in the field of numerical modelling techniques has allowed us to assess the stability of the walls of subterranean structures such as large underground caverns. A cavern is a hollow passage beneath the earth, which has one of its openings to the surface of earth. The main concern is to ensure longstanding stability of these structures, which notifies us for everlasting operational necessities. One example of such debacle pertaining to underground structures include subsidence of the Seoul subway tunnel in South Korea [1].

The Hoek-Brown empirical failure criteria have been extensively utilized for asserting rock-mass parameters [2]. Other popular empirical approaches pertaining to behaviour of rock mass have also been bestowed by several researchers [3, 4]. Stability assessment of specific underground projects with the usage of various numerical modelling tools has been explored over the past decades. A parametric study performed using Universal Distinct Element Code (UDEC) concluded that some parameters of faults were really crucial for asserting the stability of these structures [5]. Research study pertaining to the assessment of stress variations between a slope and tunnel was carried out for both single as well as multiple tunnel scenarios [6]. Three-dimensional numerical modelling code (3DEC) has also been utilized by researchers to assess the promulgation of cracks along the walls of underground structures as well as asserting their responses under the dynamic loads [7, 8]. A research

*Corresponding Author Email: rijukuili@gmail.com (S. Kuili)

study utilized Intelligent Committee Machines for forecasting the Peak Particle Velocity (PPV) generated due to bench blasting on rock slopes [9]. The stability aspect due to different extreme loading conditions has been given a lot of importance over the past decades. However, the depletion of static stability on account of poor geological formations along with presence of joints still needs in-depth assessments for mitigating future catastrophic failures. A jointed rocky medium is an accumulation of intact rock separated by the presence of discontinuities. The presence of discontinuities substantially weakens the in-situ rock mass. Researchers had adopted discrete element method in order to evaluate the implications of existing joints to ascertain the hydro-mechanical response of an underground storage facility [10]. However, the static response of any underground structures constructed under jointed geological formations is also crucial to investigate. The deleterious implication of underground openings substantially increases when the existing geological formations comprises of weak rock types. This study has shed light into the response of an underground cavern under different types of rock formations along with various joint sets. Studies have also been extended to analyze the behaviour of rocks under nonlinear loading which forecasted increment of dynamic Young's Modulus with amplitudes [11]. A study highlighted the behaviour of jointed rock mass under different types of loads by proposing a failure criterion which accounts for major principal strain as it was observed that the state of strain gains equal importance to the stress state [12]. A research study looked into the extent of ground subsidence due to the construction of tunnels [13]. Assessment of tunnel stability has also been carried out by various researchers [14, 15]. Researchers have also looked into implications of tunnel stability in liquified soil conditions [16]. All the aforementioned literatures convey the stability aspect of underground structures under various scenarios but fails to dispatch the quantitative responses of underground structure peripheries which is highly linked to the type of surrounding rock masses as well as presence of discontinuities.

Application of distinct element code to ascertain the stability of underground caverns have gained an impetus over the past years due to its robustness in handling large discontinuities. In recent years, many studies have been conducted to ascertain the stability of underground openings using 3DEC, which is a distinct element code [17-19]. An investigation on predicting lateral displacement of rock mass at locations situated away from cavern walls using distinct element code in interconnected medium has also been performed with in-depth insight into the squeezing action of cavern walls [20]. However, the aforementioned study negated the aspect of surrounding geological rock types and conveyed the lateral deformations at various locations located transverse to the cavern walls. Stability analysis

of large underground cavern has also been performed via FEM which aided in obtaining significant insights regarding the stresses of the neighboring rocks as well as rock supports [21]. Predictive modelling study has also been performed via Artificial Neural Network (ANN) for proper assessment of underground opening and surrounding soil interaction on the settlement of surface and subsurface soil layers [22]. Stability analysis on tunnels were also performed using a discontinuum model generated by 3DEC numerical code [23]. Significant insights were attained through the aforementioned studies; however, the quantitative assessments of deformations of underground openings due to jointing as well as type of geological formations were not emphasized till date. The present study has been focused on attaining quantitative estimates of deformations along cavern periphery and provides a holistic insight regarding its stability under various jointed geological formations. When underground excavations are carried out, the displacements due to overburden are found to occur at the crown and side walls of the cavern. Due to such opening, the equilibrium of stress is disturbed and it adjusts to achieve a new state of equilibrium by undergoing deformations resulting in sagging of roof as well as inward movement of side walls. Based on the aforementioned literatures presented, it has been observed that, there persists scanty studies to assess the displacements of cavern walls in different types of rocky formations as well as caverns constructed in fractured rocks. This study emphasizes on the assessment of underground cavern's response in terms of peripheral displacement by incorporating joints as well as numerous joint sets in the rock mass with the aid of 3DEC. The existing geological formations as well as presence of discontinuities are one of the crucial aspects which needs utmost supervision before the construction of any underground structures. The presence of fractured rock mass substantially weakens the neighboring rock strata which proliferates drastically when the strength of the surrounding rock mass is even less. The novelty of this study has been acquired by considering two different types of geological formations as well as different types of joint sets with varying frequencies which are quite prevalent at different places globally and the deformations encountered along the walls of horseshoe cavern due to the aforementioned aspects have been delineated in this study. The following subsections provides insight into the numerical modeling aspect via 3DEC software followed by the modelling details which has been adhered in this study. The second section of this article conveys the utilized rock mass parameters along with properties of discontinuities as well as sheds light into the application of in-situ stresses in the generated model. Finally, both the lateral as well as vertical displacements has been procured along the cavern periphery due to different types of geological formations as well as various joint sets which has been incorporated

in the model. The terminating part of this article presents the significant insights via concluding remarks attained through this numerical modelling study.

1. 1. Numerical Modelling   Stability analysis of a horseshoe cavern was conducted under two different types of ground conditions having intact rock of different rock strength. Spacing of discontinuities and inclusion of joint sets has also been varied in this study to ascertain the change in displacements along the cavern walls. The entire cavern has been modelled using two types of geological rock formation with the usage of discontinuum 3D numerical models i.e., 3DEC. 3DEC is a three-dimensional modelling tool based on Distinct Element Method mainly utilized for modelling discontinuum. Discontinuities are regarded as boundary conditions between blocks and vast displacements along discontinuities as well as rotation of blocks are permitted[1]. The applicability of FEM in the simulation of large deformations is quite cumbersome, whereas, Distinct Element Method (DEM) models every particle as an individual entity and represent granular material as an idealized assembly of particles. This aspect conveys that the DEM approaches are quite suitable for investigating the phenomena occurring at the length scale of particle diameter and simulating the bulk behavior of particles. In case of 3DEC, the independent blocks act either as a rigid or deformable material. Deformable blocks are further segregated into a mesh of finite difference elements, and individual element reacts according to a specified linear or nonlinear stress-strain law.

1. 2. Model Details   The horseshoe cavern adopted for this study has a length of 1050m, width of 25m and 40m height. Cavern roof was modelled as an arch with 5m rise. Cavern considered for this study was assumed to be situated at 50m below ground level. To reduce the influence of artificial boundaries, a span of 5D was provided (where "D" refers to cavern diameter) at the sides in transverse direction and from cavern base to the model bottom. Further, different models were generated by changing the frequency of horizontal joints for a single type of rock formation and these models were analyzed to assess the cavern stability. Numerous combinations of joint sets were also incorporated in the model in similar type of rock formation for analyzing the effect of jointing.

The extent of area where discontinuities were invoked into the model along with the excavated opening as well as the sequence for initiating the excavated portion of the opening is illustrated in Figure 1. Discontinuities invoked into the model comprises of the following:

a.   Horizontal joints at spacing of 2m, 4m and 6m.
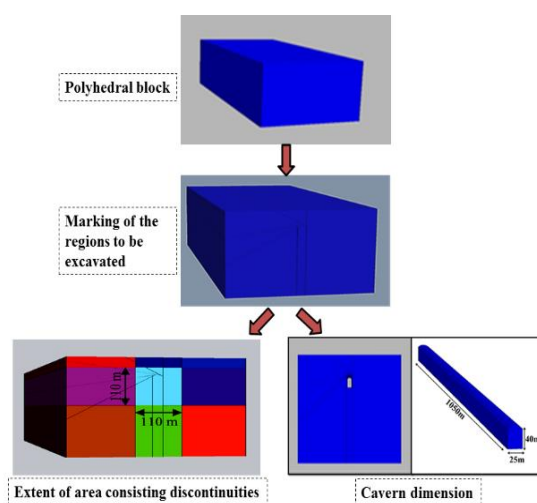
Figure 1. Generation of the model depicting cavern dimensions and extent of discontinuities

b.   Horizontal joints at 4m spacing along with vertical joints at spacing of 2m, 4m and 6m.
c.   Horizontal joints at 4m spacing along with oblique joints at spacing of 2m, 4m and 6m.

The aforementioned extent of discontinuities invoked into the model has been explored for the first time in terms of delineating the stability of horseshoe cavern. The entire domain of the generated model was divided into deformable blocks with the help of 'gen edge' command, with each block further discretized into tetrahedrons with predominant geometrical/geological features forming boundaries of different blocks. Regions lying close to excavation were meshed with smaller size and coarser mesh sizes were adopted for locations away from the cavern. The authors would like to highlight that the process of generating the model as presented in this study has been kept exactly the same as per previous published studies [8, 20]. A flowchart of the adopted research methodology is presented in Figure 2 delineating every step which have been undergone in this study for extracting the deformations along cavern periphery. Preliminary parametric assessments include assessing the cavern stability without joint sets in two different types of rock formations. Both values of horizontal and vertical displacement were noted at intervals of 210m along the length of cavern and the maximum procured displacements have been reported in this study. Later part of this study embraces inclusion of horizontal joint sets as well as horizontal joint set along with vertical or oblique joint sets at different spacings and subsequently maximum displacements in both directions have been considered as the displacements occurring along the walls of cavern.

---

[1]

https://usermanual.wiki/Document/Manualof3DECV410.1356105871.pdf
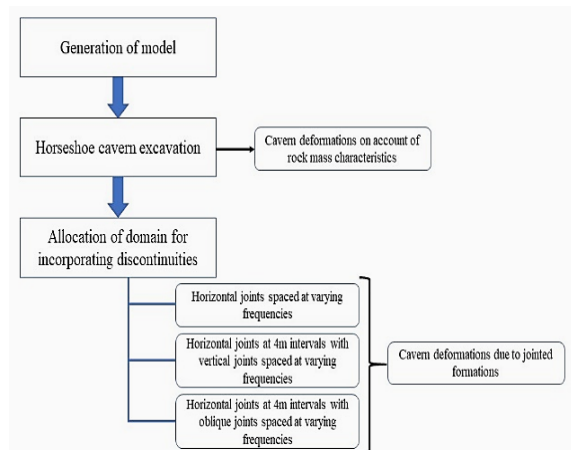
Figure 2. Flowchart of the adopted research methodology pertaining to this study

2. ROCK MASS PARAMETERS

Granitic formations with two different RMR values have been considered in this study with an overburden of 50m. The rock formations were classified into hard and moderately hard rock with RMR value of 65 and 54 respectively. Physico-mechanical properties of different materials utilized in model generation are presented in Table 1 and the joint properties are summarized in Table 2.

Material properties were introduced in the model using 'prop mat' command. Subsequently, with the usage of 'change mat' command, rock properties were assigned to the corresponding blocks. Joint properties were assigned with the help of 'change joint' command. For both ends of the generated model, displacements in x and z directions were restrained, and displacements in three different directions were restricted at the model base.

2. 1. In-situ Stress   The vertical in-situ stress of 8.12MPa and 7.25MPa were introduced by considering the density of rock mass as per Table 1. Orientation of cavern has been attained in a way such that maximum stress in horizontal direction of magnitude 12.18MPa and 10.88MPa is experienced along the cavern length and minimum horizontal stress magnitude of 8.932MPa and 7.98MPa is addressed normal to axis of cavern.
K_H (maximum horizontal stress/Vertical stress): 1.5
K_h (Minimum horizontal stress/Vertical stress): 1.1

Due to the existence of numerous discontinuities in the generated model, the estimation of existing stresses is

TABLE 1. Physico-Mechanical properties of rocks

RMR	Elastic modulus (Pa)	Shear modulus (Pa)	Cohesion (Pa)	Friction angle (Deg.)	Density (kg/m³)
65	17.3e9	10.4e9	1.2e6	70	2.8e3
54	3.8e9	2.3e9	0.56e6	60	2.5e3

TABLE 2. Input properties of joints and joint sets

Normal stiffness (Pa)	Shear stiffness (Pa)	Friction angle (Deg.)
9.0e9	0.9e9	42

very difficult via both analytical computations as well as field measurement. A research study delineated that for complex geological formations, application of proper boundary stresses should be performed for attaining the existing stresses in the generated model which has been adhered in this study also [24, 25]. The existing stress conditions were ascertained in the generated model with the usage of 'In situ' command and incorporation of gravity loading was attained with the usage of 'gravity' command. Automatic damping was used to dampen the equations of motion under applied initial as well as induced conditions and this was achieved with 'damp auto' command. Subsequently, analysis was performed in multiple stages involving in-situ equilibrium, arched roof excavation as well as excavation of cavern body both in non-fractured and fractured medium as illustrated in Figures 3 to 6.

3. RESULTS AND DISCUSSION

The model was analyzed in two types of rock formation and the maximum displacements in both directions were procured at the observation points denoted on the cavern profile as per Figure 7. Later, joint sets were included in the model by considering only hard rock properties.
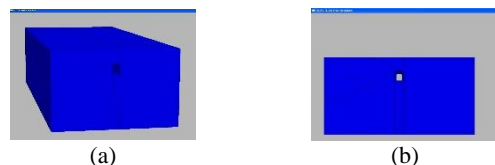
(a)   (b)
Figure 3. Cavern created within the block
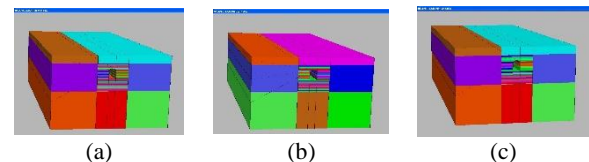
(a)   (b)   (c)
Figure 4. Cavern created within horizontal joints at spacing (a) 2m, (b) 4m and (c) 6m
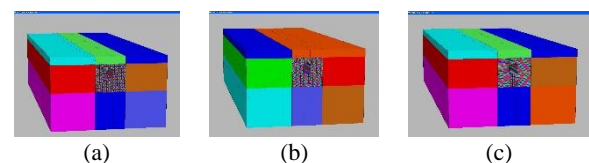
(a)   (b)   (c)
Figure 5. Cavern created with horizontal joints (4m) and vertical joints at (a) 2m, (b) 4m and (c) 6m spacings
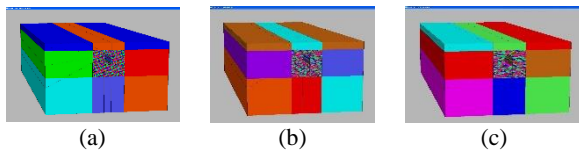
Figure 6. Cavern created with horizontal joints (4m) and oblique joints at (a) 2m, (b) 4m and (c) 6m spacings

Displacements at these corresponding points were found out varying the spacing of joint sets.

Stage 1: Investigations were performed in intact rock mass having two different types of rock properties. The displacements reported hereafter includes the direction of displacement which has been denoted with proper sign. For vertical displacements, displacements occurring in the downward direction is presented with a negative sign whereas along the cavern walls, positive displacements indicate displacements towards the right side and negative displacements indicates displacement are occurring towards the left side. Figure 8 shows the displacement at the cavern crown for both rock formations. Table 3 depicts the maximum displacements in both directions at the left wall.

The maximum vertical displacement procured at the right wall of cavern has also been assessed and the magnitudes are depicted in Table 4. It can be observed that magnitude of increase in lateral displacements along the side walls was significantly higher as compared to displacements in vertical direction.

The vertical displacement was found to be -1.89mm at the crown in case of hard rock, which increased to -6.84mm for moderately hard rock. Similar trend of
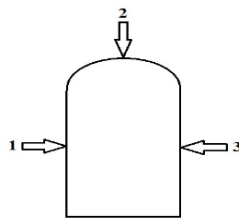
Figure 7. Observation points of cavern
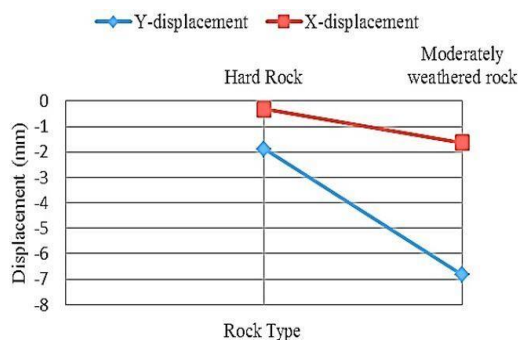
Figure 8. Displacements at the crown of cavern for two types of rock formation

TABLE 3. Displacements at left wall for both rock formations

Maximum Displacement (mm)	Hard rock	Moderately weathered rock
Vertical	-0.123	-0.854
Horizontal	9.17	24.7

TABLE 4. Displacements at right wall for both rock formations

Maximum Displacement (mm)	Hard rock	Moderately weathered rock
Vertical	-0.213	-0.735
Horizontal	-10.8	-29.2

increase in horizontal displacement was found while carrying out the analysis in both rock formations. The horizontal displacement at cavern crown was found to be -0.324mm in case of hard rock, which increased to -1.64mm in case of moderately hard rock. This aspect depicted that vertical displacement at the cavern crown is the predominant one which increased drastically in case of moderately weathered rock.

In case horizontal displacements at the side walls, similar trend of increment in the deformation magnitude has been observed for moderately weathered rock. The maximum horizontal displacement at the left wall observed to be 9.17mm for hard rock condition which substantially increased to 24.7mm in case of moderately weathered rock. The maximum horizontal displacement at the right wall was higher in moderately hard rock formation with a value of -29.2mm as compared to -10.8mm in hard rock formation. It can be observed that magnitude of increase in lateral displacements along the side walls was significantly higher as compared to displacements in vertical direction.

Stage 2: The later part of this study comprises of asserting the stability of cavern under the influence of different types of discontinuities. Horizontal (H) joint sets were incorporated in the model with different joint spacings. Three different frequencies of horizontal joint spacing have been explored in this study in order to attain comprehensive insight regarding the displacements incurred along the cavern periphery with respect to the joint spacings. Displacements in both directions were extracted at the observation points at different intervals along the cavern length and the maximum displacement has been reported hereafter.

The crown of cavern incurred maximum vertical displacement after the incorporation of horizontal joints. In case of intact rock mass, maximum displacements in vertical and horizontal direction were observed to be -1.89mm and -0.32mm, respectively; which increased considerably after the inclusion of horizontal joints. After the inclusion of horizontal joints at a spacing of 2m, the maximum vertical and horizontal displacements showed considerable increase with values of -4.14mm and -

0.955mm, respectively. This suggests that presence of discontinuities significantly proliferated the vertical displacement at cavern roof. Maximum vertical and horizontal displacements were found to be -3.48mm and -0.513mm, respectively when the spacing of joints increased to 4m. When the joint spacing was further increased to 6m, the maximum vertical and horizontal displacements were found to be -1.96mm and -0.389mm, respectively. The frequencies of the joint sets are quite a significant parameter in terms of asserting the displacements along the cavern periphery. Higher spacing of horizontal joint sets depicted less increment in both horizontal and vertical displacements at the cavern peripheries which increased drastically with the reduction of spacing of the horizontal joints. The maximum displacements at crown under horizontal jointing are depicted in Table 5. Tables 6 and 7 depicts the displacements at the left and right wall of cavern, respectively.

The presence of horizontal joints increased the magnitudes of horizontal displacements along the cavern walls as compared to intact rock mass. In the later part, along with horizontal joint sets, two different types of joint sets i.e., vertical and oblique joint sets, have also been incorporated in the model having hard rock properties. The displacements in both directions were analyzed along the periphery of cavern. The spacing of the horizontal joints has been kept as constant i.e., 4m, so that significant insights can be attained due to incorporation of other joint sets as well as variations in their frequencies. The joint sets incorporated in the model are as follows:
1. Horizontal joints and vertical joints at 4m and 2m spacing, respectively.
2. Horizontal joints along with vertical joints both at 4m spacing.
3. Horizontal joints and vertical joints at 4m and 6m spacing, respectively.
4. Horizontal joints at 4m spacing and oblique joints at 2m spacing.
5. Horizontal joints and oblique joints at 4m spacing.
6. Horizontal joints at 4m spacing along with oblique joints at 6m spacing.

TABLE 5. Displacements observed at cavern crown

Max. Displacement (mm)	No joints	H joints at 2m	H joints at 4m	H joints at 6m
Vertical	-1.89	-4.14	-3.48	-1.96
Horizontal	-0.32	-0.955	-0.513	-0.389

TABLE 6. Displacements obtained at the left wall

Maximum Displacement (mm)	No joints	H joints at 2m	H joints at 4m	H joints at 6m
Vertical	-0.12	-0.703	-0.484	-0.229
Horizontal	9.17	12.6	11.8	11.2

TABLE 7. Displacements obtained at the right wall

Maximum Displacement (mm)	No joints	H joints at 2m	H joints at 4m	H joints at 6m
Vertical	-0.21	-0.94	-0.37	-0.32
Horizontal	-10.8	-13.4	-12.6	-11.4

Figure 9 depicts that the maximum displacements procured in vertical direction at the cavern crown were -7.81mm, -6.26mm and -5.59mm with an increase in spacing of vertical joints. The maximum horizontal displacements observed at the crown were -0.682mm, -0.427mm and -0.373mm, respectively with an increase in spacing of vertical joints. This suggests that incorporation of multiple joint sets increased the vertical displacement at the cavern crown significantly, whereas, the change in horizontal displacement at the cavern crown were observed to be insignificant. Moreover, as the vertical joint spacing was increased, reduction of vertical displacement at the cavern crown was also observed.

Figure 10 shows the highlights of the displacement at the left wall of cavern. The lateral displacement procured at the left wall was significantly higher due to the inclusion of multiple joint sets. With the increment in spacing of vertical joints, maximum vertical displacements procured at left cavern were -0.802 mm, -0.696 mm and -0.494 mm, respectively; showing a decrement in the vertical displacement magnitude with increase in vertical joint spacing. Incorporating vertical joints at 2m interval along with horizontal joints spaced at 4m interval induced a lateral displacement of 40.3mm, which drastically reduced to 23.8mm in case of vertical joints spaced at 6m intervals along with horizontal joints at 4m spacing.

Further, oblique (O) joint sets at different spacings i.e., 2m, 4m and 6m, respectively, were incorporated in the model along with horizontal (H) joint set spaced at 4m interval and the displacements at cavern crown have been reported in Table 8 and displacement at the right wall has been illustrated in Figure 11.

The maximum displacements in vertical direction observed at the cavern crown after inclusion of oblique
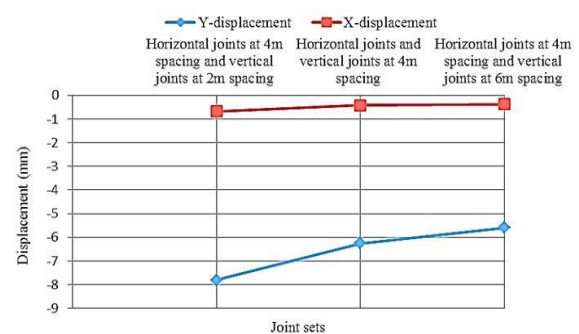
Figure 9. Displacements at cavern crown after vertical joint set inclusion
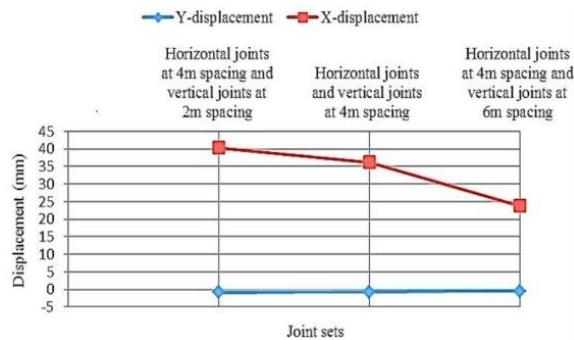
Figure 10. Displacements at left wall of cavern after vertical joint set inclusion

TABLE 8. Displacements with horizontal and oblique joints at cavern crown

Maximum Displacement (mm)	H joints (4m) with O joints (2m)	H joints and O joints (4m)	H joints (4m) with O joints (6m)
Vertical	-8.10	-7.40	-7.17
Horizontal	-1.47	-1.21	-1.19
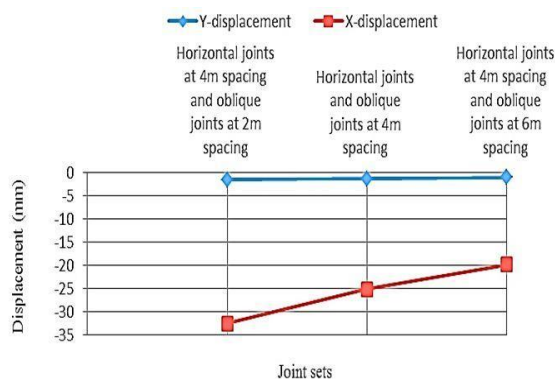
Figure 11. Displacements at right wall of cavern after inclusion of oblique joint set

joint sets were -8.1mm, -7.40mm and -7.17mm. Similar trend of decrement in the magnitude of vertical displacement was procured for the cavern roof with the increment in the spacing of the oblique joint set. Maximum displacement in the horizontal direction also reduced with the increment in spacing of oblique joints. At the right wall of cavern, maximum vertical displacements observed were -1.48mm, -1.27mm and -1.03mm comprising of horizontal joints at 4m intervals along with oblique joints spaced at 2m, 4m and 6m respectively. Maximum lateral displacements observed at the right wall of cavern for the aforementioned scenario were -32.6mm, -25.1mm, and -19.8mm respectively with the increase in spacing of oblique joints. The incorporation of oblique joints along with horizontal joints substantially increased the magnitude of lateral displacements along the right wall of cavern, however,

the magnitude of lateral displacements procured for the oblique joint with horizontal joints was lower as compared to lateral displacements pertaining to the model having vertical joints along with horizontal joints.

The assessment of both displacements attained along the cavern periphery as per this study depicts a crucial insight into the stability of underground cavern under both intact rock mass formation as well as in jointed medium. The agglomeration of discontinuities increases the chances of collapse of underground structures which has been highlighted in this study. The magnitudes of both vertical as well as lateral displacements as attained in this study would aid the readers to adopt various remedial measures which would aid in asserting the stability of underground caverns constructed in fractured rock masses. Presence of multiple joints having different orientations increased the magnitudes of displacements along the cavern periphery which is crucial to consider before the construction of underground cavern at such locations. It was also observed that increased frequency of joints induces substantial increment in the displacements which reduces with the increment in spacing of joints. Table 9 conveys a comparative study of the displacements procured at the crown, left wall and right wall of the cavern for two types of joint sets as per this study. The horizontal, vertical and oblique joints have been abbreviated as H, V and O joints respectively in Table 9. It was also observed that the magnitude of horizontal displacement at crown for models consisting of oblique joints was greater in comparison to the models comprising of vertical joints; however, the magnitudes of procured lateral displacements were substantially less as compared to the vertical displacements.

It can be observed that for underground caverns constructed in a medium comprising of horizontal and vertical joint sets will induce more lateral displacement at the side wall as compared to medium comprising of horizontal and oblique joint sets. However, the vertical

TABLE 9. Comparative study of displacements due to varying joint sets

Max. Displacement (mm)	H (4m) and V (2m) joints	H (4m) and O (2m) joints	H and V joints (both 4m)	H and O joints (both 4m)	H (4m) and V (6m) joints	H (4m) and O (6m) joints
At cavern crown						
Vertical	-7.81	-8.10	-6.26	-7.40	-5.59	-7.17
Horizontal	-0.68	-1.47	-0.42	-1.21	-0.37	-1.19
At left wall						
Vertical	-0.80	-1.64	-0.69	-1.19	-0.49	-0.96
Horizontal	40.3	27.1	36.2	20.2	23.8	18.6
At right wall						
Vertical	-0.78	-1.48	-0.51	-1.27	-0.39	-1.03
Horizontal	-50.0	-32.6	-41.8	-25.1	-31.0	-19.8

displacements procured at the cavern crown depicted higher magnitudes for the model comprising of oblique and horizontal joint sets in comparison to the models consisting of horizontal and vertical joint sets. It was also observed that with proliferation in spacing of vertical or oblique joints in the model resulted in lower magnitudes of displacements in both the directions. The observed displacements for models with discontinuities were higher as compared to model having only intact rock formation. The subtle comprehension of displacements obtained in this study under various types of rocky formations aids to provide a holistic insight regarding the remedial measures to be taken into account for ascertaining long term stability of underground caverns.

4. CONCLUSIONS

The stability analysis of underground cavern has been performed in this study with the aid of 3DEC software under various types of intact rock as well as jointed rock mass formations and the maximum displacements procured at the cavern periphery has been reported in this study. Preliminary part of this study comprises of assessment of cavern wall deformations under two different types of geological rock mass formations followed by assessing the cavern stability with horizontal joints at different spacings and the following conclusions have been attained.

- The percentage increase in vertical displacement at the crown was nearly 260% when analysed with moderately hard rock properties in comparison to hard rock properties. The percentage increase in horizontal displacement when analysed with moderately hard rock properties were almost 170% for both right and left walls in comparison to hard rock properties.
- The vertical and lateral deformations were much more predominant at the cavern crown and cavern walls respectively.
- Incorporation of horizontal joints in the models resulted in increased instability to the cavern walls as compared to intact rock mass. Presence of joints especially its frequency, plays a significant role on the magnitude of both vertical and horizontal displacements.
- This study indicated that as the frequency of horizontal joints reduced, the vertical displacement at the cavern crown also reduced and similar trend in the lateral displacements were also observed at the cavern walls.

Multiple joint sets in the form of vertical as well as oblique joints were also included in the model along with horizontal joints. The vertical joints and oblique joints were varied at a spacing of 2m, 4m, and 6m whereas horizontal joint spacing was kept as 4m and following conclusions have been attained.

- Comparative study between models comprising of intact rock mass as well as horizontal joint at 4m with vertical joints at 2m depicted 313.2% increase in vertical displacement at cavern crown and percentage increase in horizontal displacements at left and right wall of cavern were found out to be 340% and 363% respectively. Whereas in comparison to model consisting of horizontal joint along with vertical joints at 6m spacing, the percentage increase in vertical displacement at crown was observed to be 196%. For the model comprising of horizontal joint set with vertical joints at 2m interval, the percentage increase in horizontal displacements was observed to be 160% and 187% at the left and right wall respectively in comparison to the model having horizontal joint along with vertical joints at 6m interval.
- Comparison between intact rock mass model and model comprising of lateral joints along with oblique joints at 2m spacing showed 329% rise in vertical displacement at cavern crown. The percentage increase in vertical displacement reduced to 279.3% when the spacing of oblique joints was increased to 6m.
- The models containing horizontal joints in combination with vertical and oblique joints revealed that displacements at the cavern crown is higher with oblique jointing and the cavern sidewalls depicted comparatively higher magnitudes of horizontal displacements in presence of vertical joints.

The executed numerical modelling study elucidates the response of massive buried caverns under various types of rocky formations. Such studies will lead to safe design and execution of cavern projects as well as aid in taking proper remedial measures while designing in intricate rocky formations.

5. REFERENCES

1. Shin, J., Lee, I., Lee, Y. and Shin, H., "Lessons from serial tunnel collapses during construction of the seoul subway line 5", *Tunnelling and Underground Space Technology*, Vol. 21, No. 3-4, (2006). doi: 10.1016/j.tust.2005.12.154.

2. Hoek, E. and Brown, E.T., "Empirical strength criterion for rock masses", *Journal of the Geotechnical Engineering Division*, Vol.   106,   No.   9,   (1980),   1013-1035. https://doi.org/10.1061/AJGEB6.0001029

3. Serafim, J., "Consideration of the geomechanical classification of bieniawski", in Proc. int. symp. on engineering geology and underground construction. Vol. 1, (1983), 33-44.

4. Evans, B., Fredrich, J.T. and Wong, T.F., "The brittle-ductile transition in rocks: Recent experimental and theoretical progress", *The Brittle-ductile Transition in Rocks*, Vol. 56, (1990), 1-20. https://doi.org/10.1029/GM056p0001

5. Hao, Y. and Azzam, R., "The plastic zones and displacements around underground openings in rock masses containing a fault", *Tunnelling and Underground Space Technology*, Vol. 20, No. 1, (2005), 49-61. https://doi.org/10.1016/j.tust.2004.05.003

6. Nikumbh, R.K. and Chandar, K.R., "Stress analysis between tunnel and slope for single as well as multiple tunnel scenarios: A numerical modelling approach", *Current Science*, Vol. 119, No. 3, (2020), 551. doi: 10.18520/cs/v119/i3/551-555.

7. Jiao, Y., Fan, S. and Zhao, J., "Numerical investigation of joint effect on shock wave propagation in jointed rock masses", *Journal of Testing and Evaluation*, Vol. 33, No. 3, (2005), 1-7. doi: 10.1520/JTE12680.

8. Kuili, S. and Sastry, V.R., "A numerical modelling approach to assess the behaviour of underground cavern subjected to blast loads", *International Journal of Mining Science and Technology*, Vol. 28, No. 6, (2018), 975-983. https://doi.org/10.1016/j.ijmst.2018.05.015

9. Azimi, Y., "Prediction of seismic wave intensity generated by bench blasting using intelligence committee machines", *International Journal of Engineering*, Vol. 32, No. 4, (2019), 617-627. doi: 10.5829/IJE.2019.32.04A.21.

10. Li, S., Wang, Z., Ping, Y., Zhou, Y. and Zhang, L., "Discrete element analysis of hydro-mechanical behavior of a pilot underground crude oil storage facility in granite in china", *Tunnelling and Underground Space Technology*, Vol. 40, (2014), 75-84. https://doi.org/10.1016/j.tust.2013.09.010

11. Guzev, M., Kozhevnikov, E., Turbakov, M., Riabokon, E. and Poplygin, V., "Experimental investigation of the change of elastic moduli of clastic rocks under nonlinear loading", *International Journal of Engineering, Transactions C: Aspects,* , Vol. 34, No. 3, (2021), 750-755. doi: 10.5829/IJE.2021.34.03C.21.

12. Fahimifar, A., "Proposals for a failure criterion applicable to discontinuous rocks", *International Journal of Engineering*, Vol. 7, No. 3, (1994), 125-132. https://www.ije.ir/article_71104_c58f622154a1a7f1f3221dad4f5b3799.pdf

13. Vafaeian, M., "Relationship between ground settlement due to tunnelling and ground physico-mechanical peroperties", *International Journal of Engineering*, Vol. 9, No. 1, (1996), 45-49. https://www.ije.ir/article_71143.html

14. Al-Saoud, M., Shlash, K. and Fattah, M., "Boundary element analysis of a lined tunnel problem", *International Journal of Engineering, Transactions B: Applications*, Vol. 25, No. 2, (2012), 89-98. doi: 10.5829/idosi.ije.2012.25.02b.02.

15. Alipenhani, B., Bakhshandeh Amnieh, H. and Majdi, A., "Application of finite element method for simulation of rock mass caving processes in block caving method", *International Journal of Engineering, Transactions A: Basics*, Vol. 36, No. 1, (2023), 139-151. doi: 10.5829/IJE.2023.36.01a.16.

16. Rasti, A. and Marandi, S.M., "Parameters analysis of the covering soil of tunnels constructed in liquefiable soils", *International Journal of Engineering, Transactions A: Basics*, Vol. 25, No. 4, (2012), 333-346. doi: 10.5829/idosi.ije.2012.25.04a.05.

17. Sherizadeh, T. and Kulatilake, P.H., "Assessment of roof stability in a room and pillar coal mine in the us using three-dimensional distinct element method", *Tunnelling and Underground Space Technology*, Vol. 59, (2016), 24-37. https://doi.org/10.1016/j.tust.2016.06.005

18. Shreedharan, S. and Kulatilake, P.H., "Discontinuum–equivalent continuum analysis of the stability of tunnels in a deep coal mine using the distinct element method", *Rock Mechanics and Rock Engineering*, Vol. 49, (2016), 1903-1922. https://doi.org/10.1007/s00603-015-0885-9

19. Cui, Z., Sheng, Q. and Leng, X., "Control effect of a large geological discontinuity on the seismic response and stability of underground rock caverns: A case study of the baihetan# 1 surge chamber", *Rock Mechanics and Rock Engineering*, Vol. 49, (2016), 2099-2114. https://doi.org/10.1007/s00603-015-0908-6

20. Kuili, S. and Sastry, V.R., "Prediction and assessment of lateral displacement of rock mass along the length of the horseshoe cavern–a numerical modelling approach", *International Journal of Geological and Geotechnical Engineering*, Vol. 3, No. 1, (2017), 17-28. https://doi.org/10.37628/jgget.v3i1.183

21. Van Kien, D., "Numerical simulation of the stability of rock mass around large underground cavern", *Civil Engineering Journal*, Vol. 8, No. 1, (2022), 81-91. doi: 10.28991/CEJ-2022-08-01-06.

22. Hassan, S.A., Shitote, S.M. and Kiplangat, D.C., "Predictive models to evaluate the interaction effect of soil-tunnel interaction parameters on surface and subsurface settlement", *Civil Engineering Journal*, Vol. 8, No. 11, (2022), 2424-2444. doi: 10.28991/CEJ-2022-08-11-05.

23. Fekete, S. and Diederichs, M., "Integration of three-dimensional laser scanning with discontinuum modelling for stability analysis of tunnels in blocky rockmasses", *International Journal of Rock Mechanics and Mining Sciences*, Vol. 57, (2013), 11-23. https://doi.org/10.1016/j.ijrmms.2012.08.003

24. Tan, W., Kulatilake, P. and Sun, H., "Influence of an inclined rock stratum on in-situ stress state in an open-pit mine", *Geotechnical and Geological Engineering*, Vol. 32, (2014), 31-42. https://doi.org/10.1007/s10706-013-9689-4

25. Tan, W., Kulatilake, P., Sun, H. and Sun, Z., "Effect of faults on in situ stress state in an open-pit mine", *Electronic Journal of Geotechnical Engineering*, Vol. 19, (2014), 9597-9629. doi: 10.15446/ejge.v19n10.5322.

Persian Abstract

چکیده

غارها دهانه‌های زیرزمینی عظیمی هستند که برای اهدافی مانند تأسیسات دفاعی و دفع زباله‌های هسته‌ای حفاری شده‌اند که برای لایه‌های ضعیف متشکل از توده‌های سنگی شکسته چالش‌برانگیز می‌شود و ممکن است منجر به فجایع آینده شود. این مطالعه به بررسی پایداری یک غار نعل اسبی در انواع مختلف توده‌های سنگی گرانیتی و همچنین سنگ‌های شکسته اختصاص دارد. دو نوع مختلف از سازندهای گرانیتی محاسبه شده و جابجایی های به دست آمده در امتداد حاشیه غار در قسمت مقدماتی این مطالعه نشان داده شده است. یک افزایش در جابجایی عمودی در تاج ۲۶۰٪ و جابجایی جانبی تقریباً ۱۷۰٪ برای هر دو دیوار برای سنگ با هوازدگی متوسط مشاهده شد. علاوه بر این، پیامدهای ناشی از جهت گیری و فرکانس مجموعه های مفصلی بر روی جابجایی های ایجاد شده نیز بررسی شده است. این مطالعه با در نظر گرفتن ترکیبی از مجموعه های مفصلی با فواصل مختلف برای بررسی تأثیر آنها بر دیواره های غار، تازگی خود را به دست می آورد. وجود ناپیوستگی‌ها نشان می‌دهد که فاصله مفصل افقی به شدت باعث افزایش بزرگی تغییر شکل می‌شود که با کاهش فرکانس اتصال کاهش می‌یابد. متعاقباً همراه با اتصالات افقی در فاصله ٤ متری، مجموعه درزهای عمودی و مایل نیز در فرکانس های مختلف گنجانده شد. در نظر گرفتن درزهای عمودی در فاصله ۲ متری با اتصالات افقی باعث افزایش ۳۱۳/۲ درصدی جابجایی عمودی در تاج غار و همچنین افزایش ۳٤۰ درصدی و ۳٦۳ درصدی تغییر شکل جانبی در دیواره چپ و راست نسبت به سنگ سالم شد. در مورد اتصالات مورب با فاصله ۲ متر با اتصالات افقی، افزایش تغییر شکل عمودی در تاج به ۳۲۹٪ در مقایسه با سنگ دست نخورده افزایش می یابد.

Performance Analysis and Optimization of Asymmetric Front and Back Pi Gates with Dual Material in Gallium Nitride High Electron Mobility Transistor for Nano Electronics Application

Y. Gowthami, B. Balaji*, K. Srinivasa Rao

Department of Electronics and Communication Engineering, Koneru Lakshmaiah Education Foundation, Green Fields, Vaddeswaram, Guntur, Andhra Pradesh, India

A B S T R A C T

The impact of aluminium nitride (AlN) Spacer, Gallium Nitride (GaN) Cap Layer, Front Pi Gate (FG) and Back Pi Gate(BG), Dual Floating material High K dielectric material such as Hafnium dioxide (HfO$_2$), Aluminium Oxide (Al$_2$O$_3$), Silicon nitride (Si$_3$N$_4$) on Aluminium Galium Nitride/ Gallium Nitride (AlGaN/GaN), Heterojunction High Electron Mobility Transistor (HEMT) of 6nm technology is simulated and extracted the results using the Silvaco Atlas Technology Computer-Aided Design (TCAD) tool.The importance of High K dielectric materials like Al$_2$O$_3$ and Si$_3$N$_4$ were studied for the proposal of GaN HEMT. AlN, GaN Cap Layers, and High K Dielectric material are layered one on another to overcome the conventional transistor draw backs like surface defects, scattering of the electron, and less mobility of electron. Hot electron effect is overcome by Pi type gate.Triple tooth floating material is placed in the buffer layer to improve breakdown voltage. Therefore, by optimizing the HEMT structure the inabilities for certain devices are converted to abilities. The dependency on DC characteristics and RF characteristics due to GaN Cap Layers, Multi gate (FG &BG), and High K Dielectric material, Dual triple tooth material in buffer layer with recessd gate is established. Further Compared Single Gate (SG) Passivated HEMT, Double Gate (DG) Passivated HEMT, Double Gate Triple (DGT) Tooth Passivated HEMT, High K Dielectric Front Pi Gate (FG) and Back Pi Gate (BG), Asymmetric High K Dielectric Front Pi Gate (FG) and Back Pi Gate (BG) with recessed gate Nanowire HEMT. It was observed that the proposed resulted with increased Drain Current (Ion) of 7.5 (A/mm), low Leakage current (I$_{off}$) 3E-15 (A), Transconductance (Gm) of 4.8 (S/mm), Drain Conductance (G$_d$) of 2.5 (S/mm), Maximum Oscillation frequency (F$_{max}$) 745 GHz, Minimum Threshold Voltage (Vth) of -4.5V, On Resistance (Ron) of 0.12(Ohms) at V$_{gs}$=0V.

doi: 10.5829/ije.2023.36.07a.08

1. INTRODUCTION

As Gallium Nitride (GaN) wide band gap material, it possesses exclusive required material properties like high thermal stability, high breakdown voltage, high saturation velocity voltage, high current density, and high saturation velocity it can be implemented in high-power microwave applications [1]. In semiconductor optoelectronics models, GaN-based transistors have its own importance. Heterostructure, high electronic mobility Transistor is formed between semiconductor material of different Band gaps where electrons are generated and travel with rapid speed (mobility of electron) [2]. The large bandgap, high velocity, high current, and less On Resistance (Ron) characteristics, reflect high efficiency for HEMT [3]. The size reduction is the current trend in implementation to result in high performance but the reduction in size of transistor, device is permissible to some extent only if the device is further decreased which leads to short channel effects, leakage current [4]. A small transistor means more numbers in the transistor in the same area with a wafer of the same size,

Corresponding Author Institutional Email: vahividi@gmail.com
(B. Balaji)

more chips per wafer the manufacturer can fabricate. It indicates the advancement of technology towards nano world [5]. High performance is obtained due to advanced nanowire technology [6]. For example, it reflects in clock time per instruction within the same time more instruction can be executed [7]. More function units in one chip can be integrated reducing the power consumption requirements [8]. Reduction in transistor size focuses on decreasing gate length [9]. When clock speed is taken into consideration for processors, the gate length is the primary to be considered. More we reduce the gate length faster than the device works; very fast calculation is performed [10-12]. High doping causes drain-induced barrier lowering (DIBL) which causes the current to leak, high subthreshold conduction is the state where FET, which is not completely ON, not completely OFF [13]. This will be presented if the transistor gate length is reduced beyond the limitation. To overcome this limitation Heterojunction High Electron Mobility Transistor came (HEMT) into existence [14, 15]. Gallium Arsenide (GaAs), Gallium Nitride (GaN), Indium Phosphide (InP), and Silicon Carbide (SiC) can meet the requirements. Among these materials, in high–power applications GaN make its use due to its high saturation velocity, high wideband gap, and high critical field properties [16, 17]. The material properties and electronic properties of GaAs, GaN, SiC, and Si are sorted in Table 5. From this table content, it is observed that Gallium Nitride ideal candidate to proceed for implementation in the advancement of Power Electronics [18]. It is observed by Johnson's figure of merit that GaN ideal candidate for high temperature and high power due to its high electron mobility, saturation velocity, and high breakdown voltage [19]. The narrow channel plays a key role that triggers the device to work at microwave frequencies, this is provided by GaN [20]. HEMT is constructed by deploying two semiconductor substances with identical lattice constant, and distant band gap materials are stacked on one another. At the inter-junction of these two material Bidirectional Electron Gas (2DEG) is formed. A broad class of HEMTs is existent namely Gama gate, T gate, Gate Field plate (GFP), Camel shape Gate (CG), Discrete Field Plate (DFP), Multiple Grating Field Plate (MGFP) Gate HEMT [21]. These are limited by Early High Leakage current, Breakdown effects, and shorter channel effects. Conventional transistors are optimized to overcome these effects [22]. For the existing HEMT to improve the characteristics of the device GaN layers, Front Pi Gate, and Back Pi Gate are incorporated [23]. These Cap layers passivation layers provide sealing the first layer of nanowire HEMT structure from external atmospheric fluctuations. The proposed Asymmetric High K Dielectric Front Pi Gate (FG) and Back Pi Gate (BG) with recessed gate Nanowire HEMT overcomes the limitation of Dual gate HEMT and exhibits optimized

nanowire HEMT Structure which gives optimistic DC and RF characteristics [24]. The results show that high K dielectric FG & BG nanowire HEMT results improved on current, trans conductance, drain conductance, maximum oscillation frequency, improved cutoff frequency, with reduced leakage current.

2. STRUCTURE

The complete structure for the proposed Asymmetric Front Pi Gate &Back Pi Gate recessed with Dual floating material in buffer layer high electron mobility transistor (HEMT) device with the gate electrode, Source & Drain is shown in Figure 1. The High K Dielectric materials HfO_2, Al_2O_3, SiO_2, TiO_2, Si, and Si_3N_4 with K values and gap (EV) are listed in Table 1.

Hafnium oxide (HfO_2), Silicon (Si). Silicon Dioxide (SiO_2) Aluminum Oxide (Al_2O_3), Titanium Dioxide (TiO_2), and Silicon Nitride (Si_3N_4) are the material with High K dielectric constant. These materials play a key role during the process of semiconductor manufacturing [25, 26].
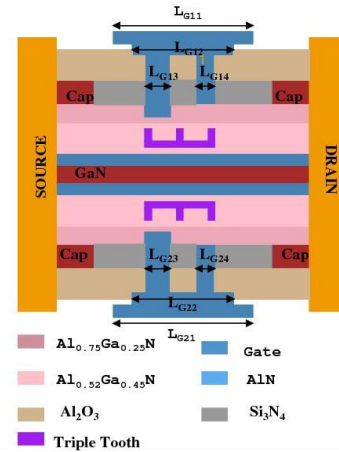
Figure 1. High K Dielectric FG-BG G13 & G23 recessed, Dual floating material GaN HEMT nanowire HEMT structure with Si_3N_4 /Al_2O_3 passivation layers

TABLE 1. High K Dielectric material HfO_2, Al_2O_3, SiO_2, TiO_2, Si, Si_3N_4 with K Values and gap (EV) are listed in table

Material	K Values	Gap(eV)
Si	3.9	1.1
SiO_2	3.9	9
Si_3N_4	7	5.3
Al_2O_3	9	8.8
TiO_2	80	3.5
HfO_2	25	5.8

Among these materials SiO_2 is conventional material where it has been used for past decades in FET, As the size of FET decreases the thickness of SiO_2 is reduced, where the gate capacitance is reduced, and thereby current improved, increasing the device performance.

As the thickness is continuously reduced beyond the limit leakage current increased and led to high power utility (consumptions) and the reliability of the device reduced (degrades). High dielectric materials lead to an increase in gate capacitance, with no leakage effects. The capacitance is related as in the following equation

$$C = \frac{kA\varepsilon_o}{t} \tag{1}$$

A is the area of the capacitance, ε_o is free space permittivity, k is dielectric constant of the material, t is capacitor oxide insulator thickness. As the capacitance is related to k by altering k we can improve the capacitance, where the derive current can be improved.

$$I_{D,Sat} = \frac{WC\mu(V_G - V_{th})^2}{2L} \tag{2}$$

The drain current equation is expressed in Equation (2). Here $I_{D,Sat}$ Saturation Drain Current is directly proportional to capacitance, W is the width of the transistor channel, the length of the channel, μ is the mobility of the carrier. V_{th} is the threshold voltage. Since Si_3N_4, Al_2O_3 are the elements that are stable thermos dynamically and have a high melting point. Al_2O_3 has low defect density, highly uniform, scalable in nanometers, is robust nature and can be manufactured. 20nm Al_2O_3 thickness was deployed. $Al_{0.75}$ $Ga_{0.25}$N, $Al_{0.52}Ga_{0.45}$N, AlN (Spacer layer), GaN, AlN, $Al_{0.52}Ga_{0.45}$N, $Al_{0.75}Ga_{0.25}$N these materials are deployed in this sequence respective with 36nm, 38nm, 34nm, 43nm, 34nm, 38nm, 36nm. Spacer Layer is to improve the density of 2DEG (2-Dimensional Electron Gas) Aluminum Nitride is stable at temperatures over 2000° in inert atmosphere. It possesses high thermal conductivity. The unique properties of AlN make its usage in lighting, renewable energy, electronics, optics, etc. It is a solid nitride of Aluminum material. At room temperature, it has approx. 6eV of the band gap. AlN layer used for carrier confinement reduction in alloy scattering improved scattering. GaN Cap layer of 2nm is deployed on the top of the structure. By using GaN cap layer carrier mobility improved, improve transport mechanism. The probability of penetrating the mobility electron into AlGaN is reduced due these layers. High conduction is possible due to the presence of cap layer. Scattering of Alloy reduced, and better confinement of carrier, improved conductivity and mobility is observed by employing the cap layer on the top of heterostructure which proposed makes easy to fabric ohmic contact.

AlGaN is the barrier layer where it is layered with various thicknesses. Leakage current is reduced I_{on}/I_{off} is increased by this employing. It shows influence in R_{on}

characteristics. High thickness of AlGaN shows the degradation of system performance. It avoids the penetration of electrons into buffer layer. Trapping effects reduction happens so that the dynamic R_{on} improved [27]. Back barrier layer (BBL) thickness results in reduction in leakage current and dynamic R_{on}; BBL can be varied from 0 to 200nm; GaN channel is wurtzite crystal structure. It possesses high bandgap of 3.49 (EV) with electron mobility of 900 (cm_2 /vs), electron peak velocity is 2.7 x 10^7 (cm/s), 2DEG sheet electron density is 20 x 10^{12} (cm^{-2}), Critical breakdown field 3.3 (MV/cm), thermal conductivity > 1.7 (W/cm-K), Relative dielectric constant (ε_r) -9.0 GaN material possess high thermal conductivity, high saturation drift velocity. These properties are required for the device to work in high frequency for having high power switching and to work at high temperatures [28]. Hetero-junction is formed when two material of different band gaps with almost the same lattice constant. The field effect transistor that incorporates hetero-junction is called the high electron mobility transistor (HEMT) [29]. The junction is the interface between two materials. In junction 2-dimensional electron gas raises and flows from the source to drain [30]. The mobility of the electron depends on the material used to form a hetero-junction. Two-dimensional gas characterizes the properties of electron mobility, electron density, gate bias ON current or drive current, Transconductance (g_m), threshold voltage (V_{th}), and cut-off frequency are determined depending on 2-dimensional electron gas. The improvement of the device's 2D Gas properties play a vital role and understanding the key mechanism of 2DEG is necessary [31]. For high power, high-frequency application AlGaN/GaN Aluminum Galium Nitride/Galium Nitride is used due to its high frequency and high-power application [32]. ∏ shaped gate formed by dividing T gate pillar into 2 symmetric halfs [33]. G13, G14 are the front gate legs and G23, G24 is right gate legs. Experimentation is performed by recessing legs of front gate and back gate with different cases. G13 leg recessed, G13 & G23 recessed, G24 & G14 recessed. Compared to T shaped gate ∏ shaped gate possess low channel temperature. When G13 and G23 is recessed ∏ shaped gate structure thermalization to electron happens and in ∏ gate energy loses so this tends to reduce peak channel temperature [34]. In ∏ structure parasitic capacitance increase which reflects on f_T reduction; this can be overcome by increasing the height of pillar Gate recess technique improves the device performed by 25 percent [35]. Triple tooth floating metal removes the gate which is virtually present between gate and drain.

The advantages of the proposed structure are to reduce hot electron effect, under which maintaining the device performance stable and well into the millimeter wave frequency range. Proposed dual gate HEMT offers improved transconductance and better immunity and

reduces short channel effects subthreshold swing compared to single gate HEMT and disadvantage is the devise should be operated in orderly manner following set of rules to sustain the device performance for longer period

3. RESULTS AND DISCUSSION

Using the Silvaco TCAD tool proposed transistor characteristics simulations are performed. Figure 1 shows high K dielectric FG-BG G13 & G23 recessed, dual floating material GaN HEMT nanowire HEMT structure with Si_3N_4 /Al_2O_3 passivation layers. The two gates play a key role in improving drain current and conductance of the Device.

Table 2 shows the dimensions of the proposed structure and Table 3 shows the physical properties of dielectric passivation materials Si_3N_4, SiO_2, and Al_2O_3. Multi combination of Al_2O_3 and Si_3N_4 showed improved results for the proposed structure

Further, the performance of the device can be optimized. GaN cap layers are placed on AlGaN layer to optimize the results. The location of the gate is an important parameter that improves the performance. It

consists of a front gate in the upper part and a back gate in the lower part of the proposed structure. The cap layers are placed using GaN material on either side of the front gate and back gate. The top layer gets protection from the external environment, and electron scattering reduces and optimizes performance.

The novel 6nm nanowire HEMT transistor is executed on the Silvaco TCAD tool, and the complete results are discussed in this section.

Figure 2 shows drain current changes concerning various drain voltage characteristics of HEMTs with various physical structures of 6 nanometers at Vgs = 0V for the proposed structure that is G13 & G23 recessed with dual floating material, G13 & G23 recessed FG (Front Gate)- BG (Back Gate) GaN HEMT, G14 & G24 recessed FG-BG GaN HEMT, G14 recessed FG-BG GaN HEMT, the proposed structure exhibits high drain current. It results in an increased drain Current (I_d) of 7.5 A/mm appearing for the proposed structure.

From Equation (3) Cutoff frequency (f_T) depends on the length of the gate (L_g) and the saturation velocity of the material and transconductance. As drain current increases, transconductance increases. As the transconductance is directly proportional to the cutoff frequency, the cutoff frequency increased to 743GHz. So, by proper placement of the transistor gate, the required cutoff frequency can be attained.

$$Cutoff\ Frequency = \frac{Vsat}{2L_G\Pi} \qquad (3)$$

Figure 3 shows the Oscillating frequency (f_{max}) concerning gate voltage, of HEMTs with various physical structures of 6 nanometers at Vgs = 0V i.e. For the proposed structure that is G13 & G23 recessed with dual floating material, at gate voltage Vds = 0.2V is shown. It resulted in maximum oscillating frequency (f_{Max}) of 743GHz appeared same as High K dielectric FG & BG nanowire HEMT for the proposed structure also.

TABLE 2. Dimension along the X-axis and Y-axis of the proposed structure

Material	X_{min}	X_{max} (nanometer)	Y_{min} (nanometer)	Y_{max} (nanometer)
$Al_{0.52}Ga_{0.45}N$	0	320	0	33
AlN	0	320	33	34
$Al_{0.75}Ga_{0.25}N$	0	320	34	36
$Al_{0.52}Ga_{0.45}N$	0	320	36	38
GaN	0	320	38	43
$Al_{0.52}Ga_{0.45}N$	0	320	43	4 9
AlN	0	320	49	50
GaN	0	320	50	350
Sapphire	0	320	350	750

TABLE 3. Physical properties of dielectric passivation materials

	SiO_2	Al_2O_3	Si_3N_4
Thermal Conductivity (w/cm/ k)	0.014	18	0.37
Melting Point (ºC)	1600	2072	1900
Density(g/cm³)	2.2	3.95	3.1
Energy gap at 300k(Ev)	9	7.6	5
Refractive index	1.46	1.77	2.05
Dielectric Constant	3.9	10	7.5
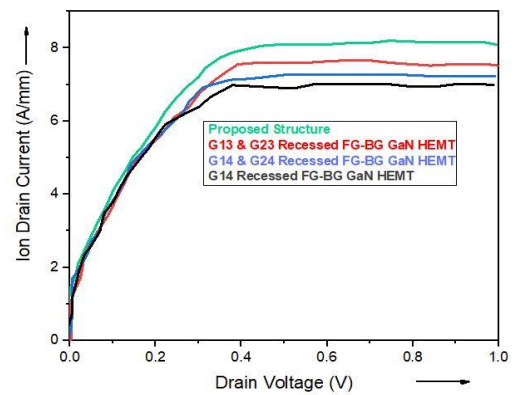
Figure 2. Drain Current changes concerning various Drain voltage characteristics for HEMTs with various physical structures of 6-nanometer technology at Vgs = 0V
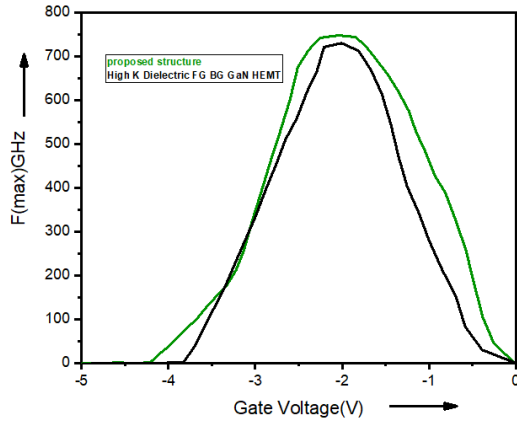
Figure 3. Maximum Oscillation frequency with various gate voltages for the proposed structure that is G13 & G23 recessed with dual floating material, high K dielectric FG & BG HEMT

Transconductance (gm) is defined as the ratio of change in drain current (I_d) to the change in the change in the gate to source voltage (V_{GS}) represented in Equation (4):

$$Transconductance = \frac{dI_D}{dV_{GS}} \qquad (4)$$

Figure 4 shows Transconductance (G_m) concerning gate Voltage V_{gs} for HEMTs with various physical structures of 6 nanometers at V_{ds} = 0.2V i.e. The proposed structure, G13 & G23 recessed with dual floating material, G13 & G23 recessed FG (Front Gate)-BG (Back Gate) GaN HEMT, G14 & G24 recessed FG-BG GaN HEMT, G14 recessed FG-BG GaN HEMT. It is shown that increased Transconductance of 4.8 (S/mm). Appeared for the proposed structure.
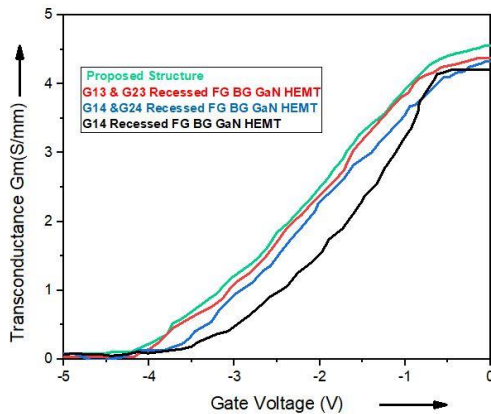
As ionized impurities scattering suppressed high mobility for the free carrier is observed and even gate to source resistance also reduced high transconductance is observed due to the usage of higher conduction band discontinuity-based materials. As sufficient space layer distance in gate to channel distance used current in active region is more which makes best use of the proposed structure in precision sensors, advanced radars, power electronics. high gain, high switch speeds, low noise and very good high frequency performance, low parasitic drain and source resistance are the required characteristics for the device to operate in millimeter range frequency. In order to obtain these requirements buffer layers, floating material, recessed gate are included in novel proposed structure.

Figure 5 shows the maximum oscillation frequency with various gate voltages for the proposed structure that is G13 & G23 recessed with dual floating material, high K dielectric FG & BG nanowire HEMT at gate voltage Vds = 0.2V is shown. It resulted same maximum oscillating frequency (f_T) of 743GHz, similar to high K dielectric FG & BG GaN HEMT.

Figure 6 shows On Resistance (R_{on}) concerning drain voltage (V_{ds}) characteristics of HEMTs with various physical structure 6 nanometers at gate Voltage = 0V i.e., for the proposed structure, G13 & G23 recessed FG (Front Gate)- BG (Back Gate) GaN HEMT, G14 & G24 recessed FG-BG GaN HEMT ,G14 recessed FG-BG GaN HEMT at gate voltage Vgs = 0V is shown. It resulted in on resistance of (R_{on}) of 0.12 (Ohms) appeared for the proposed structure.

Figure 7 shows drain conductance (G_d) concerning drain voltage (V_{ds}) characteristics of HEMTs with various physical structures of 6 nanometers at V_{ds} = 0.2V i.e., for the proposed structure, G13 & G23 recessed FG (Front Gate)- BG (Back Gate) GaN HEMT, G14 & G24 recessed FG-BG GaN HEMT ,G14 recessed FG-BG GaN HEMT, V_{gs} = 0V is shown.

Figure 4. Transconductance of various gate voltages for Proposed Structure ,G13 & G23 recessed FG(Front Gate)-BG(Back Gate) GaN HEMT ,G14 & G24 Recessed FG-BG GaN HEMT ,G14 Recessed FG-BG GaN HEMT at Vds =0.2
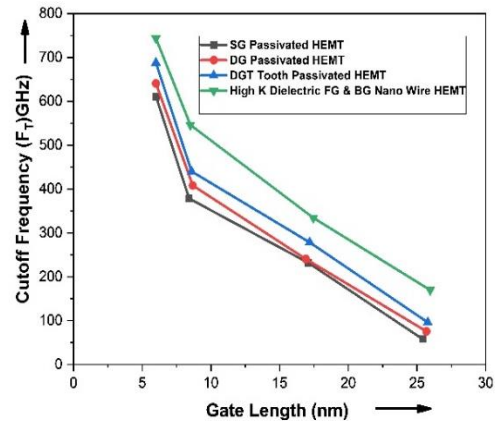
Figure 5. Cut-off frequency variations at different gate lengths for various Physical structures at Vds = 0.2V
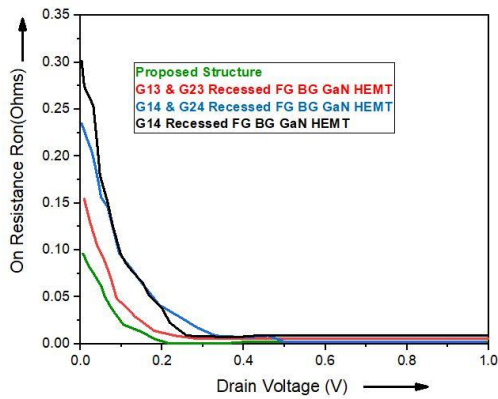
Figure 6. On Resistance variation to various Drain voltage for Proposed Structure, G13 & G23 recessed FG (Front Gate)- BG(Back Gate) GaN HEMT ,G14 & G24 Recessed FG-BG GaN HEMT ,G14 Recessed FG-BG GaN HEMT
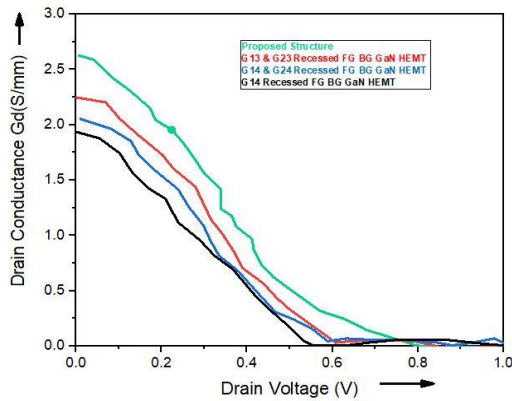
Figure 7. Drain conductance (G_d) with respect to drain voltage (V_{ds}) characteristics of HEMTs with various physical structures of 6 nanometers i.e., for Proposed Structure ,G13 & G23 recessed FG(Front Gate)- BG(Back Gate) GaN HEMT ,G14 & G24 Recessed FG-BG GaN HEMT ,G14 Recessed FG-BG GaN HEMT

It resulted in increased drain conductance (G_D) of 2.5(S/mm) appeared for the proposed structure. Tables 4, and 5 show the Electrical properties and physical properties of GaN in comparison with other available materials. This elevated differentiation shows the advantages of GaN which is used in constructing the proposed model to produce the novel structure.

The methods used in the simulation of all structures are presented here in Table 6. In Table 7 models required for the simulation for the proposed device are models required illustrated. Table 8 contains the final obtained results for the various structures like Multi gate field plated (MGFP), Discrete field plate (DFP), Gate field plate (GFP), Camel shaped gate HEMT, Gama field plate (GFP), Camel shaped gate, Gama shaped gate HEMT, proposed structure for asymmetric high K dielectric

TABLE 4. Electrical Properties of AlGaN, GaN Materials

Characteristics	Gallium Nitride	Aluminum Gallium Nitride
Saturation Velocity of electrons (cm/s)	2.5E7	11E7
Valance Band DOS (cm^{-3})	2.51E18	2.06E18
The affinity of Electron (EV)	4	3.411
Mobility of Electron (cm^2/vs)	900	300
Conduction Band DOS (cm^{-3})	2.2318	2.718

TABLE 5. Electrical and physical properties of Si, GaN,4H SiC, GaAs

Property	GaAs	Si	GaN	4H SiC
Energy band (Ev)	1.4	1.12	3.2	3.4
Thermal conductivity (W/cm/K)	0.5	1.5	4.9	1.3
Dielectric constant, ε	13.1	11.8	9.7	9.5
Electron mobility(cm^2/vs)	6000	1350	900	1300
Saturation velocity Vsat (10^7 cm/s)	1.3	1	2	3
Critical field E_{CF} (MV/cm)	0.4	0.25	3	4

TABLE 6. Methods used for simulation of Device Even power

Methods	Interpretation
Taun	Used in interface defect level electron concentration lifetime
Taup	Used in interface defect level hole concentration lifetime
f. conmun	Indicates composition, temperature, and electron models which depend on doping functionality
Material align	Specifies the fraction of the difference joining material

TABLE 7. Model used for simulation of the device

Model	Interpretation
Bgn	Indicates Bandgap narrowing. Composition, temperature, and doping-dependent bandgap narrowing.
Fldmob	Used for a model for lateral electric field
Inif	Al voltage is reset and initiated from zero
Gummel	It represents a numerical solution technique
Vsatmod	The velocity of saturation model for the mobility of electron

Front gate (FG) and Back gate (BG) caped recessed with Dual floating material GaN HEMT resulted in best results compared to other existing results. High drain current, High transconductance, High drain conductance,

TABLE 8. Comparison of existing Transistors and Proposed structure

Gate Shape	MGFT	DFP	GFP	Camel	Gama	T	Pi	SG-P	DG P	DGT TP	Proposed Structure
(L_g) nm	20	20	20	20	20	20	6	6	6	6	6
I_{on} (A/mm)	2E-2	5E-2	5.5E-2	7E-2	1	2	4	4.4	4.6	4.9	٧,٥
I_{off}(A) (E-11)	360	250	60.2	47	43.2	18	8.65	1	2.63E-1	5.6E-2	8E-4
I_{on}/I_{off} (E+8)	5.56E-05	2.00E-04	9.14E-04	0.001	0.02	0.1	4.62E-01	4.40E+00	1.75E+01	8.75E+01	0.93E+4
f_{max} (GHz)	38	50	65	80	100	425	485	490	500	520	745
f_T (GHz)	14	18	40	60	90	310	400	537	540	560	743
g_m (S/mm)	0.098	0.217	0.297	0.327	0.501	0.9	1.51	1.45	1.72	2.7	4.8
V_{th} (V)	-1	-1	-1	-1.4	-1.5	-2.8	-3.7	-3.76	-3.8	-4	-4.3.
g_d (S/mm)	0.084	0.091	0.095	0.098	0.116	0.148	0.353	0.456	0.534	0.657	2.5
R_{on} (Ωmm)	3.8	3.6	2.5	1.8	1.5	1	0.8	0.75	0.7	0.6	0.12

Low On-Resistance, High cut off frequency, High maximum oscillation frequency (f_{max}), low leakage current, and High I_{on}/I_{off} are obtained. With these obtained results further, it can be applied to suitable application.

AlGaN/GaN material exhibits high breakdown voltage and high electron mobility, with this property device can be applied for high frequency and high-power applications.

GaN possess high saturation velocity and high two-dimensional electron Gas density at the two-layer hetero interference due to this reason GaN is consider as important candidate with high power switching transistor for future nano world. This hetero combination exhibits excellent power handling capabilities. Carrier confinement is improved by introducing increased Al mole fraction in AlGaN.

Gallium Nitride High Electron Mobility Transistor provides higher power density, small passive component, higher efficiency. GaN is feasible in both vertical and lateral structure. For high power modules vertical GaN devices are used whereas for high frequency and medium power application lateral GaN are used. Only lateral GaN are in availability and are in current trend. The drawback of GaN cascade includes packing complexity when two devices are connected in series, parasitic inductance affects switching performance of the device. The device includes low Cgd gate to drain capacitance and Cgs gate to source capacitance. Due to this reason total gate charge is smaller for GaN based switch. As switching speed is directly proportional to total gate change high switching speed is efficiency is realized for GaN HEMT. For high power electric Devices GaN is prominently implemented due to its unique features such as high thermal stability and large conduction band discontinuities, high saturation drift. The thermal conductivity is lower than

Silicon and Silicon carbide. This Silicon nature tends to higher thermal resistance leads to higher operation temperature for same dissipated power.

4. CONCLUSION

Asymmetric high K dielectric front gate and back gate (BG) with recessed gates, dual triple tooth metal for 6nm HEMT are proposed in this paper and its performance is analyzed for obtaining optimized results. The proposed structure is collated with a few existing HEMT structures. The DC characteristics and RF characteristics are sorted out and reported improved increased drain current (Ion) of 7.5(A/mm), low leakage current(I_{off}) 3E-15 (A), Transconductance (Gm) of 4.8(S/mm), Drain Conductance (G_d) of 2.5(S/mm), Cutoff frequency(f_T) of 743 GHz Maximum Oscillation frequency (F_{max}) 745 GHz, Minimum Threshold Voltage (Vth) of -4.5V, On Resistance (Ron)of 0.12(Ohms) at V_{gs} =0V. The dominant characteristics of the proposed device aid to apply in millimeters wave application.

5. REFERENCES

1. Sehra, K., Kumari, V., Gupta, M., Mishra, M., Rawal, D. and Saxena, M., "Optimization of π–gate algan/aln/gan hemts for low noise and high gain applications", *Silicon*, (2020), 1-12. https://doi.org/10.1007/s12633-020-00805-7

2. Augustine Fletcher, A. and Nirmal, D., "A survey of gallium nitride hemt for rf and high power application", *Superlattice Microst*, Vol. 109, (2017), 519-537. https://doi.org/10.1016/j.spmi.2017.05.042

3. Micovic, M., Brown, D., Kurdoghlian, A., Santos, D., Grabar, B., Magadia, J., Khalaf, I., Tai, H., Prophet, E. and Burnham, S., "Gan dhfets having 48% power added efficiency and 57% drain

efficiency at $ v $-band", *IEEE Electron Device Letters*, Vol. 38, No. 12, (2017), 1708-1711. doi: 10.1109/LED.2017.2763940.

4. Jazaeri, F., Shalchian, M. and Sallese, J.-M., "Transcapacitances in epfl hemt model", *IEEE Transactions on Electron Devices*, Vol. 67, No. 2, (2019), 758-762. doi: 10.1109/TED.2019.2958180.

5. Rastogi, G., Kaneriya, R., Sinha, S. and Upadhyay, R., "Optimization of ohmic contact fabrication for al0. 3ga0. 7n/aln/gan hemts on 6h-sic using recess etching and surface plasma treatment processes", *Journal of Nanomaterials & Molecular Nanotechnology*, Vol. 8, (2019), 2. https://doi.org/10.4172/2324-8777.1000267

6. Kaneriya, R., Rastogi, G., Basu, P., Upadhyay, R. and Bhattacharya, A., "Intersubband device modeling of gallium nitride high electron mobility transistor for terahertz applications", *Radio Science*, Vol. 54, No. 12, (2019), 1172-1180. https://doi.org/10.1029/ 2019RS006844

7. Shur, M., Gaska, R., Khan, A. and Simin, G., "Wide band gap electronic devices", in Proceedings of the Fourth IEEE International Caracas Conference on Devices, Circuits and Systems (Cat. No. 02TH8611), IEEE. (2002), D051-D051.

8. Yadav, R. and Dutta, A.K., "A new charge-based analytical model for the gate current in gan hemts", *IEEE Transactions on Electron Devices*, Vol. 69, No. 4, (2022), 2210-2213. doi: 10.1109/TED.2022.3149460.

9. Van Hove, M., Boulay, S., Bahl, S.R., Stoffels, S., Kang, X., Wellekens, D., Geens, K., Delabie, A. and Decoutere, S., "Cmos process-compatible high-power low-leakage algan/gan mishemt on silicon", *IEEE Electron Device Letters*, Vol. 33, No. 5, (2012), 667-669. doi: 10.1109/LED.2012.2188016.

10. Selvaraj, S.L., Suzue, T. and Egawa, T., "Breakdown enhancement of algan/gan hemts on 4-in silicon by improving the gan quality on thick buffer layers", *IEEE Electron Device Letters*, Vol. 30, No. 6, (2009), 587-589. doi: 10.1109/LED.2009.2018288.

11. Shen, L., Heikman, S., Moran, B., Coffie, R., Zhang, N.-Q., Buttari, D., Smorchkova, I., Keller, S., DenBaars, S. and Mishra, U., "Algan/aln/gan high-power microwave hemt", *IEEE Electron Device Letters*, Vol. 22, No. 10, (2001), 457-459. doi: 10.1109/55.954910.

12. Purnachandra Rao, G., Lenka, T.R., Singh, R., Boukortt, N.E.I., Sadaf, S.M. and Nguyen, H.P.T., "Comparative study of iii-nitride nano-hemts on different substrates for emerging high-power nanoelectronics and millimetre wave applications", *Journal of Electronic Materials*, Vol. 52, No. 3, (2023), 1948-1957. https://doi.org/10.1007/s11664-022-10145-4

13. Wang, W., Yu, X., Zhou, J., Chen, D., Zhang, K., Kong, C., Kong, Y., Li, Z. and Chen, T., "Improvement of power performance of gan hemt by using quaternary inalgan barrier", *IEEE Journal of the Electron Devices Society*, Vol. 6, (2018), 360-364. doi: 10.1109/JEDS.2018.2807185.

14. Palacios, T., Chini, A., Buttari, D., Heikman, S., Chakraborty, A., Keller, S., DenBaars, S.P. and Mishra, U.K., "Use of double-channel heterostructures to improve the access resistance and linearity in gan-based hemts", *IEEE Transactions on Electron Devices*, Vol. 53, No. 3, (2006), 562-565. doi: 10.1109/TED.2005.863767.

15. Zhang, K., Kong, C., Zhou, J., Kong, Y. and Chen, T., "High-performance enhancement-mode Al_2O_3/inalgan/gan mos high-electron mobility transistors with a self-aligned gate recessing technology", *Applied Physics Express*, Vol. 10, No. 2, (2017), 024101. doi: 10.7567/APEX.10.024101.

16. Hwang, I.H., Eom, S.K., Choi, G.H., Kang, M.J., Lee, J.G., Cha, H.Y. and Seo, K.S., "High-performance e-mode algan/gan mis-hemt with dual gate insulator employing sion and hfon", *Physica status solidi (a)*, Vol. 215, No. 10, (2018), 1700650. https://doi.org/10.1002/pssa.201700650

17. Zhuge, J., Wang, R., Huang, R., Zhang, X. and Wang, Y., "Investigation of parasitic effects and design optimization in silicon nanowire mosfets for rf applications", *IEEE Transactions on Electron Devices*, Vol. 55, No. 8, (2008), 2142-2147. doi: 10.1109/TED.2008.92627.

18. Sehra, K., Kumari, V., Nath, V., Gupta, M. and Saxena, M., "Optimization of asymmetric π gate hemt for improved reliability & frequency applications", in 2019 IEEE 9th International Nanoelectronics Conferences (INEC), IEEE. (2019), 1-4.

19. Sun, W., Joh, J., Krishnan, S., Pendharkar, S., Jackson, C.M., Ringel, S.A. and Arehart, A.R., "Investigation of trap-induced threshold voltage instability in gan-on-si mishemts", *IEEE Transactions on Electron Devices*, Vol. 66, No. 2, (2019), 890-895. doi: 10.1109/TED.2018.2888840.

20. Lee, J.-W., Kuliev, A., Kumar, V., Schwindt, R. and Adesida, I., "Microwave noise characteristics of algan/gan hemts on sic substrates for broad-band low-noise amplifiers", *IEEE Microwave and Wireless Components Letters*, Vol. 14, No. 6, (2004), 259-261. doi.

21. Shinohara, K., Corrion, A., Regan, D., Milosavljevic, I., Brown, D., Burnham, S., Willadsen, P., Butler, C., Schmitz, A. and Wheeler, D., "220ghz f t and 400ghz f max in 40-nm gan dh-hemts with re-grown ohmic", in 2010 International Electron Devices Meeting, IEEE. (2010), 30.31. 31-30.31. 34.

22. Lin, J., Antoniadis, D.A. and del Alamo, J.A., "Impact of intrinsic channel scaling on ingaas quantum-well mosfets", *IEEE Transactions on Electron Devices*, Vol. 62, No. 11, (2015), 3470-3476.

23. Sharma, N., Mishra, S., Singh, K., Chaturvedi, N., Chauhan, A., Periasamy, C., Kharbanda, D.K., Parjapat, P., Khanna, P. and Chaturvedi, N., "High-resolution algan/gan hemt-based electrochemical sensor for biomedical applications", *IEEE Transactions on Electron Devices*, Vol. 67, No. 1, (2019), 289-295. doi: 10.1109/TED.2019.2949821.

24. Balaji, B., Srinivasa Rao, K., Girija Sravani, K., Bindu Madhav, N., Chandrahas, K. and Jaswanth, B., "Improved drain current characteristics of hfo2/sio2 dual material dual gate extension on drain side-tfet", *Silicon*, (2022), 1-6. https://doi.org/10.1007/s12633-022-01955-6

25. Gowthami, Y., Balaji, B. and Rao, K.S., "Design and performance evaluation of 6nm hemt with silicon sapphire substrate", *Silicon*, (2022), 1-8. https://doi.org/10.1007/s12633-022-01900-7

26. Kumar, P.K., Balaji, B. and Rao, K.S., "Performance analysis of sub 10 nm regime source halo symmetric and asymmetric nanowire mosfet with underlap engineering", *Silicon*, Vol. 14, No. 16, (2022), 10423-10436. https://doi.org/10.1007/s12633-022-01747-y

27. Balaji, B., Rao, K.S., Sravani, K.G. and Aditya, M., "Design, performance analysis of gaas/6h-sic/algan metal semiconductor fet in submicron technology", *Silicon*, (2022), 1-5. https://doi.org/10.1007/s12633-021-01545-y

28. Balaji, B., Rao, K.S., Aditya, M. and Sravani, K.G., "Device design, simulation and qualitative analysis of gaasp/6h-sic/gan metal semiconductor field effect transistor", *Silicon*, Vol. 14, No. 14, (2022), 8449-8454. https://doi.org/10.1007/s12633-022-01665-z

29. Chen, C.-H., Krishnamurthy, K., Keller, S., Parish, G., Rodwell, M., Mishra, U. and Wu, Y.-F., "Algan/gan dual-gate modulation-doped field-effect transistors", *Electronics Letters*, Vol. 35, No. 11, (1999), 933-935. doi: 10.1049/el:19990627.

30. He, J., Cheng, W.C., Wang, Q., Cheng, K., Yu, H. and Chai, Y., "Recent advances in gan-based power hemt devices", *Advanced Electronic Materials*, Vol. 7, No. 4, (2021), 2001045. doi: 10.1002/aelm.202001045.

31. Latorre-Rey, A.D., Albrecht, J.D. and Saraniti, M., "Generation of hot electrons in gan hemts under rf class a and ab pas", in 2017

75th Annual Device Research Conference (DRC), IEEE. (2017), 1-2.

32. Zhang, N.-Q., Moran, B., DenBaars, S., Mishra, U., Wang, X. and Ma, T., "Effects of surface traps on breakdown voltage and switching speed of gan power switching hemts", in International Electron Devices Meeting. Technical Digest (Cat. No. 01CH37224), IEEE. (2001), 25.25. 21-25.25. 24.

33. Ambacher, O., Smart, J., Shealy, J., Weimann, N., Chu, K., Murphy, M., Schaff, W., Eastman, L., Dimitrov, R. and Wittmer, L., "Two-dimensional electron gases induced by spontaneous and piezoelectric polarization charges in n-and ga-face algan/gan heterostructures", *Journal of Applied Physics*, Vol. 85, No. 6, (1999), 3222-3233. https://doi.org/10.1063/1.369664

34. Mishra, U.K., Shen, L., Kazior, T.E. and Wu, Y.-F., "Gan-based rf power devices and amplifiers", *Proceedings of the IEEE*, Vol. 96, No. 2, (2008), 287-305. doi: 10.1109/JPROC.2007.911060.

35. Arulkumaran, S., Egawa, T., Selvaraj, L. and Ishikawa, H., "On the effects of gate-recess etching in current-collapse of different cap layers grown algan/gan high-electron-mobility transistors", *Japanese Journal of Applied Physics*, Vol. 45, No. 3L, (2006), L220. doi: 10.1143/JJAP.45.L220.
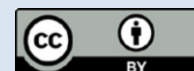
Persian Abstract

چکیده

تاثیر اسپیسر نیترید آلومینیوم (AlN)، لایه درپوش نیترید گالیم (GaN)، دروازه Pi جلو (FG)و دروازه Pi پشت (BG)، مواد شناور دوگانه مواد دی الکتریک با K بالا مانند دی اکسید هافنیوم (HfO2)، اکسید آلومینیوم (Al2O3)، نیترید سیلیکون (Si3N4)بر روی نیترید گالیم آلومینیوم/ نیترید گالیم (AlGaN/GaN)، ترانزیستور متحرک الکترون بالا (HEMT)با فناوری ۶ نانومتری شبیه سازی شده و نتایج با استفاده از طراحی به کمک رایانه فناوری (TCAD) Silvaco Atlas استخراج شده است. ابزار. اهمیت مواد دی الکتریک با پتاسیم بالا مانند Al2O3 و Si3N4 برای پیشنهاد GaN HEMT مورد مطالعه قرار گرفت. لایه‌های درپوش GaN ،AlN و مواد دی‌الکتریک با پتاسیم بالا، برای غلبه بر عقب‌نشینی‌های معمول ترانزیستور مانند نقص‌های سطحی، پراکندگی الکترون، و تحرک کمتر الکترون، روی یکدیگر لایه‌بندی می‌شوند. اثر الکترون داغ توسط گیت نوع Pi غلبه می‌کند. مواد شناور دندان سه‌گانه در لایه بافر قرار می‌گیرد تا ولتاژ شکست را بهبود بخشد. بنابراین، با بهینه‌سازی ساختار HEMT ناتوانی‌های دستگاه‌های خاص به توانایی‌ها تبدیل می‌شوند. وابستگی به ویژگی‌های DC و ویژگی‌های RF به دلیل لایه‌های درپوش GaN، گیت چندگانه (BG & FG) و مواد دی‌الکتریک با K بالا، مواد دندانه دوگانه سه‌گانه در لایه بافر با گیت فرورفته ایجاد شده است. مقایسه بیشتر HEMT غیرفعال شده تک گیت (HEMT ،SG) غیرفعال شده دو گیت (DG، HEMT) غیرفعال شده دندانه سه گانه (DGT)، گیت پی دی الکتریک بالا (FG)و گیت پی عقب (BG)، جلوی دی الکتریک با K بالا نامتقارن دروازه Pi (FG) و Back Pi Gate (BG)با گیت توکار نانوسیم .HEMT مشاهده شد که پیشنهادی منجر به افزایش جریان تخلیه (یون) ۷.۵ (A/mm)، جریان نشتی کم (Ioff) 3E-15 (A)، رسانایی (Gm) 4.8 (S/mm)، رسانایی تخلیه (Gd) 2.5 (S/mm)، حداکثر فرکانس نوسان 745 (Fmax) گیگاهرتز، حداقل ولتاژ آستانه (Vth) 4.5-V، مقاومت روی (Ron) 0.12 (اهم) در Vgs = 0V

International Journal of Engineering

An Expert System Based on Type-1 Fuzzy Logic and Digital Image Processing for Knowledge Based Edge and Contour Detection

R. Ranjan*, V. Avasthi

University of Petroleum and Energy Studies, Dehradun, India

A B S T R A C T

In computer vision, contour/edge detection is a crucial phenomenon. Edge detection is an important step in contour detection, which is helpful in the identification of important data. The accuracy of the edge detection process is heavily dependent on edge localization and orientation. In recent years, due to their versatility, soft computing approaches have been considered effective edge detection strategies. Broadly, edge detection accuracy is deeply affected by weak and dull edges. In recent works, edge detection based on fuzzy logic (FL) was proposed, and image edges were improved using guided filtering. However, guided image filtering (GIF) does not take into account the local features of an image. To include local features of an image for edge detection, an improved version, i.e., an offset enable sharpening-guided filter is used in this paper, and FL is used for edge detection. The figure of merit (FoM) and F-score are used to evaluate the method's accuracy. Using visual representations and performance metrics, the results are compared with those from cutting-edge techniques.

doi: 10.5829/ije.2023.36.07a.09

1. INTRODUCTION

Edge detection is quite vital in various processes like object detection, image processing, and computer vision. The information gained from edge detection is crucial for numerous other visual tasks [1-3]. As a result, stable detection of image edge features is necessary to effectively carry out such tasks. An edge can be defined as the black pixels in binary images with white neighbours [1]. A group of pixels with abrupt intensity fluctuations, similar to a step function, constitutes an ideal edge. An edge contour is defined by Torre et al. [4] as a collection of points with sharp brightness fluctuations. Such abrupt variations in brightness could be brought on by variations in the image's texture, grayscale, or colours. According to Shui et al. [5], the edges were discovered to be in between regions and the background. Since traditional approaches like Canny [6], Gao et al. [7], etc. are based on masks; the challenge of efficient mask generation is still an open problem. These masks additionally alter the pixel positions due to the convolution effect. Moreover, all the existing methods,

due to the behaviour of masks, are not very accurate in either accepting the correct edges or rejecting the false edges, leading to inaccurate edge identification. Edge detection methods using thresholds either accept incorrect edges or reject legitimate ones. Therefore, to address this problem in Canny Edge detection, two thresholds were used, but even using more than one threshold failed to solve the problem. Threshold-based systems are like binary systems, where if the gradient of a pixel is greater than the threshold, then the chosen pixel is considered an edge pixel; otherwise, it is chosen as a non-edge pixel. It is to be further noted that threshold will depend on the pixel values of an image; therefore, threshold-based methods fail or require other morphological operations as done in Canny method [6]. For an edge detector to be considered reasonably accurate, it must be able to recognise actual edge contours with reasonable precision [8]. This is necessary because edge contours are used in computer vision and image processing activities to link different feature regions [9]. In order to handle a variety of noise sources, it is required that the edge detectors be very resilient

Corresponding Author Email: rakeshranjanpsit@gmail.com
 (R. Ranjan)

under a variety of imaging conditions. In addition to being able to extract edge contours in real-time, the optimal edge detection method should also be manageable in terms of memory and storage requirements [8, 9].

The rest of the paper is organized as follows: in section 2, related work is presented. In section 3 of the paper, the proposed method is discussed. In section 4 of the paper, results are discussed, and finally, the major conclusions of the paper are discussed in section 5.

2. RELATED WORKS

This section provides an overview of both traditional and cutting-edge methods.

2. 1. Kernel Based Methods   The classical edge detection methods are based on masking and are very easy to implement. Some of the basic algorithms of these methods were developed by Gao an improved Sobel edge detection [7] which was based on the pixel gradient [10]. These methods generate a large number of spurious edges, and the detected edges are thick. In recent work, in place of traditional square masking, a hexagonal masking scheme is proposed where square masks are converted into hexagonal masks using the interpolation method and corresponding new pixel values are obtained [11]. Later on, the hexagonal scheme is considered under Canny edge detection method, and the superiority of hexagonal masking has been proven [12]. As an application, the usefulness of Canny edge detection in content-based image retrieval is discussed by Fadaei [13].

2. 2. Machine Learning Based Methods   A probabilistic boundary (Pb)-based edge detection method was proposed by Martin et al. [14]. In this method, a texture feature description and an approach using image local cues and logistic regression were developed for recognising edges. An advanced version of the Pb method, i.e., the multi-scale probabilistic boundary (MsPb)-based edge detection technique, was introduced by Ren et al. [15]. Arbelaez et al. [16] expanded the Pb approach [14] and proposed a global probabilistic boundary (g-Pb) approach that makes use of multi-scale and spectral clustering.

2. 3. Deep Learning Based Methods   Recently, deep learning algorithms have made incredible progress in the area of image edge identification. As explained in the following two sub-sections, the currently available deep learning-based edge detection techniques can be loosely classified into supervised and unsupervised learning-based techniques.

2. 3. 1. Supervised Learning-based Methods Currently, supervised learning is used to perform the majority of image processing tasks. Payet and Sinisa [17] applied image edges for boundary detection. Dollar et al. [18] introduced an advanced probabilistic boosting tree classification. For edge detection, Rahebi et al. [19] employed an artificial neural network. Etemad and Chelappa [20] proposed a neural network based edge detector. Lim et al. [21] used a random forest classifier for effective edge detection based on a sketch marker. The holistically nested edge detection (HED) was developed. This method considers convolutional neural networks [20] for feature extraction and a deep supervised network [22] for the classification of edges. The HED technique also has the capacity to autonomously learn and may be successfully applied to handle difficult ambiguities in edge detection. Still, edge refinement is needed, as discussed by Elharrouss et al. [23], where a cascaded convolutional neural network (CNN) is used for the refinement of edges. The summary of the discussed methods is presented in Table 1.

TABLE 1. State-of-the-art methods

Authors	Techniques
Canny et al. [6]	Masking
Gao et al. [7]	Masking
Fadaei and Abdolreza [11]	Hexagonal Masking
Firouzi, et al. [12]	Hexagonal Masking
Martin et al. [14]	Probabilistic boundary (pb)
Ren et al. [15]	Multi-scale probabilistic boundary (MsPb)
Arbelaez et al. [16]	Global probabilistic boundary (g-Pb)
Dollar et al. [18]	Probabilistic boosting tree
Rahebi et al. [19]	Artificial neural network
Lim et al. [21]	Random forest classifier
Elharrouss et al. [23]	CNN
Xiaofeng et al. [24]	Sparse code gradients (SCG)
Isola et al. [25]	Crisp boundary detection
Fano [26]	Transmission of information
Yang et al. [27]	Convolutional encoder-decoder
Anandan et al. [28]	Hierarchical model-based motion
Xia and Kulis [29]	Unsupervised image segmentation
Baterina et al. [30]	Ant Colony Optimization (ACO)
Kumar et al. [31]	ACO
Kumar et al. [32]	ACO+ Guided Filtering
Ravivarma et al. [33]	Particle Swarm Optimization (PSO)
Verma et al. [34]	Fuzzy + Guided Filtering

Kumar and Raheja [35]	Fuzzy + L$_0$ Guided Filtering
Raheja and Kumar [36]	FL
Kaur et al. [37]	Fuzzy Logic
Aborisade [38]	FL
Begol and Maghooli [39]	FL
Zhang et al. [40]	Adaptive Neuro-Fuzzy
Dorrani et al. [41]	Edge detection fuzzy ant colony
Siddharth et al. [42]	Edge detection + ANN
Ranjan et al. [43]	Fuzzy + Weighted Guided Filtering

2. 3. 2. Unsupervised Learning Based Methods

In an unsupervised learning based methods, edge contours can be identified from the main understanding of the image without the need for edge features to be manually labelled for training. As per Xiaofeng et al. [24] SCG can be used to remarkably increase the performance of edge detection methods. For extracting edge contours, Isola et al. [25] used a pointwise mutual information architecture [26]. For the purpose of extracting object contours, Yang et al. [27] proposed a completely convolutional encoder-decoder network. The basic concept behind this network was based on a full convolution network [28]. Xia and Kulis [29] proposed unsupervised semantic segmentation for edge detection using encoder-decoder architecture.

2. 4. Soft Computing Based Image Edge Detection

In soft computing techniques, the ACO technique was also employed for edge identification, but accuracy was limited because there was only one optimal solution and many of the genuine edges were ignored [30]. By employing guided image filtering to strengthen weak edges, the drawbacks of the ACO edge detection approach were reduced [31, 32]. In other recent work, the performance of a Sobel operator-based edge detection mechanism is further improved by 8-directional mask developments, and the inverse of entropy is used for threshold detection [33]. This method produces better results as compared to the traditional Sobel operator, but is still unable to detect some of the genuine edges. Verma et al. [34] considered image sharpening along with PSO for edge detection; however, the main limitation is noise in edge detection.

2. 5. FL Based Image Edge Detection

Fuzzy set-based edge detection is based on fuzzy theory. Here, the intensity of the pixels is represented in terms of membership functions. The membership functions are derived for both inputs and outputs. For pixels, neighbourhood fuzzy rules are developed, and a fuzzy inference engine is used for the output prediction. Recently, for accurate edge detection, guided image filtering was combined with FL [35, 36]. In a method based on fuzzy rules that Kaur et al. [37] explored, edge detection was performed using sixteen fuzzy rules. To address more noteworthy vulnerabilities in edge detection, more studies have been conducted with higher types of FL, particularly fuzzy type 2 [38, 39]. Zhang et al. [40] developed an adaptive neuro-fuzzy system for edge detection. An edge detection mechanism based on ACO and fuzzy logic was proposed by Dorrani et al. [41] to minimize false edges. An edge detection approach, based on Kalman filtering and ANN was proposed by Siddharth et al. [42].

2. 6. Edge Detection Based on GIF and Fuzzy Logic

Recently, edge identification based on FL and image sharpening using GIF was proposed by Ranjan et al. [43]. In the next sub-section GIF is discussed.

2. 6. 1. Guided Image Filtering (GIF)

Guided image filtering is a filtration process where edges are preserved, and the filtered image pixels are scaled and shifted version of the original unfiltered image. The scaling and shifting co-efficient are dependent on the mean and variance of input and guided image. Considering an image Y, which could be either the input image X or another image, serves as the initial filtering guide for GIF. Further assuming that 'X_p' and 'Y_p' represent the intensities values at pixel 'p' of the input and guided images, respectively. Let Ω_h represent the kernel window centred at pixel 'h'. Now, GIF is defined as:

$$GIF(X)_p = \frac{1}{\sum\limits_{q \in \Omega_h} W_{GIF_{pq}}(Y)} \sum\limits_{q \in \Omega_h} W_{GIF_{pq}}(Y) X_q \qquad (1)$$

Here, the kernel weights functions $W_{GIF_{pq}}(Y)$ can be defined as:

$$W_{GIF_{pq}}(Y) = \frac{1}{|w|^2} \sum\limits_{h:(p,q) \in \Omega_h} \left(1 + \frac{(Y_p - m_h)(Y_q - m_h)}{\sigma_h^2 + \varepsilon} \right) \qquad (2)$$

where $|w| = 9$, m_h and σ_h^2 are the mean and variance of the guided image Y in the local window. The term $\frac{(Y_p - m_h)(Y_q - m_h)}{\sigma_h^2 + \varepsilon}$ plays an important role in deciding filter weights. The above term can be positive and negative depending on the position of Y_p and Y_q and if they are on the same side of an edge or on the opposite side. The parameter ε is utilized to modify the level of smoothing. The smoothness of the image will grow as is raised.

2. 6. 2. Limitations of the Previous Works

The previous works do not consider the local patches intensity variations thus problem of broken edges occur which leads to in-accurate edge detection. In the

local patches where edges occur, variance is comparatively larger than in patches without edges. The GIF is based on the variance of local patches; if the variance exceeds a threshold, only the selected patches are kept; if the variance is below a threshold, the local patch is smoothed. Thus, in the resultant image, edges are highlighted, which leads to better edge detection. Still, this method has a shortcoming as it heavily depends on thresholds. Moreover, in Ranjan et al. [43] work, triangular membership functions are considered, which are well suited to ramp-like intensity variations that are not always evident in different images.

2. 7. Aim of Proposed Works   In this work, the broken edge problem is minimized by considering offset-based guided filtering, which considers the local intensity variations with the help of intensity offsets. The main objectives of the proposed work are:
1. To capture local intensity variation using offset enable GIF (OEGIF)
2. To use the Gaussian membership function to capture variations in intensity.

3. PROPOSED METHOD

The proposed method is an advanced version of the previous work [43]. The main problem in edge detection is the detection of weak edges; in doing so, some spurious edges are detected. The fundamental issue with guided filtering is that it smoothes the pixels without edges but does not enhance the quality of the edges. In this work, an enhanced version of guided image filtering is used, which improves the edges before FL is used for edge identification. The main steps for the proposed edge detection method are described in Algorithm 1.

Algorithm 1: Proposed Edge Detection Mechanism

Step 1: Choose input and guided image

Step 2: Apply guided filtering, choose smoothing parameter using equation 6

Step 3: Evaluate offset (η_p) based on LoG filter

Step 4: Evaluate final offset ($\eta_p^{'}$) based on LoG filter using equations 5,7

Step 5: define input and output membership function for edge and non edge pixels

Step 6: set fuzzy rules

Step 7: Get edge enhanced image from steps 4, apply FL and classify pixels as edge and non edge

Step 8: Apply performance measure to evaluate accuracy

---

3. 1. Offset Enabled Guided Image Filtering (OEGIF)   Adaptive Guided Image Filtering is based on the shifting technique of pixel value and an offset is added to the pixel under investigation. The following equations provide the AGF's filter kernel and weighting function:

$$OEGIF(X)_p = \frac{1}{\sum_{q\in\Omega_h} W_{OEGIF_{pq}}(Y)} \sum_{q\in\Omega_h} W_{OEGIF_{pq}}(Y)X_q \tag{3}$$

$$W_{OEGIF_{pq}}(Y) = \frac{1}{|w|^2} \sum_{h:(p,q)\in\Omega_h} \left(1 + \frac{\left(\left(Y_p + \eta_p^{'}\right) - m_h\right)\left(Y_q - m_h\right)}{\sigma_h^2 + \varepsilon}\right) \tag{4}$$

where ε is the smoothing parameter, and $\eta_p^{'}$ is the extra offset. The offset is chosen as

$$\eta_p^{'} = \begin{cases} Y_{max} - Y_p & if\ Y_p > m_h \\ Y_{min} - Y_p & if\ Y_p < m_h \\ 0 & if\ Y_p = m_h \end{cases} \tag{5}$$

where Y_{max} and Y_{min} is maximum and minimum values of the pixels in given window. It is further important to note that the smoothing parameter also satisfies:

$$\varepsilon = \sigma_r^2 / 255 \tag{6}$$

It is further to note that the pixel offset is also constraint by the minimum and maximum values of the pixel intensity in the chosen window using:

$$\eta_p^{'} = \begin{cases} Y_{max} - Y_p & if\ \left(Y_p + \eta_p\right) > Y_{max} \\ Y_{min} - Y_p & if\ \left(Y_p + \eta_p\right) > Y_{min} \\ \eta_p & Otherwise \end{cases} \tag{7}$$

where η_p is the optimal offset which depends on the strength of the edge and obtained from LoG filter [44].

To numerically illustrate the advantage of the proposed method, a butterfly image initial patch is considered (Figure 1(a)). In Figure 1(b), a sharpened image of Ranjan et al. [43] work along with a local patch is shown. Finally, in Figure 1(c) enhanced image with a local patch is shown. The difference in the pixel values of Figure 1(b) and Figure 1(c) is due to the offset. It is clear that the quality of the enhanced image is much

$$\begin{pmatrix} 109 & 104 & 106 \\ 107 & 103 & 104 \\ 106 & 106 & 103 \end{pmatrix} \quad \begin{pmatrix} 79 & 135 & 130 \\ 86 & 133 & 123 \\ 92 & 135 & 115 \end{pmatrix} \quad \begin{pmatrix} 83 & 140 & 134 \\ 85 & 136 & 123 \\ 86 & 132 & 112 \end{pmatrix}$$
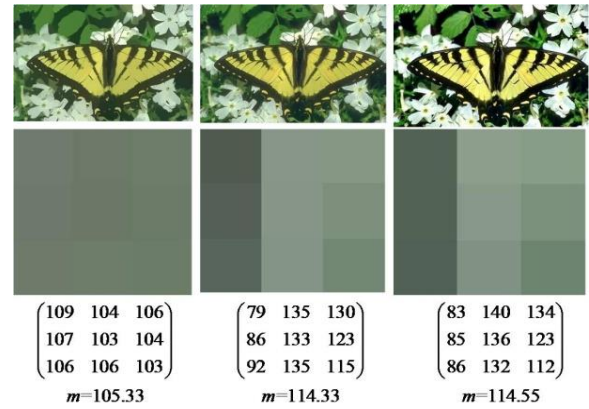
m=105.33 m=114.33 m=114.55
(a) Original Patch   (b) Ranjan et. al [43]   (c) proposed
Figure 1. Comparison of image sharpening

better in comparison to Ranjan et al. [43] work, but the mean value of the image is almost the same. Thus, the offset changes the intensity in such a way that the overall mean intensity remains the same, but edge distinction improves.

3. 2. FL Based Edge Detection   Figure 2 illustrates the design of a fuzzy-based edge detection system. In the initial step of FLED, input and output membership functions are selected, and the image's pixel values are fuzzified. The Mamdani fuzzy inference engine is then used to apply IF-ELSE rules, and lastly, defuzzification is performed to produce crisp values and the desired results.

Membership Functions:
Gaussian membership function is considered at the input, while at the output triangular membership function is considered. The Gaussian membership is of the form [29]:

$$\mu_A(x; c, u, m) = \exp\left(-\frac{1}{2}\left|\frac{x-u}{s}\right|^m\right) \tag{8}$$

While the triangular membership function is specified as [29]:

$$\mu_B(x; a, b, c, d) = \max\left(\min\left(\frac{x-a}{b-a}, \frac{c-x}{c-d}\right), 0\right) \tag{9}$$

Next fuzzy rules are devised.

Fuzzy Rules
Figure 3 depicts the rules' formation on a 3x3 mask. In the illustration, "W" stands for white pixels, "**B**" for black pixels, and "**E**" as an edge pixel. A total of 28 rules are devised for edge pixels. If a pixel is surrounded by eight white or black pixels, then the pixel under investigation is considered to be noise; similarly, a single pixel change is also considered a non edge. It is important to note that at least two white pixels surrounded by black pixels or at least two black pixels surrounded by white pixels will qualify for a possible edge.

4. RESULTS

The performance evaluation of the proposed edge detector is done on a large image dataset, and for

Figure 3. Fuzzy rules pattern for edge pixels [43]

illustration, four images, i.e., 'butterfly', 'crow', 'church, and 'Lena, are considered (Figure 4). The performance metrics FoM and F-Score are evaluated as detailed in Table 2. The FoM, measures how far the pixels have been shifted from their initial places. The optimal F-score, which is based on the confusion matrix, is 1, which indicates that the edge detection was accurate.

Figure 4. Image datasets

TABLE 2. Performance Measures

Metrics	Formula
FoM	$FoM = \dfrac{1}{\max(n_A, n_B)} \sum\limits_{i=1}^{n_B}\left(\dfrac{9}{9+d^2}\right)$ n_A = Ideal edges n_B = detected edges d = displacement between (n_A, n_B)
F Score	F-score= $2TP/(2TP+FP+FN)$ TP: True Positive

Figure 2. Diagram of FL-based edge detection [43]

In Figure 5, in the first column, three images are shown. The detected edges from the Ranjan et al. [43] work are shown in Figure 1(b), and finally, in Figure 1(c), the results for the proposed method are shown. In the case of the butterfly image, Ranjan et al. [43] fail to detect the edge in the north-west region of the image, which is successfully detected in the proposed method. In the case of the crow image, the difference is clearly visible.

Finally, in the case of the church image in Ranjan et al. [43] work, at the dome area, double edges, i.e., false edges, can be seen. However, the proposed method is free of double edges.

In the recent past, the "Lena" image was used for illustration of results; thus, for a fair comparison, the "Lena" image is used in the subsequent results. Figure 6(a) shows the original image, and Figure 6(b) shows the important marked points. In Figure 6(c), the results of guided image filtering are shown, while for adaptive guided filtering, the results are shown in Figure 6(d).

The edges in Figures 6(c) and 6(d) appear very similar, but differences can be seen in the hair edges and the face and forehead. Figure 7(a) depicts the input membership function, which has a mean (u) of 0 and a variance (s) of 0.1 and 'm'=2 (Equation (8)), and Figure 7(b) depicts the output membership function for black and white pixels. Referring to Equation (9), for black pixels a=0 and b=0.7 and for white pixels c=1 and d=0.

In Figure 8(a), demonstrate the result of canny edge detection and It is evident that while the majority of edges are correctly recognised, a disproportionate number of
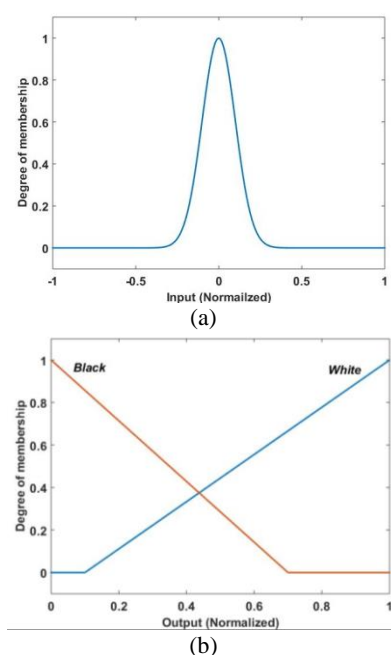
Figure 7. (a) Input membership function (Gaussian) (b) Output membership function (Triangular)

them are incorrectly accepted. For example, in comparison to the marked edges in regions 2, 4, and 5, there are numerous edges that are falsely detected. As a result, cranny edge detection is quite noisy. Sobel edge detection is displayed in Figure 8(b), and it can be seen that while some actual edges are correctly recognised, others are mistakenly rejected and can be seen in the highlighted regions 1, 2, 3, and 6.
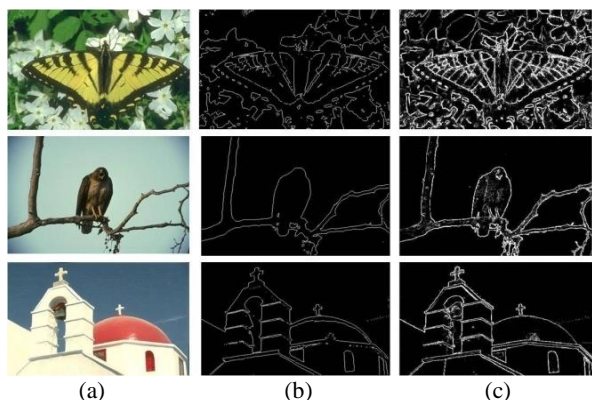
Figure 5. (a) Original image (b) Ranjan et. al. [43] (c) Proposed
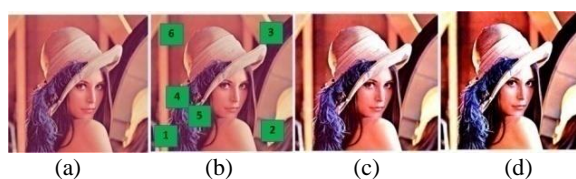
Figure 6. (a) Original Lena image (b) Marked Lena image (c) Guided filtering [40] (d) adaptive guided filtering (Proposed)

(a) Canny   (b) Sobel   (c) Fuzzy

(d) ACO   (e) ACO+ GIF   (f) FL+L₀ + GIF

(g) PSO   (h) PSO+ GIF   (i) FL+ OEGIF
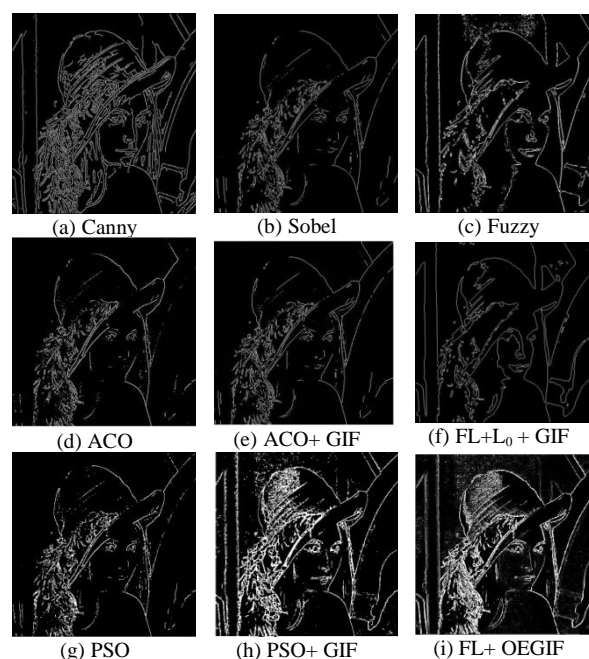
Figure 8. Comparison of edge detection methods

Although fuzzy edge identification performs better than Canny and Sobel approaches, as can be seen in marked regions 2, 3, and 4, some true edges are still mistakenly rejected (Figure 8(c)). Additionally, the face boundary is incorrectly detected, and noise can be observed across the hat area. ACO edge detection is displayed in Figure 8(d), and it can be seen that while some actual edges are correctly recognised, many of them are mistakenly rejected. These locations are indicated as 1, 2, 3, and 6. The results of Kumar et al.'s [32] edge detection method, which is based on ACO and guided filtering, are shown in Figure 8(e). As can be observed, the number of falsely rejected real edges falls as compared to the ACO method, although they are still numerous and can be seen in highlighted regions 1 and 6. Figure 8(f) shows the outcome of fuzzy + guided filtering edge detection. In this method, the problem of broken edges has been cured, but the area around the neck and face is not well identified. Results for PSO edge detection are displayed in Figure 8(g), and it can be seen that, with a little more noise, it performs remarkably similarly to Sobel approach. However, marked regions 1 and 6 still reveal missing edges. Results for Verma et al. [34] whose method is based on PSO and sharpening, are displayed in Figure 8(h), and it is evident that its performance is good. Although the majority of edges have been located, designated regions 3 still have some missing edges. The result for fuzzy and adaptive sharpening is presented in Figure 8(i), and it can be seen that performance is excellent for the most part and noise is significantly reduced as compared to the PSO+ sharpening method.

Table 3 compares the effectiveness of various edge detection techniques using FoM and F-Score. The F-score for Canny is 0.49 and FoM is 0.3, while for the Sobel method, the F-score is 0.4 and FoM is 0.42. The F-score for the learning-based sketch method token is 0.73. In the case of fuzzy and ACO-based methods, the F-score is 0.64 and 0.72, respectively, with the FoM around 0.4. Thus, various methods without edge enhancement do not perform well. Kumar et. al. [32] proposed the ACO+ Guided Filtering method, and the F-score improved to 0.81 with a FoM of 0.46. Raheja and Kumar [36] proposed Fuzzy + L_0 guided filtering method, and the F-score improved to 0.84 with a FoM of 0.5. Verma et al. [34] proposed PSO+ sharpening, and the F-Score improved to 0.851. Ranjan et al. [43] proposed Fuzzy+ Weighted Guided Filtering with an impressive FoM of 0.58. The performance of the proposed work is very impressive, with a FoM of 0.63 and an F-Score of 0.87. The result is improved due to the reduction in incorrect edges and noise.

5. CONCLUSIONS

Edge detection is a significant phenomenon that has applications in both engineering and medicine. Since edges are complex in nature, there are many different kinds of edge detection methods that have been investigated, ranging from classical masking-based methods to soft computing and deep learning-based methods. This work proposes an edge detection technique based on FL and AGIF. The adaptive guided images filtering method is useful for improving weak edges and smoothing low variance zones. The suppression of inaccurate edges is the key characteristic of the proposed edge detection method. The FoM and F-score are used to compare the performance of various edge detection methods. The FoM for the proposed method is 0.63, and the F-score is 0.87. In the future, fuzzy logic structure can be combined with deep neural network for more accurate contour/edge classification.

TABLE 3. Classical and State-of-the –art methods comparison (FoM and F-Score)

Reference	Methods	FoM	F-Score
Canny [6]	Masking	0.3	0.49
Gao et al. [7]	Masking	0.42	0.40
Lim et al. [21]	Sketch Token	-	0.73
Kumar and Raheja [35]	Fuzzy	0.4	0.64
Kumar et al. [31]	ACO	0.44	0.72
Kumar et al. [32]	ACO+ GIF	0.46	0.81
Raheja and Kumar [36]	Fuzzy+ L_0 +GIF	0.5	0.84
Setayesh et al. [45]	PSO	0.51	0.84
Verma et al. [34]	PSO+ GIF	0.51	0.851
Ranjan et al. [43]	Fuzzy+ W-GIF	0.58	0.859
Ranjan et al.	Proposed	0.63	0.87

(-) *Data Not Available

6. REFERENCES

1. Chi, Z., Li, H., Lu, H. and Yang, M.-H., "Dual deep network for visual tracking", *IEEE Transactions on Image Processing*, Vol. 26, No. 4, (2017), 2005-2015. doi: 10.1109/TIP.2017.2669880.

2. Leal-Taixé, L., Canton-Ferrer, C. and Schindler, K., "Learning by tracking: Siamese cnn for robust target association", in Proceedings of the IEEE conference on computer vision and pattern recognition workshops. (2016), 33-40.

3. Ojha, S. and Sakhare, S., "Image processing techniques for object tracking in video surveillance-a survey", in 2015 International Conference on Pervasive Computing (ICPC), IEEE. (2015), 1-6.

4. Torre, V. and Poggio, T.A., "On edge detection", *IEEE Transactions on Pattern Analysis and Machine Intelligence*, Vol., No. 2, (1986), 147-163. doi: 10.1109/TPAMI.1986.4767769.

5. Shui, P.-L. and Zhang, W.-C., "Noise-robust edge detector combining isotropic and anisotropic gaussian kernels", *Pattern*

Recognition,   Vol. 45, No. 2, (2012), 806-820. doi: 10.1016/j.patcog.2011.07.020.

6. Canny, J., "A computational approach to edge detection", *IEEE Transactions on Pattern Analysis and Machine Intelligence*, Vol., No. 6, (1986), 679-698.

7. Gao, W., Zhang, X., Yang, L. and Liu, H., "An improved sobel edge detection", in 2010 3rd International conference on computer science and information technology, IEEE. Vol. 5, (2010), 67-71.

8. Wei, Y., Liang, X., Chen, Y., Shen, X., Cheng, M.-M., Feng, J., Zhao, Y. and Yan, S., "Stc: A simple to complex framework for weakly-supervised semantic segmentation", *IEEE Transactions on Pattern Analysis and Machine Intelligence*, Vol. 39, No. 11, (2016), 2314-2320. doi: 10.1109/TPAMI.2016.2636150.

9. Rashno, A. and Fadaei, S., "Image restoration by projection onto convex sets with particle swarm parameter optimization", *International Journal of Engineering, Transactions B: Applications,* , Vol. 36, No. 2, (2023), 398-407. doi: 10.5829/ije.2023.36.02b.18.

10. Lakshmi, S. and Sankaranarayanan, D.V., "A study of edge detection techniques for segmentation computing approaches", IJCA Special Issue on "Computer Aided Soft Computing Techniques for Imaging and Biomedical Applications" CASCT, (2010), 35-40. doi.

11. Fadaei, S. and Rashno, A., "A framework for hexagonal image processing using hexagonal pixel-perfect approximations in subpixel resolution", *IEEE Transactions on Image Processing*, Vol. 30, (2021), 4555-4570. doi: 10.1109/TIP.2021.3073328.

12. Firouzi, M., Fadaei, S. and Rashno, A., "A new framework for canny edge detector in hexagonal lattice", *International Journal of Engineering, Transactions B: Applications,* , Vol. 35, No. 8, (2022), 1588-1598. doi: 10.5829/ije.2022.35.08b.15.

13. Fadaei, S., "New dominant color descriptor features based on weighting of more informative pixels using suitable masks for content-based image retrieval", *International Journal of Engineering, Transactions B: Applications,* , Vol. 35, No. 8, (2022), 1457-1467. doi: 10.5829/ije.2022.35.08b.01.

14. Martin, D.R., Fowlkes, C.C. and Malik, J., "Learning to detect natural image boundaries using local brightness, color, and texture cues", *IEEE Transactions on Pattern Analysis and Machine Intelligence*, Vol. 26, No. 5, (2004), 530-549. doi: 10.1109/TPAMI.2004.1273918.

15. Ren, X., "Multi-scale improves boundary detection in natural images", in Computer Vision–ECCV 2008: 10th European Conference on Computer Vision, Marseille, France, October 12-18, 2008, Proceedings, Part III 10, Springer. (2008), 533-545.

16. Arbelaez, P., Maire, M., Fowlkes, C. and Malik, J., "Contour detection and hierarchical image segmentation", *IEEE Transactions on Pattern Analysis and Machine Intelligence*, Vol. 33, No. 5, (2010), 898-916. doi: 10.1109/TPAMI.2010.161.

17. Payet, N. and Todorovic, S., "Sledge: Sequential labeling of image edges for boundary detection", *International Journal of Computer Vision*, Vol. 104, (2013), 15-37. doi: 10.1007/s11263-013-0612-5.

18. Dollar, P., Tu, Z. and Belongie, S., "Supervised learning of edges and object boundaries", in 2006 IEEE Computer Society Conference on Computer Vision and Pattern Recognition (CVPR'06), IEEE. Vol. 2, (2006), 1964-1971.

19. Rahebi, J. and Tajik, H.R., "Biomedical image edge detection using an ant colony optimization based on artificial neural networks", *International Journal of Engineering Science and Technology*, Vol. 3, No. 12, (2011), 8211-8218.

20. Etemad, K. and Chelappa, R., "A neural network based edge detector", in IEEE International Conference on Neural Networks, IEEE. (1993), 132-137.

21. Lim, J.J., Zitnick, C.L. and Dollár, P., "Sketch tokens: A learned mid-level representation for contour and object detection", in Proceedings of the IEEE conference on computer vision and pattern recognition. (2013), 3158-3165.

22. Eitz, M., Hays, J. and Alexa, M., "How do humans sketch objects?", *ACM Transactions on Graphics (TOG)*, Vol. 31, No. 4, (2012), 1-10. doi: 10.1145/2185520.2185540.

23. Elharrouss, O., Hmamouche, Y., Idrissi, A.K., El Khamlichi, B. and El Fallah-Seghrouchni, A., "Refined edge detection with cascaded and high-resolution convolutional network", *Pattern Recognition*,   Vol. 138, (2023), 109361. doi: 10.1016/j.patcog.2023.109361.

24. Xiaofeng, R. and Bo, L., "Discriminatively trained sparse code gradients for contour detection", *Advances in Neural Information Processing Systems*, Vol. 25, (2012).

25. Isola, P., Zoran, D., Krishnan, D. and Adelson, E.H., "Crisp boundary detection using pointwise mutual information", in Computer Vision–ECCV 2014: 13th European Conference, Zurich, Switzerland, September 6-12, 2014, Proceedings, Part III 13, Springer. (2014), 799-814.

26. Fano, R.M., "Transmission of information: A statistical theory of communications", *American Journal of Physics*, Vol. 29, No. 11, (1961), 793-794.

27. Yang, J., Price, B., Cohen, S., Lee, H. and Yang, M.-H., "Object contour detection with a fully convolutional encoder-decoder network", in Proceedings of the IEEE conference on computer vision and pattern recognition. (2016), 193-202.

28. Anandan, P., Bergen, J.R., Hanna, K.J. and Hingorani, R., "Hierarchical model-based motion estimation", *Motion Analysis and Image Sequence Processing*,   (1993), 1-22. doi: 10.1007/978-1-4615-3236-1_1.

29. Xia, X. and Kulis, B., "W-net: A deep model for fully unsupervised image segmentation", arXiv preprint arXiv:1711.08506, (2017). doi: 10.48550/arXiv.1711.08506.

30. Baterina, A.V. and Oppus, C., "Image edge detection using ant colony optimization", *Wseas Transactions on Signal Processing*, Vol. 6, No. 2, (2010), 58-67.

31. Kumar, A. and Raheja, S., "Edge detection using guided image filtering and enhanced ant colony optimization", *Procedia Computer Science*,   Vol. 173, (2020), 8-17. doi: 10.1016/j.procs.2020.06.003.

32. Kumar, A. and Raheja, S., "Edge detection using guided image filtering and ant colony optimization", in Recent Innovations in Computing: Proceedings of ICRIC 2020, Springer. (2021), 319-330.

33. Ravivarma, G., Gavaskar, K., Malathi, D., Asha, K., Ashok, B. and Aarthi, S., "Implementation of sobel operator based image edge detection on fpga", *Materials Today: Proceedings*, Vol. 45, (2021), 2401-2407.

34. Verma, A., Dhanda, N. and Yadav, V., "Binary particle swarm optimization based edge detection under weighted image sharpening filter", *International Journal of Information Technology*, Vol. 15, No. 1, (2023), 289-299. doi: 10.1007/s41870-022-01127-0.

35. Kumar, A. and Raheja, S., "Edge detection in digital images using guided l0 smoothen filter and fuzzy logic", *Wireless Personal Communications*, Vol. 121, No. 4, (2021), 2989-3007. doi: 10.1007/s11277-021-08860-y.

36. Raheja, S. and Kumar, A., "Edge detection based on type-1 fuzzy logic and guided smoothening", *Evolving Systems*, Vol. 12, No. 2, (2021), 447-462. doi: 10.1007/s12530-019-09304-6.

37. Kaur, E.K., Mutenja, V. and Gill, I.S., "Fuzzy logic based image edge detection algorithm in matlab", *International Journal of Computer Applications*, Vol. 1, No. 22, (2010), 55-58.

38. Aborisade, D.O., "Novel fuzzy logic based edge detection technique", *International Journal of Advanced Science and Technology*, Vol. 29, No. 1, (2011), 75-82.

39. Begol, M. and Maghooli, K., "Improving digital image edge detection by fuzzy systems", *World Academy of Science, Engineering and Technology*, Vol. 81, (2011), 76-79. doi.

40. Zhang, L., Xiao, M., Ma, J. and Song, H., "Edge detection by adaptive neuro-fuzzy inference system", in 2009 2nd International Congress on Image and Signal Processing, IEEE. (2009), 1-4.

41. Dorrani, Z., Farsi, H. and Mohamadzadeh, S., "Image edge detection with fuzzy ant colony optimization algorithm", *International Journal of Engineering, Transactions C: Aspects*, Vol. 33, No. 12, (2020), 2464-2470. doi: 10.5829/ije.2020.33.12c.05.

42. Siddharth, D., Saini, D. and Singh, P., "An efficient approach for edge detection technique using kalman filter with artificial neural network", *International Journal of Engineering, Transactions C: Aspects*, Vol. 34, No. 12, (2021), 2604-2610. doi: 10.5829/ije.2021.34.12c.04.

43. Ranjan, R. and Avasthi, V., "A hybrid edge detection mechanism based on edge preserving filtration and type-1 fuzzy logic", *International Journal of Information Technology*, Vol. 14, No. 6, (2022), 2991-3000. doi: 10.1007/s41870-022-01059-9.

44. Zhang, B. and Allebach, J.P., "Adaptive bilateral filter for sharpness enhancement and noise removal", *IEEE Transactions on Image Processing*, Vol. 17, No. 5, (2008), 664-678. doi: 10.1109/TIP.2008.919949.

45. Setayesh, M., Zhang, M. and Johnston, M.R., "Feature extraction and detection of simple objects using particle swarm optimisation, School of Engineering and Computer Science, Victoria University of Wellington, (2009).
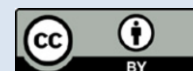
Persian Abstract

چکیده

در بینایی کامپیوتر، تشخیص کانتور/لبه یک پدیده حیاتی است. تشخیص لبه یک مرحله مهم در تشخیص کانتور است که در شناسایی داده های مهم مفید است. دقت فرآیند تشخیص لبه به شدت به محلی سازی و جهت گیری لبه بستگی دارد. در سال های اخیر، به دلیل تطبیق پذیری، رویکردهای محاسباتی نرم به عنوان استراتژی های موثر تشخیص لبه در نظر گرفته شده اند. به طور کلی، دقت تشخیص لبه عمیقاً تحت تأثیر لبه های ضعیف و کسل کننده است. در کارهای اخیر، تشخیص لبه بر اساس منطق فازی (FL) پیشنهاد شد و لبه های تصویر با استفاده از فیلتر هدایت شونده بهبود یافتند. با این حال، فیلتر تصویر هدایت‌شده (GIF)ویژگی‌های محلی یک تصویر را در نظر نمی‌گیرد. برای گنجاندن ویژگی‌های محلی یک تصویر برای تشخیص لبه، یک نسخه بهبودیافته، به عنوان مثال، یک فیلتر هدایت‌شونده شفاف‌سازی افست در این مقاله استفاده شده است، و FL برای تشخیص لبه استفاده می‌شود. برای ارزیابی دقت روش از رقم شایستگی (FoM) و امتیاز F استفاده می شود. با استفاده از نمایش‌های بصری و معیارهای عملکرد، نتایج با نتایج حاصل از تکنیک‌های پیشرفته مقایسه می‌شوند.

Experimental and Numerical Investigation of the Impact of Basalt Fibers and Tie Spacing on Short Concrete Column Behavior

Q. A. Hassan[a], A. M. Jabbar*[b], D. H. Mohammed[a]

[a] Civil Engineering Department, University of Technology, Baghdad, Iraq
[b] Civil Engineering Department, College of Engineering, Wasit University, Iraq

P A P E R   I N F O

A B S T R A C T

This paper demonstrates the effect of adding basalt fibers into a concrete matrix and altering tie spacing on the behavior of short concrete columns since short columns are more robust than long ones and are primarily used in structures. Also, the impact of changing the reinforcement ratio on column behavior is numerically discovered. Three volume fractions of basalt fiber and three-tie spacing are adopted. The results illustrate that no-fiber columns sustain more than 50 % of the failure load before cracking, while this percentage raised to 75 % upon adding basalt fiber to concrete. 0.3 % of basalt fiber increases the compressive strength, cracking and ultimate column loads better than 0.6 %. Likewise, the impact of basalt fiber on the crack load is more pronounced than on the maximum load of the column. Basalt fiber columns exhibit lower longitudinal displacement than no-fiber ones at the cracking state. The shortening increases with increasing tie spacing, whereas decreasing tie spacing barely increases the ultimate load of the column. The numerical analysis provides close results to the experimental ones and shows that increasing the reinforcement ratio raises the column's load capacity. For the same tie spacing, increasing the reinforcement ratio raises the loading capacity of columns, and the longitudinal displacement barely increases upon increasing spacing. Generally, basalt fibers delay cracking and improve the column loading capacity.

doi: 10.5829/ije.2023.36.07a.10

NOMENCLATURE

BF	Basalt fiber	Pcr/Pcro	Crack load of fiber column to crack load of analogous no fiber column ratio
BFRC	Basalt fiber reinforced concrete	Pcr/Pu	Cracking to maximum load ratio
COV	Coefficient of Variation	Pu	Maximum load, kN
f'c	Compressive strength, MPa	S	Tie-spacing, mm
FE	Finite element	SD	Standard Deviation
LVDT	Linear Variable Differential Transformer	Δcr	longitudinal displacement at cracking load, mm
Pcr	Cracking load, kN	Δu	longitudinal displacement at maximum load, mm

1. INTRODUCTION

Basalt fiber is a new natural fiber extracted from frozen lava of volcanic rocks gathered on the surface of the earth's crust [1-4]. Basalt fiber has high stability and insulating features [5, 6]. The main property that makes basalt fiber attractive for the use in concrete is its high ability to absorb strain energy upon increasing the load and enhancing the ductility [7], besides its contribution to reduce the drying shrinkage, which improves the impermeability of concrete and increasing the strength and load capacity of structural elements. Many studies investigated the impact of adding basalt fibers on the mechanical properties of concrete. Different percentages as volume fractions or as a percent of cement content were added to the concrete matrix to show their effect and to decide the best content. Each researcher selected the optimal ratio according to the added percentages in the

---

Corresponding Author Email: adilmahdi@uowasit.edu.iq
(A. M. Jabbar)

experiments where these percentages differ from one to another. Qin et al. [8] found that increasing basalt fiber content raised splitting tensile strength, and 1.25 % awarded the highest increment. Kirthika and Singh [9] decided that 0.75 % gave more increment in tensile strength, while 0.5 % accorded the best compressive strength. Ramesh and Eswari [10] found that 1.5 % basalt fiber content awarded the highest tensile strength, while Jia et al. [11] found that 0.2 % basalt fiber assigned the highest tensile strength among three percentages: 0.1, 0.2, and 0.3 %.

For compressive strength: several researchers suggested that basalt fibers have no significant effect. The researchers attributed that to reducing workability upon adding basalt fibers because of the large surface area of the microfiber and suggested using a superplasticizer to improve the concrete workability[1]. Sun et al. [12] found that the 6 mm length fiber and 0.2 % volume fraction awarded the best effect on concrete specimens. Jia et al. [11] concluded that the compressive strength was slightly enhanced upon adding basalt fiber up to 0.2 %, while at 0.3 % basalt fiber, the compressive strength decreased. Li et al. [13] found that the compressive strength slightly declined with the addition of basalt fibers as compared to plain concrete. However, the failure mode was changed from brittle to ductile in compression. Dilbas and Cakir [14] found that the 0.25 % basalt fiber awarded the best increment in compressive strength, while 1.0 % content gave the best result for tensile strength.

Ayub et al. [6] investigated the impact of 1.0 %, 2.0 %, and 3.0 % basalt fiber on the mechanical properties of high-performance concrete (HPC). The results showed that adding basalt fiber at 1.0 % and 2.0 % slightly increased compressive and tensile strength, while 3.0 % basalt fiber content decreased compressive strength by 9.45 % compared to HPC without fiber.

Ghanbari et al. [15] investigated the addition of basalt fibers to ultra-high-performance concrete (UHPC). The results showed that 0.5 %, 1.0, and 1.5 % basalt fiber raised compressive strength by 44 %, 51 %, and 41 %, respectively. High et al. [16] clarified that 1.78 kg/m^3 basalt fibers raised the compressive strength of normal concrete at 3 days by 5.48 %, at 7 days by 14.12 %, and at 28 days by 5.63 %. Krassowska and Kosior [17] showed the incorporation of 2.5 kg/m^3 and 5.0 kg/m^3 basalt fiber into normal concrete increased the compressive strength by 4.75 % and 0.98 %, respectively. Hirde and Shelar [18] clarified that the maximum increment in compressive strength was at 3 % content, while 4 % awarded the highest increment in splitting tensile strength by 33.6 %. Iyer et al. [19] showed that 18 kg/m^3 was the best content to improve compressive and flexural strengths. Incorporating basalt fibers into concrete reduced drying shrinkage and contributed to

minimizing the voids in size and quantity [20]. On the other hand, incorporating basalt fibers with the concrete matrix can enhance the absorbed energy and ductility [21]. Also, the numerous basalt filaments for any volume fraction and their orientation in different directions contribute to disrupting cracks in the concrete and impeding their progress, which highly improves the strength [15, 21]. Therefore, basalt fibers act to confine concrete internally.

Generally, it appears that adding basalt fibers to normal, high, and ultra-high-strength concrete can enhance their mechanical properties. Increasing compressive strength can affect the loading capacity of the compressive members, such as columns in buildings and infrastructures.

Columns are the prime compression members [22]. The loading capacity of short columns depends on the concrete cross-section resistance and the stresses carried by the longitudinal rebar [23]. However, steel ties are always used as transverse reinforcement to prevent the buckling of individual longitudinal bars and to hold them in place before and during concrete pouring [23]. Therefore, ACI 318-Code [7], Eurocode 2 [24], and other codes regarded only the concrete cross-section and longitudinal rebars and excluded transverse steel ties in determining the nominal strength of columns, despite the ties having a significant action in confining the concrete. The confining role of the ties for concrete can increase the compressive strength of the concrete and thus increase the bearing capacity of the column [25, 26]. Mokhtar et al. [27] investigated the influence of tie spacing on the behavior of short columns. They found that decreasing tie-spacing increases bearing capacity. Also, the longitudinal displacement increased with decreasing the tie spacing due to raising the confinement effect on concrete. Hoshitha et al. [20] also studied the effect of tie spacing on short columns. Test results showed increasing cracking and ultimate loads with decreasing spacing between ties. That was due to the enhancement of lateral confinement for the concrete core. Naji et al. [28] investigated on Columns Reinforced with Steel Fibers Mokhtar et al. [27] studied the influence of distribution ties on short-column loading capacity. The results showed that more stress occurred near the fixed end of the column. Nemati- Aghamaleki et al. [29] studied on compressive behavior of concrete-filled double-skin circular tubes with active confinement.

According to the action of basalt fibers in providing internal confinement and ties in providing external confinement for concrete in columns, the idea of this study arose. Therefore, this study aims to demonstrate the effect of tie spacing and the addition of basalt fibers to the concrete matrix on the behavior of short column and their loading capacity. Three tie-spacing and three basalt fiber volume fractions are assumed. Three columns with

---

[1] www.galencomposite.ru

variable tie spacing per mix are cast to arrive at nine columns. Furthermore, three bar diameters are adopted as additional parameters, which are numerically investigated via Abaqus software to show their impact on the short-column behavior, as illustrated in Figure 1.

2. EXPERIMENTAL INVESTIGATION

2. 1. Test Specimens   Nine identical circular section short columns were prepared for testing. The column had a diameter of 150 mm and a length of 750 mm. The longitudinal rebars were equal for all columns using 4 bars of 8 mm diameter to give a reinforcement ratio of 1.13 %. The ties were 5.5 mm diameter bars. The concrete cover was 20 mm. The tie spacing was 80 mm, 120 mm, and 180 mm, as shown in Figure 2. Another parameter adopted was the addition of basalt fibers to the concrete matrix to clarify their effects. According to the results obtained from the literature, the lower percentages of basalt fibers have a better effect on concrete strength. Therefore, three-volume fractions were assumed; 0.0, 0.3 %, and 0.6 %.

2. 2. Material Properties and Mix Proportion
The mechanical properties of steel rebars used in the columns are listed in Table 1. Tensile testing of rebars are performed according to ASTM A370 [30] and EN 10002 [31].

An identical mixture was used for all columns. The change was in chopped basalt fiber volume fraction and high-range water reducer admixture (HRWRA) dosages. Ordinary Portland cement (ASTM Type I) conforms to ASTM C150-16 [30], a fine natural aggregate with a fineness modulus of 2.75 and compacted density of 1656 kg/m^3, was used in the mixtures. Coarse aggregate was natural crushed gravel with a maximum size of 14 mm and compacted density of 1527 kg/m^3. Fine and coarse aggregate conform to Iraqi Specifications (IS No. 45/1984) [32]. Three volume fractions of basalt fiber were added to a similar concrete mixture, 0.0 %, 0.3 %, and 0.6 %. Therefore, three mixes were prepared to cast nine columns.

Chopped basalt fibers as short filaments collected in slices of 12 mm long and (16-18) μm diameter were utilized, as shown in Figure 3. Basalt fiber has a modulus of elasticity of (85-90) GPa, a density of 2800 kg/m^3, and 3.2 % elongation at breaking [3]. Basalt fiber
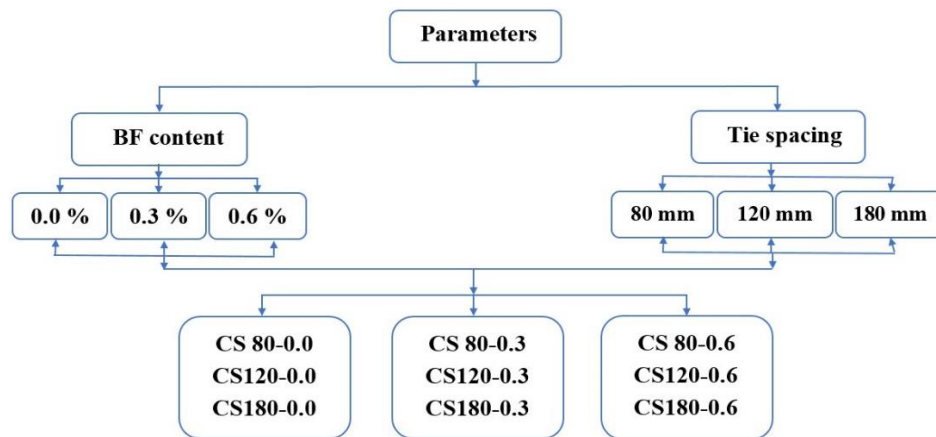

Figure 1. Parameters and experiments scheme
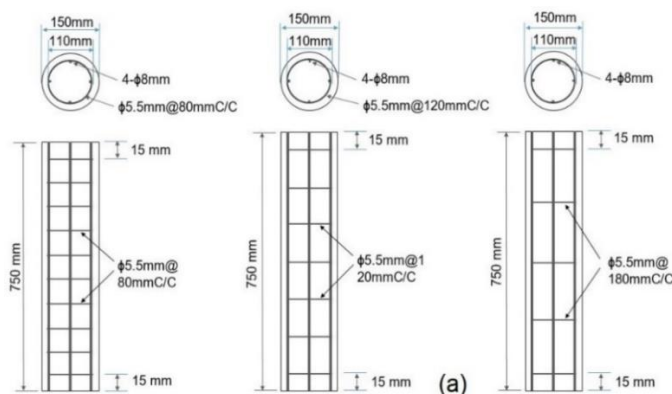
Figure 2. (a) Details of columns showing the spacing between the ties (b) Rebar configuration

TABLE 1. Mechanical properties of steel rebars used in the experiments

Nominal diameter mm	Actual diameter, mm	Rebar area, mm^2	Yield stress, f_y, MPa	SD	Ultimate strength, f_u, MPa	SD	Modulus of elasticity, Es, GPa	Maximum elongation, %	SD
8.0	7.954	49.69	563	3.64	624	4.06	200	7.678	0.19
5.5	5.100	20.43	394	1.85	443	0.83	200	1.192	0.02

is an inert substance; it does not participate in chemical reactions [6]. The mix proportion is listed in Table 2.

The water-to-cement ratio was kept constant at 0.5. Upon adding basalt fibers, the workability was excessively decreased. Therefore, Sika Viscocrete-180G has a specific gravity of 1.065 gm/cm^3 and was used as a high-range water reducer and super plasticizing admixture having a polycarboxylates polymer base.

The prepared mixture was cast into the column mold and compacted with a 16 mm steel rounded end rod to ensure that the concrete reached all parts inside the mold, as shown in Figure 4. Three or more cylinders with (100x200) mm size were also cast from the same mixture as control specimens for testing cylinder compressive

Figure 3. Chopped basalt fibers

TABLE 2. Mix proportions of concrete used in the experiments

Mix symbol	Cement content, kg/m^3	Fine aggregate, kg/m^3	Coarse aggregate, kg/m^3	Water content, kg/m^3	Basalt fibers		HRWRA	
					Vf * %	Content, kg/m^3	% **	Dosage, L/m^3
MBF0.00	430	823	847	215	0.00	0.00	0.00	0.00
MBF0.30	430	823	847	215	0.30	8.43	0.75	3.23
MBF0.60	430	823	847	215	0.60	16.90	1.25	5.38

* Volume fraction of concrete
** Percent of cement content

strength. All specimens were entirely covered with polyethylene sheets to prevent water evaporation. Twenty-four hours after casting, the specimens were de-molded, then cured in water for 28 days. One day before testing, the specimens were taken out of the water and left to dry to examine in a saturated, dry surface condition.

2. 3. Test Setup and Instrumentation   A compression bearing was subjected to the top section of the column. Two steel bolsters representing bases support the column from top and bottom. They were made of a steel ring have a diameter slightly larger than the column diameter. These bolsters were used to install the column in the testing device, as shown in Figure 5. Rubber pads of 150 mm diameter and 5 mm thickness were placed between the base of the bolsters and the concrete column at the top and bottom to avoid the impact load. A universal testing machine of 1000 kN capacity was applied to test the columns. A load cell of 1000 kN capacity was placed over the upper bolster to record the load increment. An LVDT tool was used between the upper and lower bolsters to record the axial displacement.

A data logger was used to record the loads and displacements at each increment.

For (100x200) mm concrete cylinder specimens, a Matest compressive testing device with 2500 kN capacity was used. All columns and control specimens were tested at 28-day ages.

Figure 4. Concrete pouring into a mold

Figure 5. Test setup and instrumentation

3. EXPERIMENTAL RESULTS AND DISCUSSION

The devices used to record the loads and displacements were tested before the actual loading of column specimens. The column was preloaded by 40 kN for 3 minutes to observe the measuring system. Next, the actual loading was carried out with an increase of 40 kN per grade up to 160 kN, then 20 kN until failure. Each load grade was sustained for 2 minutes to observe the appearance of cracks and allow the stability of the load to record the data. The loading system is shown in Figure 5.

3. 1. Compressive Strength Results Three or more concrete cylinders were tested per every mix at 28 days, and the average value was regarded for compressive strength. Test results are shown in Table 3.

According to the compressive strength results, it is clear that raising basalt fiber content to 0.6 % enhances compressive strength. However, 0.3 % of basalt fibers increase compressive strength more than 0.6 %. The best increase in compressive strength was 23.69% at 0.3% basalt fibers. Comparing this result to Kirthika and Singh's [9] results, they found that 0.5% increased compressive strength by 26.8%. Also, Dilbas and Cakir [15] found that 0.25% of basalt fibers (BF) awarded the best compressive strength.

The micro diameter of basalt fibers awards plenty of filaments. The low percentage of basalt fiber can orient in all directions within the concrete matrix. The bonding

TABLE 3. Cylinder compressive strength per basalt fiber content

BF content, %	Comp. strength, f'c, MPa	Percentage of increase in f'c, %	SD	COV
0.00	32.42	0.00	1.516	0.047
0.30	40.10	23.69	1.091	0.027
0.60	35.46	9.38	1.346	0.038

strength between the filament and concrete matrix increases because of its micro diameter, giving high internal confinement and reducing early shrinkage. These features enhance compressive strength.

On the other hand, the microfilament is flexible and can be bent and curled during mixing and running in a concrete mixture. When the number of filaments is extra-large, the percentage of curled ones increases to entrap dry mortar inside and form voids. Therefore, the number of voids increases inside the concrete microstructure, and the voids increment reduces the strength. Furthermore, the micro diameter of filaments raises the fibers' surface area to increase the water molecules' demand. So not all filaments will get the quantity of water they need to adhere to them. When the fiber content is relatively high, the number of non-bonded filaments increases, besides increasing the voids formed by the curled fibers; therefore, the strength comparatively decreases.

3. 2. Short Column Results Table 4 lists the test results of cracking and ultimate loads sustained by short columns with the corresponding longitudinal displacements. The columns are divided into three groups according to the basalt fiber content. Each group consists of three columns with three different tie spacing. Columns are coded with the letter "C" to indicate a circular column, the letter "S" indicates tie spacing, and the number following it refers to tie spacing value. The other number refers to the basalt fiber percentage. For instance, CS80-0.3 represents a short circular column with 80 mm tie spacing and 0.3 % of basalt fibers.

Short columns without fibers sustain more than 50 % of the failure load before cracking, whereas incorporating basalt fibers into the concrete matrix raised the cracking load to about three-quarters of the failure load.

3. 3. Effect of Basalt Fiber Content on Short Column Loading Capacity The addition of basalt fibers to the concrete matrix enhanced short column capacity. The 0.3 % of basalt fibers increased loading capacity by more than 50 % at the cracking state and between (15-19) % at the ultimate state. At 0.6 % of basalt fiber content, the cracking load was increased by about 50 % over the no-fiber short columns, while at the maximum loading, the increase was between (7.7-11.0) %. Generally, 0.3 % of basalt fiber enhanced the bearing capacity of the short column more than that of 0.6 % at cracking and ultimate state, as shown in Figures 6 and 7. The results also clarified that the effect of basalt fibers on cracking loads was more than on the maximum loads. The cracking load was about 55% of the ultimate load for no fiber columns, while this ratio increased to 75% approximately for BFRC columns, as shown in Figure 8.

On the other hand, basalt fibers reduced the longitudinal displacement at the cracking state. However, at the ultimate state, there was no evident effect for the fibers on the longitudinal shortening.

TABLE 4. Short-column test results for cracking and ultimate state

Column ID	BF content	f'c	Cracking load, Pcr, kN	Δcr, mm	Ultimate load, Pu, kN	Ultimate displacement, Δu, mm	Pcr/Pu	Pcr/Pcro
CS 80-0.00	0	32.42	256.40	1.65	470.18	3.2	0.545	1.00
CS120-0.00	0	32.42	258.89	1.86	461.64	3.0	0.561	1.00
CS180-0.00	0	32.42	257.05	1.80	453.72	3.2	0.567	1.00
CS 80-0.30	0.3	40.10	405.80	1.20	558.65	3.2	0.726	1.58
CS120-0.30	0.3	40.10	406.87	1.22	532.73	3.6	0.764	1.57
CS180-0.30	0.3	40.10	399.65	1.18	521.33	3.7	0.767	1.55
CS 80-0.60	0.6	35.46	386.50	1.28	521.67	3.7	0.741	1.51
CS120-0.60	0.6	35.46	386.02	1.34	498.73	3.7	0.774	1.49
CS180-0.60	0.6	35.46	382.50	1.33	488.50	3.2	0.783	1.49
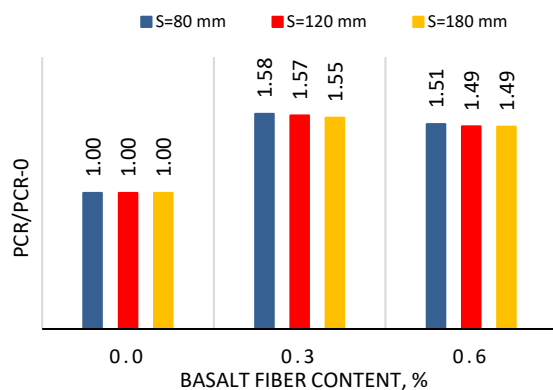
Figure 6. Cracking load increment ratio vs. basalt fiber content
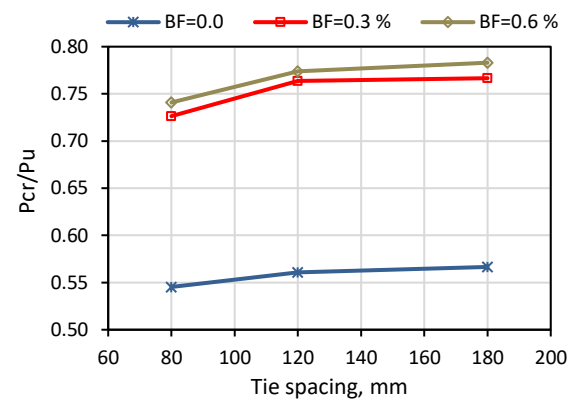
Figure 8. Effect of basalt fibers on cracking and ultimate loads
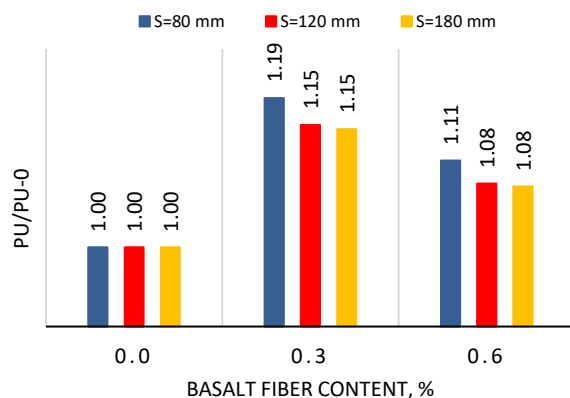
Figure 7. Ultimate load increment ratio vs. basalt fiber content

As stated previously, basalt microfilaments with 16-18 μm diameter can bond firmly with concrete matrix to form a spatial network surrounding the granules of coarse aggregate. Therefore, that network can improve the combination of concrete ingredients. The spatial network encases the coarse aggregate to hinder its movement during compression. Also, it can enhance the interfacial transition zone between coarse aggregate and cement paste and reduce the number and size of voids inside the concrete microstructure. These improvements are positively reflected in the concrete strength and are more effective when filament distribution is uniform and in all orientations. When the number of filaments steadily increases, and some remain uncombined to the matrix, the voids increase and cause reduced strength comparatively.

High bonding strength due to the micro diameter with the huge number of combined filaments requires more energy to overcome the bonding strength between filaments and concrete matrix. These features enhance cracking loading. Therefore, the cracking loads in BFRC short columns are more than in no fiber columns. Similar reasons apply to the longitudinal displacement of BFRC short columns.

3. 4. Effect of Tie Spacing On Loading Capacity
Three tie spacing were used in the three groups of columns: 80 mm, 120 mm, and 180 mm, to clarify the influence of changing tie spacing along with basalt fiber

content on the cracking and ultimate loading capacity. According to the results, the smaller the tie spacing, the slightly higher the loading capacity of the short column at the peak state.

For conventional concrete columns, the increment ratio in ultimate load was 1.85 % and 3.63 %. For BFRC columns with 0.3 %, the increment ratio was 4.9 % and 7.2 % upon reducing spacing by 40 mm and 100 mm, respectively. For 0.6 % of basalt fibers, the increment ratio in ultimate load was 4.6 % and 6.8 %, respectively, as shown in Figure 9. The increase in the loading capacity of BFRC columns was more than that of conventional concrete columns.

At a cracking state, non-apparent variation in the loads occurred for the same basalt fiber content, which is considered logical since the effect of fibers and steel ties occurs after cracking, as illustrated in Table 4.

Both ties and basalt filaments provide confinement to the concrete. Steel ties externally confine the concrete core, and basalt filaments provide internal confinement to the matrix because of their relatively high bond strength with concrete. The external and internal confinements restrict the concrete from expanding laterally. Therefore, they enhance the concrete strength in tension and compression. Additionally, the internal confinement of basalt fiber can improve the compressive strength and delay the initial cracking, which, in turn, increases the loading capacity of short columns.

However, the influence of internal confinement caused by basalt fiber on small specimens of concrete cylinders is more pronounced than on larger column specimens. That may be because the small size of concrete cylinders awards further restriction of stress transmission through small size.

3. 5. Failure Pattern   Through the test, columns did not originate transverse cracks, while vertical cracks occurred near supports before failure. Upon increasing
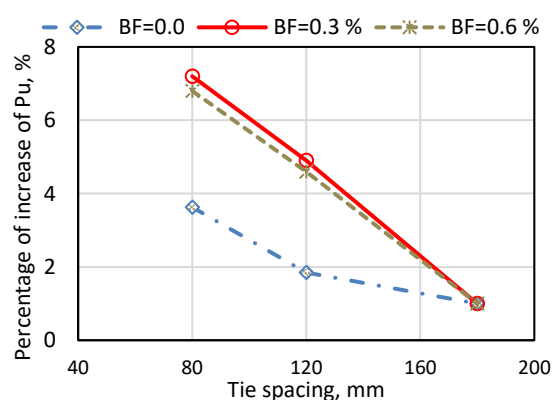
the load, the cracks developed gradually, then the concrete was crushed, and the column failed. However, the steel ties remained sound when the columns were damaged. All the columns have failed due to the crushing of concrete at the upper or lower third or both ends near the bolsters, as illustrated in Figure 10. That was because the stresses were concentrated near the loading point. During crack propagation and before failure, the concrete cover fell off. At fracture, the cracks propagated longitudinally and focused near the bolsters. After the peak, the load dropped slowly but never less than 40 % of the column loading capacity, which refers to ductility acquired by the column when adding basalt fibers. Generally, BFRC short columns were cracked later than the non-fibrous columns.

4. NUMERICAL ANALYSIS OF COLUMNS

A numerical analysis via Abaqus software was developed to trace the structural behavior of columns under axial compressive loading. It was performed by displacement control to capture the load at each increment.

4. 1. Numerical Simulation of Columns   The analyzed column consists of a concrete column with a circular section of 150 mm diameter, longitudinal rebars of 8 mm diameter, transverse ties of 5.1 mm diameter, and steel supporting plates. The concrete column and steel plates are discretized with a 3-dimensional continuum of 8 nodes and a reduced integration element (C3D8R). Steel rebars are discretized by 2 nodded link elements (T3D2). C3D8R has 8 nodes with 3 degrees of freedom per node. This element can model solids in 3 dimensions with or without reinforcement. It can consider tensile cracking, compressive crushing, and large strains [33]. T3D2 element is used to model one-dimensional rebar regarding axial strain only as a truss element[1]. Figure 11 depicts the discretization of the columns.

Figure 9. Influence of basalt fibers and tie spacing on ultimate load

Figure 10. Failure patterns of short columns

---

[1] http://www.wiley.com/go/permissions
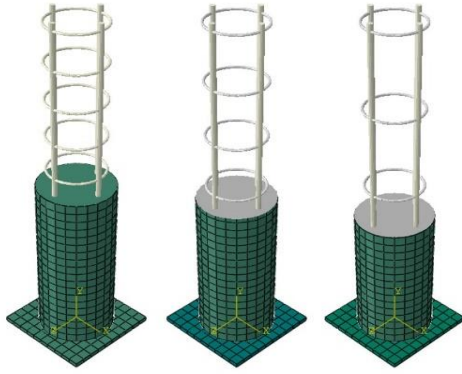
Figure 11. The meshing of concrete columns and rebars

The relationship between the concrete and rebars is assigned via the embedded region. The rebars are embedded inside the host region of concrete. The steel plates are constrained as a rigid body to prohibit deformation during loading. The lower plate is assigned as fixed support by preventing the transition and rotation in all directions. The load is applied to the upper steel plate. The elements of all parts are seeded by a 20 mm mesh size in all orientations. The interaction between the steel plates and concrete column is selected to be a contact with the normal behavior of hard contact type to prevent penetration between them and tangential behavior with a friction coefficient of 0.45 between concrete and steel. The analysis is done with a static general step.

4. 2. Material Models   The elastic behavior of concrete is defined by its modulus of elasticity and Poisson's ratio. The plastic behavior of concrete is defined by the concrete damage plasticity (CDP) model to define different transition laws of strength under compression and tension [33]. To define the CDP model, the stress-inelastic strain including compression hardening and softening, and tensile stiffening are determined according to the experimental results for compressive strength. Hognestad and Eurocode, Eu-2004 [24] formula is adopted to capture the compressive stresses at the successive strains as follows;

$$\sigma_c = f_c' \left[2 \left(\frac{\varepsilon_o}{\varepsilon_{co}} - \left(\frac{\varepsilon_o}{\varepsilon_{co}} \right)^2 \right) \right] \tag{1}$$

$$\varepsilon_o = \frac{0.4\, f_c'}{E_c} \tag{2}$$

$$E_c = 3320\sqrt{f_c'} + 6900 \tag{3}$$

$$\varepsilon_{co} = \frac{2f_c'}{E_c} \tag{4}$$

$$\varepsilon_{pl.} = \varepsilon - \frac{\sigma_c}{E} \tag{5}$$

$$d_c = 1 - \frac{\sigma_c}{f'c} \tag{6}$$

where:
σ_c = Compressive stress at corresponding strain, MPa
ε_{co} = Compressive strain at compressive strength.
ε_o = Strain at 40% of compressive strength (elastic limit).
E_c = Modulus of elasticity, MPa.
$\varepsilon_{pl.}$ = Plastic strain, and dc = damage parameter

The yield tensile strength is considered (1/10 -1/12) of compressive strength. Steel rebars are defined by the yield stresses for 5.1 mm bars and 8 mm bars, as determined experimentally. The failure surface of the finite elements is defined by the five parameters adopted in Abaqus, which are the dilation angle (ψ), eccentricity (Ɛ), the ratio of biaxial to uniaxial stress (fbo/fco), the shape of failure surface (K), and the viscosity parameter (μ). These values are illustrated in Table 5.

4. 3. Model Validation and Analysis Results   The performed finite element model was validated by comparing its results with the experimental ones. The ultimate loads, longitudinal displacements, and crack patterns are compared with the experimental results to gauge the efficiency of the simulated model for predicting the structural behavior of columns.

4. 4. Loads and Longitudinal Displacements   The finite element (FE) loads and longitudinal displacements (Δ) are illustrated in Table 6. At the cracking state, the FE loads underestimate the experimental ones because the FE results in Abaqus depend on the cracking stress of concrete, which is determined to be 40 % of compressive strength. The ratio between an experiment to FE cracking loads ranges between (1.08-1.09) for columns without fibers and between (1.21-1.23) for BFRC columns. The increase in cracking loads for no fiber columns by (8-9) % indicates that cracking does not occur at 40 % of concrete strength. That is due to the effect of ties in the columns. The additional change in fibers column experimental results refer to the influence of basalt fiber, where the microfilaments provide confinement to the concrete matrix. That confinement delays cracking and restricts crack initiation and propagation until it acquires enough energy to overcome the bonding forces between microfilaments and the matrix. For columns without fiber, the cracking displacements underestimate the experimental results. For columns with fibers, the FE cracking loads underestimate the experimental ones by (8-9) %. That reflects the action of basalt fibers in restricting the cracking and providing confinement.

At peak state, the FE loads approach the experimental ones. The ratio between an experiment to FE loads ranges between (0.94-1.03). The FE displacements are also close to the experimental results. The ratio between the experiment to FE displacement is (0.91-1.10). The results also clarify that the displacement increases with increasing tie spacing for all basalt fiber content, which is due to the increase of confinement effect of ties.

Generally, the displacement increases more than conventional concrete upon adding basalt fibers. Figures 12, 13, and 14 depict relationships between loads and longitudinal displacement for whole columns. According to these figures, the columns' behavior is similar until cracking loads, after which differences appear up to failure. After maximum loads, the columns continue in almost horizontal loads with increasing longitudinal displacement indicating the ductility of the columns.

4. 5. Crack Pattern   The numerical analysis results showed that all columns failed due to concrete crushing. The loading in Abaqus was carried out by displacement control. Upon increasing loads, the cracks initiated near the upper and lower supports then propagated to the third bottom in some columns or to the mid-length in others, as illustrated in Figure 15. However, the failure pattern of the FEA corresponded to the experimental results.

TABLE 5. The properties of materials used to simulate the short columns in Abaqus

Material	Properties				
Concrete	Elastic modulus, Ec			Poisson's ratio	
	Variable, according to f'c			0.18	
	ψ	ε	f_{bo}/f_{co}	K	μ
	25	0.1	1.16	0.67	1E-12
Steel rebars	Diameter = 8 mm			Diameter = 5.1 mm	
	Es	Yield stress	Poisson's ratio	Es	Yield stress	Poisson's ratio
	200 GPa	563 MPa	0.30	200 GPa	394 MPa	0.30

TABLE 6. The FEA results compared to experimental results

Column ID	Pcr, kN		Pcr	Δcr, mm		Δcr	Pu, kN		Pu	Δu, mm		Δu
	EXP	FEA	EXP/FEA	EXP	FEA	EXP/FEA	EXP	FEA	EXP/FEA	EXP	FEA	EXP/FEA
CS 80-0.00	256.4	237.8	1.08	1.65	0.97	1.71	470.18	495.64	0.95	3.2	3.17	1.01
CS120-0.00	258.9	238.2	1.09	1.86	0.97	1.91	461.64	489.39	0.94	3.0	3.24	0.93
CS180-0.00	257.1	237.6	1.08	1.80	0.97	1.86	453.72	482.34	0.94	3.2	3.57	0.90
CS 80-0.30	405.8	331.9	1.22	1.20	1.46	0.82	558.65	539.99	1.03	3.2	3.49	0.92
CS120-0.30	406.9	330.6	1.23	1.22	1.46	0.84	532.73	533.39	1.00	3.6	3.69	0.98
CS180-0.30	399.7	329.2	1.21	1.18	1.46	0.81	521.33	526.04	0.99	3.7	3.94	0.94
CS 80-0.60	386.5	320.2	1.21	1.28	1.46	0.88	521.67	510.83	1.02	3.7	3.37	1.10
CS120-0.60	386.0	318.9	1.21	1.34	1.46	0.92	498.73	504.37	0.99	3.7	3.46	1.07
CS180-0.60	382.5	317.3	1.21	1.33	1.46	0.91	488.50	497.25	0.98	3.2	3.51	0.91
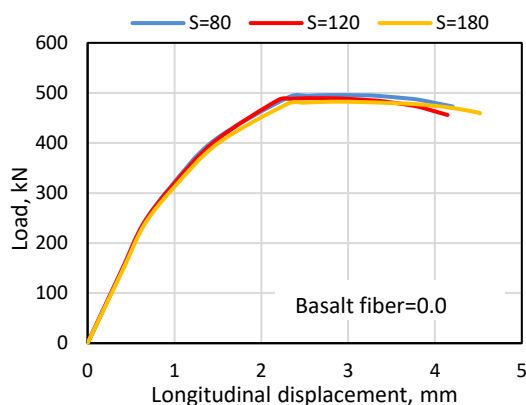
Figure 12. Load-longitudinal displacement relation of the column without basalt fiber
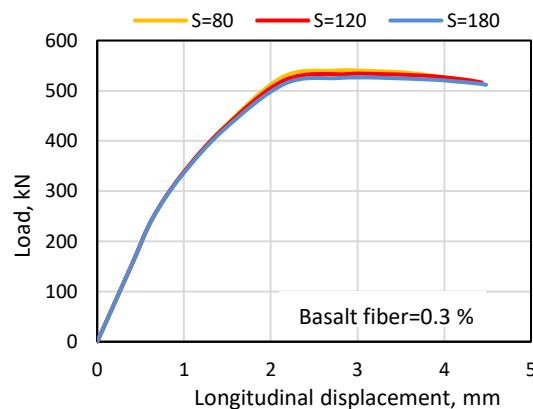
Figure 13. Load-longitudinal displacement relation of the column with 0.3% basalt fiber
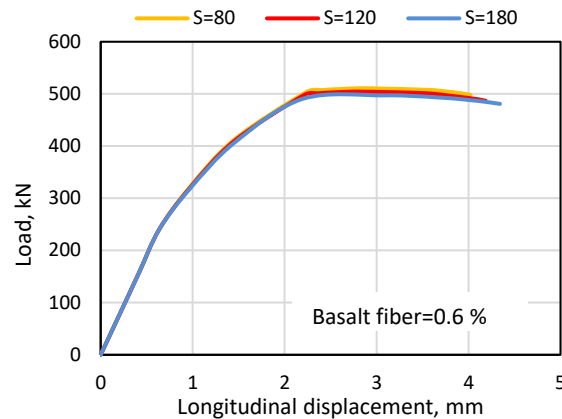
Figure 14. Load-longitudinal displacement relationship of the column with 0.6% basalt fiber
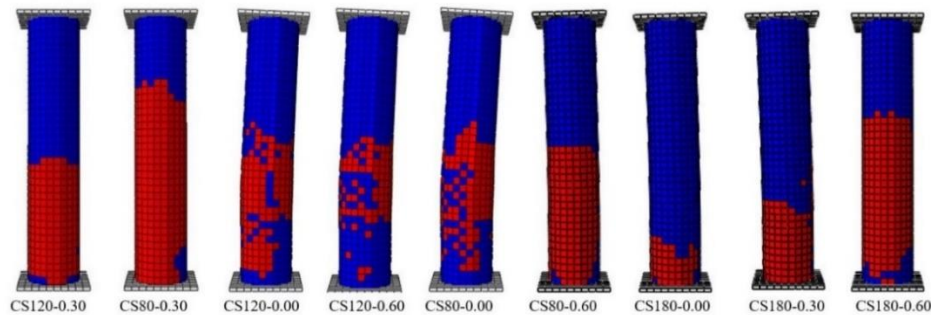
Figure 15. A crack pattern of the columns

The longitudinal bars and transverse ties did not reach yielding at the ultimate loads for all columns. That referred to the failure was occurred due to concrete crushing. The longitudinal bars sustained (70-88) % of yield stress at the maximum loads. The longitudinal bars of columns CS80-0.3, CS120-0.3, and CS180-0.3 endure the highest stress. On the other hand, the middle tie bore the higher stress at the ultimate load, which indicated a column tendency to buckle.

4. 6. Parametric Study   A numerical study was performed to demonstrate the effect of reinforcement ratio on the column loading capacity by changing the longitudinal bar diameter. Three bar diameters were adopted: 6mm, 8mm, and 10mm, to award 0.64 %, 1.13 %, and 1.78 % reinforcement ratios (ρ), respectively. The yield stress of the bar was not changed, and all other parameters remained the same. The results of FEA are illustrated in Table 7.

TABLE 7. Loading capacity and Longitudinal displacement upon changing reinforcement ratio

Column ID	db=6 mm, ρ=0.64 %		db=8 mm, ρ=1.13 %		db=10 mm, ρ=1.78 %	
	Pu, kN	**Δu, mm**	**Pu, kN**	**Δu, mm**	**Pu, kN**	**Δu, mm**
CS 80-0.00	458.54	3.24	495.64	3.17	510.57	1.95
CS120-0.00	451.36	3.47	489.39	3.24	500.00	1.99
CS180-0.00	444.83	3.58	482.34	3.57	495.24	2.10
CS 80-0.30	504.71	3.49	539.99	3.49	575.30	2.30
CS120-0.30	496.10	3.68	533.39	3.69	564.60	2.34
CS180-0.30	489.20	3.94	526.04	3.94	554.75	2.36
CS 80-0.60	473.98	3.44	510.83	3.37	530.96	2.08
CS120-0.60	465.73	3.49	504.37	3.46	521.03	2.10
CS180-0.60	460.90	3.53	497.25	3.51	514.00	2.20

According to the results of numerical analysis, increasing the reinforcement ratio raises the loading capacity of the column for all basalt fiber contents. The 0.3 % basalt fiber content causes the highest increment in column loading capacity.

At 0.0 % basalt fiber ratio, raising the reinforcement ratio from 0.64 % to 1.13 % and 1.78 % increases the maximum loading by 8 % and 11 %, respectively. While at 0.3 % and 0.6 % basalt fiber content, increasing the reinforcement ratio from 0.64 % to 1.13 % and 1.78 % raises the ultimate loading of the column by (7.5-8) % and (12-14) %, respectively.

On the other hand, for the same tie-spacing, increasing the reinforcement ratio raises the load capacity of columns where the 0.3 % basalt fiber content awarded the highest increment in all cases, as shown in Figures 16, 17, and 18.

Despite increasing reinforcement ratio in the column, the failure remained due to concrete crushing before the rebars reached yielding.

When the tie-spacing decreases and the reinforcement ratio increases, the loading capacity of the column further increases. It is well known that the stresses in columns are borne by concrete and steel rebar. Therefore, increasing the area of rebars with its relatively high yield stress increases the stresses sustained by the column section. Also, decreasing tie spacing increases external confinement on a concrete core to raise the loading capacity of the column.

The longitudinal displacement slightly increased upon increasing tie spacing. However, it decreased with increasing the reinforcement ratio. Furthermore, for a 1.78 % reinforcement ratio, the lowest longitudinal displacement was recorded numerically. Also, no significant changes occurred in longitudinal displacement at a higher reinforcement ratio.

Axial deformation is proportional to the axial load and column length and inversely proportional to the sectional area and elastic modulus. Since column length, cross-sectional area, and elastic modulus are constant, the change in rebar area is considered the prime determinant for axial deformation besides the load. Therefore, when the reinforcement area increases, the longitudinal displacement decreases.
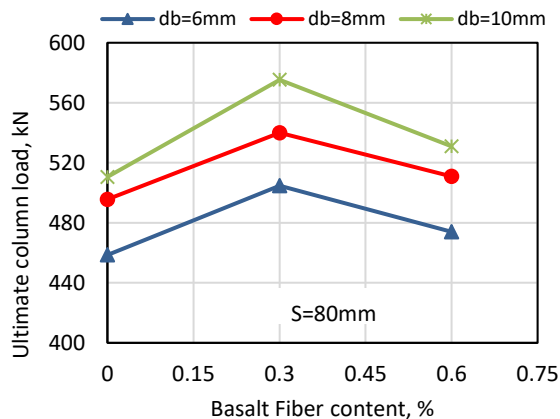
Figure 16. The effect of bar diameter on loading capacity when tie spacing is 80 mm
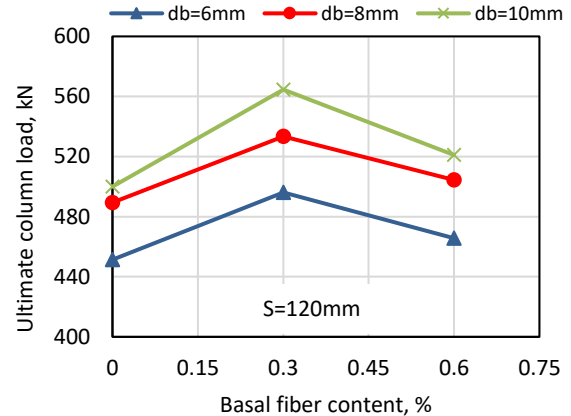
Figure 17. The effect of bar diameter on loading capacity when tie spacing is 120 mm
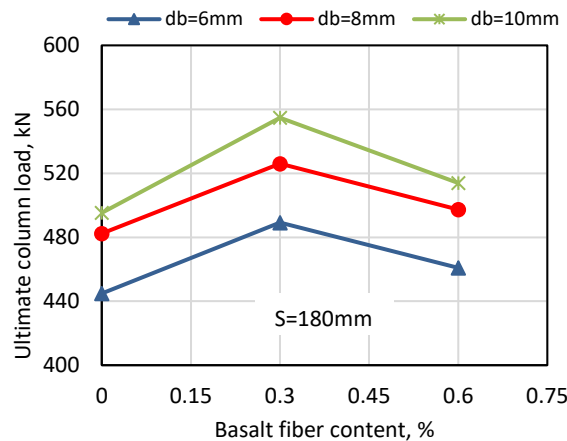
Figure 18. The effect of bar diameter on loading capacity when tie spacing is 180 mm

5. CONCLUSIONS

This research presents experimental and numerical investigations on the combined effect of basalt fibers and tie spacing on the behavior of short columns. Loading capacity at cracking and ultimate state with corresponding longitudinal displacements and the crack pattern is experimentally discovered. Then a numerical analysis is performed via Abaqus software to clarify the effect of reinforcement ratio on the loads and displacements. The following conclusion can derive:

Short concrete columns without fibers sustained more than 50 % of the failure load before cracking. Addition of basalt fiber delays cracking and increases the cracking load to about 75 % of the failure load. 0.3 % of basalt fibers increases the compressive strength and short column's load at cracking and ultimate state more than 0.6 %. The impact of basalt fibers on cracking load is more pronounced than on maximum load.

Basalt fiber reduces the longitudinal displacement at the cracking state. However, it has no evident effect on the displacement at the ultimate state.

The smaller the tie spacing, the slightly higher the ultimate load of the short column. Adding basalt fibers reduces the longitudinal displacement at cracking. The longitudinal displacement increases upon increasing tie spacing.

The numerical analysis awarded results close to the experimental ones at ultimate loading. Also, the empirical and numerical failure was the same for all columns by crushing concrete, while the longitudinal and tie rebars did not yield at maximum load.

Increasing the reinforcement ratio with keeping tie-spacing constant increases the loading capacity of columns. The increment in ultimate loads increases with decreasing tie spacing.

6. REFERENCES

1. Rajasekaran, A., Raghunath, P. and Suguna, K., "Effect of confinement on the axial performance of fibre reinforced polymer wrapped rc column", *American Journal of Engineering and Applied Sciences*, Vol. 1, No. 2, (2008), 110-117.

2. Al-Kharabsheh, B.N., Arbili, M.M., Majdi, A., Alogla, S.M., Hakamy, A., Ahmad, J. and Deifalla, A.F., "Basalt fibers reinforced concrete: Strength and failure modes", *Materials*, Vol. 15, No. 20, (2022), 7350. https://doi.org/10.3390/ma15207350

3. Aljazaeri, Z. and Al-Jaberi, Z., "Numerical study on flexural behavior of concrete beams strengthened with fiber reinforced cementitious matrix considering different concrete compressive strength and steel reinforcement ratio", *International Journal of Engineering, Transactions A: Basics*, Vol. 34, No. 4, (2021), 793-802. https://doi.org/10.5829/ije.2021.34.04a.05

4. Solhmirzaei, R. and Kodur, V., "Modeling the response of ultra high performance fiber reinforced concrete beams", *Procedia Engineering*, Vol. 210, (2017), 211-219. https://doi.org/10.1016/j.proeng.2017.11.068

5. Systèmes, D., *Getting started with abaqus: Interactive edition*. 2014, Version.

6. Ayub, T., Shafiq, N. and Nuruddin, M.F., "Mechanical properties of high-performance concrete reinforced with basalt fibers", *Procedia Engineering*, Vol. 77, (2014), 131-139. https://doi.org/10.1016/j.proeng.2014.07.029

7. Committee, A., "Building code requirements for structural concrete (aci 318-08) and commentary, American Concrete Institute. (2008).

8. Qin, J., Qian, J., Li, Z., You, C., Dai, X., Yue, Y. and Fan, Y., "Mechanical properties of basalt fiber reinforced magnesium phosphate cement composites", *Construction and Building Materials*, Vol. 188, (2018), 946-955. https://doi.org/10.1016/j.conbuildmat.2018.08.044

9. Kirthika, S. and Singh, S., "Experimental investigations on basalt fibre-reinforced concrete", *Journal of The Institution of Engineers (India): Series A*, Vol. 99, (2018), 661-670. https://doi.org/10.1007/s40030-018-0325-4

10. Ramesh, B. and Eswari, S., "Mechanical behaviour of basalt fibre reinforced concrete: An experimental study", *Materials Today: Proceedings*, Vol. 43, (2021), 2317-2322. https://doi.org/10.1016/j.matpr.2021.01.071

11. Jia, M., Xie, W., Yu, K. and Qian, K., "A comparative study of the mechanical properties of basalt fiber and basalt grille reinforced concrete composites and theoretical prediction", *Journal of Natural Fibers*, Vol. 19, No. 13, (2022), 5862-5879. https://doi.org/10.1080/15440478.2021.1902451

12. Sun, X., Gao, Z., Cao, P. and Zhou, C., "Mechanical properties tests and multiscale numerical simulations for basalt fiber reinforced concrete", *Construction and Building Materials*, Vol. 202, (2019), 58-72. https://doi.org/10.1016/j.conbuildmat.2019.01.018

13. Li, Z.-X., Li, C.-H., Shi, Y.-D. and Zhou, X.-J., "Experimental investigation on mechanical properties of hybrid fibre reinforced concrete", *Construction and Building Materials*, Vol. 157, No., (2017), 930-942. https://doi.org/10.1002/suco.201500216

14. Dilbas, H. and Çakır, Ö., "Influence of basalt fiber on physical and mechanical properties of treated recycled aggregate concrete", *Construction and Building Materials*, Vol. 254, (2020), 119216. https://doi.org/10.1016/j.conbuildmat.2020.119216

15. Ghasem Ghanbari, P., Momeni, M., Mousivand, M. and Bayat, M., "Unconfined compressive strength characteristics of treated peat soil with cement and basalt fibre", *International Journal of Engineering, Transactions B: Applications*, Vol. 35, No. 5, (2022), 1089-1095. https://doi.org/10.5829/ije.2022.35.05b.24

16. High, C., Seliem, H.M., El-Safty, A. and Rizkalla, S.H., "Use of basalt fibers for concrete structures", *Construction and Building Materials*, Vol. 96, (2015), 37-46. https://doi.org/10.1016/j.conbuildmat.2015.07.138

17. Krassowska, J. and Kosior-Kazberuk, M., "Failure mode of basalt fibre reinforced concrete beams", in IOP Conference Series: Materials Science and Engineering, IOP Publishing. Vol. 471, (2019), 052043.

18. Hirde, S. and Shelar, S., "Effect of basalt fiber on strength of cement concrete", *International Journal of Current Engineering and Technology*, Vol. 7, No. 2, (2017), 600-602.

19. Iyer, P., Kenno, S.Y. and Das, S., "Mechanical properties of fiber-reinforced concrete made with basalt filament fibers", *Journal of Materials in Civil Engineering*, Vol. 27, No. 11, (2015), 04015015. https://doi.org/10.1061/(asce)mt.1943-5533.0001272

20. Hoshitha, T.S.S., Rao, T.C. and Rao, T.G., "Effect of lateral confinement on short columns under uni-axial compression", in AIP Conference Proceedings, AIP Publishing LLC. Vol. 2297, (2020), 020015.

21. Jabbar, A.M., Hamood, M.J. and Mohammed, D.H., "Mitigation of the factors affecting the autogenous shrinkage of ultra-high performance concrete", *Engineering and Technology Journal*,

Vol. 39, No. 12, (2021), 1860-1868. https://doi.org/10.30684/etj.v39i12.2155

22. Jabbar, A.M., Hamood, M.J. and Mohammed, D.H., "The effect of using basalt fibers compared to steel fibers on the shear behavior of ultra-high performance concrete t-beam", *Case Studies in Construction Materials*, Vol. 15, (2021), e00702. https://doi.org/10.1016/j.cscm.2021.e00702

23. Jabbar, A.M., Mohammed, D.H. and Hamood, M.J., "Using fibers instead of stirrups for shear in ultra-high performance concrete t-beams", *Australian Journal of Structural Engineering*, Vol. 24, No. 1, (2023), 36-49. https://doi.org/10.1080/13287982.2022.2088654

24. En, B., "1-1. Eurocode 2: Design of concrete structures–part 1-1: General rules and rules for buildings", *European Committee for Standardization (CEN)*, (2004). https://doi.org/ICS13.220.50;91.010.30;91.080.40

25. Jamshaid, H., "Basalt fiber and its applications", *Journal of Textile Engineering & Fashion Technology*, Vol. 1, No. 6, (2017), 254-255. https://doi.org/10.15406/jteft.2017.01.00041

26. John, V.J. and Dharmar, B., "Influence of basalt fibers on the mechanical behavior of concrete—a review", *Structural Concrete*, Vol. 22, No. 1, (2021), 491-502. https://doi.org/10.1002/suco.201900086

27. Mokhtar, S.F. and Lim, N.H.A.S., "Effects of ties distributions on short column strength siti fatimah mokhtar, dr. Nor hasanah abdul shukor lim".

28. Naji, A., Al-Jelawy, H., Hassoon, A. and Al-Rumaithi, A., "Axial behavior of concrete filled-steel tube columns reinforced with steel fibers", *International Journal of Engineering, Transactions C: Aspects*, Vol. 35, No. 9, (2022), 1682-1689. https://doi.org/10.5829/ije.2022.35.09c.02

29. Nemati Aghamaleki, S., Naghipour, M., Vaseghi Amiri, J. and Nematzadeh, M., "Experimental study on compressive behavior of concrete-filled double-skin circular tubes with active confinement", *International Journal of Engineering, Transactions A: Basics*, Vol. 35, No. 4, (2022), 819-829. https://doi.org/10.5829/ije.2022.35.04a.22

30. International, A., "Astm c150/c150m-15, standard specification for portland cement, american standard for testing and materials, ASTM West Conshohocken, PA, USA. (2015).

31. EN, C., *10002-5, metallic materials–tensile testing–part 5: Method of testing at elevated temperature*. 1992, Brussels.

32. No, I.S., "For aggregates of natural resources used for concrete and construction", Baghdad, Iraq, (1984).

33. Fiore, V., Scalici, T., Di Bella, G. and Valenza, A., "A review on basalt fibre and its composites", *Composites Part B: Engineering*, Vol. 74, (2015), 74-94. https://doi.org/10.1016/j.compositesb.2014.12.034
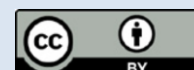
Persian Abstract

چکیده

این مقاله اثر افزودن الیاف بازالت به یک زمینه بتنی و تغییر فاصله اتصال را بر رفتار ستون‌های بتنی کوتاه نشان می‌دهد، زیرا ستون‌های کوتاه قوی‌تر از ستون‌های بلند هستند و عمدتاً در سازه‌ها استفاده می‌شوند. همچنین تأثیر تغییر نسبت آرماتور بر رفتار ستون به صورت عددی کشف شده است. سه بخش حجمی از الیاف بازالت و فاصله سه کراواتی اتخاذ شده است. نتایج نشان می دهد که ستون های بدون الیاف بیش از ۵۰ درصد بار شکست را قبل از ترک خوردگی تحمل می کنند، در حالی که این درصد با افزودن الیاف بازالت به بتن به ۷۵ درصد افزایش می یابد. ۰.۳٪ الیاف بازالت استحکام فشاری، ترک خوردگی و بارهای ستون نهایی را بهتر از ۰.۶٪ افزایش می دهد. به همین ترتیب، تأثیر الیاف بازالت بر بار ترک بیشتر از حداکثر بار ستون است. ستون های فیبر بازالتی در حالت ترک، جابجایی طولی کمتری نسبت به ستون های بدون الیاف نشان می دهند. کوتاه شدن با افزایش فاصله کراواتی افزایش می یابد، در حالی که کاهش فاصله کراواتی به سختی بار نهایی ستون را افزایش می دهد. تجزیه و تحلیل عددی نتایج نزدیک به نتایج تجربی را ارائه می دهد و نشان می دهد که افزایش نسبت آرماتور ظرفیت بار ستون را افزایش می دهد. برای همان فاصله اتصال، افزایش نسبت آرماتور ظرفیت بارگذاری ستون ها را افزایش می دهد و جابجایی طولی به سختی به سختی با افزایش فاصله افزایش می یابد. به طور کلی، الیاف بازالت، ترک خوردگی را به تاخیر می اندازد و ظرفیت بارگذاری ستون را بهبود می بخشد.

International Journal of Engineering

Journal Homepage: www.ije.ir

Efficiency Optimization Thermal Analysis and Power Output of a Modified Incinerator Plant Using Organic Rankine Cycle

P. Vanaei[a], B. Jalili[*b], M. Hosseinzadeh[a], P. Jalili[b]

[a] Department of Mechanical Engineering, Ayatollah Amoli branch, Islamic Azad University, Amol, Iran
[b] Department of Mechanical Engineering, North Tehran Branch, Islamic Azad University, Tehran, Iran

P A P E R   I N F O

A B S T R A C T

A compound of a modified incinerator system with an organic Rankine cycle (ORC) was analyzed and optimized regarding exergy and energy. This paper provides an overview of system performance considering thermal aspects in a conceptual design to understand the technical effects of the system on future energy systems; it also provides a way to increase efficiency up to an amount that did not exist before in practice by using optimization. The conceptual design uses multiple flue gas regeneration units, and R124 is used as ORC working fluid. The power plant is modeled and optimized for its thermal performance. An innovative cycle is designed to reuse the wasted heat, which makes the evaporator more efficient and increases the overall exergy efficiency of the power plant. Then, the exergy destructions and systems efficiency are observed. The results indicate that 3.19 MW output power could be generated from municipal wastes with capacity of 400 tons/day. The highest destruction of exergy for the incinerator unit and boiler were approximately 8 kW and 6.4 kW, respectively. For the primary cycle the power output capacity was almost 2.8 MW. Also, this research increased their exergy efficiency by using heating flow streams*.* The ORC cycle could not produce high power but generally improve the exergy and energy efficiency. The proposed combined cycle with flue gas reheating units and optimization increases the system output power from 3.02 to 3.19 MW. Furthermore, energy and exergy efficiency increased by 10% and 9%, respectively.

doi: 10.5829/ije.2023.36.07a.11

NOMENCLATURE

Abbreviations		Greek letters	
Cond	Condenser unit	η	Energy efficiency
ORC	Organic Rankine cycle	ε	exergy efficiency (-)
MSW	municipal solid waste	$\dot{W}_{net}$	net power output (MW)
LHV	lower heating value (kJ/kg)	**Subscripts**	
CHP	Combined Heat and Power	*ch*	chemical
e	specific physical exergy (kJ/kg)	*D*	destruction
$\dot{E}$	the flow rate of exergy (kW)	*e*	outlet
h	specific enthalpy (J/kg)	*G*	generator
$\dot{m}$	the flow rate of mass (kg/s)	*i*	inlet
$\dot{Q}$	rate of heat transfer (kW)	*p*	product exergy (kW)
R	gas constant (kJ/kg K)	*s*	supplied exergy (kW)
s	entropy (kJ/kg K)	*t*	overall
T	temperature (K)	*j*	Outlet exergy (kW)
$\dot{W}$	power (kW)		

*Corresponding Author Email: b.jalili@iau-tnb.ac.ir (B. Jalili)

1. INTRODUCTION

Over the years, humans have been disturbed by the steady increase in municipal waste generation. Municipal waste in cities and crowded areas is a significant environmental problem. Although burial or burning of these wastes is used. By using these wastes could create economic interest and decrease environmental pollution [1]. Hence, it seems that a win-win situation must be achieved to solve both problems to some extent, which many countries in the world have done by building waste incineration plants [2]. Today, an incinerator is any process in which waste burns to become harmless substances or produce energy. Many of these materials used in the combustion process and are incinerated cost much less than fossil fuels. Urban society inevitably has garbage that is increasing daily. Waste incineration is used for electricity or heat production and reduces its volume and pollution by more than 80%, which is very suitable for waste storage and disposal [3].

Electricity generation from the incineration of solid municipal waste is a proper use of such wastes; which is preservation of fossil fuel resources, leads to less pollution than the fossil fuel. In simulation software, Chen et al. [4] simulated the incineration and gasification unit of municipal waste in two reactors. The main goal is to achieve a higher heat conversion percentage and calorific value. Their results show that gas entry from the combustion chamber to the gasification chamber increases the percentage of heat conversion. Pan et al. [5] simulated a municipal waste incinerator and Organic Rankine Cycle system. They have also, reached the optimal values of the cascade supercritical CO_2 cycle. Shahnazari et al. [6] investigated the most helpful method for the thermochemical processing of MSW. Siddiqi et al. [7] estimated electricity generation via combustion of MSW along with Rankin cycle for the waste generated in Pakistan. There are various parameters for reviewing and optimizing the generated electricity from municipal waste. One of the most important parameters can be the amount of electricity generated, which can be significantly increase by changing some conditions. For example, Sajid Khan et al. [8] increased the amount of electricity generated per waste unit by integrating solar and incinerator systems. Alrobaian [9] presented an exergy, energy, and economic (3E) analysis for improving the efficiency of the incinerator plant by recycling waste heat for the feed water preheating process. Kythavone and Chaiyat [10] investigate the evaluation of an ORC and MSW incinerating for pestiferous medical waste. Escamilla-Garcia et al. [11] conducted a scientific and economic analysis of MSW incineration output power in Mexico. Mohtaram et al. [12] studied an exergy-energy efficiency analysis of an incinerator cycle coupled with a different ORC. They have reported that turbine efficiency is also raised with

decreased working fluid temperature and rising inlet pressure. Sorgulu et al. [13] experimentally designed a newly developed integrated ORC plant and reached 2.3 MW electric power. Kavatia and Prajati [14] reviewed biomass-to-energy plants using vegetable waste with an ORC. Nami and Arabkoohsar [15] designed a waste-driven combined heat and power (CHP) plant via parallel Rankine and Organic Rankine cycles and improved the power output by thermodynamic analysis. Ascanio et al. [16] presented a thermal-economic analysis of the electricity generation potential by combining the Rankine cycle and MSW incineration. The main drawback of waste incineration plants is their low efficiency of production power, which requires optimization and inventing better methods to get maximum power from waste. A steam power plant that uses an organic fluid instead of water, such as hexane, etc., is called ORC [17]. The most crucial benefit of the ORC is that it requires less heat to vaporize the working fluid [18]. The most important ability of ORC technology is utilizing all waste to generate electric power. A full review of this ORC application can be found in literature [19]. There is exhaustive literature about the combined cycle and ORC technologies, different working fluids, and benefits [20]. Therefore, more information about this technology is not explained here. In general, the design of an innovative cycle, especially about ORC, using energy and exergy analysis can help increase the efficiency of energy production and optimize as much as possible, which is the main requirement of the industry.

This study analyses an incinerator CHP plant by two Rankine and ORC parallel cycles. A general exergy and energy analysis of the incinerator plant is accomplished. The innovation of this study is the concept design of cycles and multiple regeneration streams of heat for the ORC and main cycle. Also, this proposed combined cycle is optimized by a genetic algorithm, which tries to improve the system's electricity generation by optimizing output power. Waste incinerators are one of the best ways to reuse lost resources, so their strengthening plays a key role in improving the quality of urban life. Figure 1 presents a general flowchart of the steps of this research.

1. 1. Incinerator Power Plant and the Concept of Combined Power Plant   This part gives general information about incinerator power plants. Then, the regular Rankine cycle with a schematic diagram is explained, and the combined incinerator plant is introduced and explained. As shown in Figure 2, in the first step, municipal waste with an air intake stream enters the gasifier unit. The slurry ash goes down to the ash chamber and produces syngas, which penetrates the combustion chamber with the incoming airflow. The combustion product gas with water comes from pump-fed into steam generator boiler and, superheats steam
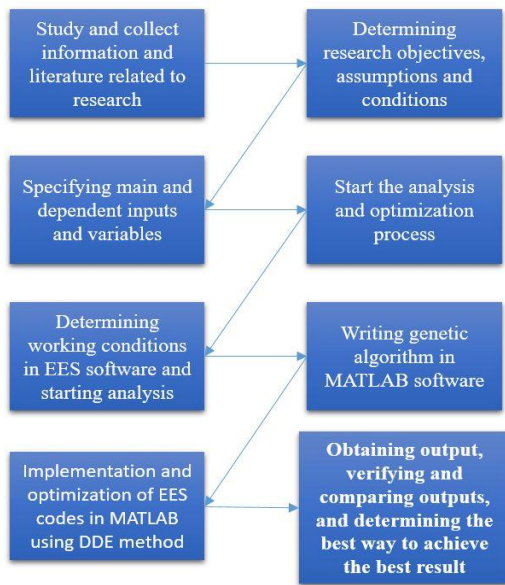
Figure 1. Steps of the research

produce, and flue gas is released from the exhaust to the air, thus superheat steam sent to the steam turbine and output power for turning on the generator is generated. Then two-phase (steam-water) fluid comes out from the steam turbine, goes to the condensing unit (that feeds with cool water from the cooling unit), and goes back to the pump.

Figure 3 shows a schematic diagram of the modified power plant. MSW and primary air initially enter the gas generator (gasifier), where syngas is produced. Complete oxidation occurs in the combustion chamber by mixing produced syngas and the air intake stream; then, syngas with high enthalpy is created. In the steam cycle, water with combustion products gas goes into the boiler to form superheat steam and then goes to the steam turbine. During the main time, the boiler's flue gas stream (8) goes into ORC. After producing power by the turbine and superheating steam, 2 phase liquid exits the turbine. Then a warm liquid stream (6a) from the steam generator turbine goes straight to the feed water tank. Water and air are used as cooling fluids (6) to cool the turbine outlet flow in the condenser. Moreover, a stream of flue released gas (11b) from the condenser and sent it to the recuperator. Two parallel cycles with similar conditions have formed this power plant, producing 3.19 MW of total output power. The ORC is the last section of the incinerator to reuse the heat output of the cycle flue gas. The waste heat from the flue gas is transferred to the organic fluid in the evaporator, and the superheated fluid goes to the turbine. After that, hot ORC liquid goes into the recuperator, gives its heat to it, and then goes to the ORC condensing unit. One flue gas stream from the recuperator enters the evaporator (11) to increase cycle thermal efficiency. At last, the waste flue gas stream exited from the exhaust. R124, as an organic working fluid, is hired in the ORC system.
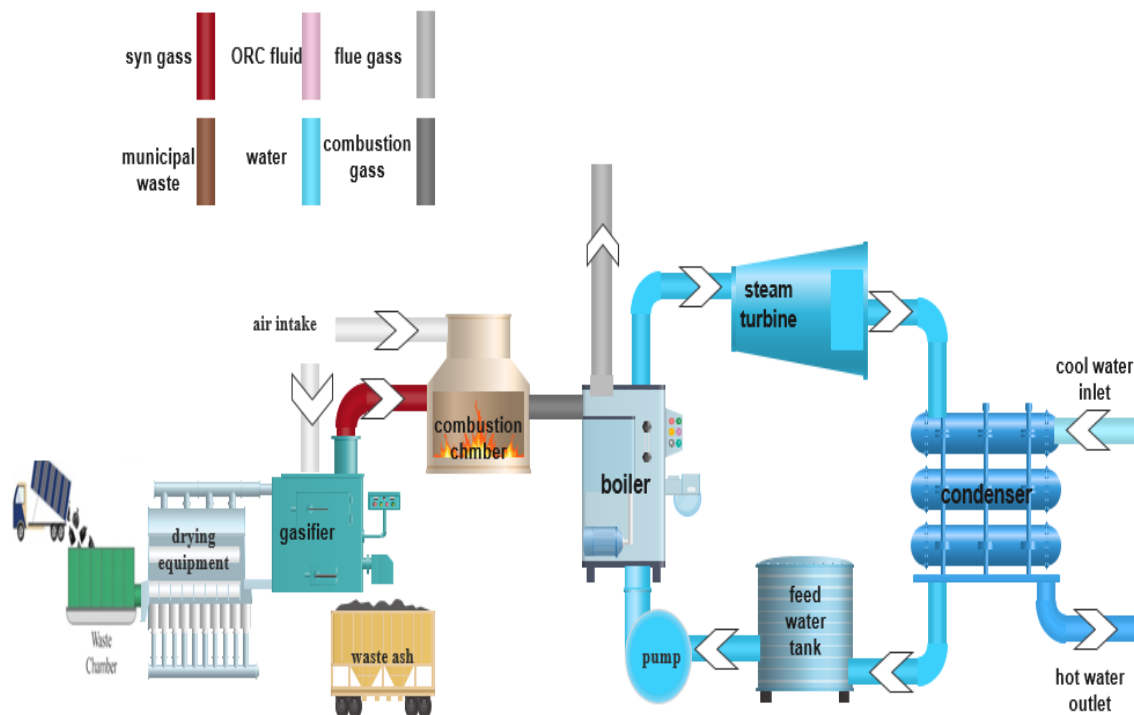
Figure 2. Schematic of the incinerator power plant [21]

Figure 3. Schematic of the concept design of incinerator CHP-ORC plant

The system is assumed to work in Steady-state conditions for the proposed cycle, and air contents are set as 79% N_2 and 21% O_2. The pressure drop in the boiler, evaporator, and condensers is 5%. Moreover, heat transfer from the combustion chamber is equal 2%. Moreover, air and flue gases are ideal [22, 23]. All operating parameters of both cycles are inserted in Table 1.

TABLE 1. Technical properties of the combined cycle incinerator system

Item	Info./Value	Reference
Orc Working Fluid	R124	
Orc Turbine Inlet Condition/Pressure (State/MPa/°C)	Sat. Vap. /Superheat P=0.8–1.2/P=1.3-2.3 T=T Sat. /T=Tsat+5	[24]
Evaporator Pinch Point (°C)	5	
Condenser Pinch Point (°C)	3	
Msw Compositions	5.91% Ash 47.18% Carbon	[25]
	6.25% Hydrogen	
	39.57% Oxygen	
	0.91% Nitrogen	
	0.18% Sulphur	
LHV of The Waste (kJ/kg)	12,500	[25]
The Volume Percentage of Air During the Incineration Process	80%	[26]
Syngas Temperature after Combustion (°C)	1100	[27]
Temp./Pressure of the Fluid after Turbine (°C/MPa)	350/2.9	
Temp./Pressure of the Fluid After Condenser (°C/MPa)	90/0.07(Condensed)	
Temp./Pressure of the Fluid Before Boiler (°C/MPa)	290/10.1	[28]
Orc Turbine Inlet Pressure (MPa)	2-4	[29]
Orc Condenser Temperature (°C)	10	[29]
The Efficiency of Orc Turbine (%)	0.9	[29]
The Efficiency of the Pump (%)	0.85	[29]

2. ANALYSIS

This part explains the energy and exergy models of the modified incinerator power plant.

2. 1. Energy Analysis   Each part is assumed to be a control volume for analyzing the system, and an energy conservation equation is created. By following the first rule of thermodynamics, works the level of steam turbine and ORC turbine ($\dot{W}$ turbine, $\dot{W}$ORC turbine), the electric power consumed by pumps ($\dot{W}$ pump, $\dot{W}$ORC pump), the pure power of each line of the system ($\dot{W}$ cycle, $\dot{W}$ORC cycle) and total power of the system ($\dot{W}$ net) are presented as follows [30-33]:

$$\dot{W}_{turbine} = \dot{m}(h_6 - h_5) \tag{1}$$

$$\dot{W}_{ORCturbine} = \dot{m}_{ORC}(h_{10} - h_9) \tag{2}$$

$$\dot{W}_{pump} = \dot{m}(h_{4a} - h_4) \tag{3}$$

$$\dot{W}_{ORC\ pump} = \dot{m}_{ORC}(h_{13c} - h_{13}) \tag{4}$$

$$\dot{W}_{cycle} = (\dot{W}_{turbine} - \dot{W}_{pump}) \tag{5}$$

$$\dot{W}_{ORC\ cycle} = (\dot{W}_{ORC\ turbine} - \dot{W}_{ORC\ pump}) \tag{6}$$

$$\dot{W}_{net} = (\dot{W}_{cycle} + \dot{W}_{ORC\ cycle}) \tag{7}$$

The efficiency of the turbines and pumps are presented as follows:

$$\eta_{turbine} = \frac{(h_5 - h_6)}{(h_5 - h_{6s})} \tag{8}$$

$$\eta_{pump} = \frac{(h_{4as} - h_4)}{(h_{4a} - h_4)} \tag{9}$$

$$\eta_{ORC\ turbine} = \frac{(h_{10} - h_9)}{(h_{10} - h_{9s})} \tag{10}$$

$$\eta_{ORC\ pump} = \frac{(h_{13cs} - h_{13})}{(h_{913c} - h_{13})} \tag{11}$$

The rate of heat transfer by the combustion chamber and condensing units is presented as follows:

$$\dot{Q}_{heating} = 12500 kw \quad (Minimum)\ [25] \tag{12}$$

$$\dot{Q}_{condenser} = \dot{m}(h_6 - h_7) \tag{13}$$

$$\dot{Q}_{ORCcondenser} = \dot{m}_{ORC}(h_{13} - h_{12}) \tag{14}$$

At last energy efficiency of the system is presented as follows:

$$\eta_{total} = \frac{\dot{W}_{net}}{\dot{Q}_{heating}} \tag{15}$$

Applied equations derived for all sections of the concept incinerator power plant are inserted in Table 2.

TABLE 2. Energy equations on the parts of the modified incinerator power plant

Parts	Equations	Numbers
Incinerator	$\dot{m}_3h_3 + \dot{m}_{3b}h_{3b} = \dot{m}_{3c}h_{3c}$	(16)
gasifier	$\dot{m}_1 LHV + \dot{m}_{1a}h_{1a} = \dot{m}_3h_3 + \dot{m}_2h_2$	(17)
Boiler	$\dot{m}_{3c}h_{3c} + \dot{m}_{4a}h_{4a} = \dot{m}_8h_8 + \dot{m}_5h_5$	(18)
Turbine	$\dot{W}_{Turbine} = \dot{m}_5(h_5 - h_6 - h_{6a})$	(19)
Pump	$\dot{W}_{Pump} = \dot{m}_8(h_{4a} - h_4)$	(20)
Evaporator	$\dot{m}_8(h_8 + h_{11} - h_{14}) = \dot{m}_9(h_9 - h_{13c})$	(21)
ORC turbine	$\dot{W}_{ORC\ Turbine} = \dot{m}_9(h_{10} - h_9)$	(22)
ORC pump	$\dot{W}_{ORC\ Pump} = \dot{m}(h_{13c} - h_{13})$	(23)
Condenser	$\dot{m}_6 = (h_6 - h_7) = \dot{m}_{7a}(h_{7b} - h_{7a})$	(24)
ORC condenser	$\dot{m}_{12} = (h_{12} - h_{13}) = \dot{m}_{13a}(h_{13b} - h_{13a})$	(25)
Recuperator	$\dot{m}_{10} = (h_{10} - h_{12}) = \dot{m}_{11a}(h_{11b} + h_{11a} - h_{11})$	(26)

2. 2. Exergy Analysis   This paper considered only physical and chemical exergies and neglected potential and kinetic exergies. The equation of exergy balance for a converting energy system is as follows [30, 31]:

$$\sum_{in} \dot{E}_i = \sum_{out} \dot{E}_j + \dot{E}_D \tag{27}$$

In here, $\sum_{out} \dot{E}_j$ and $\sum_{in} \dot{E}_i$ are, respectively, outlet and inlet exergy, while $\dot{E}_D$ is destruction of exergy [32]. A proposed correlation by Song et al. [33] is used for effectively modeling an incinerator power plant for calculating the chemical exergy of waste as a fuel e-MSW (kJ/kg). The chemical exergy of inlet waste $\dot{E}$ MSW (kW) is explained as follows:

$$\dot{E_{MSW}} = \dot{m}_{MSW} e_{msw} \tag{28}$$

With:

$$e_{MSW} = 1812.5 + 31.8\mathbf{A} + 587.354\mathbf{H} + 295.606\mathbf{C} + 17.735\mathbf{N} + 95.615\mathbf{S} + 17.506\mathbf{O} \tag{29}$$

Here, A, H, C, N, S and, O are a mass combination of ash, hydrogen, carbon, nitrogen, sulfur, and oxygen, respectively.

Song et al. [34] also presented special exergy for ash e ash (kJ/kg). So ash exergy $\dot{E}$ ash (kW) is as follows:

$$\dot{E}_{ash} = \dot{m}_{ash} e_{ash} \tag{30}$$

$$e_{ash} = 0.01057T + 0.0004056T^2 - 54.44 \tag{31}$$

That T (k) is the ash temperature.

An exergy modeling of the concept incinerator system parts is presented in Table 3 [35].

2. 3. Optimization   This part uses multi-objective optimization to optimize the hybrid power plant. So, objective functions must be defined for this purpose. The

TABLE 3. Exergy equations for each part

Parts	$\dot{E}_s$	$\dot{E}_p$	Number
Incinerator	$\dot{E}_3+\dot{E}_{3b}$	$\dot{E}_{3c}$	(32)
gasifier	$\dot{E}_1+\dot{E}_{1a}$	$\dot{E}_3-\dot{E}_2$	(33)
Boiler	$\dot{E}_{3c}$	$\dot{E}_8+\dot{E}_5$	(34)
Turbine	$\dot{E}_5-\dot{E}_6-\dot{E}_{6a}$	$\dot{W}_{Turbine}$	(35)
Pump	$\dot{W}_{Pump}$	$\dot{E}_{4a}-\dot{E}_4$	(36)
Evaporator	$\dot{E}_8+\dot{E}_{11}-\dot{E}_{14}$	$\dot{E}_9-\dot{E}_{13c}$	(37)
ORC turbine	$\dot{E}_{17}-\dot{E}_{18}$	$\dot{W}_{ORC\ Turbine}$	(38)
ORC pump	$\dot{W}_{ORC\ Pump}$	$\dot{E}_{13c}-\dot{E}_{13}$	(39)
Condenser	$\dot{E}_6-\dot{E}_7-\dot{E}_{11b}$	$\dot{E}_{7b}-\dot{E}_{7a}$	(40)
ORC condenser	$\dot{E}_{12}-\dot{E}_{13}$	$\dot{E}_{13b}-\dot{E}_{13a}$	(41)
Recuperator	$\dot{E}_{10}-\dot{E}_{12}+\dot{E}_{11a}$	$\dot{E}_{11}-\dot{E}_{11b}$	(42)

objective function is the pure outlet system's power ($\dot{W}_{net}$) and the total power plant's efficiency. The equation of the objective functions is a single equation as follows [36]:

$$\text{Objective Function} = \eta_{ex} = \frac{\sum_n \dot{W}_{net}}{Ex_f} \qquad (43)$$

The method used in multi-objective optimization maximizes the 1st objective function, and naturally, the 2nd objective function is also improved. We must have specific limits, values, and reasons for all optimization cases. The limitations are inserted in Table 4.

Exergy and energy equations for all stages of the combined cycle are written down in Engineering Equations Solver (EES) software. Exergy, Energy balance equations, and applicable auxiliary equations are applied to the system components. The plant analysis is completed, the equations are entered into the Matlab software from ESS by the DDE method, the exergy destruction of the system calculating for generations and optimized by genetic algorithm.

3. RESULTS AND DISCUSSION

The results performed on the incinerator power plant are carried out in this part. Based on the obtained results, changes in exergy and energy efficiency increase the

TABLE 4. Limits of optimization [37, 38]

Limits	Rationale
290°C < Boiler inlet < 330 °C	Material temperature limit
10MPa< P $_{Pump}$ < 13 MPa	Material pressure limit
900 °C< Steam Turbine < 1100 °C	Superheat temperature limitation
50 °C < T $_{Cond}$ < 100 °C	Thermal efficiency limitation

efficiency of the incinerator power plant. Table 5 shows the technical characteristics of the incinerator plant resulting from the energy analysis.

Table 6 reports the results of exergy performance in a waste incineration plant. This information determines the amount of exergy input and output and the exergy destruction of the critical parts when the incinerator operates at full load.

Figure 4 compares the exergy efficiency in different sections of the incinerator combined cycle. Incinerators and boilers have the lowest exergy efficiency in all cases, and a significant part of the exergy input to these parts is destructed.

Figure 5(a) shows the variability of the thermal efficiency of the two different designs of the modified cycle for the 6a stream (as shown in Figure 3). As the figure illustrates, the cycle's thermal efficiency rises with

TABLE 5. Technical parameters values

Parameter (Unit)	Value
The flow rate of fuel (kg/s)	1
The heat transferred into the boiler (MW)	9.25
The flow rate of steam (kg/s)	3.08
Energy efficiency (%)	25.49
Electrical efficiency (%)	20.9

TABLE 6. The results of exergy analysis were performed at full load before optimization

Parameters (Unit)	Values
Steam generator Boiler inlet/outlet/destructed exergy (MW)	14.57/8.1/6.47
Steam Turbine inlet/outlet/destructed exergy (MW)	7.39/5.99/1.4
Condenser inlet/outlet/destructed exergy (MW)	4.17/2.2/1.97
Recuperator inlet/outlet/destructed exergy (MW)	0.561/0.56/0.001
Exergy efficiency (%)	23.69
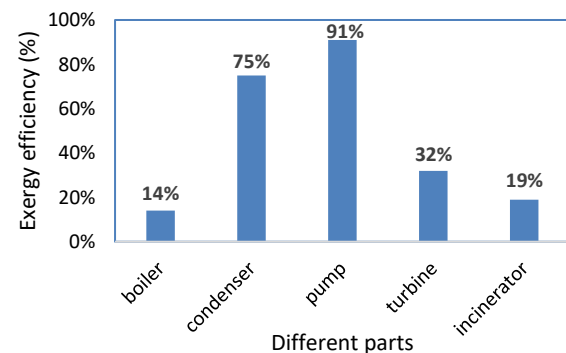
Figure 4. The exergy efficiency in different sections of the plant
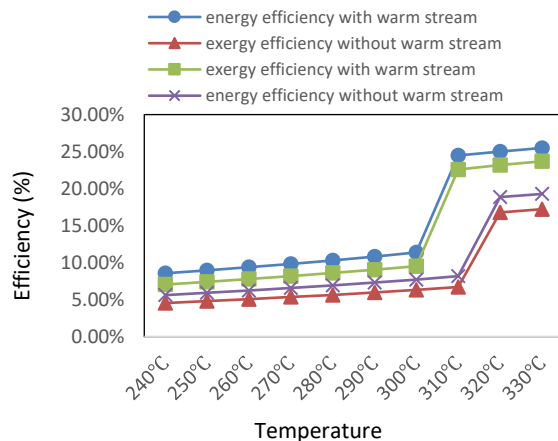
(a)
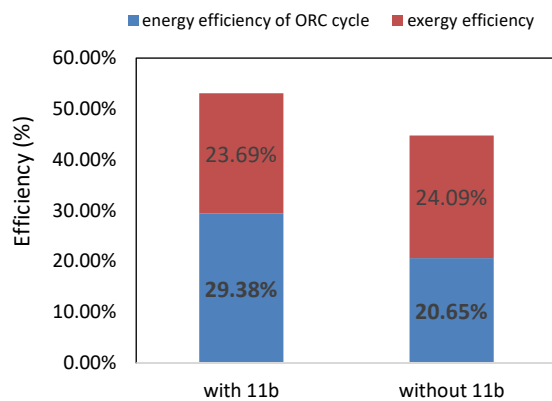
(b)

Figure 5. (a) 6a stream effects on the exergy & energy efficiencyat different inlet temp (b) Effect of 11b stream in combined cycle exergy and energy efficiency

increasing boiler inlet temperature. Furthermore, the modified cycle design increases the thermal efficiency by 15% for the same two conditions. Moreover, Figure 5(b) shows the effects of the 11b stream on the exergy and energy efficiency of the combined cycle. As shown in this figure, energy efficiency increases with the existence of the 11b stream, but exergy efficiency decreases. However, total efficiency increased.

Figure 6(a) illustrates the different values of the superheater temperature change on the cycle exergy efficiency. This figure demonstrates that increasing the temperature in the evaporator (in ORC) decreases the destruction of the exergy. In other words, flows 8 and 11 increase the inlet temperature to the evaporator and the energy and exergy efficiency of the organic Rankine cycle. Figure 6(b) shows that boiler outlet temperature decrease (Not significantly) exergy efficiency and has no effects on the energy efficiency. (The temperature varies from 900 to 1200 degrees Celsius)

Figure 7 illustrates the effects of the Boiler inlet temperature from the pump station on the exergy and

energy efficiency and confirms this trend by increasing the inlet temperature of the boiler from the pump, energy, and exergy efficiency increasing. In other words, 6a flows increase boiler inlet temperature and the energy and exergy efficiency of the main cycle.

3. 1. Optimization Results and Records   The optimization variables (genes) and thermal design results for the optimized incinerator combined cycle are shown in Table 7. Moreover, $\dot{W}_{net}$ is a rise from 3017 to 3186 kW.

Figure 8(a) shows an increase in the energy and exergy efficiency of the plant after and before optimization. Figure 8(b) shows the extracted plot of Matlab software and determines the plant's maximum output power calculated by a genetic algorithm. As it is clear in the figure, the maximum available output power
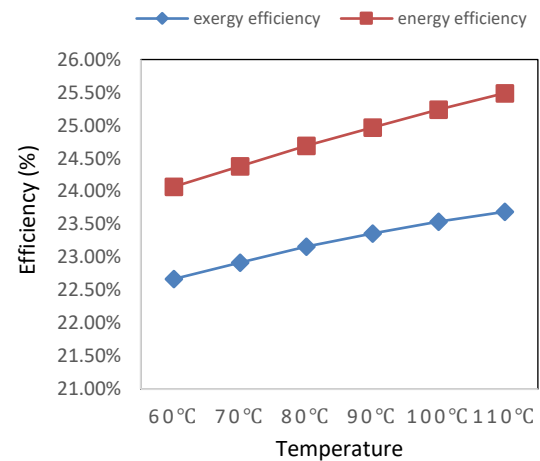
(a)
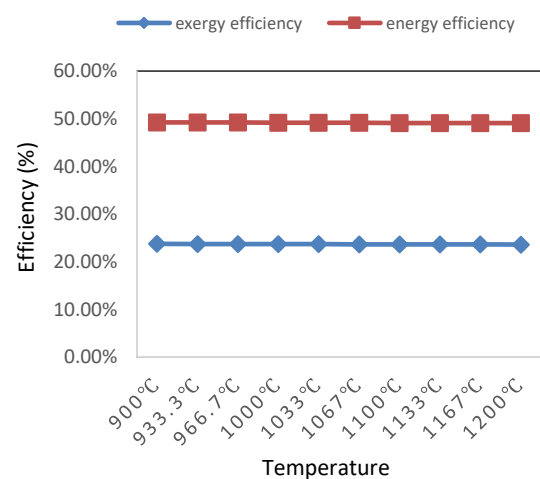
(b)

Figure 6. (a) Energy & Exergy efficiency in various evaporator temp (b) boiler outlet tempreture effects on the exergy and energy efficiency
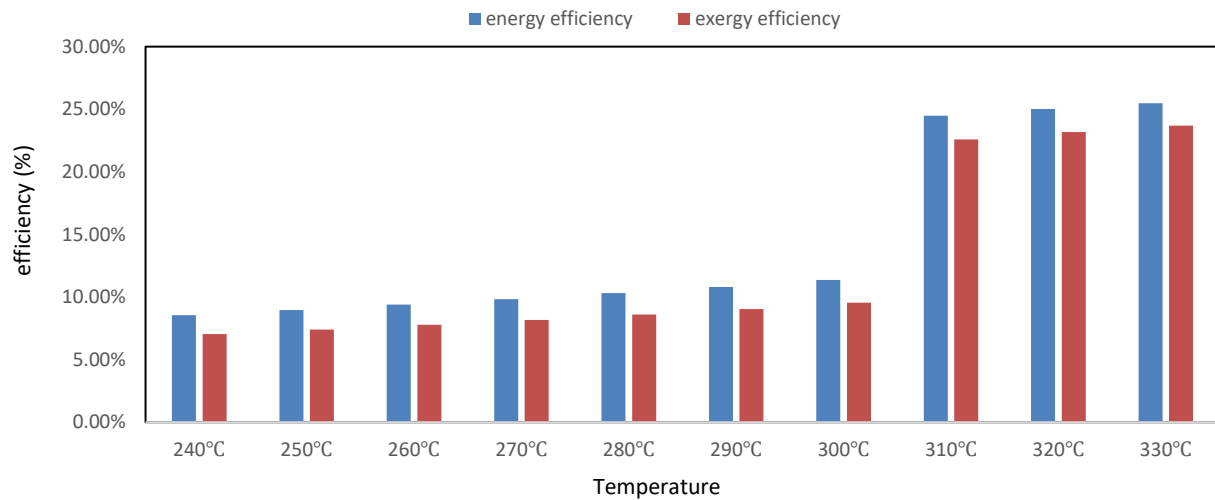
Figure 7. Boiler inlet temperature effect of energy and exergy efficiency

TABLE 7. Optimal design parameters of the CHP plant by genetic algorithm

Decision variable	Value
Boiler inlet Temperature	330 ℃
Boiler inlet Pressure	10112 kPa
condenser inlet Temperature	92.06 ℃
Condenser inlet Pressure	50.14 kPa
Incinerator outlet Temperature	976.2 ℃

can be reached at a temperature of 330 degrees Celsius (input to the boiler) and a pressure of about 10 MPa.

The increase in energy efficiency and exergy compared to nami and arabkoohsar [15] research is almost the same (both 9% and 10%), although this
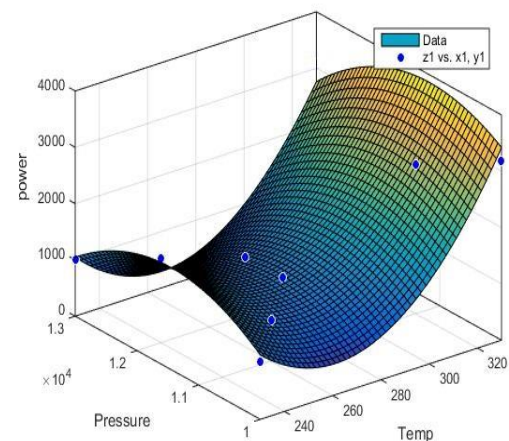
(b)

Figure 8. (a) Exergy and energy efficiency before and after optimization (b) Optimization 3D plo
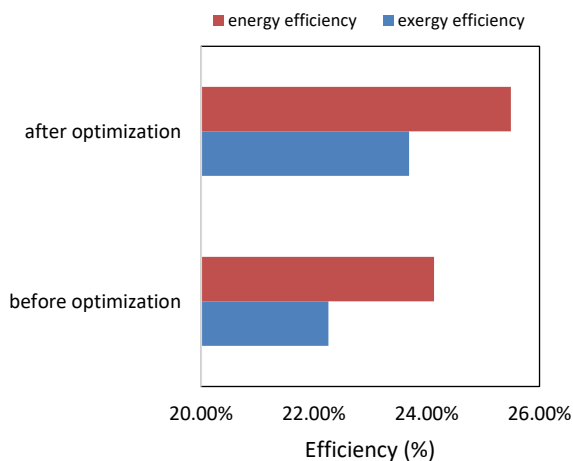
research has reached this increase in efficiency with a simpler and naturally cheaper method. Also, this research has directly increased the amount of output power, which was mentioned in the previous research implicitly and not in a clear and specific way.

4. CONCLUSION

In this paper, general analysis and optimization of the modified waste incinerator power plant were carried out and reviewed. After performing a parametric study and comparing the performance of different ORC working fluids, R124 is suggested as the best fluid from the viewpoint of exergy efficiency. Furthermore, multi-

(a)

objective optimization based on genetic algorithm is applied to find the optimum point considering both exergy and energy analysis. The main factors and their effect on the objective functions have been perused. The results show that with the increase of the steam generator boiler inlet temperature, the reduction of exergy destruction can be seen. Therefore, in the system's design, a higher inlet temperature for the boiler than the pump station should be considered. On the other hand, with the increase in the output temperature of the boiler, exergy efficiency decreases, while increasing the inlet temperature of the evaporator, the destruction of exergy decreases. As a result, the design of reheating flows from other parts of the cycle (using a recuperator) and heating the evaporator as much as possible increases the superheat steam temperature and reduces exergy destruction in the organic Rankine cycle. Also, by using optimization and genetic algorithm, the best temperature and pressure were obtained to achieve the highest output power.

5. REFERENCES

1. Tsai, W.-T. and Kuo, K.-C., "An analysis of power generation from municipal solid waste (MSW) incineration plants in taiwan", *Energy*, Vol. 35, No. 12, (2010), 4824-4830. https://doi.org/10.1016/j.energy.2010.09.005

2. Esmaeilion, F., Ahmadi, A. and Dashti, R., "Exergy-economic-environment optimization of the waste-to-energy power plant using multi-objective particle-swarm optimization (MOPSO)", *Scientia Iranica*, Vol. 28, No. 5, (2021), 2733-2750. https://doi.org/10.24200/SCI.2021.55633.4323

3. Münster, M. and Meibom, P., "Optimization of use of waste in the future energy system", *Energy*, Vol. 36, No. 3, (2011), 1612-1622. https://doi.org/10.1016/j.energy.2010.12.070

4. Chen, C., Jin, Y.-Q., Yan, J.-H. and Chi, Y., "Simulation of municipal solid waste gasification in two different types of fixed bed reactors", *Fuel*, Vol. 103, (2013), 58-63. https://doi.org/10.1016/j.fuel.2011.06.075

5. Pan, M., Chen, X. and Li, X., "Multi-objective analysis and optimization of cascade supercritical CO_2 cycle and organic rankine cycle systems for waste-to-energy power plant", *Applied Thermal Engineering*, Vol. 214, (2022), 118882. https://doi.org/10.1016/j.applthermaleng.2022.118882

6. Shahnazari, A., Rafiee, M., Rohani, A., Nagar, B.B., Ebrahiminik, M.A. and Aghkhani, M.H., "Identification of effective factors to select energy recovery technologies from municipal solid waste using multi-criteria decision making (MCDM): A review of thermochemical technologies", *Sustainable energy Technologies and Assessments*, Vol. 40, (2020), 100737. https://doi.org/10.1016/j.seta.2020.100737

7. Siddiqi, M.M., Naseer, M.N., Abdul Wahab, Y., Hamizi, N.A., Badruddin, I.A., Chowdhury, Z.Z., Akbarzadeh, O., Johan, M.R., Khan, T.Y. and Kamangar, S., "Evaluation of municipal solid wastes based energy potential in urban pakistan", *Processes*, Vol. 7, No. 11, (2019), 848. https://doi.org/10.3390/pr7110848

8. Khan, M.S., Huan, Q., Yan, M., Ali, M., Noor, O.U. and Abid, M., "A novel configuration of solar integrated waste-to-energy incineration plant for multi-generational purpose: An effort for achieving maximum performance", *Renewable Energy*, Vol.

194, (2022), 604-620. https://doi.org/10.1016/j.renene.2022.05.127

9. Alrobaian, A.A., "Improving waste incineration chp plant efficiency by waste heat recovery for feedwater preheating process: Energy, exergy, and economic (3e) analysis", *Journal of the Brazilian Society of Mechanical Sciences and Engineering*, Vol. 42, (2020), 1-14. https://doi.org/10.1007/s40430-020-02460-w

10. Kythavone, L. and Chaiyat, N., "Life cycle assessment of a very small organic rankine cycle and municipal solid waste incinerator for infectious medical waste", *Thermal Science and Engineering Progress*, Vol. 18, (2020), 100526. https://doi.org/10.1016/j.tsep.2020.100526

11. Escamilla-García, P.E., Camarillo-López, R.H., Carrasco-Hernández, R., Fernández-Rodríguez, E. and Legal-Hernández, J.M., "Technical and economic analysis of energy generation from waste incineration in mexico", *Energy Strategy Reviews*, Vol. 31, (2020), 100542. https://doi.org/10.1016/j.esr.2020.100542

12. Mohtaram, S., Sun, Y., Omidi, M. and Lin, J., "Energy-exergy efficiencies analyses of a waste-to-power generation system combined with an ammonia-water dilution rankine cycle", *Case Studies in Thermal Engineering*, Vol. 25, (2021), 100909. https://doi.org/10.1016/j.csite.2021.100909

13. Sorgulu, F., Akgul, M., Cebeci, E., Yilmaz, T. and Dincer, I., "A new experimentally developed integrated organic rankine cycle plant", *Applied Thermal Engineering*, Vol. 187, (2021), 116561. https://doi.org/10.1016/j.applthermaleng.2021.116561

14. Kavathia, K. and Prajapati, P., "A review on biomass-fired chp system using fruit and vegetable waste with regenerative organic rankine cycle (RORC)", *Materials Today: Proceedings*, Vol. 43, (2021), 572-578. https://doi.org/10.1016/j.matpr.2020.12.052

15. Arabkoohsar, A. and Nami, H., "Thermodynamic and economic analyses of a hybrid waste-driven chp–orc plant with exhaust heat recovery", *Energy Conversion and Management*, Vol. 187, (2019), 512-522. https://doi.org/10.1016/j.enconman.2019.03.027

16. Ascanio, L.S., Correa, K.T. and Quintero-Coronel, D., "Thermo-economic analysis of the potential for electricity generation by integrating a rankine cycle with municipal solid waste incineration", in Journal of Physics: Conference Series, IOP Publishing. Vol. 2163, (2022), 012007.

17. Park, B.-S., Usman, M., Imran, M. and Pesyridis, A., "Review of organic rankine cycle experimental data trends", *Energy Conversion and Management*, Vol. 173, (2018), 679-691. https://doi.org/10.1016/j.enconman.2018.07.097

18. Touaibi, R., Koten, H. and Boydak, O., "Parametric study of an organic rankine cycle using different fluids", *Emerging Science Journal*, Vol. 4, No. 2, (2020), 122-128. http://dx.doi.org/10.28991/esj-2020-01216

19. Mahmoudi, A., Fazli, M. and Morad, M., "A recent review of waste heat recovery by organic rankine cycle", *Applied Thermal Engineering*, Vol. 143, (2018), 660-675. https://doi.org/10.1016/j.applthermaleng.2018.07.136

20. Li, W. and Ling, X., "An optimization framework development for organic rankine cycle driven by waste heat recovery: Based on the radial-inflow turbine", *Case Studies in Thermal Engineering*, Vol. 34, (2022), 102054. https://doi.org/10.1016/j.csite.2022.102054

21. Teng, S., Wang, M., Xi, H. and Wen, S., "Energy, exergy, economic (3e) analysis, optimization and comparison of different orc based chp systems for waste heat recovery", *Case Studies in Thermal Engineering*, Vol. 28, (2021), 101444. https://doi.org/10.1016/j.csite.2021.101444

22. Bejan, A., Tsatsaronis, G. and Moran, M., "Thermal design and optimization, wiley, new york, 1996".

23. Alrwashdeh, S.S., Ammari, H., Madanat, M.A. and Al-Falahat, A.a.M., "The effect of heat exchanger design on heat transfer rate and temperature distribution", *Emerging Science Journal*, Vol. 6, No. 1, (2022), 128-137. http://dx.doi.org/10.28991/ESJ-2022-06-01-010

24. Quoilin, S., Van Den Broek, M., Declaye, S., Dewallef, P. and Lemort, V., "Techno-economic survey of organic rankine cycle (ORC) systems", *Renewable and Sustainable Energy Reviews*, Vol. 22, (2013), 168-186. https://doi.org/10.1016/j.rser.2013.01.028

25. Münster, M. and Lund, H., "Use of waste for heat, electricity and transport—challenges when performing energy system analysis", *Energy*, Vol. 34, No. 5, (2009), 636-644. https://doi.org/10.1016/j.energy.2008.09.001

26. Pantaleo, A.M., Ciliberti, P., Camporeale, S. and Shah, N., "Thermo-economic assessment of small scale biomass chp: Steam turbines vs orc in different energy demand segments", *Energy Proceed* Vol. 75, (2015), 1609-1617. https://doi.org/10.1016/j.egypro.2015.07.381

27. Nami, H., Ertesvåg, I.S., Agromayor, R., Riboldi, L. and Nord, L.O., "Gas turbine exhaust gas heat recovery by organic rankine cycles (ORC) for offshore combined heat and power applications-energy and exergy analysis", *Energy*, Vol. 165, (2018), 1060-1071. https://doi.org/10.1016/j.energy.2018.10.034

28. Yin, C. and Li, S., "Advancing grate-firing for greater environmental impacts and efficiency for decentralized biomass/wastes combustion", *Energy Procedia*, Vol. 120, (2017), 373-379. https://doi.org/10.1016/j.egypro.2017.07.220

29. Li, D., "Construction and environmental protection analysis of new energy power generation projects", *International Journal of Energy*, Vol. 2, No. 1, (2023), 16-19. https://doi.org/10.54097/ije.v2i1.5377

30. Eboh, F.C., Ahlström, P. and Richards, T., "Evaluating improvements in a waste-to-energy combined heat and power plant", *Case Studies in Thermal Engineering*, Vol. 14, (2019), 100476. https://doi.org/10.1016/j.csite.2019.100476

31. Nami, H., Ranjbar, F. and Yari, M., "Thermodynamic assessment of zero-emission power, hydrogen and methanol production using captured CO_2 from s-graz oxy-fuel cycle and renewable hydrogen", *Energy Conversion and Management*, Vol. 161, (2018), 53-65. https://doi.org/10.1016/j.csite.2019.100476

32. Mohammadkhani, F. and Nami, H., "Thermodynamic analysis and optimization of a novel cogeneration system: Combination of a gas turbine with supercritical CO_2 and organic rankine cycles", *International Journal of Engineering, Transactions C: Aspects*, Vol. 29, No. 12, (2016), 1765-1774. https://doi.org/10.5829/idosi.ije.2016.29.12c.16

33. Song, G., Shen, L. and Xiao, J., "Estimating specific chemical exergy of biomass from basic analysis data", *Industrial & Engineering Chemistry Research*, Vol. 50, No. 16, (2011), 9758-9766. https://doi.org/10.1021/ie200534n

34. Song, G., Shen, L., Xiao, J. and Chen, L., "Estimation of specific enthalpy and exergy of biomass and coal ash", *Energy Sources, Part A: Recovery, Utilization, and Environmental Effects*, Vol. 35, No. 9, (2013), 809-816. https://doi.org/10.1080/15567036.2011.586983

35. Boodaghi, H., Etghani, M. and Sedighi, K., "Advanced exergy scrutiny of a dual-loop organic rankine cycle for waste heat recovery of a heavy-duty stationary diesel engine", *International Journal of Engineering, Transactions A: Basics,*, Vol. 35, No. 4, (2022), 644-656. https://doi.org/10.5829/IJE.2022.35.04A.04

36. Pashapour, M., Jafarmadar, S. and Khalil Arya, S., "Exergy analysis of a novel combined system consisting of a gas turbine, an organic rankine cycle and an absorption chiller to produce power, heat and cold", *International Journal of Engineering, Transactions C: Aspects*, Vol. 32, No. 9, (2019), 1320-1326. http://doi.org/10.5829/IJE.2019.32.09C.13

37. Huang, W. and Marefati, M., "Development, exergoeconomic assessment and optimization of a novel municipal solid waste-incineration and solar thermal energy based integrated power plant: An effort to improve the performance of the power plant", *Process Safety and Environmental Protection*, Vol. 172, (2023), 562-578. https://doi.org/10.1016/j.psep.2023.02.016

38. Smith, R.W., Steam turbine cycles and cycle design optimization: Combined cycle power plants, in Advances in steam turbines for modern power plants. 2022, Elsevier.61-102.
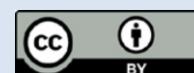
Persian Abstract

چکیده

ترکیبی از یک سیستم زباله سوز اصلاح شده بهمراه یک سیکل آلی رانکین در راستای بهبود بازدهی اگزرژی و انرژی مورد تجزیه و تحلیل و بهینه سازی قرار گرفت. این مقاله مروری بر عملکرد حرارتی سیستم در یک طراحی ابداعی برای درک اثرات فنی سیستم بر سیستم های انرژی آینده ارائه می دهد. همچنین با استفاده از بهینه سازی راهی برای افزایش بازدهی تا مقداری که قبلاً در عمل وجود نداشت، فراهم می کند. طراحی ابداعی از چندین جریان احیای گاز اتلافی استفاده می کند و از R124 به عنوان سیال عامل سیکل آلی رانکین استفاده می شود. نیروگاه برای محاسبه عملکرد حرارتی آن مدل سازی و بهینه سازی شده است. یک چرخه مبتکرانه برای استفاده مجدد از گرمای تلف شده طراحی شده است به باعث کارآمدتر شدن و افزایش راندمان کلی اگزرژی نیروگاه شد. سپس اگزرژی تخریب شده و کارایی سیستم محاسبه گردید. نتایج نشان می‌دهد که ۳/۱۹ مگاوات توان خروجی از ۴۰۰ تن زباله شهری تولید می‌شود. بیشترین تخریب اگزرژی مربوط به واحد زباله سوز و بویلر به ترتیب با حدود ۸ کیلووات و ۶/۴ کیلووات برای سیکل رانکین اولیه با ظرفیت خروجی تقریبا ۲.۸ مگاوات است. همچنین، این تحقیق با استفاده از جریانهای گرمایش مجدد، راندمان اگزرژی آنها را افزایش داد. سیکل آلی رانکین نمی تواند توان بالایی تولید کند اما به طور کلی اگزرژی و بهره وری انرژی را بهبود می‌بخشد. سیکل ترکیبی پیشنهادی با واحدهای گرمایش مجدد گاز دودکش و بهینه سازی، توان خروجی سیستم را از ۳.۰۲ به ۳.۱۹ مگاوات افزایش می دهد. علاوه بر این، بازده انرژی و اگزرژی به ترتیب ۱۰٪ و ۹٪ افزایش یافت.

International Journal of Engineering

Rescheduling Unreliable Service Providers in a Dynamic Multi-objective Cloud Manufacturing

M. M. Fazeli*, Y. Farjami, A. Jalaly Bidgoly

Department of Computer and IT, University of Qom, Qom, Iran

ABSTRACT

Cloud manufacturing (CMfg) is a new advanced manucatring model developed with the help of enterprise information technologies under the support of cloud computing, Internet of Things and service-based technologies. CMfg compose multiple manufacturing resources to provide efficient and valuable services. CMfg has a highly dynamic environment. In this environment, many disruptions or events may occur that lead the system to unplanned situations. In CMfg, a series of service providers are scheduled for production. During the production operation, some of them may be damaged, stopped, and out of service. Therefore, rescheduling is necessary for the continuation of the production process according to the concluded contracts and initial schedule. When any disruptions or other events occurred, the rescheduling techniques used to updating the inital schedule. In this paper, the dynamic rescheduling problem in CMfg is analyzed. Then the multi-objective rescheduling in CMfg is modeled and defined as a multi-objective optimization problem. Defining this problem as a multi-objective optimization problem provides the possibility of applying, checking and comparing different algorithms. For solving this problem, previous optimization methods have improved and a multi-objective and elitist algorithm based on the Jaya algorithm, called advanced multi-objective elitist Jaya algorithm (AMEJ) is proposed. Several experiments have been conducted to verify the performance of the proposed algorithm. Computational results showed that the proposed algorithm performs better compared to other multi-objective optimization algorithms.

1. INTRODUCTION

Cloud manufacturing is service-oriented and has a sharedable set of diverse and distributed production resources. CMfg aims to increase the efficiency of the production process, reduce manufacturing costs and optimize the use of resources by creating temporary, reconfigurable production lines to respond to customers' requests [1]. As a result, CMfg can satisfy users' specific manufacturing tasks by sharing on-demand networked manufacturing services [2].

CMfg compose multiple manufacturing resources to provide efficient and valuable services. With the help of CMfg resources, capabilities and manufacturing services can be shared [3]. In the CMfg environment, finding a better manufacturing resources composition is needed to achieve high-efficiency manufacturing processes [4].

CMfg has a highly dynamic environment. In this environment, many disruptions or events may occur that lead the system to unplanned situations. So the initial schedule needs to be reviewed. When any disruptions or other events occurred, the rescheduling techniques used to updating the inital schedule [5]. One of these events is service provider failures. Failure or inaccessibility of the service provider puts the initial schedule in an invalid state and it is not possible to continue the production process so reviewing the initial schedule is vital and unavoidable.

Rescheduling in CMfg should be considered as a multi-objective problem because 1) Several objectives must be simultaneously optimized 2) determining constraints in a single-objective optimization problem requires determining customer preferences, which is not always possible and correct 3) multi-objective approaches provide multiple options as result, each of which can be selected according to the system conditions and the opinion of the experts.

Coresponding Author Institutional Email: m.fazeli@stu.qom.ac.ir (M. M. Fazeli)

This paper analyses the dynamic rescheduling problem in CMfg. Then, the multi-objective rescheduling in CMfg is modeled and a multi-objective optimization problem is defiend based on the propsed model. To solve the rescheduling problem in CMfg, a multi-objective and elitist algorithm based on the Jaya algorithm, called advanced multi-objective elitist Jaya algorithm (AMEJ) is proposed.

There are various algorithms for solving multi-objective optimization problems, most of which require parameters tuning for proper execution. But AMEJ is a parameter-less algorithm that does not require any parameters for the algorithm to works correctly.

The proposed algorithm is based on Jaya algorithm. Jaya is a parameter-less simple algorithm that multiple experiments showed that it has better performance than other multi-objective optimization algorithms [6].

AMEJ adds new operators to the base Jaya algorithm, which improves its performance and results. The computational results show that the proposed algorithm performs better than the base Jaya algorithm and other compared optimization algorithms.

The innovations of this article can be summarized as follows:

1. Mathematical modelling of rescheduling problem in CMfg.
2. Defining the multi-objective rescheduling problem in CMfg as a multi-objective optimization problem that provides the possibility of applying, checking and comparing different algorithms on it.
3. Proposing a competitive and appropriate algorithm to solve this problem.

The rest of the paper is as follows. In section 2, the previous works are studied. Section 3 provides some preliminaries, mathematical model of CMfg, and objective functions for SBCOS and rescheduling problem. Section 4 proposes the AMEJ algorithm. The experiments results and analysis are presented in section 5. Finally, section 6 concludes this research and outlines the directions for future researches.

2. RELATED WORKS

In recent years, solving the SBCOS problem and scheduling in CMfg have been considered by a lot of researchers. In our previous work [7], we proposed an ensemble optimization approach that can be used as a flexible framework. This approach combins multiple optimization methods to improve service composition performance. Zhang and Ren [8] propose a multi-agent simulation model for CMfg. Their model can evaluate the manufacturing process and rescheduling strategies which can help to obtain more accurate value of parameters. Zhang et al. [9] considered disruption like random service breakdowns and proposed a framework for

rescheduling the initial schedule of multiple distributed production services. Liu et al. [10] proposed a new efficient way to scheduling a multi-task problem in CMfg based on workload criteria. This work provides general guidance to schedule multiple tasks with different workloads in CMfg under different circumstances. Yang et al. [11] have investigated on scheduling multi-population competitive field resources in CMfg. Their results showed that the FSRS-CMfg model can improve the quality of service critriation of scheduling the field manufacturing resource and proposed a higher precision of convergence without extensively increasing in the manufacturing time. Liu et al. [12] presented a model to solve the personal recommendation issue in CMfg and they proposed a swarm-based optimization algorithm named glow-worm for solving the multi-objective optimization problem. Zhou and Yao [13] proposed an artificial optimization algorithm to solve the service composition problem in CMfg based on cooperation of bees in a bee colony which uses multiple algorithms for selection of an optimal combination of services and considered QoS and randomly arriving of tasks as criterion.

Rescheduling and real-time scheduling is an interesting topic in CMfg and manufacturing. Zhang et al. [6] proposed MMSC model for composition of multi-task manufacturing services that considers multiple tasks in an uncertain environment to solve uncertainty problems such as urgent tasks and delivery delays; also a heuristic algorithm was proposed for the finding an optimal manufacturing service composition. Zhou et al. [14] proposed a model for simulation of dynamic service scheduling in CMfg. This simulation can be done from demanders, tasks, resources, or path perspective or combination of them. Zhou et al. [15] presented an event-based dynamic task scheduling approach to solve the scheduling problem in the CMfg that tasks randomly arrive into the the system. In previous researches various models and algorithms have been proposed, there are some researches that focoused on scheduling models for multi-objective or single-objective problems [16], or association analysis approach [17] and Colony based Optimization algorithms like Ant Colony. But there are less studies on CMfg dynamic scheduling [18].
Champati and Liang [19] proposed a huristic algorithm. Their algorithm can calculate the manufacturing time when a task canceled or rescheduled. They also used simulation to compare the performance of the proposed algorithm with other algorithms. Liu et al. [20] proposed a model for dynamic CMfg scheduling problem that considers dynamic task arrivals. In this model, the failure types and causes of exception conditions faced by cloud services are considered for updating programs and rescheduling production.

Most of the optimization algorithms use multiple parameters and need parameters tuning [21]. But AMEJ

is a parameter-less algorithm that does not require any parameters for the algorithm to works correctly. The Jaya algorithm and teaching-learning-based optimization (TLBO) algorithm are two popular parameter-less algorithms.

Rao et al. [22] introduced the TLBO algorithm. This algorithm has two phases; the teacher phase and the learner phase. The population of this algorithm is a group of learners. This population is updated and improved in the two phases mentioned [22]. After the success of previous algorithm, Rao [23] proposed another parameter-less algorithm named Jaya. This one-phase algorithm is simple and fast. Also Rao [23] showed that Jaya has better performance compared to other optimization algorithms.

A review of the existing research literature showed that there are a few studies that have been conducted in relation to dynamic scheduling of CMfg [18]. Various evaluation indicators currently used in CMfg scheduling; most of them evaluate service composition based on quality of service. Yang et al. [24] used six second-level indexes (importance, supply and demand, cost, remaining time, reputation and predetermined cost) as indices for the service composition evaluation. Based on the evaluation of cloud service composition reputation (CSCR), Xie et al. [25] took two types of stability and collaboration ability as the first-level evaluation indices of the service composition and three types (execution time, cost and reliability) as the second-level indices. Li et al. [26] proposed six indices (reliability, reputation, combination collaboration, combination complexity, execution time and execution cost) to evaluate service composition.

Chen et al. [27] studied real-time scheduling problem in the cloud. Resource allocation is the key feature that they considered for scheduling. They also proposed an artificial neural network model for prediction of the status of the task completion. This process can better allocate resources. In other study Zheng and Zheng [28] proposed a simulation-based approach that combines the simulation with some network models. The aims of this approach is to analysis the robustness of cloud manufacturing systems.

Other important articles in the subject area of this research are: Arkat et al. [29] on their article entitled "Reactive Scheduling Addressing Unexpected Disturbance in Cellular Manufacturing Systems" focussed on scheduling in CMfg. Puspitasari et al. [30] on their work entitled "Generator Scheduling Optimization Involving Emission to Determine Emission Reduction Costs" also paid attention on cost anlysis of CMfg. Najafi and Nikaeen [31] addressed on their work for a constraint programming approach in order to solve multi-skill resource-constrained project on scheduling problem with calendars. Torkashvand et al. [32] discussed about the distributed production assembly scheduling using hybrid flowshop in assembly lines. Maghzi et al. [33] investigated on optimization of operating room scheduling using a fuzzy uncertainty approach and metaheuristic algorithms. Halty et al. [34] discussed on Scheduling in cloud manufacturing systems. Rashidifar et al. [35] also presented a mathematical model for cloud-based scheduling using heavy traffic limit theorem in queuing process. Abtahi et al. [36] studied on stochastic model for the prioritized outpatient scheduling in a radiology center for the purose of effective and efficient services given to patients. Yazdi et al. [37] conducted an investigtaion by using a mathematical model for scheduling elective surgeries in order to minimize the waiting list in the emergency surgeries.

3. PRELIMINARIES & BACKGROUND MODELS

3. 1. Machine Breakdown and Rescheduling   In the manufacturing process, any machine may break down and be out of reach for a certain period of time. In this article, we assumed that one of the service provider's machines breaks down for T unit of times and after this amount of time it can be used again. As a result, we have two unscheduled events, one for when the machine breaks down and becomes unavailable, and the second for when it becomes available again.

Rescheduling is used to update the initial schedule when events occurred that may lead the system to a unstable state [38]. So after any unscheduled events such as machine breakdowns, the initial schedule must be reviewed and the rescheduling process must be performed.

Figures 1 and 2 show the schedules and the impact of a breakdown for three machines and four requests, each with three subtasks. For simplicity, in this example, we assumed that each service provider has only one machine. Figure 1(a) shows the Gantt chart of the initial schedule and the subtasks affected by the second machine failure. Figure 1(b) shows the modified schedule after the second machine becomes unavailable. Figure 2(a) shows the tasks that are affected by the re-availability of the second machine and Figure 2(b) shows the final schedule after the completion of the second rescheduling process.

As shown in Figure 2(a), after the second machine is available again, ongoing requests are completed and the rescheduling process is done only for requests that have not yet started.

3. 2. Non-dominated Sorting   The non-dominated sorting approach is a process for classifying the population in several ranks or Pareto fronts (PF). This approach is based on the Pareto dominance concept which is described for this research as follow [38]:
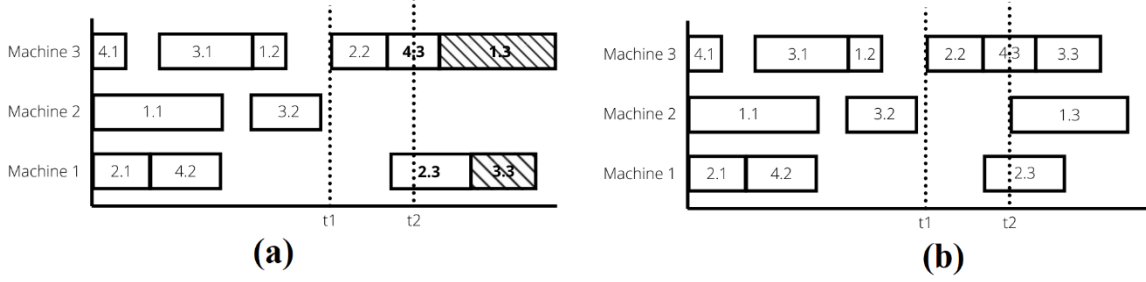
Figure 1. Schedule of 3 machines and 4 requests; (a) initial schedule; (b) reviewed schedule after the second machine breaks down
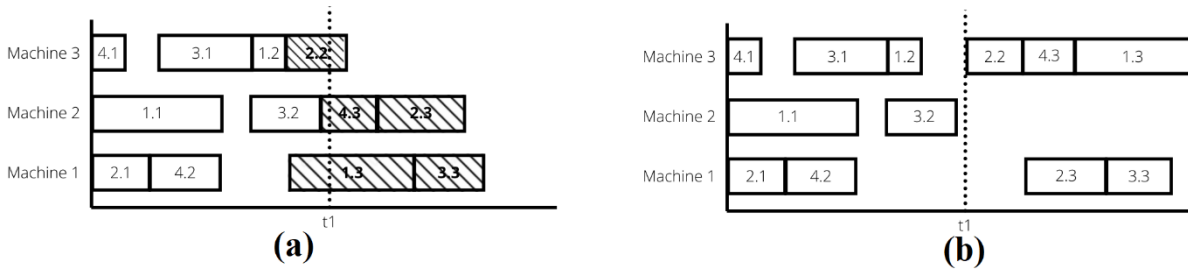
Figure 2. Schedule of 3 machines and 4 requests; (a) the schedule after the second machine breaks down and the subtasks that were affected by the re-availability of the second machine; (b) reviewed schedule after the second machine becomes available

$$Solution_j \prec Solution_i \leftrightarrow$$
$$\forall f \in \{TCT, TC, SI, STT\}\, f\left(Solution_j\right) \leq$$
$$f\left(Solution_i\right) \&$$
$$\exists f' \in \{TCT, TC, SI, STT\}\, f\left(Solution_j\right) <$$
$$f\left(Solution_i\right)$$

Where $Solution_i$ and $Solution_j$ are two solutions in result space and $Solution_j \prec Solution_i$ means $Solution_i$ dominates $Solution_j$. In the non-dominated sorting approach, for a set of populations, all non-dominated solutions that are not dominated by any other solutions are found. These solutions are rank one (first Pareto front). Then these solutions are deleted from the population and the same process is repeated until all solutions are ranked in their respective front.

3. 3. Crowding Distance   The purpose of computing crowding distance (denoted by CD_i for crowding distance of $Solution_i$) is to determine the density of solutions around each solution in the result space. The following algorithm can be used to compute the crowding distance of each solution in the front F [21]:

Crowding Distance Computation Algorithm
1. $l = |F|$
2. for each i in F set $CD_i = 0$
3. for each f in $\{TCT, TC, SI, STT\}$
   3.1 Sort F in worst order of f
   3.2 $CD_1 = CD_l = \infty$

3.3 f_{min} = minimum value of f in F
3.4 f_{max} = maximum value of f in F
3.5   for $j = 2$ to $j = l - 1$ set $CD_j = CD_j + \frac{f(j+1) - f(j-1)}{f_{max} - f_{min}}$

Based on the above algorithm, the crowded-comparison operator ($\prec_n$) is defined as follow:
$$Rank_j < Rank_i \mid (Rank_j = Rank_i \,\&\, CD_j > CD_i)$$
$$\rightarrow Solution_j \prec_n Solution_i$$

Where $Rank_i$ and $Rank_j$ are the fronts to which $Solution_i$ and $Solution_j$ belong respectively.

3. 4. Constraint-Dominance Concept   a $Solution_i$ is said to constrained-dominate a $Solution_j$ if $Solution_i$ is feasible and $Solution_j$ is not feasible or both solutions are infeasible and $Solution_i$ has a smaller overall constraint violation or both solutions are feasible and $Solution_i$ dominates $Solution_j$. This concept gives feasible solutions a higher rank than infeasible solutions. Between the feasible solutions, the superior (non-dominated) solution, and between the infeasible solutions, the solution with the lowest value of overall constraint violation will have a higher rank [21].

3. 5. Jaya Algorithm   The Jaya algorithm used by multiple researchers in thier applications. It's a parameter-less algorithm and in this algorithm, after

generating a random initial population, in each iteration, each of the solutions is updated using Equation (1):

$$Solution_{k+1,i,j} = Solution_{k,i,j} + rand_1\big(BS_{k,j} - |Solution_{k,i,j}|\big) - rand_2\big(WS_{k,j} - |Solution_{k,i,j}|\big) \quad (1)$$

where $Solution_{k,i,j}$ is jth objective function of ith solution in kth iteration and $BS_{k,j}$ and $WS_{k,j}$ are the jth objective function value of the best and worst solution in kth iteration respectively. $rand_1$ and $rand_2$ are two random numbers in between 0 and 1 [23].

3. 6. Analyzing Dynamic Rescheduling Problem in CMfg
The following flowchart shows the rescheduling problem in a dynamic CMfg environment. The following abbreviation is used to simplify the flowchart:

S: Broken service

Z: Alternative service
R(S): The time required to repair S
T(S): The time required to complete the subtask by S
W(Z): The time remaining until the start of the next subtask of Z
T(Z): The time required to complete the sub-task by Z
T'(Z): The time remaining until the completion of the current subtask of Z

After receiving, the client request is virtualized and decomposed and then saved in the subtasks database. Also, all the services, including manufacturing services and logistics services, are virtualized and saved in the services database.

Then the scheduler generates the initial schedule with the help of information stored in both databases. The schedule is given to the services and the actual manufacturing process start.
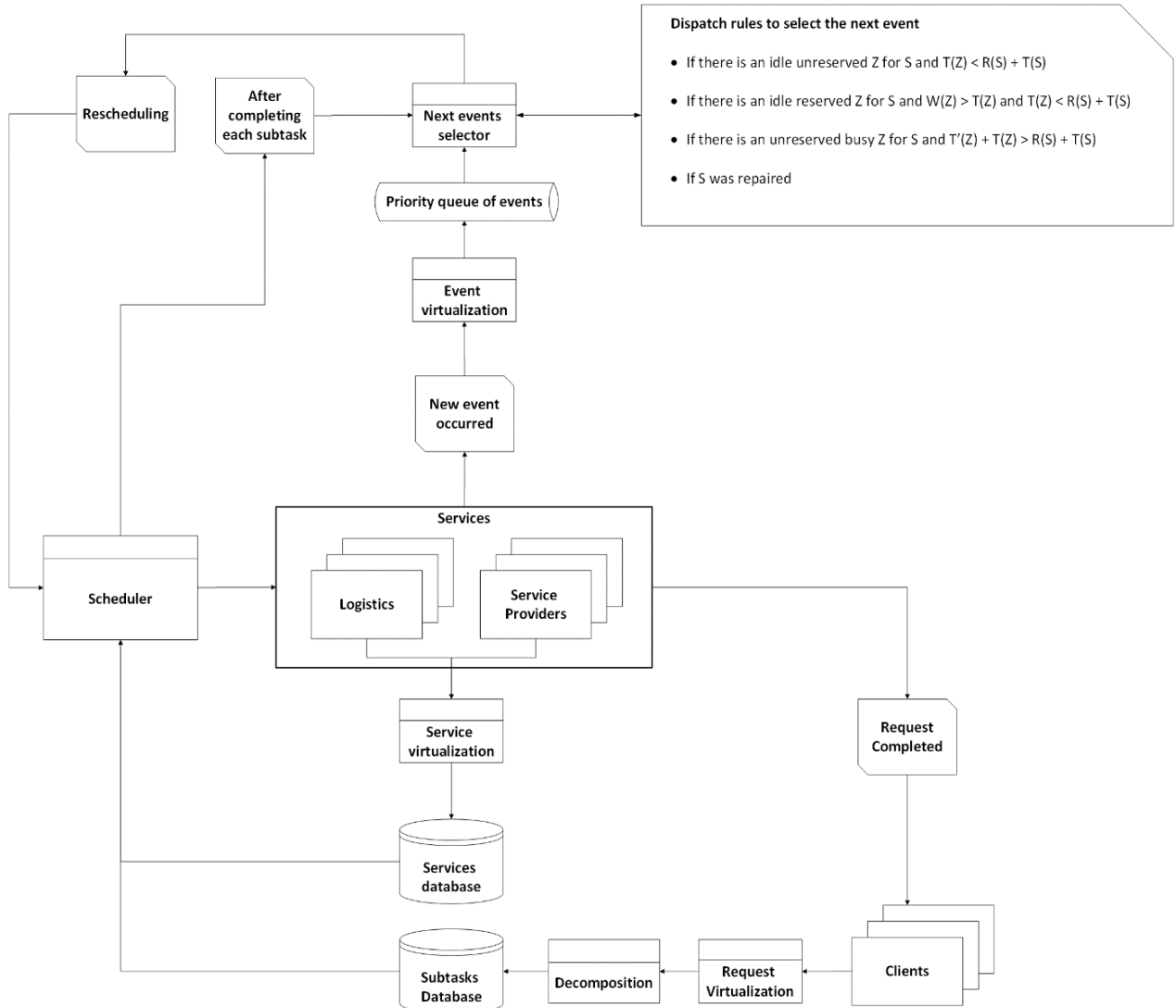

Figure 3. Dynamic rescheduling problem in CMfg

If any of the services break down during the manufacturing process, the event will be virtualized and stored in a priority queue. The next event is selected from the queue according to the following dispatching rules. These rules are in order of priority so the first rule is superior to the second one and so on.

1. If there is an idle unreserved Z for S and T(Z) < R(S) + T(S)
2. If there is an idle reserved Z for S and W(Z) > T(Z) and T(Z) < R(S) + T(S)
3. If there is an unreserved busy Z for S and T'(Z) + T(Z) > R(S) + T(S)
4. If S was repaired

Then the selected event information and the candidate services are given to the scheduler to revise the schedule and generate a new schedule.

3. 7. CMfg Model   In this article, we assume that there are several customers in the CMfg system whose requests have reached the system simultaneously. The ith request submitted by the customers denoted by Req_i where $i \in \{1,2,3, \dots, nReq\}$ and $nReq$ is the total number of requests.

Multiple subtasks (denoted by ST) should performe to complete a request. So for ith request, we have $Req_i = \{ST_{i,1}, ST_{i,2}, ST_{i,3}, \dots, ST_{i,j}\}$ where $ST_{i,j}$ is jth subtask in the subtasks sequence of Req_i. Total number of subtasks in a Req_i is shown with nST_i so $j \in \{1,2,3, \dots, nST_i\}$.

In the CMfg system, three main processes are done. First, all requests of customers are processed and decomposed, and subtasks sequences for each request are created. Then service provider (SP) send their manufacturing information to the CMfg system.

In the next process, based on subtasks data of requests and providers' data, the CMfg system tries to find the most appropriate service for each subtask of each request. In the CMfg for each subtask of a request, multiple candidate services exist that can do that subtask (candidate services for subtask j of ith request denoted by $CS_{i,j}$). If we show the total number of services in $CS_{i,j}$ with $nCS_{i,j}$, there are $\prod_{i}^{n} \prod_{j=1}^{m_i} nCS_{i,j}$ of paths to do all requests.

After fininshing the previous process, the service sequence is created based on the subtasks and services information. When the CMfg system processes are done, Based on the information like sequence of services and assigned tasks, each service provider will know its job.

3. 8. Objective Functions   The rescheduling problem in the CMfg is a multi-objective optimization problem. the priori and a posteriori approaches are the main two ways that used for solving a multi-objective optimization problem: Priori approach converts a multi-objective optimization problem into a single objective optimization problem by using some weights for the objective functions. In this approach, user preferences are considered as weights of objective functions. But the posteriori approach can find multiple solutions for a multi-objective optimization problem [21].

In this research, the posteriori approach has been used to solve the multi-objective rescheduling problem in the CMfg. The objective functions used in this problem can be divided into two categories: global objective functions such as total completion time (TCT) and total cost (TC), and rescheduling-specific objective functions such as solution instability (SI) and subtask tardiness (STT).

a. **Total Completion Time (TCT):** this objective function can be calculated by the following equation [6]:

$$TCT = TMT + TLT + TWT \qquad (2)$$

In this equation TMT is the total time needed to complete the request, TLT is the total time that consumed by the logistic processes and TWT is the total amount of time for just waiting for another proccess to be completed or receiving the material for starting a procces. These values can be calculated by Equations (2)-(4):

$$TMT = \sum_{i=1}^{nReq} \sum_{j=1}^{nST_i} MT_{i,j} \qquad (3)$$

$$TLT = \sum_{i=1}^{nReq} \sum_{j=1}^{nST_i} LT\left(SP_{i,j}, SP_{i,j+1}\right) \qquad (4)$$

$$TWT = \sum_{i=1}^{nReq} \sum_{j=1}^{nST_i} WT\left(SP_{i,j}\right) \qquad (5)$$

where $MT_{i,j}$ is the manufacturing time to complete $ST_{i,j}$, and $LT\left(SP_{i,j}, SP_{i,j+1}\right)$ is the logistic time between service providers selected to perform $ST_{i,j}$ and $ST_{i,j+1}$, and $WT\left(SP_{i,j}\right)$ is waiting time to complete $ST_{i,j}$ on its corresponding service provider.

b. **Total Cost (TC):** this objective function can be calculated by the following equation:

$$TC = TMC + TLC \qquad (6)$$

In this equation TMC and TLC are the total cost that the manufacturing and the logistic processes needed respectively. These values can be calculated by Equations (7)-(8):

$$TMC = \sum_{i=1}^{nReq} \sum_{j=1}^{nST_i} MC\left(SP_{i,j}\right) \qquad (7)$$

$$TLC = \sum_{i=1}^{nReq} \sum_{j=1}^{nST_i} LC\left(SP_{i,j}, SP_{i,j+1}\right) \qquad (8)$$

where $MC\left(SP_{i,j}\right)$ is the manufacturing cost of $SP_{i,j}$, and $LC(SP_i, SP_{i+1})$ is the logistic cost to perform logistic service between $SP_{i,j}$ and $SP_{i,j+1}$.

c. **Solution Instability (SI):** Instability is defined as the number of subtasks assigned to another service

provider for performing after rescheduling [39]. This objective function is between zero and one, and the smaller it is, the greater stability of the solution. SI can be calculated by Equation (9):

$$SI = \frac{\sum_{i=1}^{nReq} \sum_{j=1}^{nST_i} CH_{i,j}}{\sum_{i=1}^{nReq} nST_i}$$

$$CH_{i,j} = \begin{cases} 0, & SP_{i,j} \text{ remains for } ST_{i,j} \\ 1, & SP_{i,j} \text{ is changed for } ST_{i,j} \end{cases} \tag{9}$$

Where $SP_{i,j}$ is the selected service provider to perform the jth subtask of ith request.

d. **Subtask Tardiness (STT):** This objective function is the difference between the initial schedule start time of subtasks and their real start time. STT can be calculated by Equation (10):

$$STT = \sum_{i=1}^{nReq} \sum_{j=1}^{nST_i} FinalST_{i,j} - InitST_{i,j} \tag{10}$$

Where $InitST_{i,j}$ is the initial schedule start time of $ST_{i,j}$ and $FinalST_{i,j}$ is the final schedule start time of $ST_{i,j}$.

The overall multi-objective rescheduling problem is summarized as follows:

$$min \{TCT, TC, SI, STT\}$$

$$subject\ to: \begin{cases} TCT < TCT_0 \\ TC < TC_0 \\ SI < SI_0 \\ STT < STT_0 \end{cases}$$

where TCT_0, TC_0, SI_0 and STT_0 are the maximum time, cost, solution instability, and subtask tardiness based on customer preferences, respectively.

4. THE PROPOSED ALFORITHM FOR RESCHEDULING

To solve the rescheduling problem in CMfg, this paper proposed a multi-objective and elitist algorithm based on Jaya, called advanced multi-objective elitist Jaya algorithm (AMEJ). AMEJ is a parameter-less algorithm so there is no need for tuning any parameters for proper execution.

There are two lists in AMEJ: $BestList$ to maintain the best solutions and $WorstList$ to keep the worse solutions in each iteration.

In each iteration, the best solution (denoted by $best$) and the worst solution (denoted by $worst$) are found using the non-dominated sorting approach, constraint-dominance concept and crowding distance computation. Then all solutions in $BestList$ that is dominated by $best$ are removed from this list and the $best$ solution is added to $BestList$. Similarly, all solutions in $WorstList$ that dominates $worst$ are removed from this list and the $worst$ solution is added to $WorstList$. This process removes the dominated solutions (that is worse than the current $bset$ solution) from $BestList$ and the dominant

solutions (that is better than current $worst$ solution) from $WorstList$.

Then both lists are sorted by the non-dominated sorting approach, constraint-dominance concept, and crowding distance computation and the best solution from $BestList$ and the worst solution from $WorstList$ are found. These solutions are used to update the population-based on Equation 10 according to the Jaya algorithm. If these solutions have been used for more than two iterations to update the population, they will be removed from the relevant lists and other solutions will be found and used to update the population. This mechanism will lead to better dispersibility of solutions and will allow the appropriate solutions the opportunity to be reused again.

The updated population is then concatenated with the initial population and the whole population is sorted by non-dominated sorting approach, constraint-dominance concept, and crowding distance computation. Then, using a random binary variable, it is determined to separate the number of initial population or twice the initial population from the best individuals of the whole sorted population. This population is used in the next iteration. This approach allows more individuals to be used to search the problem space in some iterations randomly. The flowchart for the AMEJ algorithm is shown in Figure 4.

5. EXPERIMENTS AND DISCUSSIONS

5. 1. Experimental Setup In this section, AMEJ was compared with three multie-objective optimazation algorithms, including multi-objective Jaya algorithm (MOJaya), non-dominated sorting teaching-learning based optimization algorithm (NSTLBO), and the fast and elitist multi-objective genetic algorithm (NSGA2), based on various comparison criteria.

All the experiments are programed by Python 3.8 programing language on a 64-bit windows 10 OS with an Intel(R) Core i7 2.80 GHz processor and 16-GB RAM system. Source papers for the implementation of the comparison algorithms with explanations of their parameters are listed in Table 1.

The initial population number and the number of iterations of each algorithm were considered 300 and 20 times, respectively. In the rescheduling problem for cloud manufacturing, the constraints imposed on each of the objective functions can be considered as the min and max allowed values. In the following experiments, we considered values 75 and 100 as the min and max allowed values for all four objective functions.

These constraints can be determined by the expert depending on the type of problem. The initial population was also randomly generated in the allowed space of the problem and according to the imposed constraints.
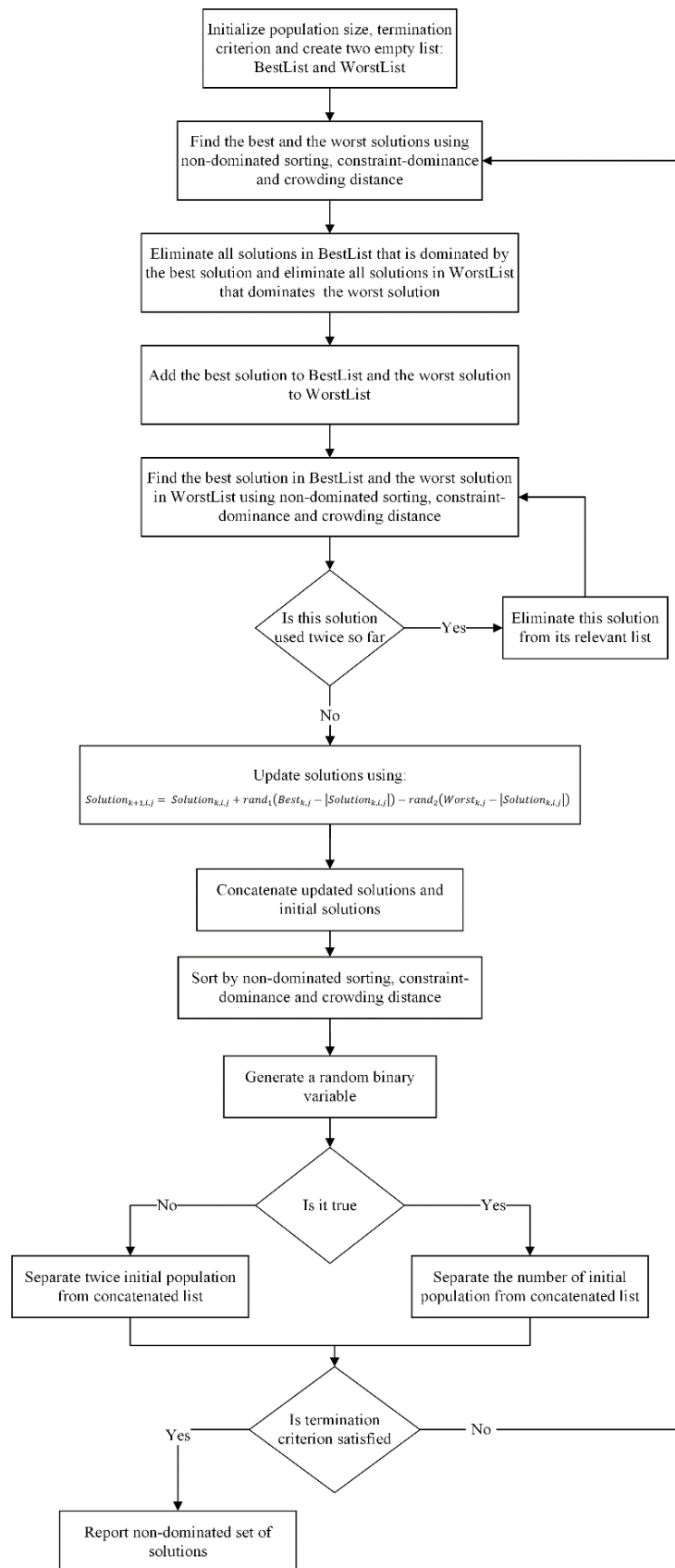
Figure 4. Flowchart of the AMEJ algorithm

TABLE 1. Source articles and parameters of comparison algorithms

Algorithm Name	Source article	Parameters
MOJaya	Rao et al. [40]	Parameter-less
NSTLBO	Rao et al. [23]	Parameter-less
NSGA2	Deb et al. [41]	crossover probability = 0.9
		mutation probability = 1/n
		n is the number of decision variables

5. 2. Experimental Results The first experiment is to compare algorithms based on the number of non-dominated solutions found in 300 individuals of population. Figure 5 shows the result of this comparison.

As shown in Figure 5, the number of non-dominated solutions found by AMEJ is more than other algorithms. This comparison criteria is simple but it can show the better performance of an algorithm in finding non-dominated solutions in the problem space compared to others.

The spacing measure is another comparison criterion used to compare multi-objective algorithms. This criterion shows how the solutions uniformly distributed in a Pareto front. The spacing measure can be calculated by the following equation:

$$Spacing = \sqrt{\frac{1}{|n-1|}\sum_{i=1}^{n}(\bar{d} - d_i)^2} \qquad (11)$$
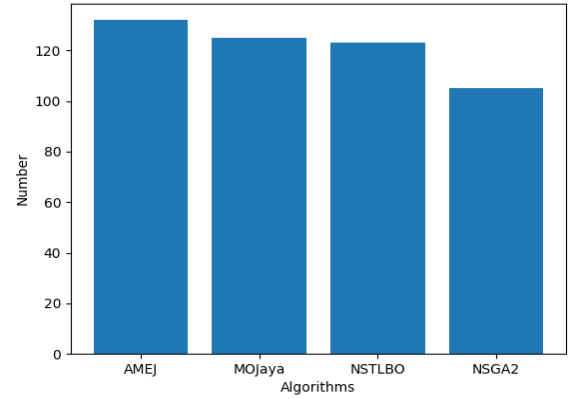
where n is the non-dominated solutions count and d_i calculated by Equation (12):

$$d_i = \min_{i, i \neq j} \sum_{m=1}^{k}|f_m^i - f_m^j|, \quad i, j = 1, 2, \dots, n \qquad (12)$$

where k is the count of objective functions and f_m is the value of the objective function for mth objective. $\bar{d}$ is the normalized value of d_i and calculated by Equation (13):

$$\bar{d} = \sum_{i=1}^{n} d_i / |n| \qquad (13)$$

The lower the value obtained for spacing measure by an

Figure 5. Number of non-dominated solutions found by each algorithm

algorithm, the better its performance based on this criterion. Figure 6 shows the comparison results of algorithms based on spacing measure:

Individual displacement in the problem space can indicate the performance of the algorithm in improving all solutions. Figures 7 shows the position of the individuals in the problem space at the beginning and after the completion of the AMEJ algorithm for each pair
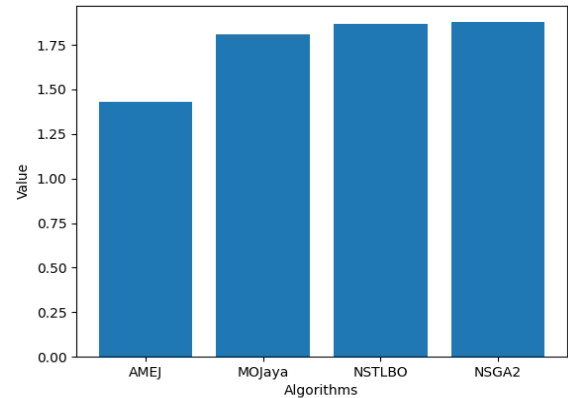
Figure 6. Comparison of algorithms based on the spacing measure
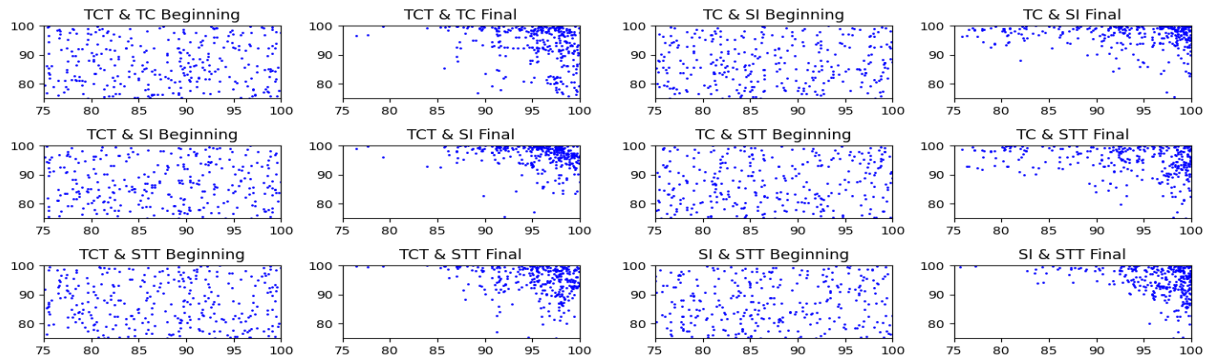
Figure 7. Distribution of individuals in the problem space at the beginning and end of AMEJ run

TABLE 2. Comparison of mean and standard division of non-dominated solutions of AMEJ and MOJaya

	TCT		TC	
	AMEJ	MOJaya	AMEJ	MOJaya
Mean	96.060076	95.186218	97.770860	97.545763
Standard Division	3.667294	4.980794	4.329043	4.597407
	SI		STT	
	AMEJ	MOJaya	AMEJ	MOJaya
Mean	96.773871	96.098727	95.059678	94.650871
Standard Division	3.954239	3.628339	4.570308	5.871844

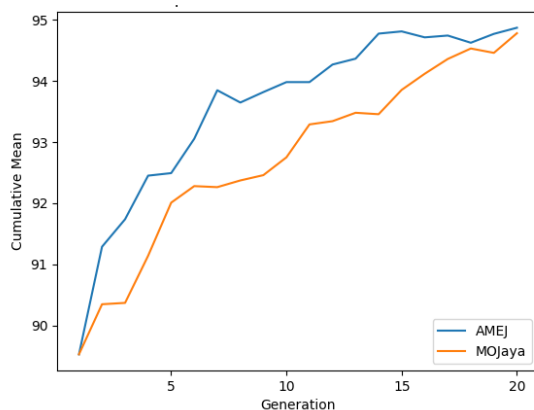**Figure 8.** comparison of AMEJ and MOJaya based on cumulative mean in 20 iterations

of objective functions. This figure shows the random distribution of individuals in the problem space at the beginning and the move towards collective improvement at the end.

Since MOJaya is the base algorithm of AMEJ, the following two comparisons were performed between these algorithms. The results show that AMEJ performance is better than MOJaya.

Table 2 shows the mean and standard deviation of non-dominated solutions of each objective functions.

Cumulative mean is another criterion used to compare AMEJ and MOJaya algorithms. To calculate this criterion in each iteration, the values of the objective functions are first normalized. Then for each solution, the sum of all objective function values with an equal weight of one is calculated. Then the mean of all calculated values is reported. For this experiment, all the solutions in the population were used.

Figure 8 shows the result of the comparison of AMEJ and MOJaya based on the cumulative mean.

6. CONCLUSION AND FUTURES WORK

CMfg has a highly dynamic environment. In this environment many disruptions or events may occur that

lead the system to unplanned situations. When any disruptions or other events occurred, the rescheduling techniques used to updating the inital schedule. First, this paper analyzes the dynamic rescheduling problem in CMfg. Then the rescheduling problem in CMfg is modeled mathematically. To solve the multi-objective rescheduling problem in CMfg, this paper proposed the AMEJ algorithm which is an advanced multi-objective and elitist algorithm based on Jaya.

To show the performance of the AMEJ algorithm, several experiments are performed. The results indicate that AMEJ has better performance than other multi-objective optimization algorithms such as MOJaya, NSTLBO, and NSGA2.

Considering the multi-objective nature of the rescheduling problem in CMfg, the procedure of modeling the rescheduling problem into a multi-objective optimization problem that was presented in this article can be considered as a suitable approach in solving rescheduling problems in future researches.

The proposed algorithm is also a generic algorithm that can be studied in other areas besides CMfg. Because the proposed algorithm can also be considered in single-objective optimization problems, we will implement a priori approach-based algorithm inspired by AMEJ in our future work and we will conduct more comparisons based on standard benchmark functions.

7. REFERENCES

1. Wu, D., Greer, M.J., Rosen, D.W. and Schaefer, D., "Cloud manufacturing: Drivers, current status, and future trends", in International Manufacturing Science and Engineering Conference, American Society of Mechanical Engineers. Vol. 55461, (2013), V002T002A003.

2. Tao, F., Zhao, D., Yefa, H. and Zhou, Z., "Correlation-aware resource service composition and optimal-selection in manufacturing grid", *European Journal of Operational Research*, Vol. 201, No. 1, (2010), 129-143. https://doi.org/10.1016/j.ejor.2009.02.025

3. Li, B.-H., Zhang, L., Ren, L., Chai, X.-D., Tao, F., Wang, Y.-Z., Yin, C., Huang, P., Zhao, X.-P. and Zhou, Z.-D., "Typical characteristics, technologies and applications of cloud manufacturing", *Computer Integrated Manufacturing System*, Vol. 18, No. 07, (2012).

4. Tao, F., Zuo, Y., Da Xu, L. and Zhang, L., "Iot-based intelligent perception and access of manufacturing resource toward cloud manufacturing", *IEEE Transactions on Industrial Informatics*, Vol. 10, No. 2, (2014), 1547-1557. doi: 10.1109/TII.2014.2306397.

5. Vieira, G.E., Herrmann, J.W. and Lin, E., "Rescheduling manufacturing systems: A framework of strategies, policies, and methods", *Journal of Scheduling*, Vol. 6, (2003), 39-62. https://doi.org/10.1023/A:1022235519958

6. Zhang, S., Xu, Y. and Zhang, W., "Multitask-oriented manufacturing service composition in an uncertain environment using a hyper-heuristic algorithm", *Journal of Manufacturing Systems*, Vol. 60, (2021), 138-151. https://doi.org/10.1016/j.jmsy.2021.05.012

7. Fazeli, M.M., Farjami, Y. and Nickray, M., "An ensemble optimisation approach to service composition in cloud manufacturing", *International Journal of Computer Integrated Manufacturing*, Vol. 32, No. 1, (2019), 83-91. https://doi.org/10.1080/0951192X.2018.1550679

8. Zhang, X. and Ren, D., "Modeling and simulation of task rescheduling strategy with resource substitution in cloud manufacturing", *Mathematical Biosciences and Engineering*, Vol. 20, No. 2, (2023), 3120-3145. doi: 10.3934/mbe.2023147.

9. Zhang, X., Han, Y., Królczyk, G., Rydel, M., Stanislawski, R. and Li, Z., "Rescheduling of distributed manufacturing system with machine breakdowns", *Electronics*, Vol. 11, No. 2, (2022), 249. https://doi.org/10.3390/electronics11020249

10. Liu, Y., Xu, X., Zhang, L., Wang, L. and Zhong, R.Y., "Workload-based multi-task scheduling in cloud manufacturing", *Robotics and Computer-integrated Manufacturing*, Vol. 45, No., (2017), 3-20. https://doi.org/10.1016/j.rcim.2016.09.008

11. Yang, B., Wang, S., Cheng, Q. and Jin, T., "Scheduling of field service resources in cloud manufacturing based on multi-population competitive-cooperative gwo", *Computers & Industrial Engineering*, Vol. 154, (2021), 107104. https://doi.org/10.1016/j.cie.2021.107104

12. Liu, Z., Guo, S., Wang, L., Du, B. and Pang, S., "A multi-objective service composition recommendation method for individualized customer: Hybrid mpa-gso-dnn model", *Computers & Industrial Engineering*, Vol. 128, (2019), 122-134. https://doi.org/10.1016/j.cie.2018.12.042

13. Zhou, J. and Yao, X., "A hybrid artificial bee colony algorithm for optimal selection of qos-based cloud manufacturing service composition", *The International Journal of Advanced Manufacturing Technology*, Vol. 88, (2017), 3371-3387. https://doi.org/10.1007/s00170-016-9034-1

14. Zhou, L., Zhang, L. and Ren, L., "Simulation model of dynamic service scheduling in cloud manufacturing", in IECON 2018-44th Annual Conference of the IEEE Industrial Electronics Society, IEEE. (2018), 4199-4204.

15. Zhou, L., Zhang, L., Sarker, B.R., Laili, Y. and Ren, L., "An event-triggered dynamic scheduling method for randomly arriving tasks in cloud manufacturing", *International Journal of Computer Integrated Manufacturing*, Vol. 31, No. 3, (2018), 318-333. https://doi.org/10.1080/0951192X.2017.1413252

16. Serrano-Ruiz, J.C., Mula, J. and Poler, R., "Smart manufacturing scheduling: A literature review", *Journal of Manufacturing Systems*, Vol. 61, (2021), 265-287. https://doi.org/10.1016/j.jmsy.2021.09.011

17. Yuan, M., Zhou, Z., Cai, X., Sun, C. and Gu, W., "Service composition model and method in cloud manufacturing", *Robotics and Computer-integrated Manufacturing*, Vol. 61, (2020), 101840. https://doi.org/10.1016/j.rcim.2019.101840

18. Wang, T., Zhang, P., Liu, J. and Zhang, M., "Many-objective cloud manufacturing service selection and scheduling with an evolutionary algorithm based on adaptive environment selection

19. strategy", *Applied Soft Computing*, Vol. 112, (2021), 107737. https://doi.org/10.1016/j.asoc.2021.107737

19. Champati, J.P. and Liang, B., "Delay and cost optimization in computational offloading systems with unknown task processing times", *IEEE Transactions on Cloud Computing*, Vol. 9, No. 4, (2019), 1422-1438. doi: 10.1109/TCC.2019.2924634.

20. Liu, Y., Liang, H., Xiao, Y., Zhang, H., Zhang, J., Zhang, L. and Wang, L., "Logistics-involved service composition in a dynamic cloud manufacturing environment: A ddpg-based approach", *Robotics and Computer-integrated Manufacturing*, Vol. 76, (2022), 102323. https://doi.org/10.1016/j.rcim.2022.102323

21. Rao, R.V., "Jaya: An advanced optimization algorithm and its engineering applications", (2019).

22. Rao, R.V., Savsani, V.J. and Vakharia, D., "Teaching–learning-based optimization: A novel method for constrained mechanical design optimization problems", *Computer-aided Design*, Vol. 43, No. 3, (2011), 303-315. https://doi.org/10.1016/j.cad.2010.12.015

23. Rao, R., "Jaya: A simple and new optimization algorithm for solving constrained and unconstrained optimization problems", *International Journal of Industrial Engineering Computations*, Vol. 7, No. 1, (2016), 19-34. doi: 10.5267/j.ijiec.2015.8.004.

24. Yang, C., Peng, T., Lan, S., Shen, W. and Wang, L., "Towards iot-enabled dynamic service optimal selection in multiple manufacturing clouds", *Journal of Manufacturing Systems*, Vol. 56, No., (2020), 213-226. doi. https://doi.org/10.1016/j.jmsy.2020.06.004 23

25. Xie, N., Tan, W., Zheng, X., Zhao, L., Huang, L. and Sun, Y., "An efficient two-phase approach for reliable collaboration-aware service composition in cloud manufacturing", *Journal of Industrial Information Integration*, Vol. 23, No., (2021), 100211. doi. https://doi.org/10.1016/j.jii.2021.10021124

26. Li, Y., Yao, X. and Liu, M., "Cloud manufacturing service composition optimization based on reliability and credibility analysis", *Computer Integrated Manufacturing Systems*, Vol. 27, No. 6, (2021), 1-33. doi. https://doi.org/10.1155/2019/7194258

27. Chen, S., Fang,S.,Tang, R., , "An ann-based approach for real-time scheduling in cloud manufacturing", *Applied Sciences*, Vol. 10 No. 7, (2020). doi: 10.3390/app10072491.

28. Zheng, X. and Zhang, X., "Robustness of cloud manufacturing system based on complex network and multi-agent simulation", *Entropy*, Vol. 25, No. 1, (2022), 45. doi: 10.3390/e25010045.

29. Arkat, J., Rahimi, V. and Farughi, H., "Reactive scheduling addressing unexpected disturbance in cellular manufacturing systems", *International Journal of Engineering, Transactions A: Basics,*, Vol. 34, No. 1, (2021), 162-170. doi: 10.5829/ije.2021.34.01a.18.

30. Puspitasari, K.M.D., Raharjo, J., Sastrosubroto, A.S. and Rahmat, B., "Generator scheduling optimization involving emission to determine emission reduction costs", *International Journal of Engineering, Transactions B: Applications*, Vol. 35, No. 8, (2022), 1468-1478. doi: 10.5829/ije.2022.35.08b.02.

31. Nikaeen, R. and Najafi, A., "A constraint programming approach to solve multi-skill resource-constrained project scheduling problem with calendars", *International Journal of Engineering, Transactions B: Applications*, Vol. 35, No. 8, (2022), 1579-1587. doi: 10.5829/ije.2022.35.08b.14.

32. Torkashvand, M., Ahmadizar, F. and Farughi, H., "Distributed production assembly scheduling with hybrid flowshop in assembly stage", *International Journal of Engineering, Transactions B: Applications*, Vol. 35, No. 5, (2022), 1037-1055. doi: 10.5829/ije.2022.35.05b.19.

33. Maghzi, P., Mohammadi, M., Pasandideh, S. and Naderi, B., "Operating room scheduling optimization based on a fuzzy uncertainty approach and metaheuristic algorithms",

International Journal of Engineering, Transactions B: Applications,   Vol. 35, No. 2, (2022), 258-275. doi: 10.5829/ije.2022.35.02b.01.

34. Halty, A., Sánchez, R., Vázquez, V., Viana, V., Pineyro, P. and Rossit, D.A., "Scheduling in cloud manufacturing systems: Recent systematic literature review", (2020). doi: 10.3934/mbe.2020377.

35. Rashidifar, R., Chen, F.F., Bouzary, H. and Shahin, M., A mathematical model for cloud-based scheduling using heavy traffic limit theorem in queuing process, in Flexible automation and intelligent manufacturing: The human-data-technology nexus: Proceedings of faim 2022, june 19–23, 2022, detroit, michigan, USA. 2022, Springer.197-206.

36. Abtahi, Z., Sahraeian, R. and Rahmani, D., "A stochastic model for prioritized outpatient scheduling in a radiology center", *International Journal of Engineering Transactions A: Basics*, Vol. 33, No. 4, (2020). doi: 10.5829/ije.2020.33.04a.11.

37. Yazdi, M., Zandieh, M. and Haleh, H., "A mathematical model for scheduling elective surgeries for minimizing the waiting times

in emergency surgeries", *International Journal of Engineering, Transctions C: Aspects*, Vol. 33, No. 3, (2020), 448-458. doi: 10.5829/ije.2020.33.03c.09.

38. Simon, D., "Evolutionary optimization algorithms, John Wiley & Sons, (2013).

39. Gao, K., Yang, F., Zhou, M., Pan, Q. and Suganthan, P.N., "Flexible job-shop rescheduling for new job insertion by using discrete jaya algorithm", *IEEE Transactions on Cybernetics*, Vol. 49, No. 5, (2018), 1944-1955. doi: 10.1109/TCYB.2018.2817240.

40. Rao, R.V., Rai, D.P. and Balic, J., "A multi-objective algorithm for optimization of modern machining processes", *Engineering Applications of Artificial Intelligence*, Vol. 61, (2017), 103-125. https://doi.org/10.1016/j.engappai.2017.03.001

41. Deb, K., Pratap, A., Agarwal, S. and Meyarivan, T., "A fast and elitist multiobjective genetic algorithm: Nsga-ii", *IEEE Transactions on Evolutionary Computation*, Vol. 6, No. 2, (2002), 182-197. doi: 10.1109/4235.996017.

Persian Abstract

چکیده

CMfg یک مدل ساخت پیشرفته جدید است که با کمک فناوری‌های اطلاعات سازمانی تحت پشتیبانی رایانش ابری، اینترنت اشیا و فناوری‌های مبتنی بر خدمات توسعه یافته است. CMfg منابع تولیدی متعددی را برای ارائه خدمات کارآمد و ارزشمند تشکیل می دهد. CMfg محیطی بسیار پویا دارد. در این محیط، اختلالات یا اتفاقات زیادی ممکن است رخ دهد که سیستم را به موقعیت های برنامه ریزی نشده سوق دهد. در CMfg، یک سری از ارائه دهندگان خدمات برای تولید برنامه ریزی شده اند. در حین عملیات تولید ممکن است برخی از آنها آسیب ببینند، متوقف شوند و از سرویس خارج شوند. لذا برای ادامه فرآیند تولید طبق قراردادهای منعقده و زمانبندی اولیه، زمانبندی مجدد ضروری است. هنگامی که هر گونه اختلال یا رویداد دیگری رخ می دهد، از تکنیک های زمان بندی مجدد برای به روز رسانی برنامه اولیه استفاده می شود. در این مقاله، مسئله زمان‌بندی مجدد دینامیک در CMfg تحلیل می‌شود. سپس زمان بندی مجدد چند هدفه در CMfg مدل شده و به عنوان یک مسئله بهینه سازی چند هدفه تعریف می شود. تعریف این مسئله به عنوان یک مسئله بهینه سازی چندهدفه امکان اعمال، بررسی و مقایسه الگوریتم های مختلف را فراهم می کند. برای حل این مشکل، روش‌های بهینه‌سازی قبلی بهبود یافته و یک الگوریتم چندهدفه و نخبه‌گرا بر اساس الگوریتم جایا به نام الگوریتم پیشرفته چندهدفه نخبه‌گرا جایا (AMEJ) پیشنهاد شد. چندین آزمایش برای تأیید عملکرد الگوریتم پیشنهادی انجام شده است. نتایج محاسباتی نشان داد که الگوریتم پیشنهادی در مقایسه با سایر الگوریتم‌های بهینه‌سازی چندهدفه بهتر عمل می‌کند.

International Journal of Engineering

J o u r n a l   H o m e p a g e :   w w w . i j e . i r

Optimal Filter Length Selection for Universal Filtered Multicarrier Systems

R. Manda*[a], A. Kumar[a], R. Gowri[b]

[a] Department of Electrical and Electronics Engineering, School of Engineering, University of Petroleum & Energy Studies, Dehradun, India
[b] Department of Electronics and Communication Engineering, Graphic Era Hill University, Dehradun, India

A B S T R A C T

Future wireless networks will use Universal Filtered Multicarrier (UFMC) as a new waveform modulation technique. The UFMC waveform sensibly considers the sub-band filter specifications such as filter order, and shape to combine the key benefits of the present generation modulation waveforms while averting their disadvantages. Therefore, in UFMC-based systems, it is important to pay attention to how the sub-band filter is made. In this paper, the sub-band filter configuration is adapted according to the sub-band size such that the UFMC symbol generates the minimum level of interference with minimum frequency selectivity. Also, the total interference caused by inter-carrier interference (ICI) and inter-sub-band interference (ISBI) was studied by finding the closed form of its change in the UFMC signal with sub-band size and filter length. From this analysis, we determined the ICI increases and ISBI decreases with filter length. Therefore, the proposed method optimizes the filter length in terms of sub-band size and interference. By this approach, the filter length is shorter than the conventional method and hence improves the symbol utilization. With the proposed method, the overall signal-to-interference ratio (SIR) improved by 1 to 3 dB.

doi: 10.5829/ije.2023.36.07a.13

1. INTRODUCTION

The fast growth in smart terminals, real-time interactive services, and the internet of everything (IoE) inspired the evolution of fifth generation (5G) networks. The key technical challenges for realizing this future network include the physical layer transmission techniques that are required to support efficient spectrum utilization to get full data rate, lower system implementation complexity, lower out-of-band emission (OBE) to minimize the interference, ultra-low latency, and artificial intelligence (AI) based estimation algorithms [1-3]. In the present broadband wireless system, Orthogonal Frequency Division Multiplexing (OFDM) is one of the most frequently used modulation waveforms. However, OFDM has several weaknesses, such as large sidelobes, high bandwidth usage, and severe synchronization requirements, which makes it ineffective for 5G and beyond. For wide-area IoT applications, the communication link must support in-depth coverage, low power consumption, and low implementation complexity

[4]. These limitations enforce to design of a new and flexible modulation waveform that needs to support asynchronous transmission, lower side lobes, and reduced latency with less baseband system complexity [5-9]. In the last few years, several waveform candidates such as Generalized Frequency Division Multiplexing (GFDM) [10], Filter Bank Multicarrier (FBMC) [11], Filtered OFDM [12], and UFMC [13] have been proposed for next-generation wireless systems with a lower OBE. Among them, the UFMC waveform is the most recommended candidate waveform in the 5G and beyond 5G wireless systems to meet the main key performance parameters such as lower OBE, flexible packet transmission, and highly suitable for short packet transmission [14, 15].

The UFMC waveform is a combined form of FBMC and F-OFDM, in which, a group of subcarriers (SCs) is filtered individually to make it more robust in relaxed synchronization conditions compared to OFDM. The sub-band filtering can be physical resource block (PRB) based, service-based, and user-based [16, 17]. The

---

UFMC is suitable for PRB-based sub-band filtering and massive machine-type communications. In case of the multi-service or multi-user approach the signaling overhead may save but the sub-band filtering disrupts the orthogonality between the subcarriers and introduces inter-carrier interference (ICI) and inter-sub band/service interference (ISBI). In addition, the UFMC system has a higher baseband complexity and computation complexity than traditional OFDM because of the quantity of IFFT blocks and sub-band filters. This computational complexity reduced with different approaches like simplified the baseband UFMC symbol to reduce the number of arithmetic operations discussed in literature [18-22]. Like a cyclic prefix (CP) in OFDM, the subband filter protects against multipath fading and inter-symbol interference (ISI) in the UFMC system. However, on both sides of the symbol, the ramp (filter tail) of the sub-band filter causes interference on neighboring sub-bands, which depends on the filter length. In practice, the sub-band filter length is preferred longer or equal to the wireless channel length to avoid the multipath fading effect [13]. But, in some scenarios, the short filter length can be sufficient to get marginal system performance, which means further the system overhead can be reduced reasonably.

Recently, there are several filter optimization and baseband signal processing approaches have been proposed to mitigate the interference in the UFMC system [23-29]. Mukherjee et al. [23], Wang et al. [30]optimized the sub-band FIR filter based on the knowledge of expected timing offset and frequency offset to reduce the out-band radiation and hence reduced the ISBI. In this method of approach, the filter is fixed and chosen arbitrary without knowledge of the adjacent sub-bands. The active interference cancellation approach is suggested by Zhang et al. [24] uses a separate subcarrier on either side of the sub-band for interference cancellation and optimizing their weights within the power constraints to maximize the overall signal-to-interference ratio (SIR). With this approach, the spectral efficiency degraded due to the use of dedicated subcarriers to cancel interference. An adaptive modulation and filter configuration was proposed by Chen et al. [25], which adaptively determined the sub-band filter impulse response parameters to reduce the interference caused by carrier frequency offset (CFO). This method used some guard band between adjacent sub-bands that causes reduction in spectral usage with better BER performance compared to the conventional method.

From the above literature, all the methods optimized the filter configuration to reduce the interference due to out of band emission, CFO and timing offset. some of these methods used extra subcarrier or guard interval, because of this the symbol utilization degraded. In this article, the filter length is adapted according to the sub-band width to minimize interference without degrading the symbol utilization. Additionally, we derived the closed form for the interference in the UFMC symbol due to filtering operation and then optimize the filter length for sub-band size. Here, each user's sub-carriers (sub-band size) allocation is determined by the service they seek, such as data, streaming video, or online interactive gaming. As a result, each sub-band has a different length and the correspondingly filter length varies. Here, the proposed method does not use any guard interval between adjacent sub-band. Consequently, the sub-band filter performs fewer calculations, increasing the symbol utilization ratio.

Following are the remaining sections of the paper: The discussion of the UFMC transmitter model and its symbol model is given in section 2. Concerning the filter length and sub-band size, Section 3 focuses on the analysis of ISBI and ICI fluctuation and covers the computation of filter parameters for 5G-NR numerology. Section 4 covers the results and discussion section, and the performance comparison of the UFMC system. Section 5 is devoted to conclusion.

2. UFMC WAVEFORM MODEL

An overview of the UFMC system model can be seen in Figure 1. The basic principle of the UFMC modulator is to divide the total number of data subcarriers N_{DC} (bandwidth) into a group of consecutive subcarriers (known as sub-band), a specific constellation modulated (Quadrature Amplitude Modulation (QAM)) data samples allocated to each sub-band and then performed N-point IFFT after subcarrier mapping on a total number of subcarriers (N) and zeros padded to the unallocated subcarriers. These time-domain sub-band signals are filtered individually with an FIR filter and summed to generate the UFMC signal. In the case of a multi-service/user-based communication system, multiple PRBs allocated to each user or service are considered sub-band.

Consider the UFMC system with B sub-bands and Q_p subcarriers in each sub-band i.e., $\sum_{p=0}^{B-1} Q_p = N_{DC}; p = 0, 1, \dots, B - 1$. The result of the subband filtering operation, which is the linear convolution of the sub-band signal $s_p(n)$ and the impulse response of the subband filter $f_p(n)$.

$$x_p(n) = \sum_{l=0}^{L_f - 1} f_p(l) s_p(n - l) = 0, 1, \dots, N + L_f - 2 \quad (1)$$

It is possible to express the final UFMC signal as:

$$x(n) = \sum_{p=0}^{B-1} \sum_{l=0}^{L_f - 1} f_p(l) s_p(n - l) \quad (2)$$

where L_f is the subband FIR filter length, $f_p(l)$ represents the filter impulse response of pth sub-band, which is the center frequency shifted of the prototype filter impulse response $(f(l))$ corresponding to the sub-band. That is:
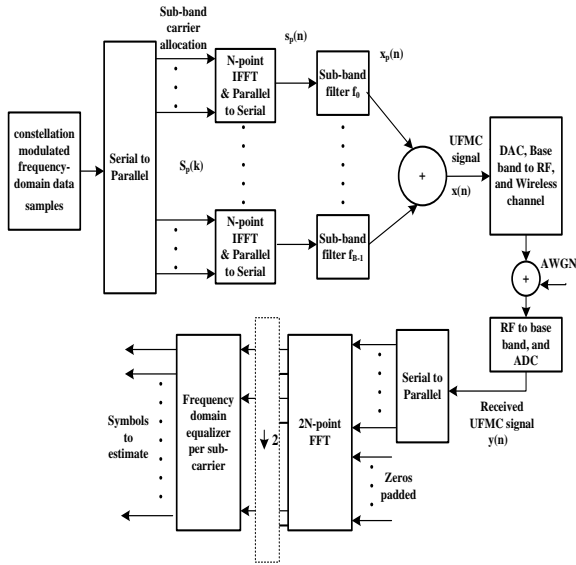
Figure 1. The UFMC system model

(a) PRB based sub-band filtering

Inter sub-band/ service/user interference

(b) User based sub-band filtering

Figure 2. Types of sub-band filtering

$$f_p(l) = f(l)e^{\frac{j2\pi}{N}(K_0+K_{pshift})l} \; ; \; l = 0, 1, \dots, L_f - 1 \qquad (3)$$

where, $K_{pshift} = \sum_{b=0}^{p-1} Q_b + Q_p/2;$ $\quad K_0 = \frac{N-N_{DC}}{2}$ signifies the beginning subcarrier index of the lowest possible sub-band of the UFMC signal. Generally, the filter length for a different sub-band is not necessarily the same. The time-domain sub-band signal $s_p(n)$ represents the N-point IFFT of pth sub-band written as:

$$s_p(n) = \frac{1}{N}\sum_{k=0}^{Q_p-1} S_p(k)e^{j\frac{2\pi}{N}(K_0+K_p+k)n} \qquad (4)$$

where the sequence $S_p(k)$ represents the pth sub-band data samples and $K_p = \sum_{b=0}^{p-1} Q_b$. At the receiver, unlike CP-OFDM, the UFMC uses the complete symbol duration of samples. Therefore, the received UFMC symbol is padded with a sufficient number of zeros for processing through 2N-point FFT. After execution of the 2N-point FFT, the even subcarriers were extracted for data detection (down sampled by a factor of 2).

3. ADAPTIVE SUB-BAND FILTER DESIGN

As we know that the FIR filtering operations provide less OBE and robustness in a relaxed synchronized system. But the filtering operation disrupts the orthogonality between the sub-carriers and causes interference. In general, the PRB-based sub-band filtering is most preferable to implemented in the UFMC waveform. In the case of multi-user and multi-services, there is design flexibility in the UFMC waveform to allocate multiple PRBs such that each service support multiple users, and one or more consecutive PRBs can be allocated to each
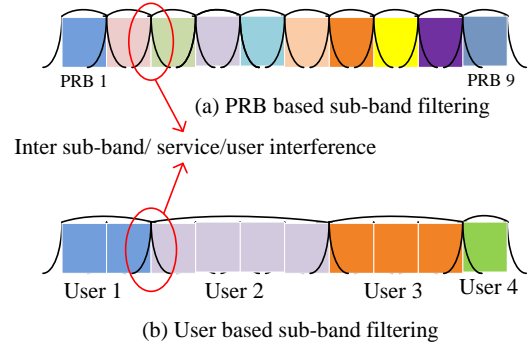
user as shown in Figure 2. The inter-symbol interference (ISI) can be minimized by sub-band filtering operation in the UFMC system, but it might be causing some significant ISBI in the case of multi-service or multi-user systems. On the other hand, for the non-adjacent sub-bands/services, the ISBI is insignificant and does not affect the system performance.

3. 1. Interference in the UFMC Symbol As stated earlier, non-orthogonality brought on by filtering operations may cause interference between nearby subcarriers and sub-bands. To analyze the interference, let us define the ISBI and ICI in terms of desired data symbols and sub-band filter metrics. Consider the following assumptions for formulation and simplification:

Assumption 1. The modulated data symbols mapping on subcarriers are uncorrelated with each other, and have zero mean (i.e., $E[S_p(k)] = 0$ and variance $E\left[|S_p(k)|^2\right] = \sigma_{S_p}^2$

Assumption 2. The sub-band filter coefficients are normalized to have $\sum_{l=0}^{L-1}|f_p(l)|^2 = 1$

Consider the energy of the UFMC symbol given as follows:

$$E_{UFMC} = \sum_{n=0}^{N+L-2}|x(n)|^2 \qquad (5)$$

The energy of the UFMC symbol can be expressed as:

$$E_{UFMC} = \sum_{n=0}^{N+L_f-2} x(n)\, x^*(n) = \\ \sum_{n=0}^{N+L_f-2}\left(\sum_{p=0}^{B-1} x_p(n)\right)\left(\sum_{q=0}^{B-1} x_q^*(n)\right) = E_{SB} + E_{ISBI} \qquad (6)$$

where x*(n) represents the complex conjugative of x(n). By substituting Equation (1) in Equation (9), the UFMC symbol energy can be composed of two components, one is the total sub-band energy (E_{SB}) for $p = q$ and another one is the ISBI component (E_{ISBI}) for $p \neq q$. These energy components can be expressed as:

$$E_{SB} = \sum_{p=q=0}^{B-1}\sum_{n=0}^{N+L_f-2}|x_p(n)|^2 = \\ \sum_{n=0}^{N+L_f-2}\sum_{p=0}^{B-1}\sum_{l=0}^{L_f-1}|f_p(l)|^2 R_{S_p,S_p} \qquad (7)$$

$$E_{ISBI} = \sum_{n=0}^{N+L_f-2} \sum_{p=0}^{B-1} \sum_{\substack{q=0 \\ q\neq p}}^{B-1} x_p(n)\, x_q{}^*(n) =$$
$$\sum_{n=0}^{N+L_f-2} \sum_{p=0}^{B-1} \sum_{\substack{q=0 \\ q\neq p}}^{B-1} \sum_{l=0}^{L_f-1} f_p(l) f_q{}^*(l) R_{s_p,s_q} \tag{8}$$

where, R_{s_p,s_q} is the correlation sequence of the two different time-domain sub-band data sequence $s_p(n)$ and $s_q(n)$, which can be defined as $R_{s_p,s_q} = s_p(n-l) s_q{}^*(n-l)$. By substituting Equation (3) here, we get:

$$R_{s_p,s_q} =$$
$$\frac{1}{N^2} \sum_{k=m=0}^{\min(Q_p,Q_q)} S_p(k) S_q{}^*(k)\; e^{j\frac{2\pi}{N}(K_p-K_q)(n-l)} +$$
$$\frac{1}{N^2} \sum_{k=0}^{Q_p-1} \sum_{\substack{m=0 \\ m\neq k}}^{Q_q-1} S_p(k) S_q{}^*(m)\; e^{j\frac{2\pi}{N}(K_p-K_q+k-m)(n-l)} \tag{9}$$

$$R_{s_p,s_q} =$$
$$\frac{1}{N^2} e^{j\frac{2\pi}{N}(K_p-K_q)(n-l)} \left(\sum_{k=0}^{\min(Q_p,Q_q)} S_p(k) S_q{}^*(k) + \right.$$
$$\left. \sum_{k=0}^{Q_p-1} \sum_{\substack{m=0 \\ m\neq k}}^{Q_q-1} S_p(k) S_q{}^*(m)\; e^{j\frac{2\pi}{N}(k-m)(n-l)} \right) \tag{10}$$

Since the modulated data sequences (frequency-domain data sequences) are uncorrelated or low correlated for $p \neq q$ and $k \neq m$. Therefore, neglecting the second term in Equation (10) we have:

$$R_{s_p,s_q} = \frac{1}{N^2} e^{j\frac{2\pi}{N}(K_p-K_q)(n-l)} \sum_{k=0}^{\min(Q_p,Q_q)} S_p(k) S_q{}^*(k) \tag{11}$$

For p = q the Equation (11) can be written as:

$$E_{ICI} = \frac{1}{N^2} \sum_{p=0}^{B-1} \sum_{k=0}^{Q_p-1} \sum_{\substack{m=0 \\ m\neq k}}^{Q_p-1} S_p(k) S_p{}^*(m) \sum_{n=0}^{N+L_f-2} e^{j\frac{2\pi}{N}(k-m)n} E_{fp}(k,m) \tag{17}$$

where

$$E_{fp}(k,m) = \sum_{l=0}^{L-1} |f_p(l)|^2\; e^{-j\frac{2\pi}{N}((k-m)l)} \tag{18}$$

$$E_{ISBI} = \frac{1}{N^2} \sum_{p=0}^{B-1} \sum_{\substack{q=0 \\ q\neq p}}^{B-1} \sum_{l=0}^{L-1} |f(l)|^2\; e^{-j\frac{2\pi}{N}\left(\frac{Q_p-Q_q}{2}\right)l} \sum_{n=0}^{N+L_f-2} e^{j\frac{2\pi}{N}(K_p-K_q)n} \sum_{k=0}^{\min(Q_p,Q_q)} S_p(k) S_q{}^*(k) \tag{19}$$

According to Equations (17) and (19), the size of the sub-band and the sub-band filter ramps have an impact on both ICI and ISBI. The filter ramps depend on the filter length, which is usually recommended to choose more than the channel length (CP length) to mitigate the multipath channel dispersion. The multipath channel effects may be partially mitigated by the filter ramp-up and ramp-down, but ISI cannot be fully removed. The sub-band filter length decides the level of non-orthogonality factor between subcarriers, the OBE, and hence the interference (ISBI and ICI). To maintain a low degree of interference, the sub-band filter order is adjusted in this article for the sub-band size. In other

$$R_{s_p,s_p} = \frac{1}{N^2} \left(\sum_{k=0}^{Q_p-1} |S_p(k)|^2 + \right.$$
$$\left. \sum_{k=0}^{Q_p-1} \sum_{\substack{m=0 \\ m\neq k}}^{Q_q-1} S_p(k) S_p{}^*(m)\; e^{j\frac{2\pi}{N}(k-m)(n-l)} \right) \tag{12}$$

From (3), we have:

$$f_p(l) f_q{}^*(l) = |f(l)|^2\; e^{j\frac{2\pi}{N}\left(K_p-K_q+\frac{Q_p-Q_q}{2}\right)l} \tag{13}$$

Substitute Equation (12) in Equation (7), the total sub-band energy can be written as:

$$E_{SB} =$$
$$\sum_{n=0}^{N+L_f-2} \sum_{p=0}^{B-1} \sum_{l=0}^{L_f-1} |f_p(l)|^2\; \frac{1}{N^2} \left(\sum_{k=0}^{Q_p-1} |S_p(k)|^2 + \right.$$
$$\left. \sum_{k=0}^{Q_p-1} \sum_{\substack{m=0 \\ m\neq k}}^{Q_q-1} S_p(k) S_p{}^*(m)\; e^{j\frac{2\pi}{N}(k-m)(n-l)} \right) \tag{14}$$

According to Equation (14), the total sub-band energy E_{SB} can be divided into two components: the sub-carrier energy (E_{SC}) component for $k = m$ and the ICI component (E_{ICI}) for $k \neq m$. Therefore, the complete UFMC symbol energy becomes:

$$E_{UFMC} = E_{SC} + E_{ICI} + E_{ISBI} \tag{15}$$

From Assumption 2 and $N \gg L_f$, the total desired data subcarriers energy of the UFMC symbol is given as:

$$E_{SC} =$$
$$\frac{1}{N^2} \sum_{n=0}^{N+L_f-2} \sum_{p=0}^{B-1} \sum_{l=0}^{L_f-1} |f_p(l)|^2\; \sum_{k=0}^{Q_p-1} |S_p(k)|^2 =$$
$$\frac{N+L_f-1}{N^2} \sum_{p=0}^{B-1} \sum_{k=0}^{Q_p-1} |S_p(k)|^2 \tag{16}$$

and

Substituting Equations (12) and (14) in Equation (9), the inter-sub-band interference energy can be written as:

words, depending on the sub-band width, the filter length or tail in the symbol duration can be adjustable. Therefore, the filter length design is an important part of the UFMC system. In the following subsection, we focus on the filter length selection according to the sub-band size.

3. 2. Filter Length Design for Sub-band Filter
The sub-band filter design flexibility is one of the most significant advantages of the UFMC waveform compared to others, which enables to adjustment of the sub-band filtering configuration according to the requirement of service, user, and channel conditions. The Gibb's

phenomenon states that the magnitude response of the filter exhibits nearly the same oscillatory behavior (i.e., ripples) after a limited value of its order. From this vantage point, we suggested an approach that modifies the FIR filter order about sub-band size, while maintaining a minimum level of OBE. In general, tolerance schemes have been used to build filter design algorithms because they give a close approximation of the ideal filter frequency response. The FIR filter design depends on the following parameters: passband (f_p) and stopband edge frequencies (f_s), maximum absolute errors known as ripples in the passband and stopband (δ_p and δ_s) and filter length (L). The sub-band filter length (L) [31] is defined approximately as:

$$L = \frac{-10\log(\delta_p\delta_s)-13}{14.36\,\Delta f} + 1 \qquad (20)$$

where Δf represents the normalized transition width, which is defined as the difference between stopband edge frequency and passband edge frequency $i.e., \Delta f = \frac{(f_s-f_p)}{F_s}$. The passband and stopband edge frequencies can be defined based on the bandwidth requirements of the sub-band/ service. The bandwidth (BW) of the filter is defined from the number of subcarriers allocated to the sub-band as $BW = Qf_{sc}$, where f_{sc} is the subcarrier spacing, typically an integer multiple of 15 kHz according to the 5G NR numerology. The lower (f_l) and upper (f_h) passband edge frequencies of the sub-band are defined as:

$$f_l = K_0 f_{sc} \ and \ f_h = (K_0 + Q_p)f_{sc} \qquad (21)$$

Here the stopband frequency is determined from the general filter assumption, i.e., half of the sampling frequency $\frac{F_s}{2}$ or the guard band between the sub-band or service bands i.e., $f_s = \frac{N}{2} f_{sc}$ and $\Delta f = \frac{1}{2} - \frac{K_0+Q_p}{N}$. Substitute Δf in Equation (20), we get:

$$L = \frac{N(-10\log(\delta_p\delta_s)-13)}{7.18(N-K_0-Q_p)} \qquad (22)$$

The sub-band filter length decides the level of non-orthogonality factor between subcarriers, the OBE, and hence the interference (ISBI and ICI). In this paper, the sub-band FIR filter order is adapted for the sub-band size as mentioned in Equation (22) to maintain a minimum level of interference. That is the filter length or tail in the symbol duration due to filtering operation can be flexible based on the sub-band width.

4. SIMULATION RESULTS AND DISCUSSION

From the discussion in Section 3, the system performance is affected by the sub-band filter design for a given width of the sub-band in different ways. In this section, the performance of the proposed method is evaluated through MATLAB simulation under various scenarios. To demonstrate the results clearly without sacrificing their generality, we adopted the 3GPP bandwidth configuration/ radio frame structure, i.e., the channel bandwidth of 10 MHz, 15 kHz subcarrier spacing, 624 data subcarriers, and the IFFT length N = 1024 for all simulation results. Let consider two different cases with different sub-band sizes (Q= 12 SCs and 36 SCs with 5 sub-bands) as shown in Figure 3. The first case depicted in Figure 3(a), here the sub-band ramps (i.e., OBE) due to filtering operation extended to more than one sub-band for smaller sub-band size (Q), and the power distribution among the subcarriers in a sub-band is approximately equal. This results in less frequency selectivity and there is a high likelihood of accurate data detection in the sub-band with a higher signal-to-interference ratio (SIR). In the second case (i.e., for larger sub-band sizes) shown in Figure 3(b), the ramp spread is less than one adjacent sub-band with a fixed filter length and ineffective power distribution along the subcarriers in a sub-band. Which leads to greater frequency selectivity and reduced performance.
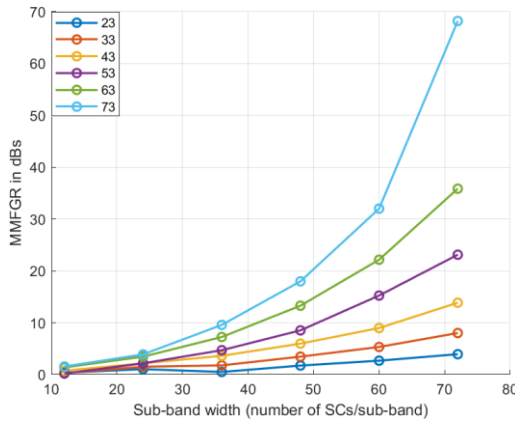

(a) 5 SB, 12 SCs each

(b) 5 SB, 36 SCs each
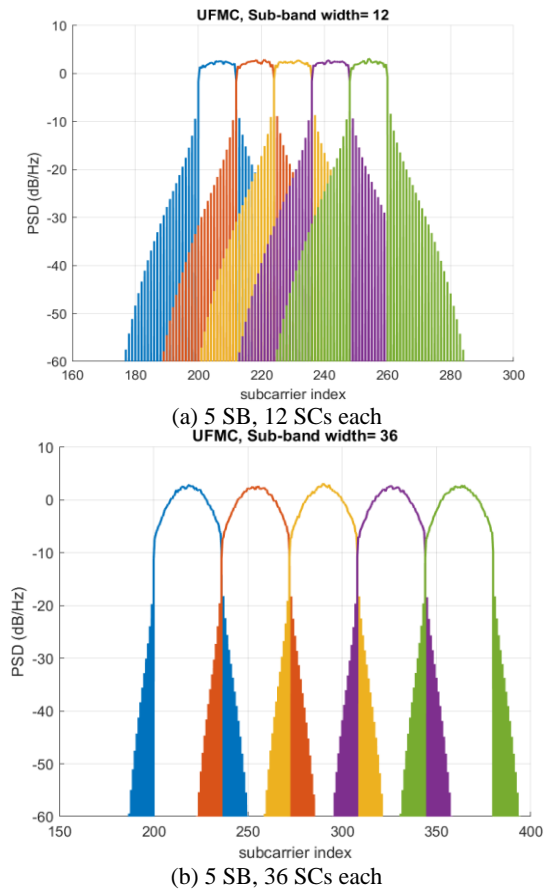
Figure 3. Power spectral density of the UFMC signal with the following specifications: 64-QAM, filter length (L_f) = 73, and N = 1024

The maximum to minimum filter gain ratio (MMFGR) can be used to define the frequency selectivity of the sub-band response shown in Figure 4. It is clear from Figure 4, for a fixed sub-band size, the MMFGR increases with filter length and for a fixed filter length, the MMFGR increase with sub-band width. The UFMC system with a longer filter length results in a larger MMFGR (i.e., non-uniform power allocation among the subcarriers within a sub-band and higher at the middle of the sub-band) and higher frequency selectivity, but it leads to a high possibility of error at the edges of the sub-band and causes a greater overall performance loss in terms of SNR. The higher value of MMFGR may also be impact on the best pilot pattern design to estimate channel impulse response and frequency offset error. Pilots should be assigned to the subcarriers with the highest filter gain (i.e., in the middle of one sub-band). This may increase the complexity of estimation algorithms at the receiver.

For instance, to obtain a specific MMFGR for a particular total number of subcarriers and filter length, we can choose the suitable sub-band bandwidth. Similarly, it is simple to calculate the corresponding MMFGR for a particular filter length and sub-band bandwidth, which can be used to assess the performance loss. To maintain a minimum level of MMFGR, here the filter length is adapted according to the allocated bandwidth of sub-bands and analyzed the variation of the interference with respect to filter length and sub-band width.

Figure 5 shows the variation of ISBI and ICI for simulation parameters (adopt from the 3GPP band configuration of 10 MHz bandwidth with 15 kHz subcarrier spacing) shown in Table 1. The simulation results from Figure 5 states that the cumulative ISBI decreases with the filter length due to lower OBE, and the ICI increases with filter length due to a higher level of non-orthogonality. In case of both uniform and non-uniform subcarrier allocation, the ISBI decreases, and

ICI increases with the filter length. There is a tradeoff between the interference and the filter length (i.e., the ISBI dominates for a smaller filter length and the ICI dominates for a longer filter length. To reduce this effect the sub-band filter length is dynamically modified with sub-band size to minimize the overall interference in the UFMC symbol according to Equation (22).

Figure 6 simulation results show how average ISBI and ICI vary for sub-band sizes of 12, 36, 48, 72, and 96 with fixed and adaptive filter lengths. From this, we

TABLE 1. Simulation parameters

Parameter Name	Value
IFFT size (N)	1024
Modulation order	64 QAM
Stopband attenuation	40 dB
Sub-band size (Q)	Integer multiple of 12 SC
Filter length (L_f)	73 for conventional Variable for proposed
Wireless channel model	Rayleigh fading
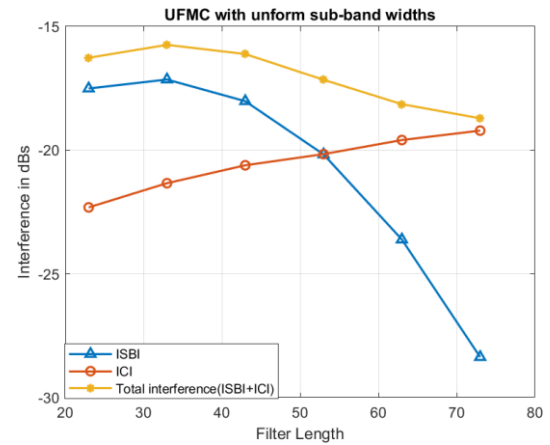
(a) uniform subabd-width allocation
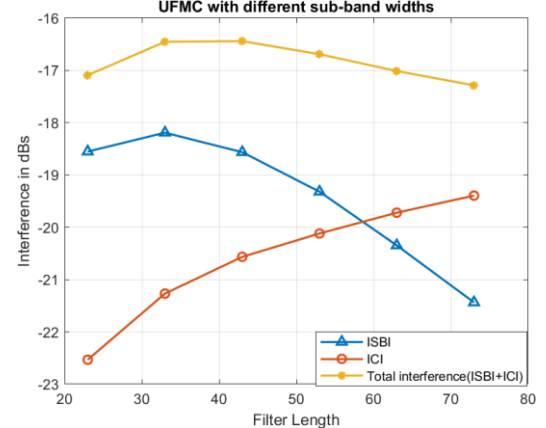
(b) non-uniform subabd-width allocation

Figure 5. Interference variation in the UFMC symbol

Figure 4. MMFGR variation according to the filter length and sub-band width

concluded that the proposed model is superior in terms of ISBI/ICI compared to the conventional UFMC system. With the proposed adaptive filter approach, the total interference (ICI+ISBI) is reduced by around 1.5 to 3 dB than the conventional method as shown in Figure 6(b). Furthermore, the proposed approach gives a better signal-to-interference ratio (SIR) compared to the conventional one as shown in Figure 7. The inclusion of the filter and the unequal power distribution to various subcarriers lead the average BER performance of the UFMC system in one sub-band to be worse than that of the OFDM system. This is because a frequency-selective filter responds more favorably in the middle of the sub-band than at the subcarriers on its edges as shown in Figure 3. As a result, there is a high likelihood of inaccurate detection at the edges, and the response at intermediate subcarriers may occasionally be excessively high.

Figure 8 illustrates the BER performance comparison between proposed and conventional method for the simulation parameters mentioned in Table 1. With the proposed method the filter length selection is based on the sub-band width, and the filter length values are 11, 13 and 15 for the sub-band widths of 12 ,36 and 60 SCs respectively. These values are shorter than the fixed filter length (i.e., 73) approach hence the symbol utilization improved with the proposed method as shown in Table 2.
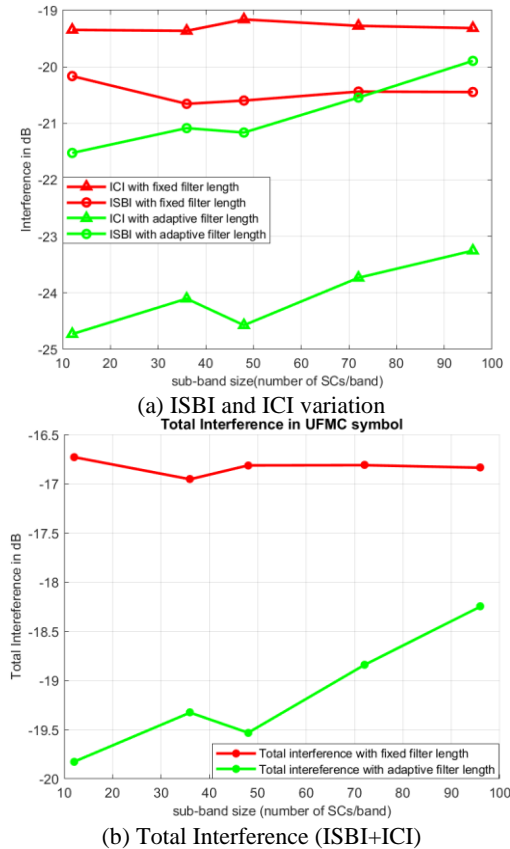

(a) ISBI and ICI variation

(b) Total Interference (ISBI+ICI)

Figure 6. Interference variation with sub-band size
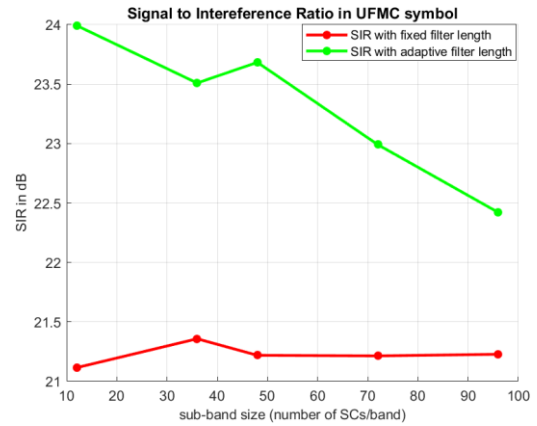

Figure 7. Signal to Interference Ratio versus sub-band size

TABLE 2. Conventional (fixed filter length) versus proposed (adaptive filter length) model

	BW (MHz)/ f_{SC} (kHz)	Data SCs/ IFFT size N	CP length	Filter length			Tail due to filtering
Subcarrier per band				12	36	60	
Conventional [12]	10/ 15	624/ 1024	72		73		72
	100/60	1200/ 2048	144		145		144
Proposed	10/ 15	624/1024	72	11	13	15	10 to 14
	100/60	1200/2048	144	9	11	11	8 to 10
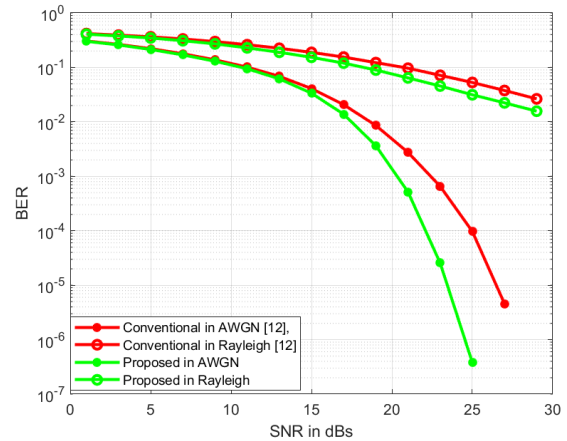
Figure 8. The UFMC system performance

By proposed method, the total interference contributed from ISBI and ICI is less than the conventional fixed filter length method results in improved SIR and hence improved the average BER performance of the system shown in Figure 8. Here, we can observe that the system attained the acceptable BER of 10^{-3} at around 21 dB and 23 dB with proposed and conventional methods, respectively. Finally, the overall simulation results

indicate that the proposed adaptive filter is appropriate for the UFMC system with multi-services.

5. CONCLUSION

The sub-band filtering process may affect the system performance in different ways directly. It is necessary to consider every subcarrier within the sub-band when selecting a filter to achieve a particular performance. Here is an idea for simplifying the filter length choice process in terms of filter response metrics. The filter length is dynamically modified to minimize interference with sub-band width. The resultant filter length obtained from the proposed method is shorter than the conventional fixed length approach. As a result, the SIR improved by 1 to 3 dBs thus improving the BER performance of the UFMC system. The computational complexity due to the filtering operation can be further reduced by applying the machine learning algorithms, this is the future scope of this work in progress.

6. REFERENCES

1. Zhang, P., Li, L., Niu, K., Li, Y., Lu, G. and Wang, Z., "An intelligent wireless transmission toward 6g", *Intelligent and Converged Networks*, Vol. 2, No. 3, (2021), 244-257. doi: 10.23919/ICN.2021.0017.

2. Matthaiou, M., Yurduseven, O., Ngo, H.Q., Morales-Jimenez, D., Cotton, S.L. and Fusco, V.F., "The road to 6g: Ten physical layer challenges for communications engineers", *IEEE Communications Magazine*, Vol. 59, No. 1, (2021), 64-69. doi: 10.1109/MCOM.001.2000208.

3. Yang, P., Xiao, Y., Xiao, M. and Li, S., "6g wireless communications: Vision and potential techniques", *IEEE Network*, Vol. 33, No. 4, (2019), 70-75. doi: 10.1109/MNET.2019.1800418.

4. Singh, S., "Environmental energy harvesting techniques to power standalone iot-equipped sensor and its application in 5g communication", *Emerging Science Journal*, Vol. 4, (2020), 116-126. doi: 10.28991/esj-2021-SP1-08.

5. Wunder, G., Jung, P., Kasparick, M., Wild, T., Schaich, F., Chen, Y., Ten Brink, S., Gaspar, I., Michailow, N. and Festag, A., "5gnow: Non-orthogonal, asynchronous waveforms for future mobile applications", *IEEE Communications Magazine*, Vol. 52, No. 2, (2014), 97-105. doi: 10.1109/MCOM.2014.6736749.

6. Farhang-Boroujeny, B., "Filter bank multicarrier modulation: A waveform candidate for 5g and beyond", *Advances in Electrical Engineering*, Vol. 2014, (2014). doi: 10.1155/2014/482805.

7. Banelli, P., Buzzi, S., Colavolpe, G., Modenini, A., Rusek, F. and Ugolini, A., "Modulation formats and waveforms for 5g networks: Who will be the heir of ofdm?: An overview of alternative modulation schemes for improved spectral efficiency", *IEEE Signal Processing Magazine*, Vol. 31, No. 6, (2014), 80-93. doi: 10.1109/MSP.2014.2337391.

8. Elkourdi, M., Peköz, B., Güvenkaya, E. and Arslan, H., "Waveform design principles for 5g and beyond", in 2016 IEEE 17th annual wireless and microwave technology conference (WAMICON), IEEE., (2016), 1-6.

9. Demir, A.F., Elkourdi, M., Ibrahim, M. and Arslan, H., "Waveform design for 5g and beyond", arXiv preprint arXiv:1902.05999, (2019).

10. Fettweis, G., Krondorf, M. and Bittner, S., "Gfdm-generalized frequency division multiplexing", in VTC Spring 2009-IEEE 69th Vehicular Technology Conference, IEEE., (2009), 1-4.

11. Nissel, R., Schwarz, S. and Rupp, M., "Filter bank multicarrier modulation schemes for future mobile communications", *IEEE Journal on Selected Areas in Communications*, Vol. 35, No. 8, (2017), 1768-1782. doi: 10.1109/JSAC.2017.2710022.

12. Zhang, L., Ijaz, A., Xiao, P., Molu, M.M. and Tafazolli, R., "Filtered ofdm systems, algorithms, and performance analysis for 5g and beyond", *IEEE Transactions on Communications*, Vol. 66, No. 3, (2017), 1205-1218. doi: 10.1109/TCOMM.2017.2771242.

13. Vakilian, V., Wild, T., Schaich, F., ten Brink, S. and Frigon, J.-F., "Universal-filtered multi-carrier technique for wireless systems beyond lte", in 2013 IEEE Globecom Workshops (GC Wkshps), IEEE., (2013), 223-228.

14. Schaich, F. and Wild, T., "Waveform contenders for 5g—ofdm vs. Fbmc vs. Ufmc", in 2014 6th international symposium on communications, control and signal processing (ISCCSP), IEEE., (2014), 457-460.

15. Schaich, F., Wild, T. and Chen, Y., "Waveform contenders for 5g-suitability for short packet and low latency transmissions", in 2014 IEEE 79th Vehicular Technology Conference (VTC Spring), IEEE., (2014), 1-5.

16. Zhang, L., Ijaz, A., Xiao, P. and Tafazolli, R., "Multi-service system: An enabler of flexible 5g air interface", *IEEE Communications Magazine*, Vol. 55, No. 10, (2017), 152-159. doi: 10.1109/MCOM.2017.1600916.

17. Zhang, L., Ijaz, A., Xiao, P., Quddus, A. and Tafazolli, R., "Subband filtered multi-carrier systems for multi-service wireless communications", *IEEE Transactions on Wireless Communications*, Vol. 16, No. 3, (2017), 1893-1907. doi: 10.1109/TWC.2017.2656904.

18. Lin, T.-T. and Chen, T.-C., "Complexity-reduced receiver for universal filtered multicarrier systems", *IEEE Wireless Communications Letters*, Vol. 8, No. 6, (2019), 1667-1670. doi: 10.1109/LWC.2019.2935191.

19. Manda, R. and Gowri, R., "Universal filtered multicarrier receiver complexity reduction to orthogonal frequency division multiplexing receiver", *International Journal of Engineering, Transactions A: Basics,* Vol. 35, No. 4, (2022), 725-731. doi: 10.5829/ije.2022.35.04A.12.

20. Saad, M., Al-Ghouwayel, A. and Hijazi, H., "Ufmc transceiver complexity reduction", in 2018 25th International Conference on Telecommunications (ICT), IEEE., (2018), 295-301.

21. Nadal, J., Nour, C.A. and Baghdadi, A., "Novel uf-ofdm transmitter: Significant complexity reduction without signal approximation", *IEEE Transactions on Vehicular Technology*, Vol. 67, No. 3, (2017), 2141-2154. doi: 10.1109/TVT.2017.2764379.

22. Matthé, M., Zhang, D., Schaich, F., Wild, T., Ahmed, R. and Fettweis, G., "A reduced complexity time-domain transmitter for uf-ofdm", in 2016 IEEE 83rd Vehicular Technology Conference (VTC Spring), IEEE., (2016), 1-5.

23. Mukherjee, M., Shu, L., Kumar, V., Kumar, P. and Matam, R., "Reduced out-of-band radiation-based filter optimization for ufmc systems in 5g", in 2015 international wireless communications and mobile computing conference (IWCMC), IEEE., (2015), 1150-1155.

24. Zhang, Z., Wang, H., Yu, G., Zhang, Y. and Wang, X., "Universal filtered multi-carrier transmission with adaptive active interference cancellation", *IEEE Transactions on*

Communications,   Vol. 65, No. 6, (2017), 2554-2567. doi: 10.1109/TCOMM.2017.2681668.

25. Chen, X., Wu, L., Zhang, Z., Dang, J. and Wang, J., "Adaptive modulation and filter configuration in universal filtered multi-carrier systems", *IEEE Transactions on Wireless Communications*,   Vol. 17, No. 3, (2017), 1869-1881. doi: 10.1109/TWC.2017.2786231.

26. Wen, J., Hua, J., Lu, W., Zhang, Y. and Wang, D., "Design of waveform shaping filter in the ufmc system", *IEEE Access*, Vol. 6, (2018), 32300-32309. doi: 10.1109/ACCESS.2018.2837693.

27. Yarrabothu, R.S. and Nelakuditi, U.R., "Optimization of out-of-band emission using kaiser-bessel filter for ufmc in 5g cellular communications", *China Communications*,   Vol. 16, No. 8, (2019), 15-23. doi: 10.23919/JCC.2019.08.002.

28. Zhang, L., Ijaz, A., Xiao, P., Wang, K., Qiao, D. and Imran, M.A., "Optimal filter length and zero padding length design for universal filtered multi-carrier (UFMC) system", *IEEE Access*, Vol. 7, (2019), 21687-21701. doi: 10.1109/ACCESS.2019.2898322.

29. Manda, R. and Gowri, R., "Filter design for universal filtered multicarrier (UFMC) based systems", in 2019 4th International Conference on Information Systems and Computer Networks (ISCON), IEEE. (2019), 520-523.

30. Wang, X., Wild, T. and Schaich, F., "Filter optimization for carrier-frequency-and timing-offset in universal filtered multi-carrier systems", in 2015 IEEE 81st Vehicular Technology Conference (VTC Spring), IEEE. (2015), 1-6.

31. Rabiner, L.R., McClellan, J.H. and Parks, T.W., "Fir digital filter design techniques using weighted chebyshev approximation", *Proceedings of the IEEE*, Vol. 63, No. 4, (1975), 595-610. doi: 10.1109/PROC.1975.9794.

Persian Abstract

چکیده

شبکه های بی سیم آینده از (UFMC) Universal Filtered Multicarrier به عنوان یک تکنیک مدولاسیون شکل موج جدید استفاده خواهند کرد. شکل موج UFMC به طور معقولی مشخصات فیلتر زیر باند مانند ترتیب فیلتر و شکل را در نظر می گیرد تا مزایای کلیدی شکل موج های مدولاسیون نسل فعلی را ترکیب کند و در عین حال از معایب آنها جلوگیری کند. بنابراین در سیستم های مبتنی بر UFMC توجه به نحوه ساخت فیلتر فرعی حائز اهمیت است. در این مقاله، پیکربندی فیلتر زیر باند با توجه به اندازه زیر باند تطبیق داده شده است به طوری که نماد UFMC حداقل سطح تداخل را با حداقل انتخاب فرکانس ایجاد می کند. همچنین کل تداخل ناشی از تداخل بین حامل (ICI) و تداخل بین زیر باند (ISBI) با یافتن شکل بسته تغییر آن در سیگنال UFMC با اندازه زیر باند و طول فیلتر مورد بررسی قرار گرفت. از این تجزیه و تحلیل، ما تعیین کردیم که ICI با طول فیلتر افزایش و ISBI کاهش می‌یابد. بنابراین، روش پیشنهادی طول فیلتر را از نظر اندازه زیر باند و تداخل بهینه می‌کند. با این روش، طول فیلتر کمتر از روش معمولی است و از این رو استفاده از نماد را بهبود می بخشد. با روش پیشنهادی، نسبت کلی سیگنال به تداخل (SIR) بین ۱ تا ۳ دسی بل بهبود یافت.

Power and Ventilation Performance Study in a Modified Vertical Axis Wind Turbine Based on Semi-analytical Approach

S. Karimian*, S. Saham

Mechanical Faculty, Tarbiat Modares University, Tehran, Iran

P A P E R   I N F O

A B S T R A C T

In the current research, a novel vertical axis wind turbine producing both power and ventilation is presented. The idea is similar to an ancient wind catchers. The wind capacity of the Manjil city in Iran has been studied and a typical home-scale wind turbine has been assessed. To modify the geometry, a 3D semi-analytical code has been developed based on Double Multiple Stream Tube (DMST) theory. The validation analysis has been accomplished by the reference turbine. Using this code, the turbine performance including power coefficient and flow diversion index was studied. Particularly the effect of blade cone angle on the power deficiency and ventilation ratio was investigated. The results of the parameter study would reveal that for the optimal range of tip speed ratio, 2.9-3.2 based on the power curve, it is feasible to produce up to 400 m^3/h ventilation flow and 50-200 W shaft power. It would be obtained by 20-degree blade inclination and is equivalent to 2.5% of the total flow entering the rotor. The power deficiency due to this change is 30% which is compromised by the ventilation capability. The results also revealed the optimal range of tip speed ratio is 2.9-3.2. . It is depicted that, power attenuation could be minimum when the suitable TSR and the appropriate geometry are selected. Finally, some generalized trends of the objective functions also have been drawn. The methodology is versatile for the ongoing problems in the field of vertical axis wind turbines.

doi: 10.5829/ije.2023.36.07a.14

NOMENCLATURE

a	Induction factor	$\dot{m}$	Mass flow rate
V_∞	Wind speed	Q	Local torque
V_e	Induced equilibrium velocity	$\bar{Q}$	Mean torque
V_n	Normal velocity	$C_{\bar{Q}}$	Mean torque coefficient
V_t	Tangential velocity along the blade chord	C_P	Power coefficient
V_s	Tangential velocity along the blade length	C_L	Lift coefficient
W	Relative velocity	C_D	Drag coefficient
V_z	Velocity along the rotor axis	L	Lift
V_a	Axial induction velocity	D	Drag
C_n	Normal force coefficient	r	The local radius of the rotor
C_t	Tangential force coefficient	Δz	Blade element height
f	Blade function	B	Number of Blades
N	Normal force	**Greek Symbols**	
T	Tangential force	λ	Tip speed ratio
c	Blade chord	ω	Rotating speed
A	Swept area	α	Angle of attack
		η	Non-dimensional blade length

1. INTRODUCTION

The growth of science, technology, and industries, as well as the increase in population and the need for extra energy, has led to the world dealing with environmental problems and renewable energy sources. Wind turbines are one of the best ways to supply green energy as they are cost-effective and environmentally friendly. It is

Corresponding Author Institutional Email: karimian@modares.ac.ir
(S. Karimian)

estimated that they can provide more than 20% of the world's energy demand [1]. Wind turbines come in different dimensions and types and can be installed in various sites from wind farms to rooftops. Wind energy systems also have a wide variety of components such as wind turbines, vibration absorbers, airborne systems, and flapping mechanisms. Wind turbines can be classified into two types: horizontal axis and vertical axis. Horizontal axis turbines have more power but require more investment and space. Vertical axis wind turbines (VAWTs) have several key advantages, including smaller dimensions, insensitivity to wind direction, and lower construction and service costs. VAWTs are suitable for installation in workshops, roofs, highways, and urban thoroughfares.

Iran is located in a low-pressure region that is affected by strong summer and winter currents originating from the Atlantic and Indian Oceans. Studies on Iran's wind potential have been conducted in the southeastern regions, including Zahedan, and the northern regions, including Manjil. Iran's first experience of producing industrial wind energy was achieved by installing a series of 500 kW wind turbines in Manjil and Rudbar in 2015, providing 1800 MW.h energy per year [2]. While the wind potential for using large scale horizontal axis wind rotors in Iran has been frequently studied, this article focuses on vertical axis turbines due to their lower cost, versatility, and suitability for small scale wind systems. The article reviews several new works dealing with Iran's wind potential and presents recent literature on related VAWT studies. Alamdari et al. [3] compared wind speeds at altitudes of 10, 30, and 40 meters above the ground in different climates across Iran. They estimated the average and distribution functions, as well as the probability density function, using data from 68 stations [3]. Mostafaeipour [4] studied wind energy feasibility in the Yazd region, measuring wind speeds monthly and annually at various altitudes between 1992 and 2005 at 11 meteorological stations. In another study, researchers evaluated the economic potential of small wind turbines in Kerman. They examined three small turbines and demonstrated that the region has potential for wind energy utilization [5]. Many researchers have explored the potential of wind energy in various regions of Iran, such as Kerman and Manjil [6], and compared it with regions in Germany [7], Turkey [8], and Greece [9, 10].

In 2009, Paraschivoiu et al. [11] analyzed the performance of a vertical axis wind turbine with pitch angle control capabilities using the coupling method of the genetic algorithm with the DMST model. Their study focused on the performance and pitch control mechanism of the H-shaped turbine. The results showed that continuous pitch angle control has a relatively better performance than sinusoidal control and can increase turbine power by about 30% annually [11]. In 2017, Cheng et al. [12] compared the results of a two-

dimensional study and three-dimensional simulation of a vertical axis wind turbine with helical blades using the LES and RANS methods. They found that changes in the angle of attack and the wake created across the rear blade had a significant effect on the turbine power coefficient. They also observed that the tip vortices of the blade were one of the effective factors in power and noise factors in the three-dimensional simulation [12]. In 2018, Zanforlin and Deluca [13] examined the effects of Reynolds number and blade tip loss factor on the performance of a vertical axis wind turbine with straight blades. They found that both factors could affect turbine performance, with the effect of blade tip loss being predominant in medium and large turbine sizes and the Reynolds number effect being greater in small turbines [13].

Rasekh et al. [14] in 2018 examined dynamic stall in the wind turbine blade and used two models, the Leishman-Beddoes semi-analytical dynamic stall and the numerical method. They compared results and revealed that dynamic stall in both methods depended on factors such as the initial and mean angle of attack, reduced frequency, and phase angle. They also observed that the Leishman-Beddoes method would have acceptable results with less computational cost. In 2021, Karimian and Rasekh [15] discussed the relation between power performance, acoustics, and geometry of a vertical axis turbine. They found that implementing some small changes in blade pitch angle could effectively enhance the power coefficient, with the greatest effect occurring at a low tip speed ratio. They also observed that small changes in pitch angle could reduce undesirable noise, especially at low turbine speed ratios [15].

In 2019, Moghimi and Motawej [16] used the DMST method to study the aerodynamic performance of H-rotor turbines and Gorlov turbines. They examined the impact of various geometric parameters, including airfoil shape and chord, number of blades, helix angle, wind speed, and aspect ratio. The researchers concluded that thicker airfoils with longer chords were more suitable for turbine operation. Utilizing fewer blades, shorter chord lengths, and smaller aspect ratios can cover a wider range of tip speed ratios. They also claimed that the helical angle of the blade has little effect on the power coefficient, although it was expected to reduce torque oscillations [16]. In 2014, Sedaghat et al. [17] investigated a horizontal axis wind turbine with a continuous change in wind speed. They improved the BEM method by generalizing the quadratic equations about the angular induction factor. The researchers also determined the optimal point of turbine operation in terms of maximum power coefficient and maximum lift-to-drag ratio. Finally, they stated that using a turbine with a continuously variable speed has a higher power coefficient than conventional constant-speed wind turbines [17]. In 2015, Sedaghat et al. [18] attempted to achieve a higher lift-to-drag ratio by circulating the

turbine blades. They were able to achieve a lift-to-drag coefficient of 278 by applying this change and utilizing the Magnus effect. The researchers stated that this was true for a wide range of symmetrical airfoils [18].

Liu and Mak [19] investigated windcatchers in 2007, examining the impact of wind speed and direction. They found that the wind speed entering the windcatcher was approximately equal to the free wind speed in the environment, which created suitable conditions for ventilation. They also observed that as wind speed increased, the flow rate through the windcatcher could be expedited by utilizing a small azimuth angle between 5-15 degrees. However, increasing this azimuth angle could decrease the flow rate through the windcatcher. They also noted that in cases of higher wind velocity or larger angles, the uniformity of the flow entering the wane would be decreased [19].

In 2017, Chong et al. [20] introduced a cross-axis wind turbine design that used three vertical-axis blades and six horizontal-axis blades perpendicular to each other. They also used additional blades to divert the flow and installed them in the rotor plan of the horizontal-axis turbine blades. This design allowed the vertical-axis turbine blades to operate initially, followed by the horizontal-axis turbine blades, improving turbine performance [20]. While Iran has suitable windy areas, its contribution to the use of wind energy is still below average due to cheap fossil fuel energy resources in the Middle East hindering the development of large-scale wind farms and high-power offshore horizontal axis turbines. Therefore, it is more attractive and effective to use wind energy in domestic and urban applications, focusing on small and medium-sized vertical-axis turbines. These turbines can be more efficient and effective on an urban scale, achieving economic and environmental benefits. Adanta et al. [21] in 2023, conducted a study to optimize a pico-hydro-type crossflow turbine's performance by curving the upper surface of the blade and increasing the lift force. Their numerical solution results revealed that the upper CFT blade has a parabolic effect on the turbine's performance and specific speed. They recommended that a CFT with a curved blade is generally more suitable for low-pressure conditions with extreme fluctuations [21].

The central idea and innovation of this study is to combine the power generation index with the home air-conditioning concept. By using angled blades in the vertical-axis turbine, it is possible to divert the output current from the turbine in addition to power generation. After evaluating the wind energy potential in Manjil as a sample area, the power and ventilation characteristics of a V-shaped turbine with proposed dimensions and geometry were investigated, and the effect of cone angle on turbine performance and flow rate was examined assuming a separating baffle. The researchers developed a semi-analytical code based on the DMST method and made some corrections, which is another achievement of this study. The steps for analyzing and evaluating the desired turbine are shown in Figure 1.

2. BASIC EQUATIONS AND MODELING

In this research, the analysis of the turbine is conducted based on the DMST method, which is implemented in MATLAB software. The momentum theory forms the foundation of this method, where the turbine rotor is divided into upwind and downwind semi-cycles, and the momentum equations of the flow are applied separately to each phase. The DMST method used in this study is an analytical method that offers the important advantage of quickly obtaining accurate results. Other similar methods include SST and MST. The DMST method outperforms similar analytical methods since it incorporates two operating discs and considers correction factors such as the Prandtl's factor. Figure 2 illustrates the division of the turbine rotor into stream tubes along the flow direction, with the azimuth angle $\Delta\theta$ corresponding to the segmentation of the stream tubes. When the free stream strikes the rotor blades upwind, it loses a part of its energy, and the velocity reduces to V_e. Similarly, the velocity V_e reduces due to the downwind blades' passage. Eventually, the flow leaving the rotor reaches its minimum velocity, V_w. The velocities at the upwind and downwind sections are abbreviated as V_{au} and V_{ad}, respectively, and are affected by the induction factors in the upwind and downwind strokes [22]. These factors represent the effect of blade wake history on the current flow passing through the rotor, and they can be computed iteratively using the momentum equations in two actuator discs, upwind and downwind.

$$V_\infty > V_{au} > V_e > V_{ad} > V_w \tag{1}$$
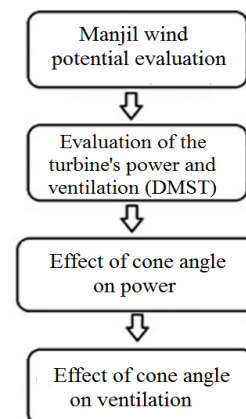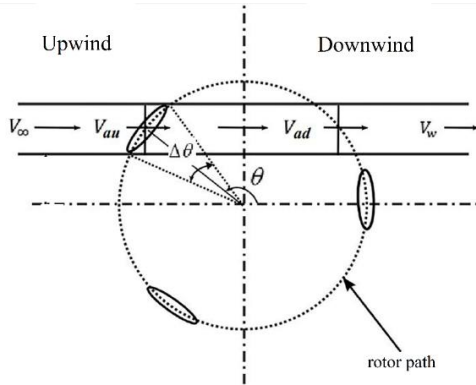
$$V_{au} = a_u V_\infty \tag{2}$$

Figure 1. Evaluation of the V-shaped wind turbine structure

Figure 2. One typical Stream-tube used in the DMST method [22]

Figure 3. Flow angle, forces, and velocity vector [22]

$$V_e = V_\infty (2a_u - 1) \tag{3}$$

$$V_{ad} = a_d V_e \tag{4}$$

Initially assuming some values for the induction factor a, the flow velocity can be calculated in the desired section. Relative flow velocity is crucial in estimating aerodynamic performance, the instantaneous relative velocity and the corresponding apparent angle of attack are determined by Equations (5) and (6) [19]. Figure 3 illustrates the position of a specific blade at four different moments during one cycle, demonstrating considerable variation in the magnitude and direction of the relative velocity and angle of attack. Using the prior quantities to obtain the lift and drag forces, one can easily determine the tangential and perpendicular force components. Figure 4 shows the DMST algorithm. Because the turbine blades have a finite length, some flow at the tip of the blade is diverted from the high-pressure surface to the low-pressure surface, causing blade tip vortices. These tip vortices generate a downwash flow and change the relative velocity vector, leading to a reduction in the effective angle of attack, particularly at the blade's tip, decreasing aerodynamic performance.

To improve the DMST method, Prandtl's tip loss factor correction is used, based on Equation (8). The 3D-lift coefficient and induced drag are determined according to Equations (7) to (9). The parameters η and α represent the nodal non-dimensional spanwise position and geometric angle, respectively [22].
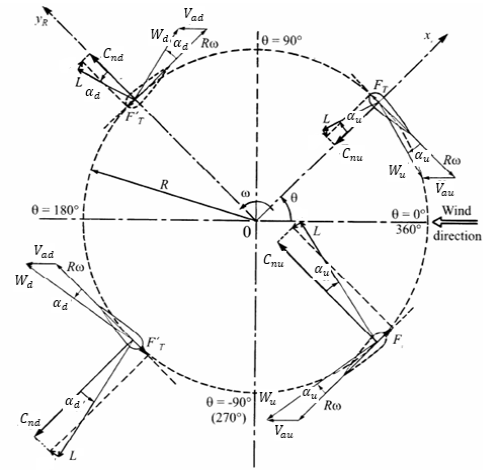
$$W = \sqrt{(V_n)^2 + (V_t)^2 + (V_s)^2} \tag{5}$$

$$\alpha = \sin^{-1}(V_n/W) \tag{6}$$

$$f = N/2 \left((1 - \eta)/(\eta \sin|\alpha|) \right) \tag{7}$$

$$C_{L(3D)} = C_{L(2D)} (2/\pi) \cos^{-1}(e^{-f}) \tag{8}$$

$$C_{D(ind)} = \left(C_{L(3D)}^2 / (0.95 \pi . AR) \right) \tag{9}$$

Moving on to the next step, the lift and drag coefficients are estimated. The normal and tangential force coefficients can be computed. Once the force coefficients are obtained, the force magnitudes in each section can be determined according to Equations (10) and (11) [22]. In these equations, ρ is the air density, c is the blade chord, Δh is the blade element increment, W is the relative flow velocity, and C_n and C_t are the normal and tangential force coefficients, which are transformed by the lift and drag coefficients. By calculating the normal and tangential force coefficients, the new estimation of the induction factor can be obtained using Equations (12) and (13) [22].

$$F_N(\theta) = \left(\frac{1}{2} C_n . \rho . c . \Delta h . W^2 \right) \tag{10}$$

$$F_T(\theta) = \left(\frac{1}{2} C_t . \rho . c . \Delta h . W^2 \right) \tag{11}$$

Consequently, the new approximations of relative flow velocity, angle of attack, and normal and tangential force coefficients are determined. The loop is repeated for each element of the blade and each azimuth angle until convergence is achieved. It is notable that the induction factor iterations are different upwind and downwind and must be examined separately. The final values of normal and tangential forces on each blade section can then be integrated to calculate the total forces applied to the entire turbine. One of the most interesting components of the total force is the one parallel to the turbine axis (z-direction of the fixed coordinate axis).

According to the simple momentum theory, the downward flow velocity and the related discharge rate $(\dot{V})$ can be predicted using Equations (14) and (15).

$$f = \frac{Bc}{8\pi r} \int_{-\pi/2}^{\pi/2} \left(C_n \frac{\cos \theta}{|\cos \theta|} - C_t \frac{\sin \theta}{|\cos \theta| \cos \delta} \right) \left(\frac{W}{V_a} \right)^2 d\theta \tag{12}$$
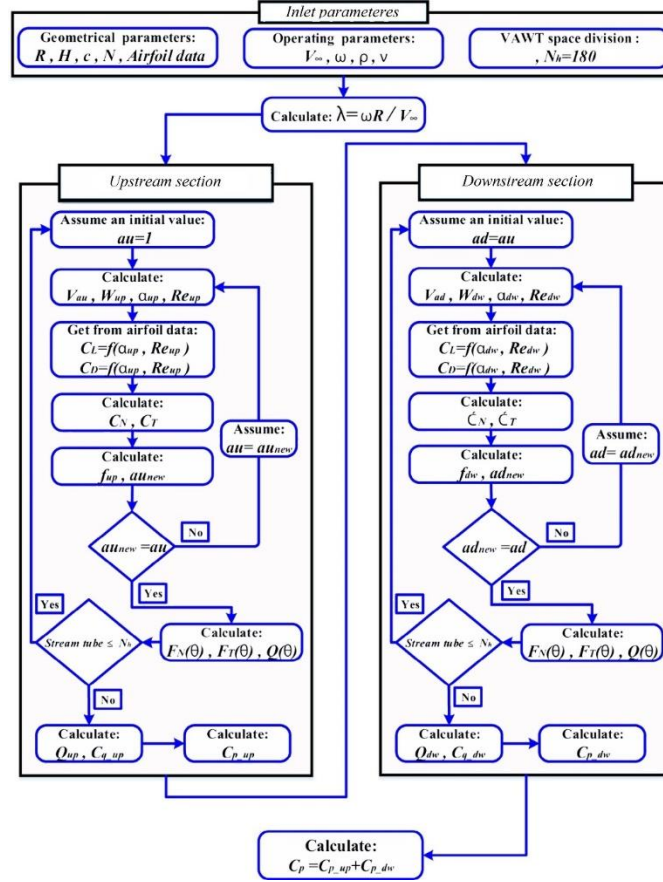
$$a_{new} = \pi/(f + \pi) \tag{13}$$

Figure 4. DMST algorithm [16]

$$V_z = \sqrt{(F_N \sin \delta) \cos \theta / \rho . A} \qquad (14)$$

$$\dot{V} = A . V_z \qquad (15)$$

In the subsequent step, Equation (16) to (18) are used to obtain the torque due to the tangential force and the turbine power [19]. The parameter $\bar{Q}$ represents the rotor's average torque and the parameter λ represents the blade tip speed ratio.

$$\bar{Q} = \frac{N}{2\pi} \int r . F_T(\theta) \, d\theta \qquad (16)$$

$$C_P = \lambda . C_{\bar{Q}} \qquad (17)$$

$$P = \frac{1}{2} \rho V^3 C_P \qquad (18)$$

The DMST algorithm is based on the upwind and downwind computation of the rotor. To initialize the process, some input variables such as blade length, rotor diameter, blade chord, airfoil type, rotational speed, and free wind speed must be defined and set. Then, the blade is discretized, and the azimuth angles are divided, which

can affect the accuracy of the method. After calculating the tip speed ratio for blade elements, one can proceed to the next step, i.e., the calculations related to the upwind of the rotor. In this step, the induction factor is scheduled to be found, as mentioned before. It may be accomplished by trial and error and by applying some default values for the induction factor. When the appropriate induction factor is obtained, key parameters of aerodynamic performance, such as relative speed and effective angle of attack, can be calculated.

By calculating the relative velocity and angle of attack, as well as the airfoil lift and drag coefficients, the blade's normal and tangential forces are calculated. Then, with proper transformation, the forces applied to the blade can be obtained, which include three force components: (1) in the direction of wind speed (x-axis), (2) perpendicular to the wind speed (y-axis), and (3) parallel to the turbine axis direction (z-axis). The torque applied to the blade is also calculated. The same process as for the upwind is repeated for the downwind stroke. The main difference is the lower inlet flow velocity. This intermediate velocity (V_e) is derived as stated at the beginning of this section. Finally, the velocity of the

downward flow parallel to the z-axis and the corresponding discharge is being estimated. This issue is addressed by ventilation capacity in the subsequent sections. Similar to the moment formula, the power extracted in upwind and downwind strokes will be estimated separately, and the overall performance can be achieved.

3. BASELINE TURBINE AND VENTILATION OF SEMI-ANALYTICAL CODE

To validate the method, an H-type turbine suitable for urban and home scales, with geometric characteristics are summarized in Table 1. The power coefficient obtained from the proposed method and implemented code is compared with both experimental data given by Castelli et al. [23] and numerical analysis are given by Mohamed [24]. As depicted in Figure 5, the horizontal axis represents the blade tip speed ratio, and the vertical axis represents the turbine power coefficient.

According to this figure, it can be seen that the DMST method presented in this study could appropriately estimate the power coefficient of the baseline turbine within a 14% relative error, which is acceptable when experiencing separation and complex wake interactions.

By evaluating the proposed model, the baseline H-type turbine (Figure 6) has been modified to meet both power and flow diversion objectives. Applying a conical angle would make the blade inclined concerning the turbine axis, resulting in a V-type turbine similar to
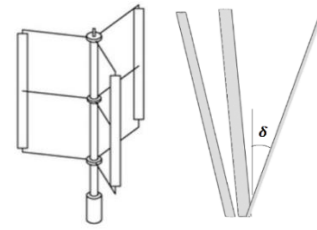
TABLE 1. characteristics of basic turbine [23]

Airfoil type	NACA 0021
Number of blades	3
Blade chord	0.08 m
Blade height	1.5 m
Rotor diameter	1 m

Figure 5. DMST method validation

Figure 6. Baseline and modified V-type turbine ($\delta = 20^\circ$)

Figure 6. Assessing the wind energy potential of Manjil city, the V-type turbine will be modeled via the proposed DMST code, and its power and ventilation performance will be examined. The appropriate range of turbine operation in terms of production power and ventilation capacity is based on the presented parametric study.

Case study: Manjil city wind energy potential
Manjil, a city with a population of about 20,000 in Gilan province in northern Iran, is one of the most promising locations for wind energy in the country. The city experiences its strongest winds during spring and summer, which are commonly referred to as the "seven days Manjil winds." The establishment of different pressure patterns in the area is one of the reasons for the strong winds. This has resulted in one of the most robust local winds in the south of Caspian Sea. Additionally, the Sefidrood valley acts as a communication channel between Caspian Sea in the north and the vast land of Central Iran in the south. The difference in latitude and climate between these two zones results in significantly different conditions in air circulation patterns, pressure distribution, and temperature profiles. This leads to a massive rate of air exchange between Caspian Sea and the central land of Iran, although the Alborz mountain prevents it from being sustained continuously.

Figure 7 displays the average wind speed profile for Manjil city between 2018 and 2020. The city has an average speed of 9.5 m/s at a height of 10 meters, with the highest average speed of 15.9 m/s occurring in July and the lowest average speed of 4.5 m/s recorded in February. Figure 8 shows the frequency/probability distribution of the realized wind speed. The turbine design is proportional to the higher wind speed and the probability of occurrence of that high wind speed. The range of wind speed considered is 8 to 10 m/s. Based on the wind speed characteristics of Manjil, the maximum available power and annual wind energy of this site can be estimated as follows:

4. TURBINE VENTILATION AND POWER PERFORMANCE

In the preceding section, examined the available power in Manjil city. As previously mentioned, the main
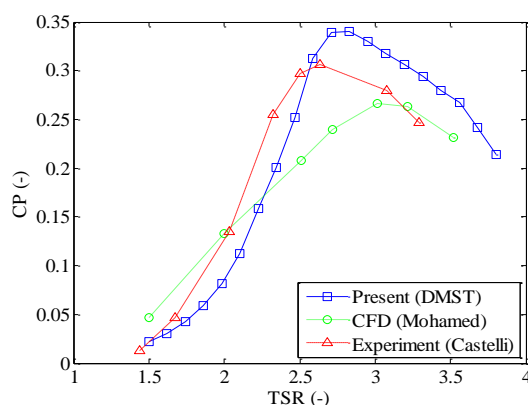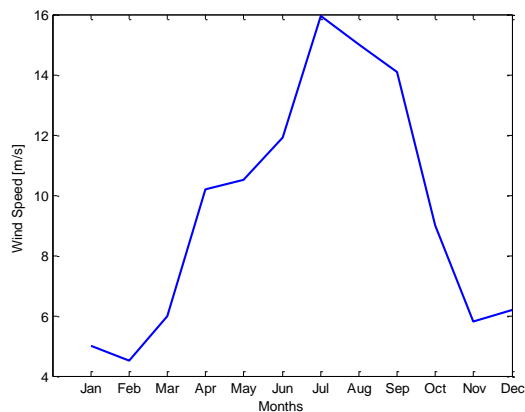
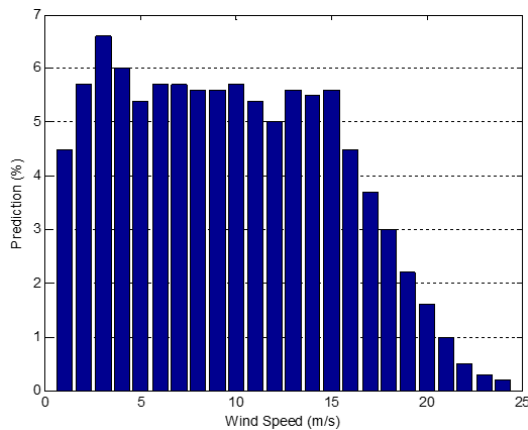**Figure 7.** Average wind speed in Manjil [7]

Figure 8. Wind speed histogram of Manjil [7]

concept is to combine the performance of old windcatchers used in desert areas of Iran with vertical axis turbines. The operation of the windcatcher can be described based on the principle of suction and discharge flow or based on the temperature difference. To build a similar mechanism, fresh air must first enter the room, and then hot and polluted air must be expelled from the room. By installing a V-shaped turbine on the roof of houses and placing a partition wall or baffle, as shown in Figure 9, it is possible to separate the supply flow from the stair flow.

Utilizing suitable V-rotor turbine, one may achieve both power generation and ventilation in a confined location. The airflow entering the upwind phase of the rotor will be partially diverted along the z-axis and used to create the inflow channel, which supplies fresh air. After circulating inside the room, it will be drawn out by the downwind phase of the turbine, which creates a suction flow in the upward z-direction. The fresh air and stale air channels are separate in order circulation occurred. They would not be mixed but are placed next to each other.
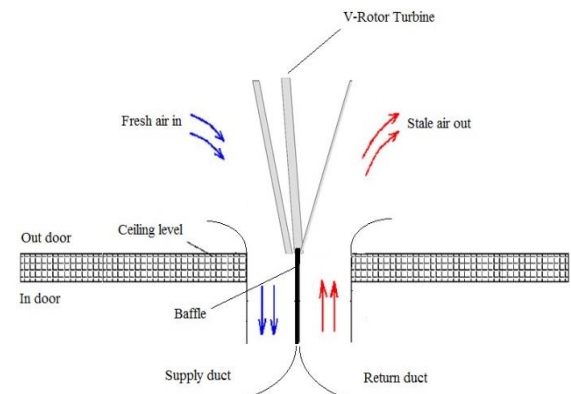

Figure 9. Schematic of the location of turbine and supply and return ducts of ventilation

Applying a conical angle on the base turbine is beneficial due to its flow-diverting and ventilation capability, but it will affect the output power of the turbine. Figure 10 shows that two cone angles of 10 and 20 degrees were applied, which caused the output power of the turbine to decrease. As the conical angle increased, the maximum extracted power decreased, but the slope of the power curve was smoothed, indicating a more extended range of wind speeds. This power reduction can be attributed to the reduction in the effective blade height and ultimately the reduction in the swept area by the rotor. Additionally, power loss at higher wind speeds decreases with increasing cone angle. In other words, the output power sensitivity to velocity change is attenuated.

The power coefficient representation based on the corrected reference area is shown in Figure 11. It can be observed that by applying the cone angle, the optimum tip speed ratio corresponding to the maximum power coefficient would be slightly increased. It still occurs within the proximity of a tip speed ratio equal to 3. By applying cone angle, the turbine would enter the stall at
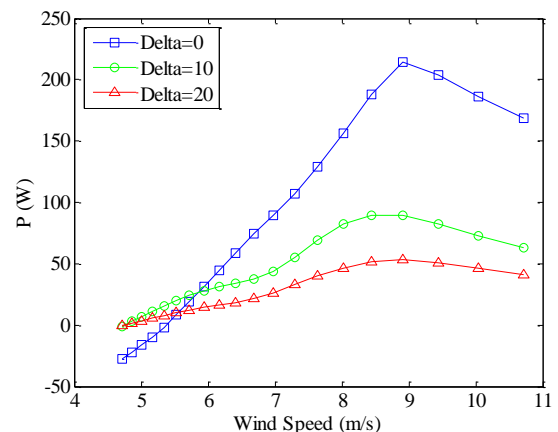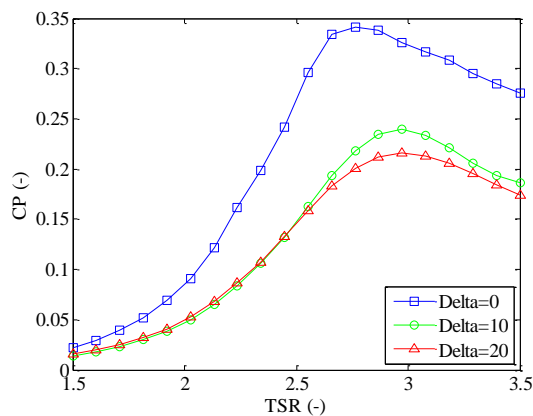

Figure 10. Effect of cone angle on the turbine power curve

Figure 11. Effect of cone angle on turbine power coefficient curve

lower wind velocities. From the power point of view, the power would be decreased by the V-rotor configuration, but the sensitivity of the power coefficient is revealed to be enhanced.

By calculating the ventilated flow in the upwind and downwind of the rotor separately, it is possible to study the diversion flow performance. For conical angles of 0, 10, and 20 degrees, it is computed independently and shown in Figure 12. As it is seen the upwind values are negative (lower curves) due to the z-axis direction and the downwind values are positive (upper curves). According to the figure, it can be founded the amount of flow diverted as ventilation flow is directly related to wind speed and cone angle. Although increasing the wind speed and cone angle will increase the ventilation flow, but the trend is nonlinear. On the other hand, the sensitivity of discharged flow to the cone angle is shown to be gradually decreased. For example, it can be seen that the amount of flow diverted in D=20 is slightly greater than D=10, while the difference in diverted flow between D=0 and D=10 is definitely more. Increasing the
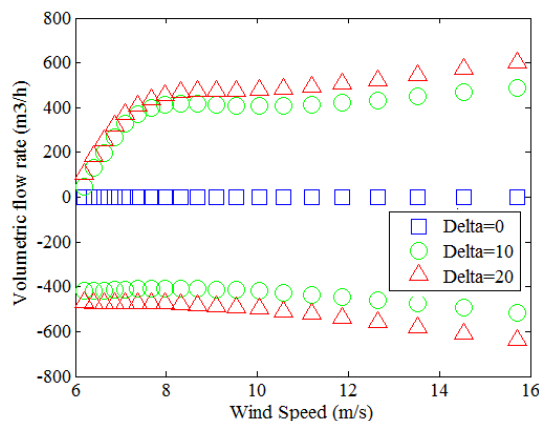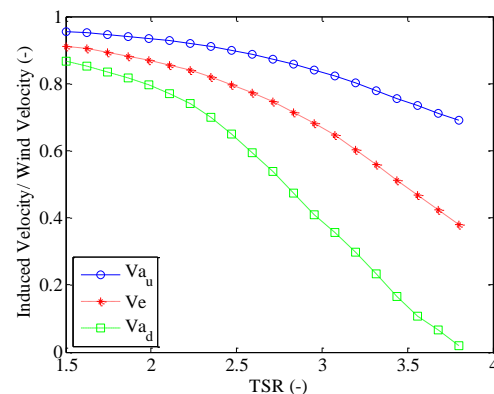
wind speed would increase the amount of ventilation, except for the Stall case which causes a sharp drop in aerodynamic performance.

The axial flow velocity is depicted in Figure 13. As can be seen, the free-stream velocity is different in the upwind and downwind, concluding the stall velocity in both regions to be different. So the upwind rotor blades would experience a stall at lower wind speeds, while the downwind blades would encounter a stall at higher wind speeds. This result together with Figure 12, could explain why the downwind curves are asymptotic. The amount of ventilation in the downwind phase is initially increasing within a range up to 7 m/s with a relatively high slope. After that, the blades would enter the stall region, and consequently flow enhancement would be attenuated. The same profile would occur in the upwind, except that the stall velocity for upwind is less (about 5 m/s). The low TSR can be considered equivalent to a higher wind speed at a constant rotational speed. Therefore, in this TSR, the blades of the turbine would face with higher speed flow, causes the wind flow coming out through the turbine to be increased. Thus, the vertical component of the flow also would be higher. Increasing this velocity component will increase the ventilation flow rate.

At a low Tip Speed Ratio (TSR), the blades of the turbine collide with the wind flow at a higher speed, equivalent to a higher wind speed at a constant rotational speed. This collision causes the wind flow coming out of the turbine to increase, including the vertical flow component, increasing the ventilation flow rate. As expected from the modeling section, the induction coefficient in the downwind is higher than the upwind, causing the flow velocity in the downwind to decrease more relatively.

Figure 13 illustrates the axial flow velocity, demonstrating different free-stream velocities in the upwind and downwind, concluding the stall velocity in both regions to be different. Therefore, the upwind rotor blades would experience a stall at lower wind speeds, while the downwind blades would encounter stall at

Figure 12. Diverted flow from the turbine (negative values for upwind and positive values for downwind)

Figure 13. Wind speed at upwind and downwind at $\delta = 20°$

higher wind speeds. This result, together with Figure 12, explains why the downwind curves are asymptotic. The amount of ventilation in the downwind phase increases within a range up to 7 m/s with a relatively high slope. After that, the blades enter the stall region, and consequently, flow enhancement is attenuated. The same profile occurs in the upwind, except that the stall velocity for upwind is less (about 5 m/s).

Figure 14 shows the Q-blade simulation for a cone angle of 20 degrees, a wind velocity of 8 m/s, and a tip speed ratio of 3. Separating the up and down current would enhance the ventilation process and establish a desired cycle within a room. The amount of flow diverted in the downwind phase is close to the upwind, except for the direction of the diverted flow.

To achieve a tradeoff between maximum power absorption and maximum ventilation, it is necessary to consider the type of use. According to Figures 10 and 12, wind speed around 10 m/s can be declared as a suitable point for absorbing power and ventilation. At high tip speed ratios corresponding to lower wind velocities, the flow downwind may be blinded due to the difference in flow velocity. Angling the blades reduces the power, and therefore, it is necessary to create a balance between power absorption and ventilation.
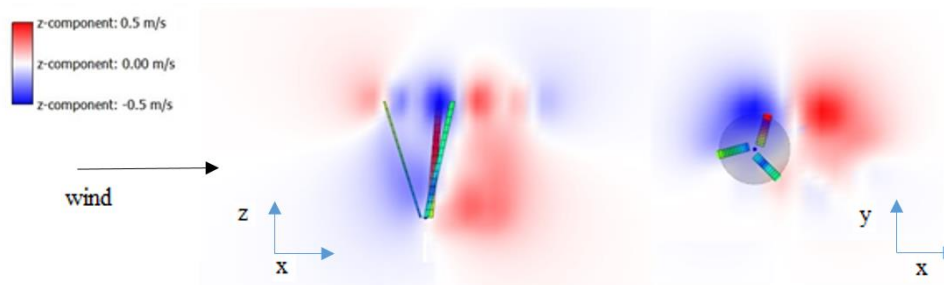
5. PARAMETRIC STUDY OF POWER AND VENTILATION COEFFICIENT

To achieve a downward relative flow rate for ventilation purposes, the diverted flow rate along the turbine axis should be normalized relative to the free-stream flow entering the rotor. This normalized quantity can be referred to as the ventilation coefficient. Figure 15 depicts changes in the ventilation coefficient for various conical angles in terms of the blade tip speed ratio. Both axes are dimensionless and can be generalized appropriately. Generally, it can be observed that the ventilation coefficient increases with the tip speed ratio. For instance, at a tip speed ratio of 3, approximately 2.5% of the flow entering the turbine vertically comes out from the upwind and downwind phases of the rotor. Assuming constant turbine angular velocity, the ventilation coefficient increases as wind speed decreases. The stall area for the upwind and downwind phases of this blade occurs at tip speed ratios of 5 and 3, respectively. At low tip speed ratios (high wind speeds), rotor blades enter the stall, leading to a decrease in relative performance but an increase in the diverted flow due to drag force effects. The ventilation coefficient initially increases with the tip speed ratio until a maximum is reached, corresponding to

Figure 14. Flow velocity gradient along the turbine axis (Z-axis)
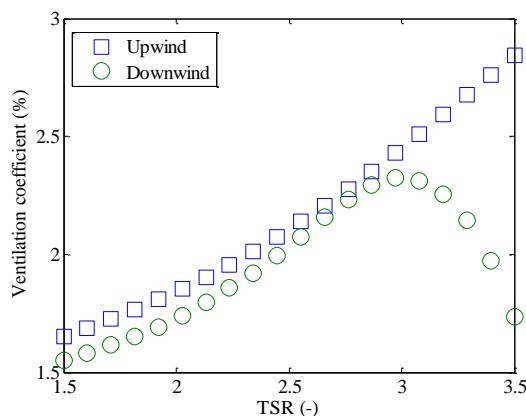
Figure 15. Downward flow rate (ventilation coefficient) at $\delta = 20°$

the stall vicinity point. After that, it decreases due to low wind speed.

As shown in Figure 12, low tip speed ratios always increase the ventilation flow. Conversely, Figure 15 indicates that reducing the tip speed ratio will decrease the ventilation coefficient due to stall. To achieve optimal performance from a ventilation perspective, a speed range of 8 m/s and a tip speed ratio of 3 can be used in this special turbine. This design point is suitable for both power and ventilation. Increasing the tip speed, would reduce the downward flow of the entire rotor and thus the ventilation coefficient and conversely, reducing tip speed, would result the turbine blades experiencing stall, leading to a degradation of both the ventilation and the power coefficients. The same argument can be drawn in terms of the tangential and normal force components.

Figure 16 shows the maximum turbine power coefficient at different cone angles. It can be observed that the maximum power coefficient decreases with increasing conical angle. From a conical angle of 15 degrees, the power coefficient experiences a local minimum. It would slightly be increased at higher conical angles, i.e., 20 degrees. This issue is partly related to the power coefficient definition. Applying a conical angle reduces the turbine power (similar to Figure 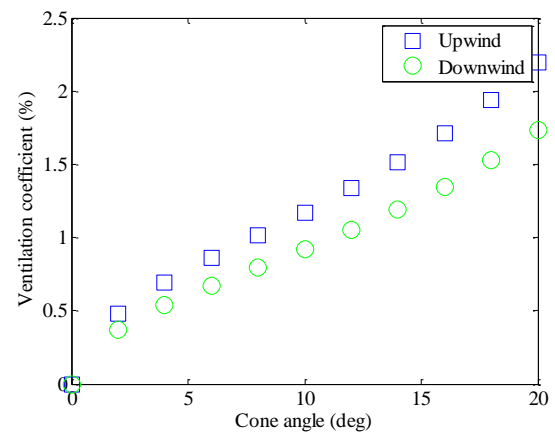10) while simultaneously reducing the swept area introduced by this new geometry. At high conical angles, the rate of reduction of turbine power is lower than the rate of wind power reduction. As a result, the power coefficient slightly increases on the right side of the axis (larger conical angles).

Figure 17 shows the ventilation coefficient or relative flow rate plotted against cone angle variation, computed using the TSR averaging scheme. The plot indicates a nearly linear behavior in terms of the cone angle, suggesting that increasing the cone angle can improve ventilation efficiency. Additionally, the difference between the ventilation coefficient in the upwind and downwind could be increased with the cone angle, which is expected due to lower suction efficiency in the downwind section. However, this does not significantly affect ventilation performance.

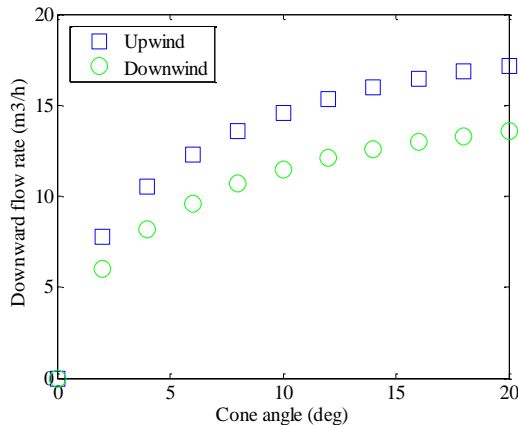In summary, Table 2 compares the performance of the turbine at different cone angles in terms of both power

Figure 17. Equation of the average ventilation coefficient to the cone angle

and ventilation. The table shows that increasing the cone angle decreases annual energy production as well as the maximum turbine power coefficient, while increasing the average ventilation coefficient. The challenge is to find a compromise between these two objectives. Since the maximum power is achieved at a TSR of about 3, the table also addresses the ventilation performance corresponding to the optimal TSR.

According to the argument mentioned in the previous section, the optimal tip speed ratio from the power curve point of view was shown to be in the range of TSR=2.6 to TSR=2.8 (Figure 11). The maximum power coefficient will be achieved in this range of TSR in terms of cone angle selection. It is interesting that having the ventilation point of view, also the optimum TSR interval is 2.9 to 3.1 (Figure 15). It shows that a matching between the essential operation conditions for two objectives could be established. The required TSR for both power and ventilation coincided in the vicinity of TSR=3. Therefore, along with finding a suitable operating point, the TSR=3 is shown to be justified. Another design parameter to be selected is the cone angle. Considering the possible variation in the angular velocity of the rotor and the geometry, it would be suggested as 10-20 degrees range. The turbine can approach this suitable operating point in the range of wind speed between 4 m/s and 10 m/s by adjusting the RPM of the turbine.

Figure 16. The relation between the maximum power coefficient and cone angle

TABLE 2. Comparison of turbine power and ventilation indicators

Cone angle (deg)	Max power (W)	AEP ($kW \cdot h$)	Max power coefficient (%)	Upwind average ventilation factor (%)	Downwind average ventilation factor (%)	Upwind ventilation flow rate at TSR=3 (m^3/h)	Downwind ventilation flow rate at TSR=3 (m^3/h)
0	215	660	34	0	0	0	0
10	90	295	24	1.1	1	410	400
20	52	185	21	2.1	1.9	480	450

Figure 18. Equation of the average ventilation to the cone angle

Comparing the amount of ventilation in the three different cone angles for the optimal tip speed ratio, it is observed that the relative ventilation enhancement at a cone angle of 20 degrees compared to 10 degrees, is lower than the same difference for 10 degrees and zero (Figure 18). On the other hand, the power attenuation for a cone angle change from 20 to 10 is also less than the power loss for a change from 10 to 0. The relative progress in ventilation after cone angle 10 is lower than the relative penalty in the power for the same change in cone angle. Therefore, one may think that angle 10 is a suitable point for the two purposes. The power reduction in the 10-20 interval is more significant than the ventilation improvement, while it is vice versa for the 0-10 interval. Finally, it is concluded that the cone angle close to 10 degrees and the tip speed ratio of 3 (wind speed 7-9 m/s which was assumed a priori constraint of the target city) could be a good design point for the proposed turbine geometry in terms of both power generation and ventilation demand.

6. CONCLISION

The recent research presents a statistical survey of wind capacity for Manjil city in Iran based on the latest 3-year interval data. The territory exhibits an average wind velocity of 9.5 m/s, indicating a wind energy potential of 1000 W/m², as estimated from the wind probability curve. This makes it an ideal location for implementing home-scale wind turbines. The proposed turbine can yield an annual energy production of 600 kWh, 295 kWh, and 185 kWh for cone angles of 0, 10, and 20 degrees, respectively. Additionally, the implementation of the cone/inclined blade layout can lead to a further diversion or ventilation flow, suitable for internal circulation and cooling purposes. The addition of a baffle or vane can

enhance the ventilation flow. By separating the inflow and outflow from the home, natural circulation can be maintained.

The inclined blade Darrieus-type turbine has a suitable power generation range of TSR=3 and higher, while the proper range of ventilation is TSR=3 and lesser. Therefore, operating the turbine at an optimum TSR of 3 would result in minimum penalties in power. The average flow entering the home can be adjusted up to 400 m³/h, making it an adequate value for cooling during summer. Other findings from the semi-analytical code developed in the current research include:

1. The efficiency of the turbine decreases as the cone angle increases. For instance, the power coefficient at cone angles of 0, 10, and 20 degrees is 0.34, 0.24, and 0.21, respectively.
2. At a cone angle of 20 degrees and a TSR of 3, the ventilation coefficient is 2.5%.
3. The V-shaped turbine's average ventilation flow rate is 400 m³/h.
4. The annual energy production at a conical angle of 10 degrees will be approximately half that of the H-shaped turbine, and at a conical angle of 20 degrees, it will be approximately one-third.

To improve the performance of home-scale wind turbines and satisfy power and ventilation needs, implementing a simple control mechanism is recommended. Changes should be made in the turbines' control system to ensure that their geometric characteristics are suitable for the weather conditions of the region. Further research can also be conducted on how to channel the flow under the turbine, as well as its proper position and geometry to efficiently absorb the diverted flow and bring it to the desired location.

7. REFERENCES

1. Kumar, A., Tausinga, S., Kishore, K., Nair, K. and Rao, D.K., "Technical and economic prospect of wind energy at lapaha, tonga", *Resources and Environmental Economics*, Vol. 2, No. 1, (2020), 136-142. https://doi.org/10.1016/j.renene.2009.07.021

2. Mirhosseini, M., Sharifi, F. and Sedaghat, A., "Assessing the wind energy potential locations in province of semnan in iran", *Renewable and Sustainable Energy Reviews*, Vol. 15, No. 1, (2011), 449-459. https://doi.org/10.1016/j.rser.2010.09.029

3. Alamdari, P., Nematollahi, O. and Mirhosseini, M., "Assessment of wind energy in iran: A review", *Renewable and Sustainable Energy Reviews*, Vol. 16, No. 1, (2012), 836-860. https://doi.org/10.1016/j.rser.2011.09.007

4. Mostafaeipour, A., "Feasibility study of harnessing wind energy for turbine installation in province of yazd in iran", *Renewable and Sustainable Energy Reviews*, Vol. 14, No. 1, (2010), 93-111. https://doi.org/10.1016/j.rser.2009.05.009

5. Mostafaeipour, A., "Economic evaluation of small wind turbine utilization in kerman, iran", *Energy Conversion and Management*, Vol. 73, (2013), 214-225. https://doi.org/10.1016/j.enconman.2013.04.018

6. Mostafaeipour, A. and Abarghooei, H., "Harnessing wind energy at manjil area located in north of iran", *Renewable and Sustainable Energy Reviews*, Vol. 12, No. 6, (2008), 1758-1766. https://doi.org/10.1016/j.rser.2007.01.029

7. Weigt, H., "Germany's wind energy: The potential for fossil capacity replacement and cost saving", *Applied Energy*, Vol. 86, No. 10, (2009), 1857-1863. https://doi.org/10.1016/j.apenergy.2008.11.031

8. Eskin, N., Artar, H. and Tolun, S., "Wind energy potential of gökçeada island in turkey", *Renewable and Sustainable Energy Reviews*, Vol. 12, No. 3, (2008), 839-851. https://doi.org/10.1016/j.rser.2006.05.016

9. Fyrippis, I., Axaopoulos, P.J. and Panayiotou, G., "Wind energy potential assessment in naxos island, greece", *Applied Energy*, Vol. 87, No. 2, (2010), 577-586. https://doi.org/10.1016/j.apenergy.2009.05.031

10. Xydis, G., Koroneos, C. and Loizidou, M., "Exergy analysis in a wind speed prognostic model as a wind farm sitting selection tool: A case study in southern greece", *Applied Energy*, Vol. 86, No. 11, (2009), 2411-2420. https://doi.org/10.1016/j.apenergy.2009.03.017

11. Paraschivoiu, I., Trifu, O. and Saeed, F., "H-darrieus wind turbine with blade pitch control", *International Journal of Rotating Machinery*, Vol. 2009, (2009). https://doi.org/10.1155/2009/505343

12. Cheng, Q., Liu, X., Ji, H.S., Kim, K.C. and Yang, B., "Aerodynamic analysis of a helical vertical axis wind turbine", *Energies*, Vol. 10, No. 4, (2017), 575. https://doi.org/10.3390/en10040575

13. Zanforlin, S. and Deluca, S., "Effects of the reynolds number and the tip losses on the optimal aspect ratio of straight-bladed vertical axis wind turbines", *Energy*, Vol. 148, (2018), 179-195. https://doi.org/10.1016/j.energy.2018.01.132

14. Rasekh, S., Hosseini Doust, M. and Karimian, S., "Accuracy of dynamic stall response for wind turbine airfoils based on semi-empirical and numerical methods", *Journal of Applied Fluid Mechanics*, Vol. 11, No. 5, (2018), 1287-1296. https://doi.org/10.29252/jafm.11.05.28668

15. Karimian, S. and Rasekh, S., "Power and noise performance assessment of a variable pitch vertical axis darrieus type wind turbine", *Journal of the Brazilian Society of Mechanical Sciences and Engineering*, Vol. 43, No. 9, (2021), 437. https://doi.org/10.1007/s40430-021-03103-4

16. Moghimi, M. and Motawej, H., "Developed dmst model for performance analysis and parametric evaluation of gorlov vertical axis wind turbines", *Sustainable Energy Technologies and Assessments*, Vol. 37, (2020), 100616. https://doi.org/10.1016/j.seta.2019.100616

17. Sedaghat, A., Assad, M.E.H. and Gaith, M., "Aerodynamics performance of continuously variable speed horizontal axis wind turbine with optimal blades", *Energy*, Vol. 77, (2014), 752-759. https://doi.org/10.1016/j.energy.2014.09.048

18. Sedaghat, A., Samani, I., Ahmadi-Baloutaki, M., Assad, M.E.H. and Gaith, M., "Computational study on novel circulating aerofoils for use in magnus wind turbine blades", *Energy*, Vol. 91, (2015), 393-403. https://doi.org/10.1016/j.energy.2015.08.058

19. Li, L. and Mak, C.M., "The assessment of the performance of a windcatcher system using computational fluid dynamics", *Building and Environment*, Vol. 42, No. 3, (2007), 1135-1141. https://doi.org/10.1016/j.buildenv.2005.12.015

20. Chong, W.-T., Muzammil, W.K., Wong, K.-H., Wang, C.-T., Gwani, M., Chu, Y.-J. and Poh, S.-C., "Cross axis wind turbine: Pushing the limit of wind turbine technology with complementary design", *Applied Energy*, Vol. 207, (2017), 78-95. https://doi.org/10.1016/j.apenergy.2017.06.099

21. Adanta, D., Sari, D.P., Syofii, I., Prakoso, A.P., Saputra, M.A.A. and Thamrin, I., "Performance comparison of crossflow turbine configuration upper blade convex and curvature by computational method", *Civil Engineering Journal*, Vol. 9, No. 1, (2023), 154-165.

22. Paraschivoiu, I., "Wind turbine design: With emphasis on darrieus concept, Presses inter Polytechnique, (2002).

23. Castelli, M.R., Englaro, A. and Benini, E., "The darrieus wind turbine: Proposal for a new performance prediction model based on CFD", *Energy*, Vol. 36, No. 8, (2011), 4919-4934. https://doi.org/10.1016/j.energy.2011.05.036

24. Mohamed, M., "Performance investigation of h-rotor darrieus turbine with new airfoil shapes", *Energy*, Vol. 47, No. 1, (2012), 522-530. https://doi.org/10.1016/j.energy.2012.08.044
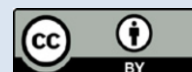
Persian Abstract

چکیده

در تحقیق حاضر، یک توربین بادی محور عمودی نوین ارائه شده که توانایی ایجاد تهویه ضمن تولید انرژی را دارا است. ایده این روش از بادگیرهای باستانی گرفته است. در این مطالعه ابتدا ظرفیت باد شهر منجیل در ایران مورد بررسی قرار گرفته و یک توربین بادی معمولی در مقیاس خانگی متناسب با اقلیم این شهر ارزیابی شده است. برای طراحی هندسه توربین از یک کد نیمه تحلیلی سه بعدی بر اساس تئوری دابل مولتیپل استریم تیوب یا به اختصار دی ام اس تی استفاده شده است. تجزیه و تحلیل اعتبار سنجی روش حل نیز توسط توربین مرجع انجام شده است. با استفاده از این کد، عملکرد توربین شامل شاخص ضریب توان و انحراف جریان بررسی شده است. همچنین تأثیر زاویه مخروطی پره بر ضریب توان و تهویه مورد بررسی قرار گرفته است. نتایج این مطالعه پارامتر نشان می‌دهد که برای محدوده بهینه نسبت سرعت نوک پره ۲.۹-۳.۲ و با زاویه مخروطی ۲۰ درجه پره بر اساس منحنی توان، امکان تولید جریان تهویه تا ۴۰۰ متر مکعب در ساعت و توان خروجی ۵۰-۲۰۰ وات وجود دارد که این میزان معادل ۲.۵٪ از کل جریان ورودی به روتور است. همچنین مشاهده شد که در صورت استفاده از هندسه متناسب با اقلیم منطقه، می‌توان افت توان را کاهش داد. در نهایت، برخی از روندهای تعمیم یافته توابع هدف نیز بیان شده و می‌توان از این روش برای حل مشکلات جاری در حوزه انرژی و تهویه مطبوع استفاده کرد.

International Journal of Engineering

Feature Engineering Methods in Intrusion Detection System: A Performance Evaluation

F. Zare, P. Mahmoudi-Nasr*

Department of Compute Engineering, University of Mazandaran, Mazandaran, Iran

A B S T R A C T

Today, the number of cyber-attacks has increased and become more complex with an increase in the size of high-dimensional data, which includes noisy and irrelevant features. In such cases, the removal of irrelevant and noisy features, by Feature Selection (FS) and Dimensions Reduction (DR) methods, can be very effective in increasing the performance of intrusion detection systems (IDS). This paper compares some FS and DR methods for detecting cyber-attacks with the best accuracy using implementation on KDDCUP99 dataset. A Deep Neural Network (DNN) is used for training and simulating them. The results show the filter methods are faster than wrapper methods but less accurate. Whereas the Wrapper methods have more accuracy but are computationally costlier. Embedded methods have the best output and maximum values, which is 99% for all the metrics, comparing to it the DR methods have shown a good performance and speed, among them Linear Discriminant Analysis (LDA) method even better than embedded method.

doi: 10.5829/ije.2023.36.07a.15

1. INTRODUCTION

With the increasing use of internet, the threats have also increased and become more complicated, so the protection of networks in the modern world has become increasingly important. A key technology for ensuring the security of networks is intrusion detection systems [1], which are referred to as the first line of defense for securing networks [2].

In general, IDSs are divided into Signature-based and Behavior-based, with the former using Machine Learning algorithms (ML), which have been widely used by data scientists recently [3-5]. The first step in working with ML algorithms is feature engineering for reducing and cleaning the input data to make it faster and more accurate. Feature engineering techniques improve the detection performance by extracting relationships between data and removing irrelevant information [6].

Two important parts of feature engineering are Feature Selection (FS) and Dimensions Reduction (DR), which play an important role in machine learning classification problems [7]. Therefore, the detection process will be faster and more intensive, which in turn

leads to a lower demand for computing resources. Some of the advantages of these methods are as follows:

1. Reduce the probability of overfitting the model and get a better generalization.
2. Give a better data visualization to get a good comprehension.
3. The unsupervised methods are useful when there is no labeled data or not enough labeled data.
4. Reduce the training time by removing the noisy and redundant data.
5. Improve the performance and accuracy of the model by removing the irrelevant data.

Since there are different types of FS and DR methods, it's necessary to select the best one. The purpose of this paper is to compare various methods of feature engineering.

Due to the increasing complexity and different types of attacks, this paper prefers to work on a behavior-based IDS, and due to the better performance of neural networks among the ML algorithms [8]. A Deep Neural Network (DNN) is selected as the final classifier. In this paper, we trained a DNN as a classifier for a behavior-based IDS to compare the performance of FS methods, i.e., filtering, wrapper, and embedded methods, as well as

Corresponding Author Institutional Email: *P.mahmoudi@umz.ac.ir*
(P. Mahmoudi-Nasr)

DR methods that categorize into linear and non-linear methods. As a classifier in FS methods, some ML algorithms like Support Vector Machine (SVM) [9] and Random Forest (RF) [10] are used to find the best features.

The rest of the paper is organized as follows: In section 2, the related works are presented. Details and explanations of the FS and DR methods are examined in section 3. The reports and experimental results are conducted in section 4 and the conclusion is given in section 5.

2. RELATED WORK AND CONTRIBUTIONS

Feature engineering is one of the most time-consuming parts in ML problems [11], FS trying to find the good features that are selected from the data and are not redundant, are related to the output, also cause more difference between classes and minimize the internal variance and maximize the external variance. FS Algorithms need to search in the data space, so four basic essential problems in their diversity have explained starting point, search organization, evaluation method and algorithms elimination metric data structure, model structure and data diversity make impression on FS. Each FS algorithm can give different results on an individual data set. FS is suitable to obtain the nature of the data, otherwise there are other methods such as feature extraction, which have become very popular in recent years.

Ghasemi and Esmaily [12] presented an IDS using KDDcup99 and NSL-KDD datasets based on machine learning algorithms. They pointed out that feature selection plays an important role in standard benchmark datasets. Therefore, the GA algorithm was used to select the optimal features. In this paper, it was shown that the data dimensions have an important effect on the performance of the algorithm, and finally the DT algorithm together with the feature selection method achieved the highest evaluation scores.

Venkatesh and Anuradha [13] have shown the importance of dimensionality reduction due to the increase of noisy data, which affects the performance of the algorithm. They have explained the FS methods and divided them into filter, wrapper and embedded methods. They have explained six stages for FS methods which consist of search direction, search strategy, evaluation criteria, stopping criteria and validation of results.

Biglari et al. [14] claimed that high-dimensional data posed a major challenge to the data mining problem. They presented a four-step feature selection method to improve the efficiency of machine learning algorithms on high-dimensional data. The proposed method was applied to two high-dimensional data and achieved a prediction accuracy of 0.92 and 0.99 (99%).

Kou et al. [15] tried 10 FS methods to get the best result on a text classification problem with 10 different data sets. The authors declared the evaluation of a FS method to be a Multiple Criteria Decision Making (MCDM) problem. They also used nine evaluation measures for binary classification and seven evaluation measures for multi-class classification. According to the results, it is obvious that MCDM-based methods are effective in evaluating the methods of FS.

Mohammadi et al. [16] have proposed a FS method to improve the performance of IDS using KDDcup99. It is a combination of a filtering method, where the linear correlation coefficient reduces the computational complexity, and a wrapper method, which is the Cuttlefish algorithm; in addition, the ID3 algorithm was used as a classifier. The results show a significant improvement in performance compared to using only the filter method or the wrapper method.

Meza and Touahria [17] have created a helpful review of FS methods to improve an IDS, they have explained many approaches in FS for IDS. They have proposed a new taxonomy of FS algorithms and presented their properties depending on different datasets, selection mechanisms, selection approaches, selection techniques, classifiers, selection features and multi-objective aspects.

Gündüz and Çeter [18] have conducted an experiment to improve the performance of IDS, which classifies attacks using four classification algorithms, namely Multi Layers Perceptron, Support Vector Machine (SVM), Decision Tree and a fuzzy-based algorithm on the KDDcup99 dataset. The FS is created first by correlation and then using the Best First Search (BFS) algorithm, where the 11 most important features were selected. The classification results show an improvement in performance after applying the FS.

Umar and Zhanfang [19] have tested five classification algorithms, i.e. Artificial Neural Network (ANN), SVM, Naïve Bayes (NB), K Nearest Neighbors (KNN) and Random Forest (RF) for improvement and IDS with two datasets, NSL-KDD and UNSW-NB15. The chosen FS. Method is wrapper-based. They compared the classification with and without FS, and the results show an increase in speed for all algorithms except ANN and a negligible decrease in accuracy. This shows the importance of FS in reducing execution time.

Zhao et al. [20] have proposed a novel model for intrusion detection using PCA and a classifier for the KDDcup99 dataset. To choose the best classifier, two algorithms were compared: soft max regression, an extended version of logistic regression, and K Nearest Neighbor. The experimental results show that the dimensions reduced by PCA contain negligible loss of useful information, but the redundant data are significantly reduced. For the classification algorithms, both achieved similar performance, with Soft max Regression having lower execution time.

Saranya et al. [21] have presented an investigation of ML algorithms to improve IDS for the Internet of Things (IoT) using the KDDcup99 dataset. They have implemented three algorithms: Linear Discriminant Analysis (LDA), Classification and Regression Trees (CART), and the RF. Experimental results show an accuracy of 99.65% for RF, 98.1% for LDA and 98% for the CART algorithm. The work has also compared different ML algorithms, i.e. K-means, J.48, SVM, PCA, logistic regression, decision tree (DT) and ANN. The results show that ANN and DT are the classifiers with the highest accuracy (99.65%).

Considering the above context, the key contributions to this paper are as follows:

- Find out the best way to make intrusion detections faster and more accurate with less use of computational resources.

- A detailed comparison between most popular DR and FS methods from prediction performance point of view.

- Examine the application of SVM and DNN to the problem of FS and DR in IDS.

3. RESEARCH METHODOLOGY

The overall view of the methods evaluated and implemented in this research is shown in Figure 1.

3. 1. Filtering Methods   Filtering methods [22] are independent of ML algorithms, so they are more optimal than other methods in terms of computational load. Figure 2 shows the overall structure of filtering methods. In these methods, FS is done according to the feature ranking by statistical characteristics such as Distance, Correlation, Information and Consisting.
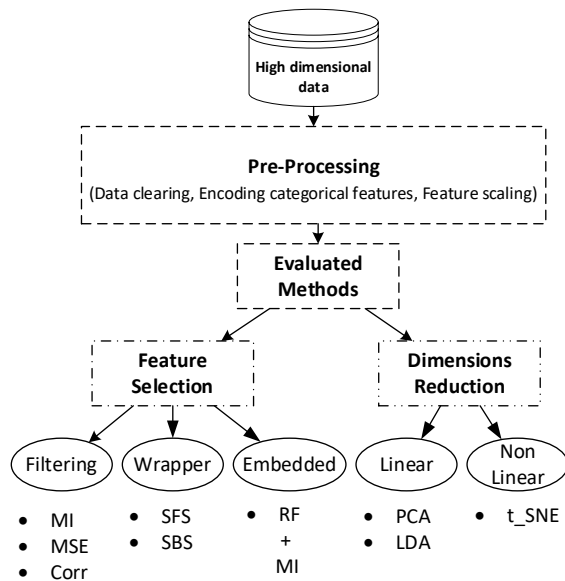

Figure 1. overall view of evaluated methods
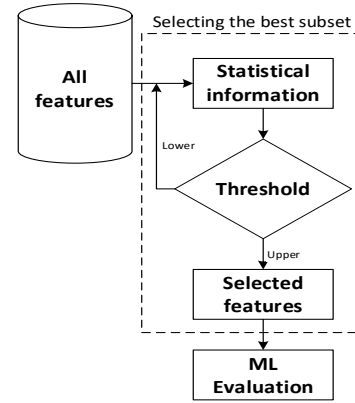

Figure 2. Overall structure of Filtering methods

3. 1. 1. Mutual Information (MI)   In this method, the MI of each feature is calculated according to Equation (1) and the best features are selected according to the maximum value of MI.

$$MI(x_k, y) = Exy\left[log\frac{P(x,y)}{P(x)P(y)}\right] \qquad (1)$$

If there is no relevance between x and y, they are considered independent and the value MI would be equal to 0.

3. 1. 2. Mean Squared Error (MSE)   This method also provides a value called MSE according to Equation (2), which gives the mean squared error.

$$MSE = \frac{1}{N}\sum_{i=1}^{N}(y_i - \hat{y}_i)^2 \qquad (2)$$

This method uses the output errors obtained with a ML algorithm that also requires a predefined threshold to select the best features.

3. 1. 3. Correlation   The correlation metric selects the features that have the greatest relevance to the output, as the lower correlation indicates the separable and redundant features [23]. The correlation is determined according to Equation (3).

$$Correlation = \frac{Cov(\chi_k, d)}{\sqrt{Var(x_k)}\sqrt{Var(y)}} \qquad (3)$$

A threshold value for the correlation value should be considered and the features with a correlation value below the threshold value should be removed. This metric works linearly and is not suitable for the nonlinear relevancies.

3. 2. Wrapper Methods   As shown in Figure 3, wrapper methods use ML evaluation algorithms to select a subset of features. These methods require more processing time than filtering methods because the evaluation algorithm is run multiple times and each time a subset of features is selected and then performance is examined according to the predefined learning model
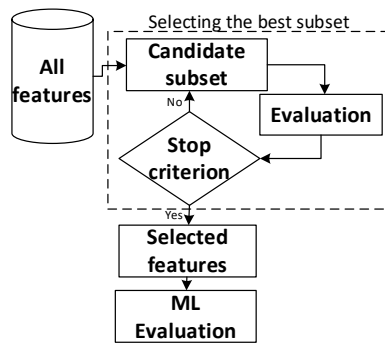
Figure 3. Overall structure of Wrapper Methods

with an evaluation metric. Since the wrapper methods naturally operate during model training, they cause a heavy computational load when processing big data.

These methods divide into greedy and non-greedy. This section presents the greedy methods, which select the features that seem best at the time and are usually trapped in a local minimum. Some of the greedy methods are as follows:

3. 2. 1. Best Individual *n* Features   In this method, to select *n* features, the cost function is calculated *t* times, then the features with the best value are selected. So, the training is repeated *t* times to find *n* best features. This method works blindly and has the disadvantage that the duplicate features are not considered and a good repeated feature appears several times in the output features.

3. 2. 2. Sequential Forward Search (SFS)   At the beginning, there is a single feature that is updated in each step. First the best single feature is selected, in the next step a feature is selected that is best related to the previous feature, and so on until the end of all features. It goes forward in the same way through all features to find *n* number features, but this has the following weaknesses:
1. The selection of the first feature follows the method of the *best individual feature* and therefore has its disadvantages.
2. The features selected in the next steps are based on the previously selected features, so the removed features have no chance to serve as the main component of the feature set.
3. Each selected feature is frozen and remains until the end, even if it could not form the best feature set.

3. 2. 3. Sequential Backward Search (SBS)   This method starts with a totality of all features as a set and in each step one of them is removed. In the initial state, the cost function has the maximum value and is reduced by the elimination in each step, so the feature chosen for removal should have the least influence on the cost function. This method has 2 weaknesses:
1. After deleting a feature, there is no way to select it in the next steps.

2. Unlike SFS, it starts with a large number of features, which reduces the reliability of the cluster, which is why the SFS method is more popular than SBS.

3. 3. Embedded Methods   Filtering methods do not use clusters reduce performance, and wrapper methods are also computationally intensive. Thus, embedded methods proposed to use the clusters to determine the criteria during training and usually use for specific ML algorithm. As can be seen in Figure 4, in these methods, the search for the optimal subset of features would occur in the cluster design phase and can be viewed as a search in a combined space of subsets and hypotheses.

Random Forest is a very powerful model for both regression and classification, which can also provide its own interpretation of feature importance. Each tree of the random forest can calculate the importance of an attribute according to its ability.

The higher the importance of the feature, the more appropriate feature to choose, and according to the importance of each feature, feature selection is done.

3. 4. Comparison Between Feature Selection Methods   Table 1 summarizes the comparison between the above methods. Filtering methods are appropriate when the speed of FS is more important, and wrapper methods are appropriate for systems that are delay tolerant and have the ability to provision the computational resources, and for systems that care about both, embedded methods are good.

As it is mentioned in Table 1, interaction with the classifier can be an advantage. The filtering methods select the features just according to statistical criteria to score the correlation or dependence between the input variables and determine the relationship between them, but the wrapper and embedded methods work with the classifier and select the features according to the main problem and evaluate and categorize effective features and introduce them to the model.

3. 5. Dimensions Reduction (DR)   As can be seen in Figure 5, the DR methods are generally divided into linear and nonlinear methods. These methods change the
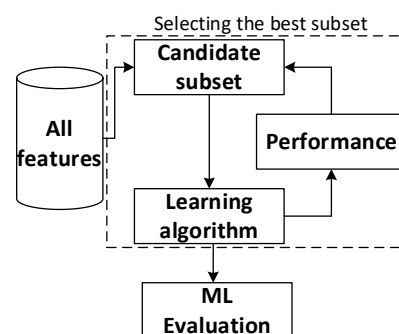

Figure 4. Overall structure of Embedded Methods

TABLE 1. Methods Comparison

Methods	Advantages	Disadvantages
Filtering	Independent of classifier, less computational cost, short running time,	No interaction with classifier
Wrapper	Interaction with classifier, Recording attribute dependency	High computational cost, Overfitting feasibility, dependent on classifier
Embedded	Interaction with classifier, less computational cost, Recording attribute dependency	Dependent on classifier
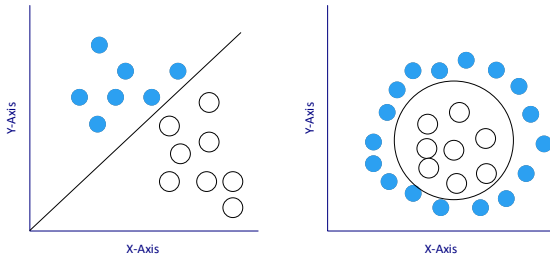
Figure 5. Structure of linear and none linear methods

distribution of data points to the distribution in which the data can be visually classified.

As part of this category, Principal Component Analysis (PCA) [24] and Linear Discriminant Analysis (LDA) [25] as linear methods, and t-distributed stochastic neighbor embedding (t-SNE) as nonlinear technique are described.

3. 5. 1. Principal Component Analysis   To reduce computational costs and process complexity when using high-dimensional data, features must be reduced and combined rather than deleted, although the combination should contain the information of all features.

There are many methods to do this, but PCA is one of the first and most important methods in the field DR. PCA doesn't consider the data labels, which is why it's also called an unsupervised method. When projecting data, some data information is inevitably lost. Therefore, the PCA method selects the axis that preserves the most information, and when projecting data with this axis, the loss of data information is the least.

PCA requires preprocessing of the data before the dimensions are reduced, which can be done using formula 4.a, or to compensate for the deviation of the data points according to Equation (4.b), the standard deviation can also be part of the preprocessing.

$$X = x_j^i - \mu_j \tag{4.a}$$

$$X = \frac{x_j^i - \mu_j}{\sigma_j} \tag{4.b}$$

X refers to input data with $m*n$ dimensions (m is the number of samples and n is the number of features).

3. 5. 2. Linear Discriminant Analysis   The LDA algorithm is a kind of counterparty to PCA, since it uses the data labels and falls into the category of supervised methods. In the following, this method is studied as a binary and multiclass method.

3. 5. 3. Multi-Classes   For multiple class data needed to determine the median, it must be determined for each class and for the entire classes in general according to Equations (5) and (6), respectively.

$$\mu_i = \frac{1}{n_i} \sum_{x_i \in c_i} x_i \tag{5}$$

$$\mu = \frac{1}{n} \sum x_i \tag{6}$$

The variance is calculated in two parts, first the variance between classes (SB) and then the variance within classes (SW) according to Equations (7) and (8), respectively.

$$S_B = \sum_{i=1}^{c} n_i (\mu_i - \mu)(\mu_i - \mu)^\top \tag{7}$$

$$S_w = \sum_{i=1}^{c} s_i; s_i = \sum_{i=1}^{c} \sum_{x_k \in c_i} (x_k - \mu_i)(x_k - \mu_i)^\top \tag{8}$$

The eigenvalues and vectors are determined using Equation (9).

$$S_B v = \alpha s_w v \; ; \; s_w^{-1} S_B v = \alpha v \tag{9}$$

3. 5. 4. t-distributed Stochastic Neighbor Embedding (t-SNE)   LDA and PCA reduce the data by finding a linear relationship between the data, but if there are too many features in the data, it's better to use a nonlinear method, which is called one of the most famous nonlinear methods t_SNE and is newer than PCA and LDA. The t_SNE algorithm is a complicated calculation [26].

The t_SNE method doesn't use labels, so it's also unsupervised and reduces data dimensions by extracting a nonlinear relationship. This section contains a brief explanation of its steps.

Step 1: The similarity rate between data points in high dimensions is calculated according to Equation (10) and the similarity for each data point is determined using the Guassian distribution.

$$P_{j|i} = \frac{exp\left(-\|x_i - x_j\|^2\right)/2\sigma^2}{\sum_{k \neq i} exp(-\|x_i - x_k\|^2)/2\sigma^2} \tag{10}$$

Step 2: This step is a repeat of the previous step, but using a different distribution called Student's t_distribution with freedom of 1, called the Cauchy distribution, so that the Qj|i for each data point are calculated according to Equation (11).

$$Q_{j|i} = \frac{exp\left(-\|x_i - x_j\|^2\right)}{\sum_{k \neq i} exp(-\|y_i - y_k\|^2)} \tag{11}$$

Step 3: in this step, the Kull-Back-Leibler divergence metric (KL) plays the role of the cost function. Each distribution tries to keep the parameters as small as possible by making the best use of the gradient decent.

3. 5. 5.   Comparison Between Feature Selection Methods   PCA and LDA are linear methods and can not handle complex and high dimensional data, but t_SNE is non-linear and suitable for high dimensional data. More over the LDA versus PCA and t_SNE is supervised and requires labeled data. On the speed discussion according to the done experiments, the fastest algorithm is LDA and the lowest one is t_SNE.

4. IMPLEMENTATION

Implementation is done using python 3.9 and on a on a machine with Intel(R) Core(TM) i7-10510U CPU @ 1.80GHz -2.30 GHz, 1 NVIDIA GP108 PCIe 2GB and 12GB RAM, using the Visual Studio Code environment with Keras and SKlearn library.

As can be seen in Figure 6, this paper attempts to find the best way to reduce the data before training a Deep Neural Network (DNN) for a classification problem. The DNN works as a supervised method and uses the labels of the data to be trained. Feature selection methods (FS) are also evaluated using Support Vector Machine (SVM) and the results can be seen in Table 2.

4. 1. Dataset And Performance Evaluation   The dataset that has been chosen for evaluation and FS is KDDcup99, which is still working as an useful dataset
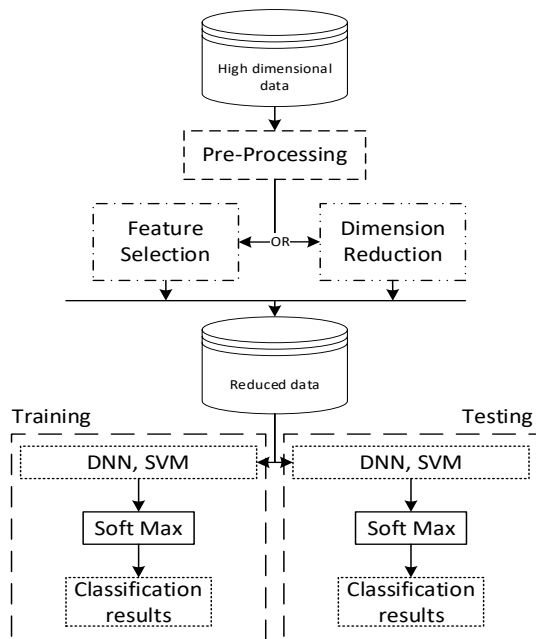

Figure 6. Implementation Structure

TABLE 2. Evaluation results for feature selection methods by SVM (Acc, Pre stand for Accuracy and Precision respectively)

Method	Selected Features	Acc	Pre	Recall	F1-Score
MI	2,4,22	99%	98%	99%	98%
Correlation	9,15,28	79%	78%	79%	71%
MSE	2,4,22	99%	98%	99%	98%
SFS	2,3,4	99%	99%	99%	99%
SBS	2,4,29	99%	98%	99%	99%
Embedded	-	99.9%	99.9%	99.9%	99.9%

[21, 27]. This dataset is selected base on: (i) lack of public benchmark datasets for network-based intrusion detection, (ii) popularity and frequent use of KDDcup99 dataset by many researchers as a good bench mark dataset, (iii) various number of attack classes in this dataset, (iv) arrangement of records in such a way that there is no need to randomly select a part of the dataset to well train a model.

This dataset has 41 features which three of them are object type (Protocol_type, Service and Flag). Totally there are four types of attacks in this dataset:
- **DoS:** Denial-of-Service, e.g. syn flood
- **R2L:** Remote to Local, unauthorized access from a remote machine, e.g. guessing password
- **U2R:** User to Root, unauthorized access to local superuser (root) privileges, e.g., buffer overflow
- **Probe:** surveillance and other probing, e.g., IP sweeping.

The dataset consists of totally 1,072,992 records which divided into 812,814 normal, 247,267 DoS, 13,860 Probe, 999 R2L and 52 U2R records.

In this work, the results and the selected features are denoted by their indices from 0 to 41.

The performance scores used in this work are **accuracy**, **precision**, **Recall** and **F1 score**, which are given in the Equations (12)-(15), respectively.

$$accuracy = {TP+TN}\big/{TP+TN+FP+FN} \tag{12}$$

$$precision = {TP}\big/{TP+FP} \tag{13}$$

$$recall = {TP}\big/{TP+FN} \tag{14}$$

$$F1-score = \frac{2*precision*recall}{precision+recall} \tag{15}$$

4. 2. Pre-processing   Before start working with the algorithms of ML, it's necessary to preprocess the input data. The 3 main steps of preprocessing are as follows:
1. *Missing value*: the selected KDD is complete and doesn't need this phase.

4. 2. 1. Encoding the Categorical Data   In this paper the label encoding method was used for the protocol_type, service, flag and label columns.

4. 2. 2. Feature Scaling   In this phase, the standard scaler is used to set the values between -1 and 1. The standardization was performed according to Equation (16).

$$Standard\ x = \frac{x_j - \overline{x_j}}{\sigma_j} \tag{16}$$

4. 3. Filtering Methods   In this method, FS is based on the classification of features in terms of their statistical properties. To perform the filtering methods such as MI, MSE and correlation, *n* (number of selected features) was set to 3, so that the 41 original features of KDD are reduced to 3. In this section, a SVM was implemented to validate the methods.

4. 3. 1. Mutual Information (MI)   This method calculates the MI and then selects the features with the most MI. Then, depending on the importance of accuracy or speed, the *n* numbers of the best selected features must be selected.

As can be seen in Figure 7, according to the result of the MI method, the 3 best features (No. 2, No. 4 and No. 22) were selected. To validate the selected features, they are applied to a SVM as input, and according to Table 2, the results show satisfactory values for the validation metrics.

4. 3. 2. MSE   Decision tree was selected as a ML algorithm to evaluate each feature to predict the target, and finally the *n* number of features with the minimum MSE are selected.

According to the plot in Figure 8, which shows the results of applying the MSE method to the KDD, the top three features (No. 2, No. 4, and No. 22) are selected to be scored with SVM. As can be seen in Table 2, the metrics scores are very similar to the method MI.

4. 3. 3. Correlation   The correlation of a variable indicates the degree of its relationship with the
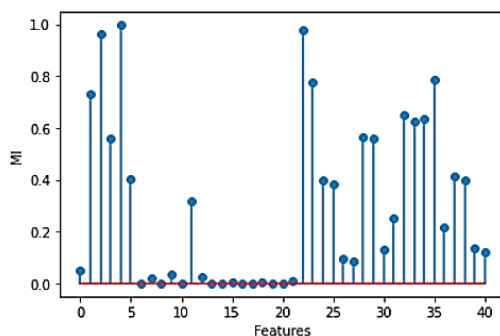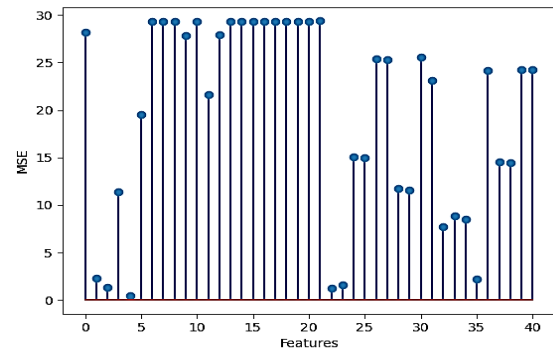

Figure 7. Features based on MI

Figure 8. features based on MSE

corresponding target. If the correlation is equal to "1", it means that they are strongly correlated, and if it is equal to "-1", it means that there is an inverse relationship between them. Then, a threshold of *α* must be set and a number of *n* must be selected for the remaining features.

In this work, the correlation between the features is calculated first, and the features whose correlation is greater than 'α" are selected, which is 0.8 in this implementation. As can be seen in Table 3, seven groups with correlation greater than 0.8 were found, from each of which one feature was selected and the others were removed. By running the Random Forest (RF) for each feature group, the features with the highest significance are selected (Table 4). Next, the three best features (No. 9, No. 15, and No. 28) have been examined with SVM, as shown in Table 2.

TABLE 3. Correlated Features (F stands for Feature)

Group1			Group 4		
F 1	**F 2**	**Correlation**	**F 1**	**F 2**	**Correlation**
38	25	0.999334	32	33	0.973634
38	37	0.998142	32	28	0.898427
38	24	0.997839	32	2	0.867102
38	28	0.857570	-	-	-
-			Group 5		
-	-	-	**F 1**	**F 2**	**Correlation**
-	-	-	21	9	0.83892
Group 2			Group 6		
F 1	**F 2**	**Correlation**	**F 1**	**F 2**	**Correlation**
26	27	0.994817	35	23	0.944650
26	39	0.986782	35	1	0.860319
26	40	0.984970	35	22	0.860243
Group 3			Group 7		
F 1	**F 2**	**Correlation**	**F 1**	**F 2**	**Correlation**
15	13	0.995016	3	28	0.851775

TABLE 4. Important Feature of each group

Group number	Most Important Feature	Importance
1	28	0.576205
2	40	0.426946
3	15	1.0
4	2	0.541133
5	9	1.0
6	22	0.527443
7	28	1.0

4. 4. Wrapper Methods   This category includes several methods. To implement the wrapper methods, the variable *n* was set to 3. The implemented wrapper methods are as follows:

4. 4. 1. Sequential Forward Search (SFS)   The SFS method attempts to eliminate the redundant features and selects a number of *n* remaining features to achieve satisfactory accuracy and speed. In this step, useful algorithms can be used to select the best features.

For simplicity, the correlation matrix is used in this implementation and the features with high correlation were removed. About 14 features were removed and the number of features was reduced to 27. Then, K Neighbors was used to find the 3 best features.

After removing 14 features through the correlation matrix, the selected algorithm for the SFS method found the three best features according to the accuracy metric. As can be seen in Table 2, the SFS selected the three best features (No. 2, No. 3, and No. 4) with accuracy greater than 99%.

4. 4. 2. Sequential Backward Search (SBS) Backward FS starts with all features and builds a model that deletes one feature at each step to get the best result. In this algorithm, the termination metric is reaching a certain number of features, so the *n* numbers of features needed can be determined at this stage.

To implement this algorithm, the RF algorithm is used to find the 3 best features according to the accuracy. Table 2 shows that the three best features (No. 2, No. 4 and No. 29) selected by the SBS method have an accuracy of more than 99%. As can be seen, the results are too close to the SFS method.

4. 5. Embedded Method   The results of this method depend on the chosen machine learning algorithm (ML) that FS uses during the training phase. After that, another method such as MI is applied to the results of the algorithm to capture the 'n" number of features needed.

4. 5. 1. RF   In this phase, the features are clustered using RF as the classification algorithm and ordered by MI.

As can be seen in Figure 9, which shows the feature group evaluated by the RF algorithm, the top three features with the most MI were selected. Table 2 and a comparison between the presented methods show that the embedded method using RF and MI received the most values for the validation metrics and outperformed the filtering and wrapper methods.

4. 6. Dimensions Reduction   In this section, a DNN was implemented to validate the methods. Figure 10 shows the structure of implemented DNN. The implemented DNN has only 2 neurons in the first layer, 10 neurons in the second layer, and finally 23 neurons for the last layer due to the 23 types of attacks that exist in the KDD dataset.

ReLU was chosen for the activation function in the first layer, *tanh* was chosen for the second layer, and *SoftMax* was chosen for the last layer, and *dropout* was also applied between layers to suppress the overfitting of the model.

Due to the existence of different types of neural networks (LSTM, CNN, TCN, DNN...), it can be claimed that there are different types of feature extraction and the most suitable network should be selected according to the type of problem. Therefore, apart from the fact that neural networks are able to extract features, when it comes to performance comparison and in all comparison modes the number of training epochs is fixed, the model in the mode that receives inputs that pass through the FS or DR stages can make better use of the limited number of epochs to be trained better than a model that is faced with raw input data with the same number of epochs. So, in the first phase of implementation, the DNN is trained and tested with all 41 features of KDD, and the results are
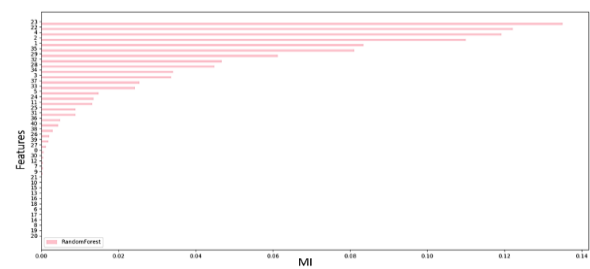
Figure 9. Random Forest Output
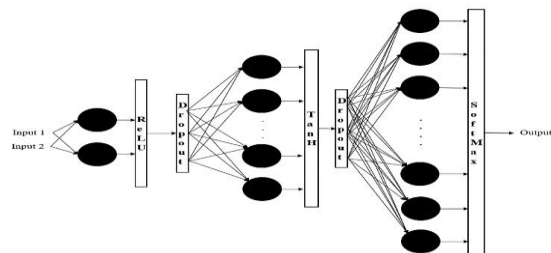
Figure 10. Structure of Deep Neural Network

shown in Table 5. As can be seen, the accuracy of the model is about 78%, which is very low compared to the other implementations.

In the next stage, Dimensions Reduction (DR) methods such as PCA, LDA and t_SNE are applied to the data.

4. 6. 1. PCA   In order to perform PCA as a linear method DR, the number n of required dimensions must be defined, which can be determined, for example, according to the number of neurons in a Deep Neural Network.

The PCA applied to KDD is set to $n=2$, so that all 41 features are mapped into 2 dimensions and passed as input to the DNN. The validation results can be seen in Table 5. As can be seen, the DNN with the PCA method outperformed the validation without applying any FS method.

4. 6. 2. LDA   The LDA method works as a linear method, and to reduce the dimensions of the data, the n numbers for the dimensions of the output data must first be specified. These may vary depending on computational resources, speed required, or accuracy needed.
To compare the results of the methods of DR, the output dimensions of LDA were also set to 2 and the mapped data was used as DNN input. As can be seen in Table 5, the LDA method outperformed PCA.

4. 6. 3. t_SNE   This method is useful for complicated data with too many features. Since it is a nonlinear method, it takes more time to reduce the dimensions of the data. The number of training epochs may be different, so it takes time to determine the number of epochs.

The t_SNE method was applied with two different iterations, first with 500 and then with 1000, and the

TABLE 5. Evaluation results for dimension reduction and feature selection methods by DNN

Method	Accuracy	Precision	Recall	F1-Score
Without FE	0.7853	1.0000	0.5685	0.7209
PCA	0.9401	0.9454	0.9400	0.9426
LDA	**0.9776**	**0.9783**	**0.9774**	**0.9778**
t-SNE (500 iter)	0.6749	0.8536	0.5218	0.6446
t-SNE (1000 iter)	0.6917	0.8203	0.5934	0.6865
MI (22, 4)	0.9466	0.9567	0.9180	0.9366
Correlation	0.5698	0.5733	0.5698	0.5698
MSE (4, 22)	0.7854	0.7854	0.7854	0.7854
SFS (3, 4)	0.7852	0.7852	0.7852	0.7852
SBS (2, 29)	0.7852	0.9184	0.9183	0.9183
Embedded (22, 23)	**0.9701**	**0.9704**	**0.9698**	**0.9701**

output dimension was set to 2. According to Table 5, the t_SNE method did not perform well on KDD, it might work better on datasets with many more features.

5. DISCUSSION

For comparison and further evaluation, three best features were selected from those chosen by the above methods and the performance of each was evaluated using the SVM algorithm on the KDDCUP99 dataset. As can be seen from Table 2, the SFS and SBS methods are close to each other, although the running time of SBS is much longer than that of SFS. Among the algorithms in Table 2, the correlation method has the lowest accuracy but also the shortest running time. Using MI method in embedded methods leads to maximum performance and satisfactory running speed.

So, the 3 different methods such as PCA, LDA, and t_SNE were applied before training the DNN to see the difference in performance. To have a complete comparison, the DNN model was also trained and tested using the selected features by FS methods.

The comparison results can be found in Table 5. As can be seen, the LDA method has the best accuracy, even compared to the embedded method, which was the best among the FS methods.

6. CONCLUSION

In this paper, the methods of Feature Selection (FS) and Dimensions Reduction (DR) are presented and compared using a DNN. The importance of DR for Big Data was shown as it increases performance, and a comparison was made between FS methods using the implementation on the KDDCUP99 dataset. The wrapper methods have higher accuracy but are more computationally expensive. Embedded methods had the best results and maximum values that are 99% for all metrics.

This paper also compares the methods of DR. Based on the implementation results, it can be seen that LDA has the best performance among the mentioned methods, even ahead of the embedded method. The t_SNE method is also very accurate, it can achieve better results on data sets with very high dimensions.

The experimental results of this paper show that:
Among the FS methods:
1. The filtering methods have the minimum run time.
2. The wrapper methods have the best accuracy.
3. The embedded methods present a trade-off between run time and accuracy.
Among the DR methods:
4. The LDA has the best value.
5. The t-SNE methods takes too long to response, it may show better results on very high dimensional data.

6. The PCA is also very close to LDA, but still among them all, the LDA has shown the best results.

In future works, the FS method will be discussed by heuristic algorithms on a more complicated data with more dimensions. Deep Learning methods that go forward by feature extraction will be also studied.

7. REFERENCES

1. Li, X., Chen, W., Zhang, Q. and Wu, L., "Building auto-encoder intrusion detection system based on random forest feature selection", *Computers & Security*, Vol. 95, (2020), 101851. https://doi.org/10.1016/j.cose.2020.101851

2. Kasongo, S.M. and Sun, Y., "A deep learning method with wrapper based feature extraction for wireless intrusion detection system", *Computers & Security*, Vol. 92, (2020), 101752. https://doi.org/10.1016/j.cose.2020.101752

3. MR, G.R., Somu, N. and Mathur, A.P., "A multilayer perceptron model for anomaly detection in water treatment plants", *International Journal of Critical Infrastructure Protection*, Vol. 31, (2020), 100393. https://doi.org/10.1016/j.ijcip.2020.100393

4. ur Rehman, S., Khaliq, M., Imtiaz, S.I., Rasool, A., Shafiq, M., Javed, A.R., Jalil, Z. and Bashir, A.K., "Diddos: An approach for detection and identification of distributed denial of service (ddos) cyberattacks using gated recurrent units (GRU)", *Future Generation Computer Systems*, Vol. 118, (2021), 453-466. https://doi.org/10.1016/j.future.2021.01.022

5. Abdelaty, M., Doriguzzi-Corin, R. and Siracusa, D., "Daics: A deep learning solution for anomaly detection in industrial control systems", *IEEE Transactions on Emerging Topics in Computing*, Vol. 10, No. 2, (2021), 1117-1129. DOI: 10.1109/TETC.2021.3073017

6. Butcher, B. and Smith, B.J., *Feature engineering and selection: A practical approach for predictive models: b*y Max Kuhn and Kjell Johnson. Boca Raton, FL: Chapman & Hall/CRC Press, (2019), https://doi.org/10.1080/00031305.2020.1790217

7. Tran, M.-Q., Liu, M.-K. and Elsisi, M., "Effective multi-sensor data fusion for chatter detection in milling process", *ISA Transactions*, Vol. 125, (2022), 514-527. https://doi.org/10.1016/j.isatra.2021.07.005

8. Chalapathy, R. and Chawla, S., "Deep learning for anomaly detection: A survey", *Computer Science*, (2019). https://doi.org/10.48550/arXiv.1901.03407

9. Guo, Y., Zhang, Z. and Tang, F., "Feature selection with kernelized multi-class support vector machine", *Pattern Recognition*, Vol. 117, (2021), 107988. https://doi.org/10.1016/j.patcog.2021.107988

10. Nazir, A. and Khan, R.A., "A novel combinatorial optimization based feature selection method for network intrusion detection", *Computers & Security*, Vol. 102, (2021), 102164. https://doi.org/10.1016/j.cose.2020.102164

11. Chio, C. and Freeman, D., "Machine learning and security: Protecting systems with data and algorithms, " O'Reilly Media, Inc.", (2018).

12. Ghasemi, J. and Esmaily, J., "A novel intrusion detection systems based on genetic algorithms-suggested features by the means of different permutations of labels' orders", *International Journal of Engineering, Tansactions A: Basics,* Vol. 30, No. 10, (2017), 1494-1502. DOI: 10.5829/ije.2017.30.10a.10

13. Venkatesh, B. and Anuradha, J., "A review of feature selection and its methods", *Cybernetics and Information Technologies*, Vol. 19, No. 1, (2019), 3-26. https://doi.org/10.2478/cait-2019-0001

14. Biglari, M., Mirzaei, F. and Hassanpour, H., "Feature selection for small sample sets with high dimensional data using heuristic hybrid approach", *International Journal of Engineering, Tansactions B: Applications* Vol. 33, No. 2, (2020), 213-220. DOI: 10.5829/IJE.2020.33.02B.05

15. Kou, G., Yang, P., Peng, Y., Xiao, F., Chen, Y. and Alsaadi, F.E., "Evaluation of feature selection methods for text classification with small datasets using multiple criteria decision-making methods", *Applied Soft Computing*, Vol. 86, (2020), 105836. https://doi.org/10.1016/j.asoc.2019.105836

16. Mohammadi, S., Mirvaziri, H., Ghazizadeh-Ahsaee, M. and Karimipour, H., "Cyber intrusion detection by combined feature selection algorithm", *Journal of Information Security and Applications*, Vol. 44, (2019), 80-88. https://doi.org/10.1016/j.jisa.2018.11.007

17. Maza, S. and Touahria, M., "Feature selection algorithms in intrusion detection system: A survey", *KSII Transactions on Internet and Information Systems*, Vol. 12, No. 10, (2018), 5079-5099. https://doi.org/10.3837/tiis.2018.10.024

18. Gündüz, S.Y. and ÇETER, M.N., "Feature selection and comparison of classification algorithms for intrusion detection", *Anadolu University Journal of Science and Technology A-Applied Sciences and Engineering*, Vol. 19, No. 1, (2018), 206-218. https://doi.org/10.18038/aubtda.356705

19. Umar, M.A. and Zhanfang, C., "Effects of feature selection and normalization on network intrusion detection", (2020).

20. Zhao, S., Li, W., Zia, T. and Zomaya, A.Y., "A dimension reduction model and classifier for anomaly-based intrusion detection in internet of things", in 2017 IEEE 15th Intl Conf on Dependable, Autonomic and Secure Computing, 15th Intl Conf on Pervasive Intelligence and Computing, 3rd Intl Conf on Big Data Intelligence and Computing and Cyber Science and Technology Congress (DASC/PiCom/DataCom/CyberSciTech), IEEE. (2017), 836-843. DOI: 10.1109/DASC-PICom-DataCom-CyberSciTec.2017.141

21. Saranya, T., Sridevi, S., Deisy, C., Chung, T.D. and Khan, M.A., "Performance analysis of machine learning algorithms in intrusion detection system: A review", *Procedia Computer Science*, Vol. 171, (2020), 1251-1260. https://doi.org/10.1016/j.procs.2020.04.133

22. Zhang, Y., Yang, C., Yang, A., Xiong, C., Zhou, X. and Zhang, Z., "Feature selection for classification with class-separability strategy and data envelopment analysis", *Neurocomputing*, Vol. 166, (2015), 172-184. https://doi.org/10.1016/j.neucom.2015.03.081

23. El Bilali, A., Taleb, A. and Brouziyne, Y., "Groundwater quality forecasting using machine learning algorithms for irrigation purposes", *Agricultural Water Management*, Vol. 245, (2021), 106625. https://doi.org/10.1016/j.agwat.2020.106625

24. Shlens, J.J.a.p.a., "A tutorial on principal component analysis", arXiv preprint arXiv:1404.1100, (2014). https://doi.org/10.48550/arXiv.1404.1100

25. Izenman, A.J., Linear discriminant analysis, in Modern multivariate statistical techniques. 2013, Springer. 237-280.

26. Van der Maaten, L. and Hinton, G.J.J.o.m.l.r., "Visualizing data using t-sne", Vol. 9, No. 11, (2008).

27. Ravipati, R.D. and Abualkibash, M., "Intrusion detection system classification using different machine learning algorithms on kdd-99 and nsl-kdd datasets-a review paper", *International Journal of Computer Science & Information Technology*, Vol. 11, No. 3, (2019). http://dx.doi.org/10.2139/ssrn.3428211
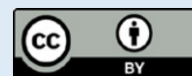
Persian Abstract

چکیده

امروزه تعداد حملات سایبری با افزایش حجم داده‌های با ابعاد بالا که شامل ویژگی‌های نویزدار و نا مرتبط است، افزایش یافته و پیچیده‌تر شده است. در چنین مواقعی حذف ویژگی های نامرتبط و نویزی می تواند در افزایش عملکرد سیستم های تشخیص نفوذ بسیار موثر می‌باشد. این مقاله برخی از روش‌های انتخاب ویژگی و کاهش ابعاد را برای تشخیص حملات سایبری با استفاده از پیاده‌سازی روی مجموعه داده KDDCUP99 مقایسه می‌کند. یک شبکه عصبی عمیق برای آموزش و پیاده سازی آنها نیز استفاده می شود. نتایج نشان می‌دهد که روش‌های فیلتر سریع‌تر از روش‌های بسته بندی هستند اما دقت کمتری دارند. در حالی که روش های بسته بندی دقت بیشتری دارند اما از نظر محاسباتی پرهزینه تر هستند. روش‌های تعبیه شده، بهترین خروجی را دارند که برای همه معیارها به میزان ۹۹ درصد رسیده است، در مقایسه با آن روش‌های کاهش بعد، عملکرد و سرعت خوبی از خود نشان داده‌اند که در میان آنها روش تحلیل تفکیک خطی، بهتر از روش های تعبیه شده می‌باشد.

A New Generalized Step-up Multilevel Inverter Topology Based on Combined T-type and Cross Capacitor Modules

S. J. Salehi, M. A. Shmasi-Nejad*, H. R. Najafi

Department of Electrical and Computer Engineering, University of Birjand, Birjand, Iran

P A P E R I N F O	*A B S T R A C T*
	This paper presents a new symmetrical switched-capacitor (SC) multilevel inverter topology which can convert the input DC voltage to a step-up multilevel AC waveform on the load. This proposed multilevel inverter consists of one T-type and several cross-capacitor modules. The structure of the generalized multilevel inverter is such that the peak inverse voltage (PIV) remains constant as the number of cross-capacitor modules increases which leads to reduce the total standing voltage (TSV) of the switches and cost function compared to other traditional topologies. The introduced structure can inherently generate the positive, negative, and zero voltage levels on the output without the back-end H-bridge section. The capacitor's voltages in the T-type and cross modules are inherently balanced, simplifying the control system under the nearest level control (NLC) switching strategy. To verify the performance of the proposed topology, several simulations and experimental results for a type 13-level inverter are provided by MATLAB and TMS320F28379D DSP, respectively.

1. INTRODUCTION

Nowadays, multilevel inverters (MLIs) are being developed for application in renewable energy resources, high voltage DC (HVDC) systems, electrical vehicles, microgrid systems, and so on [1, 2]. They can generate a staircase voltage which leads to reducing the total harmonic distortion (THD) and size of the passive filter on the output. The other advantages of multilevel inverters consist of low voltage stress on the semiconductor devices (switches and diodes), low dv/dt stress, and high efficiency [3, 4]. Generally, the MLIs are divided into three conventional groups: neutral point clamped (NPC), flying capacitor (FC), and cascaded H-bridge (CHB). The NPC and FC-type inverters have many diodes and capacitors in their structures, respectively. However, some topologies such as active-NPC and transistor-NPC have been developed by researchers for overcoming it, but these configurations still require extra auxiliary circuits for balancing the

neutral point [5-7]. The CHB-based topologies need several isolated input DC sources to obtain a number of high voltage levels on the output. For many applications such as photovoltaic (PV) systems and wind turbines, it is necessary that a step-up inverter is applied to increase the input DC voltage [8, 9]. It must be stated that none of the three conventional topologies mentioned above can boost the input DC voltage. So, researchers introduced several approaches to achieve this purpose. One of the approaches is to use a coupling inductor or transformer in a multilevel inverter structure [10-14]. However, in low frequencies (lower than 50 Hz), the inductors and transformers make the system drastically bulky and expensive. Alemi-Rostami and Rezazadeh [10] introduced a boost multilevel inverter with the presence of a coupling inductor. Nevertheless, the voltage gain has not been assessed for various frequency ranges. Moreover, using an H-bridge as a polarity generation circuit increases the PIV of switches when the number of modules is increased. An increase in PIV leads to an

Corresponding Author Institutional Email: mshamsi@birjand.ac.ir
(M. A. Shamsi-Nejad)

increase in the voltage rating of switches and thus increases the volume and cost of the whole system. Ghanbari, and Tousi [11] presented a boost transformer-based binary hybrid multilevel inverter which is required only a single DC source instead of several isolated DC sources. However, in this scenario, in addition to increasing the volume of the system, it requires several H-bridge cells leading to an increase in the TSV. Another approach to obtain the boost capability of MLIs is to use circuits based on switched-capacitor (SC) which inherently have the self-balancing ability [15, 16]. However, there are two concerns about this type of MLIs. One is the complexity of the system due to a high number of device counts such as switches and capacitors and another is the performance in high-frequency (HF) conditions for many applications such as high-speed motors, induction heating, and electric vehicles. Several SC-based MLIs have been reported with a reduction in the number of semiconductor devices, but with an increase in the modules, the PIV of switches has been drastically increased [17-23]. Hussan et al. [17] introduced an SC topology for smart grid application with two T-type capacitor modules. The T-type modules can inherently balance the capacitor voltages. However, using three isolated DC power sources is the most important challenge related to this topology. Taheri et al. [18] presented a 17-level SC multilevel inverter topology with several cross-capacitor modules. In this configuration, the number of switches has been drastically reduced. Nevertheless, by increasing the cross-capacitor modules (especially in asymmetrical mode), the PIV of switches is increased to achieve the number of high voltage levels. Recently, Khenar et al. [24] introduced a boost self-balancing SC multilevel inverter based on combined T-type and cross-capacitor modules which can keep PIV constant by increasing the capacitor modules. However, obtaining the 13-level output voltage, it requires 23 switches, 4 diodes, and 6 capacitors. So, in the number of high voltage levels, the inverter introduced by Khenar et al. [24] needs a high number of capacitors. According to the discussion made above, this paper presents a new structure of SC multilevel inverter with the following properties,

  i. Step-up capability without the presence of any transformer and inductor.
  ii. Constant PIV in the switches with increasing the number of modules.
  iii. 13-level topology with single DC bus, 20 switches, 4 capacitors, and without power diode.
  iv. Performance in low frequency (LF) and HF conditions.

Generally, the proposed topology has two important characteristics. First, it provides a high gain voltage on the load (as much as 6). Secondly, by increasing the number of cross-module, the peak inverse voltage (PIV) remains constant, leading drastically to reduce the total

standing voltage of the switches. The rest of this paper has been arranged as follows: section 2 introduces the proposed topology with switching states. Section 3 gives the comparison of the new SC multilevel inverter with other conventional topologies. Section 4 elaborates on the nearest level control as the switching technique. The calculations of capacitance values and power losses in the proposed topology are performed in section 5. In section 6, several simulations and experimental results are conducted to verify the performance of the proposed topology. Finally, the conclusions are organized in section 7.

2. CIRCUIT OF THE PROPOSED TOPOLOGY

2. 1. 13-level Structure   The circuit structure of the proposed 13-level inverter is shown in Figure 1.

This figure contains one T-type module and two cross-capacitor modules. The T-type module includes six switches ($S_1S_2S_3S_4S_5S_6$) and two capacitors (C_{t1} and C_{t2}). The cross-capacitor modules consist of a non-expandable part with switches ($S_7S_8S_9S_{10}S_{11}S_{12}$) and capacitor C_f and an expandable part with switches ($S_{13}S_{14}S_{15}S_{16}S_{17}$) and capacitor C_m. In general, the proposed 13-level topology consists of 20 switches (with 3 bi-directional switches), 4 capacitors, a zero diode, and one DC bus (V_{dc}). For achieving the high voltage gain on the output, the capacitors C_f and C_m can be connected together as parallel with the sum of the capacitors C_{t1} and C_{t2}. Table 1 and Figure 2 show the switching states and current commutation paths of the proposed multilevel inverter, respectively. The current commutation paths are arranged to obtain the voltage levels $\pm 1V_{dc}$, $\pm 2V_{dc}$, $\pm 3V_{dc}$, $\pm 4V_{dc}$, $\pm 5V_{dc}$, $\pm 6V_{dc}$, and $0V_{dc}$. According to states 6 and 8 in Table 1, and Figures (2h) and (2b), the capacitors C_{t1} and C_{t2} are charged by T-type throughout switches $S_1S_4S_5S_3$ and $S_1S_2S_5S_6$, respectively, up to $1V_{dc}$ in a self-balancing manner.

On the other hand, referring to states 5 and 10, and Figures (2g) and (2j), the capacitors C_f and C_m can be
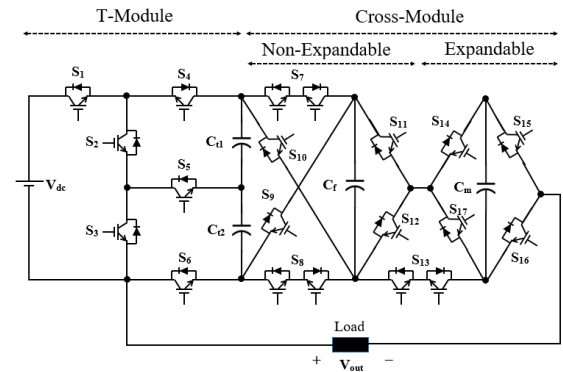

Figure 1. Proposed step-up 13-level inverter topology

TABLE 1. Switching states for the proposed 13-level inverter. The symbols C, D, and W indicate charge, discharge, and without change, respectively

Process	States	T-module	Cross-module		$C_{t1}C_{t2}C_fC_m$	V_{out}
			Non-Expandable	Expandable		
		$S_1S_2S_3S_4S_5S_6$	$S_7S_8S_9S_{10}S_{11}S_{12}$	$S_{13}S_{14}S_{15}S_{16}S_{17}$		
	1	011100	001001	01010	D-D-D-D	$+6V_{dc}$
	2	001010	001001	01010	W-D-D-D	$+5V_{dc}$
	3	011100	001000	10010	D-D-D-W	$+4V_{dc}$
	4	001010	001000	10010	W-D-D-W	$+3V_{dc}$
	5	011100	110010	11010	D-D-C-C	$+2V_{dc}$
	6	001010	010000	10010	C-D-W-W	$+1V_{dc}$
Switching states/capacitor states/voltage levels	7	101111	010000	10010	W-W-W-W	$0V_{dc}$
	8	110011	010000	10010	W-C-W-W	$0V_{dc}$
	9	001010	100010	01100	D-W-W-W	$-1V_{dc}$
	10	000001	110010	11100	D-D-C-C	$-2V_{dc}$
	11	001010	100010	00101	D-W-W-D	$-3V_{dc}$
	12	000001	100010	00101	D-D-W-D	$-4V_{dc}$
	13	001010	000110	00101	D-W-D-D	$-5V_{dc}$
	14	000001	000110	00101	D-D-D-D	$-6V_{dc}$
PIV/1V_{dc}		1-1-1-1-1-2	4-4-4-4-2-2	4-2-2-2-2	-------	-------

(a)

(b)

(c)

(d)

(e)

(f)

(g)

(h)
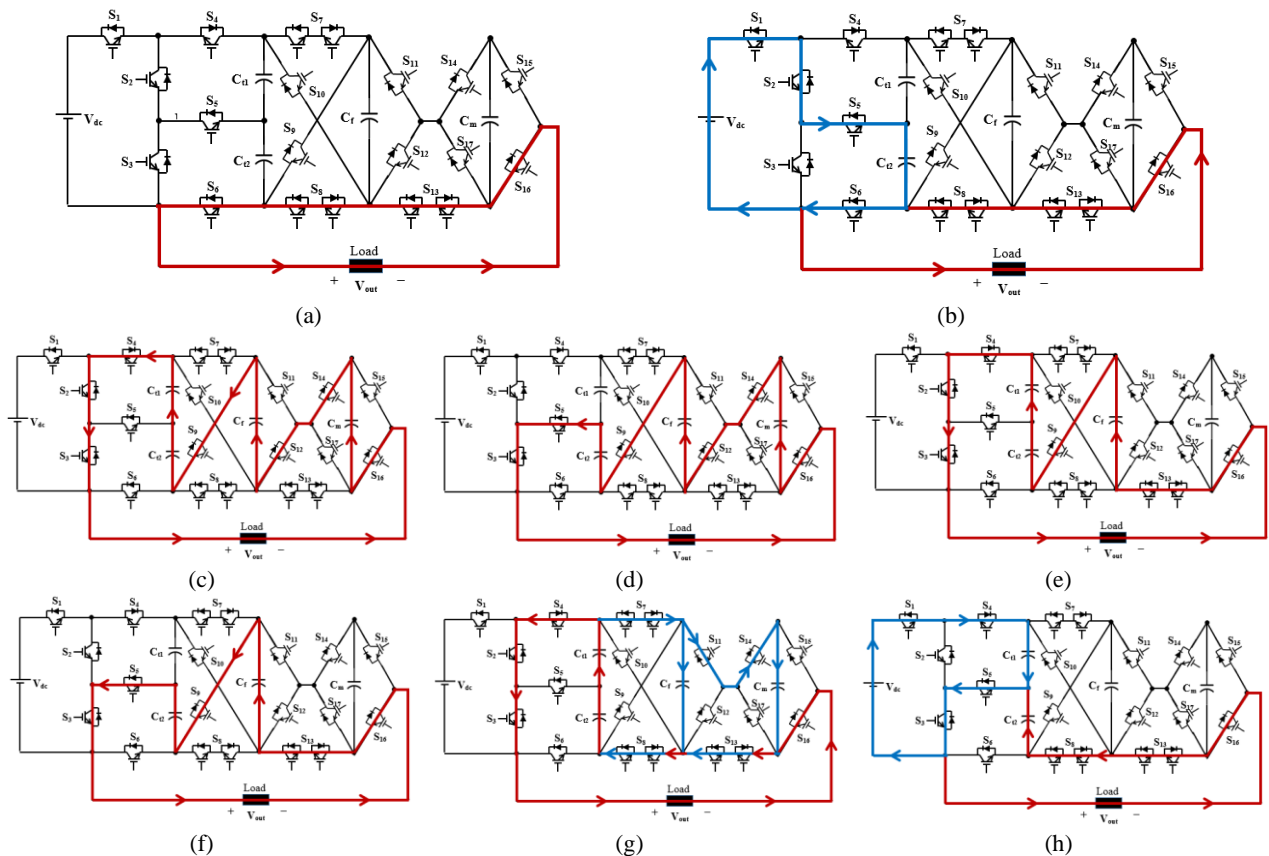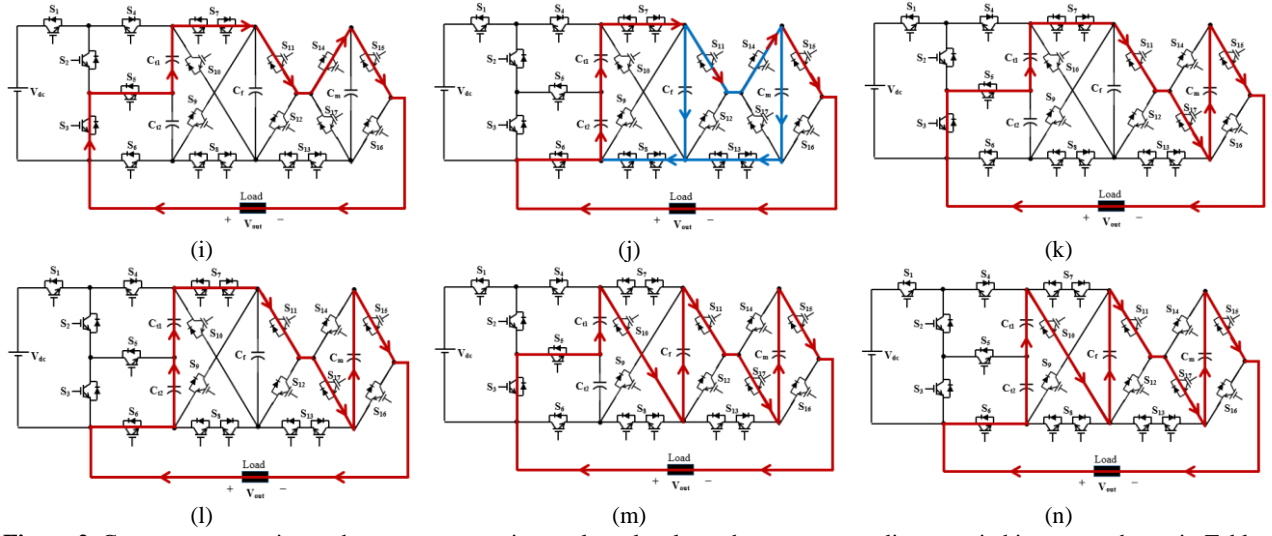
Figure 2. Current commutation paths to generate various voltage levels on the output according to switching states shown in Table 1. (a) $0V_{dc}$, (b) $0V_{dc}$, (c) $+6V_{dc}$, (d) $+5V_{dc}$, (e) $+4V_{dc}$, (f) $+3V_{dc}$, (g) $+2V_{dc}$, (h) $+1V_{dc}$, (i) $-1V_{dc}$, (j) $-2V_{dc}$, (k) $-3V_{dc}$, (l) $-4V_{dc}$, (m) $-5V_{dc}$, and (n) $-6V_{dc}$.

simultaneously charged up to $2V_{dc}$ through the sum of the voltages of capacitors C_{t1} and C_{t2}. Hence, the total voltage of the capacitors is obtained as $6V_{dc}$, which is equal to the voltage gain and the number of voltage levels in the half-cycle of the output in the proposed 13-level multilevel inverter.

2. 2. Generalized Structure   According to Figure 3, the proposed SC multilevel inverter can be extended by several cross-modules consecutively to obtain the high number of voltage levels on the output. With the addition of each expandable module, the PIV of the switches remains constant. Table 2 shows the number of device counts and blocking voltage of switches for the N-level proposed topology.

As shown in this table, the switches ($S_1S_2S_3S_4S_5$) and (S_9S_{10}) have the lowest ($1V_{dc}$) and the highest ($4V_{dc}$) blocking voltage, respectively. So, the PIV of the switches in the proposed multilevel inverter is $4V_{dc}$.

3. COMPARISON WITH OTHER TOPOLOGIES

In this section, the proposed SC multilevel inverter is compared with other topologies [20-24] in view of the number of switches, number of diodes, number of capacitors, TSV, and cost function (CF). According to Table 3, which lists these parameters, the proposed topology has the lowest number of capacitors and TSV. For instance, in the 13-level case, the number of capacitors in the literature [20-24] is 5, 5, 5, 5, and 6,
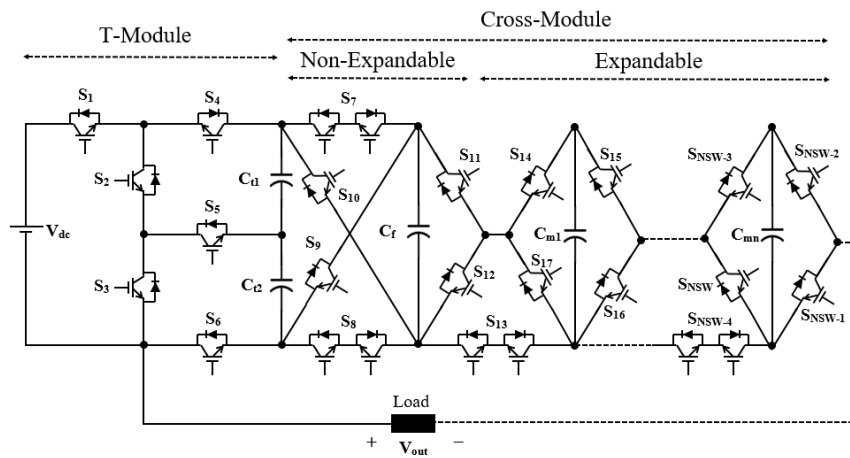
Figure 3. Generalized proposed SC multilevel inverter

TABLE 2. characteristics of proposed SC multilevel inverter for N level and N_{sw} switch

Parameter	Value
Number of switches (N_{sw})	1.5N+0.5 (N=9, 13, 17, 21, …)
Number of gate drivers (N_g)	1.25N+0.75 (N=9, 13, 17, 21, …)
Number of capacitors (N_C)	0.25N+0.75 (N=9, 13, 17, 21, …)
Blocking voltage for T-module	$1V_{dc}$ for all switches expect S_6 ($2V_{dc}$)
Blocking voltage for Non-Expandable module	$4V_{dc}$ for all switches expect S_{11} and S_{12} ($2V_{dc}$)
Blocking voltage for Expandable module	$2V_{dc}$ for all switches expect (N_{SW}-4)-th switch ($4V_{dc}$)

respectively while it is equal to 4 in the proposed topology. Now, lets the CF be defined as follows:

$$CF = N_{semiconductor} + N_C + \alpha \times \frac{TSV}{V_{dc}} + \beta \times \frac{PIV}{V_{dc}} \qquad (1)$$

where $N_{semiconductor}$ is the number of switches and diodes. Moreover, α and β are the weight of TSV and PIV against the number of device counts ($N_{semiconductor}$ + N_C), respectively. α and β are selected more than 1 when the TSV and PIV are more important than the device counts. On the other hand, α and β are selected less than 1 when the TSV and PIV are less important than the device counts. For a more detailed review, Figure 4 is shown graphically the comparison of the proposed multilevel inverter with others. As shown in Figure 4(b), the PIV for [24] and proposed topologies remain constant with increasing the number of levels.

Moreover, according to Figure 4(d), the proposed multilevel inverter has the lowest CF than other topologies whether with α=β=0.5 or with α=β=1.5. In a general view, it seems that the introduced inverter has close competition with the literature [24]. However, the number of capacitors and the CF in the proposed topology are more favorable.

TABLE 3. Comparison of the proposed multilevel inverter with other topologies for an N-level output voltage

Parameters	[20]	[21]	[22]	[23]	[24]	Proposed
number of switches	$\frac{3N-1}{2}$	$\frac{2N+6}{2}$	$\frac{N+7}{2}$	$\frac{3N-1}{2}$	$\frac{3N+7}{2}$	$\frac{3N+1}{2}$
Number of capacitors	$\frac{N-3}{2}$	$\frac{N-3}{2}$	$\frac{N-3}{2}$	$\frac{N-3}{2}$	$\frac{N-1}{2}$	$\frac{N+3}{4}$
Number of diodes	0	$N-1$	$N-3$	0	0	0
PIV for H-bridge switches	$\frac{N-1}{2}V_{dc}$	$\frac{N-1}{2}V_{dc}$	$\frac{N-1}{2}V_{dc}$	$\frac{N-1}{2}V_{dc}$	No need	No need
Maximum PIV for switches	$\frac{N-1}{2}V_{dc}$	$\frac{N-1}{2}V_{dc}$	$\frac{N-1}{2}V_{dc}$	$\frac{N-1}{2}V_{dc}$	$4V_{dc}$	$4V_{dc}$
TSV($\times 1V_{dc}$)	$\frac{7N-13}{2}$	$\frac{N^2}{4}+2N-\frac{5}{4}$	$\frac{N^2}{4}+\frac{3}{2}N-\frac{7}{4}$	$\frac{N^2+18N-19}{8}$	$\frac{7N-11}{2}$	3N

(a)

(b)
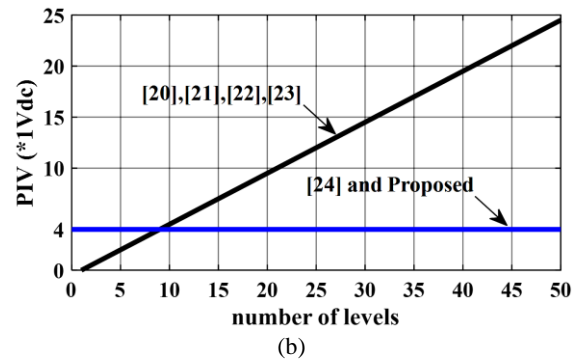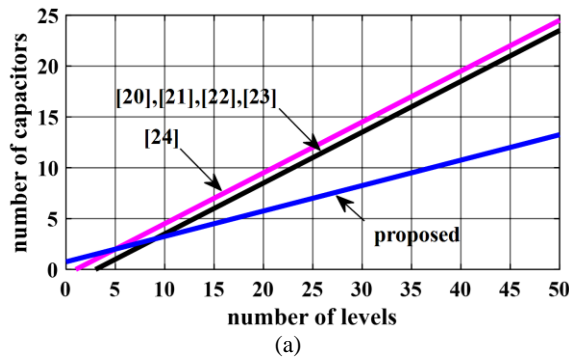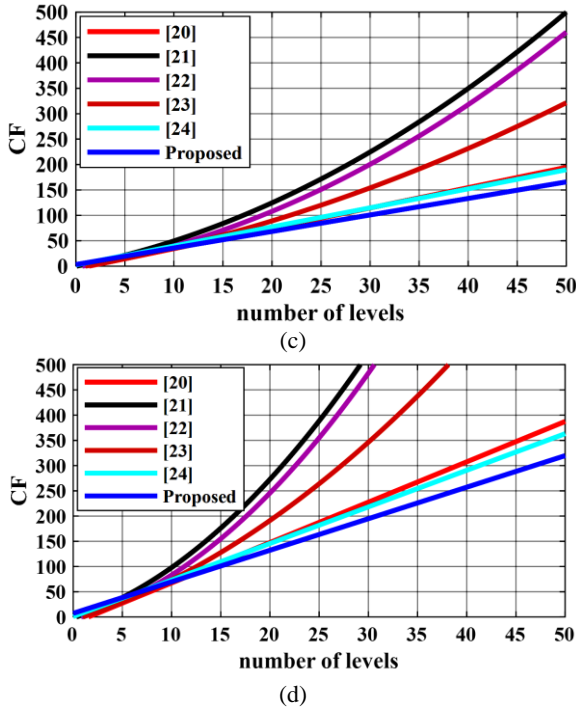
Figure 4. Comparison of the proposed topology with others. (a) number of capacitors, (b) PIV, (c) CF for α=β=0.5, and (d) CF for α=β=1.5

4. NEAREST LEVEL CONTROL

There are two general switching techniques for the multilevel inverter which are called as high switching frequency (HSF) and fundamental switching frequency (FSF) [25]. In the HSF switching techniques such as multi-carrier pulse width modulation (MC-PWM), one full sinusoidal wave is compared with several sawtooth waves with switching frequencies higher than 2kHz. This technique is used mostly for closed-loop control systems [26]. On the other hand, switching techniques based on FSF cause lower power losses on the inverter than HSF techniques. The most famous of the FSF techniques are nearest level control (NLC) and selective harmonic elimination (SHE). In the SHE scheme, by solving several non-linear equations using the Newton-Raphson method, the switching angles for generating gate pulses are obtained. However, at a high number of voltage levels, solving equations becomes very complicated and boring [27]. In the NLC switching technique, a full sinusoidal wave as the reference signal (V_{ref}) is compared with a multi-step signal so that the output voltage is close to a multilevel wave, leading to simplifying the control of the switches. For this purpose, first, the reference signal is normalized by the maximum voltage level factor (V_{omax}) then it is quantized in form of a multi-step wave. Finally, the quantized wave decides which switch to activate [28, 29]. Figure 5 shows briefly how to implement the NLC switching technique which has been considered in this work. In this figure, t_i is the switching time of the ith level, and it is described as follows:

$$t_i = \frac{1}{\omega}\sin^{-1}\left(\frac{2i-1}{N-1}\right), \quad i = 1, 2, 3, ..., \frac{N-1}{2}. \quad (2)$$

where ω is the reference angular frequency and it is formulated as ω=2πf_s.

5. CAPACITANCE AND POWER LOSSES CALCULATIONS

In this section, the capacitance and power losses are calculated for a type 13-level proposed topology. In all cases, it is assumed the load is purely resistive.

5. 1. Capacitance Calculation   As shown in Figure 1, there are four capacitors in the proposed 13-level inverter which can be charged and discharged at various instant intervals. The capacitors C_{t1}, C_{t2}, C_f, and C_m are charged up to $1V_{dc}$, $1V_{dc}$, $2V_{dc}$, and $2V_{dc}$, respectively. To charge these capacitors at the mentioned voltages, it is necessary to know the optimal value of the capacitance values.

For this purpose, the largest discharging cycle (LDC) of the capacitors is considered. Using Table 1, it can be depicted the charging and discharging time intervals of the capacitors which are shown in Figure 6. As shown in this figure, the LDC of the capacitors C_{t1}, C_{t2}, C_f, and C_m is between (t_1 to T/2-t_1), (t_1+T/2 to (T-t_1), (t_3 to T/2-t_3), and (t_5 to T/2-t_5), respectively. It should be noted that the
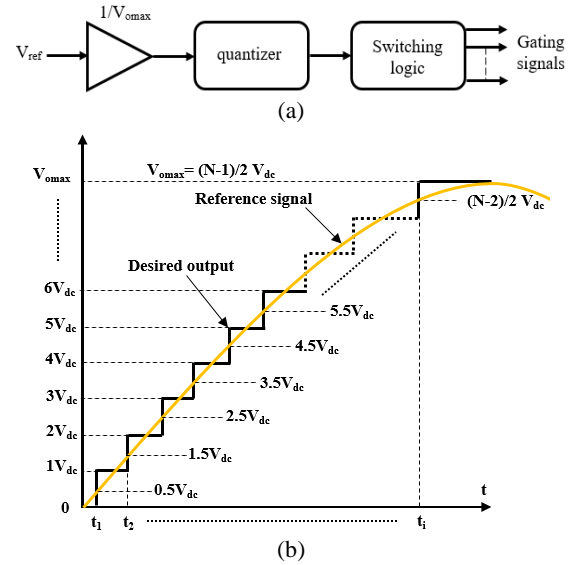
Figure 5. NLC switching technique for the pulse generation in the proposed multilevel inverter (a) block diagram (b) graphical presentation
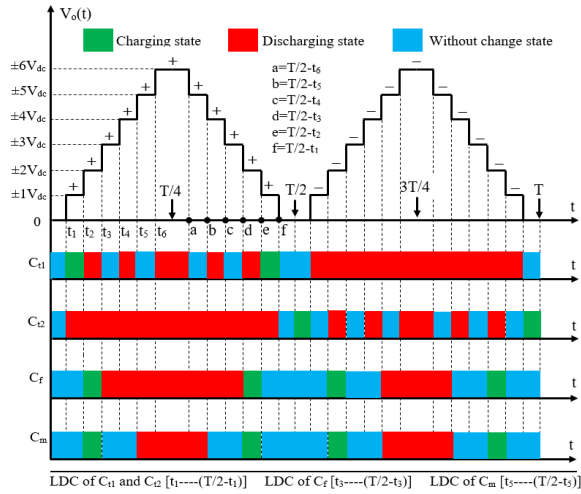
Figure 6. Charging and discharging time intervals of the capacitors C_{t1}, C_{t2}, C_f, and C_m used in the proposed topology

LDC of the capacitors C_{t1} and C_{t2} is equal to each other, leading to equalize of capacitances C_{t1} and C_{t2} (i.e. $C_{t1}=C_{t2}$). So, the calculation of the capacitance is only performed for one of them.

The expression for the discharging states of the capacitors C_{t1}, C_{t2}, C_f, and C_m in the LDC time interval are described as follows:

$$\Delta Q_{C_{t1}} = \Delta Q_{C_{t2}} = \int_{t_1}^{T/2-t_1} i_L(t)dt \tag{3}$$

$$\Delta Q_{C_f} = \int_{t_3}^{T/2-t_3} i_L(t)dt \tag{4}$$

$$\Delta Q_{C_m} = \int_{t_5}^{T/2-t_5} i_L(t)dt \tag{5}$$

where $i_L(t)$ is the instantaneous load current and it can be written as,

$$i_L(t) = i_m \sin(\omega t) \tag{6}$$

where i_m is the peak of the load current. From Equations (3) to (5), the values of the C_{t1}, C_{t2}, C_f, and C_m can be formulated as,

$$C_{t1} = C_{t2} = \frac{1}{\Delta V_{C_{t1}}} \int_{t_1}^{T/2-t_1} i_L(t)dt \tag{7}$$

$$C_f = \frac{1}{\Delta V_{C_f}} \int_{t_3}^{T/2-t_3} i_L(t)dt \tag{8}$$

$$C_m = \frac{1}{\Delta V_{C_m}} \int_{t_5}^{T/2-t_5} i_L(t)dt \tag{9}$$

where ΔV_{Ct1}, ΔV_{Cf}, and ΔV_{Cm} are the permissible voltage ripple of the capacitors C_{t1}, C_f, and C_m, respectively. By considering the value of $V_{dc}=20v$ (to achieve the maximum output voltage level $V_{omax}=120v$), the capacitors C_{t1}, C_{t2}, C_f, and C_m are charged up to 20v, 20v, 40v, and 40v, respectively. Hence, the values of ΔV_{Ct1}, ΔV_{Cf}, and ΔV_{Cm}, which are usually considered as 10% of the corresponding capacitor voltage, can be obtained as:

$$\begin{cases} \Delta V_{Ct1} = \Delta V_{Ct2} = 2v \\ \Delta V_{Cf} = 4v \\ \Delta V_{Cm} = 4v \end{cases} \tag{10}$$

The solution of Equations (7), (8), and (9) leads to appear the values of $C_{t1}=C_{t2}$, C_f, and C_m which are expressed as:

$$C_{t1} = C_{t2} = \frac{2 \times i_m \cos(\omega t_1)}{2\pi f_s \times \Delta V_{C_{t1}}} \tag{11}$$

$$C_f = \frac{2 \times i_m \cos(\omega t_3)}{2\pi f_s \times \Delta V_{C_f}} \tag{12}$$

$$C_m = \frac{2 \times i_m \cos(\omega t_5)}{2\pi f_s \times \Delta V_{Cm}} \tag{13}$$

By using Equation (2), for N=13 and f_s=50Hz, the switching times are obtained as t_1=0.00026s, t_2=0.0008s, t_3=0.0014, t_4=0.002s, t_5=0.0027s, and t_6=0.0037s. Using these switching times and Equation (10), for i_m=2A, the final solution of C_{t1}, C_{t2}, C_f, and C_m come out to be 6300µF, 6300µF, 2900µF, 2100µF, respectively. The available values of the capacitors in the laboratory are 2200µF and 4700µF. For this reason, in the experimental setup, the capacitors C_{t1}, C_{t2}, C_f, and C_m are equally chosen as much as (3×2200µF), (3×2200µF), 4700µF, and 2200µF, respectively.

5. 2. Power Losses Calculation   Generally, power losses in the proposed SC multilevel inverter are classified into three groups consisting of switching losses, conducting losses, and capacitor losses which are described as follows.

5. 2. 1. Switching Losses   The switching losses are created due to delays in turning on and turning off the switches and reverse recovery time on the diodes. when the pulse reaches the gate of a switch, it takes a t_{on} of seconds for the collector-emitter voltage and collector current to reach their final values. In addition, when the pulse is removed from the gate, it takes a t_{off} of seconds for the switch to turn off. These delays t_{on} and t_{off} cause switching losses on the switches. The switching losses during the on ($P_{sw,on}$) and off ($P_{sw,off}$) states of a typical switch are calculated by Equations (1) and (2), respectively [30].

$$P_{sw,on} = \frac{1}{6} f_s \times V_{off} \times I_{on} \times t_{on} \tag{14}$$

$$P_{sw,off} = \frac{1}{6} f_s \times V_{off} \times I_{on} \times t_{off} \tag{15}$$

where t_{on} and t_{off} are turning on and off time of switches, f_s is the switching frequency, V_{off} is the voltage rating of the switch and I_{on} is the average load current. Moreover, the switching losses on the diodes are calculated as follows:

$$P_{sw,D} = \frac{1}{6} f_s \times V_{RM} \times I_{RM} \times t_B \tag{16}$$

Where V_{RM} and I_{RM} are the maximum voltage and current of the reverse recovery, respectively. In addition, t_B is the delay time of reverse current. The total switching losses are formulated as follows:

$$P_{sw,total} = \sum_{i=1}^{N_{sw}} \left(\sum_{j=1}^{N_{on}} \left(P_{sw,on,ij} \right) + \sum_{j=1}^{N_{off}} P_{sw,off,ij} \right) + \sum_{k=1}^{N_D} \left(\sum_{h=1}^{N_{off}} \left(P_{sw,D,kh} \right) \right) \tag{17}$$

Where N_{sw} and N_D are the numbers of the switch and diode, respectively. Moreover, N_{on} and N_{off} are the numbers of the on and off states of the switch and diode during a fundamental cycle (1/Ts).

5. 2. 2. Conducting Losses   Conducting losses are created in the proposed SC topology due to the resistance and voltage drop on the switches and antiparallel diodes during turning on. The average conducting losses for the transistor (P_{cT}) and antiparallel diode (P_{cD}) can be expressed as [31]:

$$\begin{cases} P_{cT} = V_{CEO} I_{c,ave} + R_c I_{c,rms}^2 \\ P_{cD} = V_{DO} I_{D,ave} + R_d I_{D,rms}^2 \end{cases} \tag{18}$$

where I_{ave} and I_{rms} represent the average root-mean-square (RMS) values for the collector current. Moreover, V_{DO} and R_d are the forward voltage drop and on-state resistance of the antiparallel diode, respectively. Equation (18) elaborates on the conducting losses for each switch and diode. In another approach, it can be described by each output voltage level. For this purpose, consider Figure 6 in which there are six non-repetitive voltage levels (level 1: $\pm 1V_{dc}$, level 2: $\pm 2V_{dc}$, level 3: $\pm 3V_{dc}$, level 4: $\pm 4V_{dc}$, level 5: $\pm 5V_{dc}$, and level 6: $\pm 6V_{dc}$) for a 13-level output. Here, the zero level is not considered because it does not produce the conducting losses. By assuming the pure resistive load, the average conducting losses in transistors (P_{cT}) and their antiparallel diodes (P_{cD}) for mentioned six non-repetitive voltage levels can be formulated as follows:

$$\begin{cases} P_{cT,leveli} = (k_{Ti}) \left[V_{CEO} I_{c,ave,leveli} + R_c I_{c,rms,leveli}^2 \right] \\ P_{cD,leveli} = (k_{Di}) \left[V_{DO} I_{D,ave,leveli} + R_d I_{D,rms,leveli}^2 \right] \end{cases} \tag{19}$$

K_T and K_D coefficients are the numbers of switches and diodes, respectively. For each voltage level, these coefficients have been shown in Table 4.
Eventually, the sum of the conducting losses can be formulated as follows:

$$P_{c,total} = \sum_{i=-6}^{6} (P_{cT,leveli} + P_{cD,leveli}) \tag{20}$$

5. 2. 3. Capacitor Losses   In a capacitor, there are two types of losses. One is conduction losses ($P_{c,r}$) due to inner resistance (R_c) and another is voltage ripple losses ($P_{c,ripple}$). The capacitor voltage ripple losses are created by the difference between the DC bus voltage and the voltage across capacitors in charging mode. These losses are formulated as follows [32]:

$$P_{C,r} = \frac{2\pi f_{ref}}{\pi} \sum_{i=1}^{6} \left(\int_{t_{a,i}}^{t_{b,i}} R_c i_{Ci}^2 dt \right) \tag{21}$$

$$P_{C,ripple} = \frac{f_{ref}}{2} \sum_{i=1}^{6} \left(C_i \Delta V_{Ci}^2 \right) \tag{22}$$

where ($t_{a,i}$, $t_{b,i}$) are LDC intervals for the ith capacitor. Thus, capacitor losses are given as follows:

$$P_{loss,cap} = P_{c,r} + P_{C,ripple} \tag{23}$$

using Equations (18), (21), and (24), it can be written the efficiency of the proposed topology as:

TABLE 4. Coefficients of K_T and K_D in each voltage level for a 13-level output

Output level	K_T	K_D
$+1V_{dc}$	4	3
$+2V_{dc}$	6	2
$+3V_{dc}$	4	2
$+4V_{dc}$	6	1
$+5V_{dc}$	5	1
$+6V_{dc}$	7	0
$-1V_{dc}$	4	3
$-2V_{dc}$	4	2
$-3V_{dc}$	5	2
$-4V_{dc}$	5	1
$-5V_{dc}$	5	1
$-6V_{dc}$	5	0

$$\eta = \frac{Pout}{Pin} = \frac{P_{out}}{P_{out} + P_{loss}}$$

$$= \frac{P_{out}}{P_{out} + P_{sw,total} + P_{c,total} + P_{loss,cap}}$$

(24)

It should be noted that the switching losses in the proposed multilevel inverter can be ignored due to the use of the NLC switching technique. Therefore, for calculating the efficiency, it can be modeled a switch IGBT on the simulation environment which is shown in Figure 7.

Figure 8 depicts the efficiency curve in term of multiple load powers. To bring the results of simulation and experimental efficiency closer, three types of switches with specifications listed in Table 5 are considered.

According to Figure 8, the efficiency of the proposed multilevel inverter with the switch IRG4IBC30 is higher than the other two switches. This is because the V_{CEO} and R_C in the IRG4IBC30 are lower than others. For this reason, in this work, the switch IRG4IBC30 is used in the laboratory setup. Moreover, its model is applied to the simulation results.

6. SIMULATION AND EXPERIMENTAL RESULTS

To validate the proposed SC multilevel inverter topology, several simulations and experimental results are performed for a type 13-level inverter under various impedance loads and LF and HF conditions.
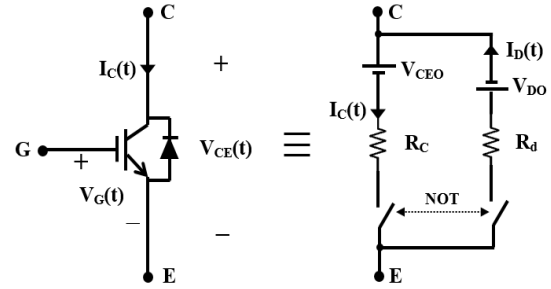

Figure 7. The equivalent circuit of a switch IGBT with an antiparallel diode to calculation of the efficiency

6. 1. Simulation Results In the simulation environment, the DC bus and capacitance parameters are set at (V_{dc}=20v) and (C_{t1}=6300μF, C_{t2}=6300μF, C_f=3300μF, C_m=3300μF), respectively. Moreover, the frequency of the reference signal is set at two values f_s=50Hz and 500Hz. To achieve high-precision processing, the sample time is regulated at 10μs. Figure 9 shows the output voltage and its harmonic spectrum under frequency f_s=50Hz. As shown in this figure, the THD of output voltage is 6.33%, which is less than 8% complying with the IEEE-519 standards. Figure 10 depicts the output parameters under pure resistive load (Z=60Ω) and f_s=50Hz. Firstly, considering that the voltage gain in the proposed topology is equal to 6, the maximum voltage level V_{omax} is close to (6×20=120) volts according to Figure 10(a). Secondly, as shown in Figure 10(b), the peak of load current agrees with ohm law (120v/60Ω=2A).

TABLE 5. The parameters values of the three types of switches IGBT for assessing the efficiency of the proposed topology

Switch IGBT	Antiparallel diode	External antiparallel diode	V_{CEO} (v)	R_C (Ω)	V_{DO} (v)	R_d (Ω)
STGH20N50FI	No	MBRF20100CT	2.5	0.125	0.85	0.085
IRGP35B60	Yes	------	1.85	0.084	2	0..075
IRG41BC30	No	MBRF20100CT	1.4	0.077	0.85	0.085
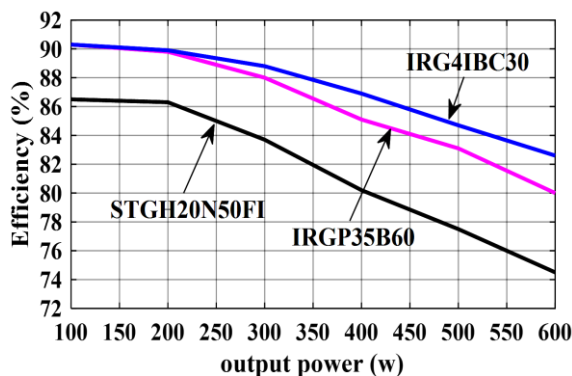
Figure 8. Efficiency curve of proposed topology for three types of IGBT switch

According to Figures 10(c), 10(d), 10(e), and 10(f), the voltage of capacitors C_{t1}, C_{t2}, C_f, and C_m are close to 20v, 20v, 40v, and 40v, respectively to product a 13-level output voltage. Figure 11 shows the output parameters of a 13-level inverter with a change in load impedance from Z=60Ω to Z=30Ω at t=1s under f_s=50Hz. As shown in this figure, the peak of output current has been increased approximately from i=2A to 4A with a fast dynamic behavior. From Figures 11(c), 11(d), 11(e), and 11f, it seems that, with increasing the load, the voltages of the capacitors have been slightly decreased. This is because of the increase in voltage drop on the IGBT switches. Figure 12 depicts the output parameters with a change in impedance load from Z=60Ω to Z=60Ω+100mH at t=1s
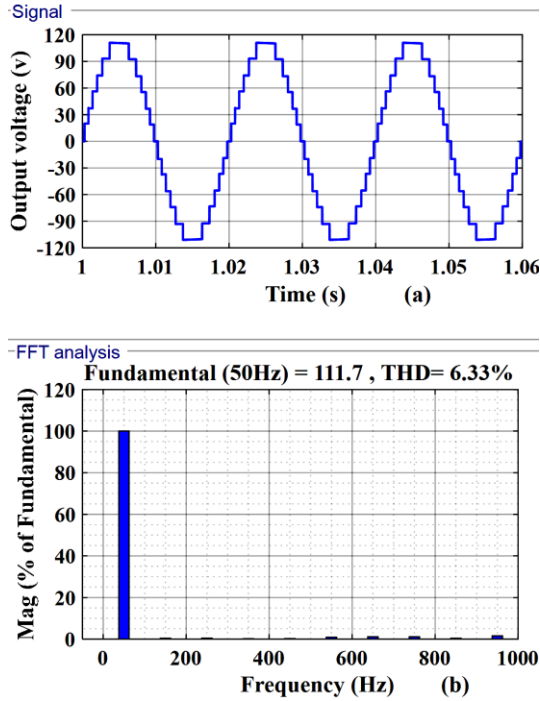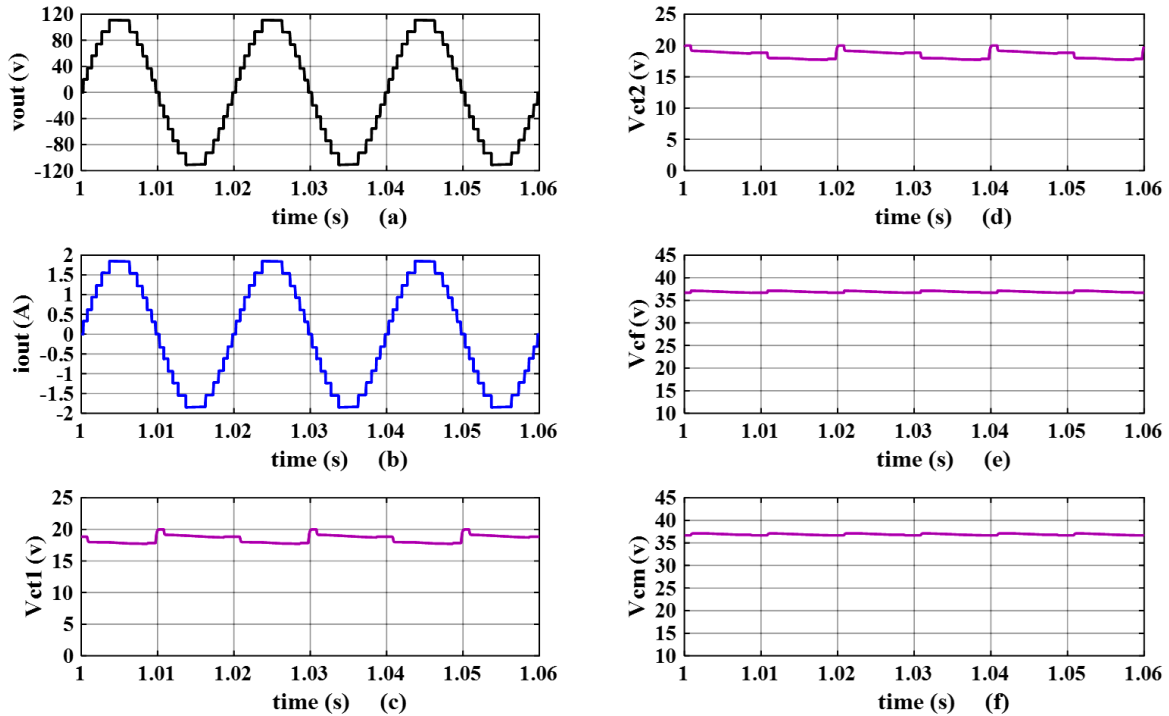
Figure 9. Simulation results for (a) output voltage, and (b) harmonic spectrum of output voltage with f_s=50Hz under NLC switching technique

under f_s=50Hz. For an inverter, the inductive load act as a low pass filter. So, it is expected that the output current is close to a pure sinusoidal waveform. This phenomenon has been clearly seen in Figure 12(b). To evaluate the proposed topology in HF conditions, a simulation result has been performed according to Figure 13 with f_s=500Hz. In this frequency, the output current is strongly diminished when the load is changed from pure resistive to induction case, as shown in Figure 13(b). This is because of the increasing the induction reactance from zero to X_L=Lω=(L×2×π×500) Ω. In other words, in f_s=500Hz, the inductive load impedance is higher than the resistive load.

Moreover, in HF conditions, according to Figures 13(c), 13(d), 13(e), and 13(f), the voltage ripple of capacitors is less than the LF conditions. This issue is compatible with Equations (11), (12), and (13) by considering the capacitances as constant.

6. 2. Experimental Results　　　According to Figure 14, a laboratory system has been provided to implement the proposed 13-level inverter topology. The experimental setup contains a DSP, a gate driver circuit, several capacitor banks, the proposed multilevel inverter, multiple power supplies for gate driver circuit, several resistive loads, an inductive load, a current sensor and a

Figure 10. Simulation results for constant pure resistive load (Z=60Ω) under f_s=50Hz. (a) output voltage, (b) output current, (c) capacitor voltage C_{t1}, (d) capacitor voltage C_{t2}, (e) capacitor voltage C_f, and (f) capacitor voltage C_m
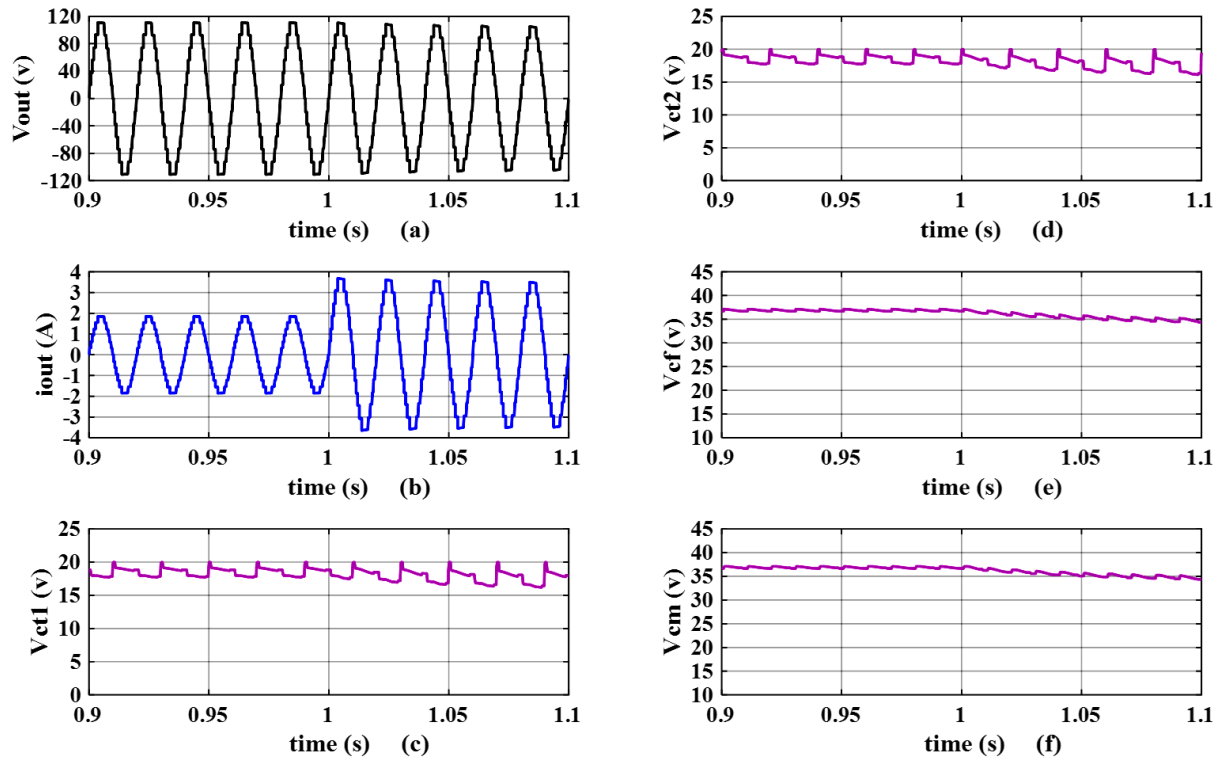
Figure 11. Simulation results under change in pure resistive load from Z=60Ω to Z=30Ω at t=1s under f_s=50Hz. (a) output voltage, (b) output current, (c) capacitor voltage C_{t1}, (d) capacitor voltage C_{t2}, (e) capacitor voltage C_f, and (f) capacitor voltage C_m
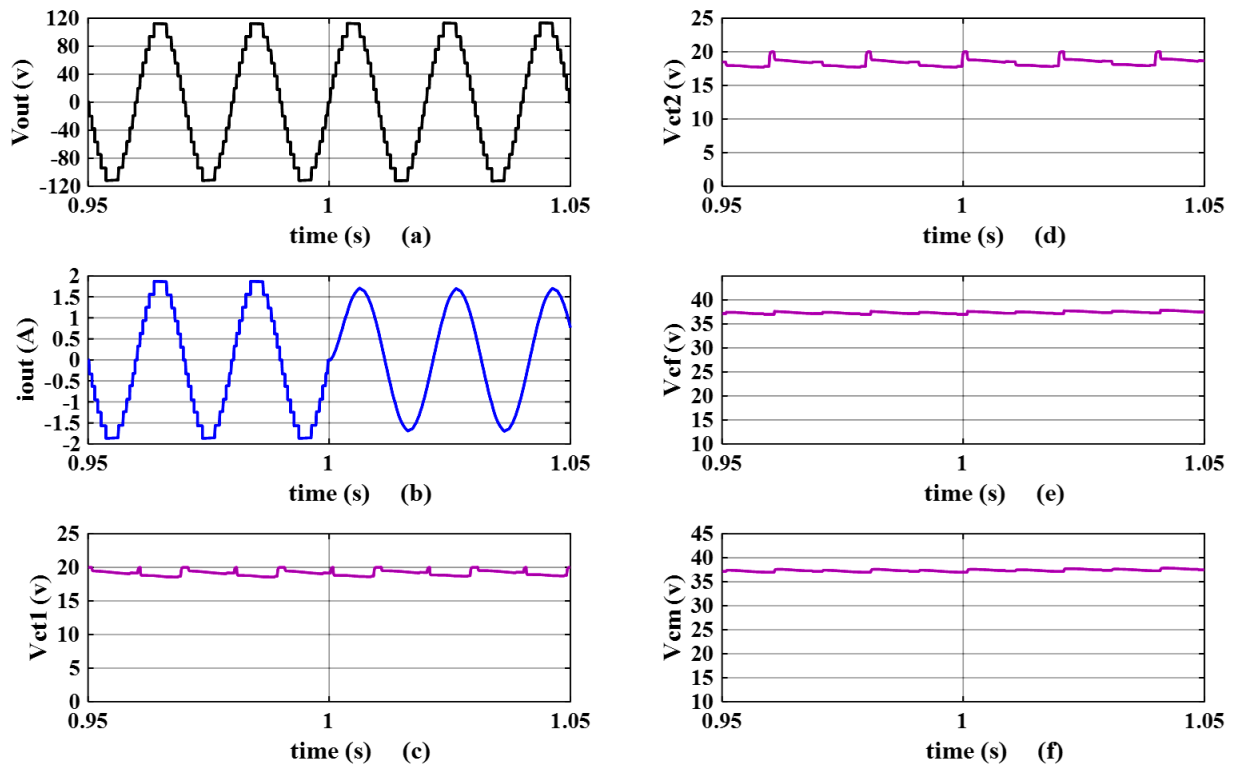
Figure 12. Simulation results under change in impedance load from Z=60Ω to Z=60Ω + 100mH at t=1s under f_s=50Hz. (a) output voltage, (b) output current, (c) capacitor voltage C_{t1}, (d) capacitor voltage C_{t2}, (e) capacitor voltage C_f, and (f) capacitor voltage C_m
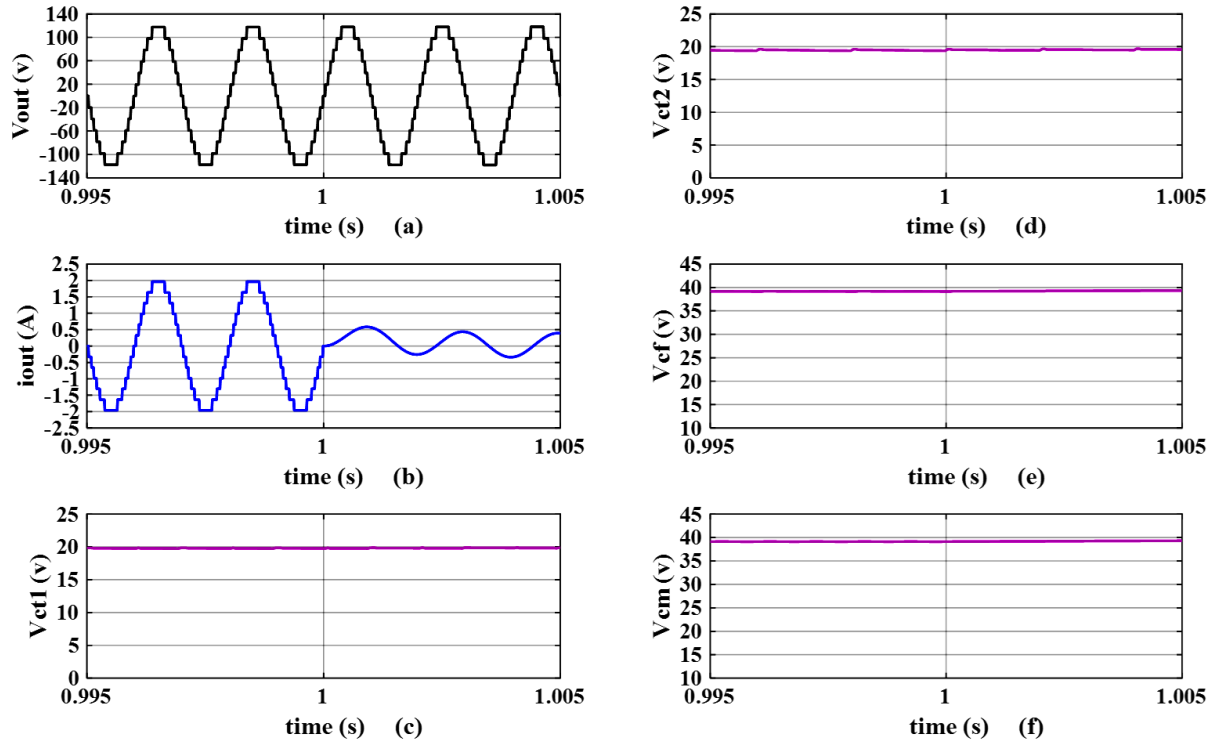
Figure 13. Simulation results under change in impedance load from Z=60Ω to Z=60Ω + 100mH at t=1s under f_s=500Hz. (a) output voltage, (b) output current, (c) capacitor voltage C_{t1}, (d) capacitor voltage C_{t2}, (e) capacitor voltage C_f, and (f) capacitor voltage C_m

Figure 14. The experimental setup

resistive voltage sensor. The details of the whole system have been listed in Table 6. In the gate driver circuit, there are two groups ICs for transferred pulse gates from DSP to the multilevel 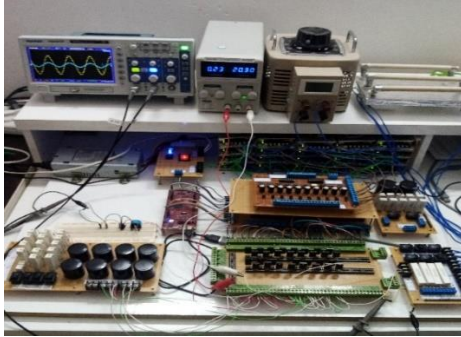inverter. One is 74HC245 buffer and another is HCPL-3120 as the main IGBT driver. The buffer IC is created an infinite impedance between DSP and multilevel inverter which prevents more currents from by the DSP. The most important of the HCPL-3120 is that it acts as isolator and driver, simultaneously. In this study, it has been used a ZMCT103C as the hall-effect current sensor. A prominent feature of this sensor is that its output is isolated from other parts of the setup.

Moreover, to measure the load current, it does not need any interface circuit. Figure 15 shows the

experimental results for the output voltage and current under pure resistive load at f_s=50Hz. Generally, when a resistive load is used, the voltage and current have no

TABLE 6. The parameters and devices applied to the laboratory setup

Parameter/ Device	Value/ Type
DSP	TMS320F28379D
V_{dc}	20v
Maximum expected voltage level	120v
Output voltage frequency	50Hz and 500Hz
Capacitors	$C_{t1}=C_{t2}=6300\mu F$ and $C_f=C_m=3300\mu F$
IGBT	IRG4IBC30
Antiparallel diode	MBRF20100CT
Driver	HCPL-3120
Buffer	74HC245
Resistive loads	50Ω and 300Ω
Inductive load	500mH
Current sensor	ZMCT103C (1:4)
Output voltage sensor	Resistive divider (1:15)
Capacitor voltage sensor for V_{cf} and V_{cm}	Resistive divider (1:1.5)

(a)

(b)
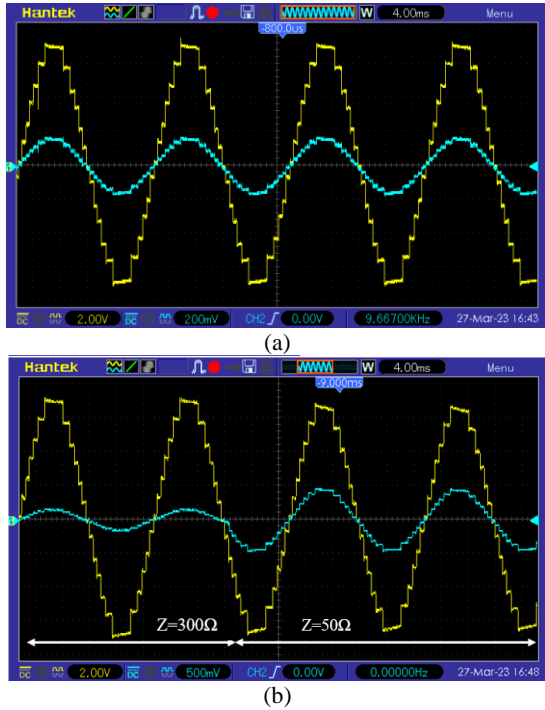
Figure 15. Experimental results for output voltage (yellow) and current (blue) with pure resistive load at f_s=50Hz. (a) with constant impedance Z=300Ω. (b) with changing the load impedance from Z=300Ω to 50Ω. To obtain the actual voltage and current values, the vertical axis must be multiplied by factors 15 and 4, respectively (see Table 6).

phase difference from each other and the waveform of the output current is a multilevel form same as the output voltage. Considering table 6, the peak value of the output voltage is about (3.5×2×15=105v).

However, this value is slightly different from the maximum expected voltage level (120v) because of the voltage drop on the IGBTs and diodes in the laboratory setup. As shown in Figure 15(b), the load impedance has increased six times. For this reason, the output current peak has been reached from (0.15×0.5×4=0.3A) to (0.9×0.5×4=1.8A).

Figure 16 depicts the experimental results with a purely inductive load as Z=500mH under f_s=50Hz. In relation to this figure, there are two outstanding points. First, the output current is close to a sinusoidal waveform same as in Figure 12(b). secondly, a 90-degree phase difference has been shown between the output voltage and current.

Figure 17 shows the capacitors voltage waveform of the C_{t1}, C_{t2}, C_m, and C_f under output frequency f=50Hz. According to Figure 6, because the discharging time of the capacitors C_{t1}, and C_{t2} is more than the capacitors C_f, and C_m, the voltage ripple of the capacitors C_{t1} and C_{t2} is more than others which can be seen in Figure 17. From the view of the voltage range, the capacitor's voltages of C_{t1} and C_{t2} are equal to V_1=15v as shown in Figure 17(a).
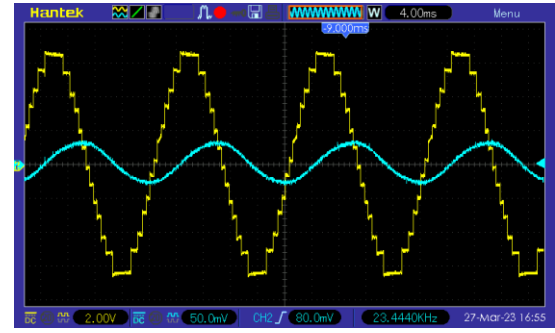
Figure 16. Experimental results for output voltage (yellow) and current (blue) with pure inductive load Z=500mH at f_s=50Hz. To obtain the actual voltage and current values, the vertical axis must be multiplied by factors 15 and 4, respectively (see Table 6)

Moreover, according to Figure 17(b), the capacitor's voltages of C_f and C_m are about V_2=37v. The V_1 and V_2 must be 20v, and 40v, respectively but the voltage drop of the switches and diodes has caused such an issue. For assessing the HF condition, an experimental result is performed at f_s=500Hz which is shown in Figure 18. In this figure, with horizontal zoom, it can be shown that the 13-level waveform is well produced at the output without the voltage levels going out of order.

(a)

(b)
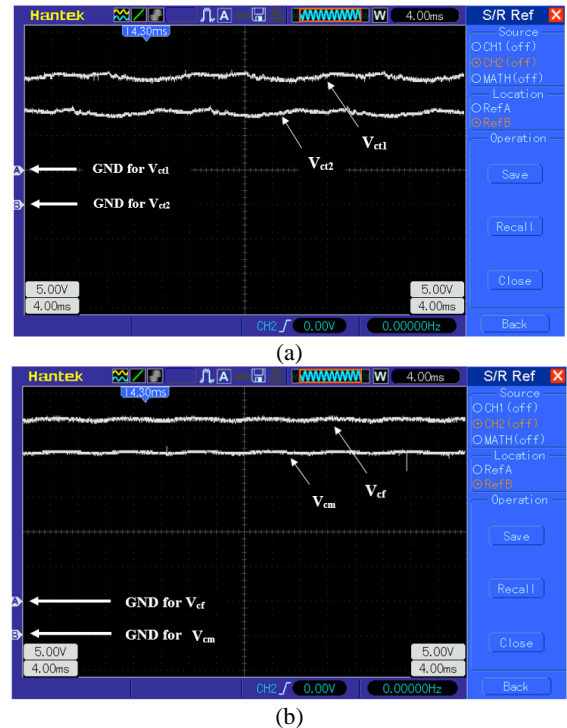
Figure 17. Experimental results for capacitor voltages under pure resistive load at f_s=50Hz. (a) capacitors voltage V_{ct1} and V_{ct2} (b) capacitors voltage V_{cf} and V_{cm}. To obtain the actual voltage value of capacitors C_f and C_m, the vertical axis must be multiplied by factor 1.5 (see Table 6)
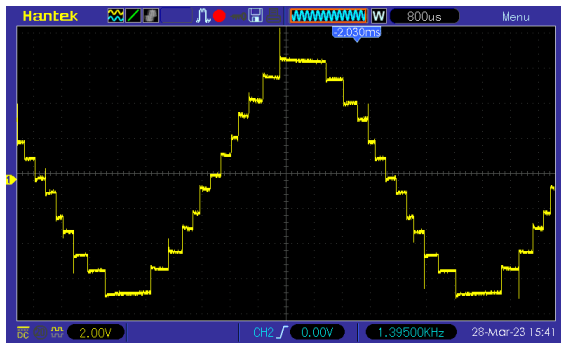
Figure 18. Experimental results for output voltage under pure resistive load at f_s=500Hz

7. CONCLUSION

A new switched-capacitor multilevel inverter based on combined T-type and cross modules without H-bridge was introduced in this work. The proposed topology has the ability to boost as well as modularity with only one DC-link source. In the case of 13-level conditions, the proposed multilevel inverter includes 20 switches and 4 capacitors to produce a voltage gain of 6. In modularity conditions, the PIV of switches remains constant as the number of cross-modules increases. Hence, the TSV and CF can be drastically decreased compared to other topologies. Under the NLC switching technique, the THD of output voltage in the proposed multilevel inverter is 6.33% which conforms to the IEEE standards. The simulation and experimental results confirm the validity of the proposed topology under steady state and transient conditions as well as performance in HF and LF domains.

8. REFERENCES

1. Fang, J., Blaabjerg, F., Liu, S. and Goetz, S.M., "A review of multilevel converters with parallel connectivity", *IEEE Transactions on Power Electronics*, Vol. 36, No. 11, (2021), 12468-12489. doi: 10.1109/TPEL.2021.3075211.

2. Gupta, K.K., Ranjan, A., Bhatnagar, P., Sahu, L.K. and Jain, S., "Multilevel inverter topologies with reduced device count: A review", *IEEE Transactions on Power Electronics*, Vol. 31, No. 1, (2015), 135-151. doi: 10.1109/TPEL.2015.2405012.

3. Arif, M.S.B., Mustafa, U., Siddique, M.D., Ahmad, S., Iqbal, A., Ashique, R.H. and Ayob, S.b., "An improved asymmetrical multi-level inverter topology with boosted output voltage and reduced components count", *IET Power Electronics*, Vol. 14, No. 12, (2021), 2052-2066. https://doi.org/10.1049/pel2.12119

4. Wang, L., Wu, Q. and Tang, W., "Novel cascaded switched-diode multilevel inverter for renewable energy integration", *IEEE Transactions on Energy Conversion*, Vol. 32, No. 4, (2017), 1574-1582. doi: 10.1109/TEC.2017.2710352.

5. Salehi, S.J., Shmasi-Nejad, M. and Najafi, H.R., "A new multilevel inverter based on harvest of unused energies for photovoltaic applications", *International Journal of Engineering, Transaction C: Aspects,* Vol. 35, No. 12, (2022), 2377-2385. doi: 10.5829/IJE.2022.35.12C.14.

6. Kopacz, R., Harasimczuk, M., Trochimiuk, P., Wrona, G. and Rąbkowski, J., "Medium voltage flying capacitor dc–dc converter with high-frequency tcm-q2l control", *IEEE Transactions on Power Electronics*, Vol. 37, No. 4, (2021), 4233-4248. doi: 10.1109/TPEL.2021.3122329.

7. Abdelhamid, E., Corradini, L., Mattavelli, P., Bonanno, G. and Agostinelli, M., "Sensorless stabilization technique for peak current mode controlled three-level flying-capacitor converters", *IEEE Transactions on Power Electronics*, Vol. 35, No. 3, (2019), 3208-3220. doi: 10.1109/TPEL.2019.2930011.

8. Nandhini, G.M. and Ganimozhi, T., "New hybrid cascaded multilevel inverter", *International Journal of Engineering Transactions B: Applications*, Vol. 26, No. 1, (2013). doi: 10.5829/idosi.ije.2013.26.11b.13.

9. Rahimi Mirazizi, H. and Agha Shafiyi, M., "Evaluating technical requirements to achieve maximum power point in photovoltaic powered z-source inverter", *International Journal of Engineering Transactions C: Aspects*, Vol. 31, No. 6, (2018), 921-931. doi: 10.5829/IJE.2018.31.06C.09.

10. Alemi-Rostami, M. and Rezazadeh, G., "Selective harmonic elimination of a multilevel voltage source inverter using whale optimization algorithm", *International Journal of Engineering, Transactions B: Applications*, Vol. 34, No. 8, (2021), 1898-1904. doi: 10.5829/IJE.2021.34.08B.11.

11. Tousi, B. and Ghanbari, T., "Transformer-based single-source multilevel inverter with reduction in number of transformers", *International Journal of Engineering, Transactions B: Applications*, Vol. 29, No. 5, (2016), 621-629. https://doi.org/10.1049/iet-pel.2018.5420

12. Lopez-Santos, O., Jacanamejoy-Jamioy, C.A., Salazar-D'Antonio, D.F., Corredor-Ramírez, J.R., Garcia, G. and Martinez-Salamero, L., "A single-phase transformer-based cascaded asymmetric multilevel inverter with balanced power distribution", *IEEE Access*, Vol. 7, (2019), 98182-98196. https://doi.org/10.22214/ijraset.2021.38989

13. Arthy, G. and Marimuthu, C., "A novel center-tapped transformer based multilevel inverter with common dc source", *Journal of Vibroengineering*, Vol. 20, No. 8, (2018), 3040-3053. https://doi.org/10.21595/jve.2018.20029

14. Salem, A., Van Khang, H., Jiya, I.N. and Robbersmyr, K.G., "Hybrid three-phase transformer-based multilevel inverter with reduced component count", *IEEE Access*, Vol. 10, (2022), 47754-47763. doi: 10.1109/ACCESS.2022.3171849.

15. Taghvaie, A., Adabi, J. and Rezanejad, M., "A self-balanced step-up multilevel inverter based on switched-capacitor structure", *IEEE Transactions on Power Electronics*, Vol. 33, No. 1, (2017), 199-209. doi: 10.1109/TPEL.2017.2669377.

16. Lakshmipriya, N. and Anathamoorthy, N., "Using fpga real time model for novel 33-level switched-capacitor multilevel inverter for pmsm drive", *Microprocessors and Microsystems*, Vol. 76, No., (2020), 103078. doi: 10.3390/mi13020179.

17. Hussan, M.R., Sarwar, A., Siddique, M.D., Mekhilef, S., Ahmad, S., Sharaf, M., Zaindin, M. and Firdausi, M., "A novel switched-capacitor multilevel inverter topology for energy storage and smart grid applications", *Electronics*, Vol. 9, No. 10, (2020), 1703. https://doi.org/10.3390/electronics9101703

18. Taheri, A., Rasulkhani, A. and Ren, H.P., "A multilevel inverter using switched capacitors with reduced components", *IET Power Electronics*, Vol. 13, No. 17, (2020), 3954-3962. https://doi.org/10.1049/iet-pel.2020.0473

19. Zamiri, E., Vosoughi, N., Hosseini, S.H., Barzegarkhoo, R. and Sabahi, M., "A new cascaded switched-capacitor multilevel inverter based on improved series–parallel conversion with less number of components", *IEEE Transactions on Industrial*

Electronics,   Vol. 63, No. 6, (2016), 3582-3594. doi: 10.1109/TIE.2016.2529563.

20. Hinago, Y. and Koizumi, H., "A switched-capacitor inverter using series/parallel conversion with inductive load", *IEEE Transactions on Industrial Electronics*, Vol. 59, No. 2, (2011), 878-887. doi: 10.1109/TIE.2011.2158768.

21. Mak, O.-C. and Ioinovici, A., "Switched-capacitor inverter with high power density and enhanced regulation capability", *IEEE Transactions on Circuits and Systems I: Fundamental Theory and Applications*, Vol. 45, No. 4, (1998), 336-347. doi: 10.1109/81.669056

22. Ye, Y., Cheng, K.W.E., Liu, J. and Ding, K., "A step-up switched-capacitor multilevel inverter with self-voltage balancing", *IEEE Transactions on Industrial Electronics*, Vol. 61, No. 12, (2014), 6672-6680. doi: 10.1109/TIE.2014.2314052.

23. Barzegarkhoo, R., Kojabadi, H.M., Zamiry, E., Vosoughi, N. and Chang, L., "Generalized structure for a single phase switched-capacitor multilevel inverter using a new multiple dc link producer with reduced number of switches", *IEEE Transactions on Power Electronics*, Vol. 31, No. 8, (2015), 5604-5617. doi: 10.1109/TPEL.2015.2492555.

24. Khenar, M., Taghvaie, A., Adabi, J. and Rezanejad, M., "Multi-level inverter with combined t-type and cross-connected modules", *IET Power Electronics*, Vol. 11, No. 8, (2018), 1407-1415. https://doi.org/10.1049/iet-pel.2017.0378

25. Tashiwa, I.E., Dung, G.D. and Adole, B.S., "Review of multilevel inverters and their control techniques", *European Journal of Engineering and Technology Research*, Vol. 5, No. 6, (2020), 659-664. https://doi.org/10.24018/ejeng.2020.5.6.1707

26. Yu, H., Chen, B., Yao, W. and Lu, Z., "Hybrid seven-level converter based on t-type converter and h-bridge cascaded under

spwm and svm", *IEEE Transactions on Power Electronics*, Vol. 33, No. 1, (2017), 689-702. doi: 10.1109/TPEL.2017.2664068.

27. Yang, K., Lan, X., Zhang, Q. and Tang, X., "Unified selective harmonic elimination for cascaded h-bridge asymmetric multilevel inverter", *IEEE Journal of Emerging and Selected Topics in Power Electronics*, Vol. 6, No. 4, (2018), 2138-2146. doi: 10.1109/JESTPE.2018.2808539.

28. Yadav, S.K., Mishra, N. and Singh, B., "Three-phase single pv array fed scott-ternary multilevel converter with nearest level control", in 2020 IEEE 7th Uttar Pradesh Section International Conference on Electrical, Electronics and Computer Engineering (UPCON), IEEE. (2020), 1-5.

29. Thakre, M.P., Jadhav, T.K., Patil, S.S. and Butale, V.R., "Modular multilevel converter with simplified nearest level control (NLC) strategy for voltage balancing perspective", in 2021 Innovations in Energy Management and Renewable Resources (52042), IEEE. (2021), 1-8.

30. Siddique, M.D., Mekhilef, S., Shah, N.M., Sarwar, A., Iqbal, A., Tayyab, M. and Ansari, M.K., "Low switching frequency based asymmetrical multilevel inverter topology with reduced switch count", *IEEE Access*, Vol. 7, (2019), 86374-86383. doi: 10.1109/ACCESS.2019.2925277.

31. Hasari, S.A.S., Salemnia, A. and Hamzeh, M., "Applicable method for average switching loss calculation in power electronic converters", *Journal of Power Electronics*, Vol. 17, No. 4, (2017), 1097-1108. https://doi.org/10.6113/JPE.2017.17.4.1097

32. Lin, W., Zeng, J., Liu, J., Yan, Z. and Hu, R., "Generalized symmetrical step-up multilevel inverter using crisscross capacitor units", *IEEE Transactions on Industrial Electronics*, Vol. 67, No. 9, (2019), 7439-7450. doi: 10.1109/TIE.2019.2942554.

Persian Abstract

چکیده

این مقاله یک توپولوژی اینورتر چند سطحی متقارن نوع خازن سوئیچ شده ارائه می‌کند که می‌تواند ولتاژ DC ورودی را به شکل موج AC چند سطحی افزاینده بر روی بار تبدیل کند. این اینورتر چند سطحی پیشنهادی از یک ماژول نوع T و چندین ماژول خازن Cross تشکیل شده است. ساختار اینورتر چند سطحی تعمیم یافته به گونه ای است که ولتاژ پیک معکوس با افزایش تعداد ماژول های خازن ثابت می ماند که این موضوع منجر به کاهش ولتاژ استرس کلیدها و عملکرد هزینه در مقایسه با سایر توپولوژی های سنتی می شود. . ساختار معرفی شده به طور ذاتی می تواند سطوح ولتاژ مثبت، منفی و صفر را در خروجی بدون ساختار H-bridge ایجاد کند. ولتاژهای خازن در ماژول های نوع T و Cross ذاتاً متعادل هستند و سیستم کنترل را تحت استراتژی سوئیچینگ کنترل نزدیکترین سطح (NLC) ساده می کنند. برای تأیید عملکرد توپولوژی پیشنهادی، چندین شبیه‌سازی و نتایج آزمایشگاهی برای یک اینورتر ۱۳ سطحی به ترتیب توسط MATLAB و TMS320F28379D DSP ارائه شده‌اند.

International Journal of Engineering

Investigation of the Damping Performance of a Shape Memory Alloy Beam

N. Danesh[a], M. J. Mahmoodabadi[*b], A. R. Fathi[c]

[a] Department of Mechanical Engineering, University of Texas at Arlington, Arlington, TX, USA
[b] Department of Mechanical Engineering, Sirjan University of Technology, Sirjan, Iran
[c] Department of Mechanical Engineering, Babol Noushirvani University of Technology, Babol, Iran

PAPER INFO

ABSTRACT

The aim of this research is to introduce a semi-analytical approach for the analysis of the free and forced nonlinear vibrations of a bending shape memory alloy (SMA) beam; while, considering the effect of its pseudo-elastic behavior. In order to create a primary deflection, an appropriate pre-strain is applied to the SMA beam using a compression spring. A new material model was utilized to simulate the nonlinear hysteric behavior of the SMA beam, while the differential equations of motion of the beam were derived based on Euler–Bernoulli beam theory and Hamilton principle. The extracted nonlinear partial differential equations of motion are semi-analytically solved by utilizing the Galerkin method. The pseudo-elastic behavior and energy dissipation of the SMA beam were studied in the free and forced nonlinear vibration regimes. Finally, the influences of the system parameters such as the spring constant, amplitude, and frequency of the excitation force on the absorber efficiency were investigated, and its stability was studied. The numerical results depict that the SMA beam exhibits a highly nonlinear dynamical behavior, and can be used as an actuator for energy dissipation.

NOMENCLATURE

ε	Total strain	e	Deviatoric strain
ε^e	Thermo-elastic strain	θ	Volumetric strain
ε^{tr}	Transformation strain	s	Deviatoric stress
ε_L	Maximum hysteresis strain	I_i	Identify tensor
σ	Total stress	p	Volumetric stress
K	Lame constant of the material	G	Lame constant of the material
τ_M	Proper function of temperature	β	Material's parameter
T_0	Initial temperature	I_{ε_L}	Indicator function of ε^{tr}
x^{tr}	Transformation stress	ψ	The Helmholtz free energy
R	Radius of the elastic area in the material	u	Displacement parallel to x direction
v	Displacement parallel to y direction	w	Displacement parallel to z direction
π	Strain energy	T	Kinetic energy
W	The work is done by external force	E	Young's modulus
I	Mass of inertia	η_i	The ith generalized coordinate
ϕ_i	The ith shape function	L	Length of the beam
r	Radius of the beam	ρ	Density of the beam
ν	Material's parameter	ω	Excitation force frequency
ς	Loss factor	A_i	he ith vibration amplitude

1. INTRODUCTION

Special features of the smart materials that make them an appropriate choice in various fields of engineering. Among different kinds of them, Shape Memory Alloys (SMAs) have their own exclusive characteristics that make them proper alternatives to other smart substances such as piezoelectrics. Some of these features could be listed as follows:

*Corresponding Author Institutional Email
mahmoodabadi@sirjantech.ac.ir (M. J. Mahmoodabadi)

- Very effective for low frequency vibration or shape control
- Easy machinability into different shapes and sizes
- Energy dissipation more than piezoelectric materials.

These behaviors of the SMAs are related to the reversible thermo-elastic martensitic phase transformation between high symmetry, austenitic and low symmetry martensitic situations which are characterized by the superelasticity and shape memory effects. The former is the ability of a material to experience large recoverable strains without notable residual strains. The latter effect refers to the capability of restoring the original shape of materials that are plastically deformed by temperature variations. These unique characteristics provide new possibilities in use of smart materials; for example, aerospace, medical industry, vibration damping, robotics, and automotive [1-12]. Particularly, the SMA actuators can make large displacements and have a high force/weight ratio in compare with the conventional actuators. The following superiorities were also ascribed to the SMA actuators: uncomplicated design, smooth motivation, bio-adaptability, silent operation, easy actuation, and low power expenditure [13].

Extensive experimental investigations have shown that phase transformation of SMAs is a thermomechanical coupled process, with heat production due to latent heat and intrinsic dissipation [14, 15]. Based on these experimental findings, a few models that take into account thermomechanical coupling were proposed [16-19]. However, these models are either limited to small deformations [18, 19] or developed without thermal deformation gradient involved [16, 17].

In fact, at high temperature and large stress magnitude the martensite structures have a much lower Young's modulus and can be readily deformed by application of an external force or heat, indicating that thermoelastic deformations cannot be neglected [20, 21]. Due to the essential role of the beams in structural mechanics, many scientists have given particular attentions to the composition of flexible beams with SMA wires and strips. Among them, some researchers [22-31]have applied analytical solutions for studying pseudo-elastic beams, while others have used numerical approaches for them [32-34]. Razavilar et al. [35] presented a semi-analytical approach to analyze free and forced vibrations of a clamped-free SMA beam. They illustrated that the phase transformation has a significant effect on the region near the clamped end; whereas, the free end stays within the elastic domain. Hashemi and Khadem [36] analyzed dynamical behaviors of clamped-free and simply supported SMA beams. They considered the superelastic property of the SMA and introduced a mathematical model based on the Auricchio material theory. Regarding this paper, it can be concluded that there is no residual stress at the end of loading under the superelastic condition, while increasing in temperature initiates a growth in stresses at the start and end of transformation. Jose et al. [37] performed an analysis on a vibration isolator made of a SMA bar under isothermal and non-isothermal conditions. Their results exhibited that the amplitude of the response to an external excitation is limited due to the hysteretic behavior of the SMA material, while the energy of the system is well dissipated. Pan and Cho [38] proposed a shape memory alloy micro-damper to apply the pseudo-elastic behavior of NiTi wires for dissipation of the system energy. They conducted a series of tension tests to analyze the damping behavior, while the NiTi wires were subjected to different temperatures, strain rates and strain amplitudes. The experimental results displayed that the energy dissipation of the wires is practically independent of the temperature, while intensely dependent on the strain rate and amplitude. Damanpack et al. [39] investigated the vibration control ability of SMA composite beams subjected to impulsive loads by applying the 1-D model proposed by Panico and Brinson [40]. It can be seen from the results that the SMA layers with high pre-strain at low temperatures have an acceptable ability for passive vibration control. Brinson et al. [41] considered active shape control of a cantilever beam with outside-attached SMA wires. Brinston's constitutive law was used for modeling the thermo-mechanical behavior of the SMA by applying linear and nonlinear beam theories as well as temperature variations. Moallem [42] suggested a nonlinear method inspired by the sliding mode control to reduce the deflection of a flexible beam using shape memory alloy wires. On the other hand, Sohn, Han, Choi, Lee [4]] investigated vibration control and position tracking of a smart flexible system by employing SMA wire actuators and robust sliding mode control. Sayyaadi and Zakerzadeh [43] carried out a nonlinear scheme for a flexible beam with two outside-attached active SMA actuators. Andrade et al. [44] developed influences of the strain rate on stress-induced martensite, rupture strain, ultimate strength and residual strain for a CuAlMnTiB SMA. Billah et al. [45] studied the properties of the shape memory alloys suitable for the civil engineering domain and prospects of forthcoming opportunities. An integrated microstructural-mechanical model is proposed by Bellini et al. [46] for an equiatomic NiTi shape memory alloy to predict its pseudoelastic cyclic behaviour.

The aim of the current study is to investigate the dynamical behavior of a simply supported SMA beam with a compression spring to make a pre-strain on it. The three-dimensional constitutive material model presented by Souza et al. [47] is utilized to simulate the hysterical behavior of the SMA, and a semi-analytical method is introduced to analyze the dynamical behavior of the system. It should be noted that most of the previous researches have been focused on the composite beams embedded with the SMA wires, and in other few cases, finite element methods have been implemented for

analyzing. Unlike these works, the current contribution proposes a novel scheme to acquire the state-space equations of the regarded SMA structure for modeling and design of a control system. The advantages of this strategy are reducing the number of required equations and decreasing the computational time.

The organization of this article is as follows. In section 2, the structure of the considered SMA beam as well as the Souza model [47] and its mathematical equations are reviewed. Moreover, the nonlinear formulation of the SMA beam under a compression force is derived in this section. The simulation and results are presented in section 3. Finally, section 4 concludes the paper.

2. SMA DAMPER AND ITS STRUCTURE

Most of the shape memory alloy actuators have been made of shape memory alloy wires or rods [47, 48]. In this research, an SMA actuator is proposed that works based on the bending of a shape memory alloy beam. The suggested system has a higher force/weight ratio and can undergo more amounts of the force in comparison with the wire or rod types. It contains a shape memory alloy beam under an excitation force (Figure 1) as well as a compression spring attached to it. The spring produces a pre-strain to create a reversible plastic deformation in the beam and to associate with a phase transformation between the twinned and detwinned martensite phases. By passing the electrical current through the SMA beam, its temperature would increase (because of the beam's electrical resistance). Increasing the temperature causes the transformation from the detwinned martensite phase to the austenite phase, which returns the beam to its original shape. By switching off the electrical current and decreasing the beam temperature, the spring changes the beam shape back again, and its phase would change to twinned martensite.

2. 1. Material Model   As it was mentioned before, the most important and complicated phenomenon of SMA materials is the metallurgical phase transformation which has a significant effect on its performance. The prediction of the phenomenological hysteretic behavior of the SMAs can be understood from their governing mathematical models [49-51]. Based on the experimental observations, there are two points of view about phenomenological constitutive models, i.e., microscopic and macroscopic [52-58]. The microscopic models are applied to realize fundamental principles in the molecular scale, but those are not good choices for the structural scale. On the other hand, the macroscopic models, related to the phenomenological features of the SMA, are able to represent phase transformation kinetics using simple mathematical functions [59-64]. To name but a few, Simo and Taylor [65] developed a stable algorithm based

on a return mapping approach for plane stress elastoplasticity in large time steps. Bertram [66] suggested a three-dimensional thermomechanical model based on an expanded classical theory of plasticity to describe shape memory effects as an explanation of incremental iterations. Leclercq [67] extended a phase transition model to simulate the behavior of the SMA with isothermal or non-isothermal loadings. Further, Souza, Mamiya and Zouain [47] proposed a three-dimensional model having superelasticity behaviors and shape memory effects by means of plasticity concepts.

In this study, Souza's material model [47] is used to identify the hysteric behavior of the SMA based on the theory of irreversible thermodynamics under small deformations. According to this model, a series of external and internal variables illustrate the thermo-dynamical state of a homogenized volume element at each moment. In this way, the total strain is divided into elastic and inelastic parts as follows:

$$\varepsilon = \varepsilon^{te} + \varepsilon^{tr} \tag{1}$$

where, ε, ε^{te} and ε^{tr} are the total, thermo-elastic and transformation strains, respectively. Moreover, strain ε and stress σ are decomposed as follows:

$$\varepsilon = e + \frac{\theta}{3}I_i \tag{2}$$

$$\sigma = s + pI_i \tag{3}$$

where, e is the deviatoric strain, $\theta = \mathrm{tr}(\varepsilon)$ denotes the volumetric strain, s represents the deviatoric stress, $p = tr(\sigma)/3$ signifies the volumetric stress, and I_i indicates the identity tensor.

In this model, volumetric θ and deviatoric e strains, as well as temperature T are determined as the control variables, while transformation strain ε^{tr} is regarded as an internal variable. The transformation strain is with the phase transformation from the twinned martensite to the detwinned martensite. Due to the phase transformation, the norm of ε^{tr} is zero when the material is without oriented martensite and has maximum value ε_L when the material is completely transformed into the martensite as follows:

$$\|\varepsilon^{tr}\| \le \varepsilon_L \tag{4}$$

where, $\|\varepsilon^{tr}\|$ shows the Euclidean norm of the transformation strain.
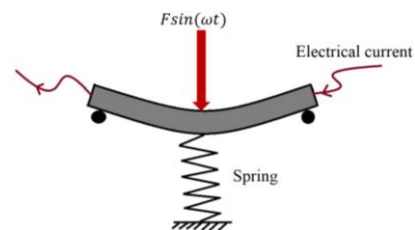
Figure 1. Schematic of the considered shape memory alloy beam

In this model, the Helmholtz free energy, suggested by Souza [47], could be represented as follows:

$$\psi(\theta, \varepsilon, \varepsilon^{tr}, T) = \frac{1}{2}K\theta^2 + G\|\varepsilon - \varepsilon^{tr}\|^2 + \tau_M(T)\|\varepsilon^{tr}\| + \frac{1}{2}h\|\varepsilon^{tr}\|^2 + I_{\varepsilon_L}(\|\varepsilon^{tr}\|) \tag{5}$$

In Equation (5), K and G signify the Lame constants of the material, $\tau_M(T)$ denotes a function of temperature, and h represents a material parameter related to its hardening. $\tau_M(T)$ is considered as $\tau_M(T) = \beta\langle T - T_0\rangle$, where β is a constant parameter, T_0 shows an initial temperature, and operator '$\langle . \rangle$' illustrates the positive part of a function.

In addition, function I_{ε_L} is defined as follows:

$$I_{\varepsilon_L}(\|\varepsilon^{tr}\|) = \begin{cases} 0 & if \ \|\varepsilon^{tr}\| \le \varepsilon_L \\ +\infty & otherwise \end{cases} \tag{6}$$

From Equation (5), the following constitutive relations could be written.

$$p = \frac{\partial\psi}{\partial\theta} = K\theta \tag{7}$$

$$s = \frac{\partial\psi}{\partial\varepsilon} = 2G(\varepsilon - \varepsilon^{tr}) \tag{8}$$

$$x^{tr} = -\frac{\partial\psi}{\partial\varepsilon^{tr}} = s - x \tag{9}$$

where, x^{tr} indicates the transformation stress having the following relation.

$$x = [\tau_M(T) + h\|\varepsilon^{tr}\| + \gamma]\frac{\varepsilon^{tr}}{\|\varepsilon^{tr}\|} \tag{10}$$

where,

$$\begin{cases} \gamma = 0 & if \ \|\varepsilon^{tr}\| < \varepsilon_L \\ \gamma \ge 0 & if \ \|\varepsilon^{tr}\| = \varepsilon_L \end{cases} \tag{11}$$

The following equation is regarded for satisfying the second law of thermodynamics:

$$\dot{\varepsilon}^{tr} = \zeta\frac{\varepsilon^{tr}}{\|\varepsilon^{tr}\|} \tag{12}$$

Based on the evolution of the phase transformation, f is determined as follows:

$$f = \|x^{tr}\| - R \tag{13}$$

where, R is the radius of the elastic area in material.
Finally, Souza's model [47] would be accomplished if the stability and Kuhn-Tucker conditions are satisfied, therefore.

$$\dot{\zeta} \ge 0, \quad f \le 0, \quad \dot{\zeta}f = 0 \tag{14}$$

2. 1. 1. Return Mapping
In this sub-section, a return mapping algorithm is presented to merge Equations (7) through (13) within the imperceptible plasticity situation. Generally, the solving procedure includes three steps as follows:

(i) A trial state and an elastic behavior are assumed for the material.
(ii) Comparing whether the calculated trial state is actually elastic.
(iii) If the trial state does not have any elastic behavior, then the state variables are designed to validate all the constraints enforced by the problem.

In this algorithm, prescribed strain ε_{n+1} is determined as a mechanical loading for the SMA material. At first, the algorithm calculates the trial state $(s_{n+1}^{trial}, x_{n+1}^{trial})$ and then the elastic condition is assumed by making $\varepsilon_{n+1}^{tr^{trial}} = \varepsilon_n^{tr}$. Therefore, by employing Equation (4), the following relations are found.

$$s_{n+1}^{trial} = 2G\left(\varepsilon_{n+1} - \varepsilon_{n+1}^{tr^{trial}}\right) \tag{15}$$

$$x_{n+1}^{trial} = s_{n+1}^{trial} - \left(\tau_M(T) + h\left\|\varepsilon_{n+1}^{tr^{trial}}\right\|\right)\frac{\varepsilon_{n+1}^{tr^{trial}}}{\left\|\varepsilon_{n+1}^{tr^{trial}}\right\|} \tag{16}$$

The material has an elastic behavior if the following conditions are satisfied.

$$\begin{cases} 0 < \|\varepsilon_n^{tr}\| < \varepsilon_L \\ \|x_{n+1}^{trial}\| \le R \end{cases} \tag{17}$$

If $\varepsilon_n^{tr} = 0$, trial force x_{n+1}^{trial} cannot be calculated by Equation (16), whereas s_{n+1}^{trial} could be computed by Equation (15). The elastic behavior would occur in the parent phase, if:

$$\begin{cases} \varepsilon_n^{tr} = 0 \\ s_{n+1}^{trial} \le \tau_M(T) + R \end{cases} \tag{18}$$

Finally, the case for which $\|\varepsilon_n^{tr}\| = \varepsilon_L$ has to be considered. Here, the step is elastic whenever there exists $\gamma \ge 0$ such that:

$$\begin{cases} \|\varepsilon_n^{tr}\| = \varepsilon_L \\ \|\hat{s} + \hat{\gamma}n\| \le R \quad n = -\frac{\varepsilon_{n+1}^{tr^{trial}}}{\|\varepsilon_{n+1}^{tr^{trial}}\|}, \\ \hat{s} = \|s_{n+1}^{trial} + (\tau_M(T) + h\varepsilon_L)n\|, \quad \hat{\gamma} = < -\hat{s}.n > \end{cases} \tag{19}$$

The step would be elastic, if one of the three conditions mentioned in Equations (17), (18) or (19) holds. At time $n + 1$, the actual state is a trial state; therefore, the following relations could be mentioned.

$$\varepsilon_{n+1}^{tr} = \varepsilon_{n+1}^{tr^{trial}}$$
$$s_{n+1} = s_{n+1}^{trial} \tag{20}$$

Finally, if none of conditions stated in Equations (17), (18) or (19) are approved, a phase transformation would occur, and ε_{n+1}^{tr} could be calculated by the following equation.

$$R\frac{\varepsilon_{n+1}^{tr} - \varepsilon_n^{tr}}{\|\varepsilon_{n+1}^{tr} - \varepsilon_n^{tr}\|} - 2G(\varepsilon_{n+1} - \varepsilon_{n+1}^{tr}) + (\tau_M(T) + h\|\varepsilon_{n+1}^{tr}\|)\frac{\varepsilon_{n+1}^{tr}}{\|\varepsilon_{n+1}^{tr}\|} = 0 \tag{21}$$

If $\|\varepsilon_{n+1}^{tr}\| > \varepsilon_L$, then the solution for ε_{n+1}^{tr} and γ_{n+1} can be achieved via the following set of nonlinear equations:

$$\left\{ \begin{array}{c} R\frac{\varepsilon_{n+1}^{tr}-\varepsilon_n^{tr}}{\|\varepsilon_{n+1}^{tr}-\varepsilon_n^{tr}\|} - 2G(\varepsilon_{n+1}-\varepsilon_{n+1}^{tr}) + \\ (\tau_M(T) + h\varepsilon_L + \gamma_{n+1})\frac{\varepsilon_{n+1}^{tr}}{\|\varepsilon_{n+1}^{tr}\|} \\ \|\varepsilon_{n+1}^{tr}\| - \varepsilon_L \end{array} \right\} = 0 \qquad (22)$$

$$s_{n+1} = 2G(\varepsilon_{n+1}-\varepsilon_{n+1}^{tr}) \qquad (23)$$

2. 2. Constitutive Equation of the Shape Memory Alloy Beam   In this study, the Euler-Bernoulli beam with the circular cross-section is considered to derive the set of the governing equations for simulation of the SMA system behavior using a semi-analytical solution method. While the transverse displacement of the centerline of the beam is w, the displacement of any points in the cross-section is w too. As shown in Figure 2, the plane sections stay normal to the centerline.

$$u = -z\frac{\partial w(x,t)}{\partial x} \qquad v = 0 \qquad w = w(x,t) \qquad (24)$$

where, u, v and w designate the components of displacement in x, y and z directions, respectively. The components of the strain and stress corresponding to this displacement field are given by the following equations:

$$\varepsilon_{xx} = \frac{\partial u}{\partial x} = -z\frac{\partial^2 w(x,t)}{\partial x^2}, \varepsilon_{yy} = 0 \ , \ \varepsilon_{zz} = 0 \ , \ \varepsilon_{xy} = 0 \ , \ \varepsilon_{xz} = 0 \ , \ \varepsilon_{yz} = 0$$

$$\sigma_{xx} = -Ez\frac{\partial^2 w(x,t)}{\partial x^2}, \qquad \sigma_{yy} = 0 \ , \ \sigma_{zz} = 0 \ , \ \sigma_{xy} = 0 \ , \ \sigma_{xz} = 0 \ , \ \sigma_{yz} = 0$$

$$(25)$$

The strain energy of the system (π) as well as its kinetic energy (T) can be expressed as:

$$\pi = \frac{1}{2}\iiint \sigma_{xx}\varepsilon_{xx}dV = \frac{1}{2}\iiint E(\varepsilon - \varepsilon^{tr})^2 dV \qquad (26)$$

$$T = \frac{1}{2}\int_0^L \rho A\left(\frac{\partial w(x,t)}{\partial t}\right)^2 dx \qquad (27)$$

The work done by the mechanical load (F_0), excitation force ($F\sin(\omega t)$) and simple spring (F_k) is given by:

$$W = \int_0^L \left(F_0\left(\frac{L}{2},t\right) + F\left(\frac{L}{2},t\right)\sin(\omega t) - F_k\left(\frac{L}{2},t\right) \right) w(x,t)dx \qquad (28)$$
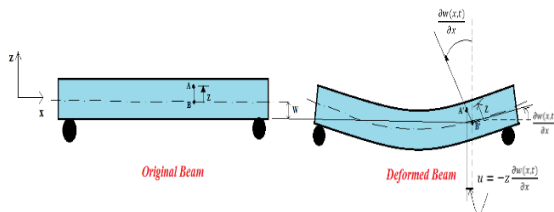

Figure 2. Bending of an Euler–Bernoulli beam

where, ω is the frequency of the excitation force. The dirac delta function could be employed to enter these forces into the equation as follows:

$$F_0\left(\frac{L}{2},t\right) = f_0\ \delta\left(x - \frac{L}{2}\right),$$

$$F\left(\frac{L}{2},t\right)\sin(\omega t) = f\sin(\omega t)\ \delta(x - \frac{L}{2}), \qquad (29)$$

$$F_k\left(\frac{L}{2},t\right) = f_k\left(\frac{L}{2},t\right)\delta\left(x - \frac{L}{2}\right)$$

In order to extract the governing equations of the motion and boundary conditions for the SMA beam, the Hamilton's principle is utilized as follows:

$$\delta\int_{t_1}^{t_2}(\pi - T - W)\ dt = 0 \qquad (30)$$

where, δ denotes the variation operator, and $[t_1, t_2]$ describes an arbitrary time interval. By substituting Equations (26), (27), (28) and (29) into Equation (30), the following equation is obtained.

$$\int_{t_1}^{t_2}\int_0^L EI\frac{\partial^4 w(x,t)}{\partial x^4}\delta w(x,t)dx\ dt +$$
$$\int_{t_1}^{t_2}\left[EI\frac{\partial^2 w(x,t)}{\partial x^2}\delta\left(\frac{\partial w(x,t)}{\partial x}\right)\Big|_0^L\right]dt +$$
$$\int_{t_1}^{t_2}\int_0^L \frac{\partial^2 Q}{\partial x^2}dx\ dt + \int_{t_1}^{t_2} EQ\ \delta\left(\frac{\partial w(x,t)}{\partial x}\right)\Big|_0^L dt +$$
$$\int_{t_1}^{t_2}\int_0^L \rho A\frac{\partial^2 w(x,t)}{\partial t^2}\delta w(x,t)\ dx\ dt -$$
$$\int_{t_1}^{t_2}\int_0^L \left(F_k\left(\frac{L}{2},t\right) - F_0\left(\frac{L}{2},t\right) - \right.$$
$$\left. F\left(\frac{L}{2},t\right)\sin(\omega t)\right)\delta w(x,t)\ dx\ dt = 0 \qquad (31)$$

where, $Q = \int \varepsilon^{tr}z\ dA$. Therefore, the differential equation of motion for the SMA beam would be presented as follows:

$$EI\frac{\partial^4 w(x,t)}{\partial x^4} + E\frac{\partial^2 Q}{\partial x^2} + \rho A\frac{\partial^2 w(x,t)}{\partial t^2} - F_0\left(\frac{L}{2},t\right) - F\left(\frac{L}{2},t\right)\sin(\omega t) + F_k\left(\frac{L}{2},t\right) = 0 \qquad (32)$$

While the boundary conditions are:

$$w(x,t)_{x=0} = 0$$
$$w(x,t)_{x=L} = 0$$
$$\left[EI\frac{\partial^2 w(x,t)}{\partial x^2} + EQ\right]_{x=0} = 0 \qquad (33)$$
$$\left[EI\frac{\partial^2 w(x,t)}{\partial x^2} + EQ\right]_{x=L} = 0$$

The solution for Equation (32) can be regarded as:

$$w(x,t) = \sum_{i=1}^n \eta_i(t)\ \phi_i(x) \qquad (34)$$

where, $\eta_i(t)$ and $\phi_i(x)$ denote the ith generalized coordinate and shape function, respectively. For this problem, the following form for the shape function is introduced that satisfies the boundary conditions.

$$\phi_i(x) = \sin\left(\frac{i\pi x}{L}\right) \qquad (35)$$

Therefore, the following equation would be achieved.

$$W(X, \tau) = \sum_{i=1}^{n} \eta_i(\tau) \, sin(i\pi X) \qquad (36)$$

Besides, the following non-dimensional parameters are selected.

$$X = \frac{x}{L}, \; W(X, \tau) = \frac{w(x,t)}{L}, Z = \frac{z}{r}, \quad \tau = \omega_0 t, \quad \omega =$$
$$\left(\frac{\pi}{L}\right)^2 \sqrt{\frac{EI}{\rho A}} \qquad (37)$$

In this study, the Galerkin method is used to change the partial differential equation to an ordinary differential equation [60]. In this way, if Equation (36) is substituted into Equation (32), and by applying Equation (37), the following nonlinear differential equation is achieved.

$$\frac{1}{2}\eta_i(\tau)(i\pi)^4 - \frac{4L\pi i^2}{R} \int_0^1 sin(i\pi X) \left(\int \varepsilon^{tr} Z dA \right) dX +$$
$$\frac{1}{2}\ddot{\eta}_i(\tau)(\pi)^4 - \frac{f_0 L^3}{EI} sin\left(\frac{i\pi}{2}\right) - \frac{fL^3}{EI} sin(\tau) sin\left(\frac{i\pi}{2}\right) + \qquad (38)$$
$$\frac{KL^3}{EI} \sum_{j=1}^{n} \eta_j(\tau) sin\left(\frac{j\pi}{2}\right) sin\left(\frac{i\pi}{2}\right) = 0$$

where, ε^{tr} could be computed by using Equation (22). Therefore,

$$\ddot{\eta}_i(\tau) = -\eta_i(\tau)i^4 +$$
$$\frac{8Li^2}{R\pi^3} \int_0^1 sin(i\pi X)(\int \varepsilon^{tr} Z dA) dX + \frac{2f_0 L^3}{EI\pi^4} sin\left(\frac{i\pi}{2}\right) \quad +$$
$$\frac{2fL^3}{EI\pi^4} sin(\tau) sin\left(\frac{i\pi}{2}\right) - \qquad (39)$$
$$\frac{2KL^3}{EI\pi^4} \sum_{j=1}^{n} \eta_j(\tau) sin\left(\frac{j\pi}{2}\right) sin\left(\frac{i\pi}{2}\right)$$

3. SIMULATION RESULTS AND DISCUSSIONS

In this section, the fourth-order Runge–Kutta method is implemented to solve the semi-analytical equation found by the Galerkin approach in section 2 for computing the strain, transformation strain, and stress quantities. Furthermore, the considered SMA beam has length

TABLE 1. Mechanical properties of Nitinol alloy implemented for simulations [44]

Value	Parameter
6450	$\rho \left(\frac{Kg}{m^3}\right)$
0.33	ν
70000	$E \, (MPa)$
0.03	ε_L
253.15	$T_0 \, (°K)$
323.15	$T \, (°K)$
45	$R \, (MPa)$
7.5	$\beta \left(\frac{MPa}{°K}\right)$
500	$h \, (MPa)$

$15 \, mm$ and diameter $1.5 \, mm$. The spring constant is $100 \left[\frac{N}{mm}\right]$, and results are presented for Nitinol alloy having the mechanical properties mentioned in Table 1 [47].

In the following, at first, the static behavior of the SMA beam is studied. Then, the dynamical behaviors of both ordinary and SMA beams are presented to investigate the effects of the SMA on the beam performance.

3. 1. Analysis of the Static Behavior   In order to analyze the static behavior of the beam, it is meshed in two dimensionless directions X and Z (51×15). According to the mesh convergence study performed by the authors, the appropriate meshing steps in both directions were obtained as $\Delta X = 0.02 \, and \, \Delta Z = 0.07$. Figure 3 shows the static behavior of the SMA beam with distribution load $f_0 = -35 \, [N]$ and spring constant $K =$
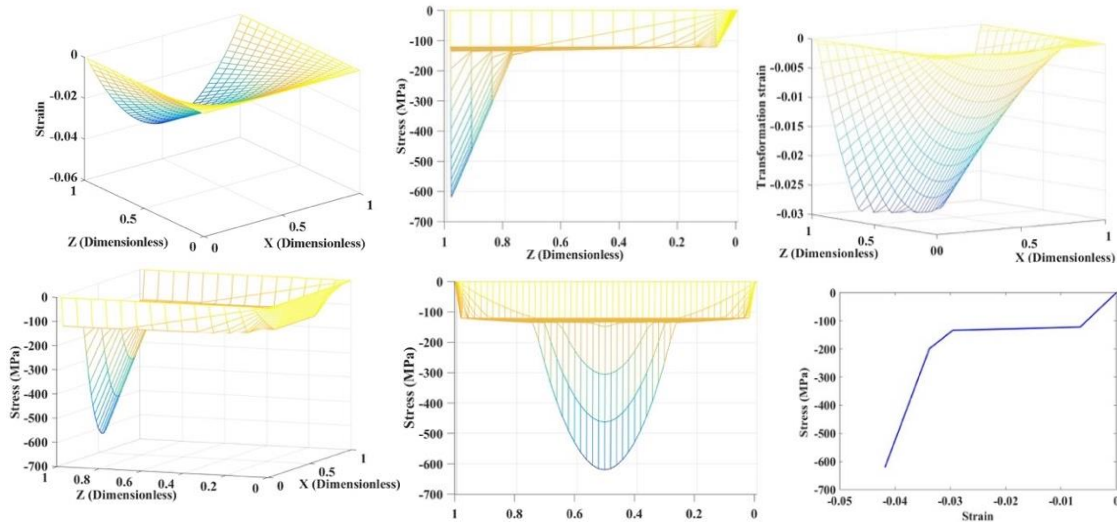
Figure 3. Static behavior of the introduced SMA beam with distribution load $f_0 = -35 \, [N]$ and spring constant $K = 0$.

0. In this figure, contour map of strain, stress, and transformation strain which show all aspects of the beam behavior are being taken into consideration. As it is demonstrated, the stress distribution along direction X is symmetric. Furthermore, in order to valid the found results, Figure 4 illustrates a hysteresis loop appeared in the SMA stress-strain static response by applying variable distribution load $f_0 = -35\sin(i\pi)\,[N]$, $i \in [0,2]$ and spring constant $K = 0$. As it is represented in this figure, the hysteresis loop has the same behavior as Souza's model [47].

3. 2. Analysis of the Dynamic Behavior
3. 2. 1. Free Vibration   The damping property of the regarded structure is analyzed by comparing the vibration response of the SMA beam with an elastic one. Furthermore, this comparison helps to illustrate the effect of energy dissipation mechanism of SMA materials due to their hysteresis property. To this end, the SMA beam is subjected to an initial deflection which undergoes phase transformation within the SMA beam. The amount of this initial deflection is set so that the beam deflection remains on the validity domain of the Euler‑Bernoulli beam theory. Figure 5 depicts the free vibration response of an elastic (non-SMA) beam for $f_0 = -15\,[N]$ and $K = 0$. It can be seen from this figure that there is no decreasing in the vibration amplitude (undamped harmonic response). The steady state response of the results illustrates that the SMA beam vibrates as an elastic member and its frequency is the same as its equivalent elastic beam. This behavior can be explained by the stress/strain variations as shown in Figure 6. Whereas Figure 6 exhibits the free vibration [67, 68] of the SMA beam when the temperature of the beam is $323.15°K$ and the spring has an initial compression force $f_0 = -15\,[N]$. At this temperature, the austenite phase is active, and the initial compression is so high. Therefore, the phase transformation from austenite to martensite would be initially induced within the beam. Hence, the hysteresis loop, depicted in Figure 6(a), makes an intense decreasing for the vibration amplitude. This process continues until the vibration amplitude cannot make any other phase transformation; therefore, the elastic response is activated only for the SMA beam. In this way, the whole beam vibrates elastically with a constant amplitude around steady state deflection $Z = -0.045$. As it is illustrated in Figure 6, the nonlinear behavior of the SMA does not affect the natural frequency of the system, and it remains constant. Indeed, there is only one damping term which is effective and practical for vibration control. In this study, contour map of strain, stress, and transformation strain which show all aspects of the beam behavior are being taken into consideration. In the free vibration study, as shown in Figure 6, an adequate initial condition was imposed onto the system

to make it undergo phase transformation over the beam. The strain contour map and longitudinal distribution of strain in each layer of the cross section are depicted in Figure 6 for early oscillations when SMA beam is fully deflected.

The corresponding loss factor could be calculated by employing the following logarithmic relation.

$$\varsigma = \frac{1}{2\pi r}\ln\left(\frac{A_i}{A_{i+r}}\right) \tag{40}$$

where, A_i and A_{i+r} are vibration amplitudes ith and $(i + r)$th, respectively. In order to investigate the effect of the shape memory alloy on the vibrating behavior of the beam, the time responses of the dissipated energy for the SMA beam are generated in Figure 7. It can be seen from this figure that the total dissipated energy reduces over time until the zero value is attained.

These observations could be verified through the results presented in Figure 6. Indeed, the diagrams in Figure 6 clearly depict that the oscillation amplitude and the total energy of the system decrease via the generated hysteresis loops. The vibration amplitude of the beam becomes constant in the steady state condition, as shown in Figure 6. Figure 7 depicts the dissipated energy of the SMA beam with respect to time for the free vibrations.
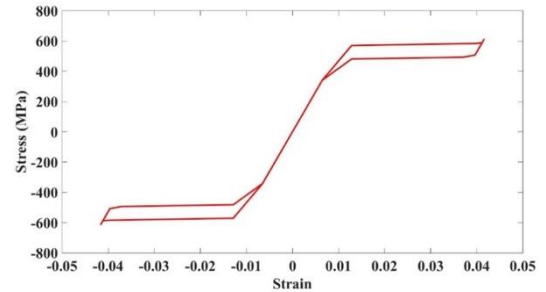
Figure 4. Stress-strain diagram to study the static behavior of the SMA beam with variable distribution load $f_0 = -35\sin(i\pi)\,[N]$, $i \in [0,2]$ and spring constant $K = 0$
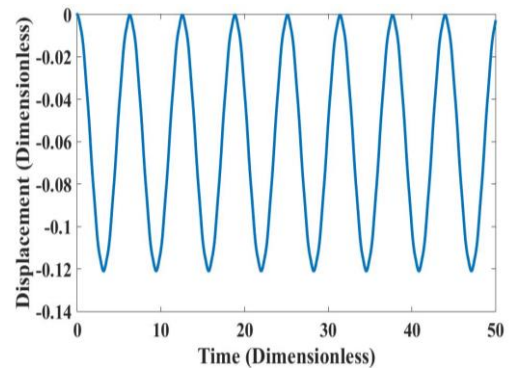
Figure 5. Free vibration of the midpoint of an ordinary beam with initial compression force $f_0 = -15\,[N]$ and spring constant $K = 0$
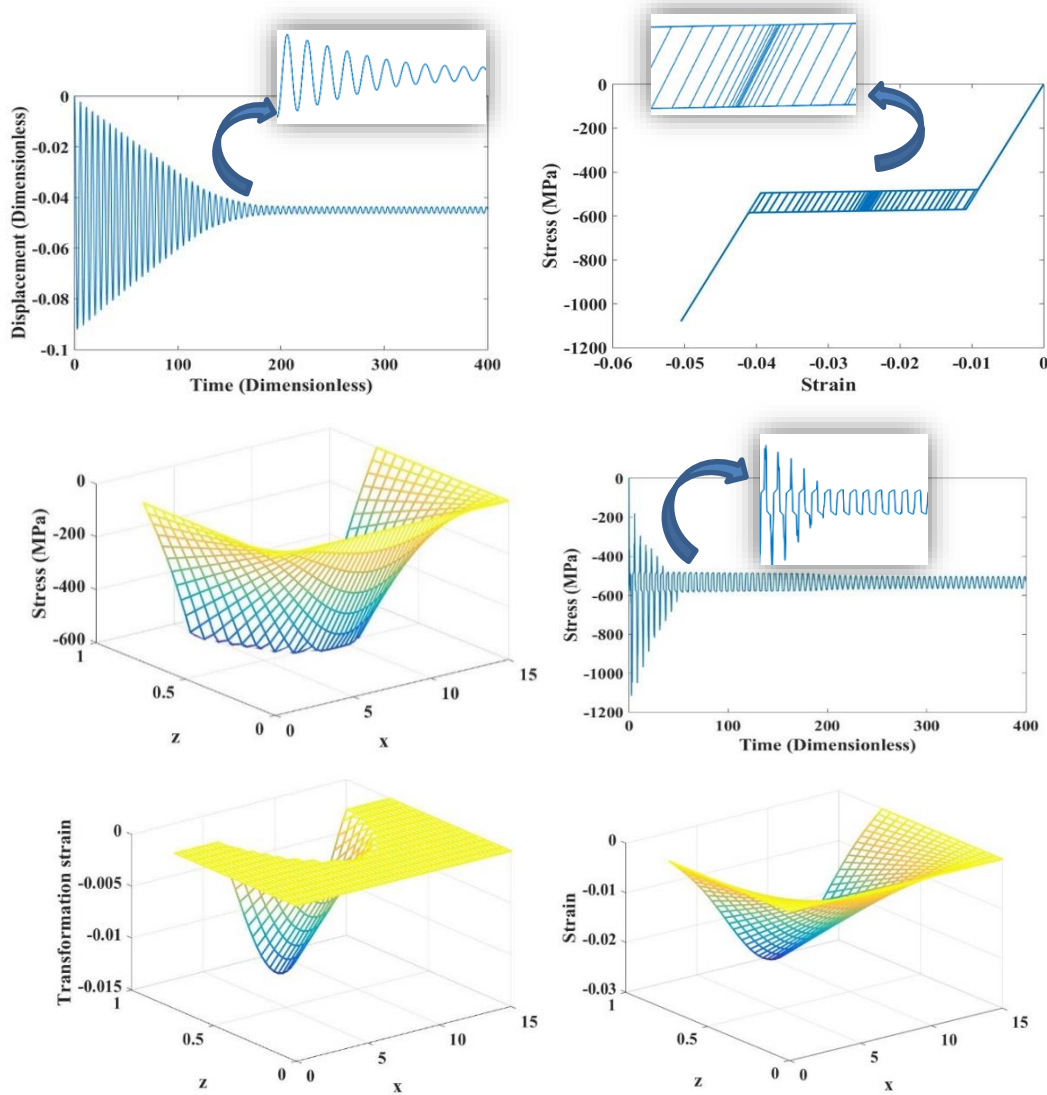
Figure 6. Dynamical behavior of the proposed SMA beam for free vibration with compression force $f_0 = -15 \, [N]$ spring constant and $K = [100 \, ^N/_{mm}]$
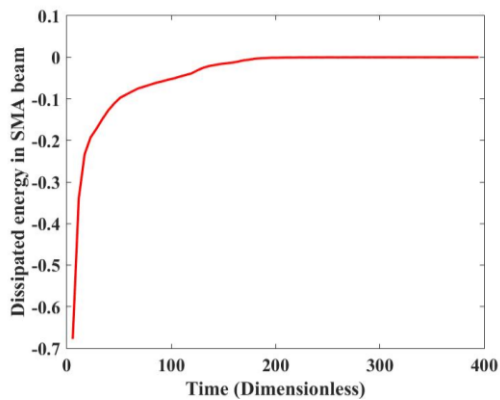
Figure 7. Dissipated energy related to the SMA beam versus time for free vibration.

Moreover, the phase plane diagram for the free vibration of the midpoint is plotted in Figure 8. This figure displays the pseudo elastic behavior of the SMA beam at the beginning of the vibration, whereas the elastic behavior can be seen at the end of the vibration.

3. 2. 2. Forced Vibration   In this sub-section, the forced vibration behavior of the proposed SMA beam with excitation force $F = -15 \sin\left(\frac{3\omega_0}{4}t\right) [N]$ and spring constant $K = 100[^N/_{mm}]$ is investigated. The stress-strain diagram demonstrated in Figure 9(a) indicates the hysteretic behavior of the SMA with inner loops. The time history of the displacement and stress of the midpoint are illustrated in Figures 9(b) and 9(c),

respectively. Finally, Figure 9(d) shows the amount of the dissipated energy in the SMA beam versus time for the forced vibration. From Figures 9(b) and (d), it could be realized that the area of the dissipated energy reduces and consequently, the reduction rate of the vibration amplitude decreases too. With continuing vibration, the beam will oscillate with a constant amplitude. In other words, according to the hysteresis phenomenon of the SMA, the amplitude initially tends to decrease as well as

approach to the elastic situations and after that, indicate a constant response.

3. 3. Parametric Analysis   Here, the vibrational behavior of the SMA beam is analyzed to evaluate the influence of system parameters such as the spring constant, excitation force magnitude and excitation force frequency on the displacement and stress of the midpoint.
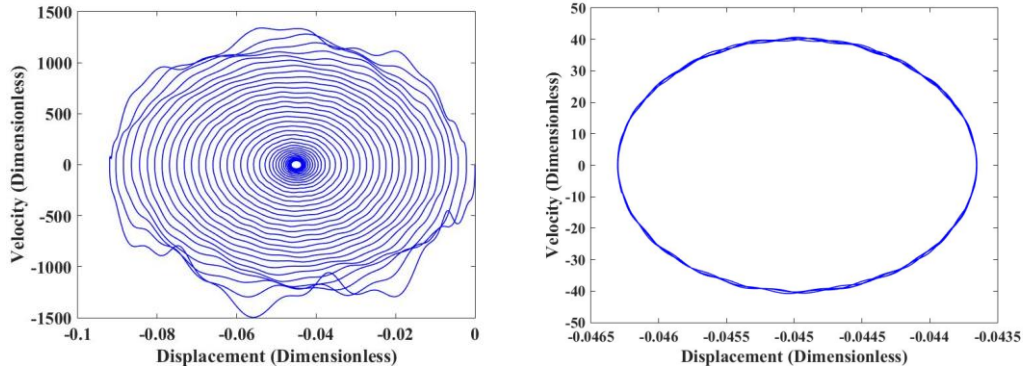
Figure 8. Phase plane diagrams corresponding to free vibration of the midpoint of the beam for $f_0 = -15(N)$: (a) $\tau = 1:400$, (b) $\tau = 380:400$

(a)

(b)

(c)

(d)
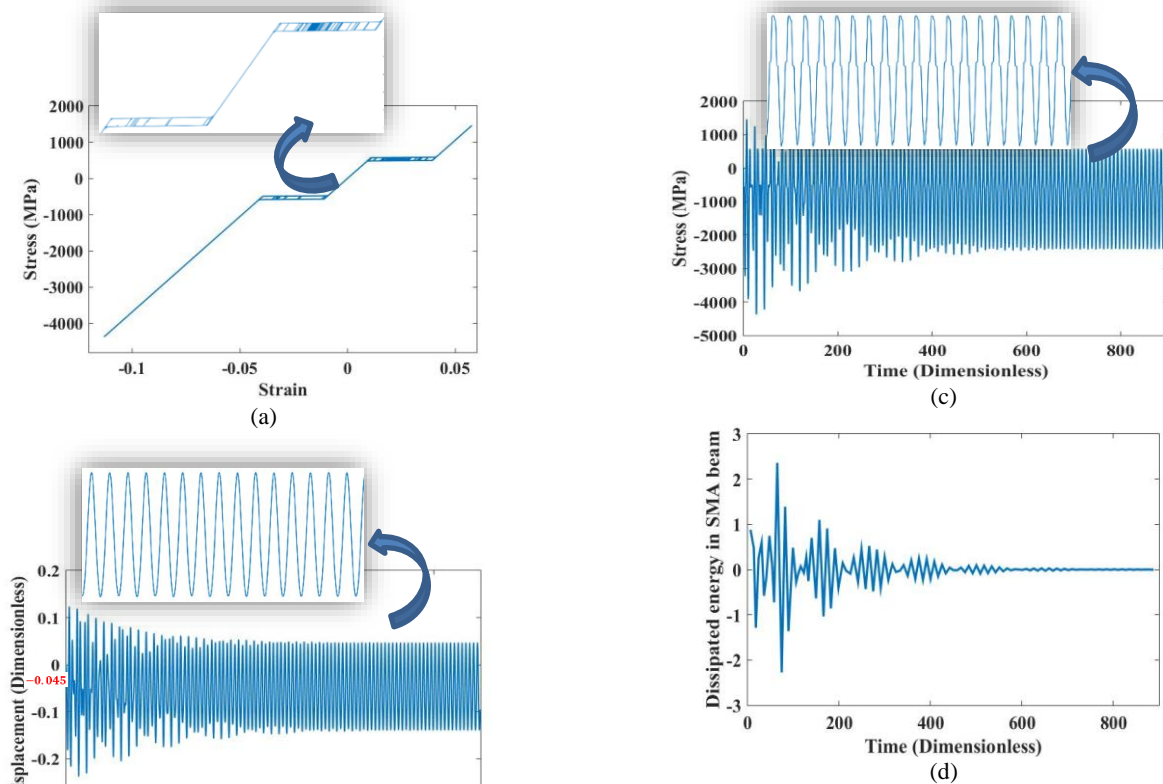
Figure 9. Dynamical behavior of the regarded SMA beam for forced vibration with excitation force $F = -15\sin\left(\frac{3\omega_0}{4}t\right)[N]$ and spring constant $K = 100[{}^{N}/_{mm}]$

In this way, the results in Figure 11 show that by increasing the value of spring constant K, the vibration amplitude and the stress at the midpoint are reduced, while the frequency of the vibration is increased. Therefore, it can be realized that the spring constant has a great effect on the vibration response of the beam. Moreover, Figure 12 exhibits the results of the forced vibration at the midpoint of the SMA beam with different values of the excitation force frequency. Figures 13 and 14 depict the variations of the oscillation amplitude when the excitation force has different values of magnitude and frequency, respectively. As it is understood from Figure 13, by increasing the magnitude of the excitation force, the oscillation amplitude would be increased, too. Besides, it can be observed from Figure 14 when the frequency of the excitation force coincides with the natural frequency ($\omega = \omega_0 = 0.1587$), the oscillation amplitude reaches its maximum value.

Figure 15 presents the energy dissipation rate of the SMA beam for frequency range [0-0.5]. As it is seen from this figure, although the energy dissipation is effective at all frequencies, it is more significant at low frequencies. Indeed, the SMA is potentially a sluggish element and very effective at low frequencies, therefore, it would display a great impact on the energy dissipation at these circumstances. However, it is ideal to have such dominant frequencies, as it can be easily tuned for any system. This frequency could coincide with the natural frequency of the system and prevent from the resonance phenomenon.

Figure 13. Variations of the oscillation amplitude versus different values of the excitation force magnitude
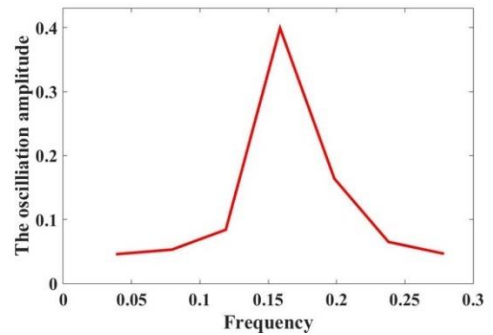
Figure 14. Variations of the oscillation amplitude versus different values of the excitation force frequency
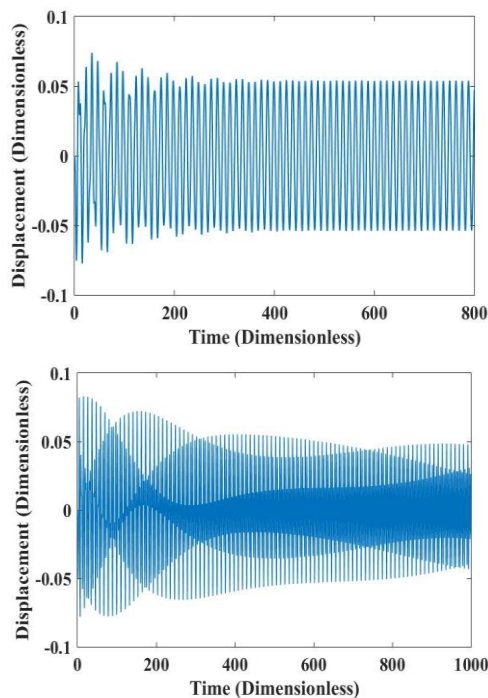

Figure 12. Time responses of the midpoint for different values of the excitation force frequency
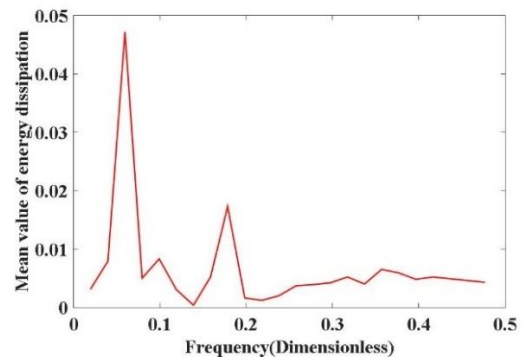
Figure 15. Broad band damping of the SMA beam with the loading condition

In the following, the Discrete Fourier Transformation (DFT) is applied to transform the time domain signal to its representation in the frequency domain. To determine the vibration frequency through the simulation results, the Fast Fourier Transformation (FFT) is implemented to provide the fast computation of the DFT [69]. In this regard, Figure 16 shows the last fourth of the period, regarding the DFT versus the frequency, for the forced vibration in $\omega = \frac{3\omega_0}{4}$Hz. As it can be observed from this diagram, only one frequency component could be

identified, which is about $\omega = 0.119$ Hz. Since this is the oscillation frequency of the SMA beam under the forced vibration, the shape memory alloy has no effect on the frequency of the system.

In Table 2, a comparison is made between the frequencies produced by the FFT and those of the excitation force. As it is observed from these results, the two types of frequencies match well, and the shape memory alloy of the beam has no effect on the frequency of the system.
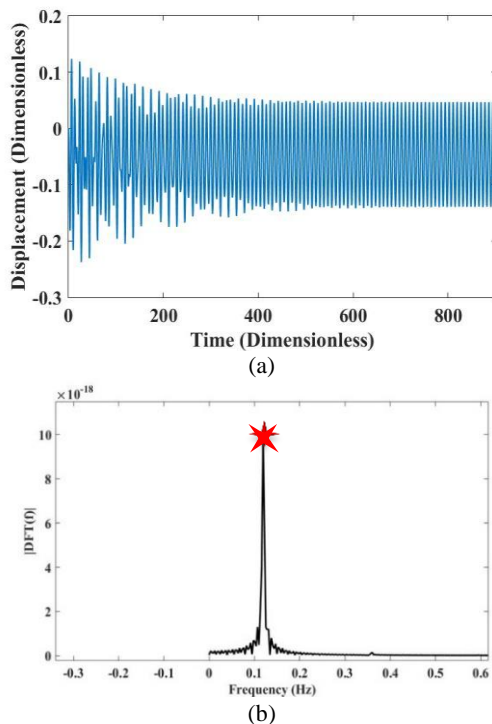
Figure 16. Simulation results of the SMA beam for forced vibration with $\omega = \frac{3\omega_0}{4}$: (a) time history of the midpoint displacement. (b) Last fourth of the period for the discrete Fourier transformation versus frequency

TABLE 2. Comparisons of the frequencies produced by the FFT and those of the excitation force.

Excitation force frequency	Frequency from FFT	Oscillation amplitude
$\omega = {\omega_0}/{4}$	0.039	0.046
$\omega = {\omega_0}/{2}$	0.079	0.053
$\omega = {3\omega_0}/{4}$	0.119	0.084
$\omega = \omega_0$	0.158	0.399
$\omega = {5\omega_0}/{4}$	0.198	0.164
$\omega = {3\omega_0}/{2}$	0.238	0.065
$\omega = {7\omega_0}/{4}$	0.277	0.047

4. CONCLUSIONS

In this article, the free and forced vibrations of a bending shape memory alloy beam having nonlinear hysteresis, were analyzed regarding the effect of the pseudo-elastic behavior. The three-dimensional constitutive equation of Souza's model was used to simulate the hysteric behavior of the SMA beam.

The time responses and states of strain, transformation strain and stress-strain for the SMA beam were investigated. To shed light on the influences of the SMA on the vibrations, the time histories of the displacement and the stress at midpoint of the beam as well as velocity-displacement and stress- strain diagrams were studied. Moreover, the average of the total dissipated energy was studied for the FFT frequency during the time. The effects of parameters such as the spring constant, excitation force magnitude and excitation force frequency on the displacement and stress of the midpoint were discussed in details. Pursuant to the numerical results, some conclusions could be mentioned as follows.

- The SMA beam exhibits highly nonlinear dynamical behavior.
- The pseudo-elastic behavior of the SMA is a hysteretic energy-dissipation behavior, which causes drastic decreasing in the vibration amplitude of the beam.
- The FFT and excitation force frequencies reveal that the pseudo-elastic behavior of the SMA does not have any effect on the frequency of the system.
- The broad response of the SMA beam due to varying the hysteretic damping with the loading condition displays that it has a great effect on the energy dissipation at low frequencies and could be employed as an effective absorber for slow motion applications.
- The energy absorbing behavior of the SMA beam makes it suitable for suspension systems, or vibrating structures.

5. REFERENCES

1. Kabla, M., Ben-David, E. and Shilo, D., "A novel shape memory alloy microactuator for large in-plane strokes and forces", *Smart Materials and Structures*, Vol. 25, No. 7, (2016). doi: 10.1088/0964-1726/25/7/075020.

2. Barzegari, M.M., Dardel, M., Fathi, A. and Ghadimi, M., "Aeroelastic characteristics of cantilever wing with embedded shape memory alloys", *Acta Astronautica*, Vol. 79, (2012), 189-202. doi: 10.1016/j.actaastro.2012.04.023.

3. Pittaccio, S., Garavaglia, L., Ceriotti, C. and Passaretti, F., "Applications of shape memory alloys for neurology and neuromuscular rehabilitation", *Journal of Functional Biomaterials*, Vol. 6, No. 2, (2015), 328-344. doi: 10.3390/jfb6020328.

4. Sohn, J., Han, Y., Choi, S., Lee, Y. and Han, M., "Vibration and position tracking control of a flexible beam using sma wire

actuators", *Journal of Vibration and Control*, Vol. 15, No. 2, (2009), 263-281. doi: 10.1177/1077546308094251.

5. She, Y., Chen, J., Shi, H. and Su, H.-J., "Modeling and validation of a novel bending actuator for soft robotics applications", *Soft Robotics*, Vol. 3, No. 2, (2016), 71-81. doi: 10.1089/soro.2015.0022.

6. Bellini, A., Colli, M. and Dragoni, E., "Mechatronic design of a shape memory alloy actuator for automotive tumble flaps: A case study", *IEEE Transactions on Industrial Electronics*, Vol. 56, No. 7, (2009), 2644-2656. doi: 10.1109/TIE.2009.2019773.

7. Burugupally, S.P., Koppolu, B., Danesh, N., Lee, Y., Indeewari, V. and Li, B., "Enhancing the performance of dielectric elastomer actuators through the approach of distributed electrode array with fractal interconnects architecture", *Journal of Micromechanics and Microengineering*, Vol. 31, No. 6, (2021), 064002. doi: 10.1088/1361-6439/abf632.

8. Kang, Z. and James, K.A., "Multiphysics design of programmable shape-memory alloy-based smart structures via topology optimization", *Structural and Multidisciplinary Optimization*, Vol. 65, No. 1, (2022), 24. doi: 10.1007/s00158-021-03101-z.

9. Ozturk, B., Cetin, H., Dutkiewicz, M., Aydin, E. and Noroozinejad Farsangi, E., "On the efficacy of a novel optimized tuned mass damper for minimizing dynamic responses of cantilever beams", *Applied Sciences*, Vol. 12, No. 15, (2022), 7878. doi: 10.3390/app12157878.

10. Aydin, E., Öztürk, B. and Dutkiewicz, M., "Analysis of efficiency of passive dampers in multistorey buildings", *Journal of Sound and Vibration*, Vol. 439, (2019), 17-28. doi: 10.1016/j.jsv.2018.09.031.

11. Aydin, E., Dutkiewicz, M., Öztürk, B. and Sonmez, M., "Optimization of elastic spring supports for cantilever beams", *Structural and Multidisciplinary Optimization*, Vol. 62, (2020), 55-81. doi: 10.1007/s00158-019-02469-3.

12. Coşkun, S.B., Atay, M.T. and Öztürk, B., "Transverse vibration analysis of euler-bernoulli beams using analytical approximate techniques", *Advances in Vibration Analysis Research*, Vol. 1, (2011), 22. doi: 10.5772/15891.

13. Rogers, C.A., "Active vibration and structural acoustic control of shape memory alloy hybrid composites: Experimental results", *The Journal of the Acoustical Society of America*, Vol. 88, No. 6, (1990), 2803-2811. doi: 10919/52280.

14. Peyroux, R., Chrysochoos, A., Licht, C. and Löbel, M., "Thermomechanical couplings and pseudoelasticity of shape memory alloys", *International Journal of Engineering Science*, Vol. 36, No. 4, (1998), 489-509. doi: doi:10.1016/S0020-7225(97)00052-9.

15. Grabe, C. and Bruhns, O.T., "On the viscous and strain rate dependent behavior of polycrystalline niti", *International Journal of Solids and Structures*, Vol. 45, No. 7-8, (2008), 1876-1895. doi: 10.1016/j.ijsolstr.2007.10.029.

16. Müller, C. and Bruhns, O., "A thermodynamic finite-strain model for pseudoelastic shape memory alloys", *International Journal of Plasticity*, Vol. 22, No. 9, (2006), 1658-1682. doi: 10.1016/j.ijplas.2006.02.010.

17. Christ, D. and Reese, S., "A finite element model for shape memory alloys considering thermomechanical couplings at large strains", *International Journal of Solids and Structures*, Vol. 46, No. 20, (2009), 3694-3709. doi: 10.1016/j.ijsolstr.2009.06.017.

18. Andani, M.T. and Elahinia, M., "A rate dependent tension–torsion constitutive model for superelastic nitinol under non-proportional loading; a departure from von mises equivalency", *Smart Materials and Structures*, Vol. 23, No. 1, (2013), 015012. doi: 10.1088/0964-1726/23/1/015012.

19. Chatziathanasiou, D., Chemisky, Y., Chatzigeorgiou, G. and Meraghni, F., "Modeling of coupled phase transformation and reorientation in shape memory alloys under non-proportional thermomechanical loading", *International Journal of Plasticity*, Vol. 82, (2016), 192-224. doi: 10.1016/j.ijplas.2016.03.005.

20. Jani, J.M., Leary, M., Subic, A. and Gibson, M.A., "A review of shape memory alloy research, applications and opportunities", *Materials & Design (1980-2015)*, Vol. 56, (2014), 1078-1113. doi: 10.1016/j.matdes.2013.11.084.

21. Chemisky, Y., Chatzigeorgiou, G., Kumar, P. and Lagoudas, D.C., "A constitutive model for cyclic actuation of high-temperature shape memory alloys", *Mechanics of materials*, Vol. 68, (2014), 120-136. doi: 10.1016/j.mechmat.2013.07.020.

22. Plietsch, R., Bourauel, C., Drescher, D. and Nellen, B., "Analytical description of the bending behaviour of niti shape-memory alloys", *Journal of Materials Science*, Vol. 29, No. 22, (1994), 5892-5902. doi: 10.1007/BF00366873.

23. Auricchio, F. and Sacco, E., "A one-dimensional model for superelastic shape-memory alloys with different elastic properties between austenite and martensite", *International Journal of Non-Linear Mechanics*, Vol. 32, No. 6, (1997), 1101-1114. doi: 10.1016/S0020-7462(96)00130-8.

24. Rajagopal, K.R. and Srinivasa, A.R., "On the bending of shape memory wires", *Mechanics of Advanced Materials and Structures*, Vol. 12, No. 5, (2005), 319-330. doi: 10.1080/15376490590953581.

25. Eshghinejad, A. and Elahinia, M., "Exact solution for bending of shape memory alloy superelastic beams", in ASME conference proceedings. Vol. 54723, (2011), 345-352.

26. Rizzoni, R., Merlin, M. and Casari, D., "Shape recovery behaviour of niti strips in bending: Experiments and modelling", *Continuum Mechanics and Thermodynamics*, (2013), 1-21. doi: 10.1007/s00161-012-0242-0.

27. Mirzaeifar, R., DesRoches, R., Yavari, A. and Gall, K., "On superelastic bending of shape memory alloy beams", *International Journal of Solids and Structures*, Vol. 50, No. 10, (2013), 1664-1680. doi: 10.1016/j.ijsolstr.2013.01.035.

28. Ostadrahimi, A., Arghavani, J. and Poorasadion, S., "An analytical study on the bending of prismatic sma beams", *Smart Materials and Structures*, Vol. 24, No. 12, (2015), 125035. doi: 10.1088/0964-1726/24/12/125035.

29. Atanacković, T. and Achenbach, M., "Moment-curvature relations for a pseudoelastic beam", *Continuum Mechanics and Thermodynamics*, Vol. 1, No. 1, (1989), 73-80. doi: 10.1007/BF01125887.

30. Liu, M.X., J. Li, Q. , "Design and experiment of piezoelectric-shape memory alloy composite shock absorber", *Materials Letters*, Vol. 304, (2021). doi: 10.1016/j.matlet.2021.130538.

31. Sattari, M.K., M. Akbarzadeh, S. Gholami, R. Beheshti, A. , "Wear in superelastic shape memory alloys: A thermomechanical analysis", *Wear* (2022), 488-489. doi: 10.1016/j.wear.2021.204139.

32. De la Flor, S., Urbina, C. and Ferrando, F., "Asymmetrical bending model for niti shape memory wires: Numerical simulations and experimental analysis", *Strain*, Vol. 47, No. 3, (2011), 255-267. doi: 10.1111/j.1475-1305.2009.00679.x.

33. Hartl, D., Lagoudas, D., Calkins, F. and Mabe, J., "Use of a ni60ti shape memory alloy for active jet engine chevron application: I. Thermomechanical characterization", *Smart Materials and Structures*, Vol. 19, No. 1, (2009), 015020. doi: 10.1088/0964-1726/19/1/015021.

34. Hartl, D., Mooney, J., Lagoudas, D., Calkins, F. and Mabe, J., "Use of a ni60ti shape memory alloy for active jet engine chevron application: Ii. Experimentally validated numerical analysis", *Smart Materials and Structures*, Vol. 19, No. 1, (2009), 015021. doi: 10.1088/0964-1726/19/1/015021.

35. Razavilar, R., Fathi, A., Dardel, M. and Arghavani Hadi, J., "Dynamic analysis of a shape memory alloy beam with pseudoelastic behavior", *Journal of Intelligent Material Systems and Structures*, Vol. 29, No. 9, (2018), 1835-1849. doi: 10.1177/1045389X17754268.

36. Hashemi, S. and Khadem, S., "Modeling and analysis of the vibration behavior of a shape memory alloy beam", *International Journal of Mechanical Sciences*, Vol. 48, No. 1, (2006), 44-52. doi: 10.1016/j.ijmecsci.2005.09.011.

37. Jose, S., Chakraborty, G. and Bhattacharyya, R., "Coupled thermo-mechanical analysis of a vibration isolator made of shape memory alloy", *International Journal of Solids and Structures*, Vol. 115, (2017), 87-103. doi: 10.1016/j.ijsolstr.2017.03.001.

38. Pan, Q. and Cho, C., "The investigation of a shape memory alloy micro-damper for mems applications", *Sensors*, Vol. 7, No. 9, (2007), 1887-1900. doi: 10.3390/s7091887.

39. Damanpack, A., Bodaghi, M., Aghdam, M. and Shakeri, M., "On the vibration control capability of shape memory alloy composite beams", *Composite Structures*, Vol. 110, No., (2014), 325-334. doi: 10.1016/j.compstruct.2013.12.002.

40. Panico, M. and Brinson, L., "A three-dimensional phenomenological model for martensite reorientation in shape memory alloys", *Journal of the Mechanics and Physics of Solids*, Vol. 55, No. 11, (2007), 2491-2511. doi: 10.1016/j.jmps.2007.03.010.

41. Brinson, L., Huang, M., Boller, C. and Brand, W., "Analysis of controlled beam deflections using sma wires", *Journal of Intelligent Material Systems and Structures*, Vol. 8, No. 1, (1997), 12-25. doi: 10.1177/1045389X9700800103.

42. Moallem, M., "Deflection control of a flexible beam using shape memory alloy actuators", *Smart Materials and Structures*, Vol. 12, No. 6, (2003), 1023. doi: 10.1088/0964-1726/12/6/022.

43. Sayyaadi, H. and Zakerzadeh, M., "Nonlinear analysis of a flexible beam actuated by a couple of active sma wire actuators", *International Journal of Engineering, Transactions A: Basics*, Vol. 25, No. 3, (2012), 249-264. doi: 10.5829/idosi.ije.2012.25.03a.07.

44. Andrade, B.H., Silva, D.D., Brito, I.C., Caluête, R.E., Sousa, A.R., Gomes, R.M. and Oliveira, D.F., "Influence of strain rate on mechanical properties of a cualmntib shape memory alloy", *Journal of Materials Research and Technology*, Vol. 16, No., (2022), 1667-1672. doi: 10.1016/j.jmrt.2021.12.100.

45. Billah, A.M., Rahman, J. and Zhang, Q., "Shape memory alloys (smas) for resilient bridges: A state-of-the-art review", in Structures, Elsevier. Vol. 37, (2022), 514-527.

46. Bellini, C., Berto, F., Di Cocco, V. and Iacoviello, F., "A cyclic integrated microstructural-mechanical model for a shape memory alloy", *International Journal of Fatigue*, Vol. 153, (2021), 106473. doi: 10.1016/j.ijfatigue.2021.106473.

47. Souza, A.C., Mamiya, E.N. and Zouain, N., "Three-dimensional model for solids undergoing stress-induced phase transformations", *European Journal of Mechanics-A/Solids*, Vol. 17, No. 5, (1998), 789-806. doi: 10.1016/S0997-7538(98)80005-3.

48. Paik, J.K., Hawkes, E. and Wood, R.J., "A novel low-profile shape memory alloy torsional actuator", *Smart Materials and Structures*, Vol. 19, No. 12, (2010), 125014. doi: 10.1088/0964-1726/19/12/125014.

49. Chung, J.-H., Heo, J.-S. and Lee, J.-J., "Modeling and numerical simulation of the pseudoelastic behavior of shape memory alloy circular rods under tension–torsion combined loading", *Smart Materials and Structures*, Vol. 15, No. 6, (2006), 1651. doi: 10.1088/0964-1726/15/6/018.

50. Viet, N. and Zaki, W., "Analytical investigation of the behavior of concrete beams reinforced with multiple circular superelastic shape memory alloy bars", *Composite Structures*, Vol. 210, (2019), 958-970. doi: 10.1016/j.compstruct.2018.11.080.

51. Viet, N. and Zaki, W., "Bending model for functionally graded porous shape memory alloy/poroelastic composite cantilever beams", *Applied Mathematical Modelling*, Vol. 97, (2021), 398-417. doi: 10.1016/j.apm.2021.03.058.

52. Auricchio, F., Taylor, R.L. and Lubliner, J., "Shape-memory alloys: Macromodelling and numerical simulations of the superelastic behavior", *Computer methods in applied mechanics and engineering*, Vol. 146, No. 3-4, (1997), 281-312. doi: 10.1016/S0045-7825(96)01232-7.

53. Sun, Q.P. and Hwang, K.C., "Micromechanics modelling for the constitutive behavior of polycrystalline shape memory alloys—i. Derivation of general relations", *Journal of the Mechanics and Physics of Solids*, Vol. 41, No. 1, (1993), 1-17. doi: 10.1016/0022-5096(93)90060-S.

54. Auricchio, F., Bonetti, E., Scalet, G. and Ubertini, F., "Theoretical and numerical modeling of shape memory alloys accounting for multiple phase transformations and martensite reorientation", *International Journal of Plasticity*, Vol. 59, (2014), 30-54. doi: 10.1016/j.ijplas.2014.03.008.

55. Arghavani, J., Auricchio, F. and Naghdabadi, R., "A finite strain kinematic hardening constitutive model based on hencky strain: General framework, solution algorithm and application to shape memory alloys", *International Journal of Plasticity*, Vol. 27, No. 6, (2011), 940-961. doi: 10.1016/j.ijplas.2010.10.006.

56. Gao, X., Huang, M. and Brinson, L.C., "A multivariant micromechanical model for smas part 1. Crystallographic issues for single crystal model", *International Journal of Plasticity*, Vol. 16, No. 10, (2000), 1345-1369. doi: 10.1016/S0749-6419(00)00013-9.

57. Patoor, E., Lagoudas, D.C., Entchev, P.B., Brinson, L.C. and Gao, X., "Shape memory alloys, part i: General properties and modeling of single crystals", *Mechanics of Materials*, Vol. 38, No. 5, (2006), 391-429. doi: 10.1016/j.mechmat.2005.05.027.

58. Lagoudas, D.C., Entchev, P.B., Popov, P., Patoor, E., Brinson, L.C. and Gao, X., "Shape memory alloys, part ii: Modeling of polycrystals", *Mechanics of Materials*, Vol. 38, No. 5, (2006), 430-462. doi: 10.1016/j.mechmat.2005.08.003.

59. Boyd, J.G. and Lagoudas, D.C., "Thermomechanical response of shape memory composites", *Journal of Intelligent Material Systems and Structures*, Vol. 5, No. 3, (1994), 333-346. doi: 10.1177/1045389X9400500306.

60. Tanaka, K. and Nagaki, S., "A thermomechanical description of materials with internal variables in the process of phase transitions", *Archive of Applied Mechanics*, Vol. 51, No. 5, (1982), 287-299. doi: 10.1007/BF00536655.

61. Liang, C. and Rogers, C.A., "One-dimensional thermomechanical constitutive relations for shape memory materials", *Journal of Intelligent Material Systems and Structures*, Vol. 8, No. 4, (1997), 285-302. doi: 10.1177/1045389X9000100205.

62. Brinson, L.C., "One-dimensional constitutive behavior of shape memory alloys: Thermomechanical derivation with non-constant material functions and redefined martensite internal variable", *Journal of Intelligent Material Systems and Structures*, Vol. 4, No. 2, (1993), 229-242. doi: 10.1177/1045389X9300400213.

63. Ivshin, Y. and Pence, T.J., "A thermomechanical model for a one variant shape memory material", *Journal of Intelligent Material Systems and Structures*, Vol. 5, No. 4, (1994), 455-473. doi: 10.1177/1045389X9400500402.

64. Ivshin, Y. and Pence, T.J., "A constitutive model for hysteretic phase transition behavior", *International Journal of Engineering Science*, Vol. 32, No. 4, (1994), 681-704. doi: 10.1016/0020-7225(94)90027-2.

65. Simo, J. and Taylor, R., "A return mapping algorithm for plane stress elastoplasticity", *International Journal for Numerical*

Methods in Engineering, Vol. 22, No. 3, (1986), 649-670. doi: 10.1002/nme.1620220310.

66. Bertram, A., "Thermo-mechanical constitutive equations for the description of shape memory effects in alloys", *Nuclear Engineering and Design*, Vol. 74, No. 2, (1983), 173-182. doi: 10.1016/0029-5493(83)90054-7.

67. Leclercq, S., Bourbon, G. and Lexcellent, C., "Plasticity like model of martensite phase transition in shape memory alloys", *Le*

Journal de Physique IV, Vol. 5, No. C2, (1995), C2-513-C512-518. doi: 10.1051/jp4:1995279.

68. Courant, R. and Hilbert, D., "Methods of mathematical physics: Partial differential equations, John Wiley & Sons, (2008).

69. Brigham, E.O. and Morrow, R., "The fast fourier transform", *IEEE Spectrum*, Vol. 4, No. 12, (1967), 63-70. doi: 10.1109/MSPEC.1967.5217220.
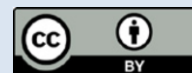
Persian Abstract

چکیده

هدف از این تحقیق معرفی یک رویکرد نیمه تحلیلی برای تحلیل ارتعاشات غیرخطی آزاد و اجباری تیر آلیاژ حافظه دار خمشی (SMA) با در نظر گرفتن تأثیر رفتار شبه الاستیک آن است. به منظور ایجاد یک انحراف اولیه، یک کرنش پیش مناسب با استفاده از فنر فشاری به تیر SMA اعمال می شود. یک مدل ماده جدید برای شبیه‌سازی رفتار هیستریک غیرخطی تیر SMA استفاده می‌شود، در حالی که معادلات دیفرانسیل حرکت تیر بر اساس نظریه تیر اویلر–برنولی و اصل همیلتون نوشته شده‌اند. معادلات دیفرانسیل جزئی غیرخطی استخراج شده با استفاده از روش گالرکین و به صورت نیمه تحلیلی حل می‌شوند. رفتار شبه الاستیک و اتلاف انرژی تیر SMA در وضعیت‌های ارتعاش غیرخطی آزاد و اجباری مورد مطالعه قرار می‌گیرد. در نهایت، تأثیر پارامترهای سیستم مانند ثابت فنر، دامنه و فرکانس نیروی تحریک بر راندمان جاذب بررسی شده و پایداری آن مورد بررسی قرار می‌گیرد. نتایج عددی نشان می‌دهد که تیر SMA رفتار دینامیکی بسیار غیرخطی از خود نشان می‌دهد و می‌تواند به عنوان یک محرک برای میرایی انرژی استفاده شود.

Effect of Combined Different Sources of Alumina Silicate on Mechanical Properties and Carbonation Depth of Environmentally Friendly Geopolymeric Composite Based on Metakaolin

A. Esparham*, N. Mehrdadi

Department of Environmental Engineering, University of Tehran, Tehran, Iran

A B S T R A C T

Today, concrete is the most widely used building material. Cement production releases about 7% of carbon dioxide gas into the atmosphere and increases greenhouse gases, so it seems necessary to use an alternative to Portland cement. In recent years, geopolymers (mineral polymers) have been proposed as a new environmentally friendly cement. Metakaolin, bentonite, zeolite, iron blast furnace slag and fly ash can be mentioned as aluminosilicate sources. In the field of geopolymer concrete construction, few articles have been working on the composition and effect of replacing aluminosilicate sources. In this experimental study, the effect of replacing slag aluminosilicate sources, class F fly ash and bentonite with proportions of 5-45% with metakaolin on the mechanical properties and durability of geopolymer concrete based on metakaolin was investigated. After making the samples, compressive, bending, tensile and carbonation tests were performed on the geopolymer concrete samples to obtain the optimal strength and carbonation depth of the samples. Also, to determine the validity of the tests, machine learning estimation analysis was performed on the samples. The findings showed that bentonite leads to a decrease in strength, while fly ash and slag lead to an increase in strength. The predicted R^2 values showed the highest matching of the correlation matrix (more than 93%) for the pressure samples. In addition, the results of the tests showed that the metakaolin-based geopolymer concrete sample replaced with fly ash (35%) had a lower penetration depth (carbonation) and higher mechanical properties than other samples.

doi: 10.5829/ije.2023.36.07a.18

1. INTRODUCTION

The World Environment Commission has defined the concept of sustainable development as the ability to meet our current needs without compromising the ability of future generations to meet their needs. This definition requires us to consider all aspects of a particular industry through raw material supply, energy consumption and reuse or recycling. As the main component of ordinary concrete, Portland cement is the most widely used cement material in the construction industry [1, 2]. But the production of Portland cement has major environmental disadvantages, including: high energy consumption, consumption of primary resources, and carbon dioxide emissions [3, 4]. So that the production of

one ton of Portland cement causes the release of approximately one ton of carbon dioxide into the environment and the consumption of 1.5 tons of raw materials [5-8]. On the other hand, pollution and global warming have become the most important concerns of developed countries [1]. The main cause of the global warming phenomenon is the emission of greenhouse gases, and carbon dioxide plays the biggest role in the global warming phenomenon [9]. In the process of producing each ton of Portland cement, on average, 125 liters of fossil fuel and 118 kilowatt hours of electricity are consumed, and polluting gases enter the environment due to the burning of fuel oil and electricity consumed in cement factories [10]. In recent years, in order to produce environmentally friendly building materials,

Corresponding Author Email: alireza.esparham@ut.ac.ir
(A. Esparham)

geopolymers have been proposed as a green cement element and a suitable alternative to Portland cement all over the world. Geopolymer was first introduced in the late 1970s by Davidovits, a prominent French chemist, as a new binder from the inorganic polymer family. The use of geopolymer cement can reduce carbon dioxide emissions by 44-64% compared to Portland cement [11]. Also, geopolymer concrete makes optimal use of available waste, which has a positive impact on the environment [12]. In terms of properties, geopolymer concretes have better mechanical and chemical properties than conventional concretes, including higher compressive, tensile and flexural strengths [13-15], faster hardening [13, 16], longer durability [17], resistance to fire, and high temperatures [18-20], less permeability and resistance to attack by salts and acids [21, 22] and less creep [23, 24]. Geopolymers are inorganic aluminosilicate materials obtained from the polymerization reaction between a silica-rich aluminosilicate source (SiO_2) and alumina (Al_2O_3) with an alkaline activating solution [1, 2]. Geopolymerization is a rapid chemical reaction in alkaline conditions between Si and Al elements, which causes the formation of a three-dimensional Si-O-Al polymer chain [3, 4]. In this article, metakaolin was used as the main source of aluminosilicate. Blast furnace slag, which is called a slag for short, is a by-product of the iron blast furnace, which is one of the most potential sources of aluminosilicate due to its structural nature.

The alkaline activating solution, as one of the two main parts of geopolymers, plays an important role in breaking down and forming the crystal structure of Si and Al, and it is usually selected based on sodium or potassium, which are soluble alkaline metals. The most common alkaline activator solution used in polymerization is a combination of sodium hydroxide (NaOH) or potassium hydroxide (KOH) solution with sodium or potassium silicate solution [4]. The source of aluminosilicate, which is known by other names, such as the source of polymerization, base material, and adhesive, as a supplier of Si and Al, plays the most important role in geopolymer cements. Aluminosilicate sources can be natural, such as bentonite; industrial, such as: metakaolin; Or waste materials or by-products [5], the most common of which are fly ash [6] and iron blast furnace slag [7-12]. The type of source, the content of source elements, molecular structure and crystalline degree of the source, alkali substances in the source, Si/Al ratio in the source, etc. are some of the influencing parameters in the strength of geopolymer concretes. Metakaolin is one of the aluminosilicate sources . Fly ash is a by-product of coal-fired power plants, which can be one of the best primary sources of geopolymerization due to its amorphous structural nature [10, 13]. Fly ash is classified into two classes: C (containing high amounts of calcium oxide) and F (containing low amounts of calcium oxide). Bentonite is another source of aluminosilicate. It is a type of fine-grained clay that has at least 85% of montmorillonite clay. Bentonite is a material from the category of clays and consists of swelling minerals, which are mainly montmorillonite and a small amount of beadlite. Most bentonites are formed by the weathering and alteration of volcanic ash, often in the presence of water, and their source rock is the most basic [14, 15]. In this article, class F fly ash, bentonite and slag were used as aluminosilicate sources to replace metakaolin to make geopolymer concrete.

Some researches have been done in the field of the composition of aluminosilicate sources, which will be briefly discussed. Zhang et al. [16] studied on the thermal resistance of geopolymers used in combination of metakaolin and fly ash. They have concluded that the replacement of fly ash by 50% increases the compressive strength. Fernández et al. [17] also reported similar results. Rajamma et al [18]observed the positive effects of replaced fly ash up to 40% instead of metakaolin. Bernal et al. [19], in research using the slag and metakaolin combination, concluded that 40% of slag is used instead of metakaolin, which causes a significant increase in the compressive strength of geopolymer concrete. Yip et al. [20] also concluded in their research that the combination of slag (below 40%) and metakaolin increases the compressive strength and durability of concrete and also improves the microstructure of geopolymer cement. Esparham [21] in research on geopolymer cement paste, used the combination of metakaolin and zeolite in different replacement percentages as a source of aluminosilicate. In a research on geopolymer cement paste, they used the combination of metakaolin and zeolite in different replacement percentages as a source of aluminosilicate. These researchers concluded that replacing zeolite instead of metakaolin increases the compressive strength of geopolymer concrete. Cheng et al. [22] also reported similar results in their research.

Soft Programming, Machine Learning (ML) and Artificial Neural Networks (ANNs) are new methods to predict the mechanical behavior of concrete. Currently, engineers prefer to practice using computer programming including machine studying, data mining, and other types to forecast concrete mechanical properties. Computer prediction techniques can reduce time and material. Furthermore, classical programming can transfer equations to commuter programs, and algorithms to find the precise outcomes [23-31] Topçu and Saridemir [32] investigated the prediction of concrete mixture with extra fly ash through ANNs and FL techniques separately. They concentrated on aggregate diameter to forecast the mechanical properties of concrete. At the end, their outcomes showed that the R^2 was extra than 0.9, and their method turned into reliable. Another researcher, Kashyzadeh et al. [33] also applied Data Mining to

predict the concrete mechanical properties based on the mechanical properties of aggregate. They found that features of data mining of aggregate properties affect compressive strength. Data mining can predict the mechanical properties of concrete. Kumar et al. [34] used ML techniques, Gaussian Progress Regression (GPR), Support Vector Machine Regression (SVMR), and Ensemble Learning (EL) to predict lightweight-concrete mechanical properties. They concluded that R^2 was 0.98 for GPR forecasting. In another example, Hematibahar et al. [35] used classical programming to predict compressive strength They used classical programming to forecast the compressive strength and compressive stress-strain of concrete. Their results show that R^2 was more than 0.97. Hasanzadeh et al. [36] studied the prediction of the mechanical properties of concrete with ML. Their results showed that the Polynomial Regression (PR) for basalt fibred high-performance concrete can predict mechanical properties ($R^2>0.99$).

In this experimental study, the role of the combination of fly ash, bentonite and slag with metakaolin on the compressive, flexural and tensile strength and depth of carbonation of geopolymer concrete was investigated. Because, the research conducted on the effect of the combination of different sources of alumina silicate on the mechanical properties and durability of concrete Geopolymer is low and insufficient. In this experimetal investigation research, fly ash, slag and bentonite - types of aluminosilicate sources - were used instead of metakaolin (geopolymer concrete based on metakaolin) in ratios of 5, 10, 15, 20, 25, 30, 35, 40 and 45, respectively. Then the samples were tested in terms of

compressive strength, indirect tensile strength and three-point bending at the age of 7 and 28 days, and also to obtain the carbonation depth, 7 and 14 day carbonation tests were performed on the samples. The correlation matrix was used to determine the relationship between the mechanical properties of concrete. Finally, the results were collected, analyzed and presented.

2. MATERIALS AND METHODS

2. 1. Materials   The main source of aluminosilicate in this study was metakaolin. Also, the fly ash was of class F type. Bentonite used was in this study as well. XRF of these 4 materials are presented in Table 1. The alkaline activator solution in this research was sodium hydroxide with 98% purity and liquid sodium silicate solution with a ratio of SiO_2 to Na_2O equal to 2. The chemical breakdown of these two substances is summarized in Table 2. Consumable sand is also obtained from mines. Around Tehran, the sand used was broken sand, which was sieved according to ASTM C33 standard [37] and granulated. In this research, specific gravity and water absorption test were performed according to ASTM standard C127 [38]. It was taken from used sand. This test was performed on the used sand according to ASTM standard C128 [39]; whose results are provided in Table 3. Also, the coefficient of softness of sand according to ASTM standard C136 [40] equal to 8.2, the amount rejected from sieve No. 200, 9.0% and the value of sands was also measured according to ASTM D2419 standard [41]. The water used was the tap water

TABLE 1. XRF of mineral materilas

Chemical analysis		SiO$_2$	Al$_2$O$_3$	CaO	Fe$_2$O$_3$	Na$_2$O	K$_2$O	MgO	MnO	SO$_3$	Cl	LOI
Slag	**wt.%**	15.4	7.3	20.4	38.20	0.62	0.68	9.8	5.19	1.2	0.23	0.5
Metakaolin	**wt.%**	54.98	17.54	5.40	5.33	0.95	0.86	0.20	0.12	-	-	1.4
Fly ash	**wt.%**	70.7	21.1	1.13	3.9	0.26	1.09	0.77	0.05	-	-	1.8
Bentonite	**wt.%**	68.93	11.14	2.68	1.08	0.41	0.59	2.54	-	-	-	15.06

TABLE 2. Chemical Analysis of Sodium Hydroxide and Sodium Silicate

NaOH			KOH		
Chemical substance	**Result**	**Unit**	**Chemical substance**	**Result**	**Unit**
NaOH	98	%	**NaOH**	90.7	%
Na$_2$CO$_3$	1	%	**Na$_2$CO$_3$**	0.2	%
NaCl	200	ppm	**NaCl**	0.006	ppm
Fe	6	ppm	**Fe**	0.2	ppm
SiO$_2$	15.7	ppm	**SiO$_2$**	0.6	ppm
Appearance	**White flake**		**Appearance**	**White flake**	

of Tehran city. The superplasticizer used was polycarboxylate with a specific weight of 1.1 grams per cubic centimeter the detailed of sand and gravels are shown in Figure 1 and Table 3.

2. 2. Experimental Methods   The main aluminosilicate source in this study was metakaolin. Also, the fly ash was of class F type. The bentonite used was natural bentonite and clinoptilolite. XRF analysis of these 4 materials is presented in Table 1.

The alkaline activating solution in this research was sodium hydroxide with 98% purity and liquid sodium silicate solution with a ratio of SiO_2 to Na_2O equal to 2.
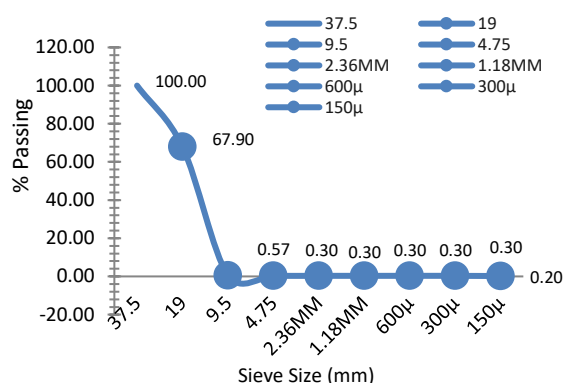
Figure 1. Gradation curves of fine and coarse aggregates

TABLE 3. Water absorption, specific density of aggregates and Fineness modulus

	Specific density of aggregates (g/cm³)	Water absorption (%)	Fineness modulus
Gravel	2.69	0.8	6.5
Sand	2.65	2.2	1.2

The chemical analysis of these two materials is summarized in Table 2. The used sand was broken sand, which after preparation, was granulated by ASTM C33 [37] standard sieve. In this research, sand with a maximum diameter of 12.5 mm was used. The test of specific gravity and water absorption according to ASTM C127 standard [38] was taken from the used sand. This test was carried out using sand according to ASTM C128 standard [39], the results of which are presented in Table 3. Also, the softness coefficient of sand according to ASTM C136 [40] standard was equal to 2.8, the amount rejected from sieve No. 200 was 0.9% and the sand value was also measured according to ASTM D2419 [41] standard, 74. The water used was the tap water of Tehran

city. The superplastiziter used was polycarboxylate with a specific weight of 1.1 grams per cubic centimeter.

After conducting preliminary tests and using the results of previous research [42], the geopolymer concrete mixing plan based on metakaolin was selected and metakaolin was replaced with slag, fly ash and bentonite in proportions of 5, 10, 15-45%. Mixing schemes are presented in Table 4. To make the samples, the alkaline activating solution was first prepared. For this purpose, first, sodium hydroxide solution with a concentration of 12 M was mixed with sodium silicate solution and supreplaseter according to the mixing plans. In the day of the test, first, dry materials including: sand, sand, metakaolin, slag, bentonite and fly ash were poured into the concrete mixer according to the mixing plans and mixed for 3 minutes in order to distribute evenly. Then, alkaline activator solution and additional water were added to the mixer and the concrete mixture was mixed for 2 minutes. After finishing the mixing, concrete compressive, tensile and bending samples were molded. The samples were compacted for 10 seconds on the vibrating table. Then the samples were processed for 24 hours in an oven at a temperature of 80 degrees Celsius. After the processing, the samples were removed from the oven and placed at ambient temperature. 7 and 28 days compressive, tensile and bending strength tests were taken from the samples. It is worth mentioning that the dimensions of compression samples were 10x10x10 and bending 50x10x10 cm. Also, the dimensions of the cylindrical tensile samples were 10 x 20 cm. In this term, the concrete cylinder has been locked between four steels, and at the moment of of the failure splitting in two parts (see Figure 2).

The tests performed on concrete samples include: compressive strength test based on Part 116: BS1881, indirect tensile test (Brazilian) based on ASTM C496 [43] and three-point bending strength test based on ASTM C293.

TABLE 4. The mixture of the first part

Mix ID	Metakoalin	Fly ash	Slag	Bentonite	NaOH	Na₂SiO₃	Coarse aggregates	Fine sand	SP	Unit
M	350	0	0	0	140	210	840	840	10	**kg/m³**
MF5	3320.5	17.5	0	0	140	210	840	840	10	**kg/m³**
MF10	315	35	0	0	140	210	840	840	10	**kg/m³**
MF15	297.5	52.5	0	0	140	210	840	840	10	**kg/m³**
MF20	280	70	0	0	140	210	840	840	10	**kg/m³**
MF25	262.5	87.5	0	0	140	210	840	840	10	**kg/m³**
MF30	245	105	0	0	140	210	840	840	10	**kg/m³**
MF35	227.5	122.5	0	0	140	210	840	840	10	**kg/m³**
MF40	210	140	0	0	140	210	840	840	10	**kg/m³**

MF45	192.5	192.5	0	0	140	210	840	840	10	**kg/m³**
MS5	3320.5	0	17.5	0	140	210	840	840	10	**kg/m³**
MS10	315	0	35	0	140	210	840	840	10	**kg/m³**
MS15	297.5	0	52.5	0	140	210	840	840	10	**kg/m³**
MS20	280	0	70	0	140	210	840	840	10	**kg/m³**
MS25	262.5	0	87.5	0	140	210	840	840	10	**kg/m³**
MS30	245	0	105	0	140	210	840	840	10	**kg/m³**
MS35	227.5	0	122.5	0	140	210	840	840	10	**kg/m³**
MS40	210	0	140	0	140	210	840	840	10	**kg/m³**
MS45	192.5	0	192.5	0	140	210	840	840	10	**kg/m³**
MB5	3320.5	0	0	17.5	140	210	840	840	10	**kg/m³**
MB10	315	0	0	52.5	140	210	840	840	10	**kg/m³**
MB15	297.5	0	0	52.5	140	210	840	840	10	**kg/m³**
MB20	280	0	0	70	140	210	840	840	10	**kg/m³**
MB25	262.5	0	0	87.5	140	210	840	840	10	**kg/m³**
MB30	245	0	0	105	140	210	840	840	10	**kg/m³**
MB35	227.5	0	0	122.5	140	210	840	840	10	**kg/m³**
MB40	140	0	0	210	140	210	840	840	10	**kg/m³**
MB45	157.5	0	0	192.5	140	210	840	840	10	**kg/m³**

Figure 2. Tensile, flexural, and compression samples made

2. 3. Machine Learning   An AI calculation generally works by taking a gander at a great deal of information to sort out the principles, new encounters, and information (the "preparing process") prior to utilizing these guidelines, encounters, and information to tackle and foresee future issues (the "testing process"). As a result, developing a database is a crucial and essential step in the development of machine learning.

The types of materials and their properties were the subjects of the input data in this kind of database. The experimental data that led to the collection of these data. The target of this strategy was found the compressive strength by means of polynomial relapse. The data set was split into two parts: one for training and one for

testing. Note that Equation (1) shows that the kinds of polynomial relapse (PR) which can anticipate the compressive strength.

According to the current study, the polynomial regression has been provided to predict the compressive, tensile and flexural strengths, the polynomial regression equeation followed by :

$$y_{(x)} = a_n x^n + a_{n-1} x^{n-1} + a_{n-2} x^{n-3} + \ldots + a_1 x^1 + a_0 , \quad (1)$$

The a_n, is the coefficient of a polynomial function has different value at various conditions. As well as, the a_0, is the Y-intercept of polynomial function or constant value [44]. Where a known as the polynomial function coefficient, x is variable, and $y_{(x)}$ is dependent variables to x in Equation (1).

The machine learning method was performed according by Python and Spyder Plugin. In this regard, the concrete experimental results has been classification and next divided to "train and test". The "polynomial regression" has been imported from "skylearn". Finally the polynomial regression has been applied to data.

To find the verify of prediction, the Correlation Coefficient (R^2), Mean Absolute Errors (MAE) and Root Mean Squared Errors (RMSE) have been established. Equation (2) illustrates the R^2 formula:

$$R^2 = 1 - \frac{\sum_{}^{n}(y - \hat{y})^2}{\sum_{}^{n}(y - \bar{y})^2} \qquad (2)$$

where y, ˆy, and −y are the actual, predicted, and mean of the actual value, respectively.

The MAE equation is equal the sum of the numerical differences of the values of community set divided by whole numbers (Equation (2)). The MAE equation is defined as (Equation (3)):

$$MAE = \frac{1}{n}\sum_{}^{n}\left|y - \hat{y}\right| \qquad (3)$$

RMSE calculate the average deviation of each actual data point and the predicted results (Equation (4)):

$$RMSE = \sqrt{\frac{1}{n}\sum_{}^{n}(y - \hat{y})^2} \qquad (4)$$

2. 4. Deep Learning   An idea in machine learning called deep learning is based on artificial neural networks. Deep learning models perform better than basic machine learning models and conventional data analysis techniques for many applications. The structure is deeper and includes a perceptron with multiple hidden layers and multiple layers of layers. By combining low-level features to discover distributed feature representations of data, deep learning creates more abstract attribute categories of high-level representation or features.

The correlation matrix can able to find the maximum relationship among the properties of the materials of concrete with deep learning and machine learning.

This article found the correlation matrix between mechanical properties and the properties of concrete.

2. 5. Carbonation   One of the most important failures of reinforced concrete is steel corrosion in concrete. Corrosion starts for two reasons, one is carbonation in concrete and the other is the penetration of chloride ions into concrete.

Due to the alkalinity of the concrete, the steels in the concrete have a thin surface layer on them, and the carbonation process begins when this surface layer that protects the concrete against corrosion is destroyed and the pH of the concrete reach below 9.

The phenomenon of carbonation in concrete is one of the main reasons for the corrosion of reinforcements.

To carry out carbonation tests, a special device has been installed that reduces the time required to measure the depth of carbonation of concrete with the increase in the concentration of carbon dioxide gas. The procedure is as follows: two chambers were made to place a small cylindrical sample with a length of 20 cm and a diameter of 5 cm, which are placed in a closed circuit. In the

mentioned closed circuit, a flow of a mixture of 50% air and 50% carbon dioxide gas is established. Considering that water is produced in the carbonation reactions of concrete, the relative humidity will change, for this reason, chemical dryers (moisture absorbent silicate gel) are used in the mentioned circuit to achieve relative humidity. It is accompanied by an increase by placing the above-mentioned chambers inside the water tanks, controlled and kept constant at around 27 degrees Celsius by circulating the water at a lower temperature and adjusting its heigh

2. 5. 1. Determining the Depth of Carbonation of Concrete   According to the RILEM CPC-18 standard, first the selected samples are placed lengthwise in the force application device and divided into two halves like the Brazilian test. Then, a solution of phenolphthalein and ethyl alcohol is sprayed on the fracture surface, and the distance between the purple color and no color change compared to the outer surface of the sample is reported as the carbonation depth of the geopolymer concrete sample [45-48].

3. RESULTS

3. 1. Compressive Strength   The results of the compressive strength test of the samples and the effect of replacing fly ash, bentonite and slag are presented in Figure 5. As shown in Figure 5, the 7- and 28-day compressive strength of sample M (100% metakaolin) is 18 and 26 MPa was measured. The replacement of 5% fly ash (MF5) increased the compressive strength by approximately 12%. Also, with a further increase in the replacement percentage of fly ash up to 35% (MF15, MF10, and... MF35), the compressive strength of the samples also increased. So that in the ratio of 35%, the maximum compressive strength of 7 and 28 days of MF35 sample reached more than 25.9 and 37 MPa with a 30% increase compared to M. In the case of replacement with slag, it can be seen that the compressive strength increases in general, so that the maximum compressive strength of 7 and 28 days corresponds to the MS15 sample (containing 15% slag and 85% metakaolin), which were measured as 25.2 and 36 MPa, respectively. (approximately 12% increase compared to 100% metakaolin). By replacing 35% more slag (MS35), the process of improving the compressive strength compared to sample M (100% metakaolin) also increased and the 7 and 28 days compressive strength of this sample was measured as 19.6 and 28 MPa. But with more slag replacement of 35% (MS35), (unlike fly ash), the compressive strength of the sample decreased with respect to M. Yet, on account of bentonite, the outcomes were unique. According to the findings, the samples' compressive strength decreased by 100% (M) when

bentonite was substituted for metakaolin, from 5 to 45%. For instance, the 7-day compressive strength of the MB30 design was measured at 13.8 MPa, while the 28-day compressive strength was measured at 23.46 MPa, which is approximately 8% lower than the M sample (see Figures 3 and 5).

3. 2. Tensile Strength   The tensile strength test results of the samples are also presented in Figures 4 and 6. As the results of Figure 6 show, the 7- and 28-day tensile strength of sample M was measured as 2.26 and 2.7 MPa, respectively. Replacing 15-45% fly ash instead of metakaolin increased the 28-day tensile strength by approximately 4-19% compared to design M; so that the maximum 7 and 28-day tensile strength was observed in design MF35 with values of 2.7 and 3.22. In the samples replaced with slag (up to 35 observations of replacement), the tensile strength of the samples has increased so that at 15% replacement (MS 15) the tensile strength reached to its maximum (7 and 28 days resistances were 2.66 and 3.15 MPa, respectively). But by replacing 40% and 45% more slag instead of metakaolin, similar to the compressive strength, the 28-day tensile strength compared to M, also decreased by 10% and 12%, respectively. The replacement of bentonite instead of metakaolin, similar to the

Figure 3. Failure sample of geopolymer concrete

Figure 4. Failure sample of geopolymer concrete

compressive strength in all replacement ratios, decreased the 7 and 28 day tensile strength of the samples compared to the M plan. For example, at 5% replacement ratio (MB5), the tensile strength at 7 and 28 days, it faced a very slight reduction compared to the M plan. Also, with an increase in the replacement percentage from 10 to 45%, the tensile strength of the samples gradually decreased. So that the tensile strength of 7 and 28 days of sample MB45 was measured as 1.91 and 2.50 MPa, respectively, which is approximately 26 and 15% less than that of sample M (see Figures 4 and 6).

3. 3. Flexural Strength   The trend of bending strength results was similar to the trend of compressive and tensile strength. Specimen M (100% metakaolin) had a flexural strength of 4.18 and 4.9 MPa at days 7 and 28, as shown in Figure 7, when fly ash was replaced with 5 to 45% metakaolin, the flexural strength increased, so that the greatest increase in strength in 7 and 28 days was related to the replacement of 35% with fly ash compared to other samples (flexural strength of 7 days, 4.98 MPa and 28 days, 5.96 MPa, respectively). Similar to the compressive and tensile strength results, in the replacement of metakaolin with 15% slag, the highest flexural strength of 7 and 28 days was obtained (4.92 and 5.88 MPa, respectively). In replacement of 40 and 45% with slag, compared to the 100% sample of metakaolin (M), the resistance was determined at 7 and 28 days.
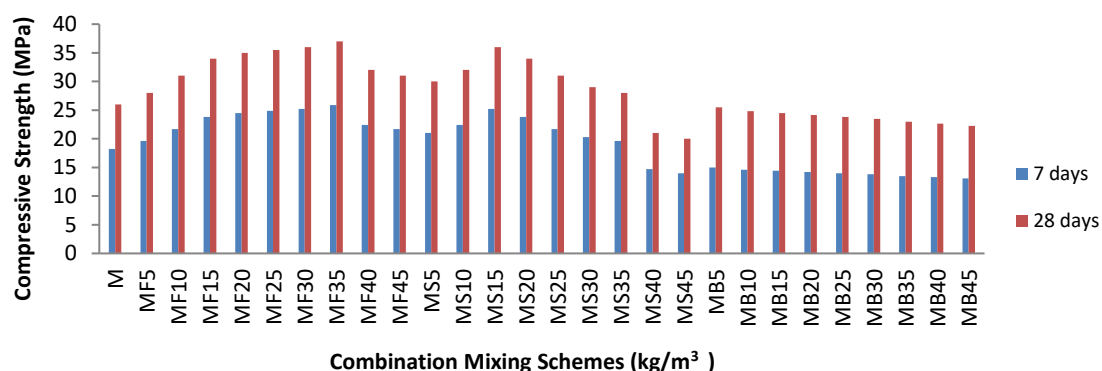

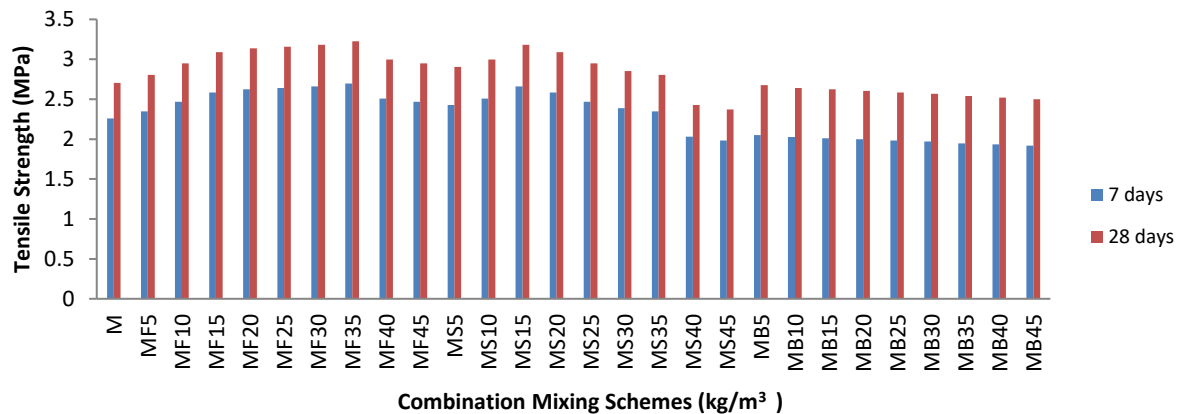**Figure 5.** Compressive Strength results
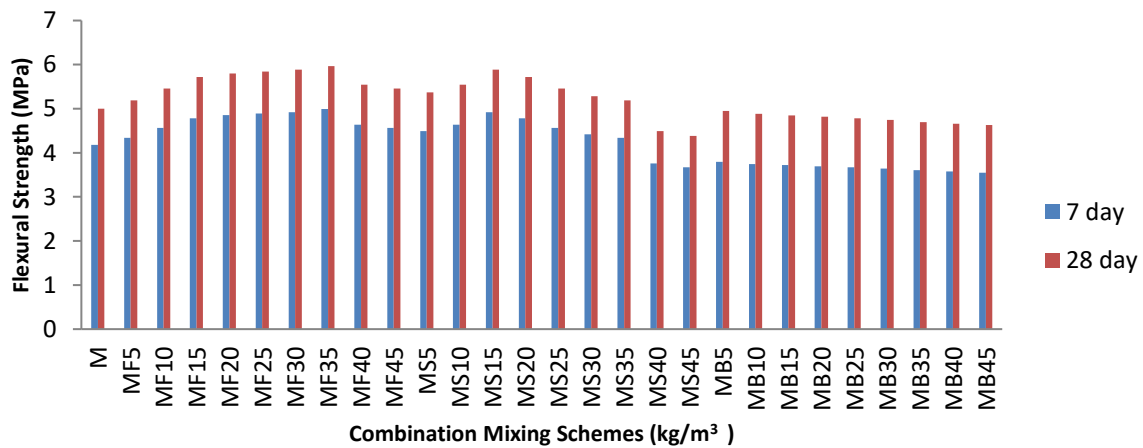
Figure 6. Tensile Strength results

Figure 7. Flexural Strength results

Fasting decreased by 11 to 14%. In replacing metakaolin with bentonite, the tensile strength values faced a gradual decreasing trend, so that the greatest amount of reduction in tensile strength in 7 and 28 days occurred in 45% replacement with bentonite (approximately 12 to 13%) (see Figure 7).

3. 4. Machine Learning The results show a good polynomial regression for all strengths between the predictive data and the experimental data. It can be the experimental data overestimated or underestimated than predicted results in each types of results (Figures 8-11).

The R^2 RMSE, and MAE results has been shown in Table 5. According to Table 5 the Polynomial regression had the best results for compressive strength and next, flexural strength. The results shows that the compressive strength was experimental and prediction results was similar together.

The tensile strength prediction according to machine learning is illustrated in Figure 9, the results show that the R^2 was more than 0.8 and the closet sample was

MB25 to experimental results. MAE, and RMSE results was 1.2 and 3.4 respectively

The flexural strength shows that the close relationship between experimental results and predictably results the R^2 was more than 0.75. In fact the polynomial function was able to predict the flexural strength with 75% accuracy (Figure 10).

The results can be provided for the other type of concrete and other type of consept as well. For example Hasanzadeh et al [36] has been predicted the compressive, tensile and flexural strengths with 99% for basalt fibred high performance concrete via polynomial regression.

3. 5. Correlation Regarding the relationship between the compressive, tensile and flexural strength, the correlation matrix is provided by the Python Software Spyder extension (Figure 11). Based on the results, the compressive strength with tensile and flexural strength is more than 0.96 and 0.93%, respectively. In the mortar, fly ash had a large Impact with more than 60%

compressive strength, followed by slag with 33%. Bentonite and methicillin had -77 and -20% effect on compressive strength.

According to samples and experimental results, the relationship between compressive strength and tensile strength (Equation (5)) and flexural strength (Equation (6)) has been provided.

$$f_t' = 0.3f_c' + 0.96 \tag{5}$$

$$f_f' = 0.011f_c' + 0.3 \tag{6}$$

where f_c' is compressive strength, f_f' is flexural strength and f_t' is tensile strength. Tables 6 and 7 shows the tensile and flexural strengths for 28 days for prediction and experimental results.
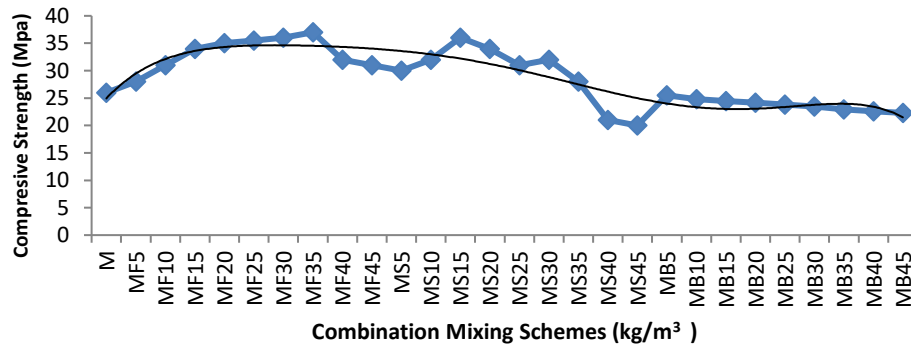

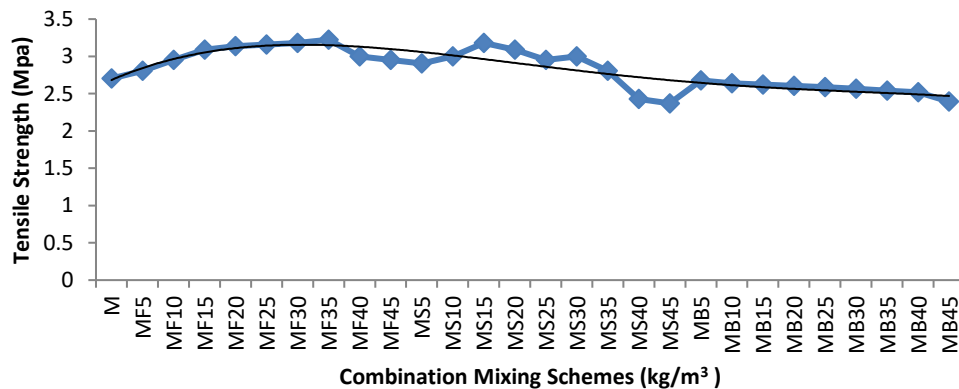**Figure 8.** Polynomial prediction for compressive strength
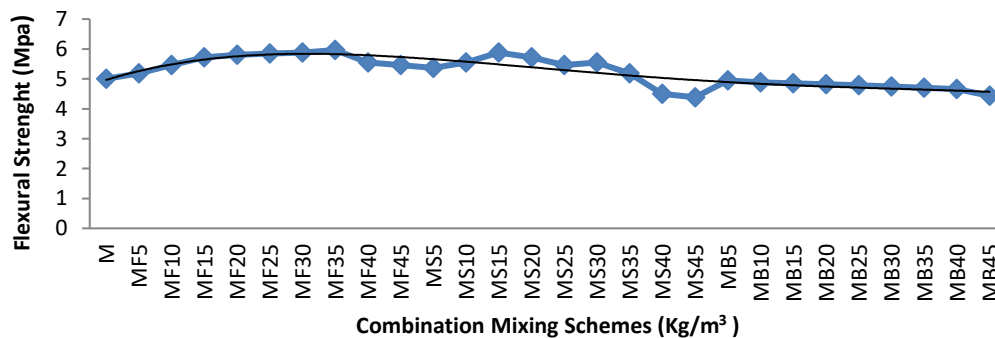

Figure 9. Polynomial prediction for tensile strength

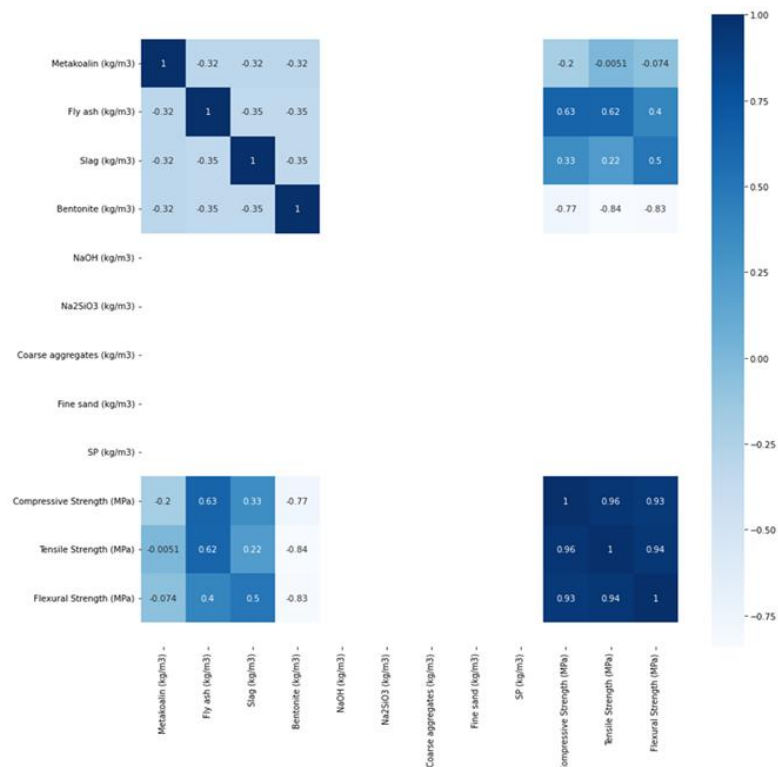**Figure 10.** Polynomial prediction for Flexural strength

Figure 11. The correlation matrix of geopolymer concret

TABLE 5. R² , RMSE, MAE results

	R²(MPa)	RMSE(MPa)	MAE(MPa)
Compressive (MPa)	0.93	1.4	4.2
Tensile (MPa)	0.8	1.2	3.4
Flexural (MPa)	0.75	0.9	3.2

TABLE 6. The results of prediction tensile strength according to Equation (5)

Mix ID	Prediction	Experimental	Errors
M	1.8869	1.955	0.0681
MF10	2.06515	2.185	0.11985
MF15	2.1721	1.725	0.4471
MF20	2.20775	2.3	0.09225
MF25	2.225575	2.07	0.15558
MF30	2.2434	2.415	0.1716
MF35	2.27905	2.0125	0.26655
MS10	2.07104	1.9075	0.16354
MS15	2.20992	1.8857	0.32422
MS20	2.14048	2.0165	0.12398
MS25	2.03632	2.0056	0.03072
MS30	2.07104	1.962	0.10904
MS35	1.93216	1.8857	0.04646

MB10	1.58062	1.001	0.57962
MB15	1.594725	0.9646	0.63013
MB20	1.60883	0.9919	0.61693
MB25	1.63704	0.9828	0.65424
MB30	1.69346	1.08	0.61346
MB35	1.72167	1.025	0.69667

TABLE 7. The results of prediction flexural strength according to Equation (6)

Mix ID	Prediction	Experimental	Errors
M	1.8869	3.5085	0.0585
MF10	2.06515	3.819	0.254
MF15	2.1721	3.9225	0.346
MF20	2.20775	3.97425	0.23675
MF25	2.225575	4.026	0.254
MF30	2.2434	4.1295	0.1045
MF35	2.27905	3.5256	0.7294
MS10	2.07104	3.9288	0.4188
MS15	2.20992	3.7272	0.0552
MS20	2.14048	3.4248	0.3552
MS25	2.03632	3.5256	0.384
MS30	2.07104	3.1224	0.8196

MS35	1.93216	2.1018	1.8726
MB10	1.58062	2.14275	0.56775
MB15	1.594725	2.1837	0.5637
MB20	1.60883	2.2656	0.5556
MB25	1.63704	2.4294	0.5394
MB30	1.69346	2.5113	0.4863
MB35	1.72167	2.3	0.23

3. 6. Durability (Carbonation Test)   Carbonation test was done as durability test. Carbonation of concrete is a chemical reaction between carbon dioxide permeated into concrete and alkaline products resulting from the hydration of cement in concrete and the production of calcium carbonate. The penetration of CO_2 reduces the alkalinity of concrete and destroys the alkaline protective layer around the reinforcement, and as a result, the rebars are exposed to corrosion. Carbonation test results of the selected mixture designs (M, MF35, MS15, MB5) are shown in graphs of Table 8 below.

4. DISCUSSION

4. 1. Analysis of Compressive, Tensile and Flexural Strengths   According to the summary of the obtained results, it can be said that the replacement of fly ash instead of metakaolin increased the compressive, tensile and bending strength of the samples compared to the 100% metakaolin sample. This issue can be related to various reasons. The first parameter is the degree or degrees of amorphous crystallization of the aluminosilicate source. This parameter is ignored in most cases, but it is one of the important conditions of the source of aluminosilicate. due to lack of reactivity and having a strong and regular crystal structure, they cannot effectively participate in the geopolymerization process, because breaking the structures of SiO_2 and Al_2O_3 to become SiO_4 and AlO_4 monomers in these sources is done less and harder [10]. Structurally, fly ash has a more suitable structure than metakaolin for making geopolymer. As a result, replacing fly ash instead of

TABLE 8. The results carbonation of selected mixture designs

	80°C		Density (M)
Sample	Carbonation Depth (mm) 28 days	Carbonation Depth (mm) 14 days	
M	10.4	8.2	
MF35	7.3	6.5	12
MS15	9.1	7.6	
MB5	16.8	12.8	

metakaolin increases the geopolymerization process and increases the mechanical resistance of geopolymer concrete [8-12].

On the other hand, another important and influencing parameter on the mechanical strength of geopolymeric concrete is the Al/Si ratio of the aluminosilicate source. Many researchers consider the Al/Si ratio as the most effective parameter in the compressive strength of geopolymer concrete. These researchers have reported the optimal value of this ratio between 3.3 and 5.3, which results in achieving the highest compressive strength [7, 13, 45, 46]. Al/Si ratio in metakaolin used in this research was equal to 1/8. This ratio is 35.3 in fly ash. In fact, with the addition of fly ash instead of metakaolin, in addition to the amorphousness of the cement material, the Al/Si ratio also increases and approaches the optimal level (3.3 to 5.3). As a result, the compressive, tensile and flexural strength increases and also with the increase of the replacement ratio, the increase and improvement of the compressive, tensile and flexural strength also increases. The optimal amount of fly ash replacement in this research was measured at 25%.

Regarding replacing slag instead of metakaolin, the summary of the obtained results showed that replacing slag also increased the mechanical resistance of geopolymer concrete based on metakaolin. This issue can have various reasons. One of the reasons similar to fly ash is the more amorphous and reactive structure of slag compared to metakaolin. But other reasons can be different from fly ash. Although the Al/Si ratio of slag is equal to 3 and similar to fly ash, it can increase the mechanical resistance of concrete, but there are other important parameters that cause differences in the results of replacing slag with fly ash. Another influential parameter is the CaO content of the aluminosilicate source. According to the results of this article and our previous research [10] this parameter has a significant role on the compressive strength of geopolymer concrete. In a research on geopolymers, van Jaarsveld et al. [46] concluded that the characteristics of the aluminosilicate source, especially the amount of calcium oxide CaO, determines the properties of the geopolymer. Xu et al. [47] also consider the amount of CaO of the aluminosilicate source, along with the parameters of the alkaline solution and the Al/Si ratio, as one of the important and influencing factors on the properties and mechanical resistance of geopolymers. In the case of using fly ash and metakaolin, considering that both materials have a very low percentage of CaO (13.1 percent in fly ash and 3.1% in metakaolin), so the role of CaO in the mechanical resistance of geopolymer concrete is not key. But regarding slag, due to the high percentage CaO in slag (37%), this role can be important and influential. Replacing slag up to 20%, due to having large amounts of CaO and increasing the Si/Ca ratio, as well as the potential of CaO for ion geopolymerization and chain

formation with this ion [34, 35] leads to an increase in the compressive, tensile and bending strengths of $+Ca_2$ Geopolymer concrete.

On the other hand, with a further increase in the replacement ratio of slag from 25 to 35%, the mechanical resistance of concrete decreased compared to the case of 25% slag replacement. The reason for this issue can be another important parameter of the sources in the source [34]. Likewise, the amount of Al in the aluminosilicate $2O_3$, which was mentioned and the results of this article showed, with the increase in the amount of CaO (Si/Ca) in the aluminosilicate source, the compressive and tensile strengths and the bending of geopolymer concrete increases, but on the other hand, in aluminosilicate sources with a high CaO, the amount of Al_2O_3 in the source is very important. In these aluminosilicate sources, if there are large amounts of Al2O3, scale is also produced. This substance reacts with Ca and causes the formation of +3 calcium aluminate compounds next to the geopolymer network and H-S-C gel, which reduces the compressive strength of the geopolymer [13, 14]. As can be seen in Table 1, metakaolin has large amounts Al_2O_3 is (2.30%). As a result, when using the combination of metakaolin and slag, if the amount of slag is too much (35%), the mechanical resistance of geopolymer concrete will decrease. As a result, the optimal amount of slag replacement for the greatest effect in improving compressive and tensile strengths flexural in this research was measured at 25%. Regarding the replacement of bentonite instead of metakaolin, the summary of the results showed that the replacement of this material instead of metakaolin has caused a significant reduction in the compressive, tensile and bending strengths of geopolymer concrete compared to the case of using 100% metakaolin. The reason for this can be related to the structure of bentonite. bentonite has a strong crystal structure [49] and among the aluminosilicate sources used in this article, it has the strongest crystal structure, and as mentioned, the aluminosilicate source must have a suitable amorphous structure. Compared to metakaolin, bentonite has a more crystalline structure. As a result, replacing a material with a higher crystalline degree instead of a material with a lower crystalline degree causes a relative decrease in the geopolymerization process and, as a result, a decrease in compressive, tensile and bending resistances. On the other hand, with the increase of bentonite replacement percentage from 5 to 45%, the reduction of compressive, tensile and flexural strengths of the samples slightly increased. The reason for this increase in resistance can be related to the tetrahedral structure of clinoptilolite, which strengthens the metakaolin geopolymer matrix [15, 49, 50].

4. 2. Analysis of Durability (Carbonation Test)
According to the carbonation test results, it can be seen

that the composite samples with fly ash(MF15) and slag(MS25) have a lower carbonation depth compared to the control sample based on metakaolin (M). This can be due to the increase in the amount of calcium oxide in the aluminosilicate source and help in the formation of gel C-S-H, which itself causes the denser and improved microstructure of the samples combined with fly ash and thermally slag. It can also be seen that the lowest amount of carbonation depth belongs to sample MF15 (28 days-7.3 mm and 14 days -6.5 mm). On the other hand, it can be seen that by combining metakaolin with bentonite(MB5), the degree of crystallization of the aluminosilicate source has increased and the amorphous ratio(SI/AL) has decreased, which itself causes a decrease in geopolymerization, as a result, the depth of carbonation increases. According to the results, it can be concluded that corrosion potential Rebar in metakaolin geopolymer concrete samples combined with fly ash and slag decreases and samples combined with bentonite increases [13, 14, 49, 51].

5. CONCLUSION

In this experimental research, an attempt was made to study the role of replacing F-class fly ash, natural clinoptilolite bentonite, and slag of the slag furnace instead of metakaolin on the compressive, tensile, and bending strengths of geopolymer concrete based on metakaolin. In this regard, after conducting related experiments and data analysis, the following are presented as specific results of this article.

1. The replacement of class F fly ash instead of metakaolin in the composition of geopolymer concrete increased the compressive, tensile and flexural strengths of concrete. The optimal amount of fly ash replacement in this research was measured as 35%, which caused an increase of approximately 25.9 and 37 and in the 7 and 28 days gor compressive strength of geopolymer concrete.

2. The replacement of slag instead of metakaolin in the composition of geopolymer concrete increased the compressive, tensile and flexural strengths of concrete. The optimal amount of slag replacement in this research was measured to be 15%, which caused an increase of approximately 25.2, and 36 for compressive strength in 7 days and 28 days .

3. The replacement of bentonite instead of metakaolin in the composition of geopolymeric concrete caused a significant decrease in the compressive, tensile and flexural strength.

4. The correlation matrix shows that the compressive strength with tensile and flexural strength had more than 90% relationship. Moreover, the strength of materials has related to fly ash more than other addictive.

5-The Machine learning results shows that the compressive strength R^2 was more than 0.93, tensile

strength was more than 0.8 and flexural strength was more than 0.75.

6. The carbonation depth was decreased when fly ash and slag were used to replace metakaolin (metakaolin-based geopolymer concrete). The lowest carbonation penetration depth was associated with a 35% replacement with fly ash. However, substituting bentonite for metakaolin resulted in a deeper carbonation.

6. REFRENCESS

1. Esparham, A., "A review of the features of geopolymer cementitious composites for use in green construction and sustainable urban development", *Central Asian Journal of Environmental Science and Technology Innovation*, Vol. 3, No. 3, (2022), 64-74. doi: 10.22034/CAJESTI.2022.03.01.

2. Esparham, A., Moradikhou, A.B. and Jamshidi Avanaki, M., "Investigating the environmental properties and energy consumption of geopolymer concrete as a sustainable material", *Advance Researches in Civil Engineering*, Vol. 4, No. 2, (2022), 44-53. doi: 10.30469/arce.2022.157272.

3. Gao, K., Lin, K.-L., Wang, D., Hwang, C.-L., Tuan, B.L.A., Shiu, H.-S. and Cheng, T.-W., "Effect of nano-SiO₂ on the alkali-activated characteristics of metakaolin-based geopolymers", *Construction and Building Materials*, Vol. 48, (2013), 441-447. https://doi.org/10.1016/j.conbuildmat.2013.07.027

4. Görhan, G. and Kürklü, G., "The influence of the naoh solution on the properties of the fly ash-based geopolymer mortar cured at different temperatures", *Composites Part B: Engineering*, Vol. 58, (2014), 371-377. doi. https://doi.org/10.1016/j.compositesb.2013.10.082

5. Esparham, A. and Ghalatian, F., "The features of geopolymer concrete as a novel approach for utilization in green urban structures", *Journal of Composites and Compounds*, Vol. 4, No. 11, (2022), 89-96. doi. https://doi.org/10.52547/jcc.4.2.4

6. Adesina, A., "Recent advances in the concrete industry to reduce its carbon dioxide emissions", *Environmental Challenges*, Vol. 1, (2020), 100004. https://doi.org/10.1016/j.envc.2020.100004

7. Hardjito, D., Wallah, S.E., Sumajouw, D.M. and Rangan, B.V., "On the development of fly ash-based geopolymer concrete", *Materials Journal*, Vol. 101, No. 6, (2004), 467-472. doi. https://doi.org/10.14359/13485

8. Ramón-Álvarez, I., Marugán-Cruz, C., Enríquez, E., Sánchez-Delgado, S. and Torres-Carrasco, M., "Alkali-activated and hybrid materials: Alternative to portland cement as a storage media for solar thermal energy", *Boletín de la Sociedad Española de Cerámica y Vidrio*, (2021). https://doi.org/10.1016/j.bsecv.2021.11.006

9. Palankar, N., Shankar, A.R. and Mithun, B., "Air-cured alkali activated binders for concrete pavements", *International Journal of Pavement Research and Technology*, Vol. 8, No. 4, (2015), 289. http://dx.doi.org/10.6135/ijprt.org.tw/2015.8(4).289

10. Moradikhou, A.B. and Esparham, A., "Water absorption, density, mechanical strengths and high-temperature resistance of metakaolin-based geopolymer concrete reinforced with hybrid polyolefin and simple polypropylene fibers", *Advance Researches in Civil Engineering*, Vol. 3, No. 2, (2021), 1-15. https://doi.org/10.30469/arce.2021.135121

11. Mithun, B., Narasimhan, M., Nitendra, P. and Ravishankar, A., "Flexural fatigue performance of alkali activated slag concrete mixes incorporating copper slag as fine aggregate", *Selected Scientific Papers-Journal of Civil Engineering*, Vol. 10, No. 1, (2015), 7-18. https://doi.org/10.30469/arce.2021.135121

12. Esparham, A., "Investigation of the effects of nano silica particles and zeolite on the mechanical strengths of metakaolin-based geopolymer concrete", *International Journal of Innovation in Engineering*, Vol. 1, No. 4, (2021), 82-95. https://doi.org/10.52547/ijie.1.4.82

13. Yu, Q., Li, S., Li, H., Chai, X., Bi, X., Liu, J. and Ohnuki, T., "Synthesis and characterization of mn-slag based geopolymer for immobilization of co", *Journal of Cleaner Production*, Vol. 234, (2019), 97-104. https://doi.org/10.1016/j.jclepro.2019.06.149

14. Esparham, A. and Moradikhou, A.B., "A novel type of alkaline activator for geopolymer concrete based on class c fly ash", *Advance Researches in Civil Engineering*, Vol. 3, No. 1, (2021), 1-13. https://doi.org/10.30469/arce.2021.130143

15. Esparham, A., Vatin, N.I., Kharun, M. and Hematibahar, M., "A study of modern eco-friendly composite (geopolymer) based on blast furnace slag compared to conventional concrete using the life cycle assessment approach", *Infrastructures*, Vol. 8, No. 3, (2023), 58. https://doi.org/10.3390/infrastructures8030058

16. Zhang, H.Y., Kodur, V., Qi, S.L., Cao, L. and Wu, B., "Development of metakaolin–fly ash based geopolymers for fire resistance applications", *Construction and Building Materials*, Vol. 55, (2014), 38-45. https://doi.org/10.1016/j.conbuildmat.2014.01.040

17. Fernández-Jiménez, A., Monzó, M., Vicent, M., Barba, A. and Palomo, A., "Alkaline activation of metakaolin–fly ash mixtures: Obtain of zeoceramics and zeocements", *Microporous and Mesoporous Materials*, Vol. 108, No. 1-3, (2008), 41-49. doi. https://doi.org/10.1016/j.micromeso.2007.03.024

18. Rajamma, R., Labrincha, J.A. and Ferreira, V.M., "Alkali activation of biomass fly ash–metakaolin blends", *Fuel*, Vol. 98, (2012), 265-271. https://doi.org/10.1016/j.fuel.2012.04.006

19. Bernal, S.A., Rodríguez, E.D., Mejía de Gutiérrez, R., Gordillo, M. and Provis, J.L., "Mechanical and thermal characterisation of geopolymers based on silicate-activated metakaolin/slag blends", *Journal of Materials Science*, Vol. 46, (2011), 5477-5486. https://doi.org/10.1007/s10853-011-5490-z

20. Yip, C.K., Lukey, G. and Van Deventer, J.S., "The coexistence of geopolymeric gel and calcium silicate hydrate at the early stage of alkaline activation", *Cement and Concrete Research*, Vol. 35, No. 9, (2005), 1688-1697. https://doi.org/10.1016/j.cemconres.2004.10.042

21. Esparham, A., "Synthesis of environmentally friendly activated alkali concrete (geopolymer) based on bentonite", *Journal of Environmental Friendly Materials*, Vol. 6, No. 2, (2022), 1-8.

22. Cheng, T., Lee, M., Ko, M., Ueng, T. and Yang, S., "The heavy metal adsorption characteristics on metakaolin-based geopolymer", *Applied Clay Science*, Vol. 56, (2012), 90-96. https://doi.org/10.1016/j.clay.2011.11.027

23. Farooq, F., Czarnecki, S., Niewiadomski, P., Aslam, F., Alabduljabbar, H., Ostrowski, K.A., Śliwa-Wieczorek, K., Nowobilski, T. and Malazdrewicz, S., "A comparative study for the prediction of the compressive strength of self-compacting concrete modified with fly ash", *Materials*, Vol. 14, No. 17, (2021), 4934. https://doi.org/10.3390/ma14174934

24. Khan, M.A., Memon, S.A., Farooq, F., Javed, M.F., Aslam, F. and Alyousef, R., "Compressive strength of fly-ash-based geopolymer concrete by gene expression programming and random forest", *Advances in Civil Engineering*, Vol. 2021, (2021), 1-17. https://doi.org/10.1155/2021/6618407

25. Erdal, H.I., "Two-level and hybrid ensembles of decision trees for high performance concrete compressive strength prediction", *Engineering Applications of Artificial Intelligence*, Vol. 26, No. 7, (2013), 1689-1697. https://doi.org/10.1016/j.engappai.2013.03.014

26. Kabiru, O.A., Owolabi, T.O., Ssennoga, T. and Olatunji, S.O., "Performance comparison of svm and ann in predicting

compressive strength of concrete", (2014). http://dx.doi.org/10.9790/0661-16518894

27. Yang, D., Yan, C., Liu, S., Jia, Z. and Wang, C., "Prediction of concrete compressive strength in saline soil environments", *Materials*, Vol. 15, No. 13, (2022), 4663. https://doi.org/10.3390/ma15134663

28. Peng, X., Zhuang, Z. and Yang, Q., "Predictive modeling of compressive strength for concrete at super early age", *Materials*, Vol. 15, No. 14, (2022), 4914. https://doi.org/10.3390/ma15144914

29. Agrawal, R., "Sustainable design guidelines for additive manufacturing applications", *Rapid Prototyping Journal*, (2022). https://doi.org/10.1108/RPJ-09-2021-0251

30. Khorasani, M., Loy, J., Ghasemi, A.H., Sharabian, E., Leary, M., Mirafzal, H., Cochrane, P., Rolfe, B. and Gibson, I., "A review of industry 4.0 and additive manufacturing synergy", *Rapid Prototyping Journal*, No. ahead-of-print, (2022). https://doi.org/10.1108/RPJ-08-2021-0194

31. AlAlaween, W., Abueed, O., Gharaibeh, B., Alalawin, A., Mahfouf, M., Alsoussi, A. and Albashabsheh, N., "The development of a radial based integrated network for the modelling of 3d fused deposition", *Rapid Prototyping Journal*, Vol. 29, No. 2, (2023), 408-421. https://doi.org/10.1108/RPJ-04-2022-0121

32. Topcu, I.B. and Sarıdemir, M., "Prediction of properties of waste aac aggregate concrete using artificial neural network", *Computational Materials Science*, Vol. 41, No. 1, (2007), 117-125. https://doi.org/10.1016/j.commatsci.2007.03.010

33. Reza Kashyzadeh, K., Amiri, N., Ghorbani, S. and Souri, K., "Prediction of concrete compressive strength using a back-propagation neural network optimized by a genetic algorithm and response surface analysis considering the appearance of aggregates and curing conditions", *Buildings*, Vol. 12, No. 4, (2022), 438. https://doi.org/10.3390/ buildings12040438

34. Kumar, A., Arora, H.C., Kapoor, N.R., Mohammed, M.A., Kumar, K., Majumdar, A. and Thinnukool, O., "Compressive strength prediction of lightweight concrete: Machine learning models", *Sustainability*, Vol. 14, No. 4, (2022), 2404. https://doi.org/10.3390/su14042404

35. Hematibahar, M., Vatin, N.I., Ashour Alaraza, H.A., Khalilavi, A. and Kharun, M., "The prediction of compressive strength and compressive stress–strain of basalt fiber reinforced high-performance concrete using classical programming and logistic map algorithm", *Materials*, Vol. 15, No. 19, (2022), 6975. https://doi.org/10.3390/ma15196975

36. Hasanzadeh, A., Vatin, N.I., Hematibahar, M., Kharun, M. and Shooshpasha, I., "Prediction of the mechanical properties of basalt fiber reinforced high-performance concrete using machine learning techniques", *Materials*, Vol. 15, No. 20, (2022), 7165. doi. https://doi.org/10.3390/ma15207165

37. ASTM, A., "C33/c33m-18 standard specification for concrete aggregates", ASTM International: West Conshohocken, PA, USA, (2018).

38. Standard, A., "C127-15 (2015)"standard test method for relative density (specific gravity) and absorption of coarse aggregate."", Annual Book of ASTM Standards, Vol. 9, No. 49.

39. ASTM, A., *C128-15, standard test method for relative density (specific gravity) and absorption of fine aggregate, astm international, west conshohocken, pa, 2015*. 2015.

40. ASTM, *Astm c136/c136m-19, standard test method for sieve analysis of fine and coarse aggregates*. 2019, ASTM International West Conshohocken, PA.

41. ASTM, D., "2419-14. Standard test method for sand equivalent value of soils and fine aggregate", ASTM International: West Conshohocken, PA, USA, (2017).

42. Moradikhou, A.B., Hosseini, M.H., Mousavi Kashi, A., Emami, F. and Esparham, A., "Experimental study of the effect of 2-element hybrid copolymer fibers and nano-silica particles on compressive, tensile and flexural strengths of metakaolin-based geopolymer concrete", *Journal of Concrete Structures and Materials*, Vol. 4, No. 2, (2019), 100-113. https://doi.org/10.30478/jcsm.2019.187332.1123

43. International, A., *Astm c496/c496m-17, standard test method for splitting tensile strength of cylindrical concrete specimens*. 2017, ASTM International West Conshohocken, PA.

44. Riener, C. and Schabert, R., "Linear slices of hyperbolic polynomials and positivity of symmetric polynomial functions", arXiv preprint arXiv:2203.08727, (2022).

45. Fernández-Jiménez, A. and Palomo, A., "Characterisation of fly ashes. Potential reactivity as alkaline cements☆", *Fuel*, Vol. 82, No. 18, (2003), 2259-2265. doi. https://doi.org/10.1016/S0016-2361(03)00194-7

46. Van Jaarsveld, J., Van Deventer, J. and Lukey, G., "The characterisation of source materials in fly ash-based geopolymers", *Materials Letters*, Vol. 57, No. 7, (2003), 1272-1280. https://doi.org/10.1016/S0167-577X(02)00971-0

47. Xu, H. and Van Deventer, J.S., "Geopolymerisation of multiple minerals", *Minerals Engineering*, Vol. 15, No. 12, (2002), 1131-1139. https://doi.org/10.1016/S0892-6875(02)00255-8

48. De La Rilem, R., "Cpc-18 measurement of hardened concrete carbonation depth", (1988).

49. Waqas, R.M., Butt, F., Danish, A., Alqurashi, M., Mosaberpanah, M.A., Masood, B. and Hussein, E.E., "Influence of bentonite on mechanical and durability properties of high-calcium fly ash geopolymer concrete with natural and recycled aggregates", *Materials*, Vol. 14, No. 24, (2021), 7790. https://doi.org/10.3390/ma14247790

50. Jithendra, C. and Elavenil, S., "Parametric effects on slump and compressive strength properties of geopolymer concrete using taguchi method", *International Journal of Engineering, Transactions C: Aspects*, Vol. 34, No. 3, (2021), 629-635. doi: 10.5829/ije.2021.34.03c.06.

51. Zhuguo, L. and Sha, L., "Carbonation resistance of fly ash and blast furnace slag based geopolymer concrete", *Construction and Building Materials*, Vol. 163, (2018), 668-680. https://doi.org/10.1016/j.conbuildmat.2017.12.127
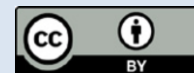
Persian Abstract

چکیده

امروزه بتن پرمصرف ترین مصالح ساختمانی است .تولید سیمان باعث انتشار حدود ۷ درصد گاز دی اکسید کربن در جوو افزایش گازهای گلخانه ای میباشد بنابراین استفاده از جایگزینی برای سیمان پرتلند ضروری به نظر می رسد. در سال های اخیر ژئوپلیمرها (پلیمرهای معدنی)، به عنوان یک عنصر سیمانی جدید مطرح شده است. متاکائولین، بنتونیت، زئولیت، سرباره کوره بلند آهن و خاکستر بادی (بقایای نیروگاه های حرارتی) را می توان به عنوان منابع آلومینوسیلیکات نام برد. در زمینه ساخت بتن ژئوپلیمری، مقالات کمی در مورد ترکیب و اثر جایگزینی منابع آلومینوسیلیکات کار شده است. در این مطالعه آزمایشگاهی، تأثیر جایگزینی منابع آلومینوسیلیکات: سرباره، خاکستر بادی کلاس F و بنتونیت با نسبت‌های ۱۰، ۱۵، ۲۰، ۲۵، ۳۰، ۳۵، ۴۰ و ۴۵ درصد با متاکائولین بر خواص مکانیکی و دوامی(کربناتسیون)بتن ژئو پلیمری بر پایه متاکائولین مورد بررسی قرار گرفت. پس از ساختنمونه ها، آزمایش های فشاری، خمشی ، کششی و کربناتاسیون بر روی نمونه های بتن ژئوپلیمری انجام شد تا مقاومت بهینه و عمق کربناسیون نمونه ها به دست آید. همچنین برای تعیین اعتبار آزمون ها، تحلیل تخمین یادگیری ماشین بر روی نمونه ها انجام شد. در این بخش به دلیل دقت بالا، رگرسیون چندلیلی انتخاب شده است. یافته ها نشان داد که بنتونیت منجر به کاهش استحکام می شود در حالی که خاکستر بادی و سرباره منجر به افزایش استحکام می شود. مقادیر R2 پیش‌بینی بیش از ۹۳ درصد برای نمونه‌های فشاری، بیش از ۸۰ درصد برای نمونه‌های کششی، و بیش از ۷۵ درصد برای نمونه‌های خمشی با ماتریس همبستگی مطابقت دارند. علاوه بر این، نتایج آزمایشات نشان داد که نمونه بتن ژئوپلیمری MF ۳۵(متاکائولین جایگزین شده با خاکستر بادی (۳۵٪)) نسبت به سایر نمونه‌ها ، عمق نفوذ کمتر(کربناته شدن) و خواص مکانیکی بالاتری داشت.

AIMS AND SCOPE

The objective of the International Journal of Engineering is to provide a forum for communication of information among the world's scientific and technological community and Iranian scientists and engineers. This journal intends to be of interest and utility to researchers and practitioners in the academic, industrial and governmental sectors. All original research contributions of significant value focused on basics, applications and aspects areas of engineering discipline are welcome.

This journal is published in three quarterly transactions: Transactions A (Basics) deal with the engineering fundamentals, Transactions B (Applications) are concerned with the application of the engineering knowledge in the daily life of the human being and Transactions C (Aspects) - starting from January 2012 - emphasize on the main engineering aspects whose elaboration can yield knowledge and expertise that can equally serve all branches of engineering discipline.

This journal will publish authoritative papers on theoretical and experimental researches and advanced applications embodying the results of extensive field, plant, laboratory or theoretical investigation or new interpretations of existing problems. It may also feature - when appropriate - research notes, technical notes, state-of-the-art survey type papers, short communications, letters to the editor, meeting schedules and conference announcements. The language of publication is English. Each paper should contain an abstract both in English and in Persian. However, for the authors who are not familiar with Persian, the publisher will prepare the latter. The abstracts should not exceed 250 words.

All manuscripts will be peer-reviewed by qualified reviewers. The material should be presented clearly and concisely:

- *Full papers* must be based on completed original works of significant novelty. The papers are not strictly limited in length. However, lengthy contributions may be delayed due to limited space. It is advised to keep papers limited to 7500 words.
- *Research* notes are considered as short items that include theoretical or experimental results of immediate current interest.
- *Technical notes* are also considered as short items of enough technical acceptability with more rapid publication appeal. The length of a research or technical note is recommended not to exceed 2500 words or 4 journal pages (including figures and tables).

Review papers are only considered from highly qualified well-known authors generally assigned by the editorial board or editor in chief. Short communications and letters to the editor should contain a text of about 1000 words and whatever figures and tables that may be required to support the text. They include discussion of full papers and short items and should contribute to the original article by providing confirmation or additional interpretation. Discussion of papers will be referred to author(s) for reply and will concurrently be published with reply of author(s).

INSTRUCTIONS FOR AUTHORS

Submission of a manuscript represents that it has neither been published nor submitted for publication elsewhere and is result of research carried out by author(s). Presentation in a conference and appearance in a symposium proceeding is not considered prior publication.

Authors are required to include a list describing all the symbols and abbreviations in the paper. Use of the international system of measurement units is mandatory.

- On-line submission of manuscripts results in faster publication process and is recommended. Instructions are given in the IJE web sites: www.ije.ir-www.ijeir.info
- Hardcopy submissions must include MS Word and jpg files.
- Manuscripts should be typewritten on one side of A4 paper, double-spaced, with adequate margins.
- References should be numbered in brackets and appear in sequence through the text. List of references should be given at the end of the paper.
- Figure captions are to be indicated under the illustrations. They should sufficiently explain the figures.
- Illustrations should appear in their appropriate places in the text.
- Tables and diagrams should be submitted in a form suitable for reproduction.
- Photographs should be of high quality saved as jpg files.
- Tables, Illustrations, Figures and Diagrams will be normally printed in single column width (8cm). Exceptionally large ones may be printed across two columns (17cm).

PAGE CHARGES AND REPRINTS

The papers are strictly limited in length, maximum 8 journal pages (including figures and tables). For the additional to 8 journal pages, there will be page charges. It is advised to keep papers limited to 3500 words.

Page Charges for Papers More Than 8 Pages (Including Abstract)	
For International Author ***	**$55 / per page**
For Local Author	**100,000 Toman / per page**

AUTHOR CHECKLIST

- Author(s), bio-data including affiliation(s) and mail and e-mail addresses).
- Manuscript including abstracts, key words, illustrations, tables, figures with figure captions and list of references.
- MS Word files of the paper.